PHOTOREDOX CATALYSIS MEDIATED BY TRANSITION METAL COMPLEXES. TOWARDS CHALLENGING ORGANIC REDUCTIONS

David Pascual Gascón

UNIVERSITAT ROVIRA i VIRGILI

Photoredox catalysis mediated by transition metal complexes. Towards challenging organic reductions.

DAVID PASCUAL GASCÓN

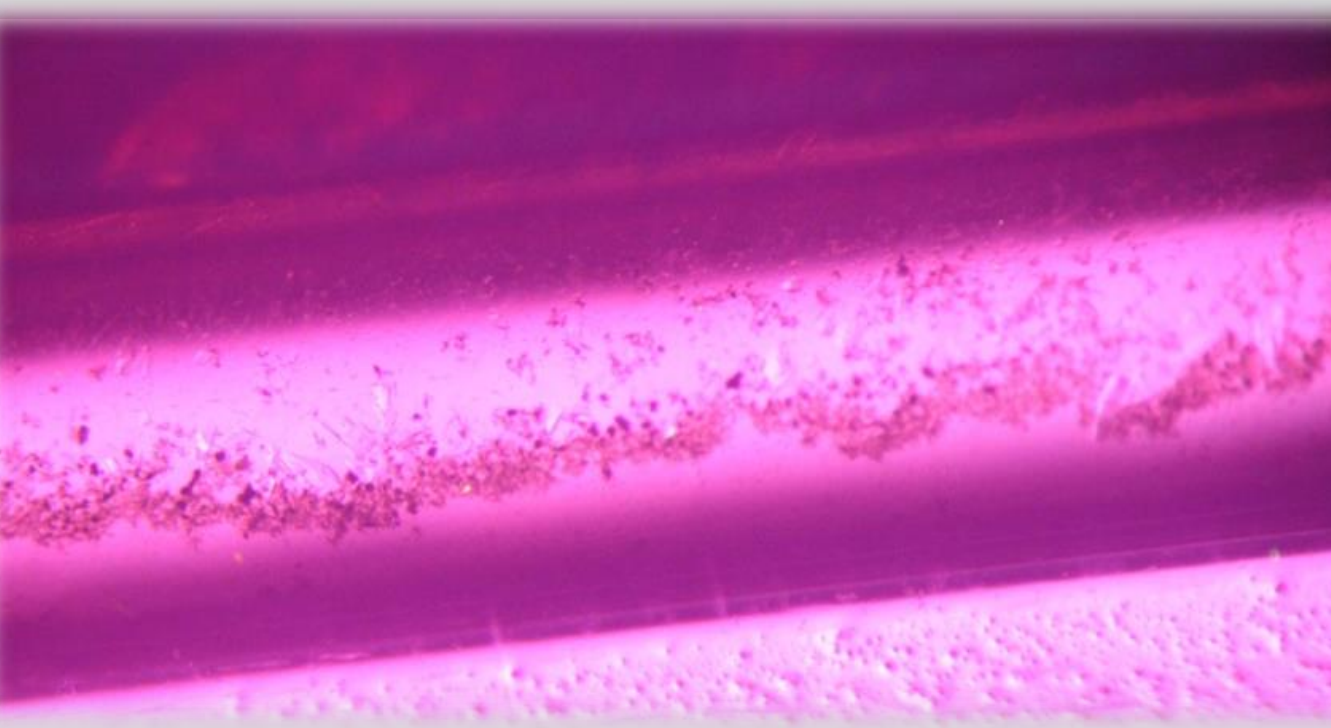

DOCTORAL THESIS
2022

UNIVERSITAT ROVIRA I VIRGILI
PHOTOREDOX CATALYSIS MEDIATED BY TRANSITION METAL COMPLEXES.
TOWARDS CHALLENGING ORGANIC REDUCTIONS
David Pascual Gascón

UNIVERSITAT ROVIRA I VIRGILI
PHOTOREDOX CATALYSIS MEDIATED BY TRANSITION METAL COMPLEXES.
TOWARDS CHALLENGING ORGANIC REDUCTIONS
David Pascual Gascón

UNIVERSITAT ROVIRA I VIRGILI
PHOTOREDOX CATALYSIS MEDIATED BY TRANSITION METAL COMPLEXES.
TOWARDS CHALLENGING ORGANIC REDUCTIONS
David Pascual Gascón

PhD Thesis

Photoredox catalysis mediated by transition metal complexes. Towards challenging organic reductions.

David Pascual Gascón

Supervised by Prof. Dr. Julio Lloret-Fillol

Tarragona

October 2022

UNIVERSITAT ROVIRA I VIRGILI
PHOTOREDOX CATALYSIS MEDIATED BY TRANSITION METAL COMPLEXES.
TOWARDS CHALLENGING ORGANIC REDUCTIONS
David Pascual Gascón

Prof. Dr. Julio Lloret-Fillol, Group Leader at the Institute of Chemical Research of Catalonia (ICIQ) and Research Professor at the Catalan Institution for Research and Advanced Studies (ICREA),

I STATE that the present Doctoral Thesis, entitled "**Photoredox catalysis mediated by transition metal complexes. Towards challenging organic reductions.**" presented by David Pascual Gascón to receive the degree of Doctor with International Mention, has been carried out under my supervision at the Institute of Chemical Research of Catalonia (ICIQ).

Tarragona, 22nd November 2022

Doctoral Thesis Supervisor
Prof. Dr. Julio Lloret-Fillol

UNIVERSITAT ROVIRA I VIRGILI
PHOTOREDOX CATALYSIS MEDIATED BY TRANSITION METAL COMPLEXES.
TOWARDS CHALLENGING ORGANIC REDUCTIONS
David Pascual Gascón

A todos los míos, soy todo vuestro.

'*No queda otra, hay que echarle huevos*', '*No reblar*'

Mi tío, **J. M. Artal**

'*Si tiene solución, ya está. Y si no tiene solución, ya está*'

Mi hermanito, **D. Pérez**

'*Lo bueno de lo malo es que se aprende. Lo malo de lo bueno es que se acaba'*

Anónimo

UNIVERSITAT ROVIRA I VIRGILI
PHOTOREDOX CATALYSIS MEDIATED BY TRANSITION METAL COMPLEXES.
TOWARDS CHALLENGING ORGANIC REDUCTIONS
David Pascual Gascón

Agradecimientos

En primer lugar, quiero agradecer a mi supervisor Julio Lloret-Fillol por acogerme y haber apostado por mí, no cualquiera tiene esta oportunidad. Creo que he crecido un poquito y la experiencia adquirida es un privilegio que va más allá de la ciencia. Es por ti que he vivido estos 4 años, y ha sido un camino muy largo del que me quedo con cosas muy buenas. Gracias por lo anterior y por el trocito de camino que nos queda.

Pero el árbol no sería árbol sin sus raíces. Y yo debo ser como un bonsái con las raíces de secuoya….

Mi familia estuvo ahí desde semilla, me regaron con valores y palabras sencillas pero nutritivas. El primero en ir a la universidad, esta es mi forma de devolvéroslo papa y mamá. 27 años después es una suerte que los cuatro seguís aquí para ver esto, disfrutadlo porque es vuestro. Hubo muchos más seres queridos alrededor, no me olvido y con los años os devuelvo vuestro amor.

Desde el 98, los primeros de mi tribu aún son mi tribu y se ha sumado alguno más por el camino. Zaragoza siempre estuvo y estará en mi corazón, especial dedicación, por orden de duración: a persona-barba y a maestro-chancla, a Calimbo, Ferrick B y D. Pérez, a un trozo de pan, una nutria y una cabra. *Solo los locos entienden de lo que hablan*. A mis zagales del local, aunque ya no haya local, amistades de la uni y letujanas, sé que os volveré a encontrar. Tenemos mucho por contar… Por fortuna si los lazos son fuertes no son fáciles de cortar.

Sin mis anteriores tutores no habría hecho tesis. Desde el laboratorio de Procesos Estereoselectivos donde un día el éter llegó al punto flash (algún día tenía que contártelo, Jose Antonio), al 408 donde me pasaron 100 historias más... Gracias a Nuria por confiar en mí, mis tan buenos últimos resultados son también gracias a ti; pues en esta tesis he de confesar que no brilló la mente, brilló la

frente: esfuerzo y sudor solamente. Por haberme valorado e inspirado determinación. No hay mejor catalizador que la motivación.

No solo a Julio sino también al resto de la orquesta, thanks to all previous and following labmates who helped creating a good working environment. That's very professional and very human, you've learnt your ABC. From all of you I have learnt. Sin olvidarme de los otros postdocs (Carla, Sergio, Fede, Alberto, Vlad, Katia, Felix, Noufal, Suvendu), PhDs (Miguel, Klaudia, Suyun, Ahmed, Jing, Liu, Mattia), no puedo no hacer mención especial a los estudiantes con los que más he conectado y compartido estos 4 años: Sergi, Jordi, Geyla y Luis. No cabe aquí lo que me alegro mucho de haber recorrido estos años junto a vosotros, gracias por todo, que no ha sido poco. Also, my two students Ajdin and Marina, you did a great work to be proud of. A todos os deseo lo mejor.

Thanks to James for hosting my great short stay, and all my people in UK, perhaps we meet again someday. Fabio se merece también mi agradecimiento por hacerme espabilar a tiempo, su empuje desatascó el proyecto. Y hay bastante más gente del instituto en general a quienes doy gracias por el apoyo en estos años y el tramo final. ICIQ no sería ICIQ sin los talleres de Xavi, León y Aleix, bien es sabido, como tampoco sin los miembros de los distintos servicios de investigación o sin recepción. Muchísimas gracias también a las personas que me han dejado sus comentarios y revisiones en estos dos meses de escritura, ha sido ayuda inmensa y significa mucho para mi. Indiscutible la especial dedicación a los amigos que me llevo de estos 4 años, bendita vuestra paciencia, sois la mejor recompensa… en concreto gracias a Andrea, Ricardo, Nico, Cris, Stef y Clau, incluso Paulita, ¡qué importantes habéis sido para que esto llegase al final, y qué afortunado me siento!

En conjunto, si yo he hecho esto, lo puede hacer cualquiera que ponga la actitud, trust the process; ánimo para los que aun os queda, contad con mi apoyo. Empieza una nueva etapa, David está de vuelta.

Financial Support

The present doctoral thesis has been made possible thanks to funding received from the Institute of Chemical Research of Catalonia (ICIQ) CERCA Programme (Generalitat de Catalunya) for financial support and MINECO (CTQ2016-80038-R, Severo Ochoa Excellence Accreditation 2014– 2018; SEV-2013-0319).

UNIVERSITAT ROVIRA I VIRGILI
PHOTOREDOX CATALYSIS MEDIATED BY TRANSITION METAL COMPLEXES.
TOWARDS CHALLENGING ORGANIC REDUCTIONS
David Pascual Gascón

Curriculum Vitae

David Pascual Gascón was born on October 9th, **1995** in Zaragoza (Spain). He obtained his Bachelor's degree in Chemistry in **2017** from the University of Zaragoza (Spain) defending his final project under the supervision of Prof. J. A. Gálvez. Later on, he started the university Master's degree in Organic Chemistry at the Autonomous University of Madrid (UAM). For the Master thesis, he was in the group of Prof. J. C. Carretero for six months, under the supervision of Dr. N. Rodriguez and Dr. I. Alonso in the project named 'Theoretical and experimental mechanistic study of direct dialkenylation of *N*-benzylpicolinamide derivatives using 1,3-enynes'. In October 2018 he joined to Prof. Julio Lloret-Fillol group at the Institute of Chemical Research of Catalonia (ICIQ). Last year, he was awarded with Severo Ochoa International Mobility fellowship to spend three months in Prof. James Durrant group in Imperial College London (London, United Kingdom). The research studies performed during his PhD are described in this thesis, and have been communicated at different conferences, such as the III ICIQ PhD day (**2019**), ISOC-MMM2019 (**2019**), the EUGSC IV in Tarragona (**2019**), the 'Spectroscopic Methodologies for Elucidation of Reaction Mechanisms - ICIQ seminar' (**2021**) and XXXVIII Bienal RSEQ in Granada, Spain (**2022**).

UNIVERSITAT ROVIRA I VIRGILI
PHOTOREDOX CATALYSIS MEDIATED BY TRANSITION METAL COMPLEXES.
TOWARDS CHALLENGING ORGANIC REDUCTIONS
David Pascual Gascón

List of Publications

Carla Casadevall, **David Pascual**, Jordi Aragón, Arnau Call, Alicia Casitas, Irene Casademont-Reig and Julio Lloret-Fillol. 'Light-Driven Reduction of Aromatic Olefins in Aqueous Media Catalysed by Aminopyridine Cobalt Complexes', Chem. Sci., 2022, (DOI:10.1039/d1sc06608k)

Jordi Aragón, Suyun Sun, **David Pascual**, Sebastian Jaworski and Julio Lloret-Fillol. 'Photoredox activation of inert alkyl chlorides for the reductive cross-coupling with aromatic alkenes', Angew. Chem. Int. Ed. 2022, e2024365, (DOI: 10.1002/anie.202114365).

UNIVERSITAT ROVIRA I VIRGILI
PHOTOREDOX CATALYSIS MEDIATED BY TRANSITION METAL COMPLEXES.
TOWARDS CHALLENGING ORGANIC REDUCTIONS
David Pascual Gascón

Preface

The work presented in this dissertation has been performed at the Institute of Chemical Research of Catalonia (ICIQ), during the period of October 2018 until November 2022 under the supervision of Professor Julio Lloret-Fillol. This thesis is divided into six sections: a general introduction containing the aims and outline of the thesis, the objectives of the thesis, three research chapters, and a chapter in which the overall conclusions of the work are presented. Each of the research chapters includes a brief introduction on the topic, followed by the collected results and their discussion, the main conclusions, and finally a detailed experimental section. References and their numbering are independently organized in each chapter.

UNIVERSITAT ROVIRA I VIRGILI
PHOTOREDOX CATALYSIS MEDIATED BY TRANSITION METAL COMPLEXES.
TOWARDS CHALLENGING ORGANIC REDUCTIONS
David Pascual Gascón

Table of Contents

CHAPTER 5. Metal to Ligand Concern Transfer: $[Ir(bpy)(ppy)_2]^+$

ABSTRACT

Photoredox catalysis exploits visible light as energy source to carry out chemical reactions that involve electron transfer processes. On the one hand, implementing water as hydrogen equivalents for reductive organic transformations is essential from a sustainable perspective. In that direction, given that transition metal complexes are good candidates for the transference of hydrogen equivalents, metallaphotoredox catalysis is a promising platform for reducing functionalities such as double bonds.

In the present thesis, a dual photocatalytic system previously reported in our group for reducing aryl ketones using visible light as the driving force and H_2O/amine as the hydride source has been used to reduce aryl olefins. The catalytic system involved a robust and well-defined cobalt complex with an aminopyridine ligand, and a copper photoredox catalyst. Furthermore, based on our mechanistic understanding, evaluation of other photosensitizers and conditions reached a dual Co/Ir system capable of selectively reducing styrene *versus* acetophenone and *vice versa*.

In parallel, we explored the asymmetric reduction of aromatic ketones in aqueous media by utilizing chiral-at-ligand cobalt complexes. Using synthetic modifications in the chiral ligand, we found that the *ortho*-position of the pyridine ring must remain non-substituted, while the *meta*-substitution could positively affect chirality transfer.

On the other hand, in the main project of the thesis, we have revisited the reductive quenching mechanism of $[Ir(bpy)(ppy)_2]PF_6$ as a model iridium photoredox catalyst. After the isolation and well-defined characterization of the reduced intermediate $[Ir(bpy)(ppy)_2]^0$, we found that it can catalyze more reductive transformations under irradiation. Furthermore, our theoretical and experimental mechanistic studies support that the reactivity comes from the reduced bipyridine ligand.

This thesis paves the way for new selective organic reductions using visible light as the driving force and H_2O as a clean source of hydrides, as well as sheds light

on the current mechanistic understanding of multiphoton photoredox cycles, disclosing the crucial role of bipyridine derivatives.

RESUMEN

La catálisis fotorredox utiliza la luz visible como fuente de energía para llevar a cabo reacciones químicas que implican procesos de transferencia de electrones. Por un lado, la implementación del agua como fuente de equivalentes de hidrógeno para llevar a cabo reducciones orgánicas es fundamental desde una perspectiva sostenible. Dado que los complejos de metales de transición son buenos candidatos para la transferencia de equivalentes de hidrógeno, su combinación con catalizadores fotorredox es una estrategia prometedora para la reducción de funcionalidades como los dobles enlaces.

En la presente tesis, un sistema fotocatalítico dual previamente reportado en nuestro grupo para la reducción de cetonas aromáticas aromáticas usando luz visible como fuerza motriz y H_2O/amina como fuente de hidruro, se ha utilizado para la reducción de olefinas. El sistema catalítico se compone de un complejo de cobalto robusto y bien definido con un ligando de aminopiridina y un catalizador fotorredox de cobre. De acuerdo a nuestra comprensión del mecanismo, la evaluación de otros fotosensibilizadores y condiciones llevó a un sistema dual (Co/Ir) capaz de reducir selectivamente estireno frente a acetofenona y *viceversa*.

Paralelamente, exploramos la reducción asimétrica de cetonas aromáticas en medios acuosos mediante la utilización de complejos de cobalto quirales en el ligando. Mediante modificaciones sintéticas en el ligando quiral, encontramos que la posición *orto* del anillo de piridina debe permanecer sin sustituir, mientras que la posición *meta* podría tener un efecto positivo en la transferencia de quiralidad.

Por otro lado, en el proyecto principal de la tesis, hemos revisado el mecanismo de quencheo reductivo de $[Ir(bpy)(ppy)_2]PF_6$ como modelo de catalizador fotorredox de iridio. Después del aislamiento y la caracterización bien definida del intermedio reducido $[Ir(bpy)(ppy)_2]^0$, encontramos que puede catalizar transformaciones más reductoras al ser irradiado con luz visible. Nuestros estudios mecanísticos teóricos y experimentales respaldan claramente que la reactividad proviene del ligando de bipiridina reducido.

Esta tesis allana el camino para nuevas reducciones orgánicas selectivas utilizando luz visible como fuerza motriz y H_2O como fuente limpia de hidruros, y arroja luz sobre la comprensión mecanística actual de los ciclos fotorredox multifotónicos, revelando el papel crucial de los derivados de bipiridina.

List of abbreviations

In this doctoral thesis, the abbreviations and acronyms most commonly used in organic chemistry are based on the recommendations of the ACS "Guidelines for authors". Additional abbreviations are listed below:

4CzIPN	1,2,3,5-Tetrakis(carbazol-9-yl)-4,6-dicyanobenzene
AcOEt	Ethyl Acetate
anh	anhydrous
AP	Artificial Photosynthesis
APSET	Assembly promoted single electron transfer
aq	Aqueous
Ar	Aromatic group
ATH	Asymmetric transfer hydrogenation
atm	atmosphere
BET	Back Electron Transfer
BNAH	1-benzyl-1,4-dihydropyridine-3-carboxamide
BP	biphenyl
bpy	2,2'-bipyridine
cat	catalyst
C60	Fullerene
CD	Cyclodextrine
COD	Cyclooctadiene
conv	Conversion
Cp	Cyclopentadiene
Cp*	1,2,3,4,5-Pentamethylcyclopentadiene
CPE	Controlled potential electrolysis
CPME	Cyclopentyl methyl ether
CT	Charge transfer
CV	Cyclic voltammetry
BARF	Tetrakis(3,5-bis(trifluoromethyl)phenyl)borate
DCA	Dicyanoanthracene
DCM	Dichloromethane
DCE	Dichloroethane
Dcob	2,2′-Bipyridine-4,4′-dicarboxylic acid
DFT	Density functional theory
DIPEA	N,N-Diisopropylethylamine
DMA	*N*,*N*-Dimethylacetamide

DMAP	4-dimethylaminopyridine
DMF	*N*,*N*-Dimethylformamide
DMSO	Dimethylsulfoxide
DMPU	*N*,*N*′-Dimethylpropyleneurea
DPZ	Dicyanopyrazine
EA	Electron Acceptor
ED	Electron Donor
EDA	Electron donor acceptor complex
EDG	Electron donating group
EDTA	Ethylenediaminetetraacetic acid
ee	Enantiomeric excess
en	Ethylenediamine
EnT	Energy transfer
Eox	Oxidation potential
Eox*	Excited state oxidation potential
equiv	equivalents
Ered	Reduction potential
Ered*	Excited state reduction potential
Et	Ethyl group
ET	Electron transfer
Et_3N	Triethylamine
EtOH	Ethanol
EPR	Electron Paramagnetic Resonance
EWG	Electron withdrawing group
EXAFS	Extended X-ray absorption fine structure
FAD	Flavin adenine dinucleotide
FID	Flame ionization detector
FMN	riboflavin-5′-phosphate
GC	Gas chromatography
GC-MS	Gas chromatography-mass spectrometry
HAT	Hydrogen atom transfer
HOMO	Highest occupied molecular orbital
HPLC	High-performance liquid chromatography
HRMS	High-resolution mass spectrometry
IC	Internal Conversion
iPr	Isopropyl group
iPrOH	isopropanol
IR	Infrared
ISC	Intersystem crossing

kq	Quenching constant
KRA	Ketyl radical anion
LC	Ligand centered
LED	Light-emitting diode
LKADH	Alcohol dehydrogenase from Lactobacillus kefir
LLCT	Ligand to ligand charge transfer
LMCT	Ligand to metal charge transfer
LSV	Linear square voltammetry
LUMO	Lowest occupied molecular orbital
MA	Mandelic acid
MC	Metal centered
MCP	(1*S*,2*S*)-*N*1,*N*2-dimethyl-N1,N2-bis(pyridin-2-ylmethyl)cyclohexane-1,2-diamine
Me	Methyl group
MeOH	Methanol
MLCT	Metal to ligand charge transfer
MO	Molecular orbital
MPA	3-mercaptopropionic acid
MV	Methyl viologen
NAD	Nicotinamide adenine dinucleotide
NADP	Nicotinamide adenine dinucleotide phosphate
NMe2	Dimethylamino group
NMR	Nuclear Magnetic Resonance
NpMI	2-(2,6-diisopropylphenyl)-1H-benzo[de]isoquinoline-1,3(2H)-dione
NT	Nanotubes
NT-COOH	Nanotubes functionalized with carboxylic groups
OTf	Triflate
ovn	Overnight
ox	oxalate
PC	Photoredox Catalyst
PC*	Excited photoredox catalyst
PDP	(2*S*,2'*S*)-1,1'-bis(pyridin-2-ylmethyl)-2,2'-bipyrrolidine)
phen	Phenantroline
ppm	Parts per million
ppy	2-phenylpyridine
Q	Quencher
QD	Quantum dots
rGO	Reduced graphene oxide

RVC	Reticular vitreous carbon
rt	Room temperature
SCE	Saturated calomel electrode
SDS	Sodium dodecyl sulfate
SET	Single electron transfer
S_N1	Unimolecular nucleophilic substitution
S_N2	Bimolecular nucleophilic substitution
SPEC	Spectroelectrochemical
SPS	Solvent Purification System
tacn	1,4,7-Triazacyclononane
TAEA	Tris(2-aminoethyl)amine
TAS	Transient absorption spectroscopy
TBS	tert-butyldimethylsilyl
TBA_2ox	Bis(tetrabutylammonium) oxalate
TBA	Tetrabutylammonium
tBu	Tert-butyl group
TEOA	triethanolamine
THF	Tetrahydrofuran
TD-DFT	Time dependent density functional theory
TLC	Thin layer chromatography
TMB	Trimethoxybenzene
TMS	trimethylsilyl
TON	Turnover Number
TS	Transition state
TsOYE	old yellow enzyme homologue from Thermus scotoductus SA-01
Ur	Urate
UV	Ultraviolet
vis	visible
XANES	X-ray absorption near edge structure
XAT	Halogen atom transfer
XR	X-ray

Structures and abbreviations of studied catalysts

Pentadentate catalysts

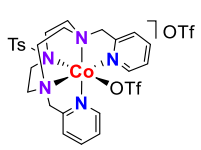

$\mathbf{1}_{Co}$

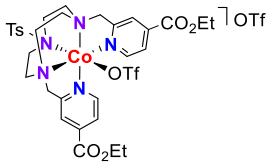

$^{CO2Et}\mathbf{1}_{Co}$

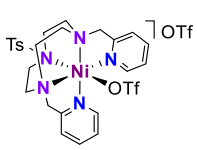

$\mathbf{1}_{Co}$

Tetradentate cobalt catalysts

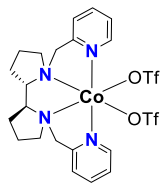

$\mathbf{2}_{Co}$ (*S*,*S*)

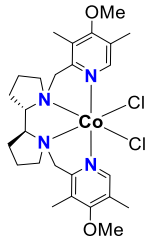

J1 (*S*,*S*)

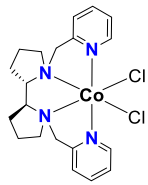

J2 (*S*,*S*)

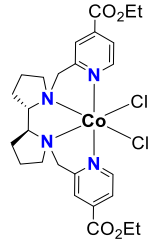

J3 (*S*,*S*)

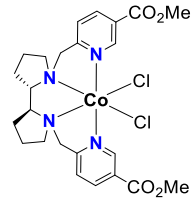

K1 (*S*,*S*)

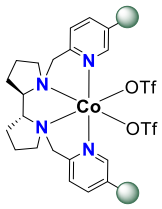

K2 (*R*,*R*)

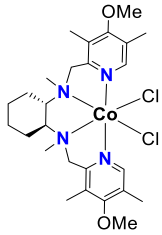

J4 (*S*,*S*)

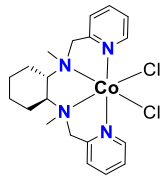

J5 (*S*,*S*)

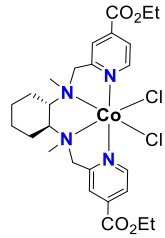

J6 (*S*,*S*)

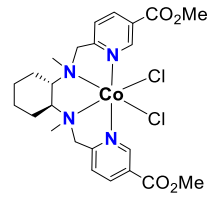

K3 (*S*,*S*)

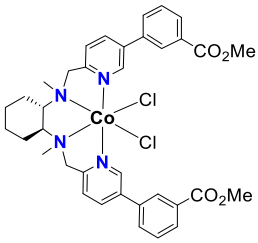

K4 (*S*,*S*)

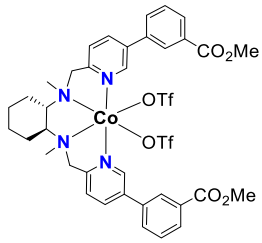

K5 (*S*,*S*)

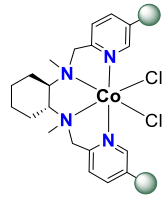

K6 (*R*,*R*)

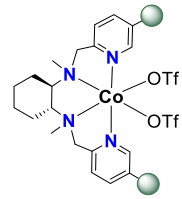

K7 (*R*,*R*)

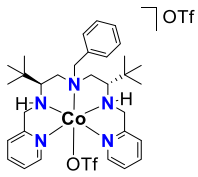

S1 (*S*,*S*)

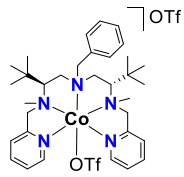

S2 (*S*,*S*)

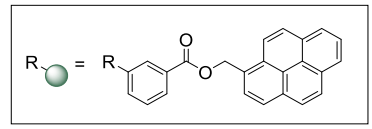

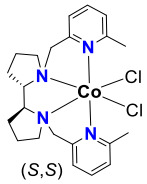

$^{o\text{-}Me}$PDPCo$_{Cl}$

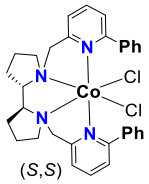

$^{o\text{-}Ph}$PDPCo$_{Cl}$

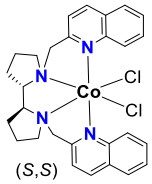

^{quin}PDPCo$_{Cl}$

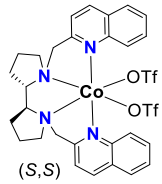

^{quin}PDPCo$_{OTf}$

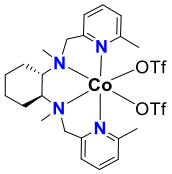

$^{o\text{-}Me}$MCPCo$_{OTf}$

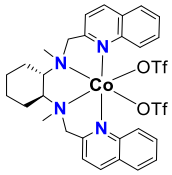

^{quin}MCPCo$_{OTf}$

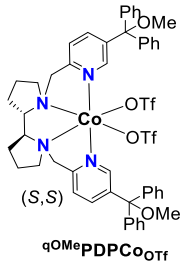

^{qOMe}PDPCo$_{OTf}$

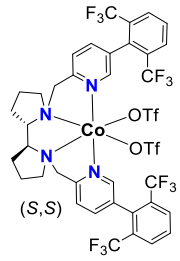

$^{Ar\text{-}CF3}$PDPCo$_{OTf}$

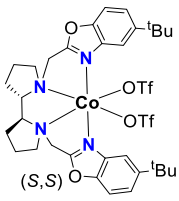

^{oxaz}Co$_{OTf}$

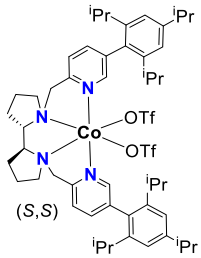

$^{Ar\text{-}Pr}$PDPCo$_{OTf}$

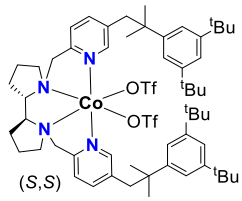

$^{Ar\text{-}tBu}$PDPCo$_{OTf}$

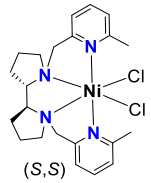

$^{o\text{-}Me}$PDPNi$_{Cl}$

Tetradentate nickel catalysts

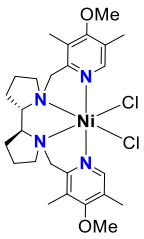

J1-Ni (*S*,*S*)

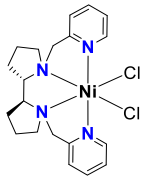

J2-Ni (*S*,*S*)

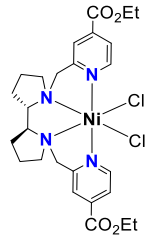

J3-Ni (*S*,*S*)

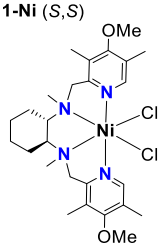

J4-Ni (*S*,*S*)

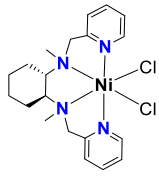

J5-Ni (*S*,*S*)

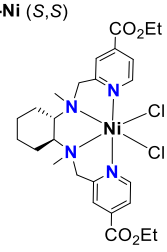

J6-Ni (*S*,*S*)

Copper-based photoredox catalysts

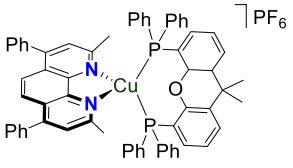

PC_{Cu}

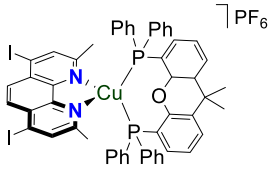

$^{I}PC_{Cu}$

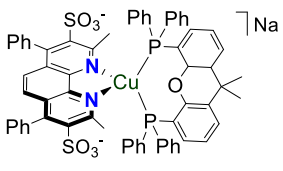

$^{SO3}PC_{Cu}$

Ruthenium and rhenium-based photoredox catalysts

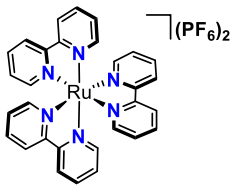

PC_{Ru}

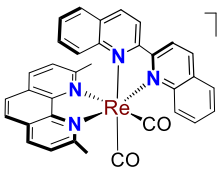

$^{1}PC_{Re}$

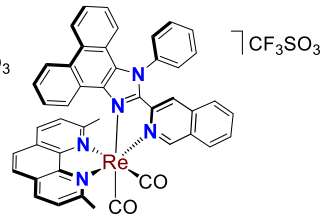

$^{2}PC_{Re}$

Iridium-based photoredox catalysts

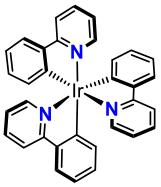

fac-[Ir(ppy)$_3$]

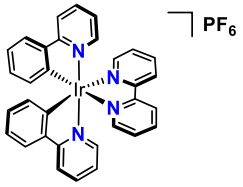

PC_{Ir}

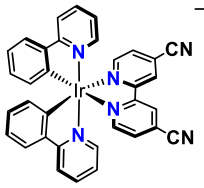

$^{CN}PC_{Ir}$

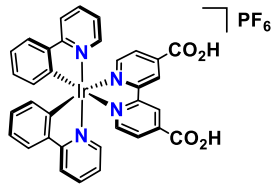

$^{CO2H}PC_{Ir}$

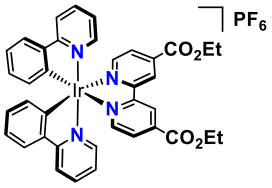

$^{CO2Et}PC_{Ir}$

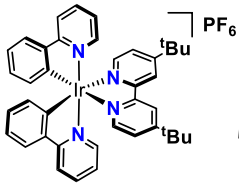

$^{tBu}PC_{Ir}$

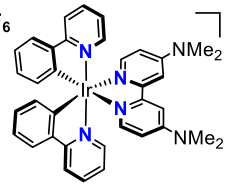

$^{NMe2}PC_{Ir}$

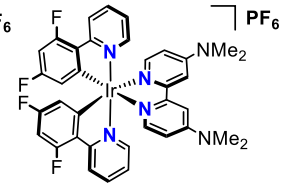

$^{NMe2\text{-}F}PC_{Ir}$

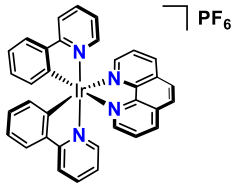

$^{phen}PC_{Ir}$

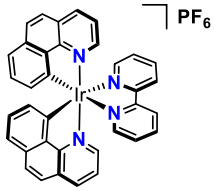

$^{bzq}PC_{Ir}$

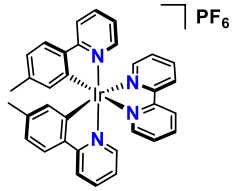

$^{Me}PC_{Ir}$

Disambiguation for iridium intermediates

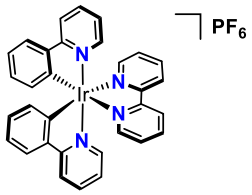

PC_{Ir}
salt

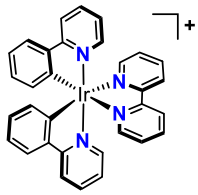

PC_{Ir}^{+}
monocationic

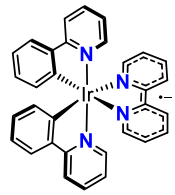

PC_{Ir}^{0}
neutral

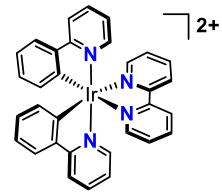

PC_{Ir}^{2+}
dicationic

'And all this science I don't understand, It's just my job five days a week' -

Elton John

Chapter 1

General Introduction

UNIVERSITAT ROVIRA I VIRGILI
PHOTOREDOX CATALYSIS MEDIATED BY TRANSITION METAL COMPLEXES.
TOWARDS CHALLENGING ORGANIC REDUCTIONS
David Pascual Gascón

1.1. What is photoredox catalysis?

1.1.1. Short prelude

Chemists traditionally relied on harsh reagents or high temperatures to enable reactions. Alternatively, light is a clean and relatively inexpensive energy source that can accelerate specific processes at room temperature. Moreover, it can provide pathways to access different products and permit temporal reaction control.[1] The ability of chemical reagents to absorb photons and undergo different transformations has been explored since the end of the eighteenth century,[2] but 'Photocatalysis', the utilisation of light-absorbing compounds to catalyse energetically-demanding reactions under illumination, is not that old.[3, 4] Indeed, it remained unexploited until Fujishima and Honda observed the photocatalytic effect of TiO_2 in electrochemical water splitting that fascinated scientists.[5] By that time, the term 'photoredox catalyst' (PC) was coined to be a type of photocatalyst with the ability to donate or remove one electron to or from organic substrates, generally under UV light irradiation.[6] Then, photoredox catalysis emerged as a promising branch of photocatalysis. Nonetheless, 15 years ago, the field experimented its renaissance with the utilization of visible light for activating a molecular ruthenium catalyst in the contributions of Yoon,[7] MacMillan,[8] and Stephenson.[9] Their work attracted an exponentially growing interest of the scientific community, and photoredox catalysis evolved into an accessible and well-established research area (Figure 1. 1).

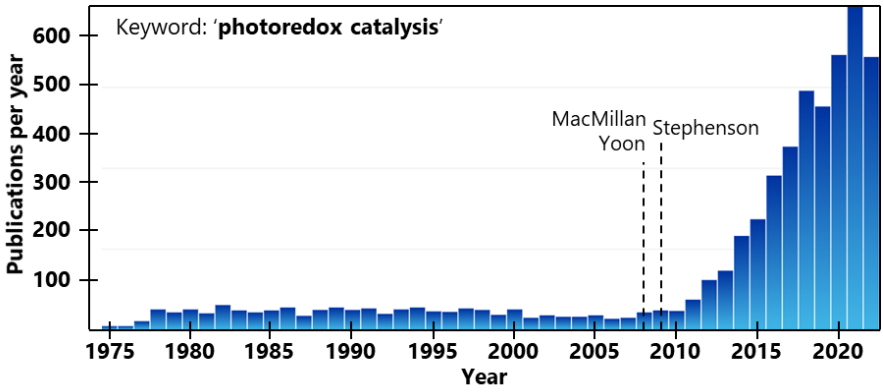

Figure 1.1. Number of publications per year using keyword: "photoredox catalysis" Scifinder search conducted on 10/11/2022.

The vast field of photocatalysis explores light-driven catalytic processes that proceed *via* three main types of reactivity: energy transfer (EnT)[10, 11] atom transfer,[12, 13]

or reductive and oxidative single electron transfer events (SET).[14, 15] In particular, photocatalytic SET reactions define the area of photoredox catalysis (Scheme 1.1c).

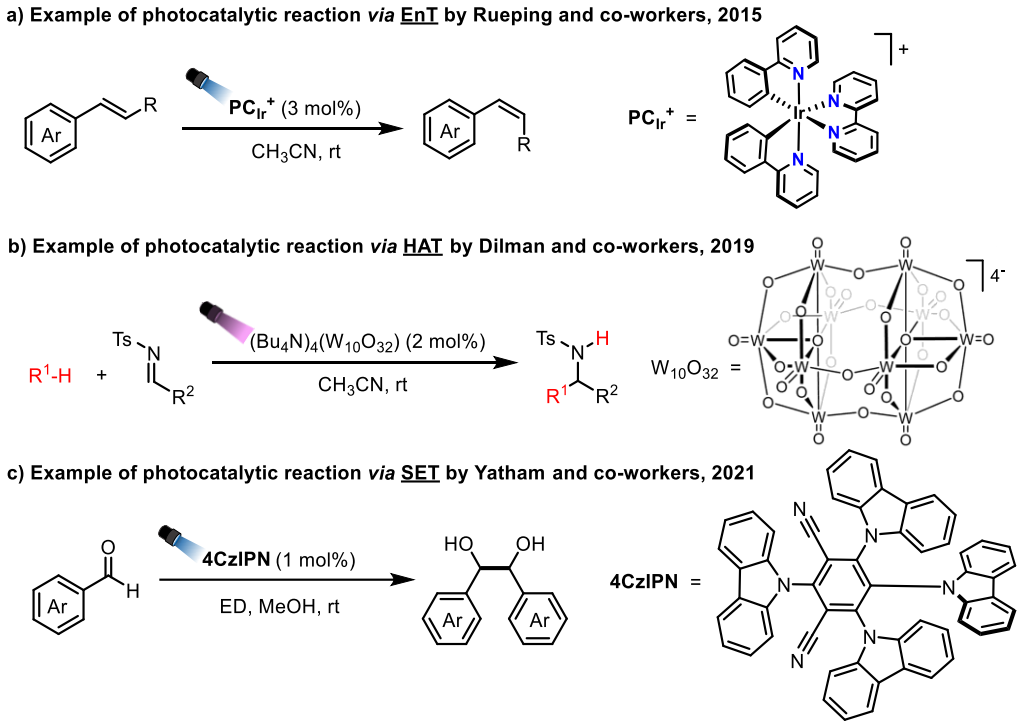

Scheme 1.1. Selected examples of photocatalytic reactions where the excited photocatalyst performs (a) SET = single electron transfer, (b) EnT = energy transfer and (c) HAT = hydrogen atom transfer. ED = Electron donor.

The present thesis focuses on challenging photoredox transformations, specifically using transition-metal-based PCs.[16] But, we first introduce concepts critical to understand photoredox catalysis. The next section contains a walkthrough that starts from the photoactivation of a given complex, followed by its possible deactivation pathways, and ends in its reactivation to engage (photoredox) catalysis.[17]

1.1.2. Photocatalyst activation: absorption of light energy

When being introduced to photocatalysis, some of the initial questions can be 'why does light alter the chemical behaviour of certain molecules?', or 'how does the photocatalyst structure change after irradiation?'. The answer is found in the first event present in any photochemical process: the electronic photoactivation or **excitation** of the photocatalyst.[18, 19] Under appropriate irradiation, the photocatalyst can absorb a photon with enough energy to promote one electron from the lowest (ground) electronic

states to an excited state (higher energy orbital). This **electronic transition** is very fast and has no direct effect on the relative disposition of the atoms of the photocatalyst (Franck-Condon principle). However, it can significantly alter the charge redistribution or bond strength, affecting its chemical behaviour (*vide infra*). A visual way to illustrate the changes in an excited PC is the three-dimensional representation of the different orbitals that the excited electron populates (Figure 1.2), which will be addressed in deeper detail in the following sections.

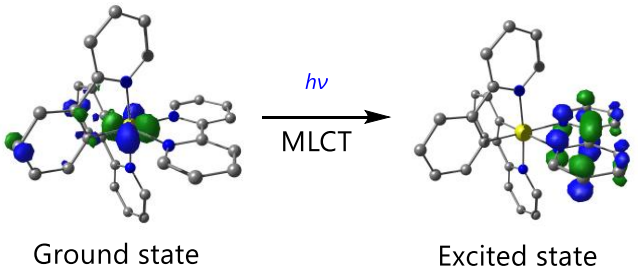

Figure 1.2. Illustration of the charge redistribution between different orbitals as a consequence of electronic excitation of a complex, $[Ir(bpy)(ppy)_2]^+$. Coloured areas indicate the orbitals populated by the excited electron. MLCT = Metal to ligand Charge Transfer. This complex is an example for this introductory section because it will be a relevant PC along the thesis, but it can be taken as a generic model to illustrate charge redistribution.

To draw a more precise picture of electronic transitions in transition metal complexes, it can help to describe the **molecular orbitals (MO)**.

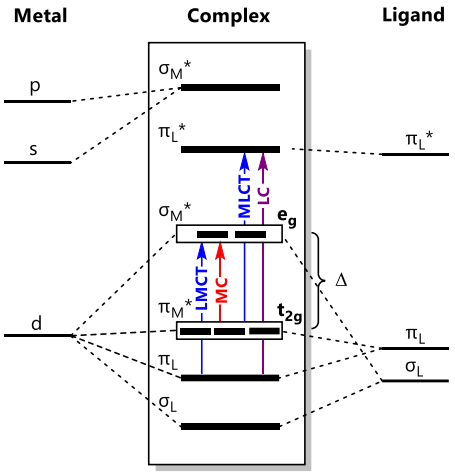

Figure **1. 3** illustrates the MO diagram of a generic octahedral complex.[20, 21] Crystal field theory describes how MO of a coordination complex is derived from the combination of the degenerated atomic d orbitals of the metal ion with the orbitals of

the ligands, producing their destabilization and splitting. The two resulting groups of MOs have different energy depending on their symmetry: t_{2g} (lower energy) or e_g (higher energy).[22] The interaction caused by orbital overlap between metal d- and ligand σ-orbitals is stronger than with ligand π-orbitals. Therefore, the destabilized t_{2g} and e_g correspond with π_M^* (lower energy) and σ_M^* (higher energy) respectively, where the subscript M indicates that the MO is predominantly metal centred rather than ligand centred (subscript L, as the case of σ_L and π_L^*).

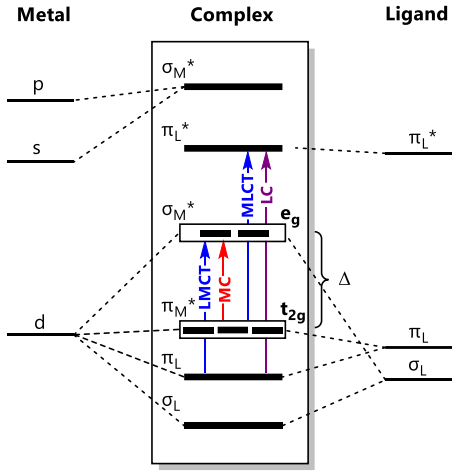

Figure 1. 3. Simplified molecular orbital diagram for a generic transition metal complex with octahedral symmetry. This diagram includes possible sigma-donor, pi-donor, and pi-acceptor orbitals.

The difference in energy between the -occupied and unoccupied- MO of a photocatalyst allows us to estimate if a particular electronic transition requires a photon of lower or higher energy. In particular, the energetic difference between t_{2g} and e_g is called ligand field splitting (Δ), and it is smaller for first-row transition metals than for second- and third-row. Other important factor that affects Δ is the nature of the ligand: those ligands which most favour metal to ligand back bonding also produce most splitting, as deduced from the empirical trend observed in the spectrochemical series ($CO > CN^- > PPh_3 > NO_2^- > SO_3^{2-} >$ phen > bpy > en > NH_3 > py > $CH_3CN > ONO^- > NCS^-$ (S-bonded) > $OH_2 > C_2O_4^{2-} > ONO_2^- > OSO_3^{2-} > OCHO^- > OH^- > OCO_2^{2-} > OCOR^- > S_2O_3^{2-} > F^- > N_3^- > Cl^- > SCN^- > S^{2-} > Br^- > I^-$).[23]

Now that we have described the types of MOs, we can describe the main **classes of electronic transitions** between them.

- On the one hand, electronic transitions within metal-centred orbitals (MC, $t_{2g} \rightarrow e_g$ in Figure 1.3, red line) or ligand-centred orbitals (LC, $\pi_L \rightarrow \pi_L^*$ in Figure 1.3, purple

line) occur without significant charge redistribution. Although these transitions can cause important changes in the bonding properties of the ligands, they are not relevant in photoredox catalysis, and these classes will not be discussed further.

- On the other hand, charge-transfer (CT) transitions are the ones responsible of the photoredox properties of the PCs, and are named either MLCT (metal to ligand, exemplified in Figure 1.2, blue line) or LMCT (ligand to metal) depending on the original and final involved orbitals. The charge redistribution implies the formal oxidation (MLCT) or reduction (LMCT) of the metal centre while respectively reducing or oxidising the ligand. The nature of these events is dictated by the individual redox properties of the metal and the ligand: for instance, MLCT will be favoured when the metal is easier to oxidise than the ligand, while the opposite is true for LMCT. A third possible CT transition involves orbitals in two different ligands (called inter-ligand or ligand-to-ligand charge transfer, LLCT).[24] Once a given CT excited state is formed, its redox properties are very different from the ground state, and oxidative/reductive events can be unlocked; but it has to be considered that depending on the PC, also changes in pK_a can favour protonation/deprotonation events,[25] as well as changes in bond strength, can alter the coordination sphere.[26, 27]

Moreover, the selection rules dictate the probability of a certain electronic transition happening, which also determines the intensity of absorption (or emission). A transition is generally allowed only if it involves a change in the orbital quantum number (specifically, $\Delta L = \pm 1$), so d-d transitions are forbidden. Besides, the spin multiplicity does not change for an allowed transition ($\Delta S = 0$), and the total angular momentum should follow $\Delta J = 0$ or ± 1. Yet, the selection rules can be broken (*vide infra*) mainly by spin-orbit coupling or by vibrational changes in symmetry.[18, 19]

1.1.3. Deactivation: different pathways

After the fast absorption of the photon, the excited state survives only for a particular lifetime (τ) and tends to decay back to the more stable ground state (S_0) by different possible deactivation pathways. The electronic deactivation transition involves an electronic decay from the excited state (S_n) to the initial ground electronic state (S_0), typically passing through multiple excited states before returning to the S_0. (Activation: $S_0 \rightarrow S_n$; Deactivation $S_n \rightarrow \ldots \rightarrow S_0$). Jablonski diagrams summarize the different electronic transitions between ground and excited states of a given photocatalyst and their dynamics (Figure 1.4), which can be summarised in two main groups: non-radiative and radiative.

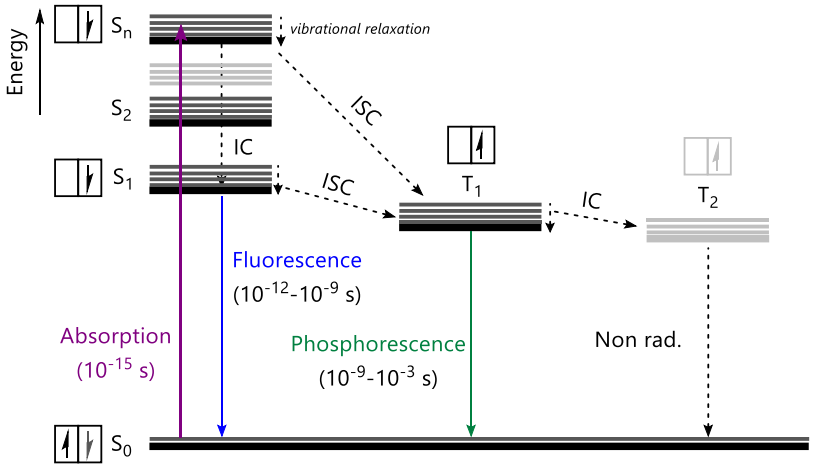

Figure 1.4. Jablonski diagram of a generic photocatalyst. S = Singlet; T = Triplet; IC = Internal Conversion; ISC = Intersystem Crossing.

- Non-radiative transitions (indicated with dashed lines in Figure 1.4):
  - Vibrational relaxation: to the lowest vibrational level of the same electronic level.
  - Internal conversion (IC): from a vibrational state in an excited state to the vibrational state in a lower electronic level.
  - Intersystem crossing (ISC): a transition to a level with a different spin multiplicity (in Figure 1.4, from singlet S to triplet T). This means that the spin selection rule is not followed (*vide supra*), which is characteristic of metal complexes with strong spin-orbit coupling effects (second- and third-tow transition metals).[28]
- Radiative transitions:
  - Fluorescence: an electronic transition from excited to ground state that occurs without being preceded by an ISC event. The excited state's lifetime is short and decays very fast (ps-ns).[29]
  - Phosphorescence is an electronic transition from excited to ground state after an ISC event. The spin selection rule forbids the relaxation to the ground state; thus, the excited state lifetime is longer (ns-ms).[29] The longer an exciting state lives, the more likely it is to engage in bimolecular encounters.[30]

As a practical example, Figure 1.5 illustrates the photophysical processes unchained after excitation of the photocatalyst $[Ir(bpy)(ppy)_2]^+$ ($\mathbf{PC_{Ir}}^+$, bpy = 2,2'-bipyridine, ppy = monodeprotonated 2-phenylpyridine). The excitation from the ground state (S_0) to an excited ^{1}MLCT state has been generally accepted in the literature.[31-33]

Then, the strong spin-orbit coupling effect of Ir^{+3} facilitates ISC to a $^3MLCT_{ppy}$ (<100 fs, predominantly located in the ppy ligand), which after vibrational relaxation (700 fs) is followed by a LLCT (16 ps) to a $^3MLCT_{bpy}$ (predominantly located in the bpy ligand). This is the resting excited state ($\tau \simeq 300$ ns in acetonitrile)[34] from which the complex emits a photon by phosphorescence.

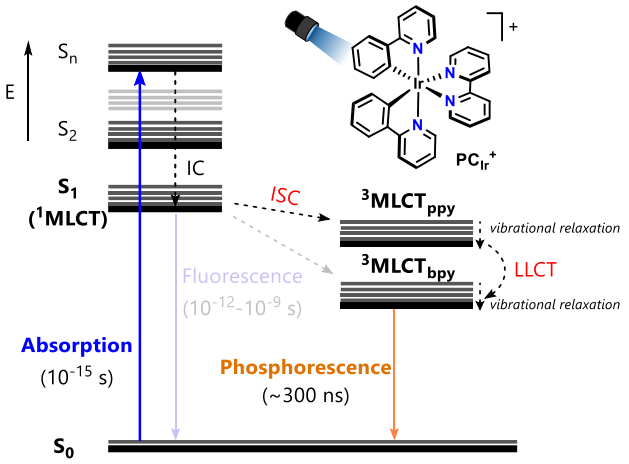

Figure 1.5. Jablonski diagram of $\mathbf{PC_{Ir}^+}$. S = Singlet; T = Triplet; IC = Internal Conversion; ISC = Intersystem Crossing. This complex is an example for this introductory section because it will be a relevant PC along the thesis, but it can be taken as a generic model to illustrate electronic transitions.

Notably, an excited photocatalyst (PC*) can play simultaneously two roles: first, the high energy of the excited electron (Figure 1.4, T_1) makes the PC* to be a potential reductant *via* single electron transfer (SET) in the presence of electron acceptors. Second, the excitation of the ground state PC also leaves a low energy hole (Figure 1.4, S_0) that acts as a potential oxidant in front of electron donors. Likewise, if an irradiated photocatalyst rests in an excited state that lives long enough to diffuse in solution (at least a few nanoseconds), collisional bimolecular events called dynamic quenching processes can occur instead of radiative or non-radiative deactivation. Moreover, if the excited photocatalyst encounters an appropriate quencher, its emission intensity and lifetime will decrease (*vide infra*). For PCs, the quenching process can be reductive (the quencher donates one electron to the PC, Scheme 1.2a1) or oxidative (the quencher accepts one electron from the PC, Scheme 1.2a2). Third, energy transfer events result in the excitation of the quencher (Scheme 1.2b), but this process is not related to photoredox catalysis and will not be further discussed.

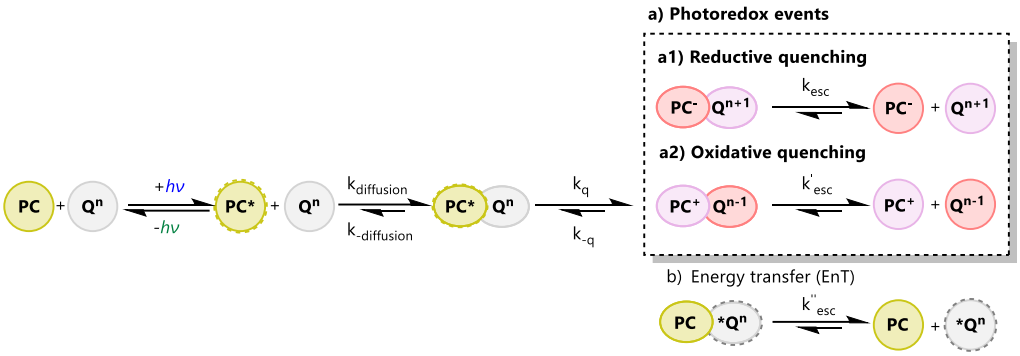

Scheme 1.2. Kinetic steps in a dynamic quenching process. PC = photoredox catalyst; Q = quencher.

Alternatively, static quenching processes can happen if the PC and the quencher form a donor-acceptor complex in the ground state. Then once excited, no diffusion events are required. It is noteworthy to mention that after the electron transfer (either *via* reductive or oxidative quenching), the PC* is not being 'deactivated' towards its original pre-excitation form because the resultant species have been either mono-reduced ($PC^{–}$) or mono-oxidised (PC^{+}) in one electron. The reductant or oxidant behaviour of the excited state will depend on the matching redox potentials between the different species in the media. In general, electron donors (EDs) and electron acceptors (EAs) are economical molecules expected to respectively transfer one electron to the excited PC (such as tertiary amines, ascorbate, alcohols…)[35] or to remove one electron from the PC (more limited, such as Ag^{+}, $S_2O_8^{2-}$…).[36] For the SET to take place, the redox partners need suitable redox potentials. This implies that the E_{ox} of the ED or the E_{red} of the EA, match with $E(PC^*/PC^{–})$ or $E(PC^{+}/PC^*)$, resulting in an exergonic event according to the formulas:

$$\Delta G_{redox} = E_{red}(ED^{+}/ED) – E_{red}(PC^*/PC^{–}) \textit{ (for reductive quenching)}$$

$$\Delta G_{redox} = E_{red}(PC^{+}/PC^*) – E_{red}(EA/EA^{–}) \textit{ (for oxidative quenching)}$$

The redox potentials of a ground-state molecule can be measured by cyclic voltammetry.[37] From the different ways known to estimate **excited state redox potentials**,[38-40] the most common approach is the use of simplified Rehm-Weller equations:[41]

$$E(PC^{+}/PC^*) = E(PC^{+}/PC) - E_{00}$$

$$E(PC^*/PC^{–}) = E(PC/PC^{–}) + E_{00}$$

In these expressions, the value E_{00} is the energy gap between the zeroth vibrational state in the ground and the excited state, and it has been generally approximated as the

crossing point of the absorption and emission spectra[40] (or directly from the emission peak).[42] It is important to recall that the excited state redox potential will not be as strong as the ground state potential. To put an example of what compounds are predicted to be reactive in SET event, we can look again at $\mathbf{PC_{Ir}}^+$ (Scheme 1.3). In its ground state,[42] only reductants with E_{red} more negative than -1.4 V (*vs* SCE) will be effective (such as Na^0),[43] as well as oxidants over +1.2 V *vs* SCE (such as NO^+).[44] However, on its excited state,[20, 42, 45] the compound can be reductively quenched by molecules with an oxidation potential as low as 0.7 V. A clear example of a good reductive quencher is the oxalate anion $C_2O_4^{2-}$,[46] and also triethylamine[35, 47] (because the ET events do not only happen at the E_{red} value but in a certain redox range as can be detected in voltammetry measurements).[37] In the opposite way, the excited state $\mathbf{PC_{Ir}}^{+*}$ is expected to be oxidatively quenched by molecules with a reduction potential milder than -0.8 V, such as MV^{2+}.[48]

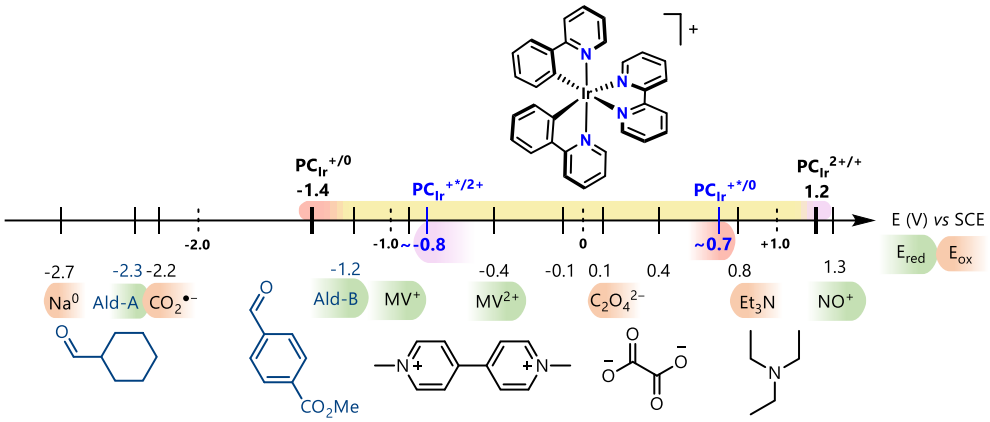

Scheme 1.3. Collection of reported redox values for $\mathbf{PC_{Ir}}^+$ in its ground (black letters) and excited state (blue letters), as well as for a series of potential single electron donors (in orange background) and acceptors (in green background).

Stern-Volmer quenching studies can quantify the quenching effect between a particular PC* and the quencher. Both the original lifetime (τ_0) and emission (I_0) of the pure PC, will decrease with higher concentrations of quencher [Q], as dictated by the Stern-Volmer equation:

$$I_0/I = 1 + K_{SV}\cdot[Q]$$

$$\tau_0/\tau = 1 + K_{SV}\cdot[Q]$$

From where K_{SV} (Stern-Volmer quenching constant) correspond with the slope at which the quenching evolves, and can be calculated from the linear plot of the ratio of starting/final intensity vs [Q] as illustrated in Figure 1.6. Furthermore, when having a

purely dynamic quenching, K_{SV} can be correlated with the bimolecular quenching constant by the formula:

$$K_{SV} = k_q \tau_0$$

It is important to note that Stern-Volmer studies confirm the existence of a quenching process but cannot indicate whether the quenching mechanism is oxidative, reductive, or even EnT. Furthermore, the comparison of k_q values obtained for a given PC in front of different potential quenchers can be used to estimate the predominant reactivity of PC*.[49, 50]

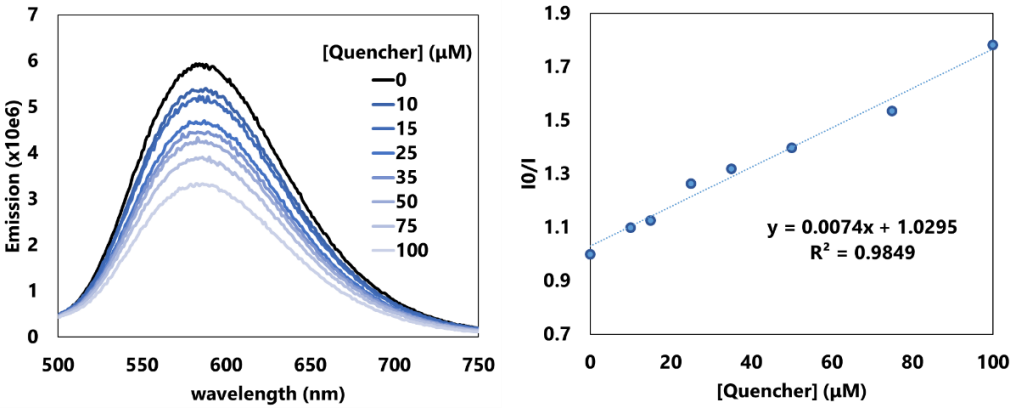

Figure 1.6. Decay of the emission and Stern-Volmer plot of a generic photocatalyst.

1.1.4. Reactivation: design of a photoredox cycle

All the information above can help identify good PC candidates: molecules that exhibit a long-lived excited state after absorption of a -visible light- photon, which facilitates the interaction with a quencher possessing matching-redox potentials.[51] Up to here, we have revisited the first two steps of a photoredox cycle: the electronic excitation and the reductive/oxidative quenching. To close the reductive quenching cycle, the intermediate PC^- has to react with a suitable EA (Scheme 1. 4, left cycle), whereas the oxidative quenching cycle requires an ED (Scheme 1. 4, right cycle). For instance, with the molecules included in Scheme 1.3, we can rationalise a simple photoredox cycle for $\mathbf{PC_{Ir}}^+$ to reduce different substrates.

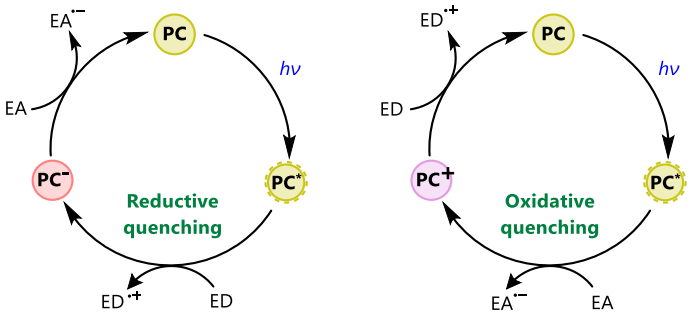

Scheme 1. 4. General mechanism of photoredox catalytic processes. PC = photoredox catalyst; ED = electron donor; EA = electron acceptor.

It was already commented that after the initial absorption of a photon, reductive quenching of $\mathbf{PC_{Ir}^{+}*}$ can happen with oxalate or even triethylamine (Scheme 1.5, left cycle). The resultant $\mathbf{PC_{Ir}^{0}}$ is expected to transfer one electron to substrates with E_{red} up to -1.4 V *vs* SCE (Scheme 1.3). Likewise, suitable examples to close the cycle could be methyl 4-formylbenzoate (Ald-B, E_{red} = -1.2 V)[52] or methyl viologen (MV^{2+}, E_{red}=-0.4 V),[48] whereas cyclohexanecarboxaldehyde (Ald-A, E_{red}=-2.3V)[47] is not expected to be reduced under these conditions. Moreover, since the one-electron reduction of methyl viologen is also accessible *via* oxidative quenching of $\mathbf{PC_{Ir}^{+}*}$, both alternative mechanisms can be operative for this substrate. Which of the two pathways is preferential will be dictated by the quenching rate of $\mathbf{PC_{Ir}^{+}*}$ *vs* each potential quencher, what depends on the bimolecular quenching constant k_q and the concentration of each quencher ([Q]).

$$\text{rate} = -\frac{d[PC^*]}{dt} = k_q \cdot [PC^*] \cdot [Q]$$

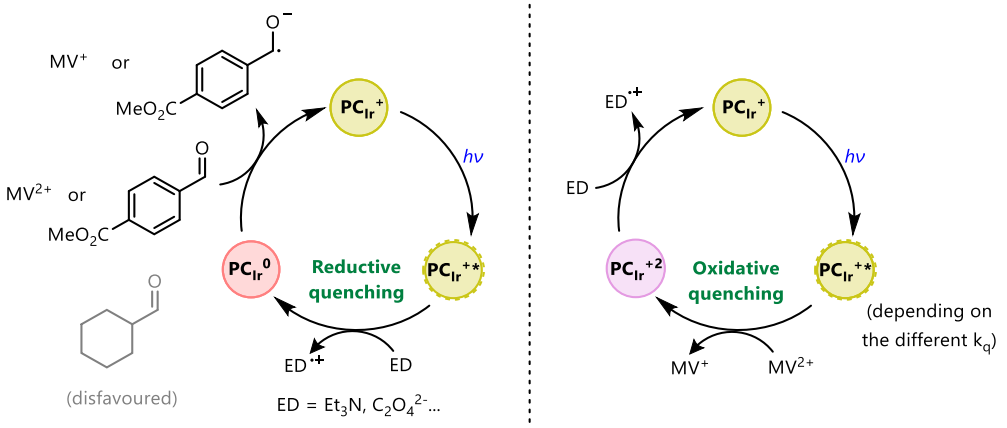

Scheme 1.5. Hypothetical photoredox catalytic cycles for selected substrates. MV^{2+} = Methyl viologen; ED = Electron donor; $C_2O_4^{2-}$ = oxalate anion.

1.1.5. Combining cycles: dual photoredox catalysis

As illustrated in the previous section, the illuminated PC can mediate transferences of electrons that would not happen under darkness between a given ED and an EA. Nonetheless, this electron circuit can also be connected with a non-photoactive second catalyst. The simultaneous combination of two catalytic cycles is known as cooperative or dual catalysis (Scheme 1. 6),[53] and it embraces the combination of PCs with enzymes, organic molecules[8] or transition metal complexes.[54] In the present thesis, we will study the latter case, also termed metallaphotoredox catalysis, which can present multiple advantages regarding direct ET reactions: first, (1) the energy barrier is divided in a multi-step electron transfer process. Moreover, (2) the chemistry of many organometallic complexes is well known, so (3) the co-catalyst can be designed to improve the selectivity and (4) prevent electron-hole recombination *via* back electron transfer (especially when using heterogeneous PC). Likewise, (5) rational catalyst design can unlock otherwise inaccessible transformations, as we will describe in the next section.

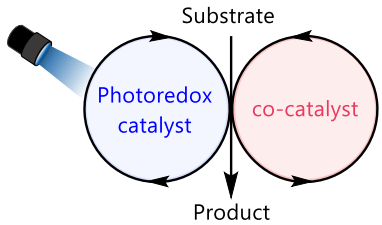

Scheme 1. 6. Schematic representation of the concept of dual photoredox catalysis.

1.2. Artificial photosynthesis for organic transformations

1.2.1. Context

Through natural photosynthesis, plants and other organisms convert light energy into chemical energy. In essence, sunlight is used to split water into oxygen and hydrogen equivalents, which reduce carbon dioxide to carbohydrates (and other energy-rich organic compounds). The process relies on combining multiple natural catalysts, which are very specific (bio)organic molecules and organometallic complexes. Inspired by nature, the concept of artificial photosynthesis (AP) has been defined in many different ways.[55-58] In general, based on the use of (sun)light to produce another energy source employing an heterogeneous or homogeneous catalyst. Similarly, in the present

thesis, we employ the AP as catalysts combination that uses visible light's energy with water as a source of hydrogen equivalents to drive chemical reductions (storing luminous energy into chemical bonds).

In this context, archetypical AP examples are the visible-light-induced fixation of carbon dioxide[59, 60] or the reduction of aqueous protons[61-64] to carry out H_2 evolution (a profitable fuel), coupled with O_2 evolution as the only by-product. This last reaction, called 'water splitting' has been performed since 1972 using light-driven electrochemistry.[5] In their pioneering experiment, Fujishima and Honda connected a TiO_2 electrode to a Pt electrode in a divided cell containing an aqueous electrolyte. The irradiation of the TiO_2 electrode with ultraviolet light activated the oxidation of water on its surface, while the released protons were reduced to hydrogen in the Pt cathode chamber (Figure 1.7). Nonetheless, when looking at the thermodynamics of light-driven water splitting, it is clear that water oxidation half-reaction is highly endergonic, what represents an arduous bottleneck to bypass (the overall process results in ΔG = 113 kcal/mol).[65, 66] In fact, performing visible-light-driven water splitting by a homogeneous system is still a challenging and inefficient process.[67]

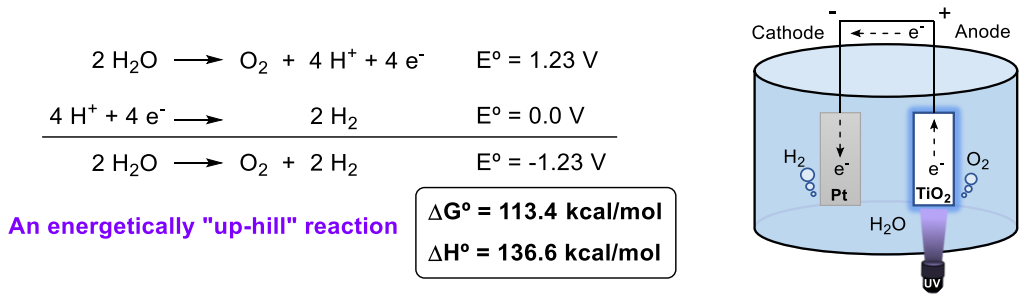

Figure 1.7. Thermodynamics of water splitting half-reactions and schematic representation of Fujishima and Honda experiment.

With this context in mind, it can be envisioned that those catalytic systems developed for water splitting could also facilitate the use of water as a source of H equivalents for reducing organic functionalities (Scheme 1.7).[56] Nevertheless, although much attention has been put on using water molecules as electron donors, the photocatalytic reduction of organic substrates in combination with oxygen evolution remains underdeveloped. Its limited implementation is a direct consequence of the thermochemically challenging half-reaction of water oxidation. In addition, the generation of O_2 in a reductive environment can lead to unfavourable side reactivity such as PC quenching, oxidation of the co-catalyst or even oxygenation of the substrates. Under those circumstances, until now, photocatalytic reduction studies have

been forced to disregard the exciting approach of being complemented with O_2 evolution half-reaction. Instead, the use of water as a clean, economical and environmentally benign source of hydrogen atoms has been explored in photocatalysis by coupling the reduction of organic substrates with the oxidation of sacrificial ED (Scheme 1.7). This approach matches with our definition of AP (*vide supra*), focused on organic reductions with molecular catalysts.

Moreover, it is remarkable that using D_2O in these organic methodologies provide direct access to valuable deuterated products obtained under mild conditions and from the most economical deuterium source. The highest limitation of this approach using homogeneous catalysts could be to control the selective reaction of catalytic [M–H] species *vs* the substrate rather than *vs* water. Although controlling this selectivity is complicated, there has been progress in the field, and selected contributions will be discussed in the following section.

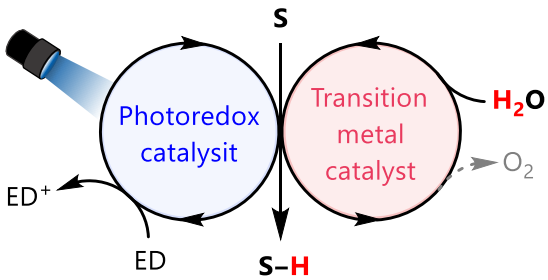

Scheme 1.7. Schematic representation of artificial photosynthesis concept applied to organic reductions. S = Substrate; ED = electron donor.

1.2.2. Artificial photosynthesis for the reduction of double bonds

Substantial work has been devoted to exploiting water as H source for the photocatalytic reduction of organic functionalities.[68, 69] In the present section, we focus our attention on the reduction of double bonds. At this point, it must also be highlighted that, despite that water being a good proton donor (pKa = 14),[70] is not a good H atom donor compared with other abundant compounds such as alcohols, amines or alkanes (Table 1. 1).

Table 1. 1. Bond dissociation energies and pK_a of some selected common molecules.

Entry	Bond (substance)	BDE (kJ/mol)	pK_a
1	O–H (water)	498.7	14
2	O–H (methanol)	436.8	16
3	H–H	436	35
4	N–H (ammonia)	435	37
5	C–H (methane)	431	~50
6	O–H (phenol)	368	10

Consequently, using co-catalysts that can undergo hydride or hydrogen atom transfer is convenient to exploit water as a co-substrate to reduce organic compounds. Transition metal complexes are good candidates to perform selective transference of reducing equivalents. However, this transference frequently implies the formation of very reactive organometallic [M–H] species. Compromised by the accessible pK_a of water, [M–H] can unselectively react with protons instead of the desired organic substrate. In addition, water does not always match with organic compounds in terms of solubility and pK_a. Over decades, many of the systems developed for the reduction of organic double bonds have relied on non-purely aqueous mixtures, where a proportion of alcohol or organic acid facilitated the transference of H atoms (in acid-base equilibrium with water).[71-74]

The earliest example of photocatalytic reduction of organic double bonds using water corresponds with the work of Boonstra and co-workers in 1975,[75] very close in time after the discovery of photoelectric water splitting.[5] The irradiation of TiO_2 with UV-light in the presence of ethylene gas and H_2O vapour generated a mixture of short-chain saturated alkanes (Scheme 1.8, mainly methane, ethane, propane and butane). This contribution preceded many other hydrogenations using semiconductors; however, following our definition of AP (*vide supra*), we will focus our discussion on molecular catalysis rather than purely heterogeneous.

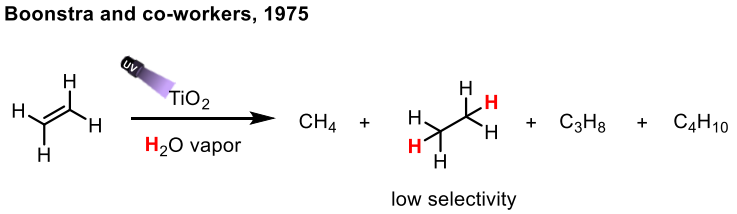

Scheme 1.8. The first photocatalytic reduction of a C=C bond using water as H source.

Examples of organometallic catalysts employed for the photoreduction of alkenes in aqueous media are very scarce. To the best of our knowledge, the first case was reported by Can Li and co-workers in 2011,[74] who employed CdS nanoparticles as PC (irradiating at $\lambda > 400$ nm) and a tetradentate anionic iridium complex as a transition metal catalyst. As illustrated in Scheme 1.10, lactic acid was used as a sacrificial reagent and benzylideneacetone was the only olefin explored. Despite the lack of solid mechanistic evidence, this was likely the first use of a photocatalytically generated [M–H] species for the reduction of C=C bond in aqueous media. The following example was the hybrid TiO_2-B_{12} system reported by Hisaeda and co-workers,[76] which could reduce the C=C bond of atropic acid in water (Scheme 1.10b). Different substrates were also explored in their work but using methanol as solvent. Other reported molecular photocatalytic systems have also relied on the utilization of alcohol/water solvent mixtures. Hence the role of water as H source was not well-defined.[72, 73]

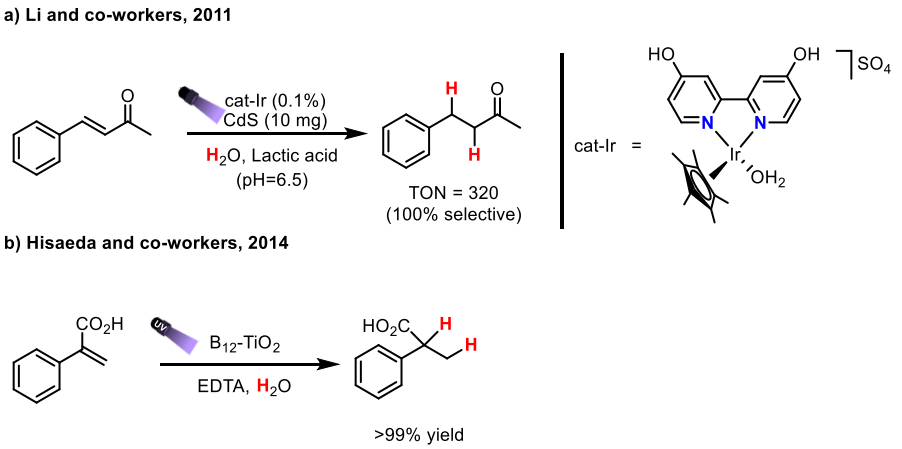

Scheme 1.9. Selected examples of the photocatalytic reduction of olefins in aqueous media using molecular complexes.

Alternatively, enzymes have been successfully employed for the photocatalytic reduction of alkenes in aqueous media with sacrificial additives, what's more, in an enantioselective fashion. Nonetheless, although protocols for broad scopes have been reported by different authors,[77-79] the state-of-the-art in AP corresponds with the bio-inspired photocatalytic system of Corma and co-workers.[80] In particular, the irradiation of Au nanoparticles supported on TiO_2 in the presence of an oxidoreductase (the old yellow enzyme homologue from *Thermus scotoductus* SA-01, TsOYE) afforded the stereoselective reduction of the C=C bond of ketoisophorone. Moreover, this reductive transformation was coupled with the thermodynamically recalcitrant O_2 evolution semirreaction (Figure 1.7, Scheme 1.12).

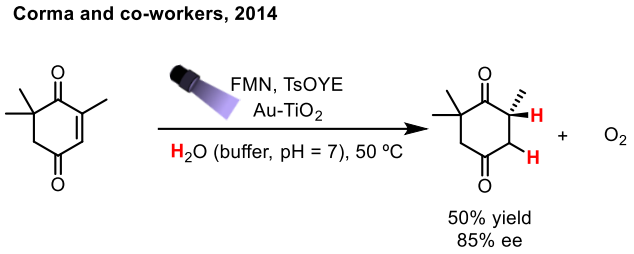

Scheme 1.10. State-of-the-art C=C photocatalytic reduction in water coupled with O_2 evolution.

In the case of the reduction of carbonyl groups, the initial examples of photocatalysis were reported by Pac and co-workers in 1983.[81-83] The system, which consisted of $[Ru(bpy)_3]Cl_2$ as PC and 1-Benzyl-1,4-dihydronicotinamide (BNAH) as sacrificial reductant, could reduce ketones with electron withdrawing groups under visible light irradiation (λ > 470 nm, Scheme 1.11a). The early use of visible light instead of UV is significant, since near-UV irradiation can directly excite aromatic ketones.[84-87]

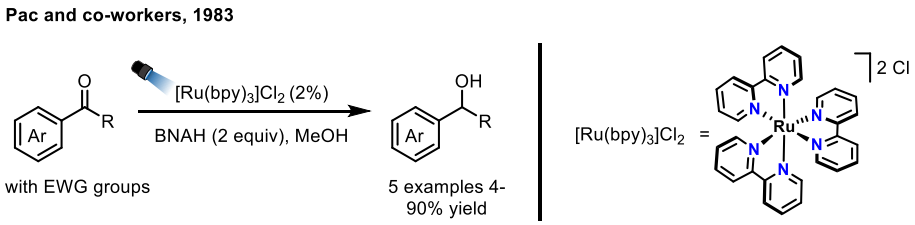

Scheme 1.11. First example of the photocatalytic reduction of C=O bonds.

On the other hand, developing organometallic catalysts to reduce carbonyl groups using water as the source of H has been unusual.[74, 88-92] In a remarkable work from Baeg and co-workers,[89] the combination of a graphene-based PC, a rhodium-based co-catalyst, and triethanolamine (TEOA) as the source of electrons rendered a [Rh–H] species that could be applied for the reduction of $NADP^+$ (nicotinamide adenine dinucleotide phosphate) to NADPH in water. The same system was utilised as a catalytic source of NADPH in the presence of alcohol dehydrogenase (*Lactobacillus kefir*, LKADH), and various acetophenone derivatives could be reduced to the corresponding chiral alcohols (Scheme 1.12a). Another example by our group[92] presented a dual system based on a copper-based PC and a cobalt-based co-catalyst. Under light irradiation, the in situ generated [Co–H] species reduced a diverse scope of ketones and three aldehydes in aqueous media (Scheme 1.12b). Moreover, competitive studies in both types of substrates revealed a very unusual selectivity: aromatic ketones were reduced in the presence of aliphatic aldehydes. This work is an example of how

the rational design of organometallic complexes for metallaphotoredox catalysis can facilitate the access to otherwise unreachable reactivity.

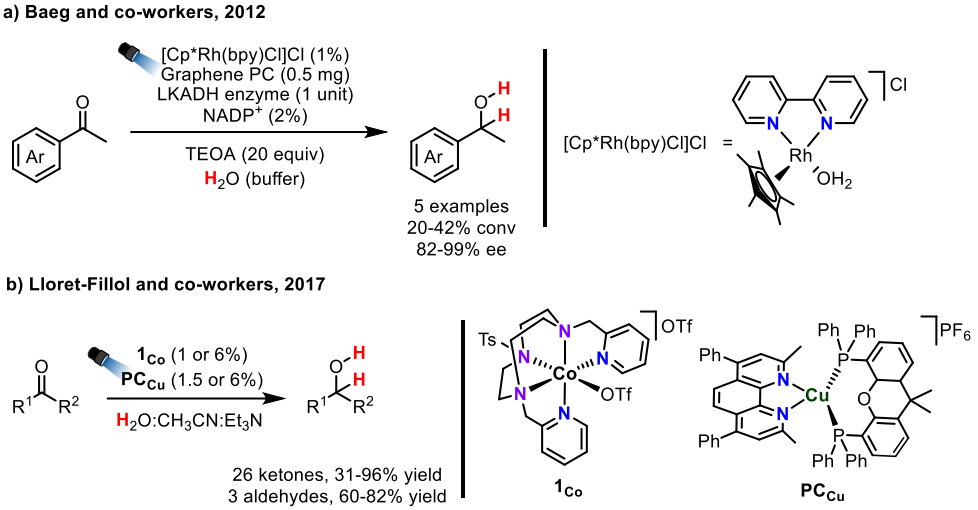

Scheme 1.12. Selected examples of the photocatalytic reduction of carbonyl groups using molecular complexes.

Lastly, the photocatalytic reduction of C=N bonds was not explored until 2018.[93-97] From those systems that operate in aqueous media,[93, 96, 97] it is remarkable the contribution of Wenger and co-workers. In the first publication,[97] hydrogen equivalents coming from 3-mercaptopropionic acid (MPA) were transferred to the C=N bonds of *in situ* generated iminium species (Scheme 1.13a). Furthermore, in a second report in collaboration with Ward,[97] the water-soluble iridium PC $Na_3[Ir(sppy)_3]$ (sppy= 3-(pyridin-2-yl)benzenesulfonate) was combined with *E. coli* (MAO-N-9) and ascorbic acid ($AscH_2$) to produce different pyrrolidine derivatives in a stereoselective fashion (Scheme 1.13b). Moreover, although reductive methodologies usually require a strictly inert atmosphere, their system was optimally operating under aerobic conditions.

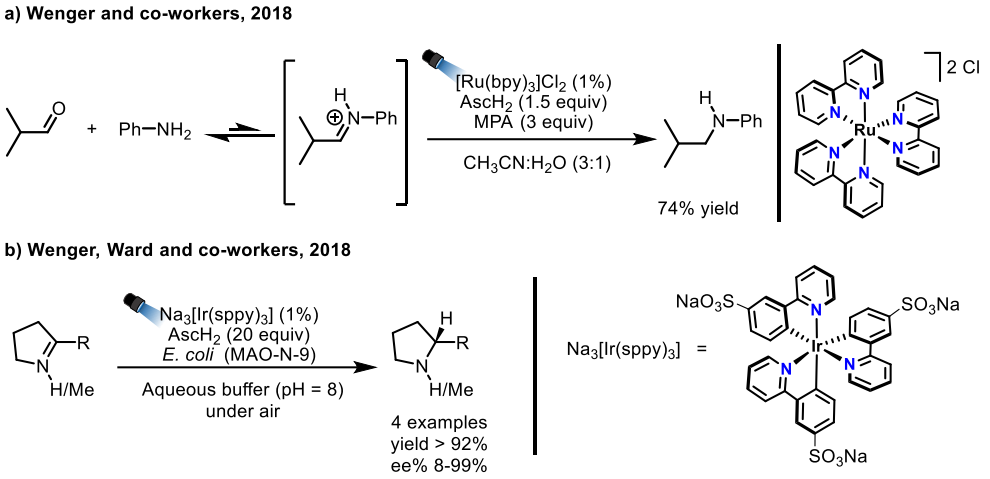

Scheme 1.13. Selected examples of the photocatalytic reduction of imines.

To sum up, various photocatalytic technologies have been developed for the saturation of double bonds, and significant examples are operating in aqueous solutions. Actually, transition metal-based co-catalysts are a promising strategy for the double incorporation of H atoms from water into the substrate, although their use is frequently compromised due to the side-reactivity of [M–H] species with aqueous protons. Nevertheless, all these studies represent a necessary progression towards environmentally-benign, efficient and well-understood organic reductions, which might be coupled with water oxidation someday.

1.3. Highly reductive photocatalytic systems

1.3.1. Two photons, one cycle

As we have introduced in the first section, excited PCs exhibit a strong reductant or oxidant character in comparison with their ground state (Scheme 1.3). Nonetheless, the excited state redox properties of a given PC* are still limited, and substrates with more extreme reduction or oxidation potentials remain inaccessible under conventional conditions. In the case of reductive photocatalysis, a practical limit for regular transformations can be considered around -2 V *vs* SCE.[98, 99] However, more challenging substrates have been activated through dual catalysis,[100] high energy irradiation wavelengths,[101] or multiphoton mechanisms.[102, 103] In the latter case, despite different multiphoton catalytic cycles have been proposed,[104-107] the most common scenario corresponded with the illustrated absorption-reduction-absorption cycle (Scheme 1.14).

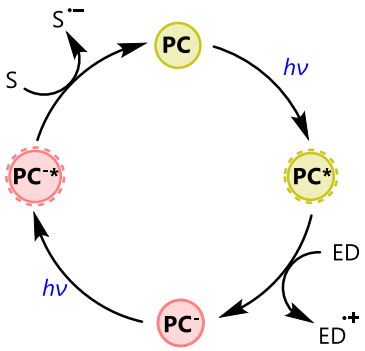

Scheme 1.14. General absorption-reduction-absorption mechanism for generating excited radical intermediates.

In recent years, the photocatalytic reduction of very challenging substrates has been performed through different PC,[107-114] mainly organic molecules based on polyaromatic structures,[107-111] which have aroused further interest for mechanistic studies.[115-118] In a notorious contribution, Nicewicz and co-workers[111] reported the characterization of a new acridinium catalyst (Mes-Acr-BF_4). The E_{ox}* of the reduced intermediate was calculated to be -3.4 V *vs* SCE, a value similar to that of the alkali metals.[43] Indeed, the system was able to reduce aryl halides with values of E_{red} up to -2.9 V *vs* SCE (Scheme 1.15a) and break the N–S bond from substrates with *N*-tosylate group (E_{red} < -2 V *vs* SCE). A very unusual feature of this system was that the excited radical intermediate could engage SET events in solution despite of having a sub-nanosecond lifetime (~100 ps).[119]

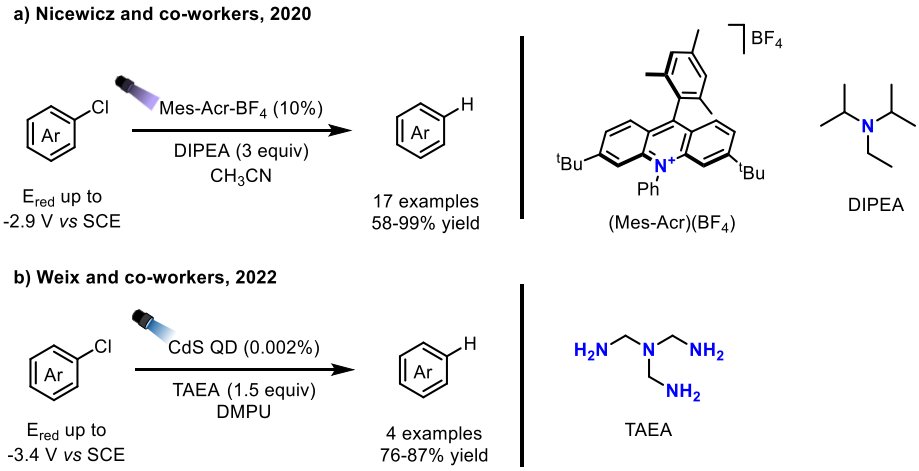

Scheme 1.15. Selected examples of two-photon catalysis.

From a distinct approach, Weix and co-workers utilised quantum dots (QD),[113] semiconductors nanoparticles (few nm) that acquire different properties than larger particles due to quantum mechanics.[120] In their methodology, the irradiation of CdS QD in the presence of tertiary amines as external ED allowed the accumulation of electrons in the nanomaterial. The reduced CdS^{-n} can absorb an additional photon. Then the excited species transfers the electron to aryl chlorides with reduction potentials beyond -3 V (Scheme 1.15b). Moreover, a catalyst loading as low as 0.002% was sufficient to functionalise the generated aryl radicals (for example with boron pinacolate), but also to perform alternative organic reductions (as cyclopropyl ring opening or *N*-detosylation).

Nonetheless, in some of these reported methodologies for challenging reductions, the authors also proposed the generation of solvated electrons as an alternative mechanism.[112-114] In theory, the promotion of electrons in reduced intermediates to extremely high energy levels can surpass the ionization potential of the catalyst. Under those circumstances, instead of the conventional relaxation pathways to the ground state, the catalyst might directly eject the electron to the solvent (Scheme 1.16).

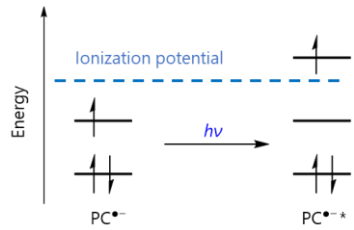

Scheme 1.16. Simplified MO diagram for a reduced PC and its excited species.

Solvated electrons have been generated in different solvents such as methanol,[121, 122] acetonitrile,[123] tetrahydrofuran (THF)[124] or ammonia,[125, 126] generally using high radiation sources, photoionization of chemical species, or dissolving alkali metals.[127] To the best of our knowledge, the generation of solvated electrons using visible light irradiation has been well-supported only in aqueous media.[106, 128] In this context, the first photocatalytic systems that employed solvated electrons (E_{red} = -3.1 V *vs* SCE)[129, 130] were designed by Goez and co-workers.[131-134] The authors demonstrated that the cycle of absorption-reduction-absorption[104] could be operative for $[Ru(bpy)_3]^{2+}$, with the ultimate ejection of a solvated electron.[128] This catalyst was employed to reduce many substrates with E_{red} beyond -2 V *vs* SCE (in dehalogenations,[134] cross couplings,[133] or the saturation of C=C bonds,[132, 134] among others).[134] Originally, their methodologies relied on SDS (sodium dodecyl sulfate) micellar compartmentalization. This anionic environment permitted the isolation of the stable cationic intermediate $[Ru(bpy)_3]^{+}$ for

its fruitful excitation, minimizing the electron recombination with the formal radical cation of the sacrificial donor. Nonetheless, in the same year, they also designed a micelle-free alternative, in which the anionic environment was replaced with a PC bearing carboxylate substituents that afforded a comparable reactivity (Scheme 1.17a).[131] Shortly after, Wenger and co-workers reported that the water-soluble PC $Na_3[Ir(sppy)_3]$ could also generate solvated-electrons, which were employed for different transformations (Scheme 1.17b).[106] However, spectroscopic data supported a different mechanism, in which the electron ejection took place after two consecutive photon absorptions (absorption-absorption-reduction), and finally the oxidised PC reacted with the sacrificial ED.

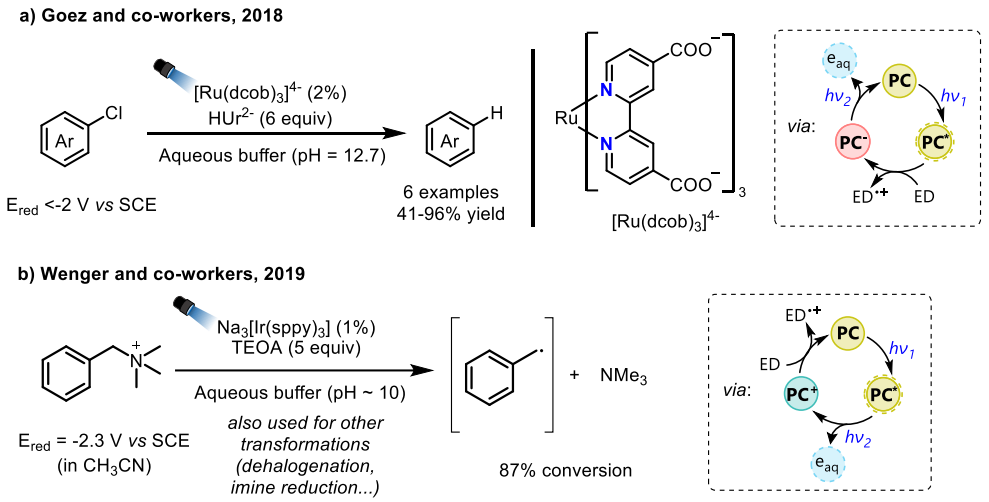

Scheme 1.17. Selected examples of two-photon transformations mediated by the generation of solvated electrons.

1.3.2. Electrophotocatalysis

In the previous section, we revisited some recent publications where the reduced intermediate of specific photoredox cycles unlocked challenging reactivity after a second excitation event (Scheme 1.14). For this reason, studying these reduced intermediates is promising both from fundamental and practical perspectives. In that direction, replacing sacrificial EDs with an external electric bias is a very convenient strategy (Scheme 1.18).[135, 136] In the first place, it has been proposed by Goez and co-workers how the presence of formal cationic sacrificial agents can dramatically quench the reactivity behind second excitation events.[131, 137] Moreover, eliminating chemical additives is a significant upgrade in economy and green chemistry. Hence,

electrophotochemistry emerges as a powerful approach to exploiting reduced PC intermediates' excitation.[137-140]

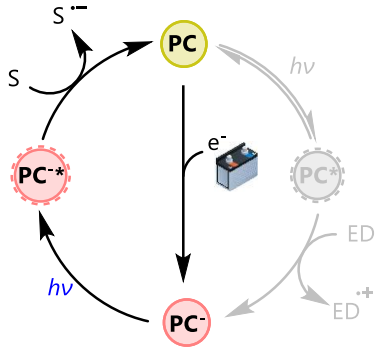

Scheme 1.18. A general mechanism for the electrophotocatalytic generation of excited radical intermediates, avoiding sacrificial electron donors.

Two pioneering contributions established the viability of reductive electrophotocatalysis using organic dyes (both were reported in 2020, the same day). On the one hand, Wickens and co-workers[138] used an *N*-naphtalimide (NpMI) under the application of a constant current and irradiation to form C–C and C–P bonds with good yields (Scheme 1. 19a). The system could activate substrates with up to -3.4 V *vs* SCE. Nonetheless, further mechanistic insights by Nocera and co-workers[141] revealed that the active species is not the non-emissive excited radical anion ($NpMI^{-}$*) but an excited i*n situ* generated organic hydride ($NpMI(H)^{-}$*). On the other hand, Lin and co-workers,[139] used dicyanoanthracene (DCA) to explore the formation of C–C, C–B and even C–Sn (Scheme 1. 19b), in this case merging irradiation with a fixed cell potential. Although an indirectly measured lifetime in the nanosecond timescale was reported for the excited radical anion, Vauthey and co-workers[118] revisited that this transient lives just a few picoseconds. Therefore, it cannot engage conventional dynamic quenching processes.

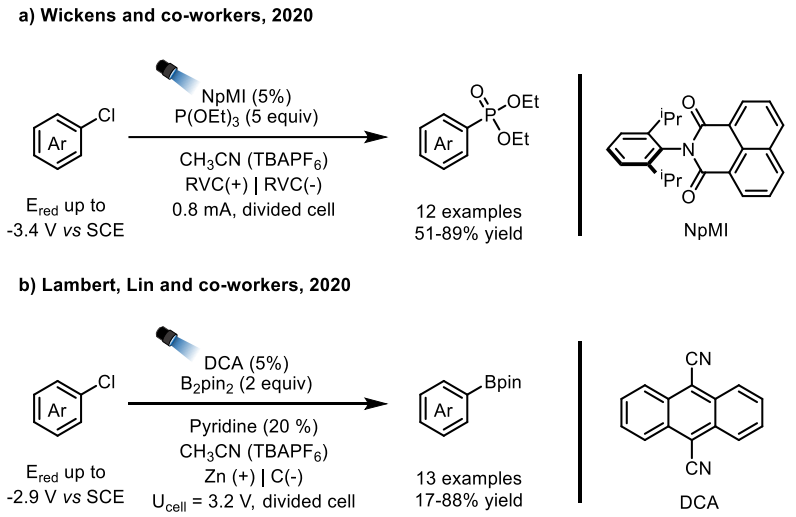

Scheme 1. 19. Selected examples of reductive electrophotocatalysis.

Hence, beyond using light as a unique driving force, its combination with an electric potential facilitates access to state-of-the-art reductions. Furthermore, this eliminates the necessity of stoichiometric additives, and new approaches and outcomes might be implemented soon (such as using dual electrophotocatalysis or multiphoton mechanisms).

1.4. References

1. Chatani, S.; Kloxin, C. J.; Bowman, C. N., The power of light in polymer science: photochemical processes to manipulate polymer formation, structure, and properties. *Polymer Chemistry* **2014,** *5* (7), 2187-2201.
2. Roth, H. D., The Beginnings of Organic Photochemistry. *Angewandte Chemie International Edition in English* **1989,** *28* (9), 1193-1207.
3. Capaldo, L.; Ravelli, D., The Dark Side of Photocatalysis: One Thousand Ways to Close the Cycle. *European Journal of Organic Chemistry* **2020,** *2020* (19), 2783-2806.
4. Coronado, J. M., A Historical Introduction to Photocatalysis. In *Design of Advanced Photocatalytic Materials for Energy and Environmental Applications*, Coronado, J. M.; Fresno, F.; Hernández-Alonso, M. D.; Portela, R., Eds. Springer London: London, 2013; pp 1-4.
5. Fujishima, A.; Honda, K., Electrochemical Photolysis of Water at a Semiconductor Electrode. *Nature* **1972,** *238* (5358), 37-38.
6. Meyer, T. J., Photoredox Catalysis. In *Fundamental Research in Homogeneous Catalysis*, Tsutsui, M.; Ugo, R., Eds. Springer US: Boston, MA, 1977; pp 169-182.
7. Ischay, M. A.; Anzovino, M. E.; Du, J.; Yoon, T. P., Efficient Visible Light Photocatalysis of [2+2] Enone Cycloadditions. *Journal of the American Chemical Society* **2008,** *130* (39), 12886-12887.

8. Nicewicz, D. A.; MacMillan, D. W. C., Merging Photoredox Catalysis with Organocatalysis: The Direct Asymmetric Alkylation of Aldehydes. *Science* **2008,** *322* (5898), 77-80.
9. Narayanam, J. M. R.; Tucker, J. W.; Stephenson, C. R. J., Electron-Transfer Photoredox Catalysis: Development of a Tin-Free Reductive Dehalogenation Reaction. *Journal of the American Chemical Society* **2009,** *131* (25), 8756-8757.
10. Strieth-Kalthoff, F.; Glorius, F., Triplet Energy Transfer Photocatalysis: Unlocking the Next Level. *Chem* **2020,** *6* (8), 1888-1903.
11. Fabry, D. C.; Ronge, M. A.; Rueping, M., Immobilization and Continuous Recycling of Photoredox Catalysts in Ionic Liquids for Applications in Batch Reactions and Flow Systems: Catalytic Alkene Isomerization by Using Visible Light. *Chemistry – A European Journal* **2015,** *21* (14), 5350-5354.
12. Capaldo, L.; Ravelli, D.; Fagnoni, M., Direct Photocatalyzed Hydrogen Atom Transfer (HAT) for Aliphatic C–H Bonds Elaboration. *Chemical Reviews* **2022,** *122* (2), 1875-1924.
13. Supranovich, V. I.; Levin, V. V.; Dilman, A. D., Radical Addition to N-Tosylimines via C–H Activation Induced by Decatungstate Photocatalyst. *Organic Letters* **2019,** *21* (11), 4271-4274.
14. Shaw, M. H.; Twilton, J.; MacMillan, D. W. C., Photoredox Catalysis in Organic Chemistry. *The Journal of Organic Chemistry* **2016,** *81* (16), 6898-6926.
15. Yedase, G. S.; John, M.; Yatham, V. R., Organophotoredox-Catalyzed Switchable Selective Transformation of Aromatic Aldehydes into Pinacols and Benzyl alcohols. *Asian Journal of Organic Chemistry* **2021,** *10* (11), 2916-2920.
16. Glaser, F.; Wenger, O. S., Recent progress in the development of transition-metal based photoredox catalysts. *Coordination Chemistry Reviews* **2020,** *405*, 213129.
17. Bell, J. D.; Murphy, J. A., Recent advances in visible light-activated radical coupling reactions triggered by (i) ruthenium, (ii) iridium and (iii) organic photoredox agents. *Chemical Society Reviews* **2021,** *50* (17), 9540-9685.
18. Kettle, S. F. A., Electronic spectra of transition metal complexes. In *Physical Inorganic Chemistry: A Coordination Chemistry Approach*, Kettle, S. F. A., Ed. Springer Berlin Heidelberg: Berlin, Heidelberg, 1996; pp 156-184.
19. Reddy, S. L.; Tamio, E.; Reddy, G. S., Electronic (Absorption) Spectra of 3d Transition Metal Complexes. In *Advanced Aspects of Spectroscopy*, Muhammad Akhyar, F., Ed. IntechOpen: Rijeka, 2012; p Ch. 1.
20. Arias-Rotondo, D. M.; McCusker, J. K., The photophysics of photoredox catalysis: a roadmap for catalyst design. *Chemical Society Reviews* **2016,** *45* (21), 5803-5820.
21. Kandoth, N.; Claros, M.; Rodriguez, N.; Lloret-Fillol, J., Photoinduced Electron-Transfer in First-Row Transition Metal Complexes. In *Springer Handbook of Inorganic Photochemistry*, Bahnemann, D.; Patrocinio, A. O. T., Eds. Springer International Publishing: Cham, 2022; pp 493-546.
22. Pearson, R. G., Crystal field theory and substitution reactions of metal ions. *Journal of Chemical Education* **1961,** *38* (4), 164.
23. Ishii, T.; Tsuboi, S.; Sakane, G.; Yamashita, M.; Breedlove, B. K., Universal spectrochemical series of six-coordinate octahedral metal complexes for modifying the ligand field splitting. *Dalton Transactions* **2009,** (4), 680-687.
24. Vogler, A.; Kunkely, H., Ligand-to-ligand and intraligand charge transfer and their relation to charge transfer interactions in organic zwitterions. *Coordination Chemistry Reviews* **2007,** *251* (3), 577-583.

25. Nazeeruddin, M. K.; Kalyanasundaram, K., Acid-base behavior in the ground and excited states of ruthenium(II) complexes containing tetraimines or dicarboxybipyridines as protonatable ligands. *Inorganic Chemistry* **1989,** *28* (23), 4251-4259.
26. Vogler, A.; Kunkely, H., Charge Transfer Excitation of Coordination Compounds. Generation of Reactive Intermediates. In *Photosensitization and Photocatalysis Using Inorganic and Organometallic Compounds*, Kalyanasundaram, K.; Grätzel, M., Eds. Springer Netherlands: Dordrecht, 1993; pp 71-111.
27. Durham, B.; Wilson, S. R.; Hodgson, D. J.; Meyer, T. J., Cis-trans photoisomerization in Ru(bpy)2(OH2)22+. Crystal structure of trans-[Ru(bpy)2(OH2)(OH)](ClO4)2. *Journal of the American Chemical Society* **1980,** *102* (2), 600-607.
28. Yoon, S.; Kukura, P.; Stuart, C. M.; Mathies, R. A., Direct observation of the ultrafast intersystem crossing in tris(2,2′-bipyridine)ruthenium(II) using femtosecond stimulated Raman spectroscopy. *Molecular Physics* **2006,** *104* (8), 1275-1282.
29. Pitre, S. P.; McTiernan, C. D.; Scaiano, J. C., Understanding the Kinetics and Spectroscopy of Photoredox Catalysis and Transition-Metal-Free Alternatives. *Accounts of Chemical Research* **2016,** *49* (6), 1320-1330.
30. Jameson, D. M., *Introduction to Fluorescence (1st ed.)*. CRC Press. : 2014.
31. Tschierlei, S.; Neubauer, A.; Rockstroh, N.; Karnahl, M.; Schwarzbach, P.; Junge, H.; Beller, M.; Lochbrunner, S., Ultrafast excited state dynamics of iridium(iii) complexes and their changes upon immobilisation onto titanium dioxide layers. *Physical Chemistry Chemical Physics* **2016,** *18* (16), 10682-10687.
32. Bevernaegie, R.; Marcélis, L.; Moreno-Betancourt, A.; Laramée-Milette, B.; Hanan, G. S.; Loiseau, F.; Sliwa, M.; Elias, B., Ultrafast charge transfer excited state dynamics in trifluoromethyl-substituted iridium(iii) complexes. *Physical Chemistry Chemical Physics* **2018,** *20* (43), 27256-27260.
33. Pomarico, E.; Silatani, M.; Messina, F.; Braem, O.; Cannizzo, A.; Barranoff, E.; Klein, J. H.; Lambert, C.; Chergui, M., Dual Luminescence, Interligand Decay, and Nonradiative Electronic Relaxation of Cyclometalated Iridium Complexes in Solution. *The Journal of Physical Chemistry C* **2016,** *120* (30), 16459-16469.
34. Lowry, M. S.; Hudson, W. R.; Pascal, R. A.; Bernhard, S., Accelerated Luminophore Discovery through Combinatorial Synthesis. *Journal of the American Chemical Society* **2004,** *126* (43), 14129-14135.
35. Pellegrin, Y.; Odobel, F., Sacrificial electron donor reagents for solar fuel production. *Comptes Rendus Chimie* **2017,** *20* (3), 283-295.
36. Schneider, J.; Bahnemann, D. W., Undesired Role of Sacrificial Reagents in Photocatalysis. *The Journal of Physical Chemistry Letters* **2013,** *4* (20), 3479-3483.
37. Elgrishi, N.; Rountree, K. J.; McCarthy, B. D.; Rountree, E. S.; Eisenhart, T. T.; Dempsey, J. L., A Practical Beginner's Guide to Cyclic Voltammetry. *Journal of Chemical Education* **2018,** *95* (2), 197-206.
38. Jones, W. E., Jr.; Fox, M. A., Determination of Excited-State Redox Potentials by Phase-Modulated Voltammetry. *The Journal of Physical Chemistry* **1994,** *98* (19), 5095-5099.
39. Oda, N.; Tsuji, K.; Ichimura, A., Voltammetric Measurements of Redox Potentials of Photo-Excited Species. *Analytical Sciences/Supplements* **2002,** *17icas*, i375-i378.
40. Buzzetti, L.; Crisenza, G. E. M.; Melchiorre, P., Mechanistic Studies in Photocatalysis. *Angewandte Chemie International Edition* **2019,** *58* (12), 3730-3747.
41. Rehm, D.; Weller, A., Kinetics of Fluorescence Quenching by Electron and H-Atom Transfer. *Israel Journal of Chemistry* **1970,** *8* (2), 259-271.

42. Goldsmith, J. I.; Hudson, W. R.; Lowry, M. S.; Anderson, T. H.; Bernhard, S., Discovery and High-Throughput Screening of Heteroleptic Iridium Complexes for Photoinduced Hydrogen Production. *Journal of the American Chemical Society* **2005,** *127* (20), 7502-7510.
43. Scordilis-Kelley, C.; Fuller, J.; Carlin, R. T.; Wilkes, J. S., Alkali Metal Reduction Potentials Measured in Chloroaluminate Ambient-Temperature Molten Salts. *Journal of The Electrochemical Society* **1992,** *139* (3), 694.
44. Connelly, N. G.; Geiger, W. E., Chemical Redox Agents for Organometallic Chemistry. *Chemical Reviews* **1996,** *96* (2), 877-910.
45. Hockin, B. M.; Li, C.; Robertson, N.; Zysman-Colman, E., Photoredox catalysts based on earth-abundant metal complexes. *Catalysis Science & Technology* **2019,** *9* (4), 889-915.
46. Kai, T.; Zhou, M.; Johnson, S.; Ahn, H. S.; Bard, A. J., Direct Observation of C2O4•– and CO2•– by Oxidation of Oxalate within Nanogap of Scanning Electrochemical Microscope. *Journal of the American Chemical Society* **2018,** *140* (47), 16178-16183.
47. Roth, H. G.; Romero, N. A.; Nicewicz, D. A., Experimental and Calculated Electrochemical Potentials of Common Organic Molecules for Applications to Single-Electron Redox Chemistry. *Synlett* **2016,** *27* (05), 714-723.
48. Iordache, A.; Kannappan, R.; Métay, E.; Duclos, M.-C.; Pellet-Rostaing, S.; Lemaire, M.; Milet, A.; Saint-Aman, E.; Bucher, C., Redox control of molecular motions in bipyridinium appended calixarenes. *Organic & Biomolecular Chemistry* **2013,** *11* (26), 4383-4389.
49. Hoffman, M. Z.; Bolletta, F.; Moggi, L.; Hug, G. L., Rate Constants for the Quenching of Excited States of Metal Complexes in Fluid Solution. *Journal of Physical and Chemical Reference Data* **1989,** *18* (1), 219-543.
50. Juneau, A.; Hope, T. O.; Malenfant, J.; Mesko, M.; McNeill, J.; Frenette, M., Methods to Predict Potential Reagents in Iridium-Based Photoredox Catalysis Calibrated with Stern–Volmer Quenching Rate Constants. *ACS Catalysis* **2022,** *12* (4), 2348-2356.
51. Wu, Y.; Kim, D.; Teets, T. S., Photophysical Properties and Redox Potentials of Photosensitizers for Organic Photoredox Transformations. *Synlett* **2021,** *33* (12), 1154-1179.
52. Thopate, S. R.; Kulkarni, M. G.; Puranik, V. G., The Paternò–Büchi Reaction of L-Ascorbic Acid. *Angewandte Chemie International Edition* **1998,** *37* (8), 1110-1112.
53. Lang, X.; Zhao, J.; Chen, X., Cooperative photoredox catalysis. *Chemical Society Reviews* **2016,** *45* (11), 3026-3038.
54. Chan, A. Y.; Perry, I. B.; Bissonnette, N. B.; Buksh, B. F.; Edwards, G. A.; Frye, L. I.; Garry, O. L.; Lavagnino, M. N.; Li, B. X.; Liang, Y.; Mao, E.; Millet, A.; Oakley, J. V.; Reed, N. L.; Sakai, H. A.; Seath, C. P.; MacMillan, D. W. C., Metallaphotoredox: The Merger of Photoredox and Transition Metal Catalysis. *Chemical Reviews* **2022,** *122* (2), 1485-1542.
55. Beller, J.-N.; Beller, M., Spiers Memorial Lecture Artificial photosynthesis: An introduction. *Faraday Discussions* **2019,** *215* (0), 9-14.
56. Reisner, E., When Does Organic Photoredox Catalysis Meet Artificial Photosynthesis? *Angewandte Chemie International Edition* **2019,** *58* (12), 3656-3657.
57. Abe, R.; Bajada, M.; Beller, M.; Bocarsly, A. B.; Butt, Julea N.; Cassiola, F.; Domcke, W.; Durrant, J. R.; Gavrielides, S.; Grätzel, M.; Hammarström, L.; Hatzell, M. C.; König, B.; Kudo, A.; Kuehnel, M. F.; Lage, A.; Lee, C.-Y.; Maneiro, M.; Minteer, S. D.; Paris, A. R.; Plumeré, N.; Reek, J. N. H.; Reisner, E.; Roy, S.; Schnedermann, C.; Shankar, R.; Shylin, S. I.; Smith, W. A.; Soo, H. S.; Wagner, A.; Wielend, D., Beyond artificial photosynthesis: general discussion. *Faraday Discussions* **2019,** *215* (0), 422-438.
58. Gust, D., Chapter One - An Illustrative History of Artificial Photosynthesis. In *Advances in Botanical Research*, Robert, B., Ed. Academic Press: 2016; Vol. 79, pp 1-42.
59. Qiao, J.; Liu, Y.; Hong, F.; Zhang, J., A review of catalysts for the electroreduction of carbon dioxide to produce low-carbon fuels. *Chemical Society Reviews* **2014,** *43* (2), 631-675.

60. Appel, A. M.; Bercaw, J. E.; Bocarsly, A. B.; Dobbek, H.; DuBois, D. L.; Dupuis, M.; Ferry, J. G.; Fujita, E.; Hille, R.; Kenis, P. J. A.; Kerfeld, C. A.; Morris, R. H.; Peden, C. H. F.; Portis, A. R.; Ragsdale, S. W.; Rauchfuss, T. B.; Reek, J. N. H.; Seefeldt, L. C.; Thauer, R. K.; Waldrop, G. L., Frontiers, Opportunities, and Challenges in Biochemical and Chemical Catalysis of CO2 Fixation. *Chemical Reviews* **2013,** *113* (8), 6621-6658.
61. Han, Z.; Eisenberg, R., Fuel from Water: The Photochemical Generation of Hydrogen from Water. *Accounts of Chemical Research* **2014,** *47* (8), 2537-2544.
62. Kaeffer, N.; Chavarot-Kerlidou, M.; Artero, V., Hydrogen Evolution Catalyzed by Cobalt Diimine–Dioxime Complexes. *Accounts of Chemical Research* **2015,** *48* (5), 1286-1295.
63. Queyriaux, N.; Jane, R. T.; Massin, J.; Artero, V.; Chavarot-Kerlidou, M., Recent developments in hydrogen evolving molecular cobalt(II)–polypyridyl catalysts. *Coordination Chemistry Reviews* **2015,** *304-305*, 3-19.
64. Zee, D. Z.; Chantarojsiri, T.; Long, J. R.; Chang, C. J., Metal–Polypyridyl Catalysts for Electro- and Photochemical Reduction of Water to Hydrogen. *Accounts of Chemical Research* **2015,** *48* (7), 2027-2036.
65. Lewis, N. S.; Nocera, D. G., Powering the planet: Chemical challenges in solar energy utilization. *Proceedings of the National Academy of Sciences* **2006,** *103* (43), 15729-15735.
66. Inoue, H.; Shimada, T.; Kou, Y.; Nabetani, Y.; Masui, D.; Takagi, S.; Tachibana, H., The Water Oxidation Bottleneck in Artificial Photosynthesis: How Can We Get Through It? An Alternative Route Involving a Two-Electron Process. *ChemSusChem* **2011,** *4* (2), 173-179.
67. Lin, L.; Hisatomi, T.; Chen, S.; Takata, T.; Domen, K., Visible-Light-Driven Photocatalytic Water Splitting: Recent Progress and Challenges. *Trends in Chemistry* **2020,** *2* (9), 813-824.
68. Tian, X.; Guo, Y.; An, W.; Ren, Y.-L.; Qin, Y.; Niu, C.; Zheng, X., Coupling photocatalytic water oxidation with reductive transformations of organic molecules. *Nature Communications* **2022,** *13* (1), 6186.
69. Zhou, R.; Ma, L.; Yang, X.; Cao, J., Recent advances in visible-light photocatalytic deuteration reactions. *Organic Chemistry Frontiers* **2021,** *8* (3), 426-444.
70. Silverstein, T. P.; Heller, S. T., pKa Values in the Undergraduate Curriculum: What Is the Real pKa of Water? *Journal of Chemical Education* **2017,** *94* (6), 690-695.
71. Valenzuela, M. A.; Albiter, E.; Ríos-Bernÿ, O.; Córdova, I.; Flores, S. O., Photocatalytic Reduction of Organic Compounds. **2010,** *13* (3), 321-340.
72. Czyz, M. L.; Taylor, M. S.; Horngren, T. H.; Polyzos, A., Reductive Activation and Hydrofunctionalization of Olefins by Multiphoton Tandem Photoredox Catalysis. *ACS Catalysis* **2021,** *11* (9), 5472-5480.
73. Kamei, Y.; Seino, Y.; Yamaguchi, Y.; Yoshino, T.; Maeda, S.; Kojima, M.; Matsunaga, S., Silane- and peroxide-free hydrogen atom transfer hydrogenation using ascorbic acid and cobalt-photoredox dual catalysis. *Nature Communications* **2021,** *12* (1), 966.
74. Li, J.; Yang, J.; Wen, F.; Li, C., A visible-light-driven transfer hydrogenation on CdS nanoparticles combined with iridium complexes. *Chemical Communications* **2011,** *47* (25), 7080-7082.
75. Boonstra, A. H.; Mutsaers, C. A. H. A., Photohydrogenation of ethyne and ethene on the surface of titanium dioxide. *The Journal of Physical Chemistry* **1975,** *79* (19), 2025-2027.
76. Shimakoshi, H.; Hisaeda, Y., B12-TiO2 Hybrid Catalyst for Light-Driven Hydrogen Production and Hydrogenation of C□C Multiple Bonds. *ChemPlusChem* **2014,** *79* (9), 1250-1253.
77. Litman, Z. C.; Wang, Y.; Zhao, H.; Hartwig, J. F., Cooperative asymmetric reactions combining photocatalysis and enzymatic catalysis. *Nature* **2018,** *560* (7718), 355-359.

78. Nakano, Y.; Black, M. J.; Meichan, A. J.; Sandoval, B. A.; Chung, M. M.; Biegasiewicz, K. F.; Zhu, T.; Hyster, T. K., Photoenzymatic Hydrogenation of Heteroaromatic Olefins Using 'Ene'-Reductases with Photoredox Catalysts. *Angewandte Chemie International Edition* **2020,** *59* (26), 10484-10488.
79. Kim, J.; Lee, S. H.; Tieves, F.; Choi, D. S.; Hollmann, F.; Paul, C. E.; Park, C. B., Biocatalytic C=C Bond Reduction through Carbon Nanodot-Sensitized Regeneration of NADH Analogues. *Angewandte Chemie International Edition* **2018,** *57* (42), 13825-13828.
80. Mifsud, M.; Gargiulo, S.; Iborra, S.; Arends, I. W. C. E.; Hollmann, F.; Corma, A., Photobiocatalytic chemistry of oxidoreductases using water as the electron donor. *Nature Communications* **2014,** *5* (1), 3145.
81. Ishitani, O.; Pac, C.; Sakurai, H., Redox-photosensitized reactions. 10. Formation of a novel type of adduct between an NADH model and carbonyl compounds by photosensitization using Ru(bpy)32+. *The Journal of Organic Chemistry* **1983,** *48* (17), 2941-2942.
82. Mandler, D.; Willner, I., Photosensitized NAD(P)H regeneration systems; application in the reduction of butan-2-one, pyruvic, and acetoacetic acids and in the reductive amination of pyruvic and oxoglutaric acid to amino acid. *Journal of the Chemical Society, Perkin Transactions 2* **1986,** (6), 805-811.
83. Ishitani, O.; Yanagida, S.; Takamuku, S.; Pac, C., Redox-photosensitized reactions. 13. Ru(bpy)32+-photosensitized reactions of an NADH model, 1-benzyl-1,4-dihydronicotinamide, with aromatic carbonyl compounds and comparison with thermal reactions. *The Journal of Organic Chemistry* **1987,** *52* (13), 2790-2796.
84. Robertson, P. A.; Bishop, H. M.; Orr-Ewing, A. J., Tuning the Excited-State Dynamics of Acetophenone Using Metal Ions in Solution. *The Journal of Physical Chemistry Letters* **2021,** *12* (23), 5473-5478.
85. El Moncef, A.; Cuquerella, M. C.; Zaballos, E.; Ramírez de Arellano, C.; Ben-Tama, A.; Stiriba, S.-E.; Pérez-Prieto, J., Efficient ultraviolet-light energy dissipation by an aromatic ketone. *Chemical Communications* **2010,** *46* (5), 800-802.
86. Cao, D.; Ataya, M.; Chen, Z.; Zeng, H.; Peng, Y.; Khaliullin, R. Z.; Li, C.-J., Light-driven transition-metal-free direct decarbonylation of unstrained diaryl ketones via a dual C–C bond cleavage. *Nature Communications* **2022,** *13* (1), 1805.
87. Pérez-Prieto, J.; Galian, R. E.; Morant-Miñana, M. C., Aromatic Ketones as Photocatalysts: Combined Action as Triplet Photosensitiser and Ground State Electron Acceptor. *ChemPhysChem* **2006,** *7* (10), 2077-2080.
88. Liu, X.; Sun, D.; Yuan, R.; Fu, X.; Li, Z., Efficient visible-light-induced hydrogenation over composites of CdS and ruthenium carbonyl complexes. *Journal of Catalysis* **2013,** *304*, 1-6.
89. Choudhury, S.; Baeg, J.-O.; Park, N.-J.; Yadav, R. K., A Photocatalyst/Enzyme Couple That Uses Solar Energy in the Asymmetric Reduction of Acetophenones. *Angewandte Chemie International Edition* **2012,** *51* (46), 11624-11628.
90. Choudhury, S.; Baeg, J.-O.; Park, N.-J.; Yadav, R. K., A solar light-driven, eco-friendly protocol for highly enantioselective synthesis of chiral alcohols via photocatalytic/biocatalytic cascades. *Green Chemistry* **2014,** *16* (9), 4389-4400.
91. Ghosh, T.; Slanina, T.; König, B., Visible light photocatalytic reduction of aldehydes by Rh(iii)–H: a detailed mechanistic study. *Chemical Science* **2015,** *6* (3), 2027-2034.
92. Call, A.; Casadevall, C.; Acuña-Parés, F.; Casitas, A.; Lloret-Fillol, J., Dual cobalt–copper light-driven catalytic reduction of aldehydes and aromatic ketones in aqueous media. *Chemical Science* **2017,** *8* (7), 4739-4749.

93. Guo, X.; Wenger, O. S., Reductive Amination by Photoredox Catalysis and Polarity-Matched Hydrogen Atom Transfer. *Angewandte Chemie International Edition* **2018,** *57* (9), 2469-2473.
94. Xi, Z.-W.; Yang, L.; Wang, D.-Y.; Pu, C.-D.; Shen, Y.-M.; Wu, C.-D.; Peng, X.-G., Visible-Light Photocatalytic Synthesis of Amines from Imines via Transfer Hydrogenation Using Quantum Dots as Catalysts. *The Journal of Organic Chemistry* **2018,** *83* (19), 11886-11895.
95. van As, D. J.; Connell, T. U.; Brzozowski, M.; Scully, A. D.; Polyzos, A., Photocatalytic and Chemoselective Transfer Hydrogenation of Diarylimines in Batch and Continuous Flow. *Organic Letters* **2018,** *20* (4), 905-908.
96. Wang, R.; Ma, M.; Gong, X.; Panetti, G. B.; Fan, X.; Walsh, P. J., Visible-Light-Mediated Umpolung Reactivity of Imines: Ketimine Reductions with Cy2NMe and Water. *Organic Letters* **2018,** *20* (8), 2433-2436.
97. Guo, X.; Okamoto, Y.; Schreier, M. R.; Ward, T. R.; Wenger, O. S., Enantioselective synthesis of amines by combining photoredox and enzymatic catalysis in a cyclic reaction network. *Chemical Science* **2018,** *9* (22), 5052-5056.
98. Liao, L.-L.; Song, L.; Yan, S.-S.; Ye, J.-H.; Yu, D.-G., Highly reductive photocatalytic systems in organic synthesis. *Trends in Chemistry* **2022,** *4* (6), 512-527.
99. von Wolff, N.; Robert, M., Taming Electron Transfers: From Breaking Bonds to Creating Molecules. *The Chemical Record* **2021,** *21* (9), 2095-2106.
100. Aragón, J.; Sun, S.; Pascual, D.; Jaworski, S.; Lloret-Fillol, J., Photoredox Activation of Inert Alkyl Chlorides for the Reductive Cross-Coupling with Aromatic Alkenes. *Angewandte Chemie International Edition* **2022,** *61* (21), e202114365.
101. Yin, H.; Jin, Y.; Hertzog, J. E.; Mullane, K. C.; Carroll, P. J.; Manor, B. C.; Anna, J. M.; Schelter, E. J., The Hexachlorocerate(III) Anion: A Potent, Benchtop Stable, and Readily Available Ultraviolet A Photosensitizer for Aryl Chlorides. *Journal of the American Chemical Society* **2016,** *138* (50), 16266-16273.
102. Glaser, F.; Kerzig, C.; Wenger, O. S., Multi-Photon Excitation in Photoredox Catalysis: Concepts, Applications, Methods. *Angewandte Chemie International Edition* **2020,** *59* (26), 10266-10284.
103. Markushyna, Y.; Savateev, A., Light as a Tool in Organic Photocatalysis: Multi-Photon Excitation and Chromoselective Reactions. *European Journal of Organic Chemistry* **2022,** *2022* (24), e202200026.
104. Goez, M.; Zubarev, V., Light intensity dependence of a two-photon catalytic cycle: photoionization via absorption–electron transfer–absorption. *Chemical Physics* **2000,** *256* (1), 107-116.
105. Connell, T. U.; Fraser, C. L.; Czyz, M. L.; Smith, Z. M.; Hayne, D. J.; Doeven, E. H.; Agugiaro, J.; Wilson, D. J. D.; Adcock, J. L.; Scully, A. D.; Gómez, D. E.; Barnett, N. W.; Polyzos, A.; Francis, P. S., The Tandem Photoredox Catalysis Mechanism of [Ir(ppy)2(dtb-bpy)]+ Enabling Access to Energy Demanding Organic Substrates. *Journal of the American Chemical Society* **2019,** *141* (44), 17646-17658.
106. Kerzig, C.; Guo, X.; Wenger, O. S., Unexpected Hydrated Electron Source for Preparative Visible-Light Driven Photoredox Catalysis. *Journal of the American Chemical Society* **2019,** *141* (5), 2122-2127.
107. Ghosh, I.; Ghosh, T.; Bardagi, J. I.; König, B., Reduction of aryl halides by consecutive visible light-induced electron transfer processes. *Science* **2014,** *346* (6210), 725-728.
108. Ghosh, I.; König, B., Chromoselective Photocatalysis: Controlled Bond Activation through Light-Color Regulation of Redox Potentials. *Angewandte Chemie International Edition* **2016,** *55* (27), 7676-7679.

109. Xu, J.; Cao, J.; Wu, X.; Wang, H.; Yang, X.; Tang, X.; Toh, R. W.; Zhou, R.; Yeow, E. K. L.; Wu, J., Unveiling Extreme Photoreduction Potentials of Donor–Acceptor Cyanoarenes to Access Aryl Radicals from Aryl Chlorides. *Journal of the American Chemical Society* **2021,** *143* (33), 13266-13273.
110. Herrera-Luna, J. C.; Díaz, D. D.; Jiménez, M. C.; Pérez-Ruiz, R., Highly Efficient Production of Heteroarene Phosphonates by Dichromatic Photoredox Catalysis. *ACS Applied Materials & Interfaces* **2021,** *13* (41), 48784-48794.
111. MacKenzie, I. A.; Wang, L.; Onuska, N. P. R.; Williams, O. F.; Begam, K.; Moran, A. M.; Dunietz, B. D.; Nicewicz, D. A., Discovery and characterization of an acridine radical photoreductant. *Nature* **2020,** *580* (7801), 76-80.
112. Cole, J. P.; Chen, D.-F.; Kudisch, M.; Pearson, R. M.; Lim, C.-H.; Miyake, G. M., Organocatalyzed Birch Reduction Driven by Visible Light. *Journal of the American Chemical Society* **2020,** *142* (31), 13573-13581.
113. Widness, J. K.; Enny, D. G.; McFarlane-Connelly, K. S.; Miedenbauer, M. T.; Krauss, T. D.; Weix, D. J., CdS Quantum Dots as Potent Photoreductants for Organic Chemistry Enabled by Auger Processes. *Journal of the American Chemical Society* **2022,** *144* (27), 12229-12246.
114. Giedyk, M.; Narobe, R.; Weiß, S.; Touraud, D.; Kunz, W.; König, B., Photocatalytic activation of alkyl chlorides by assembly-promoted single electron transfer in microheterogeneous solutions. *Nature Catalysis* **2020,** *3* (1), 40-47.
115. Li, H.; Wenger, O. S., Photophysics of Perylene Diimide Dianions and Their Application in Photoredox Catalysis. *Angewandte Chemie International Edition* **2022,** *61* (5), e202110491.
116. Marchini, M.; Gualandi, A.; Mengozzi, L.; Franchi, P.; Lucarini, M.; Cozzi, P. G.; Balzani, V.; Ceroni, P., Mechanistic insights into two-photon-driven photocatalysis in organic synthesis. *Physical Chemistry Chemical Physics* **2018,** *20* (12), 8071-8076.
117. Brandl, F.; Bergwinkl, S.; Allacher, C.; Dick, B., Consecutive Photoinduced Electron Transfer (conPET): The Mechanism of the Photocatalyst Rhodamine 6G. *Chemistry – A European Journal* **2020,** *26* (35), 7946-7954.
118. Beckwith, J. S.; Aster, A.; Vauthey, E., The excited-state dynamics of the radical anions of cyanoanthracenes. *Physical Chemistry Chemical Physics* **2022,** *24* (1), 568-577.
119. Fujitsuka, M.; Majima, T., Reaction dynamics of excited radical ions revealed by femtosecond laser flash photolysis. *Journal of Photochemistry and Photobiology C: Photochemistry Reviews* **2018,** *35*, 25-37.
120. Cotta, M. A., Quantum Dots and Their Applications: What Lies Ahead? *ACS Applied Nano Materials* **2020,** *3* (6), 4920-4924.
121. Nishitani, J.; Yamamoto, Y.-i.; West, C. W.; Karashima, S.; Suzuki, T., Binding energy of solvated electrons and retrieval of true UV photoelectron spectra of liquids. *Science Advances 5* (8), eaaw6896.
122. Hara, A.; Yamamoto, Y.-i.; Suzuki, T., Solvated electron formation from the conduction band of liquid methanol: Transformation from a shallow to deep trap state. *The Journal of Chemical Physics* **2019,** *151* (11), 114503.
123. Grills, D. C.; Lymar, S. V., Solvated Electron in Acetonitrile: Radiation Yield, Absorption Spectrum, and Equilibrium between Cavity- and Solvent-Localized States. *The Journal of Physical Chemistry B* **2022,** *126* (1), 262-269.
124. Kadhum, A. A. H.; Salmon, G. A., Reactivity of solvated electrons in tetrahydrofuran. *Journal of the Chemical Society, Faraday Transactions 1: Physical Chemistry in Condensed Phases* **1986,** *82* (8), 2521-2530.
125. Buttersack, T.; Mason, P. E.; McMullen, R. S.; Schewe, H. C.; Martinek, T.; Brezina, K.; Crhan, M.; Gomez, A.; Hein, D.; Wartner, G.; Seidel, R.; Ali, H.; Thürmer, S.; Marsalek,

O.; Winter, B.; Bradforth, S. E.; Jungwirth, P., Photoelectron spectra of alkali metal–ammonia microjets: From blue electrolyte to bronze metal. *Science* **2020,** *368* (6495), 1086-1091.
126. Chaban, V. V.; Prezhdo, O. V., Electron Solvation in Liquid Ammonia: Lithium, Sodium, Magnesium, and Calcium as Electron Sources. *The Journal of Physical Chemistry B* **2016,** *120* (9), 2500-2506.
127. Rumbach, P.; Bartels, D. M.; Sankaran, R. M.; Go, D. B., The solvation of electrons by an atmospheric-pressure plasma. *Nature Communications* **2015,** *6* (1), 7248.
128. Goez, M.; Kerzig, C.; Naumann, R., An "All-Green" Catalytic Cycle of Aqueous Photoionization. *Angewandte Chemie International Edition* **2014,** *53* (37), 9914-9916.
129. Pavlishchuk, V. V.; Addison, A. W., Conversion constants for redox potentials measured versus different reference electrodes in acetonitrile solutions at 25°C. *Inorganica Chimica Acta* **2000,** *298* (1), 97-102.
130. Buxton, G. V.; Greenstock, C. L.; Helman, W. P.; Ross, A. B., Critical Review of rate constants for reactions of hydrated electrons, hydrogen atoms and hydroxyl radicals (·OH/·O− in Aqueous Solution. *Journal of Physical and Chemical Reference Data* **1988,** *17* (2), 513-886.
131. Naumann, R.; Goez, M., First Micelle-Free Photoredox Catalytic Access to Hydrated Electrons for Syntheses and Remediations with a Visible LED or even Sunlight. *Chemistry – A European Journal* **2018,** *24* (66), 17557-17567.
132. Naumann, R.; Lehmann, F.; Goez, M., Micellized Tris(bipyridine)ruthenium Catalysts Affording Preparative Amounts of Hydrated Electrons with a Green Light-Emitting Diode. *Chemistry – A European Journal* **2018,** *24* (50), 13259-13269.
133. Naumann, R.; Goez, M., A Green-LED Driven Source of Hydrated Electrons Characterized from Microseconds to Hours and Applied to Cross-Couplings. *Chemistry – A European Journal* **2018,** *24* (39), 9833-9840.
134. Naumann, R.; Lehmann, F.; Goez, M., Generating Hydrated Electrons for Chemical Syntheses by Using a Green Light-Emitting Diode (LED). *Angewandte Chemie International Edition* **2018,** *57* (4), 1078-1081.
135. Liu, J.; Lu, L.; Wood, D.; Lin, S., New Redox Strategies in Organic Synthesis by Means of Electrochemistry and Photochemistry. *ACS Central Science* **2020,** *6* (8), 1317-1340.
136. Tay, N. E. S.; Lehnherr, D.; Rovis, T., Photons or Electrons? A Critical Comparison of Electrochemistry and Photoredox Catalysis for Organic Synthesis. *Chemical Reviews* **2022,** *122* (2), 2487-2649.
137. Jeong, D. Y.; Lee, D. S.; Lee, H. L.; Nah, S.; Lee, J. Y.; Cho, E. J.; You, Y., Evidence and Governing Factors of the Radical-Ion Photoredox Catalysis. *ACS Catalysis* **2022,** *12* (10), 6047-6059.
138. Cowper, N. G. W.; Chernowsky, C. P.; Williams, O. P.; Wickens, Z. K., Potent Reductants via Electron-Primed Photoredox Catalysis: Unlocking Aryl Chlorides for Radical Coupling. *Journal of the American Chemical Society* **2020,** *142* (5), 2093-2099.
139. Kim, H.; Kim, H.; Lambert, T. H.; Lin, S., Reductive Electrophotocatalysis: Merging Electricity and Light To Achieve Extreme Reduction Potentials. *Journal of the American Chemical Society* **2020,** *142* (5), 2087-2092.
140. Chernowsky, C. P.; Chmiel, A. F.; Wickens, Z. K., Electrochemical Activation of Diverse Conventional Photoredox Catalysts Induces Potent Photoreductant Activity**. *Angewandte Chemie International Edition* **2021,** *60* (39), 21418-21425.
141. Rieth, A. J.; Gonzalez, M. I.; Kudisch, B.; Nava, M.; Nocera, D. G., How Radical Are "Radical" Photocatalysts? A Closed-Shell Meisenheimer Complex Is Identified as a Super-Reducing Photoreagent. *Journal of the American Chemical Society* **2021,** *143* (35), 14352-14359.

Chapter 2

Main Objectives and Summary of Chapters

UNIVERSITAT ROVIRA I VIRGILI
PHOTOREDOX CATALYSIS MEDIATED BY TRANSITION METAL COMPLEXES.
TOWARDS CHALLENGING ORGANIC REDUCTIONS
David Pascual Gascón

A prerequisite for a sustainable society is to develop new efficient, economic, and greener synthetic methods. The use of sun light as a source of energy is one of the most sustainable approaches. In the same direction, water is the ideal source of hydrogen equivalents for reductive organic transformations. In this context, metallaphotoredox catalysis is a challenging but promising platform for the reduction of double bonds. On the other hand, the use of photoredox catalysts for highly reductive transformations has recently opened the door to mechanistic pathways based on multiphoton absorption. Nonetheless, the accessible reactivity is frequently attributed to intermediates with a controversial sub-nanosecond lifetime, then further research is needed to understand how these processes work.

Based on these premises, the main aims of the current thesis are:

- Optimization of reaction conditions for the selective photoreduction of aromatic ketones in the presence of aromatic olefins (and *vice versa*) in aqueous media. This will be pursued by rationally tuning the activity of the dual catalytic system.
- Revisit the photocatalytic transfer hydrogenation to aromatic ketones in aqueous media but using chiral-at-ligand [M–H] species. Study the effect of synthetic modifications in the chiral ligand.
- Develop a methodology for the isolation of reduced derivatives of iridium photoredox catalysts, in order to examine its second excitation process and shed light on current mechanistic uncertainness.

To this end, following the previously stated objectives, this thesis takes the chemistry developed in our research group in recent years as a starting point. Specifically, it starts (*Chapter 3*) from a previously reported catalytic system based on earth-abundant elements (Co/Cu) that reduced aryl ketones using visible light as the driving force and H_2O/amine as the hydride source. Further studies in the group extended this dual system for the reduction of aromatic olefins, and based on our mechanistic understanding, we have envisioned that selectivity in the reduction of

aromatic ketones *versus* aromatic olefins could be predictably tuned upon optimization of the catalytic conditions.

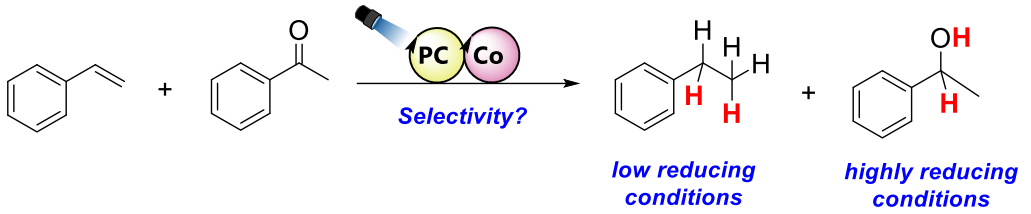

Scheme 2. 1. Light-driven competitive reduction of aromatic ketones *vs* aromatic olefins in aqueous media, *Chapter 3*.

According to our mechanistic insights, for *Chapter 4* we have contemplated that introducing chirality into the cobalt complex would lead to the enantioselective reduction of aromatic ketones. We propose to design and synthesize chiral ligands whose pyridine rings have substituents in the *ortho*- or *meta*- position, so that the introduction of steric hindrance near the reaction centre favours the chirality transfer.

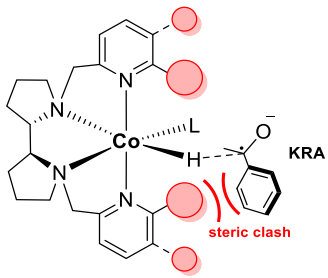

Scheme 2. 2. Enantioselective reduction of acetophenone by chiral cobalt complexes, *Chapter 4*.

The main project of this thesis is presented in *Chapter 5*. We endeavour to study if an absorption-reduction-absorption catalytic cycle can be operative in heteroleptic iridium complexes, what has been proposed but not demonstrated yet. We have designed some experiments to try to clarify this information, including transient spectroscopic studies carried out during an international stay at Imperial College London with Prof. James Durrant.

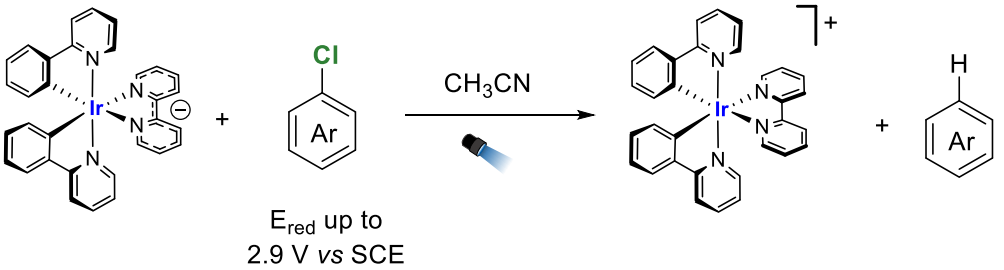

Scheme 2. 3. Studies on the intermediate of reductive quenching cycle of iridium photoredox catalysts, *Chapter 5*.

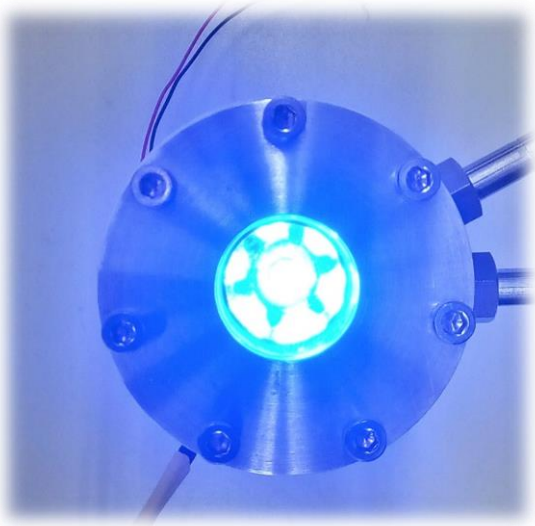

'There is no better catalyst than motivation'

Chapter 3

Studies on the photocatalytic reduction of aromatic olefins in aqueous media

The results described in this chapter have been published in:

Casadevall, C.; Pascual, D.; Aragón, J.; Call, A.; Casitas, A.; Casademont-Reig, I.; Lloret-Fillol, J. *Chem. Sci.* **2022**, *13*, 4270-4282.

UNIVERSITAT ROVIRA I VIRGILI
PHOTOREDOX CATALYSIS MEDIATED BY TRANSITION METAL COMPLEXES.
TOWARDS CHALLENGING ORGANIC REDUCTIONS
David Pascual Gascón

3.1 State of the art

Using sunlight as a driving force is a promising but challenging strategy towards sustainability in chemical production.[1-5] As introduced in Chapter 1, artificial photosynthesis (AP) exploits water and visible light to provide a clean source of reductive equivalents, what has been mainly studied in CO_2[6, 7] and H_2O[8-11] reduction. However, it is reasonable that the same or similar photocatalytic systems might also catalyse organic reductive reactions, a field with still limited progress in the context of AP. A challenging transformation in this direction is the hydrogenation of double bonds.[5] Among other difficulties, developed synthetic protocols for olefin reduction rely on the activation of H_2, silanes or alcohols, but are not suitable for operation under aqueous conditions.[12-14] Moreover, selectivity of olefin reduction *versus* water reduction is needed to use these systems practically. Besides, only a few studies used light to drive these reactions.

Initially, semiconductor materials such as TiO_2 and CdS were used as photoredox catalysts (PC) for the light-driven hydrogenation of a limited number of olefins,[15-26] what established the first connection between this transformation and AP. These systems generally required UV light or noble metals to obtain moderate selectivity for alkane formation. In 2014, Hishaeda and co-workers employed a B_{12}–TiO_2 hybrid for the UV light-driven reduction of alkenes to alkanes.[27] Unluckily, the highly energetic conditions led to the formation of dimeric products compromising the selectivity. Another remarkable example in aqueous media was presented by Qiu and co-workers, in which substituted olefins and alkynes could be reduced by Pd nanoparticles on the surface of a KCl-modified polymeric carbon nitride nanosheet (PCN-KCl) as PC.[25]

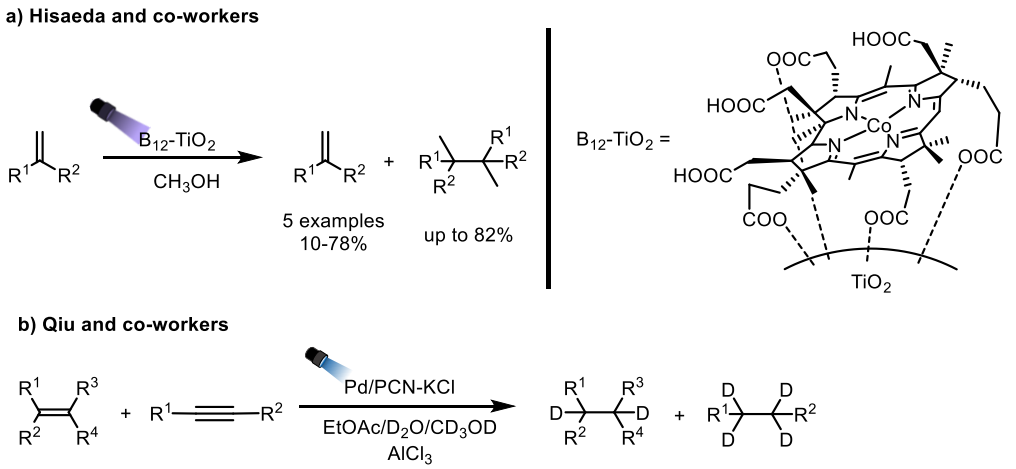

Scheme 3.1. Selected examples of the photocatalytic reduction of olefins in aqueous media using heterogeneous systems were reported by (a) Hishaeda and (b) Qiu. (references 25 and 27).

Another elegant approach to connect AP with the reduction of double bonds is using enzymes, which inherently operate in aqueous media. Holland, Corma and co-workers introduced the stereoselective hydrogenation of the C=C bond of ketoisophorone by combining the photocatalytic activity of Au nanoparticles supported on TiO_2 with the enzymatic activity of oxidoreductases, with FAD^+ as a mediator (Scheme 3.2a).[28] The uniqueness of this system lies in exploiting water as a source of protons and electrons, then releasing oxygen as a by-product. Todd Hyster used ene-reductases with $[Ru(bpy)_3]Cl_2$ as PC for the enantioselective hydrogenation of heteroaromatic olefins (Scheme 3.2b).[29] Likewise, Hartwig, Zhao and co-workers reported a cooperative chemoenzymatic reaction that combines the sequential isomerisation of inactive olefins by an iridium PC, with the hydrogenation activity of ene-reductases. Electron-deficient aromatic olefins are selectively reduced to their corresponding alkanes in high enantiomeric excess (88–99% ee, Scheme 3.2c).[30]

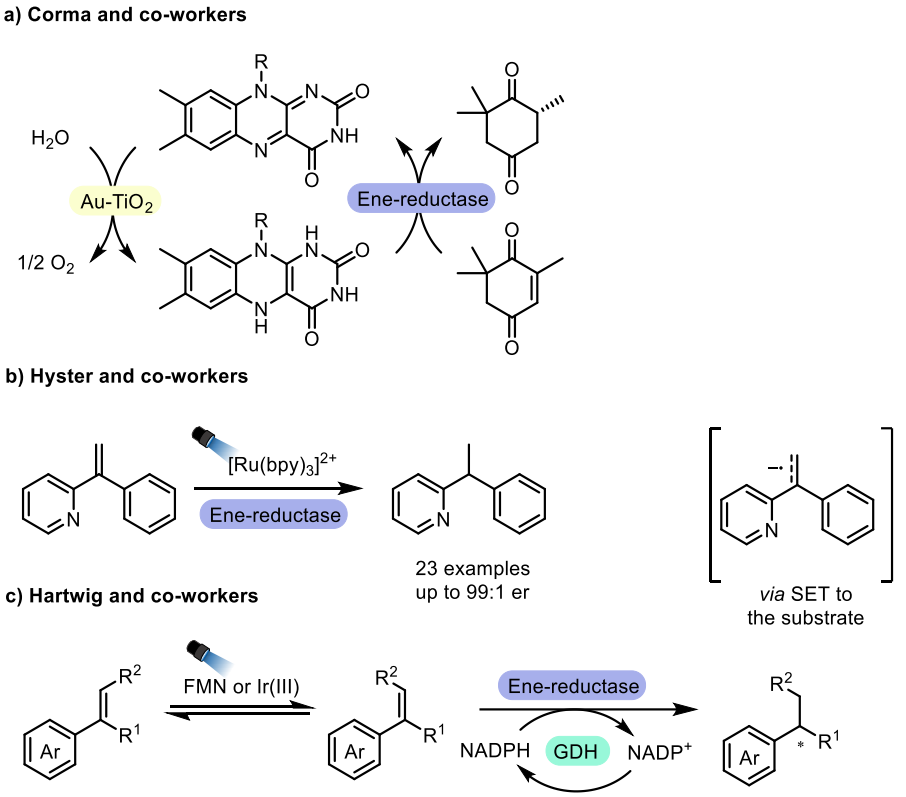

Scheme 3.2. State-of-the-art selected examples of the enantioselective reduction of olefins using photobiocatalytic systems by (a) Corma (R = 2*R*,3*S*,4*S*-trihydroxypentyl dihydrogen phosphate), (b) Hyster and (c) Hartwig. (references 28, 29 and 30).

Moving from vast enzymes to the molecular scale, the use of well-defined homogeneous catalysts permits a deeper understanding and control of the reactivity. Recently, Cambeiro and co-workers reported the reduction of aromatic 1,2-disubstituted alkenes using a Hantzsch ester for the initial HAT, and an iridium PC for the subsequent single electron transfer (SET), although good yields were obtained only for activated olefins.[31] At the same time, Kojima, Matsunaga and co-workers found that glyoxime-type complexes with a PCy_3 ligand and a ruthenium PC reduce aliphatic alkenes via a hydrogen atom transfer (HAT) mechanism (Scheme 3.3a).[32] However, aromatic alkenes have additional difficulties such as their tendency to engage in radical polymerization[33] or isomerization[34-37] reactions under reductive conditions, which makes their reduction under photocatalytic conditions more challenging. By a conceptually different

approach, Guo, Wenger and co-workers recently reported the reduction of olefins by the organometallic iridium hydride complex [Cp*Ir^{III}(phen)–H], which participates both in SET and HAT processes after excitation.[38] Alternatively, Conell and co-workers showed the reduction of aromatic olefins *via* direct photoinduced electron transfer under highly reductive conditions and light intensity (Scheme 3.3b).[39]

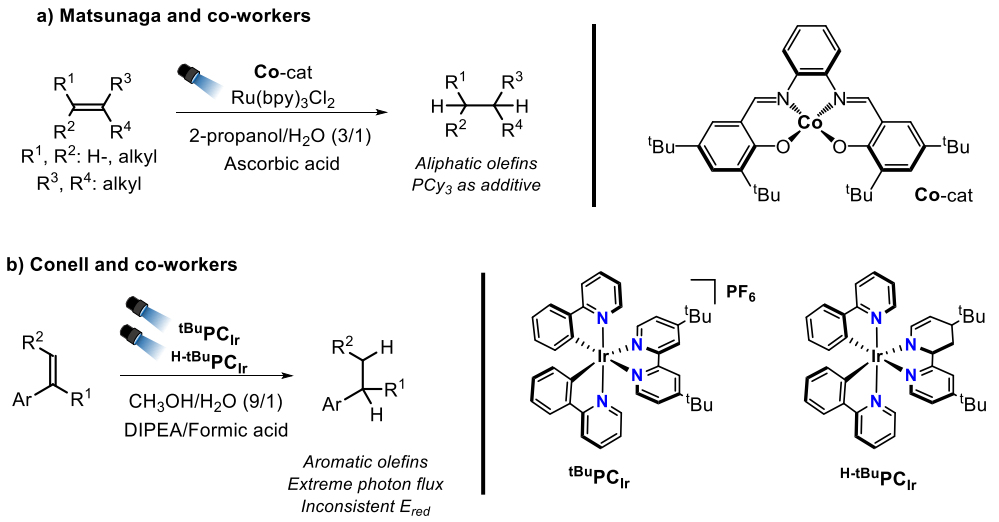

Scheme 3.3. State-of the art selected examples of the photocatalytic reduction of olefins using molecular catalysts in aqueous media (references 32 and 39).

Ideally, AP systems should employ water as an environmentally benign source of hydrogen atoms and use the PC in combination with molecular catalysts to facilitate the selective reduction of alkenes. Furthermore, such an approach should identify catalysts' hits to develop more complex AP schemes. Towards this goal, we previously reported a dual catalytic system formed by **1$_{Co}$** (formula [Co(OTf)(Py$_2$^{Ts}tacn)](OTf), where Py$_2$^{Ts}tacn = 1,4-di(picolyl)-7-(ptoluenesulfonyl)-1,4,7-triazacyclononane, OTf = trifluoromethanesulfonate anion) as reduction catalyst and **PC$_{Cu}$** (formula [Cu(bathocuproine)(xantphos)](PF$_6$))[40] as PC, which efficiently reduces water to hydrogen[41] and carbonyl groups to alcohols,[42] using water as hydrogen source. Moreover, the system presents a unique selectivity for reducing acetophenone in front of aliphatic aldehydes, unprecedented for metal-catalysed transformations (Figure 3.1).

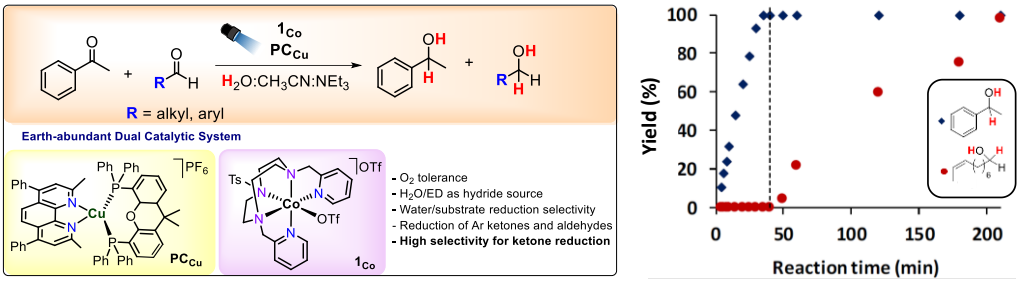

Figure 3.1 (Left) Earth-abundant dual catalytic system for the photoreduction of aromatic ketones and aldehydes. (Right) Plot of the selective reduction of an aromatic ketone in front of an aliphatic aldehyde. The dotted line indicates the point where the aldehyde starts reacting.

As summarised in Figure 3.2, our mechanistic studies suggested that the [Co^{II}] precursor undergoes SET to form the more nucleophilic [Co^{I}] species, which reacts with protons to form the [Co^{III}–H]. However, this hydride is not strong enough to react and suffers an additional SET to form the key intermediate [**Co^{II}–H**] ([Co(H)($Py_2{}^{Ts}$tacn)]$^+$), which was a common species in both reduction reactions. To close the cycle, different pathways can operate depending on the substrate: reactivity experiments support a hydride transfer step (Figure 3.2) for substrates with more negative redox potentials (>-2 V), such as aliphatic aldehydes, while those with more accessible redox potential such as aromatic ketones can be reduced via HAT to the corresponding ketyl radical anion (KRA in Figure 3.2, cycle on the right). Nevertheless, both homolytic and heterolytic pathways could coexist depending on the redox potential of the substrate.

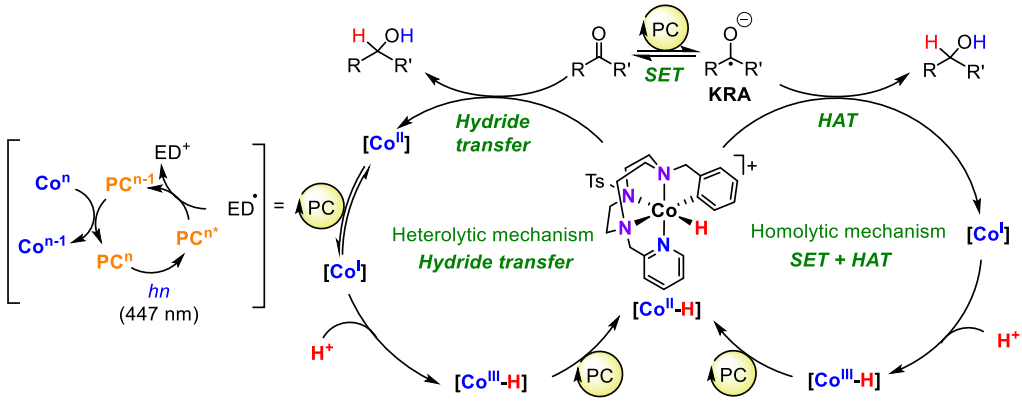

Figure 3.2 Possible mechanistic scenarios for the photoreduction of aromatic ketones and aldehydes. Acronyms stand for PC = photoredox catalyst; ED = electron donor; SET = single electron transfer and HAT = hydrogen atom transfer.

Based on these precedents, we hypothesised that [**Co^{II}–H**] should also be reactive enough to reduce other organic functionalities, such as aromatic olefins, without strong reducing agents. Indeed, we developed a dual catalytic system consisting of cobalt complexes based on nitrogenated ligands, a photoredox catalyst and an electron donor to reduce styrene derivatives using light as an energy source.[43] The reduction operates without using typical hydrogen sources such as silanes, H_2, HCO_2H or alcohols. The best-performing catalytic system is obtained by combining **1$_{Co}$** and **PC$_{Cu}$** under light irradiation employing H_2O/Et_3N as a hydride source (Scheme 3.4). Reactivity and mechanistic studies based on kinetics, isotopic labelling and radical clock experiments suggest that the reduction of aromatic olefins occurs via a HAT mechanism, most likely through a [**Co^{II}–H**] intermediate.

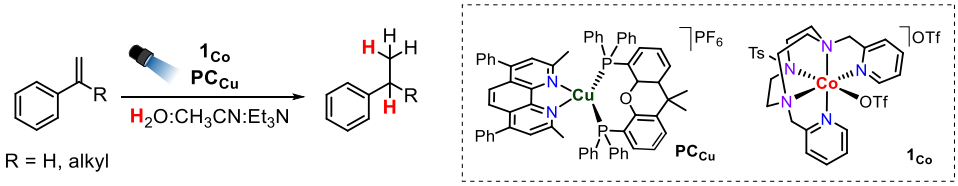

Scheme 3.4. Earth-abundant dual catalytic system for the photoreduction of aromatic olefins.

In the present chapter, we will complement the mechanistic understanding of this system with different studies, including the screening of PC, deuterium-labelling experiments, and competitive reactivity. Based on this mechanistic picture, the main focus will be to study the interplay between the catalyst/substrate redox potential, together with the light intensity, to provide a way to control the selectivity for the reduction of aromatic olefins versus aromatic ketones and *vice versa*. This unique behaviour is rationalised by the different reduction pathways that each substrate undergoes.

3.2 Results and Discussion

3.2.1 Photoredox Catalyst screening

The general conditions (solvent, temperature, atmosphere, cobalt catalyst and electron donor) for the dual earth-abundant system based on $\mathbf{1_{Co}}$ as catalyst for the transference of hydrogen atoms and $\mathbf{PC_{Cu}}$ as photoredox catalyst (Scheme 3.4), had been optimised by Dr. Carla Casadevall.[44] At this point, we screened different PC (Table 3.1) with the main aim of bringing deeper comprehension of the catalytic system.

First, two new copper-based PC synthesised were tested (Table 3.1, above). A $\mathbf{PC_{Cu}}$ in which the phenyl substituents of the bathocuproine ligand had been replaced by iodide groups, $\mathbf{^{I}PC_{Cu}}$ (E_{red} = -1.47 V *vs* SCE in CH_3CN), exhibited sluggish reactivity under these conditions (obtaining 21% yield). Then, introducing two sulphate groups to the bathocuproine ligand led to the anionic complex $\mathbf{^{SO3}PC_{Cu}}$ (E_{red} = -1.66 V *vs* SCE). The introduction of the sulphate groups was designed to make the complex highly soluble in aqueous organic mixtures as well as pure water. However, the level of performance was 78% lower than $\mathbf{PC_{Cu}}$ (91%, E_{red} = -1.6 V *vs* SCE). The previous results obtained with these three copper-based PC, indicate that the redox power of the reduced ground state is not the only factor influencing the catalytic performance of the PC.

Interestingly, the widespread $[Ru(bpy)_3](PF_6)_2$ was not compatible (11% yield), as well as *fac*-$Ir(ppy)_3$ resulted in no transformation. In the case of the latter, redox potentials do not match for a reductive quenching between the excited state *fac*-$Ir(ppy)_3$* (E_{red}* = 0.3 V *vs* SCE)[45, 46] and triethylamine (E_{ox} = 0.8 V *vs* SCE).[47, 48] Moreover neutral iridium photocatalysts are highly insoluble in aqueous media.[49]

Table 3.1. Screening of photoredox catalysts**.**

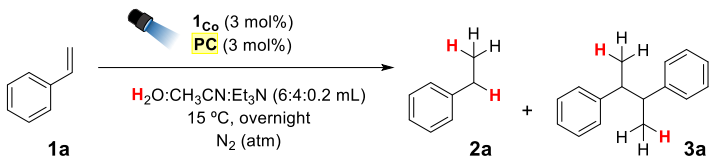

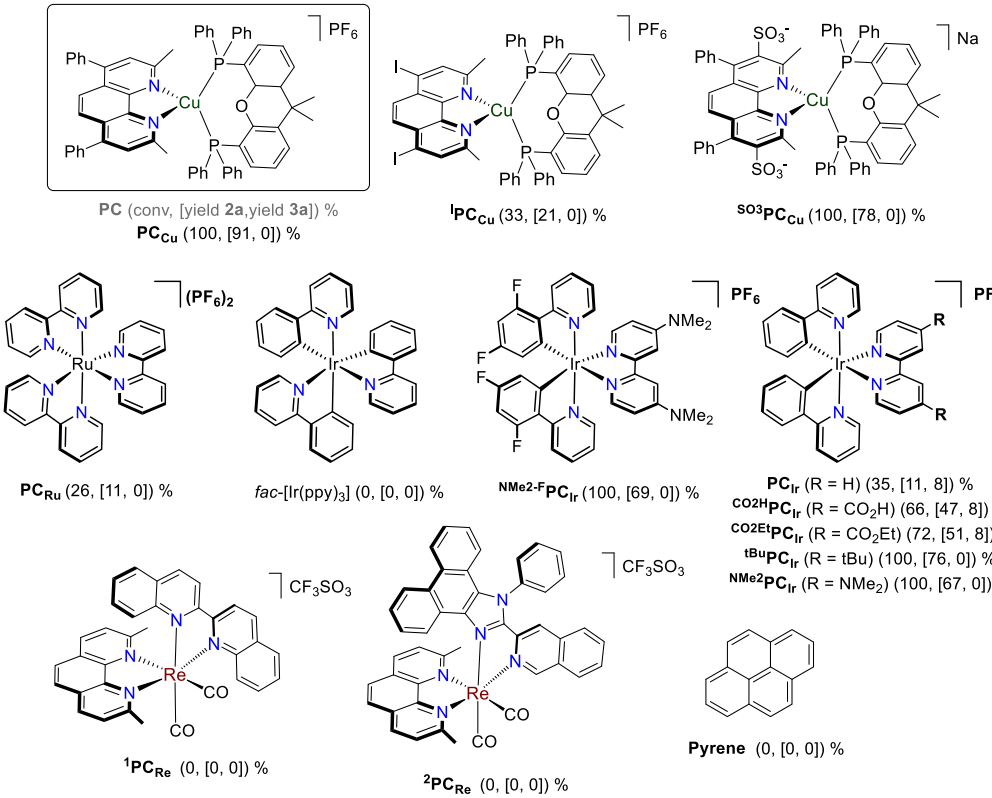

Conditions: **1**$_{Co}$ (261 mM, 3 mol%), PC (261 mM, 3 mol%), and **1a** (8.7 mM) in H_2O:CH_3CN:Et_3N (6:4:0.2 mL), irradiation (447 nm) overnight at 15 °C under N_2. Yields were determined by GC analysis after workup relative to a calibrated internal standard. Values were the average of duplicates and corresponded to conversion and [**2a**, **3a** yield].

Next, we also tested various iridium-based heteroleptic catalysts, where those with electron-donating groups in the bipyridine ligand afforded reasonable yields of 69%, 67%, 76% for $^{NMe2\text{-}F}$**PC**$_{Ir}$, ^{NMe2}**PC**$_{Ir}$, ^{tBu}**PC**$_{Ir}$, respectively. The formation of dimers was not detected in any case, whereas with complexes bearing electron-withdrawing groups, slightly lower yields were obtained (47, 51% for ^{CO2H}**PC**$_{Ir}$ and ^{CO2Et}**PC**$_{Ir}$, respectively,

and 8% of dimerisation in both cases). The most unexpected finding was that the non-substituted $\mathbf{PC_{Ir}}$ afforded only 11% yield, given that its reduction potential (-1.40 V *vs* SCE) is within the redox window of the other iridium-based complexes ($^{CO2Et}\mathbf{PC_{Ir}}$, $^{CO2H}\mathbf{PC_{Ir}}$, $^{tBu}\mathbf{PC_{Ir}}$, $^{NMe2}\mathbf{PC_{Ir}}$, E_{red} = -0.99, -1.01, -1.51, and -1.81 V *vs*. SCE). Other tested photosensitisers resulted unreactive for this transformation, in particular a couple of rhenium complexes synthesised by Koshevoy's group and the organic dye pyrene, which was also highly insoluble in the aqueous mixture.

An interplay between the different components of the system results in a non-general correlation with the redox potential or with the structure of the complexes, whereas $\mathbf{PC_{Cu}}$ clearly remains the optimal choice for the current transformation.

3.2.2 Polisubstituted double bonds

The scope of aromatic olefins had been previously explored by Dr. Carla Casadevall.[44] Here, we also studied if introducing phenyl substituents as a slightly activating group in the different positions of the double bond could unlock the reduction of other disubstituted olefins by stabilising the benzylic radical formation. For comparison, 1,1-diphenylethylene (**1b**) was reduced to **2b** in 83% yield (similar to the other 1,1-disubstituted olefins),[44] while no alkane was found in the reaction of **1c**, the tri-substituted **1d**, or the tetra-substituted **1e**. The only product found in the reaction of **1c** (trans-stilbene) resulted in **1c'** (cis-stilbene), an E→Z isomerisation (ratio Z/E 69/31) matching with an energy transfer process (EnT) from $\mathbf{PC_{Cu}}$[34-37], though the presence of $\mathbf{1_{Co}}$ could also make possible other mechanisms.[50] It is noteworthy at this point that we discard EnT as the responsible path for the reduction of olefins: despite both **1a** and Et_3N showing a similar quenching rate of $\mathbf{PC_{Cu}}$, the higher concentration of the amine backed its role as predominant quencher.[43]

Table 3.2. GC-analyses of reactions with double-bond-polysubstituted styrene derivatives.

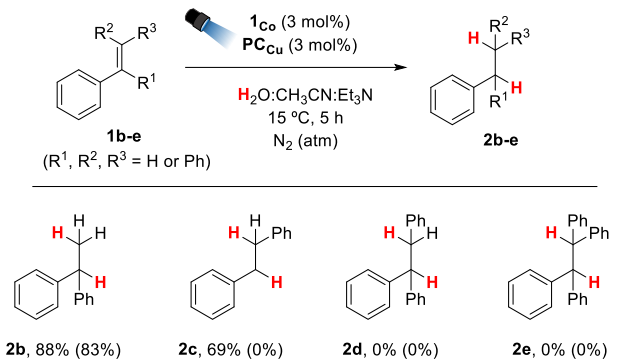

Conditions: **1**$_{Co}$ (261 mM, 3 mol%), PC (261 mM, 3 mol%), and **1** (8.7 mM) in H_2O:CH_3CN:Et_3N (6:4:0.2 mL), irradiation (447 nm) 5 h at 15 °C under N_2. Yields were determined by GC analysis (not isolated) after workup relative to a calibrated internal standard. Values were the average of duplicates and corresponded to conversion and (yield%).

In summary, the presence of substituents in the terminal position of the olefin hampers its reactivity. This result could be due to different reasons, i) an excessive steric interaction with the putative [**Co^{II}–H**] species, (in aggrement, increasing the size of the substituent at the alfa position also has a detrimental effect on the yield) ii) electronic effects, although less likely, or iii) due to a more efficient energy transfer between the PC excited state and the olefine, hampering the electron transfer process to the cobalt complex.

3.2.3 Deuteration studies and mechanistic implications

Different mechanistic studies have been performed for the current system by Dr. Carla Casadevall[44] and Dr. Jordi Aragón, including radical clock experiments, Stern-Volmer analysis, DFT calculations or electrochemical studies.[43] With all this mechanistic information, the two main possible pathways for the reduction of styrene derivatives are the insertion of the olefin into the [**Co^{II}–H**] (Scheme 3.5a) or HAT+SET (Scheme 3.5b). The pieces of evidence discard as an important pathway the direct hydride transfer from [**Co^{II}–H**] to the olefin (as supported by radical clock experiments or the observation of dimers).

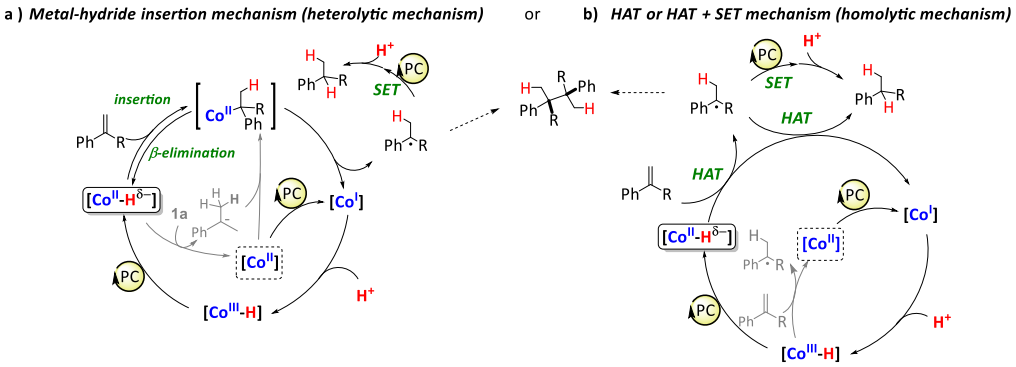

Scheme 3.5. Possible mechanistic scenarios for reducing aromatic olefins by the light-driven dual-copper–cobalt catalytic system in aqueous media. The [Co^{II}] intermediate inside each cycle indicates the beginning of the catalytic cycle. Acronyms stand for PC = photoredox catalyst; ED = electron donor; SET = single electron transfer and HAT = hydrogen atom transfer.

Since H_2O is the source of hydrogen atoms in the developed method, we also explored the possibility of obtaining deuterated products by using D_2O as a solvent. Thus, olefins **1f-j** were reduced with the dual $\mathbf{PC_{Cu}/1_{Co}}$ catalytic system in a D_2O:CH_3CN mixture.[43]

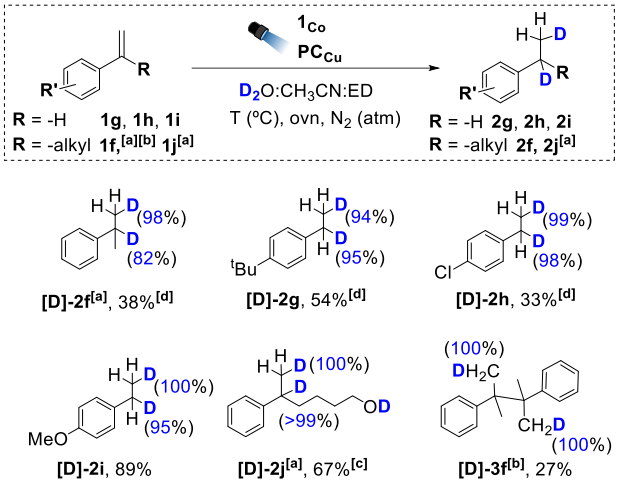

Scheme 3.6. Deuterium labelling studies of aromatic olefins. Conditions: $\mathbf{1_{Co}}$ (3 mol%), $\mathbf{PC_{Cu}}$ (3 mol%), the substrate (8.7 mM) in D_2O:CH_3CN:Et_3N (6:4:0.2 mL) irradiated for 24 h (447 nm) at 15 °C under N_2. [a] Other conditions: $\mathbf{1_{Co}}$ (6 mol%), $\mathbf{PC_{Cu}}$ (6 mol%), and the substrate (4.4 mM) in D_2O:CH_3CN:iPr_2EtN (6:4:0.2 mL), irradiated (447 nm) for 24 h at -3 °C under N_2. [b]Conditions [a] modifying [Subs.] to 16 mM and 5 h at 30 °C. [c]NMR yield. [d]Low isolated yields were obtained due to the volatility of the products. Isolated yields (average of 16 reactions). D-insertion analysed by NMR. Products **2f**, **2g**, **2h** were isolated by the PhD candidate D. Pascual, and **2i**, **2j**, **3f** by Dr. Carla Casadevall.

We observed nearly quantitative olefin deuteration (Figure 3.3Figure 3.13, Figure **3.15** and reference 43) incorporating one deuterium atom at each carbon atom of the double bond (α and β) (Scheme 3.6). This agrees with the formation of the deuteride species [Co^{II}–D] involved in a deuterium atom transfer (DAT) mechanism with the olefin (Scheme 3.5b), forming the corresponding benzylic radical, which either dimerises or undergoes deuteration in the benzylic position, affording the final product (Scheme 3.5). Moreover, in the substrates **2f**, **2h**, **2i**, **2j**, we did not observe double deuteration at the same carbon nor H/D scrambling (Figure 3.3, Figure **3.16**, reference 43). Therefore, if organometallic cobalt species are formed after the insertion of Co–D/H in the olefin, the reversibility of the reaction via *beta*-hydride elimination would be negligible in this case. Otherwise, reversible *beta*-hydride elimination would imply deuteration in both equivalent methyl groups of **2f**, but the corresponding NMR analysis is more consistent with 98% of deuterium incorporation in one unique position (the methyl group integrates 5H in ^{1}H-NMR and no significant isotopomers or isotopologues were observed in ^{13}C-NMR, Figure 3.3). Still, we found some signals that could be, in principle, associated with minor H/D scrambling in the ^{13}C-NMR spectrum for **2g** (Figure 3.14).

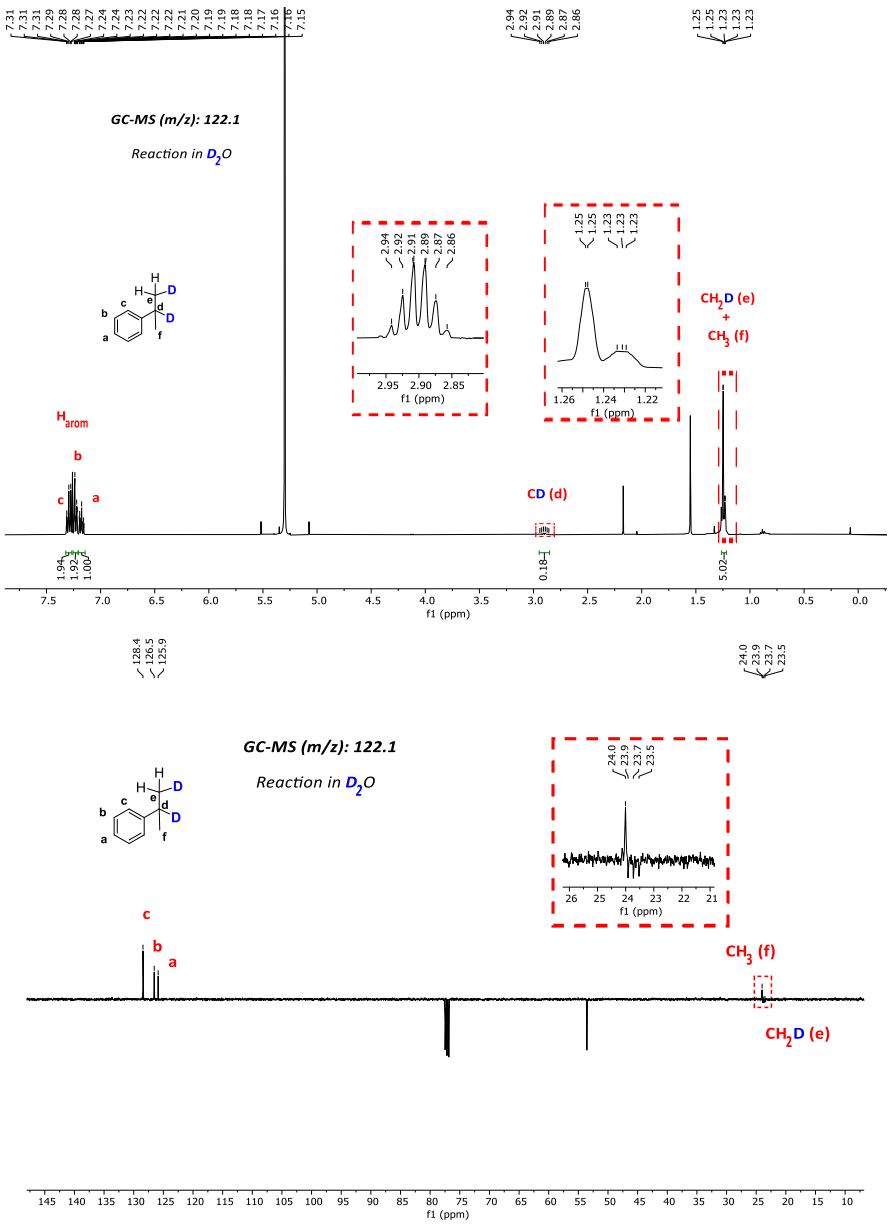

Figure 3.3. ^{1}H-NMR spectra ($CDCl_3$, 400 MHz, 300 K) and $^{13}C[^{1}H]$-DEPT-135-NMR spectra ($CDCl_3$, 100.6 MHz, 300 K) of the isolated product **[D]-2f** using D_2O (99.9 % in deuterium) in the solvent mixture. Inset in ^{1}H-NMR spectra: amplification of the area of the –CD and the -CH_2D. Inset in ^{13}C-NMR spectra: amplification of the area of the –CH_2D with the insertion of deuterium showing the triplet due to the C–D coupling**.** Conditions: $\mathbf{1_{Co}}$ (6 mol%), $\mathbf{PC_{Cu}}$ (6 mol%), substrate (0.044 mmol, 4.4 mM) in H_2O (or D_2O):CH_3CN:Et_3N (6:4:0.2 ml) irradiated at λ = 447 nm and -3 ºC for 24 h, under N_2.

Since no doubly deuterated terminal carbons in the reduced products were detected, this indicates that neither β-hydride elimination (Scheme 3.5a) nor reversible HAT occurs significantly. Although irreversible insertion cannot be ruled out, the most likely scenario is that benzylic radicals are formed *via* HAT and then undergo a reduction (E_{red} =-1.44 to -1.69 V *vs*. SCE)[43] by $\mathbf{PC_{Cu}^{0}}$ (E_{red}=-1.60 V *vs*. SCE), which after subsequent protonation gives the alkane (Scheme 3.5b). We also discard the HAT from the oxidised amine because the deuteration of the benzylic position is virtually quantitative.

Finally, when we employed 1,2-disubstituted olefin **1k**, we did not observe deuterium insertion (Scheme 3.7 and Figure 3.17), indicating that although isomerisation takes place (Table 3.2), it is most likely to proceed through a photochemically generated excited state and a diradical mechanism[34-37] without the intervention of [$\mathbf{Co^{II}–H}$] insertion–elimination steps or direct SET from $\mathbf{PC_{Cu}}$.

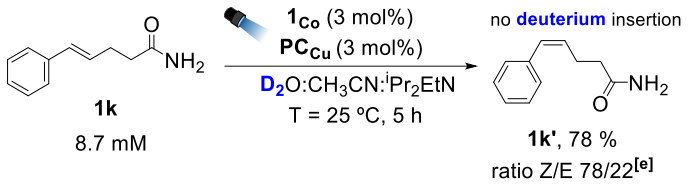

Scheme 3.7. Deuterium labelling studies of aromatic olefin **1g**. Conditions: 1 (3 mol%), $\mathbf{PC_{Cu}}$ (3 mol%), the substrate (8.7 mM) in H_2O:CH_3CN:Et_3N (6:4:0.2 mL) irradiated for 5 h (447 nm) at 15 °C under N_2. Z/E ratio analysed by NMR.

3.2.4 Amine-side reactivity

We have shown that this methodology allows the selective reduction of aromatic olefins avoiding dimerisation or oligomerisation side-processes (see Table 3.1, 91% of **2a**). However, careful examination of the chromatograms with $\mathbf{PC_{Cu}}$ revealed a small peak in the optimised reactions. The same peak also appeared when using other PC, especially with $\mathbf{^{NMe2}PC_{Ir}}$. Furthermore, GC-MS analysis of the samples revealed that the molecular mass of this by-product was 205 g/mol, which is consistent with the coupling between styrene and the α-aminoalkyl radicals generated in solution, as illustrated in Scheme 3.8.

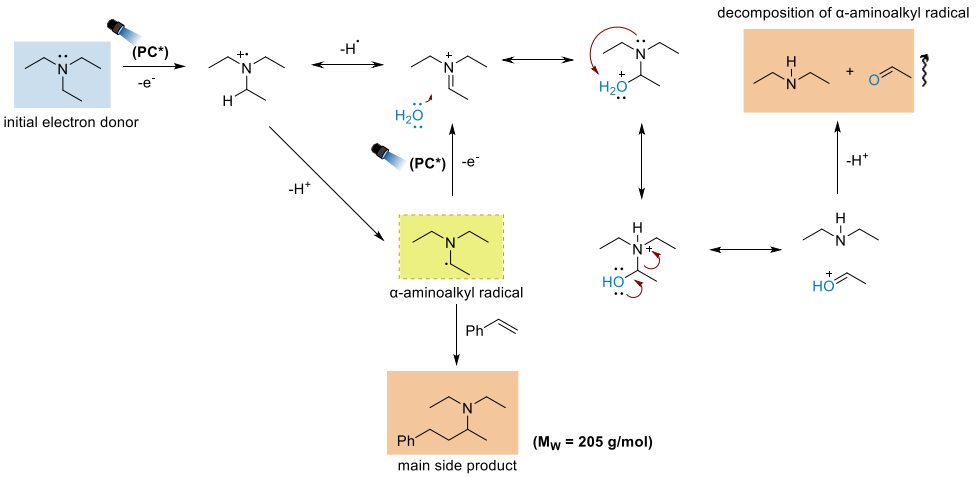

Scheme 3.8. Photogeneration of α-aminoalkyl radicals and their side reactivity.

Despite the light-driven coupling of amines and olefins having been reported elsewhere[51-56] and it is not our current target transformation, we were interested in the mechanistic information obtainable from the selectivity of the formation of **2a** *vs* **4a** by modifying our model conditions. Such information can be valuable for further methodologic developments based on this system. In that direction, we could foresee that removing $\mathbf{1_{Co}}$ from the system should result in an increment of the by-product since its formation is expected to be dictated merely by the PC reactivity. However, only a minor increment of **4a** was observed for $^{\mathbf{NMe2}}\mathbf{PC_{Ir}}$ without $\mathbf{1_{Co}}$, and there was no detection for $\mathbf{PC_{Cu}}$. Other copper and iridium PC were also tested without $\mathbf{1_{Co}}$ and neither showed an increment in the formation of **4a**. Consequently, $\mathbf{1_{Co}}$ is not responsible for suppressing the side-reactivity of α-aminoalkyl radicals.

Table 3.3. Effect of removing $\mathbf{1_{Co}}$ from the dual system for selected PC.

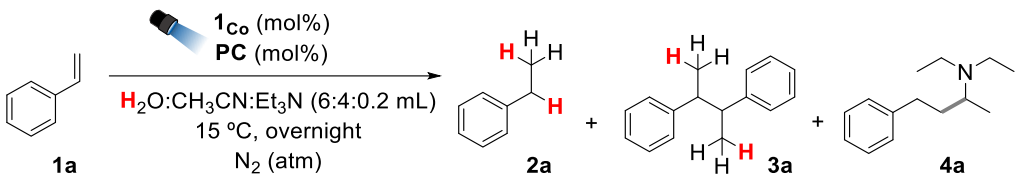

Entry	PC	[$\mathbf{1_{Co}}$] (mol%)	[PC] (mol%)	Conv (%)	Yield **2a** (%)	Yield **3a** (%)	'Yield' **4a** (%)[b]
1	$\mathbf{PC_{Cu}}$	3	3	100	91	0	3
2	$\mathbf{PC_{Cu}}$	2	3	100	81	<1	5
3	$\mathbf{PC_{Cu}}$	1	1.5	100	67	<1	4
4	$\mathbf{PC_{Cu}}$	0	3	2	0	0	0
5[b]	$\mathbf{^{NMe2}PC_{Ir}}$	3	3	100	57	0	22
6[b]	$\mathbf{^{NMe2}PC_{Ir}}$	0	3	89	4	0	30
7	$\mathbf{^{SO3}PC_{Cu}}$	3	3	100	71	0	1
8	$\mathbf{^{SO3}PC_{Cu}}$	0	3	19	0	0	1
9	$\mathbf{^{I}PC_{Cu}}$	3	3	33	21	0	5
10	$\mathbf{^{I}PC_{Cu}}$	0	3	7	0	0	5
11	$\mathbf{PC_{Ir}}$	3	3	20	11	8	1
12	$\mathbf{PC_{Ir}}$	0	3	4	2	0	1
13	$\mathbf{^{CO2H}PC_{Ir}}$	3	3	66	47	8	0
14	$\mathbf{^{CO2H}PC_{Ir}}$	0	3	3	0	0	0

Conditions: $\mathbf{1_{Co}}$ (261 mM, 3 mol%), **PC** (261 mM, 3 mol%), and **1a** (8.7 mM) in H_2O:CH_3CN:Et_3N (6:4:0.2 mL), irradiation (447 nm) overnight at 15 °C under N_2. Yields were determined by GC analysis after workup relative to a calibrated internal standard. Values were average of duplicates. Since we had not isolated **4a**, this yield was estimated using the calibration constant for styrene. [b]Diphenylcyclobutane traces were also found.

These results suggest that for the side-production of **4a**, a powerful PC is required to accumulate enough α-aminoalkyl radicals or activate styrene. In terms of redox potential, the generation of α-aminoalkyl radicals is expected to be slightly more efficient from $\mathbf{^{NMe2}PC_{Ir}}$* than $\mathbf{PC_{Cu}}$* (being their excited state reduction potential 0.6 and 0.5 V *vs* SCE, respectively, Table 3.7). On the other hand, since **1a** has E_{red} = -2.3 V *vs* SCE, a direct SET from the PC to the olefine is not possible; still, an EnT can occur.[43, 57] In this regard, the quenching effects of both $\mathbf{PC_{Cu}}$ and $\mathbf{^{NMe2}PC_{Ir}}$ with styrene

in aqueous media have been studied in our group by Dr. Jordi Aragón (Figure 3.4). Despite these two experiments were not recorded in identical conditions, they can serve for a close comparison, highlighting that ^{NMe2}**PC$_{Ir}$** (K_{SV} = 399.3 M^{-1})[58] has a superior interaction with styrene than **PC$_{Cu}$** (K_{SV} = 109.8 M^{-1}). As a matter of fact, diphenylcyclobutane traces with MW=208 g/mol were also detected by GC-MS in the case of ^{NMe2}**PC$_{Ir}$** (Table 3.3, entries 5 and 6).

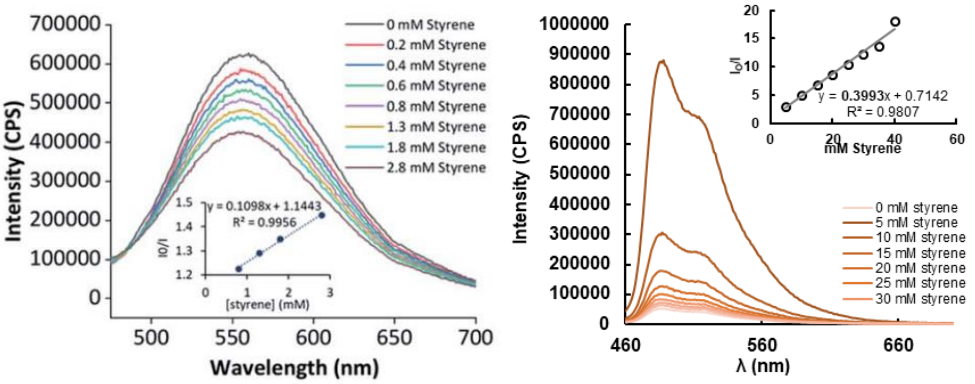

Figure 3.4. Comparison of the emission spectra of **PC$_{Cu}$** (left, graph from reference 35) and ^{NMe2}**PC$_{Ir}$** (right, graph from reference 36) in the presence of varying styrene concentrations. [**PC$_{Cu}$**]= 10 µM in CH_3CN:H_2O (800 µL/1200 µL). [^{NMe2}**PC$_{Ir}$**]= 10 µM in CH_3CN:EtOH:H_2O (400 µL/1200 µL/300 µL).

The other point we studied about this side reaction was whether the generation of **4a** is dictated by a purely photochemical or thermal effect (Table 3.4). We only observed a vague decrease in the reactivity when warming up from 15 to 40 ºC. However, the side reaction accelerated when increasing the amount of light (entries 9 and 10), especially for **PC$_{Cu}$**. These results indicate that under more reductive conditions (more powerful PC and increased photon flux), the reduction of olefins becomes less selective in favour of the coupling with α-aminoalkyl radicals.

Table 3.4. Thermal *vs* photo-response of the catalytic system.

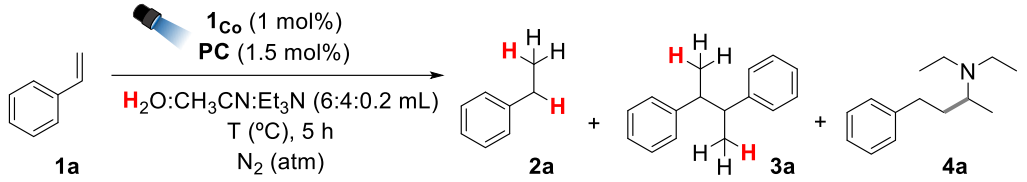

Entry	n LEDs	PC	T (°C)	Conv (%)	Yield **2a** (%)	Yield **3a** (%)	'Yield' **4a** (%)
1	1	$\mathbf{PC_{Cu}}$	5	100	74	<1	4
2	1	$\mathbf{PC_{Cu}}$	15	100	67	<1	4
3	1	$\mathbf{PC_{Cu}}$	25	100	66	3	3
4	1	$\mathbf{PC_{Cu}}$	40	100	62	3	2
5	1	$\mathbf{^{NMe2}PC_{Ir}}$	5	100	36	0	29
6	1	$\mathbf{^{NMe2}PC_{Ir}}$	15	100	50	0	27
7	1	$\mathbf{^{NMe2}PC_{Ir}}$	25	100	33	0	30
8	1	$\mathbf{^{NMe2}PC_{Ir}}$	40	100	0	30	35
9	7	$\mathbf{PC_{Cu}}$	15	100	77	<1	30
10	7	$\mathbf{^{NMe2}PC_{Ir}}$	15	100	45	0	37
11	0	$\mathbf{PC_{Cu}}$	15	0	0	0	0

Conditions: $\mathbf{1_{Co}}$ (1 mol%), **PC** (1.5 mol%), and **1a** (17.4 mmol, 8.7 mM) in H_2O:CH_3CN:Et_3N (6:4:0.2 mL), irradiation (447 nm) 5 h under N_2. Yields were determined by GC analysis after workup relative to a calibrated internal standard. Values were average of duplicates. [b]Since we had not isolated **4a,** the yield was estimated using the calibration constant for styrene.

3.2.5 Selectivity olefin *vs* ketone

The postulated HAT mechanism for olefin reduction (Scheme 3.5) implies a controllable selectivity in front of functional groups that are reduced *via* a different mechanism, such as SET. This is the case for our previously reported reduction of aromatic ketones using the dual catalytic system. Therefore, we selected styrene (**1a**) and acetophenone (**5a**) as competing substrates to test our hypothesis. As introduced in Section 3.1 (Figure 3.2), we previously determined that under equivalent photocatalytic conditions that **5a** is reduced to 1-phenylethanol (**6a**). The process is initiated by a SET mechanism from $\mathbf{PC_{Cu}^0}$ to form the ketyl radical anion (KRA) as an intermediate (E_{red} = -1.65 V *vs*. SCE).[42] Then the generated KRA is trapped by [$\mathbf{Co^{II}}$–**H**] to form the reduced product via HAT (Scheme 3.9, above).

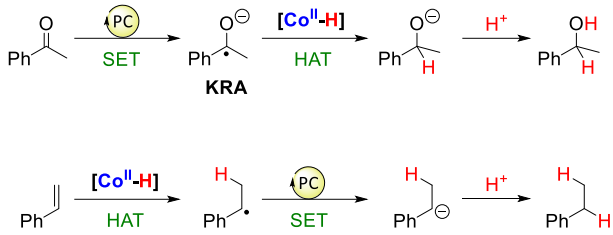

Scheme 3.9. Different substrate-dependent mechanisms for the expected selectivity. KRA stands for ketyl radical anion and PC for the photoredox catalyst (the electron donor has been omitted for simplicity).

Therefore, it should be possible to differentiate the KRA formation *via* SET from the HAT mechanism of the olefin, designing the photocatalytic conditions rationally. This rationalisation suggests, for instance, the counterintuitive idea of increasing the redox potential of the PC to make the catalytic system more selective. In this way, under more reducing conditions where the SET step is favoured, the reduction of the ketone would be preferential, while the opposite conditions in which SET is minimised would favour the reduction of the olefin.

First, when similar catalytic conditions to those previously reported for the selective reduction of aromatic ketones *vs.* aliphatic aldehydes[42] were used, **5a** was preferentially reduced in the presence of **1a** ($Sel_{\mathbf{5a/1a}}$ = 1.9, Figure 3.5, where selectivity is calculated as the ratio of converted moles of each substrate at a given reaction time).

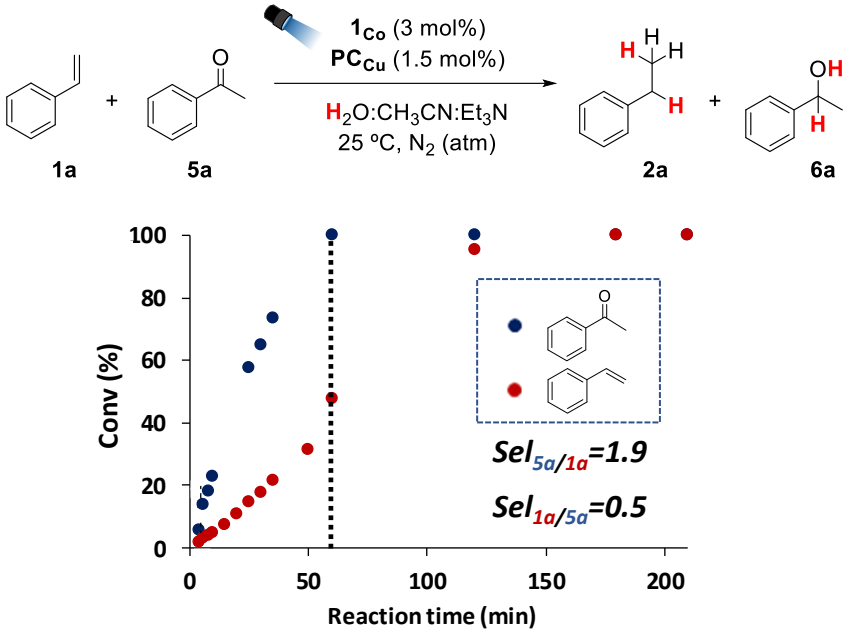

Figure 3.5. Monitoring of the competitive reaction between **1a** *vs* **5a** without any optimisation. Conditions: (**1**$_{Co}$ (1 mol%), **PC**$_{Cu}$ (1.5 mol%), total substrates (**1a** + **5a**, 16.5 mM, 1:1) in H_2O:CH_3CN:Et_3N (6:4:0.2 mL) irradiated for 4 h at 25 °C under N_2).

Then, we modified the reaction conditions to test the hypothesis of favouring either the SET to **5a** or the HAT to **1a**. According to our rational design, one of the key parameters to tune is the redox potential of the PC. With this aim in mind, we considered it more convenient to work with the set of heteroleptic iridium PC, for which the redox potential is easy to tune by modification of the substituents in the bipyridine ligand. Therefore, we monitored the competitive reduction using ^{NMe2}**PC**$_{Ir}$, ^{tBu}**PC**$_{Ir}$ and ^{CO2H}**PC**$_{Ir}$, finding a different behaviour in selectivity: the favoured reduction of **5a** or **1a** was even reversed with the different PC (Figure 3.6).

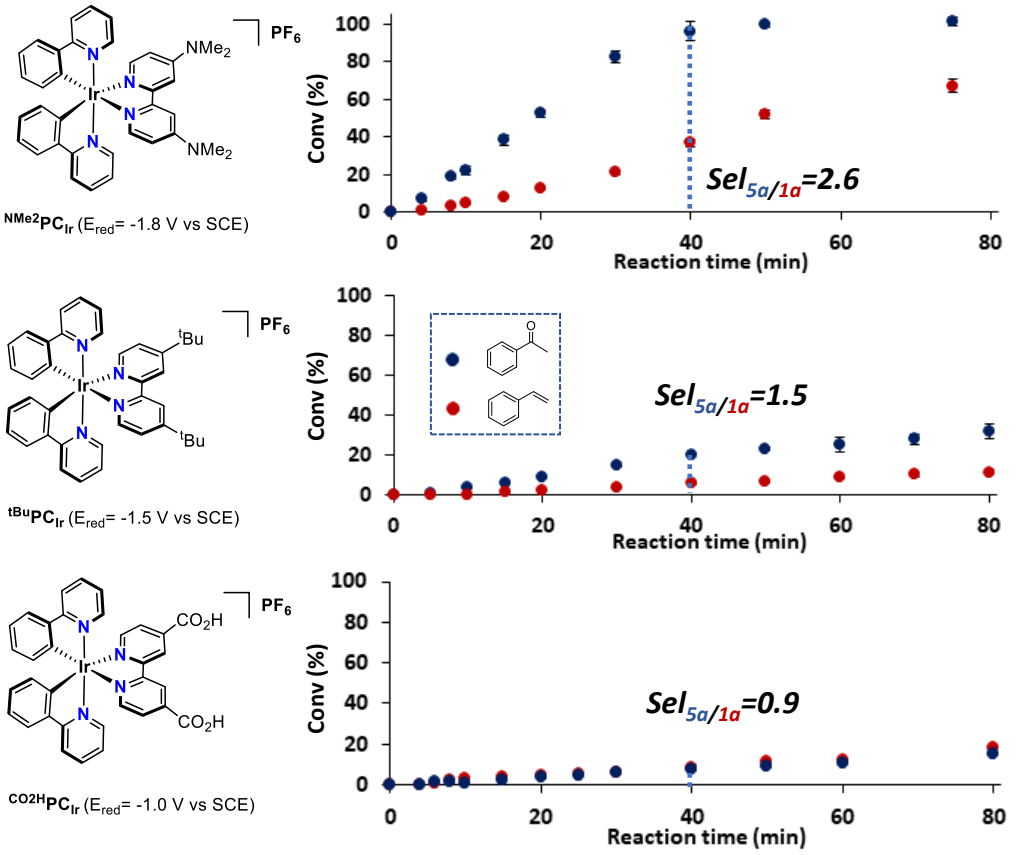

Figure 3.6. Monitoring of the competitive reaction between **1a** *vs* **5a** with different iridium **PC** to compare the effect of E_{red} in selectivity at 40 min. Conditions: $\mathbf{1_{Co}}$ (1 mol%), **PC** (1.5 mol%), total substrates (**1a** + **5a**, 16.5 mM, 1:1) in H_2O:CH_3CN:Et_3N (6:4:0.2 mL) irradiated for 4 h at 25 °C under N_2.

To our delight, the improvement in the selectivity for ketone reduction observed by using $^{NMe2}\mathbf{PC_{Ir}}$ instead of $\mathbf{PC_{Cu}}$ (from 1.9 to 2.6, Figure 3.6 and Figure **3.20**) matches with the more favourable SET step by using a more reductively powerful PC. To further promote the SET, we increased the light intensity up to $6.2\cdot10^{-3}$ mmol·hv·s^{-1} (3 LED) *vs.* the normal $2.1\cdot10^{-3}$ mmol·hv·s^{-1} (1 LED), which presumably increased the concentration of the reduced PC ($^{NMe2}\mathbf{PC_{Ir}^0}$), and thus, accelerated the reduction of the ketone (from 2.6 to 7.1, Figure 3.21). In addition, decreasing the concentration of complex $\mathbf{1_{Co}}$ to disfavour the HAT was slightly effective (from 7.1 to 9.1, Figure 3.22). In essence, total selectivity for ketone **5a** reduction was obtained in the presence of

styrene **1a** (in 2 min) using a higher amount of ^{NMe2}**PC$_{Ir}$** (3 mol%, E_{red}= -1.80 V *vs.* SCE), a lower amount of complex **1$_{Co}$** (0.25 mol%, $E(Co^{II/I})$ = -1.15 V *vs.* SCE) and irradiation at higher light intensity ($1.4\cdot10^{-2}$ mmol·hν·s^{-1}, 7 LED) (Figure 3.7bFigure 3.25).

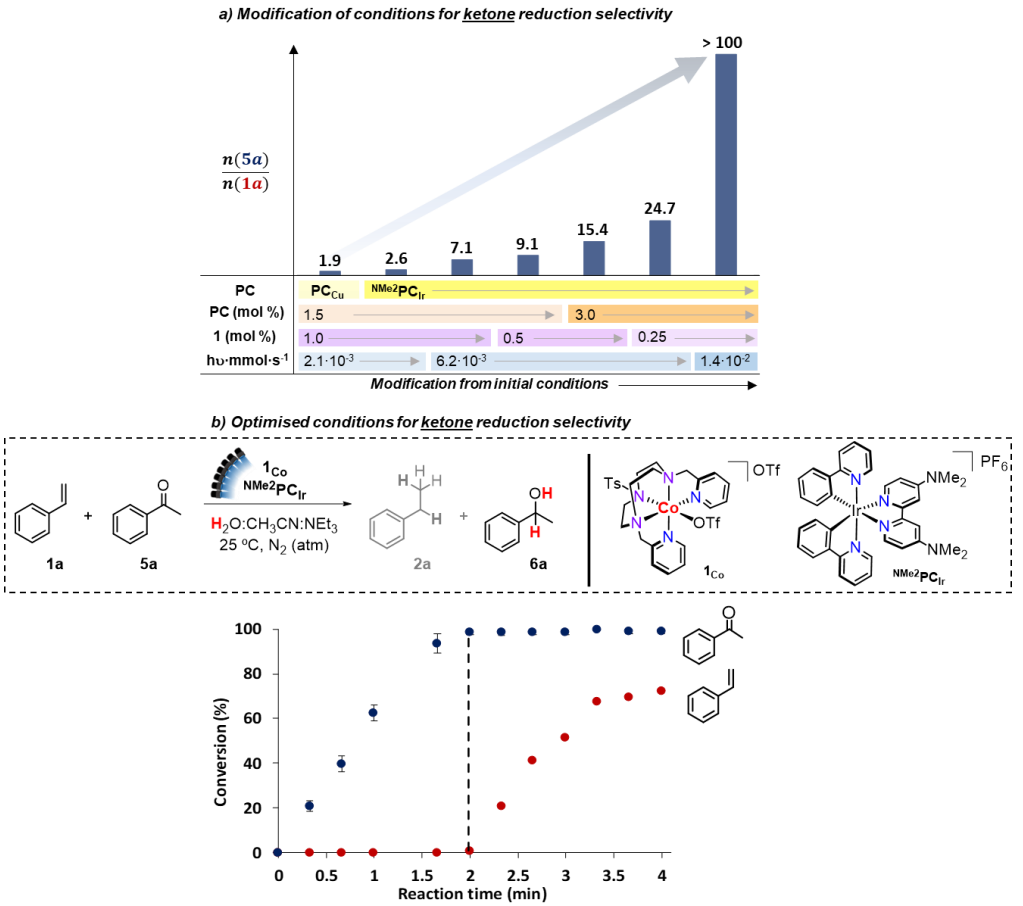

Figure 3.7. (a) Optimisation of the photocatalytic conditions for competitive reduction of acetophenone (**5a**) in the front of styrene (**1a**). (b) Conditions: **1$_{Co}$** (0.25 mol%), ^{NMe2}**PC$_{Ir}$** (3 mol%), total substrate concentration (**1a** + **5a**, 16.5 mM, 1:1) in H_2O:CH_3CN:Et_3N (3:2:0.1 mL) mixture, irradiated at 447 nm (7 LED at 700 mA, $1.44\cdot10^{-2}$ mmol·hν·s^{-1} of photons) for 4 min at 25 °C under N_2. The black dotted line indicates where substrate **1a** starts reacting.

At this point, it's noteworthy to mention that the determination of the photon flux for the LEDs was carried out by chemical actinometry. This experiment consists in measuring the yield of a simple photochemical reaction after irradiation. The reaction

must have a well-known quantum yield (ϕ), which is defined as the number of events (reactions) that occur per absorbed photon.[59] Therefore the moles of product after a particular time can be correlated with the moles of absorbed photons. A widespread actinometer is potassium ferrioxalate,[60, 61] that decomposes under irradiation following the next reaction:

$$[Fe^{III}(C_2O_4)_3]^{3-} \rightarrow Fe^{2+} + 2C_2O_4^{2-} + C_2O_4^{\bullet-}$$

In this way, the photon flux can be calculated measuring the yield of the irradiated sample (and a non irradiated sample as a blank) by UVvis absorption spectroscopy:[62]

$$\text{mol } Fe^{2+} = (V \cdot \Delta A)/(l \cdot \varepsilon)$$

$$\text{Photon flux} = (\text{mol } Fe^{2+})/(\phi \cdot t \cdot f)$$

Where V is the volume of irradiated solution, ΔA is the difference in absorbance, l is the path length and ε is the absorptivity coefficient at the irradiated wavelength, ϕ is the quantum yield of the actinometer, t is the time of irradiation and f is the fraction of light absorbed at that wavelength. In our case, Dr. Noufal Kandoth determined that the photon flux per LED was $2.05 \cdot 10^{-3}$ mmol·hν·s^{-1}.

On the other hand, we should be able to favour the HAT by modifying the reaction conditions to make them less reducing, enabling the selective reduction of the olefin without converting the ketone. Indeed, we already observed that the less reductive photoredox catalyst ^{CO2H}**PC$_{Ir}$** (E_{red} = -1.01 V *vs*. SCE) inversed the selectivity of **PC$_{Cu}$**. For ^{CO2H}**PC$_{Ir}$** the styrene reduction is slightly preferential ($Sel_{1a/5a}$ increased from 0.5 to 1.2) (Figure 3.26). Likewise, using a Co complex easier to reduce **[(Co^{II}(OTf)(^{H,CO2Et}Py$_2^{Ts}$tacn)]** (^{CO2Et}**1$_{Co}$**, $E(Co^{II/I})$ = -0.96 V *vs*. SCE, while $E(Co^{II/I})$ = -1.15 V *vs*. SCE for **1$_{Co}$**), the selectivity improved up to 2.2. Then, we increased the ^{CO2Et}**1** concentration with the idea to increase [**Co^{II}–H**] and thus the HAT product ($Sel_{1a/5a}$ = 3.1, Figure 3.28). Finally, lowering the light intensity of the LED to 8% ($1.7 \cdot 10^{-4}$ mmol·hν·s^{-1}), **1a** was reduced over **5a** with full selectivity (Figure 3.7 and Figure **3.29**). GC monitoring of the reactions showed that **5a** remained virtually intact, whereas **1a** was consumed and converted to **2a** and dimer **3a** (Figure 3.28). The

observation of **3a** under less reductive conditions also matches the fact that once benzylic radicals are formed, dimerisation becomes relevant rather than the disfavoured SET.

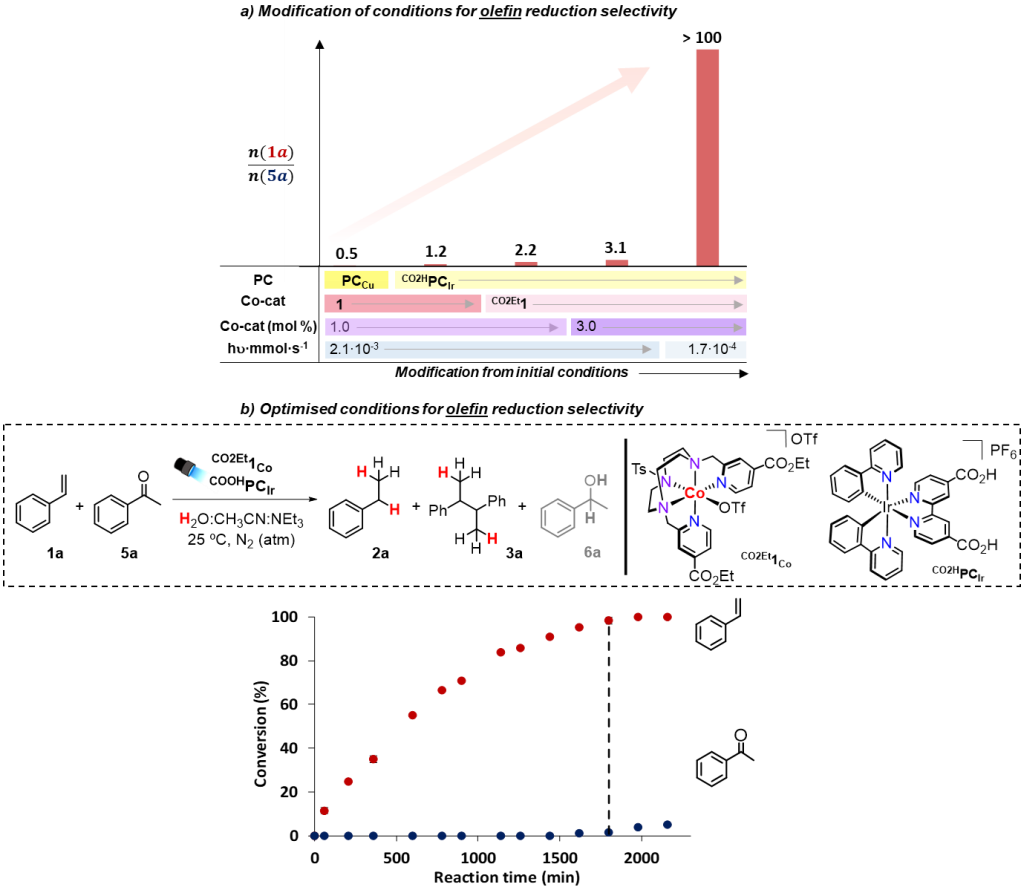

Figure 3.8. (a) Optimisation of the photocatalytic conditions for competitive reduction of styrene (**1a**) in front of acetophenone (**5a**). (b) Conditions: $^{CO2Et}\mathbf{1}_{Co}$ (3 mol%), $^{CO2H}\mathbf{PC}_{Ir}$ (1.5 mol%), total substrate concentration (**1a** + **5a**, 16.5 mM, 1:1) in a H_2O:CH_3CN:Et_3N (3:2:0.1 mL) mixture, irradiated at 447 nm (1 LED at 50 mA $1.67 \cdot 10^{-4}$ mmol·hν·s^{-1} of photons) for 36 h (2160 min) at 25 °C under N_2. The black dotted line indicates where substrate **5a** (d) starts reacting.

At this point, apart from the previous mechanistic support, it could be attractive to expand this methodology for the selective reduction of double bonds to the intramolecular fashion. Therefore, the chalcone **1l** was tested as a preliminary substrate under the optimised conditions for the competitive reduction of styrene. GC-followed

kinetic studies revealed the consumption of the substrate **1l** without any apparent product formation, but some white precipitate was significantly accumulated. The reaction was left overnight, and the filtered particles were then washed with water and ethanol. The powder quickly crystallised and X-ray diffraction revealed the obtention of a cyclopentanol structure resulting from the reductive dimerisation of the chalcone (Figure 3.9), a type of reactivity that has also been reported by other authors.[63, 64] This finding does not match with our target reactivity and indicates that, effectively, chalcone is not a suitable substrate for selective intramolecular studies.

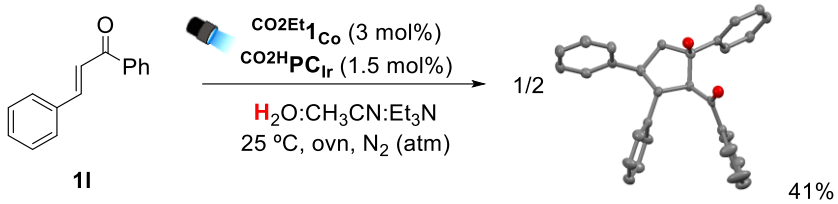

Figure 3.9. Reductive dimerisation of chalcone was observed under the optimised conditions for reducing olefins.

As a summary of this section, the observed intermolecular selectivity agrees with the existence of two competitive mechanistic scenarios involving: (i) SET + HAT for substrates that can be directly reduced, such as acetophenone, and (ii) HAT for substrates with more negative reduction potentials that cannot be directly reduced by one electron from the PC such as aromatic olefins.

3.3 Conclusions

In this chapter, we found that the methodology developed for the photocatalytic reduction of olefins in aqueous media strongly depends on the PC nature. In that sense, $\mathbf{PC_{Cu}}$ is the prevalent selection under optimised conditions for olefin reduction, and it exhibits excellent selectivity in front of side processes, such as the dimerisation of styrene. We also corroborated that despite a variety of styrene derivatives and 1,1-disubstituted aryl olefins can be reduced to the corresponding alkanes using the present methodology, 1,2-disubstituted olefins are recalcitrant to undergo the target reduction under the current reaction conditions.

The selected system was used to expand the methodology for synthesising deuterated alkanes using D_2O (99.9%), exhibiting quantitative incorporation of deuterium atoms in the olefin's alpha and beta carbons. The absence of doubly deuterated positions and scrambling was consistent with an irreversible HAT step, although a slow irreversible metal hydride insertion cannot be fully discarded. Moreover, even though 1,2-disubstituted olefins were not reduced under the optimised conditions isomerise to the cis-diastereomer without deuterium incorporation. This result matches EnT from the PC to the olefin rather than other pathways, such as reversible insertion-elimination or SET.

In addition, the side reaction of styrene with α-aminoalkyl radicals was detected, and we noted that the process is not dependent on the presence/absence of cobalt catalyst but on the nature of the PC. Consistent with that, this side reaction is not significantly affected by thermal changes but is accelerated when increasing irradiation intensity increases.

Based on our mechanistic understanding, we envisioned that selectivity in the reduction of aromatic ketones *versus* aromatic olefins could be predictably tuned upon optimisation of the catalytic conditions. Therefore, other photosensitisers and conditions were evaluated, reaching a dual Co/Ir system capable of reducing all the aryl ketone with absolute selectivity before reacting with the aryl olefin and *vice versa*. This unique behaviour is rationalised by the different reduction mechanisms that each substrate undergoes.

These results show that the selectivity of the metal hydrides in basic media can be controlled and directed to reducing organic functionalities. For this reason, we envision that other readily available H_2O reduction catalysts could also be active in reducing other functional groups and more complex organic structures. These results pave the way for the development of selective organic reductions and solar-chemical generation using artificial catalytic systems that operate entirely with earth-abundant elements, using visible light as the driving force and H_2O as a clean source of hydrides.

3.4 Experimental Section

3.4.1. Materials and reagents

Reagents and solvents were used as received from the commercial supplier unless otherwise stated. Triethylamine and diisopropylethylamine were distilled over potassium hydroxide and were stored under argon. Photocatalysts [Ir(deeb)(ppy)$_2$](PF$_6$) (**^{CO2Et}PC$_{Ir}$**), [Ir(tbbpy)(ppy)$_2$](PF$_6$) (**^{tBu}PC$_{Ir}$**), [Ir(bpy)(ppy)$_2$](PF$_6$) (**PC$_{Ir}$**), [Cu(bathocuproine)(xantphos)](PF$_6$) (**PC$_{Cu}$**), and complexes **(Py$_2$^{Ts}tacn)Co(OTf)$_2$** (**1$_{Co}$**), **(Py$_2$^{Ts}tacn)Co(OTf)$_2$**102 (**^{CO2Et}1$_{Co}$**) were synthesized according to the literature procedures. [40, 41, 65, 66] The other photocatalysts [Ir(dmabpy)(ppy)$_2$](PF$_6$) (**^{NMe2}PC$_{Ir}$**), [Ir(dcbpy)(ppy)$_2$](PF$_6$) (**^{CO2H}PC$_{Ir}$**), were synthesised from a modified procedure from the literature. [66, 67, 68]

For the synthesis of reagents, the solvents (DMF, hexane, Et$_2$O, CH$_2$Cl$_2$, CH$_3$CN and toluene) were used from a SPS-400, Innovative Technology solvent purification system and stored under argon with activated 4 Å molecular sieves. Anhydrous acetonitrile was purchased from Sigma-Aldrich® and water was purified with a Milli-Q Millipore Gradient AIS system. Water, methanol, ethanol, trifluoroethanol, acetonitrile, dimethylformamide, dimethylacetamide and tetrahydrofurane used for photoreactions were degassed by freeze-pump-thaw method (repeated 3 cycles) and were stored under argon. All the alkenes were filtered by a pad of Celite (Hyflo Super Cel from Sigma-Aldrich, CAS: 68855-54-9) before running the photoreactions.

The synthesis of air-sensitive reagents, as well as the preparation of visible light photocatalytic reactions, were conducted inside a nitrogen-filled glove box

3.4.2. Instruments

Nuclear magnetic resonance (NMR). NMR spectra were recorded on Bruker Fourier300, AV400, AV500 and AVIII500 spectrometers using standard conditions (300 K). All 1H chemical shifts are reported in ppm and have been internally calibrated to the residual protons of the deuterated solvent. The 13C chemical shifts have been

internally calibrated to the carbon atoms of the deuterated solvent. The coupling constants were measured in Hz.

Mass Spectrometry. High resolution Mass Spectrometry (HRMS) data were collected on a HPLC-QqTOF (Maxis Impact, Bruker Daltonics) or HPLC-TOF (MicroTOF Focus, Bruker Daltonics) mass spectrometer using 1 mM solution of the analysed compound.

Electrochemistry. All the electrochemical experiments were performed with a *vs*P potentiostat from BioLogic, equipped with the EC-Lab software. CV measurements were carried out under Ar atmosphere using 1 mM solutions of nickel complex or Ir photoredox catalysts in MeCN, with tetrabutylammonium hexafluorophosphate ($TBAPF_6$) as supporting electrolyte (0.1 M). A single-compartment cell was employed, with glassy carbon (GC) working electrodes (3 mm and 1 mm diameter). Additionally, a Pt wire was used as a counter electrode and a Ag/AgCl wire as a pseudo-reference, immerged in a bridge tube containing the same electrolyte solution (0.1 M $TBAPF_6$/MeCN) and separated from the working solution by a porous tip. Ferrocene (Fc) was added to the solution as an internal standard and all the potentials were first referenced *vs*. the $Fc^{+/0}$ redox couple and then *vs*. SCE. The working electrodes were polished by using 0.05 μm alumina powder (CHInstruments) on a polishing pad wet with distilled H_2O, followed by rinsing with distilled water/acetone and sonication to remove the residues of alumina over the electrode.

UV-Vis spectroscopy. UV-Vis spectra were recorded on an Agilent 8453 diode array spectrophotometer (190-1100 nm range) in 1 cm quartz cells. A cryostat from Unisoku Scientific Instruments was used for the temperature control.

Fluorescence spectroscopy. Fluorescence measurements were carried out on a Fluorolog Horiba Jobin Yvon spectrofluorimeter equipped with photomultiplier [or InGaAs if using the nitrogen-cooled detector] detector, double monochromator and Xenon light source. Sample preparation was the same as that of absorption experiments in 1 cm quartz cells.

Gas chromatography analysis. The analysis and quantification of the starting materials and products were carried out on an Agilent 7820A gas chromatograph (HP5 column, 30m or Cyclosil-B column, 30m) and a flame ionisation detector. GC-MS spectral analyses were performed on an Agilent 7890A gas chromatograph interfaced with an Agilent 5975c MS mass spectrometer.

3.4.3. In-house developed parallel photoreactors

Figure 3. 10. In house developed parallel photoreactors with (left) 25 positions for vials of 10 or 21 mL and (right) with 48 positions for vials of 1 mL.

Light source: The reactions were performed using Royal-Blue (λ = 447±20 nm) LUXEON Rebel ES LED, mounted on a 20 mm Square Saber - 1030 mW @ 700mA as a light source.

Temperature Control: Reaction temperature was controlled by a high-precision thermoregulation Hubber K6 cryostat. Likewise, aiming at ensuring stable irradiation, the temperature of the LEDs was controlled and set at 22 ºC.

3.4.4. Synthesis and characterisation of PC

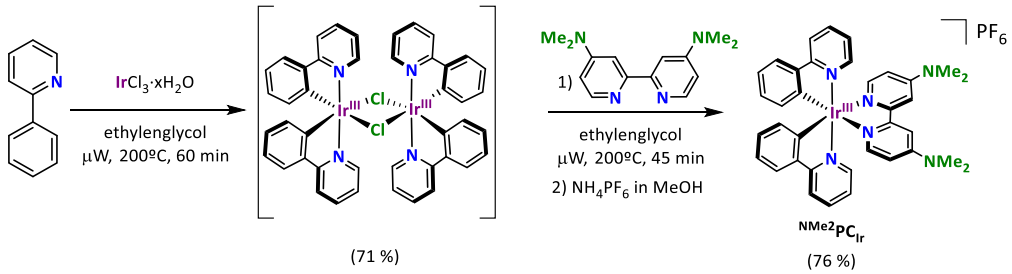

Synthesis of [Ir(ppy)$_2$(dmab)](PF$_6$), (^{NMe2}PC$_{Ir}$). $IrCl_3 \cdot xH_2O$ (405 mg, 1.356 mmol) and phenylpyridine (1.55 ml, 10.85 mmol, 8equiv) were mixed and sonicated in ethylene glycol (15 mL). The reaction was set in the microwave at 200 ºC for 60 min, obtaining a bright yellow mixture corresponding with the formation of the dimer. Next, after adding **dmab** (493 mg, 2.035 mmol, 1.5 eq) the reaction vessel was microwaved at 200 ºC for an additional 45 min, obtaining an orange solution. The reaction was allowed to cool down to room temperature to carry out liquid-liquid extraction of the organic layer in water (15 mL) and dichloromethane (3 x 150 ml). The organic phases were combined, dried over $MgSO_4$, and removed the solvent *in vacuo*. The solid was dissolved in a methanolic solution containing ammonium hexafluorophosphate (10.0 g in 100 mL of MeOH), and the precipitate was filtered and dried to afford ^{NMe2}**PC$_{Ir}$** in 76% yield (0.915 g, 1.03 mmol). ^{1}H NMR (400 MHz, Acetone-d_6) δ 8.19 (d, J = 8.1 Hz, 2H), 7.96 – 7.87 (m, 4H), 7.85 (d, J = 6.8 Hz, 2H), 7.44 (d, J = 6.7 Hz, 2H), 7.20 (t, J = 6.6 Hz, 1H), 6.97 (t, J = 7.5 Hz, 2H), 6.80 (td, J = 7.5 Hz, 2H), 6.73 (dd, J = 6.7, 2.8 Hz, 1H), 6.35 (d, J = 8.3 Hz, 2H), 3.19 (s, 12H). ^{13}C NMR (101 MHz, Acetone-d_6) δ 169.18, 156.98, 155.99, 153.72, 149.70, 149.55, 145.15, 138.86, 132.69, 130.93, 125.61, 124.00, 122.55, 120.38, 110.32, 106.61, 39.65. ^{19}F NMR (376 MHz, Acetone-d_6) δ -72.71 (d, J = 707.4 Hz). ^{32}P NMR (162 MHz, Acetone-d_6) δ -141.15 (hept, J = 707.4 Hz). MS (GC): 743.2 [M].

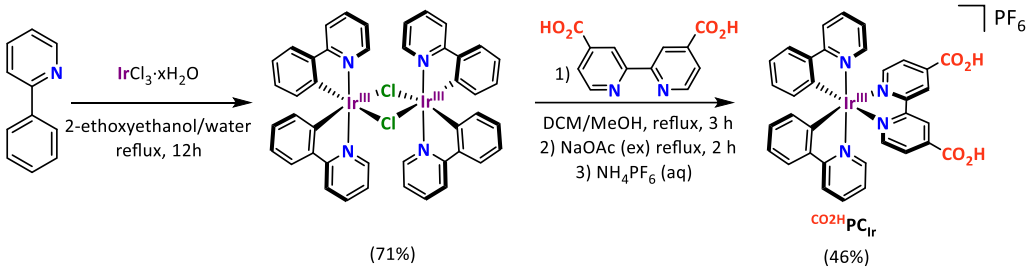

Synthesis of [Ir(ppy)$_2$(dcbpy)](PF$_6$), (^{CO2H}PC$_{Ir}$). [Ir(ppy)$_2$(μ-Cl)]$_2$ (50.0 mg, 0.047 mmol) as a solution in dichloromethane (6 mL) was added to a suspension of 4,4′-dicarboxy-2,2′-bipyridine (22.78 mg, 0.093 mmol) in methanol (6 mL). The reaction mixture was heated to reflux with stirring for 3 h under N_2 atmosphere, and then sodium

acetate (excess) in methanol (1.5 mL) was added. The mixture was heated for 2 h and then cooled to room temperature.

The solvent was removed under reduced pressure, hexafluorophosphoric acid (1 M, 5 mL) was added, and the suspension was stirred for 1 hour. The product was then filtered, washed with water (2 × 10 mL), and extracted into methanol. A saturated solution of ammonium hexafluorophosphate in methanol (2 mL) was added, and the mixture was stirred for a further 30 min. The solvent was removed under reduced pressure, and the residue was extracted into dichloromethane and filtered. The mixture was condensed and purified through a short silica path using CH_2Cl_2 for the elution. The solvent was removed under reduced pressure to give iridium [bis(C,N-phenylpyridine)-N,N-4,4′-carboxy-2,2′-bipyridine] hexafluorophosphate as a dark-red powder (39.0 mg, 46%). ^{1}H-NMR (acetone-d_6, 400 MHz, 300 K) δ, ppm: 9.34 (s, 1H), 8.33 (d, 2H, *J* = 5.6 Hz), 8.25 (d, 2H, *J* = 8.0 Hz), 8.17 (dd, 2H, *J* = 5.6, 1.6 Hz), 7.97 (td, 2H, *J* = 7.9, 1.5 Hz), 7.94-7.88 (m, 4H), 7.14 (ddd, 2H, *J* = 7.3, 5.9, 1.4 Hz), 7.06 (td, 2H, *J* = 7.6, 1.2 Hz), 6.94 (td, 2H, *J* = 7.4, 1.3 Hz), 6.34 (dd, 2H, *J* = 7.5, 0.9 Hz). ^{13}C[^{1}H]-NMR (acetone-d_6, 100.6 MHz, 300 K) δ, ppm: 168.4, 164.8, 157.6, 152.7, 150.6, 150.4, 144.9, 141.6, 139.8, 132.4, 131.4, 129.2, 125.9, 125.6, 124.6, 123.7, 120.9. MS (GC): 745.1 [M].

Table 3.5. Measured m/z: 743.2442 for **^{NMe2}PC$_{Ir}$** (expected: 743.2469).

Meas. m/z	Ion Formula	m/z	|err| [ppm]	err [mDa]	mSigma	e¯ Conf	z
741.2433	C36H34N6^191Ir	741.2445	1.7	-1.3	547.5	even	1+
	C33H36N5O3^191Ir	741.2419	1.9	-1.4	548.3	odd	1+
	C31H34N8O2^191Ir	741.2405	3.7	2.8	550.6	even	1+
743.2441	C36H34N6^193Ir	743.2469	3.8	2.8	2.4	even	1+
	C33H36N5O3^193Ir	743.2442	0.1	-0.1	16.6	odd	1+
	C31H34N8O2^193Ir	743.2429	1.7	1.2	23.0	even	1+

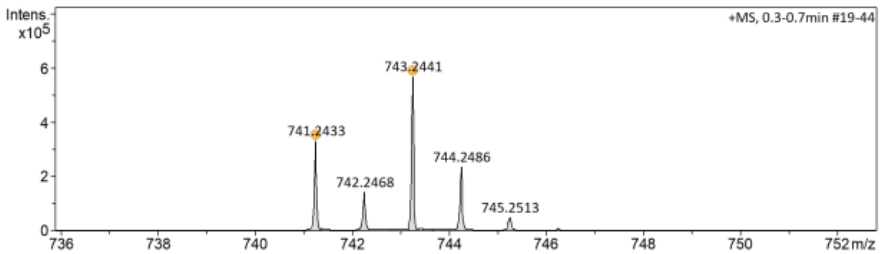

Table 3.6. Measured m/z: 745.1448 for **^{CO2H}PC$_{Ir}$** (expected: 745.1408).

Meas. m/z	Ion Formula	m/z	|err| [ppm]	err [mDa]	mSigma	e¯ Conf	z
743.1393	C34H24N4O4^191Ir	743.1398	0.6	-0.5	550.1	even	1+
	C31H26N3O7^191Ir	743.1371	3.0	-2.2	550.4	odd	1+
	C32H22N7O3^191Ir	743.1385	1.2	-0.9	552.1	odd	1+
745.1435	C32H22N7O3^193Ir	745.1408	3.7	-2.7	1.3	odd	1+
	C34H24N4O4^193Ir	745.1421	1.8	1.4	7.4	even	1+
	C37H22N5O^193Ir	745.1448	1.7	1.3	24.9	odd	1+

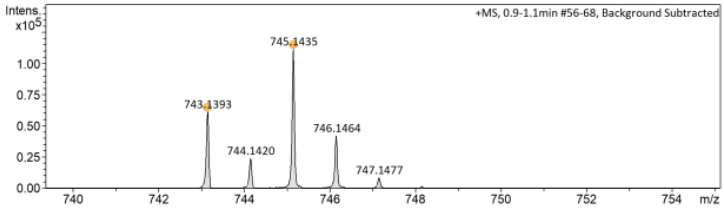

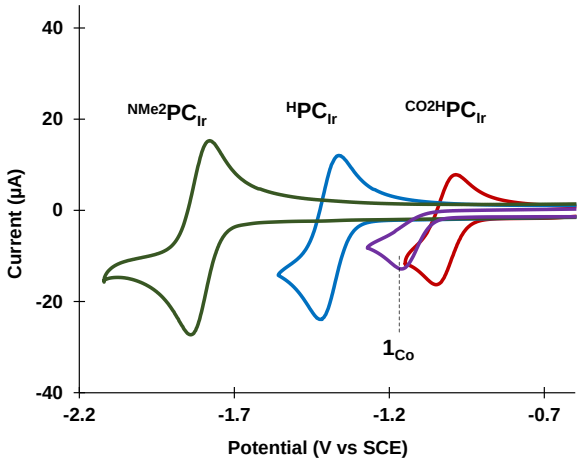

Figure 3.11. Cyclic voltammograms of ^{NMe2}**PC$_{Ir}$** (1 mM, green), **PC$_{Ir}$** (1 mM, blue), ^{CO2H}**PC$_{Ir}$** (1 mM, red) and 1 (1 mM, purple). CVs were recorded using $TBAPF_6$ (0.1 M) as a supporting electrolyte in dry acetonitrile. Scan rate = 100 mV/s, glassy carbon working electrode. Potentials are referenced *versus* SCE. E_{red}(^{NMe2}**PC$_{Ir}$**) = -1.81 V; E_{red}(**PC$_{Ir}$**) = -1.40 V; E_{red}(^{CO2H}**PC$_{Ir}$**) = -1.01 V.

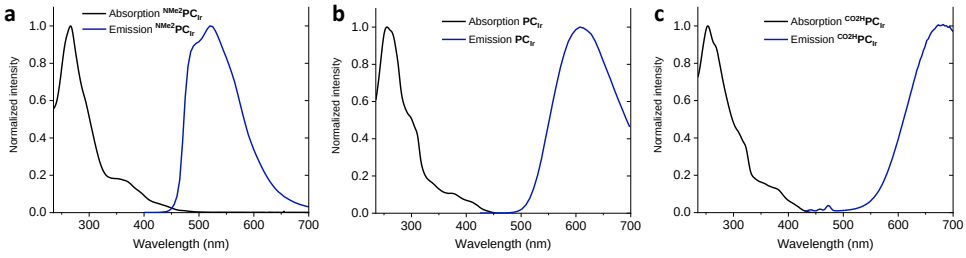

Figure 3.12. Normalised absorption and emission spectra of a) ^{NMe2}**PC$_{Ir}$**, b) **PC$_{Ir}$** and c) ^{CO2H}**PC$_{Ir}$**, at 10 µM concentration in CH_3CN, (V = 2 mL); cell path length = 1 cm; T = 25 °C.

3.4.5. Calculation of excited state redox potentials

Despite the redox potential of excited state photosensitisers can be measured experimentally,[69] in the broad literature, these values have been estimated using different approaches.[70] The most common way is probably using simplified Rehm-Weller equations, where E_{00} corresponds with the energy difference between the excited and ground state in the lowest vibrational level (0-0 transition). However, we consider that the most accurate measurement of the E_{00} from a triplet excited state should be estimated from the energy of the maximum emission wavelength (λ_{em}).[71] Then, the energy E_{00} is calculated from Planck's equation:

$$E_{00} = h\nu = hc/\lambda_{em}$$

E_{00} was calculated in Joules, taking h as $6.62607015E^{-34}$ **J·s**, c as $2.99792E^{17}$ **nm/s** and the corresponding λ_{em} in **nm**. Joules are converted to Volts divided by the Culoumbs of an electron ($1.60217733E^{-19}$ C). Then, in a simplified manner, we can calculate:

$$E^*_{red} = E_{red} + E_{00}$$

$$E^*_{ox} = E_{ox} - E_{00}$$

Table 3.7. Summary of ground state reduction potentials measured for the selected PC series and calculated for the excited state. All measurements were done in anhydrous acetonitrile.

Entry	PC	λ_{em} (nm)	E_{00} (V)	E_{red} (V)	E^*_{red} (V)
1	$\mathbf{PC_{Cu}}$	581	2.13	-1.6	0.5
2	$\mathbf{^{SO3}PC_{Cu}}$	560	2.21	-1.7	0.6
3	$\mathbf{^{I}PC_{Cu}}$	601	2.06	-1.5	0.6
4	$\mathbf{^{NMe2}PC_{Ir}}$	520	2.38	-1.8	0.6
5	$\mathbf{PC_{Ir}}$	610	2.03	-1.4	0.6
6	$\mathbf{^{CO2H}PC_{Ir}}$	670	1.82	-1.0	0.8

3.4.6. Characterisation of deuterated alkenes

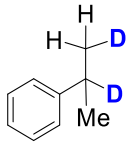

(1-methylethyl-1,2-*d*$_2$)benzene ([D]-2f). (38%, *this isolated yield was that low due to the volatility of the product and that non-optimised conditions were used: Et_3N was used instead of DIPEA) ^{1}H-NMR ($CDCl_3$, 400 MHz, 300 K) δ, ppm: 7.31-7.27 (m, 2H), 7.24-7.21 (m, 2H), 7.20-7.15 (m, 2H), 1.27-1.23 (m, 2H, C**HD**). ^{13}C[^{1}H]-NMR ($CDCl_3$, 100.6 MHz, 300 K) δ, ppm: 128.64, 126.74, 126.07, 23.93 (t, *J* = 19.4 Hz, **C**HD). MS (GC): 122.1 [M].

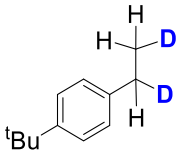

1-(tert-butyl)-4-(ethyl-1,2-*d*$_2$)benzene ([D]-2g). (54%, *this isolated yield was that low due to the volatility of the product) ^{1}H-NMR ($CDCl_3$, 400 MHz, 300 K) δ, ppm: 7.37-7.34 (m, 2H, **H$_{arom}$**), 7.19-7.17 (m, 2H, **H$_{arom}$**), 2.67-2.63 (m, 1H, C**HD**), 1.35 (s, 9H, (C**H$_3$**)$_3$), 1.29-1.23 (m, 2H, C**H$_2$D**). ^{13}C[^{1}H]-NMR ($CDCl_3$, 100.6 MHz, 300 K) δ, ppm: 148.5, 141.3, 127.6, 125.3, 34.5, 31.6, 28.0 (t, *J* = 19.5 Hz, **C**HD), 15.3 (t, *J* = 19.3 Hz, **C**H$_2$D). MS (GC): 164.0 [M].

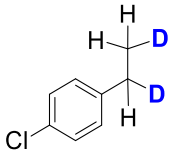

1-chloro-4-(ethyl-1,2-*d*$_2$)benzene ([D]-2h). (33%, *this isolated yield was that low due to the volatility of the product) ^{1}H-NMR ($CDCl_3$, 400 MHz, 300 K) δ, ppm: 7.26-7.23 (m, 2H), 7.14-7.10 (m, 2H), 2.63-2.57 (m, 1H, C**HD**), 1.22-1.18 (m, 2H, C**HD**). ^{13}C[^{1}H]-NMR ($CDCl_3$, 100.6 MHz, 300 K) δ, ppm: 142.7, 131.4, 129.3, 128.5, 28.0 (t, *J* = 19.4 Hz, **C**HD), 15.3 (t, *J* = 19.3 Hz, **C**H$_2$D). MS (GC): 142.0 [M].

3.4.6. Deuteration spectra collection

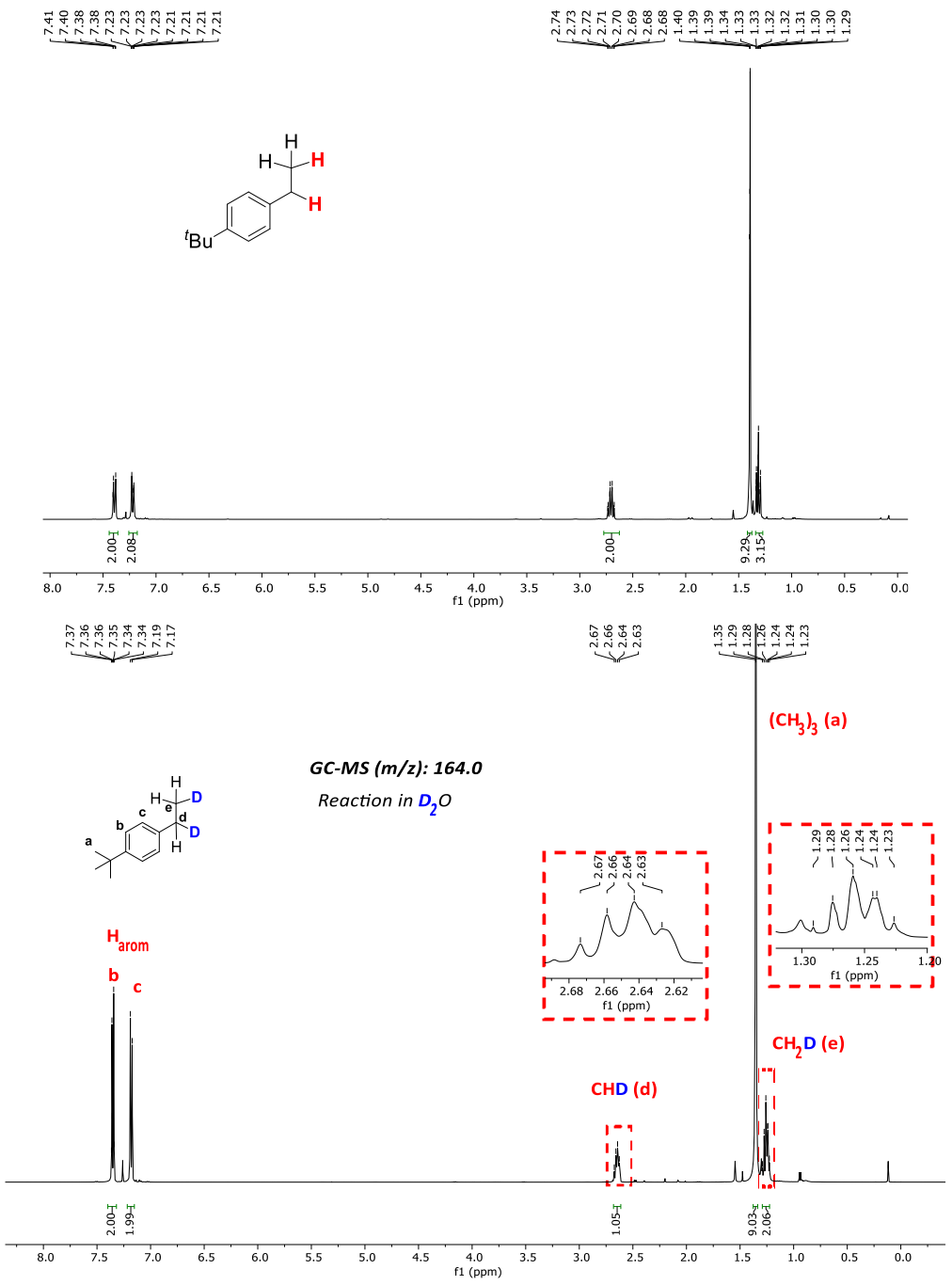

Figure 3.13. ^{1}H-NMR spectra ($CDCl_3$, 400 MHz, 300 K) of the isolated products **2g** and **[D]-2g** using H_2O (top) or D_2O (99.9 % in deuterium) (bottom) in the solvent mixture, respectively. Conditions: $\mathbf{1_{Co}}$ (3 mol%), $\mathbf{PC_{Cu}}$ (3 mol%), substrate (0.087 mmol, 8.7 mM) in H_2O (or D_2O):CH_3CN:Et_3N (6:4:0.2 ml) irradiated at λ= 447 nm and 15 ºC for 5 h, under N_2. Inset: amplification of the area of the –CHD and the -CH_2D.

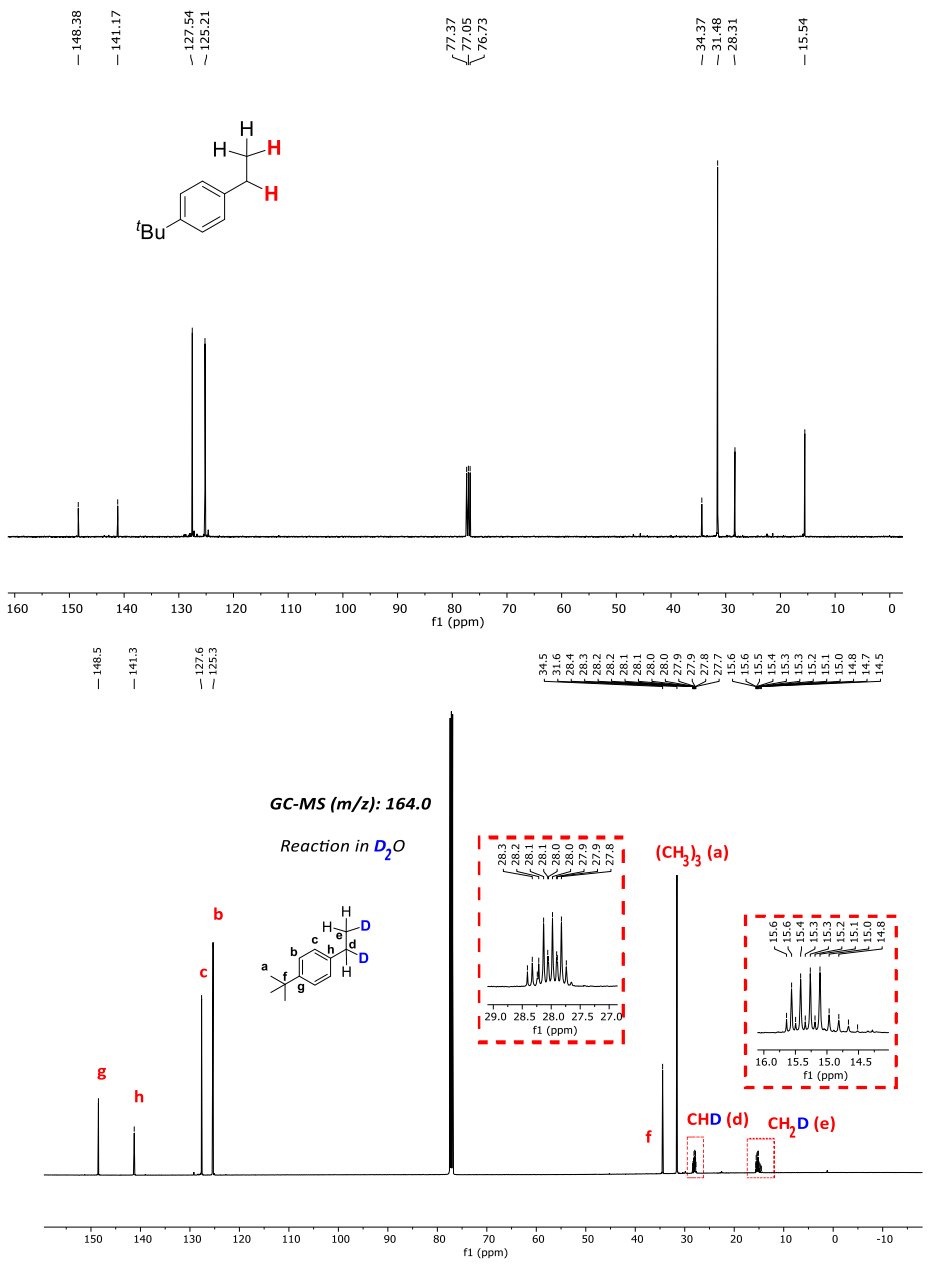

Figure 3.14. $^{13}C[^{1}H]$-NMR spectra ($CDCl_3$, 100.6 MHz, 300 K) of the isolated products **2g** and **[D]-2g** using H_2O (Top) or D_2O (99.9 % in deuterium) (Bottom) in the solvent mixture, respectively. Conditions: $\mathbf{1_{Co}}$ (3 mol%), $\mathbf{PC_{Cu}}$ (3 mol%), substrate (0.087 mmol, 8.7 mM) in H_2O (or D_2O):CH_3CN:Et_3N (6:4:0.2 ml) irradiated at λ = 447 nm and 15 ºC for 5 h, under N_2. Inset: amplification of the area of the $–CH_2D$ and –CHD with the insertion of deuterium showing the triplet due to the C–D coupling.

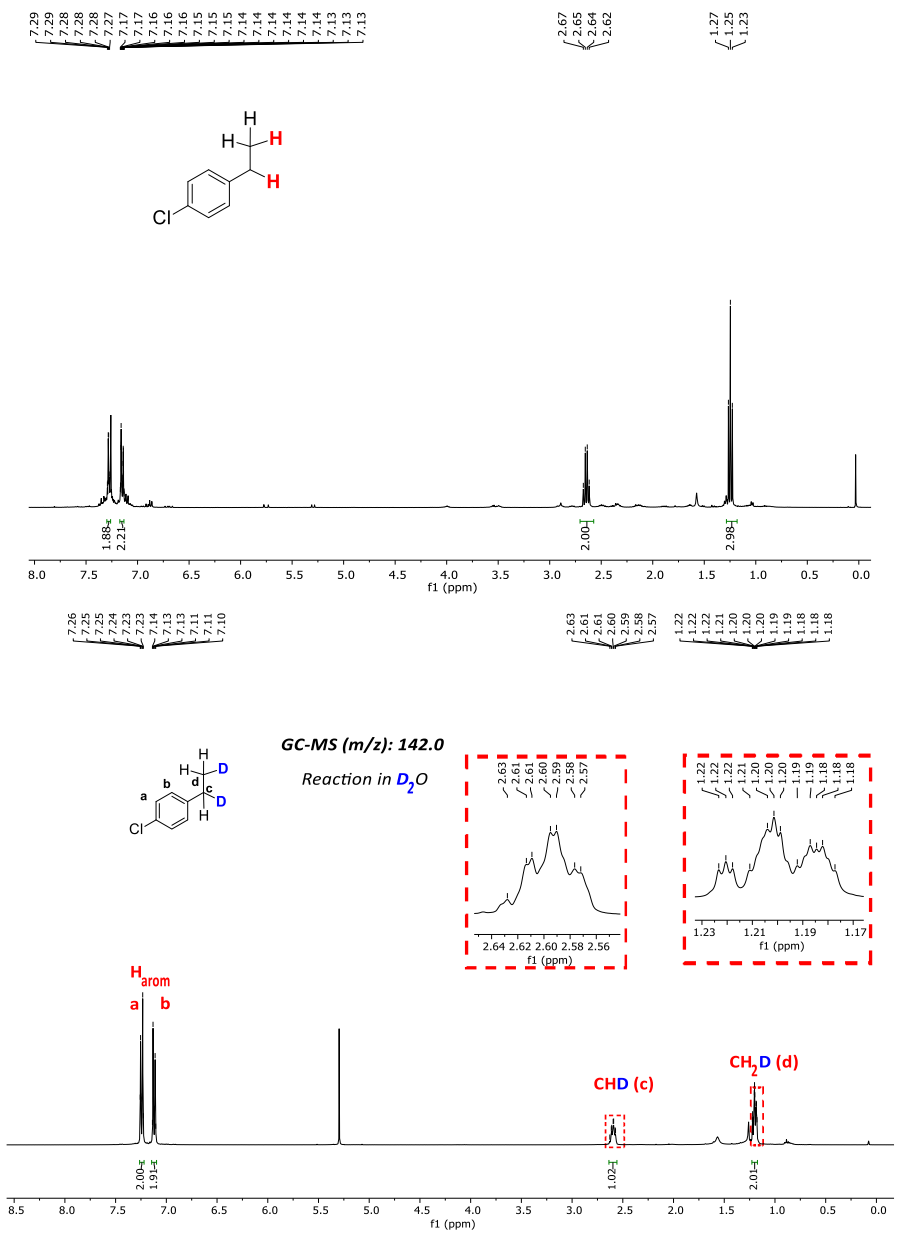

Figure 3.15. ^{1}H-NMR spectra ($CDCl_3$, 400 MHz, 300 K) of the isolated products **2h** and **[D]-2h** using H_2O (top) or D_2O (99.9 % in deuterium) (bottom) in the solvent mixture, respectively. Conditions: $\mathbf{1_{Co}}$ (3 mol%), $\mathbf{PC_{Cu}}$ (3 mol%), substrate (0.087 mmol, 8.7 mM) in H_2O (or D_2O):CH_3CN:Et_3N (6:4:0.2 ml) irradiated at λ = 447 nm and 15 ºC for 5 h, under N_2. Inset: amplification of the area of the –CHD and the -CH_2D.

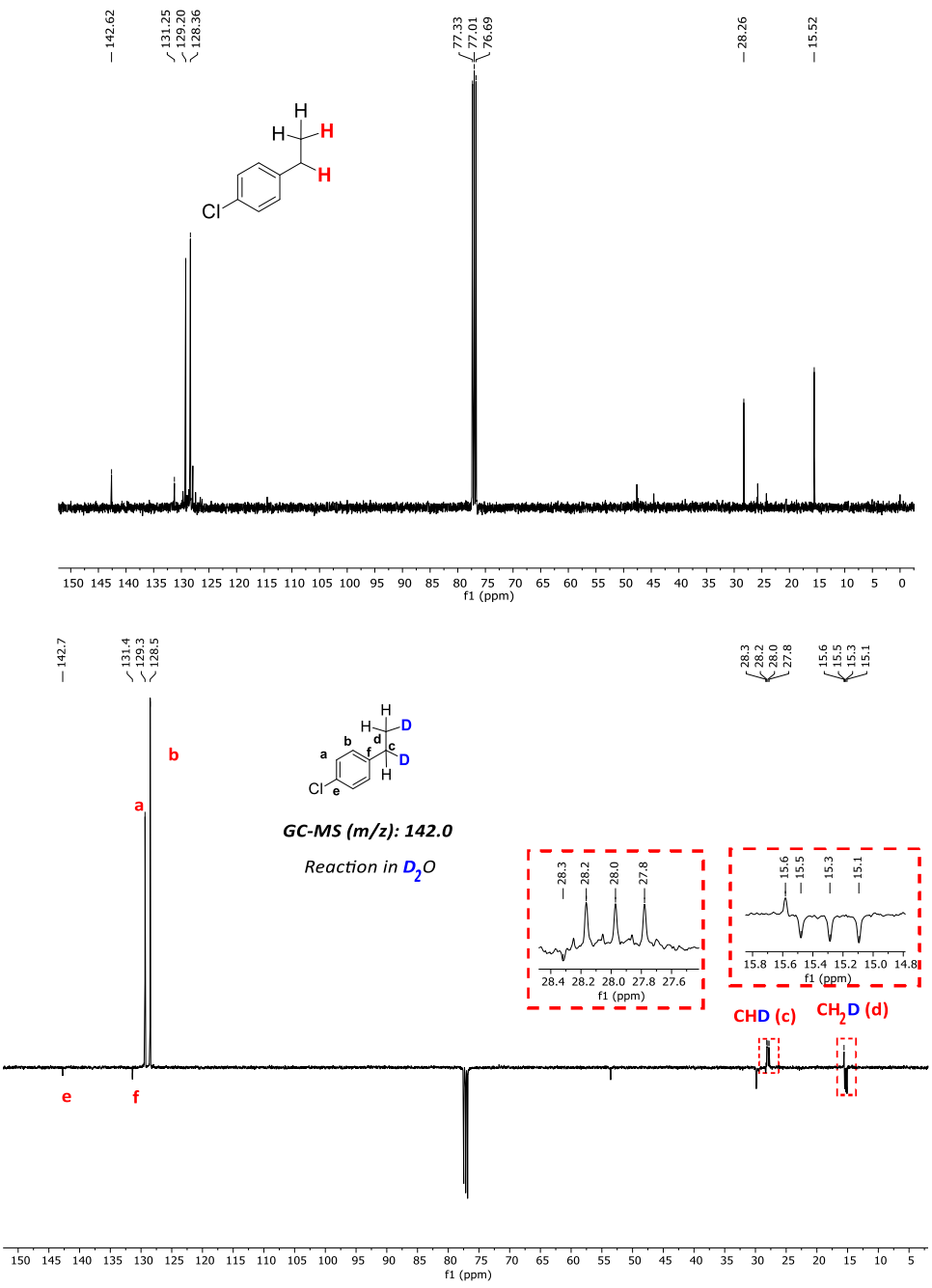

Figure 3.16. $^{13}C[^{1}H]$-NMR and $^{13}C[^{1}H]$-DEPTQ-135-NMR spectra ($CDCl_3$, 100.6 MHz, 300 K) of the isolated products **2h** and **[D]-2h** using H_2O (top) or D_2O (99.9 % in deuterium) (bottom) in the solvent mixture, respectively. Conditions: $\mathbf{1_{Co}}$ (3 mol%), $\mathbf{PC_{Cu}}$ (3 mol%), substrate (0.087 mmol, 8.7 mM) in H_2O (or D_2O):CH_3CN:Et_3N (6:4:0.2 ml) irradiated at λ = 447 nm and 15 ºC for 5 h, under N_2. Inset: amplification of the area of the $–CH_2D$ and –CHD with the insertion of deuterium showing the triplet due to the C–D coupling.

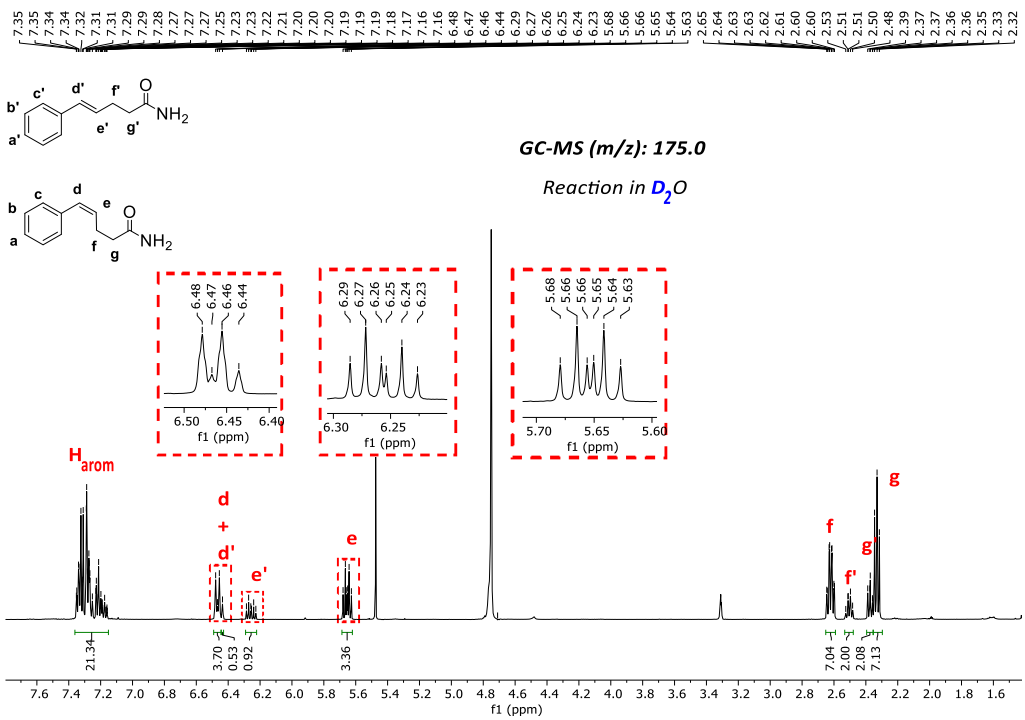

Figure 3.17. ^{1}H-NMR spectra (CD_3OD, 400 MHz, 300 K) of the mixture of products **1k** and **1k'** using D_2O (99.9 % in deuterium) in the solvent mixture, respectively. Conditions: $\mathbf{1_{Co}}$ (3 mol%), $\mathbf{PC_{Cu}}$ (3 mol%), substrate (0.087 mmol, 8.7 mM) in D_2O:CH_3CN:Et_3N (6:4:0.2 ml) irradiated at λ = 447 nm and 25 ºC for 5 h, under N_2. Inset: amplification of the area of the olefin characteristic signals.

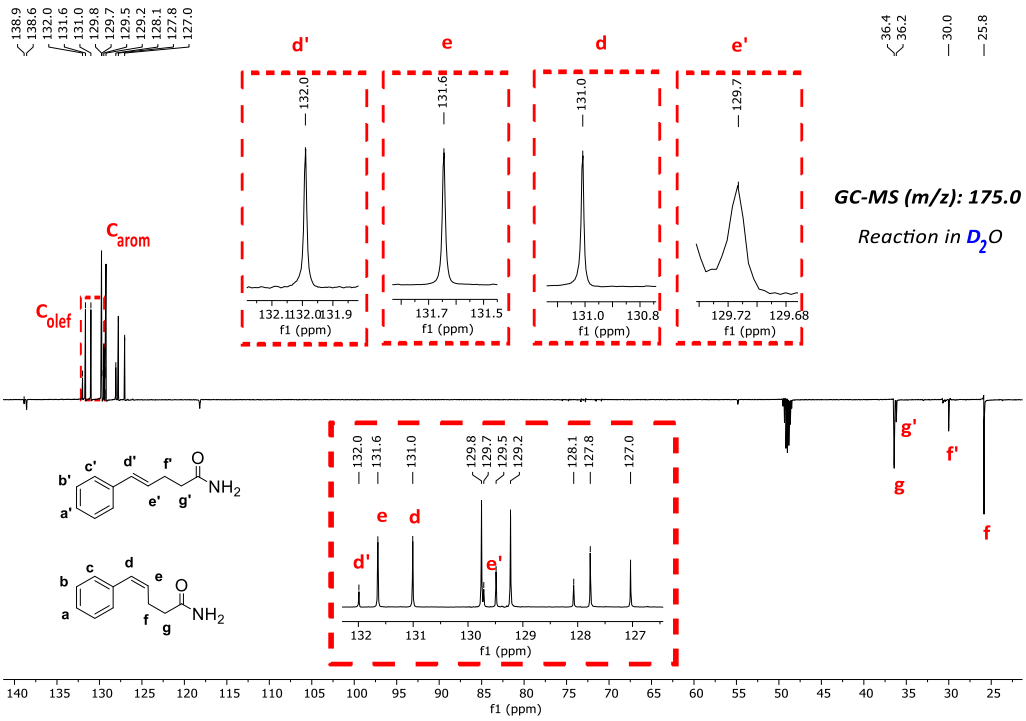

Figure 3.18. $^{13}C[^{1}H]$-NMR and $^{13}C[^{1}H]$-DEPTQ-135-NMR spectra (CD_3OD, 100.6 MHz, 300 K) of the mixture of products **1k** and **1k'** using D_2O (99.9 % in deuterium) in the solvent mixture, respectively. Conditions: $\mathbf{1_{Co}}$ (3 mol%), $\mathbf{PC_{Cu}}$ (3 mol%), substrate (0.087 mmol, 8.7 mM) in D_2O:CH_3CN:Et_3N (6:4:0.2 ml) irradiated at λ = 447 nm and 25 ºC for 5 h, under N_2. Inset: amplification of the area of the olefin characteristic signals (their appearance as singlets and not triplets correspond with no insertion of deuterium).

3.4.7. Competitive studies

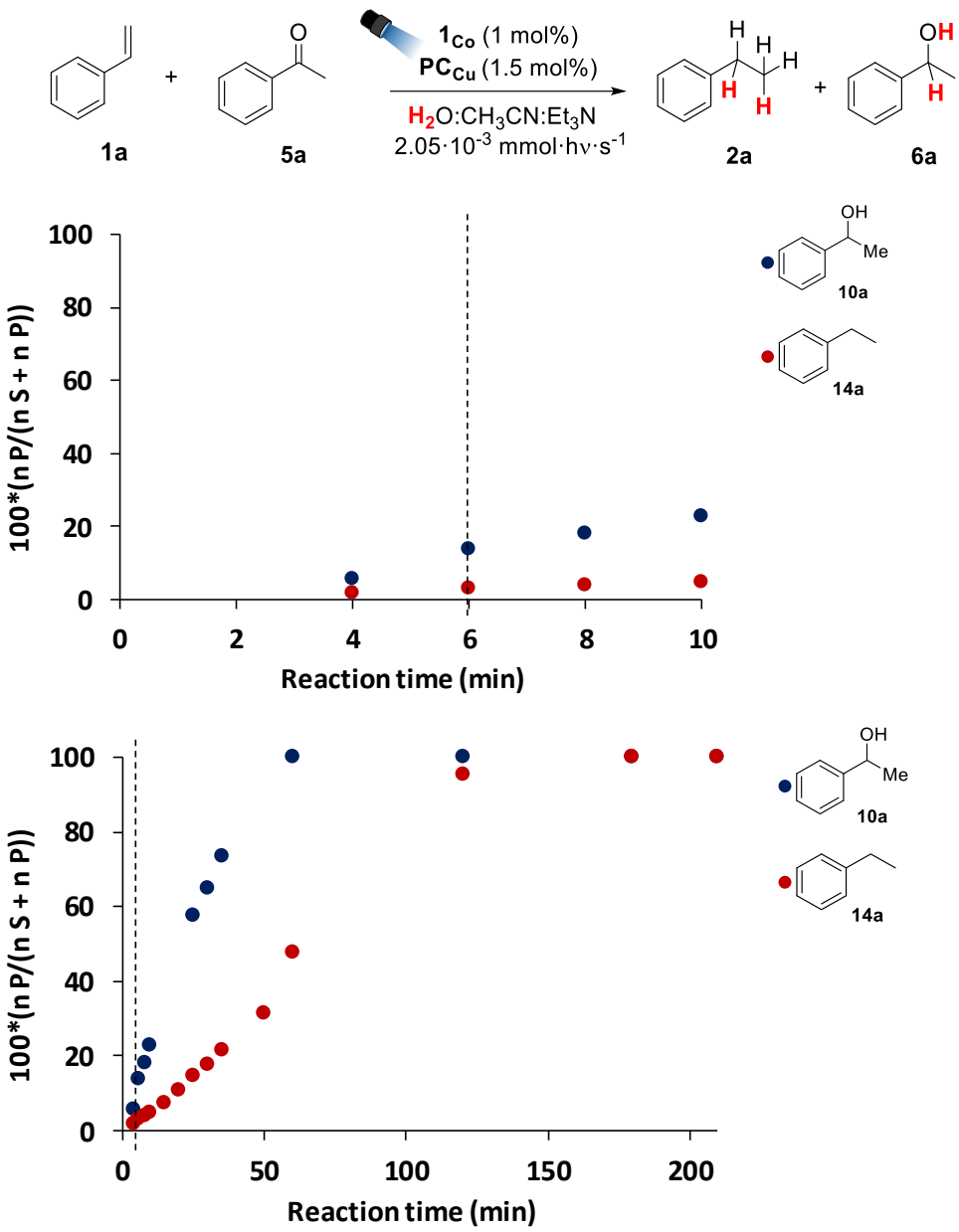

Figure 3.19. Monitoring of the competition between substrates **1a** and **5a** under catalytic conditions. Top: yield during the first 10 minutes of irradiation, it can be seen that the reduction of substrate **1a** starts when **5a** has not been totally reduced; bottom, all the reaction time monitorisation (3.5 hours). [a]Conditions: $\mathbf{1_{Co}}$ (1 mol%), $\mathbf{PC_{Cu}}$ (1.5 mol%), Substrate A + B (16.5 mM), A:B (1:1), in H_2O:CH_3CN:Et_3N (6:4:0.2 mL) irradiated (1 LED, 447 nm, $2.05\cdot10^{-3}$ mmol·hν·s^{-1} photons) for 4 h at 25 ºC under N_2. [b]The plotted data is the ratio between the amount of the reduced product formed and the sum of the amount of the reduced product formed and the unconverted starting material. [c] The black dotted line indicates where substrate **5a** reaches full conversion. Selectivity for ketone reduction 1.9 and olefin reduction 0.5.

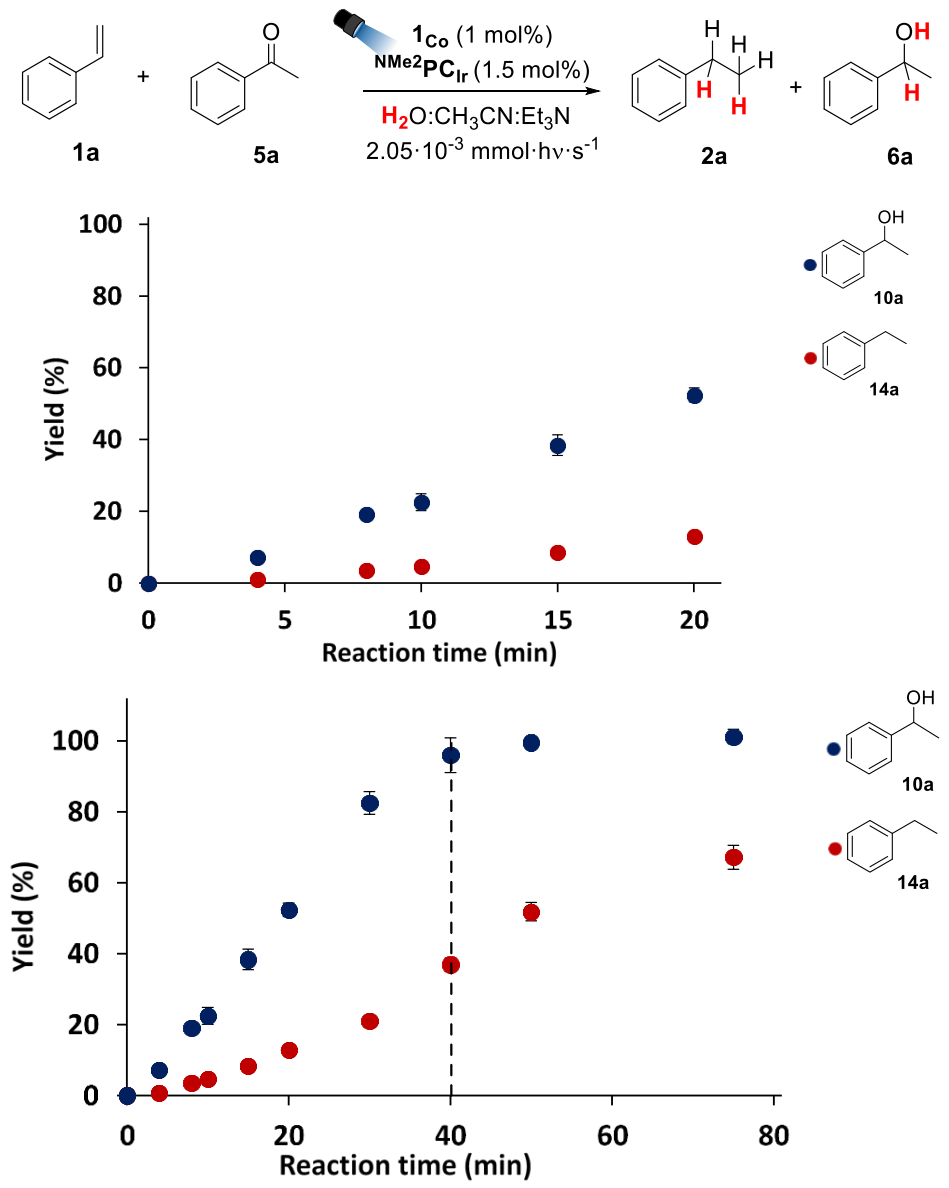

Figure 3.20. Monitoring of the competition between substrates **1a** and **5a**. Top: yield during the first 20 minutes of irradiation, it can be seen that the reduction of substrate **1a** starts when **5a** has not been totally reduced; bottom, all the reaction time monitorisation (75 min). [a]Conditions: $\mathbf{1}_{Co}$ (1 mol%), $^{NMe2}\mathbf{PC}_{Ir}$ (1.5 mol%), Substrate A + B (16.5 mM), A:B (1:1), in H_2O:CH_3CN:Et_3N (6:4:0.2 ml) irradiated (1 LED, 447 nm, $2.05\cdot10^{-3}$ mmol·hν·s^{-1} photons) for 75 min at 25 ºC under N_2. [b] The plotted data is determined by GC analysis after workup and relative to a calibrated internal standard. [c]The black dotted line indicates the point where substrate **5a** reaches full conversion. Selectivity for ketone reduction: 2.6.

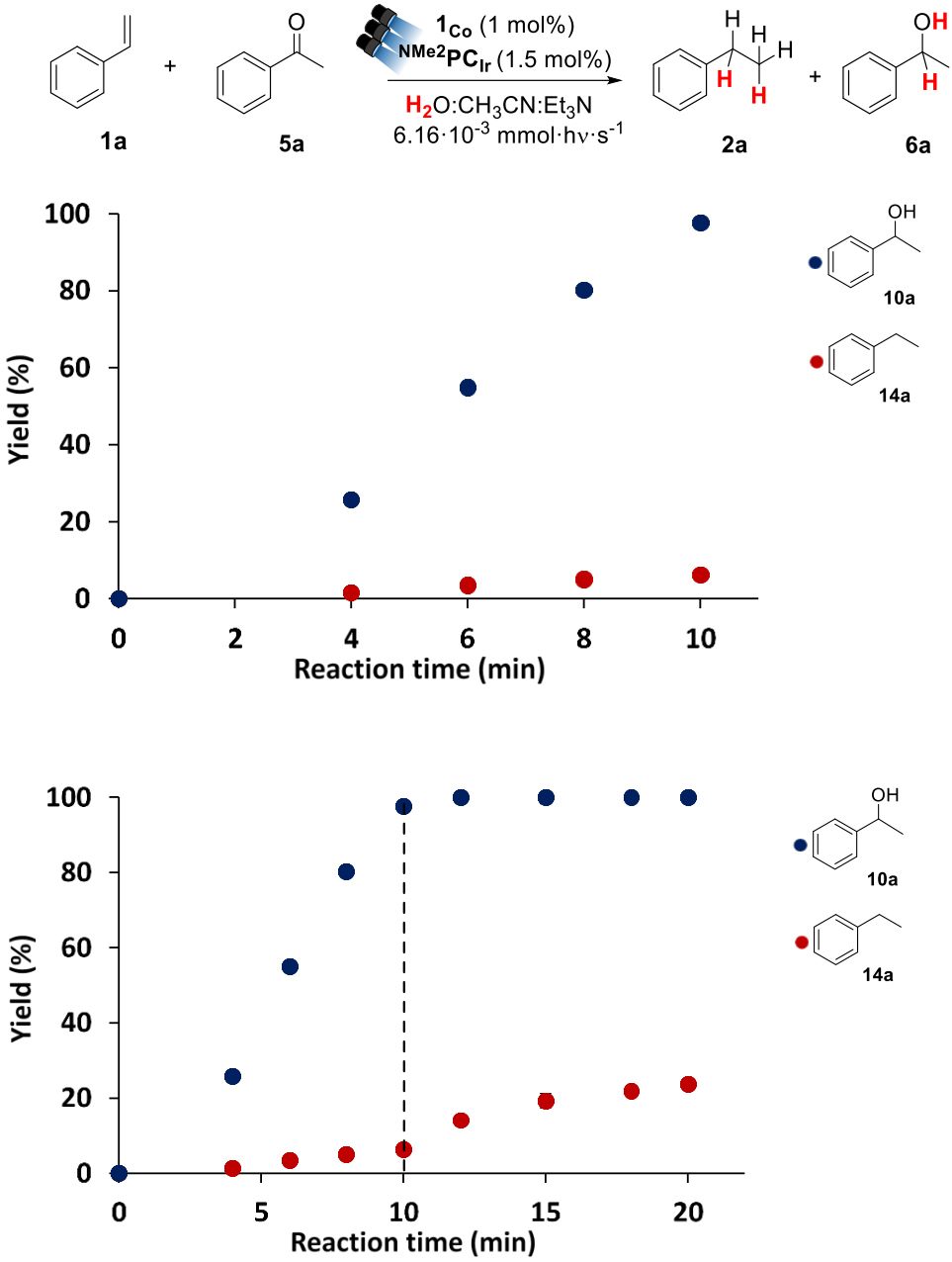

Figure 3.21. Monitoring of the competition between substrates **1a** and **5a**. Top: yield during the first 10 minutes of irradiation, it can be seen that the reduction of substrate **1a** starts when **5a** has not been totally reduced; bottom, all the reaction time monitorisation (20 min) [a]Conditions: $\mathbf{1_{Co}}$ (1 mol%), $^{NMe2}\mathbf{PC_{Ir}}$ (1.5 mol%), Substrate A + B (16.5 mM), A:B (1:1), in H_2O:CH_3CN:Et_3N (6:4:0.2 ml) irradiated (3 LEDs, 447 nm, $6.16\cdot10^{-3}$ mmol·hν·s^{-1} photons) for 20 min at 25 ºC under N_2. [b] The plotted data is determined by GC analysis after workup and relative to a calibrated internal standard. [c]The black dotted line indicates the point where substrate **5a** reaches full conversion. Selectivity for ketone reduction: 7.1.

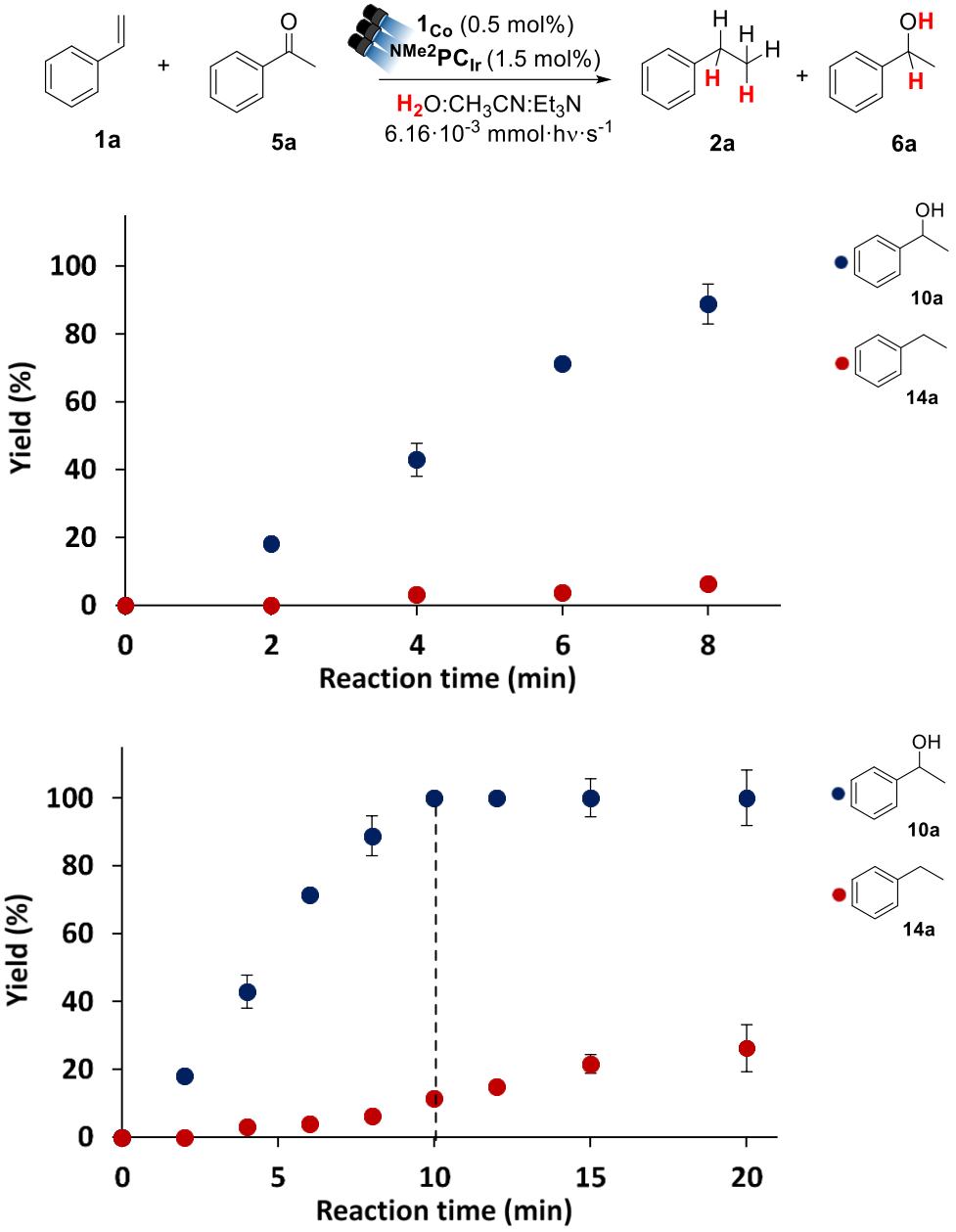

Figure 3.22. Monitoring of the competition between substrates **1a** and **5a**. Top: yield during the first 8 minutes of irradiation, it can be seen that the reduction of substrate **1a** starts when **5a** has not been totally reduced; bottom, all the reaction time monitorisation (20 min). [a]Conditions: $\mathbf{1_{Co}}$ (0.5 mol%), $^{\mathbf{NMe2}}\mathbf{PC_{Ir}}$ (1.5 mol%), Substrate A + B (16.5 mM), A:B (1:1), in H_2O:CH_3CN:Et_3N (6:4:0.2 ml) irradiated (3 LEDs, 447 nm, $6.16\cdot10^{-3}$ mmol·hν·s^{-1} photons) for 20 min at 25 ºC under N_2. [b] The plotted data is determined by GC analysis after workup and relative to a calibrated internal standard. [c]The black dotted line indicates the point where substrate **5a** reaches full conversion. Selectivity for ketone reduction: 9.1.

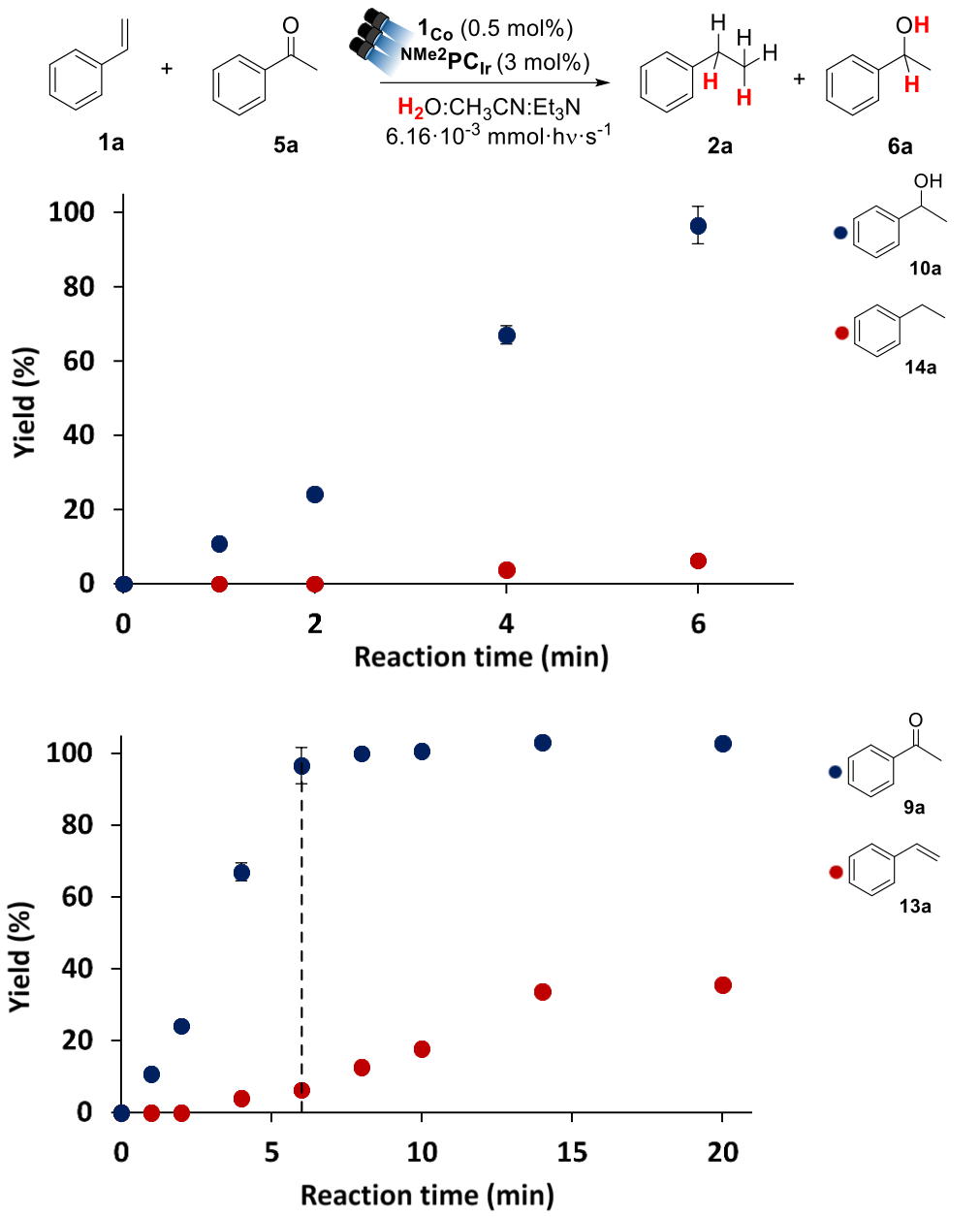

Figure 3.23. Monitoring of the competition between substrates **1a** and **5a**. Top: yield during the first 6 minutes of irradiation, it can be seen that the reduction of substrate **1a** starts when **5a** has not been totally reduced; bottom, all the reaction time monitorisation (20 min). [a]Conditions: $\mathbf{1}_{Co}$ (0.5 mol%), $^{NMe2}\mathbf{PC}_{Ir}$ (3 mol%), Substrate A + B (16.5 mM), A:B (1:1), in H_2O:CH_3CN:Et_3N (6:4:0.2 ml) irradiated (3 LEDs, 447 nm, $6.16\cdot10^{-3}$ mmol·hν·s^{-1} photons) for 20 min at 25 ºC under N_2. [b] The plotted data is determined by GC analysis after workup and relative to a calibrated internal standard. [c]The black dotted line indicates the point where substrate **5a** reaches full conversion. Selectivity for ketone reduction: 15.4.

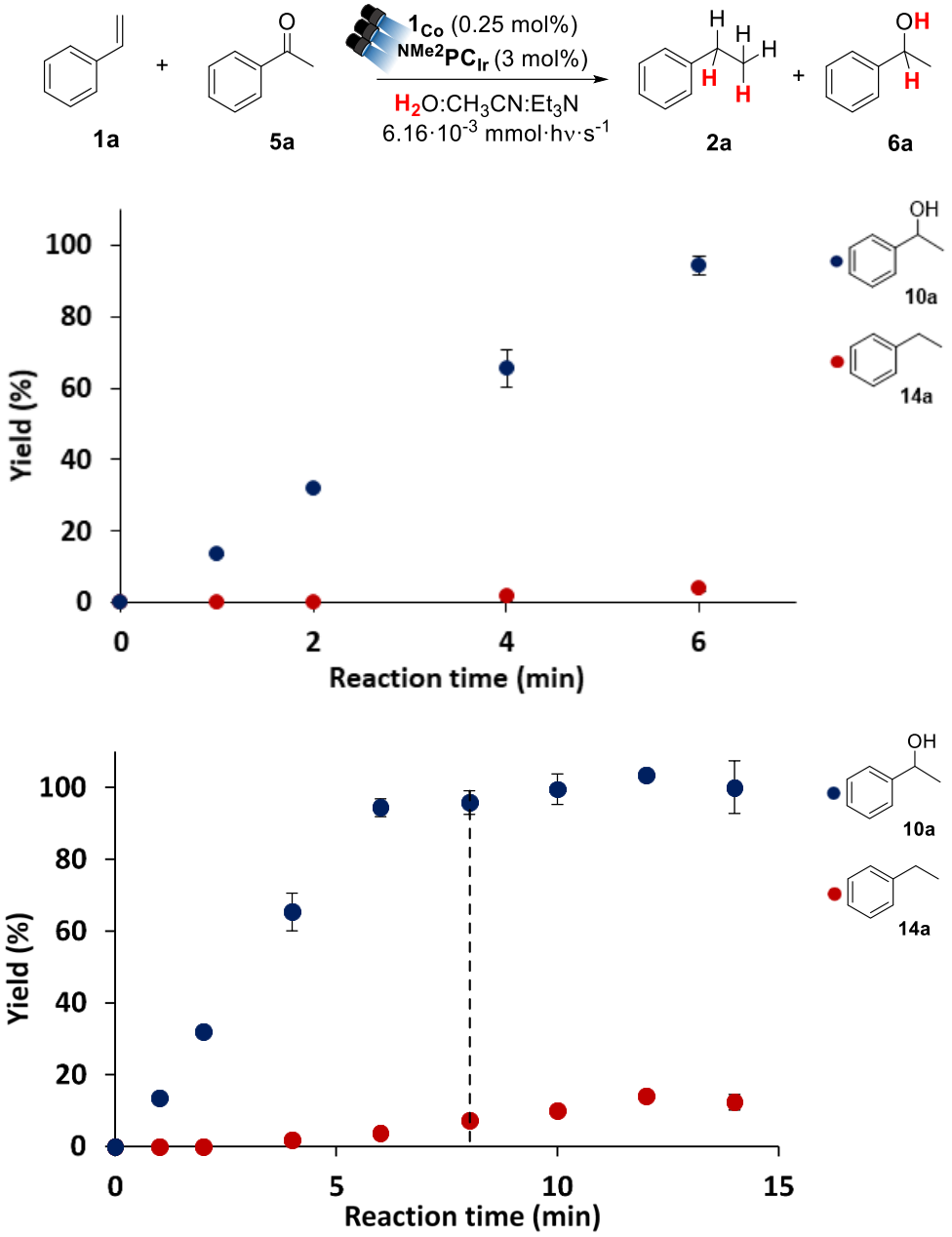

Figure 3.24. Monitoring of the competition between substrates **1a** and **5a**. Top: yield during the first 6 minutes of irradiation, it can be seen that the reduction of substrate **1a** starts when **5a** has not been totally reduced; bottom, all the reaction time monitorisation (14 min) - [a]Conditions: $\mathbf{1}_{Co}$ (0.25 mol%), $^{NMe2}\mathbf{PC}_{Ir}$ (3 mol%), Substrate A + B (16.5 mM), A:B (1:1), in H_2O:CH_3CN:Et_3N (6:4:0.2 ml) irradiated (3 LEDs, 447 nm, $6.16\cdot10^{-3}$ mmol·hν·s^{-1} photons) for 14 min at 25 ºC under N_2. [b] The plotted data is determined by GC analysis after workup and relative to a calibrated internal standard. [c]The black dotted line indicates the point where substrate **5a** reaches full conversion. Selectivity for ketone reduction: 24.7.

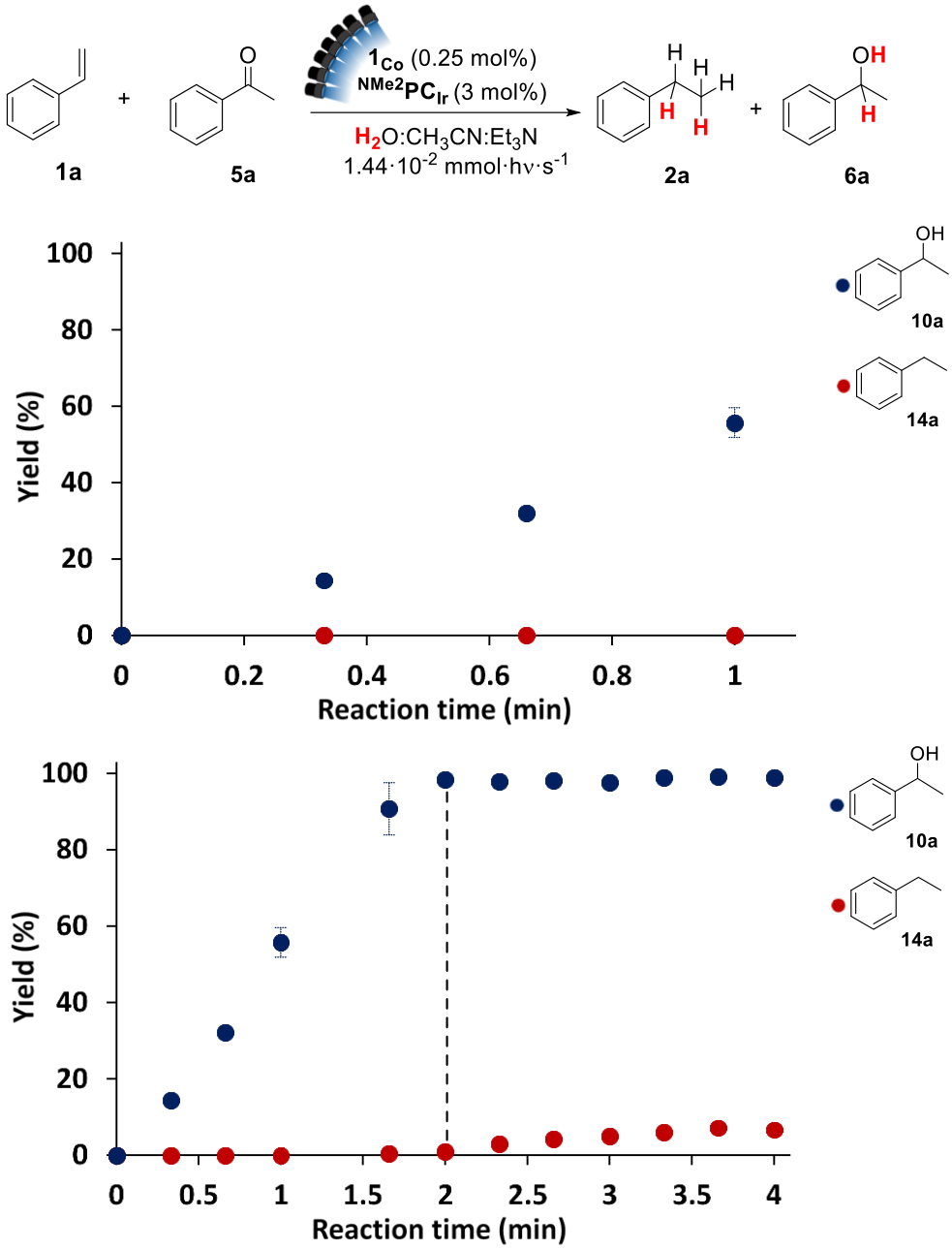

Figure 3.25. Monitoring of the competition between substrates **1a** and **5a**. Top: yield during the first 6 minutes of irradiation, it can be seen that the reduction of substrate **1a** starts when **5a** has not been totally reduced; bottom, all the reaction time monitorisation (14 min) - [a]Conditions: $\mathbf{1_{Co}}$ (0.25 mol%), $^{NMe2}\mathbf{PC_{Ir}}$ (3 mol%), Substrate A + B (16.5 mM), A:B (1:1), in H_2O:CH_3CN:Et_3N (6:4:0.2 ml) irradiated (7 LEDs, 447 nm, $1.44\cdot10^{-2}$ mmol·hν·s^{-1} photons) for 4 min at 25 ºC under N_2. [b] The plotted data is determined by GC analysis after workup and relative to a calibrated internal standard. [c]The black dotted line indicates the point where substrate **5a** reaches full conversion. Selectivity for ketone reduction: >99, full.

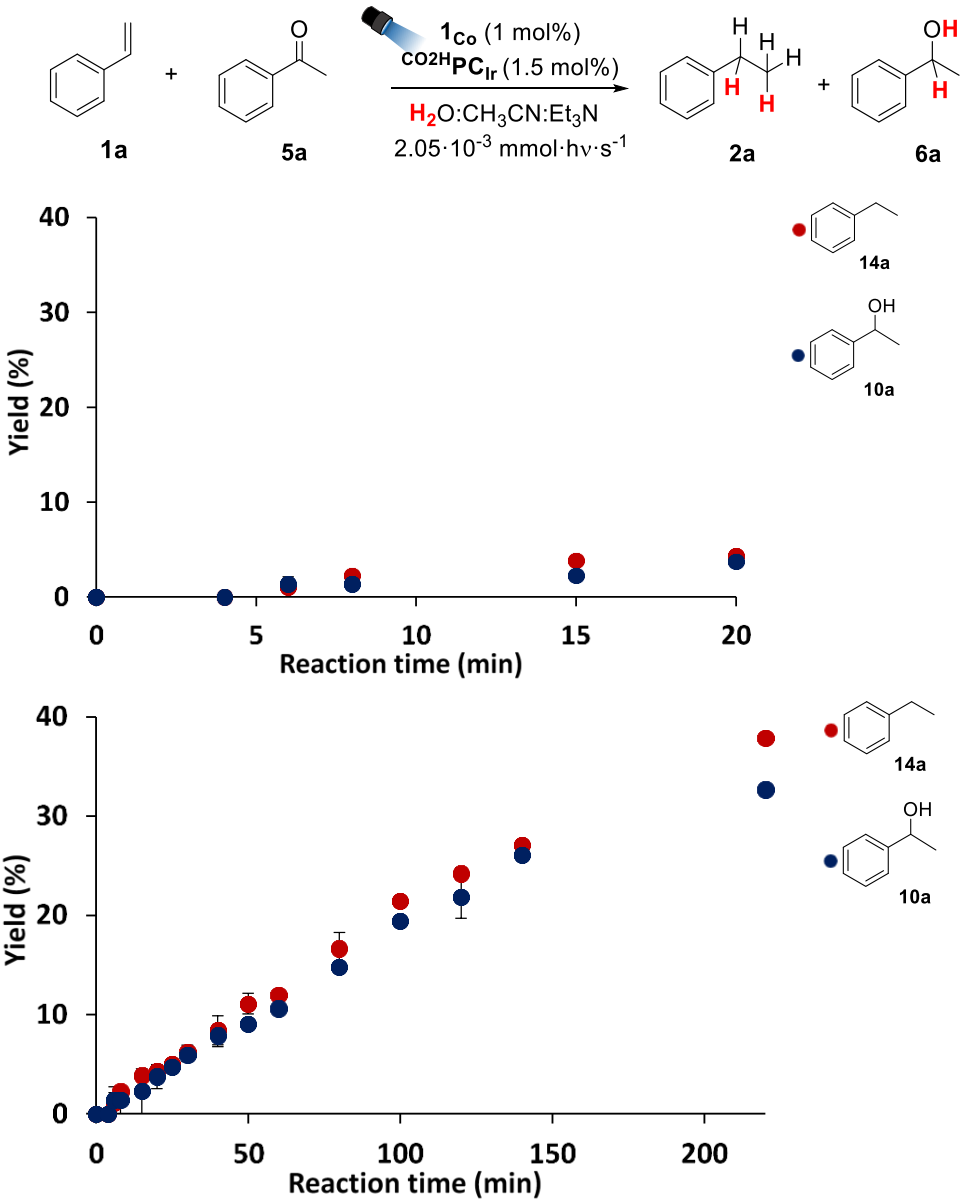

Figure 3.26. Monitoring of the competition between substrates **1a** and **5a**. Top: yield during the first 20 minutes of irradiation, it can be seen that the reduction of substrate **5a** starts when **1a** has not been totally reduced; bottom, all the reaction time monitorisation (220 min). [a]Conditions: $\mathbf{1_{Co}}$ (1 mol%), $^{CO2H}\mathbf{PC_{Ir}}$ (1.5 mol%), Substrate A + B (16.5 mM), A:B (1:1), in H_2O:CH_3CN:Et_3N (6:4:0.2 ml) irradiated (1 LED, 447 nm, $2.05\cdot10^{-3}$ mmol·hν·s^{-1} photons) for 220 min at 25 ºC under N_2. [b] The plotted data is determined by GC analysis after workup and relative to a calibrated internal standard. Selectivity for olefin reduction (taken at the end): 1.2.

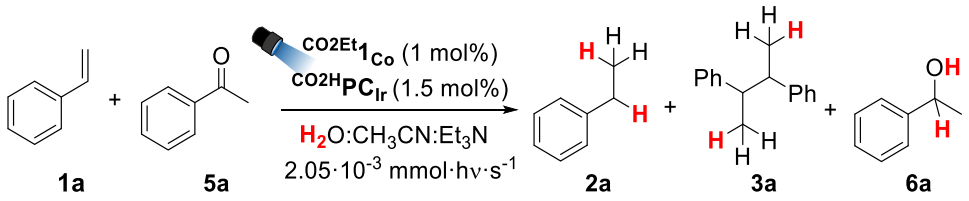
CO2Et
1Co (1 mol%)
CO2H
PCIr (1.5 mol%)
H2O:CH3CN:Et3N
2.05·10-3 mmol·hν·s-1
1a
5a
2a
3a
6a

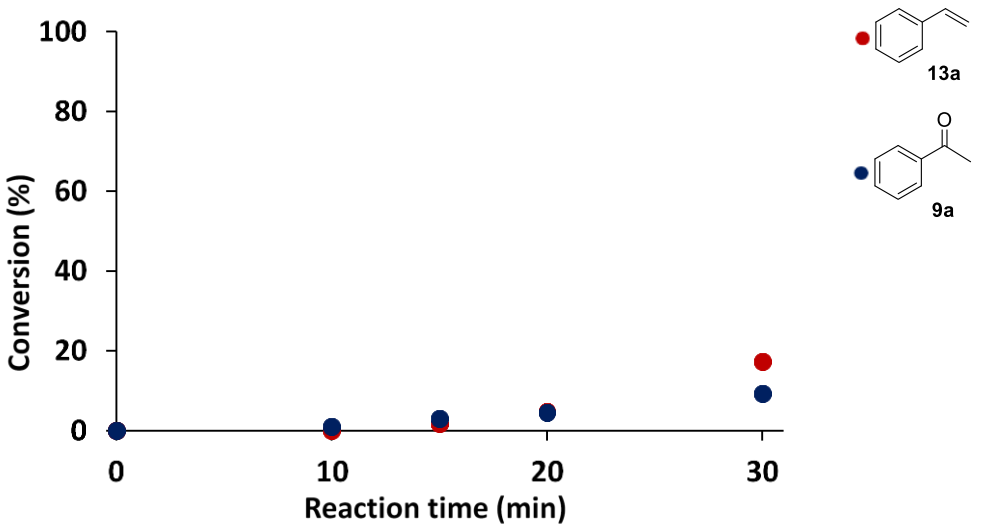
Conversion (%)
Reaction time (min)
13a
9a

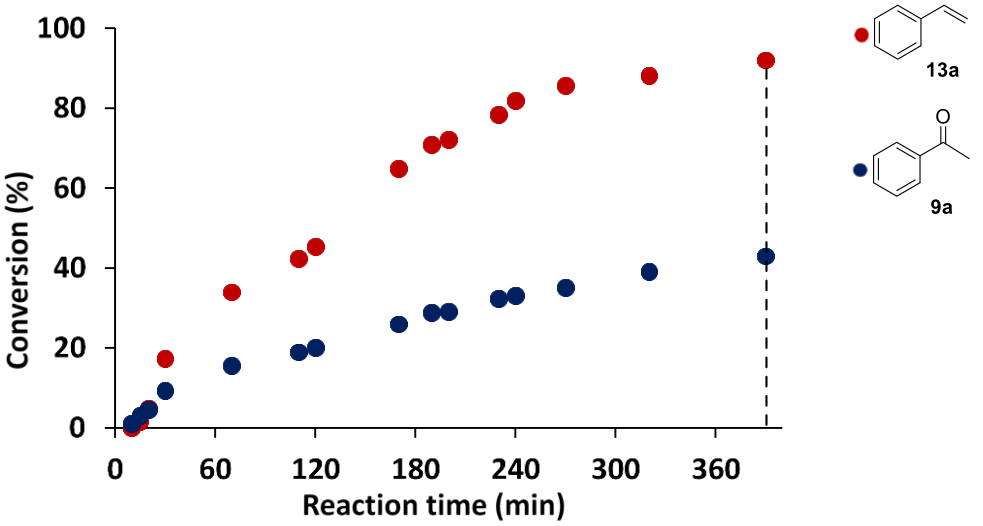
Conversion (%)
Reaction time (min)
13a
9a

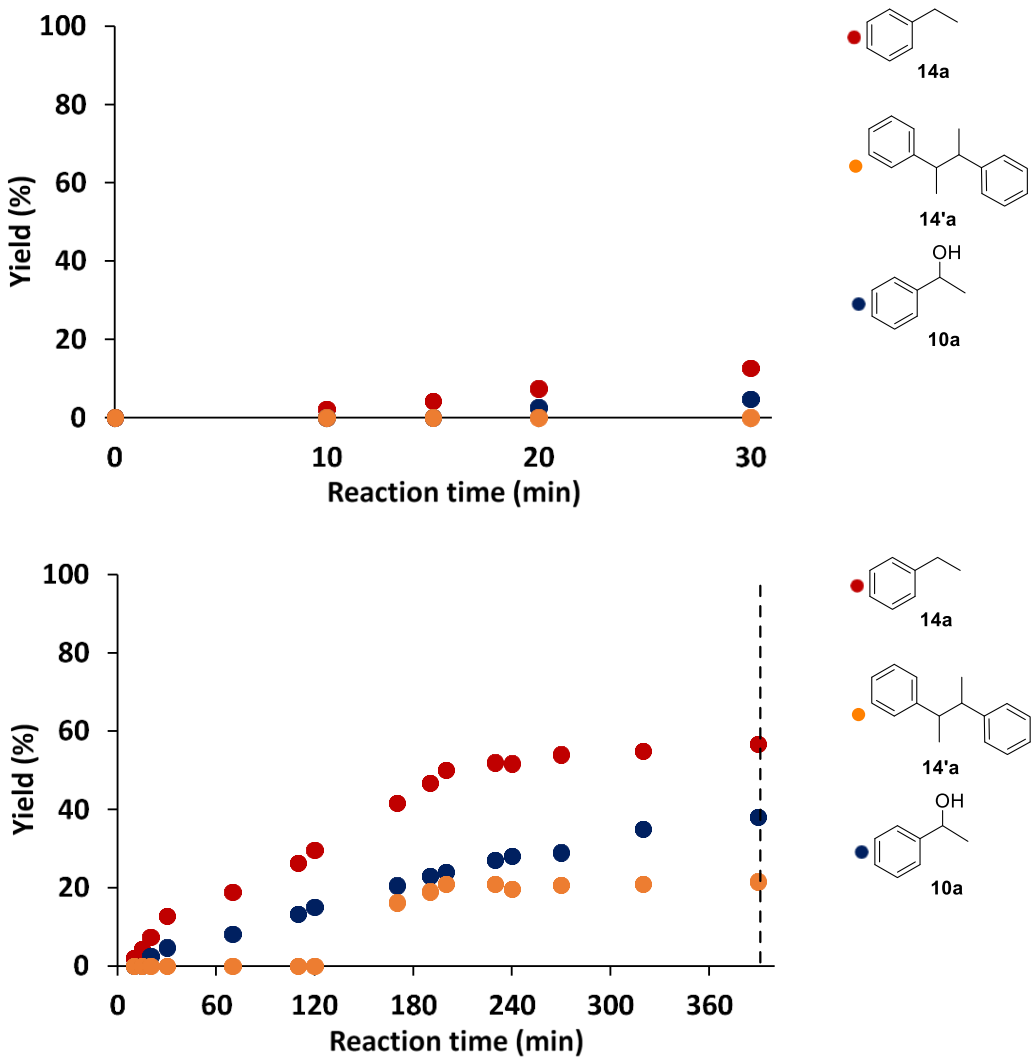

Figure 3.27. Monitoring of the competition between substrates **1a** and **5a**. Top: yield during the first 30 minutes of irradiation, it can be seen that the reduction of substrate **5a** starts when **1a** has not been totally reduced; bottom, all the reaction time monitorisation (380 min). [a]Conditions: $^{CO2Et}\mathbf{1}_{Co}$ (1 mol%), $^{CO2H}\mathbf{PC}_{Ir}$ (1.5 mol%), Substrate A + B (16.5 mM), A:B (1:1), in H_2O:CH_3CN:Et_3N (6:4:0.2 ml) irradiated (1 LED, 447 nm, $2.05 \cdot 10^{-3}$ mmol·hν·s^{-1} photons) for 380 min at 25 ºC under N_2. [b] The plotted data is determined by GC analysis after workup and relative to a calibrated internal standard. [c] The black dotted line indicates the point where substrate **1a** reaches full conversion. Selectivity for olefin reduction: 2.2.

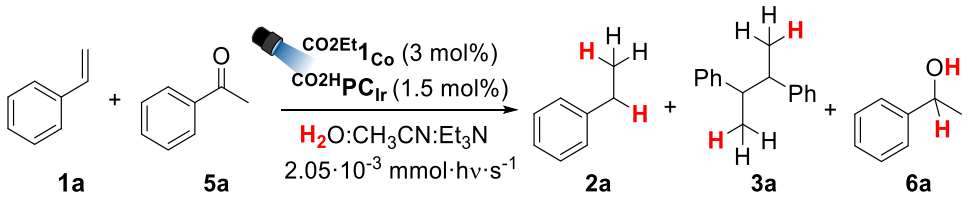
CO2Et
1Co (3 mol%)
CO2H
PCIr (1.5 mol%)
H2O:CH3CN:Et3N
2.05·10-3 mmol·hν·s-1
1a
5a
2a
3a
6a

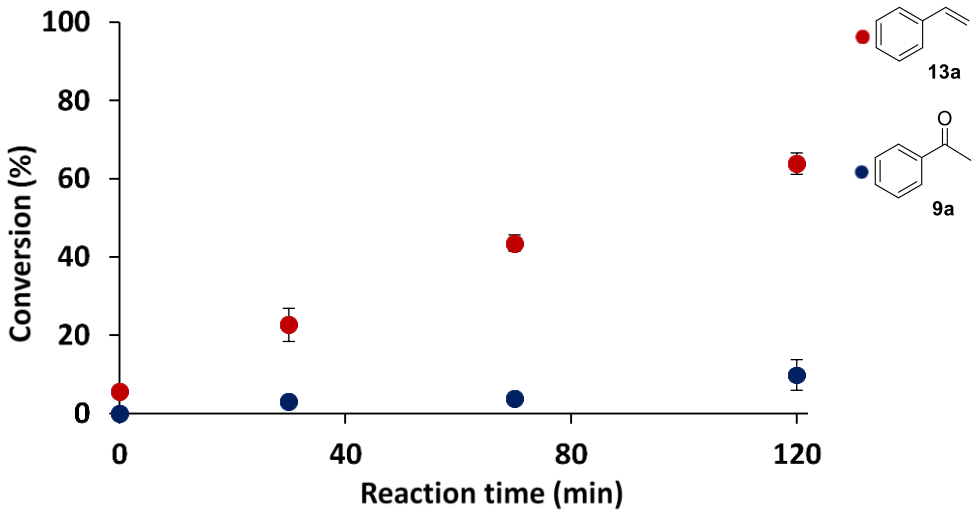
Conversion (%)
Reaction time (min)
13a
9a

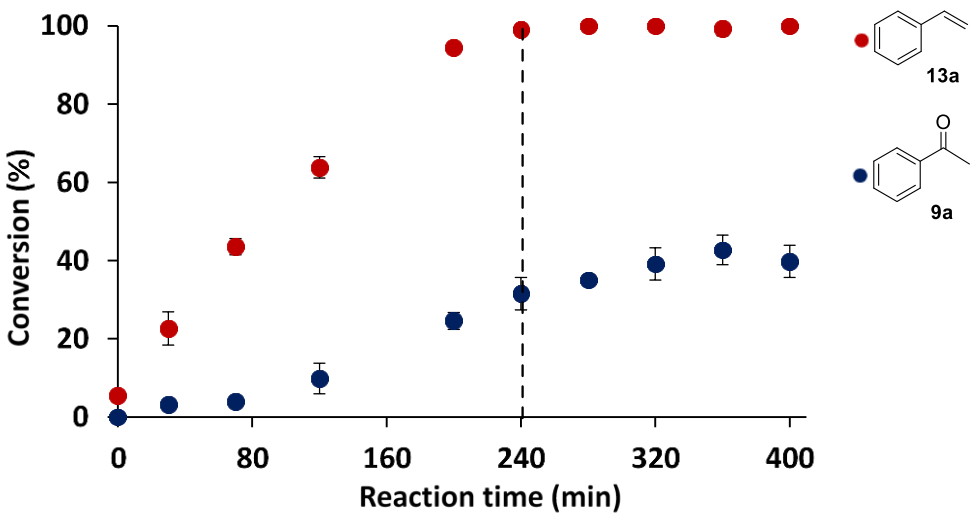
Conversion (%)
Reaction time (min)
13a
9a

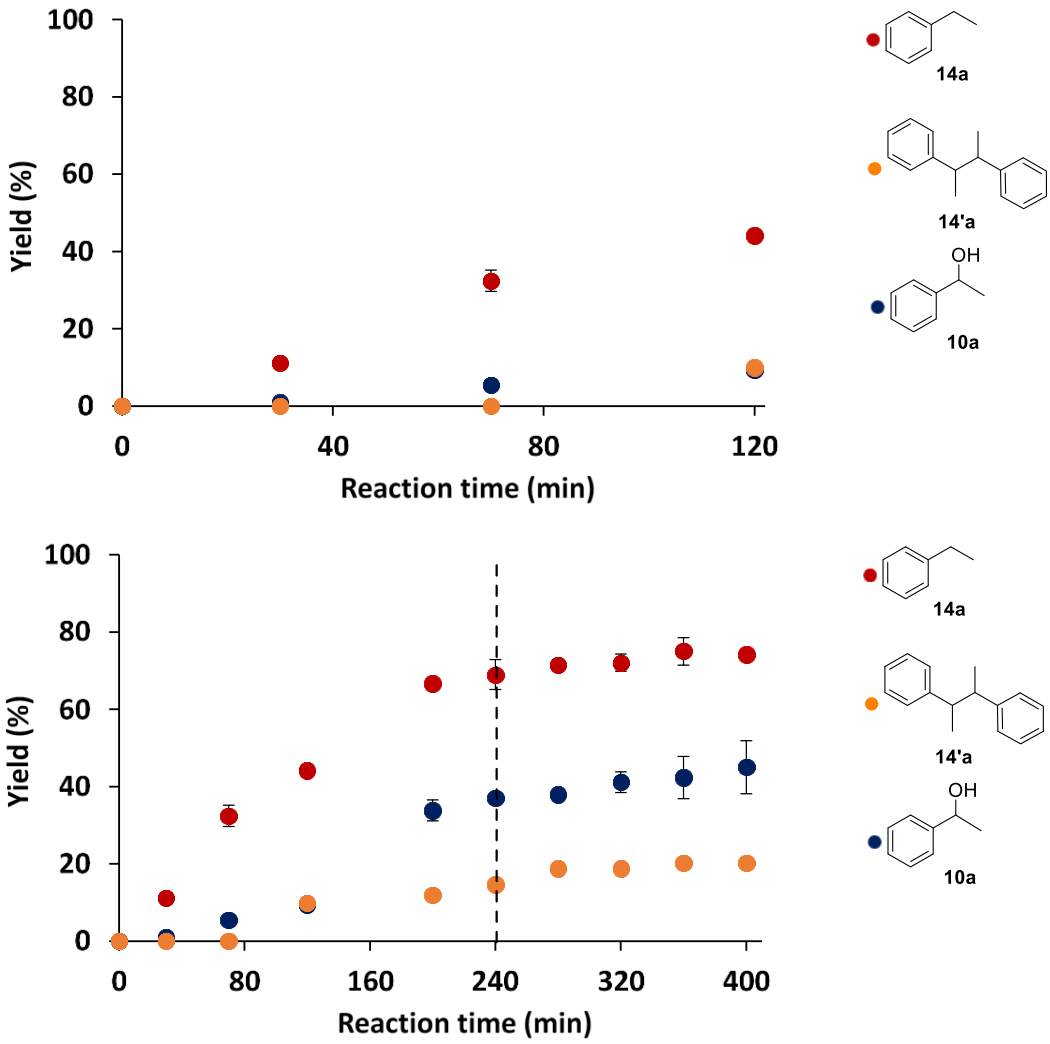

Figure 3.28. Monitoring of the competition between substrates **1a** and **5a**. Top: yield during the first 120 minutes of irradiation, it can be seen that the reduction of substrate **5a** starts when **1a** has not been totally reduced; bottom, all the reaction time monitorisation (400 min). [a]Conditions: $^{CO2Et}\mathbf{1}_{Co}$ (3 mol%), $^{CO2H}\mathbf{PC}_{Ir}$ (1.5 mol%), Substrate A + B (16.5 mM), A:B (1:1), in H_2O:CH_3CN:Et_3N (6:4:0.2 ml) irradiated (1 LED, 447 nm, $2.05 \cdot 10^{-3}$ mmol·hν·s^{-1} photons) for 400 min at 25 ºC under N_2. [b] The plotted data is determined by GC analysis after workup and relative to a calibrated internal standard. [c] The black dotted line indicates the point where substrate **1a** reaches full conversion. Selectivity for olefin reduction: 3.1.

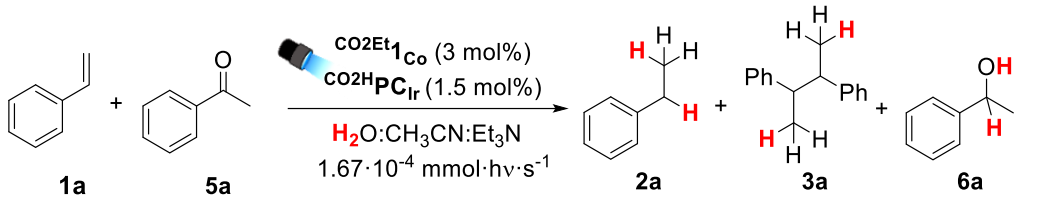
CO2Et
1Co (3 mol%)
CO2H
PCIr (1.5 mol%)
H2O:CH3CN:Et3N
1.67·10-4 mmol·hν·s-1
1a
5a
2a
3a
6a

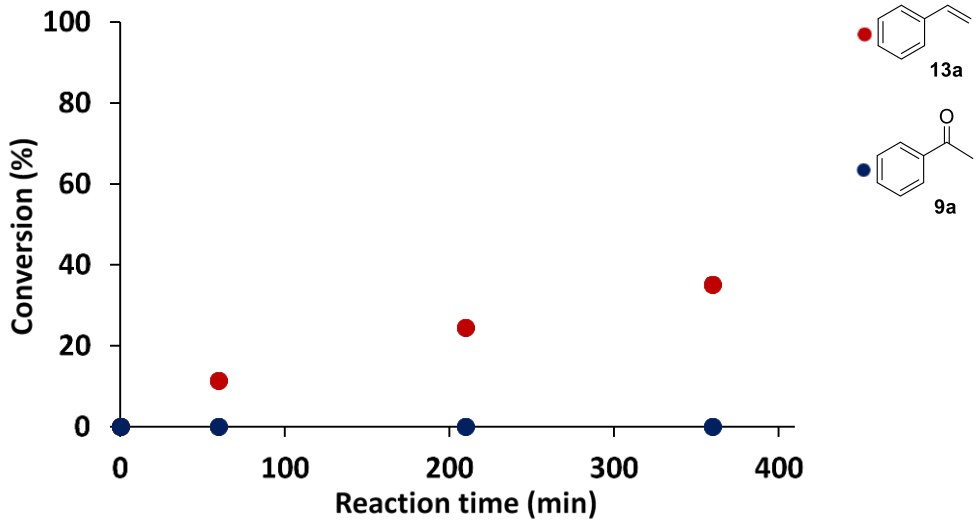
Conversion (%)
Reaction time (min)
13a
9a

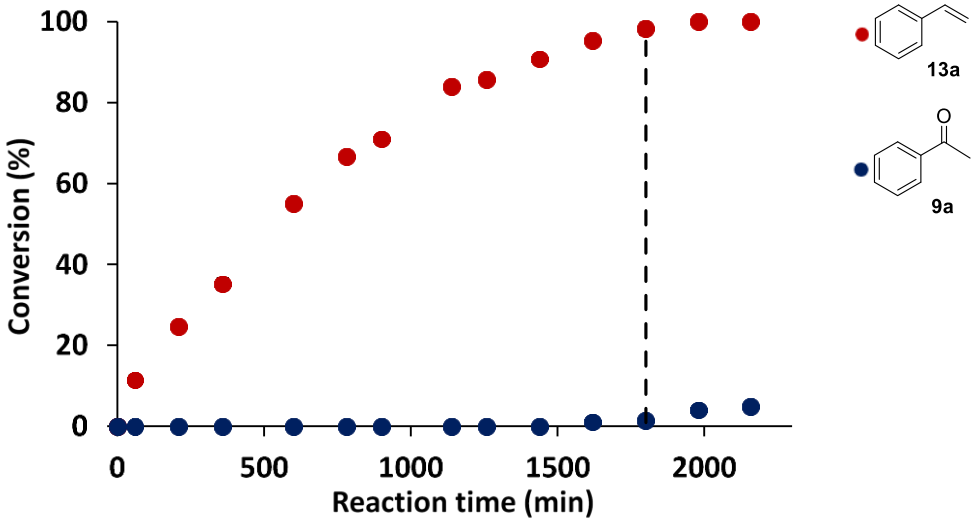
Conversion (%)
Reaction time (min)
13a
9a

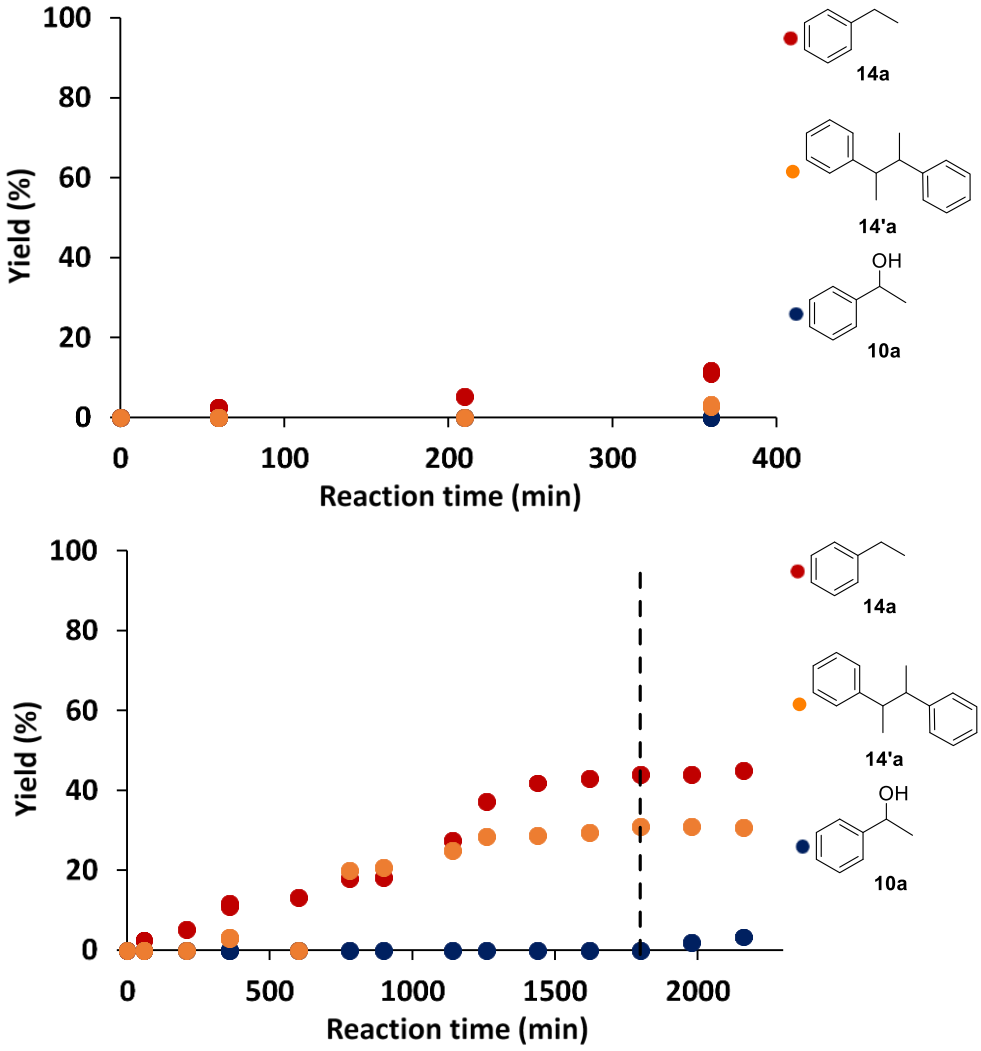

Figure 3.29. Monitoring of the competition between substrates **1a** and **5a**. Top: yield during the first 400 minutes of irradiation, it can be seen that the reduction of substrate **5a** starts when **1a** has not been totally reduced; bottom, all the reaction time monitorisation (2160 min). [a]Conditions: $^{CO2Et}\mathbf{1}_{Co}$ (3 mol%), $^{CO2H}\mathbf{PC}_{Ir}$ (1.5 mol%), Substrate A + B (16.5 mM), A:B (1:1), in H_2O:CH_3CN:Et_3N (6:4:0.2 ml) irradiated (1 LED, 447 nm, $2.05 \cdot 10^{-3}$ mmol·hv·s^{-1} photons) for 2160 min at 25 ºC under N_2. [b] The plotted data is determined by GC analysis after workup and relative to a calibrated internal standard. [c] The black dotted line indicates the point where substrate **1a** reaches full conversion. Selectivity for olefin reduction: >99, full.

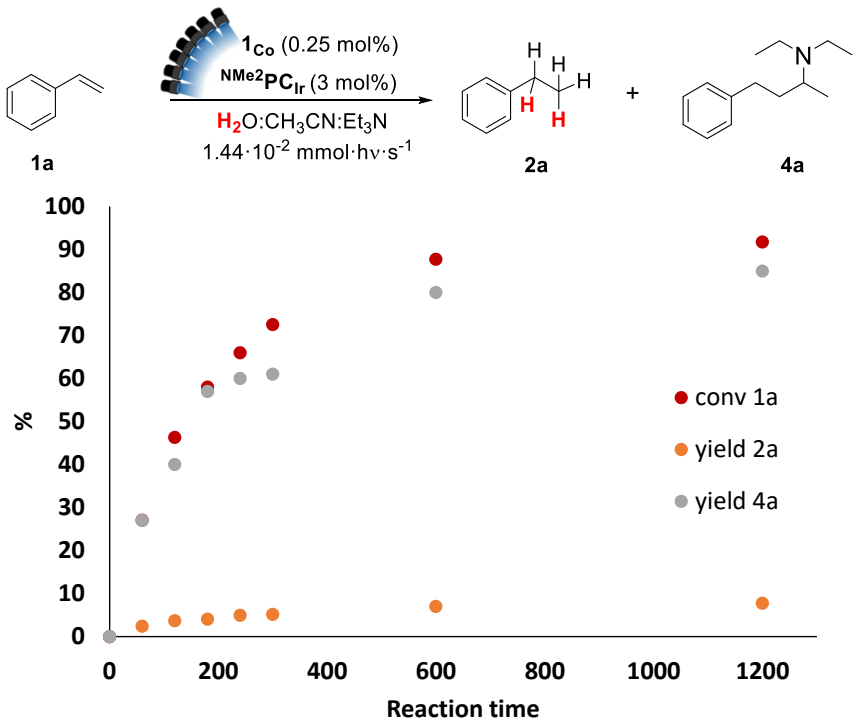

Figure 3.30. Monitoring of the reaction of **1a** under the optimised conditions for the competitive reduction of ketones, but in the absence of **5a** (20 min) .[a]Conditions: $\mathbf{1_{Co}}$ (0.25 mol%), $^{NMe2}\mathbf{PC_{Ir}}$ (3 mol%), Substrate A + B (16.5 mM), A:B (1:1), in H_2O:CH_3CN:Et_3N (6:4:0.2 ml) irradiated (7 LEDs, 447 nm, $1.44\cdot10^{-2}$ mmol·hν·s^{-1} photons) for 20 min at 25 ºC under N_2. [b] The plotted data is determined by GC analysis after workup and relative to a calibrated internal standard, except for **4a** that was not isolated (yield estimates with the calibration constant of styrene).

3.5 References

1. Barber, J.; Tran, P. D., From natural to artificial photosynthesis. *Journal of The Royal Society Interface* **2013,** *10* (81), 20120984.
2. Zhang, B.; Sun, L., Artificial photosynthesis: opportunities and challenges of molecular catalysts. *Chemical Society Reviews* **2019,** *48* (7), 2216-2264.
3. Lewis, N. S.; Nocera, D. G., Powering the planet: Chemical challenges in solar energy utilization. *Proceedings of the National Academy of Sciences* **2006,** *103* (43), 15729-15735.
4. Andreiadis, E. S.; Chavarot-Kerlidou, M.; Fontecave, M.; Artero, V., Artificial Photosynthesis: From Molecular Catalysts for Light-driven Water Splitting to Photoelectrochemical Cells. *Photochemistry and Photobiology* **2011,** *87* (5), 946-964.
5. Dalle, K. E.; Warnan, J.; Leung, J. J.; Reuillard, B.; Karmel, I. S.; Reisner, E., Electro- and Solar-Driven Fuel Synthesis with First Row Transition Metal Complexes. *Chemical Reviews* **2019,** *119* (4), 2752-2875.
6. Qiao, J.; Liu, Y.; Hong, F.; Zhang, J., A review of catalysts for the electroreduction of carbon dioxide to produce low-carbon fuels. *Chemical Society Reviews* **2014,** *43* (2), 631-675.
7. Appel, A. M.; Bercaw, J. E.; Bocarsly, A. B.; Dobbek, H.; DuBois, D. L.; Dupuis, M.; Ferry, J. G.; Fujita, E.; Hille, R.; Kenis, P. J. A.; Kerfeld, C. A.; Morris, R. H.; Peden,

C. H. F.; Portis, A. R.; Ragsdale, S. W.; Rauchfuss, T. B.; Reek, J. N. H.; Seefeldt, L. C.; Thauer, R. K.; Waldrop, G. L., Frontiers, Opportunities, and Challenges in Biochemical and Chemical Catalysis of CO2 Fixation. *Chemical Reviews* **2013,** *113* (8), 6621-6658.

8. Han, Z.; Eisenberg, R., Fuel from Water: The Photochemical Generation of Hydrogen from Water. *Accounts of Chemical Research* **2014,** *47* (8), 2537-2544.

9. Kaeffer, N.; Chavarot-Kerlidou, M.; Artero, V., Hydrogen Evolution Catalyzed by Cobalt Diimine–Dioxime Complexes. *Accounts of Chemical Research* **2015,** *48* (5), 1286-1295.

10. Queyriaux, N.; Jane, R. T.; Massin, J.; Artero, V.; Chavarot-Kerlidou, M., Recent developments in hydrogen evolving molecular cobalt(II)–polypyridyl catalysts. *Coordination Chemistry Reviews* **2015,** *304-305*, 3-19.

11. Zee, D. Z.; Chantarojsiri, T.; Long, J. R.; Chang, C. J., Metal–Polypyridyl Catalysts for Electro- and Photochemical Reduction of Water to Hydrogen. *Accounts of Chemical Research* **2015,** *48* (7), 2027-2036.

12. Trincado, M.; Bösken, J.; Grützmacher, H., Homogeneously catalyzed acceptorless dehydrogenation of alcohols: A progress report. *Coordination Chemistry Reviews* **2021,** *443*, 213967.

13. Wen, J.; Wang, F.; Zhang, X., Asymmetric hydrogenation catalyzed by first-row transition metal complexes. *Chemical Society Reviews* **2021,** *50* (5), 3211-3237.

14. Ai, W.; Zhong, R.; Liu, X.; Liu, Q., Hydride Transfer Reactions Catalyzed by Cobalt Complexes. *Chemical Reviews* **2019,** *119* (4), 2876-2953.

15. Boonstra, A. H.; Mutsaers, C. A. H. A., Photohydrogenation of ethyne and ethene on the surface of titanium dioxide. *The Journal of Physical Chemistry* **1975,** *79* (19), 2025-2027.

16. Frank, A. J.; Goren, Z.; Willner, I., Photohydrogenation of acetylene and ethylene by Pt and Rh supported on CdS semiconductor particles. *Journal of the Chemical Society, Chemical Communications* **1985,** (15), 1029-1030.

17. Yamataka, H.; Seto, N.; Ichihara, J.; Hanafusa, T.; Teratani, S., Reduction of C–C multiple bonds using an illuminated semiconductor catalyst. *Journal of the Chemical Society, Chemical Communications* **1985,** (12), 788-789.

18. Baba, R.; Nakabayashi, S.; Fujishima, A.; Honda, K., Photocatalytic hydrogenation of ethylene on bimetal-deposited semiconductor powders. *Journal of the American Chemical Society* **1987,** *109* (8), 2273-2277.

19. Shiragami, T.; Pac, C.; Yanagida, S., Visible-light-induced two-electron-transfer photoreductions on cadmium sulfide: effects of morphology. *The Journal of Physical Chemistry* **1990,** *94* (2), 504-506.

20. Shibata, T.; Kabumoto, A.; Shiragami, T.; Ishitani, O.; Pac, C.; Yanagida, S., Novel visible-light-driven photocatalyst. Poly(p-phenylene)-catalyzed photoreductions of water, carbonyl compounds, and olefins. *The Journal of Physical Chemistry* **1990,** *94* (5), 2068-2076.

21. Anpo, M.; Chiba, K.; Tomonari, M.; Coluccia, S.; Che, M.; Fox, M. A., Photocatalysis on Native and Platinum-Loaded TiO2 and ZnO Catalysts —Origin of Different Reactivities on Wet and Dry Metal Oxides—. *Bulletin of the Chemical Society of Japan* **1991,** *64* (2), 543-551.

22. Matsuoka, S.; Kohzuki, T.; Kuwana, Y.; Nakamura, A.; Yanagida, S., Visible-light-induced photocatalysis of poly(pyridine-2,5-diyl). Photoreduction of water, carbonyl compounds and alkenes with triethylamine. *Journal of the Chemical Society, Perkin Transactions 2* **1992,** (4), 679-685.

23. Shiragami, T.; Fukami, S.; Wada, Y.; Yanagida, S., Semiconductor photocatalysis: effect of light intensity on nanoscale cadmium sulfide-catalyzed photolysis of organic substrates. *The Journal of Physical Chemistry* **1993,** *97* (49), 12882-12887.

24. Li, J.; Yang, J.; Wen, F.; Li, C., A visible-light-driven transfer hydrogenation on CdS nanoparticles combined with iridium complexes. *Chemical Communications* **2011,** *47* (25), 7080-7082.
25. Fan, X.; Yao, Y.; Xu, Y.; Yu, L.; Qiu, C., Visible-Light-Driven Photocatalytic Hydrogenation of Olefins Using Water as the H Source. *ChemCatChem* **2019,** *11* (11), 2596-2599.
26. Imamura, K.; Okubo, Y.; Ito, T.; Tanaka, A.; Hashimoto, K.; Kominami, H., Photocatalytic hydrogenation of alkenes to alkanes in alcoholic suspensions of palladium-loaded titanium(iv) oxide without the use of hydrogen gas. *RSC Advances* **2014,** *4* (38), 19883-19886.
27. Shimakoshi, H.; Hisaeda, Y., B12-TiO2 Hybrid Catalyst for Light-Driven Hydrogen Production and Hydrogenation of C□C Multiple Bonds. *ChemPlusChem* **2014,** *79* (9), 1250-1253.
28. Mifsud, M.; Gargiulo, S.; Iborra, S.; Arends, I. W. C. E.; Hollmann, F.; Corma, A., Photobiocatalytic chemistry of oxidoreductases using water as the electron donor. *Nature Communications* **2014,** *5* (1), 3145.
29. Nakano, Y.; Black, M. J.; Meichan, A. J.; Sandoval, B. A.; Chung, M. M.; Biegasiewicz, K. F.; Zhu, T.; Hyster, T. K., Photoenzymatic Hydrogenation of Heteroaromatic Olefins Using 'Ene'-Reductases with Photoredox Catalysts. *Angewandte Chemie International Edition* **2020,** *59* (26), 10484-10488.
30. Litman, Z. C.; Wang, Y.; Zhao, H.; Hartwig, J. F., Cooperative asymmetric reactions combining photocatalysis and enzymatic catalysis. *Nature* **2018,** *560* (7718), 355-359.
31. Larionova, N. A.; Ondozabal, J. M.; Cambeiro, X. C., Reduction of Electron-Deficient Alkenes Enabled by a Photoinduced Hydrogen Atom Transfer. *Advanced Synthesis & Catalysis* **2021,** *363* (2), 558-564.
32. Kamei, Y.; Seino, Y.; Yamaguchi, Y.; Yoshino, T.; Maeda, S.; Kojima, M.; Matsunaga, S., Silane- and peroxide-free hydrogen atom transfer hydrogenation using ascorbic acid and cobalt-photoredox dual catalysis. *Nature Communications* **2021,** *12* (1), 966.
33. Perkowski, A. J.; You, W.; Nicewicz, D. A., Visible Light Photoinitiated Metal-Free Living Cationic Polymerization of 4-Methoxystyrene. *Journal of the American Chemical Society* **2015,** *137* (24), 7580-7583.
34. Fabry, D. C.; Ronge, M. A.; Rueping, M., Immobilization and Continuous Recycling of Photoredox Catalysts in Ionic Liquids for Applications in Batch Reactions and Flow Systems: Catalytic Alkene Isomerization by Using Visible Light. *Chemistry – A European Journal* **2015,** *21* (14), 5350-5354.
35. Singh, K.; Staig, S. J.; Weaver, J. D., Facile Synthesis of Z-Alkenes via Uphill Catalysis. *Journal of the American Chemical Society* **2014,** *136* (14), 5275-5278.
36. Saltiel, J.; Hammond, G. S., Mechanisms of Photochemical Reactions in Solution. XVII. cis-trans Isomerization of the Stilbenes by Excitation Transfer from Low Energy Sensitizers. *Journal of the American Chemical Society* **1963,** *85* (16), 2515-2516.
37. Metternich, J. B.; Gilmour, R., A Bio-Inspired, Catalytic E → Z Isomerization of Activated Olefins. *Journal of the American Chemical Society* **2015,** *137* (35), 11254-11257.
38. Schreier, M. R.; Pfund, B.; Guo, X.; Wenger, O. S., Photo-triggered hydrogen atom transfer from an iridium hydride complex to unactivated olefins. *Chemical Science* **2020,** *11* (32), 8582-8594.
39. Czyz, M. L.; Taylor, M. S.; Horngren, T. H.; Polyzos, A., Reductive Activation and Hydrofunctionalization of Olefins by Multiphoton Tandem Photoredox Catalysis. *ACS Catalysis* **2021,** *11* (9), 5472-5480.
40. Luo, S.-P.; Mejía, E.; Friedrich, A.; Pazidis, A.; Junge, H.; Surkus, A.-E.; Jackstell, R.; Denurra, S.; Gladiali, S.; Lochbrunner, S.; Beller, M., Photocatalytic Water Reduction with

Copper-Based Photosensitizers: A Noble-Metal-Free System. *Angewandte Chemie International Edition* **2013,** *52* (1), 419-423.
41. Call, A.; Codolà, Z.; Acuña-Parés, F.; Lloret-Fillol, J., Photo- and Electrocatalytic H2 Production by New First-Row Transition-Metal Complexes Based on an Aminopyridine Pentadentate Ligand. *Chemistry – A European Journal* **2014,** *20* (20), 6171-6183.
42. Call, A.; Casadevall, C.; Acuña-Parés, F.; Casitas, A.; Lloret-Fillol, J., Dual cobalt–copper light-driven catalytic reduction of aldehydes and aromatic ketones in aqueous media. *Chemical Science* **2017,** *8* (7), 4739-4749.
43. Casadevall, C.; Pascual, D.; Aragón, J.; Call, A.; Casitas, A.; Casademont-Reig, I.; Lloret-Fillol, J., Light-driven reduction of aromatic olefins in aqueous media catalysed by aminopyridine cobalt complexes. *Chemical Science* **2022,** *13* (15), 4270-4282.
44. Serrano, C. C. Mechanistic Studies of Water Oxidation Catalyzed by Homogeneous Iron and Ruthenium Complexes and Light driven Organic Reductions with a Dual Cobalt/Copper Catalytic System. Universidad Rovira i Virgili, 2019.
45. Monos, T. M.; Stephenson, C. R. J., Photoredox Catalysis of Iridium(III)-Based Photosensitizers. In *Iridium(III) in Optoelectronic and Photonics Applications*, 2017; pp 541-581.
46. Wu, Y.; Kim, D.; Teets, T. S., Photophysical Properties and Redox Potentials of Photosensitizers for Organic Photoredox Transformations. *Synlett* **2021,** *33* (12), 1154-1179.
47. Pellegrin, Y.; Odobel, F., Sacrificial electron donor reagents for solar fuel production. *Comptes Rendus Chimie* **2017,** *20* (3), 283-295.
48. Roth, H. G.; Romero, N. A.; Nicewicz, D. A., Experimental and Calculated Electrochemical Potentials of Common Organic Molecules for Applications to Single-Electron Redox Chemistry. *Synlett* **2016,** *27* (05), 714-723.
49. Jespersen, D.; Keen, B.; Day, J. I.; Singh, A.; Briles, J.; Mullins, D.; Weaver, J. D., III, Solubility of Iridium and Ruthenium Organometallic Photoredox Catalysts. *Organic Process Research & Development* **2019,** *23* (5), 1087-1095.
50. Li, G.; Kuo, J. L.; Han, A.; Abuyuan, J. M.; Young, L. C.; Norton, J. R.; Palmer, J. H., Radical Isomerization and Cycloisomerization Initiated by H• Transfer. *Journal of the American Chemical Society* **2016,** *138* (24), 7698-7704.
51. Lin, S.-X.; Sun, G.-J.; Kang, Q., A visible-light-activated rhodium complex in enantioselective conjugate addition of α-amino radicals with Michael acceptors. *Chemical Communications* **2017,** *53* (54), 7665-7668.
52. Zhu, S.; Das, A.; Bui, L.; Zhou, H.; Curran, D. P.; Rueping, M., Oxygen Switch in Visible-Light Photoredox Catalysis: Radical Additions and Cyclizations and Unexpected C–C-Bond Cleavage Reactions. *Journal of the American Chemical Society* **2013,** *135* (5), 1823-1829.
53. Ruiz Espelt, L.; McPherson, I. S.; Wiensch, E. M.; Yoon, T. P., Enantioselective Conjugate Additions of α-Amino Radicals via Cooperative Photoredox and Lewis Acid Catalysis. *Journal of the American Chemical Society* **2015,** *137* (7), 2452-2455.
54. Ruiz Espelt, L.; Wiensch, E. M.; Yoon, T. P., Brønsted Acid Cocatalysts in Photocatalytic Radical Addition of α-Amino C–H Bonds across Michael Acceptors. *The Journal of Organic Chemistry* **2013,** *78* (8), 4107-4114.
55. Miyake, Y.; Nakajima, K.; Nishibayashi, Y., Visible-Light-Mediated Utilization of α-Aminoalkyl Radicals: Addition to Electron-Deficient Alkenes Using Photoredox Catalysts. *Journal of the American Chemical Society* **2012,** *134* (7), 3338-3341.
56. Kohls, P.; Jadhav, D.; Pandey, G.; Reiser, O., Visible Light Photoredox Catalysis: Generation and Addition of N-Aryltetrahydroisoquinoline-Derived α-Amino Radicals to Michael Acceptors. *Organic Letters* **2012,** *14* (3), 672-675.

57. Szostak, M.; Spain, M.; Procter, D. J., Determination of the Effective Redox Potentials of SmI2, SmBr2, SmCl2, and their Complexes with Water by Reduction of Aromatic Hydrocarbons. Reduction of Anthracene and Stilbene by Samarium(II) Iodide–Water Complex. *The Journal of Organic Chemistry* **2014,** *79* (6), 2522-2537.
58. Aragón, J.; Sun, S.; Pascual, D.; Jaworski, S.; Lloret-Fillol, J., Photoredox Activation of Inert Alkyl Chlorides for the Reductive Cross-Coupling with Aromatic Alkenes. *Angewandte Chemie International Edition* **2022,** *61* (21), e202114365.
59. Jameson, D. M., *Introduction to Fluorescence (1st ed.)*. CRC Press. : 2014.
60. Hatchard, C. G.; Parker, C. A.; Bowen, E. J., A new sensitive chemical actinometer - II. Potassium ferrioxalate as a standard chemical actinometer. *Proceedings of the Royal Society of London. Series A. Mathematical and Physical Sciences* **1956,** *235* (1203), 518-536.
61. Hislop, K. A.; Bolton, J. R., The Photochemical Generation of Hydroxyl Radicals in the UV−vis/Ferrioxalate/H2O2 System. *Environmental Science & Technology* **1999,** *33* (18), 3119-3126.
62. Cismesia, M. A.; Yoon, T. P., Characterizing chain processes in visible light photoredox catalysis. *Chemical Science* **2015,** *6* (10), 5426-5434.
63. Kurpil, B.; Markushyna, Y.; Savateev, A., Visible-Light-Driven Reductive (Cyclo)Dimerization of Chalcones over Heterogeneous Carbon Nitride Photocatalyst. *ACS Catalysis* **2019,** *9* (2), 1531-1538.
64. Zhao, G.; Yang, C.; Guo, L.; Sun, H.; Lin, R.; Xia, W., Reactivity Insight into Reductive Coupling and Aldol Cyclization of Chalcones by Visible Light Photocatalysis. *The Journal of Organic Chemistry* **2012,** *77* (14), 6302-6306.
65. Chirdon, D. N.; McCusker, C. E.; Castellano, F. N.; Bernhard, S., Tracking of Tuning Effects in Bis-Cyclometalated Iridium Complexes: A Combined Time Resolved Infrared Spectroscopy, Electrochemical, and Computational Study. *Inorganic Chemistry* **2013,** *52* (15), 8795-8804.
66. Monos, T. M.; Sun, A. C.; McAtee, R. C.; Devery, J. J.; Stephenson, C. R. J., Microwave-Assisted Synthesis of Heteroleptic Ir(III)+ Polypyridyl Complexes. *The Journal of Organic Chemistry* **2016,** *81* (16), 6988-6994.
67. Nazeeruddin, M. K.; Wegh, R. T.; Zhou, Z.; Klein, C.; Wang, Q.; De Angelis, F.; Fantacci, S.; Grätzel, M., Efficient Green-Blue-Light-Emitting Cationic Iridium Complex for Light-Emitting Electrochemical Cells. *Inorganic Chemistry* **2006,** *45* (23), 9245-9250.
68. Waern, J. B.; Desmarets, C.; Chamoreau, L.-M.; Amouri, H.; Barbieri, A.; Sabatini, C.; Ventura, B.; Barigelletti, F., Luminescent Cyclometalated RhIII, IrIII, and (DIP)2RuII Complexes with Carboxylated Bipyridyl Ligands: Synthesis, X-ray Molecular Structure, and Photophysical Properties. *Inorganic Chemistry* **2008,** *47* (8), 3340-3348.
69. Jones, W. E.; Fox, M. A., Determination of Excited-State Redox Potentials by Phase-Modulated Voltammetry. *The Journal of Physical Chemistry* **1994,** *98* (19), 5095-5099.
70. Buzzetti, L.; Crisenza, G. E. M.; Melchiorre, P., Mechanistic Studies in Photocatalysis. *Angewandte Chemie International Edition* **2019,** *58* (12), 3730-3747.
71. Goldsmith, J. I.; Hudson, W. R.; Lowry, M. S.; Anderson, T. H.; Bernhard, S., Discovery and High-Throughput Screening of Heteroleptic Iridium Complexes for Photoinduced Hydrogen Production. *Journal of the American Chemical Society* **2005,** *127* (20), 7502-7510.

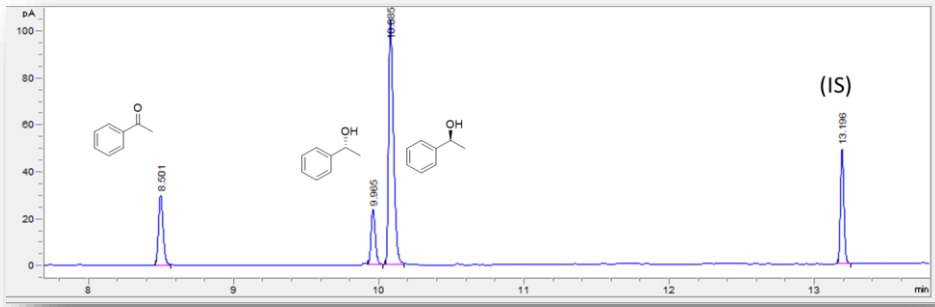

'*Confess ignorance, vindicate doubt*'

J. M. Levy-Leblond

Chapter 4

Synthesis of new chiral cobalt complexes and their use on the photocatalytic asymmetric reduction of ketones in aqueous media

UNIVERSITAT ROVIRA I VIRGILI
PHOTOREDOX CATALYSIS MEDIATED BY TRANSITION METAL COMPLEXES.
TOWARDS CHALLENGING ORGANIC REDUCTIONS
David Pascual Gascón

4.1 State of the art

Asymmetric synthesis has become pivotal for an increasing number of applications, from the synthesis of bioactive compounds to the design of optically active materials.[1-4] It also constitutes an expanding source of knowledge from the point of view of fundamental chemistry,[5-7] given that the development of novel enantioselective processes demands new levels of understanding, especially when catalyzed. Different strategies are well-established to render chirality induction catalytically, including organocatalysis,[8-11] biocatalysis,[12-14] using auxiliary chiral additives,[15, 16] or transition metal catalysis.[17, 18] For the present chapter, we focus our attention on the latter.

Catalytic asymmetric hydrogenation (Scheme 4. 1a) and hydrogen transfer hydrogenation of ketones (ATH, also called 'asymmetric hydrogen transfer', Scheme 4. 1b) have been extensively studied since Noyori presented his pioneering work in 1995.[19] These transformations represent the most efficient, environmentally-respectful and atom-economical method to prepare chiral alcohols, which are versatile building blocks for the synthesis of other chemicals (including drugs, perfumes, pesticides and natural products).[20]

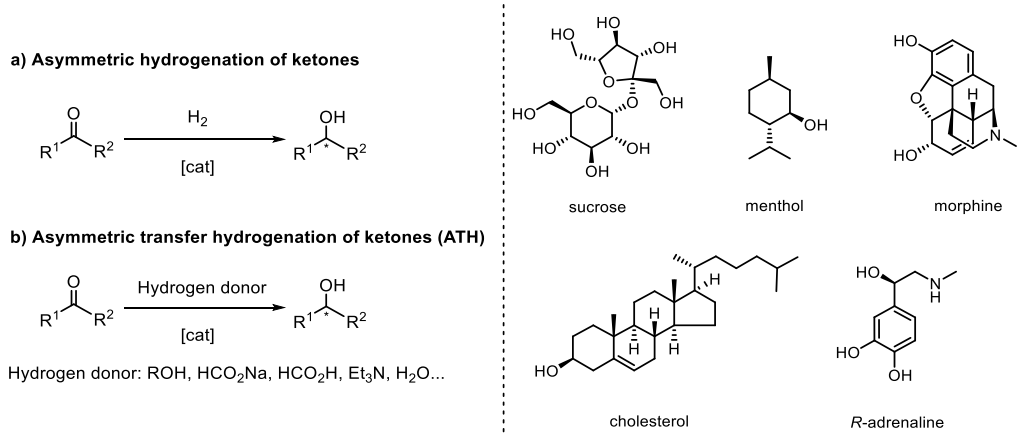

Scheme 4. 1. On the left, a general scheme of the asymmetric hydrogenation and hydrogen transfer events. On the right, selected examples of biologically relevant molecules containing chiral alcohols.

Many chiral transition metal complexes have been developed for the enantioselective reduction of ketones over the past decades.[21, 22] Furthermore, several

groups presented successful catalysts based on elements from the 1st row transition series.[23, 24] However, cobalt is an element that remains underexplored for the enantioselective ATH of ketones[25, 26] in opposition to more scarce and expensive[27] d^7 analogous Rh[28-32] and Ir.[33-35] This might be because cobalt exhibits different redox behaviour and the oxidation state M^{II} is more common for cobalt than rhodium, while for iridium is exceptional. Moreover, Cobalt can more easily access both low and high-spin electronic configurations. To the best of our knowledge, apart from the early work with 1,2-diketones by Waldron[36] and Ohgo,[37, 38] the only example of cobalt-catalysed asymmetric reduction of ketones was reported by Gao and co-workers in 2016, employing high pressure of molecular hydrogen in alkaline methanolic media (Scheme 4.2).[39]

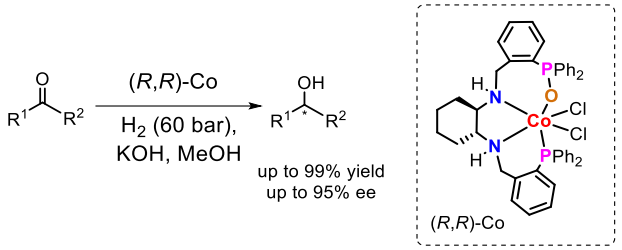

Scheme 4.2. Selected example of Co-catalysed asymmetric reduction of ketones reported by Gao and co-workers.

Following the principles of green chemistry,[40] numerous examples have also demonstrated being operative in aqueous solutions.[28, 30, 41-47] Excellent results can be highlighted from the work of Gao and co-workers, that combined the dimer $[IrHCl_2(COD)]_2$ with a chiral tetradentate ligand (Scheme 4.3a), or the more recent report from Meggers and co-workers, who utilised a chiral-at-metal iridium complex (Scheme 4.3b).

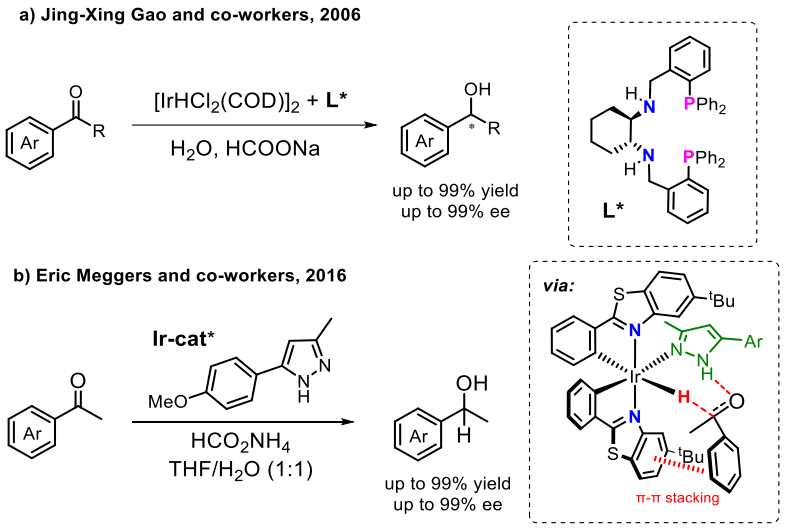

Scheme 4.3. Highlighted non-photocatalytic precedents in aqueous media.

In photoredox catalysis[48-50], a significant number of enantioselective reactions have been explored.[51-54] In particular, photocatalytic asymmetric reduction of ketones has also been achieved through different approaches. Kohtani, Miyabe and co-workers presented the ATH of ketones using TiO_2 with chiral mandelic acid (MA) adsorbed onto its surface (Scheme 4.4a).[55] This modified heterogeneous material catalysed the reduction of ketones under UV irradiation in the presence of ethanol (up to 37% ee). Jiang and co-workers combined a dicyanopyrazine-derived chromophore (DPZ) as the photoredox catalyst (PC) with a noncovalent chiral organocatalyst to asymmetrically reduce 1,2-diketones in chlorobenzene (up to 97% ee, Scheme 4.4b)[56] and azaarene-based ketones in cyclopentyl methyl ether (up to 98% ee, Scheme 4.4c).[57] Both methodologies operated under blue light irradiation at low temperatures (0 and -40 ºC) and employed a particular tertiary amine as a source of electrons.

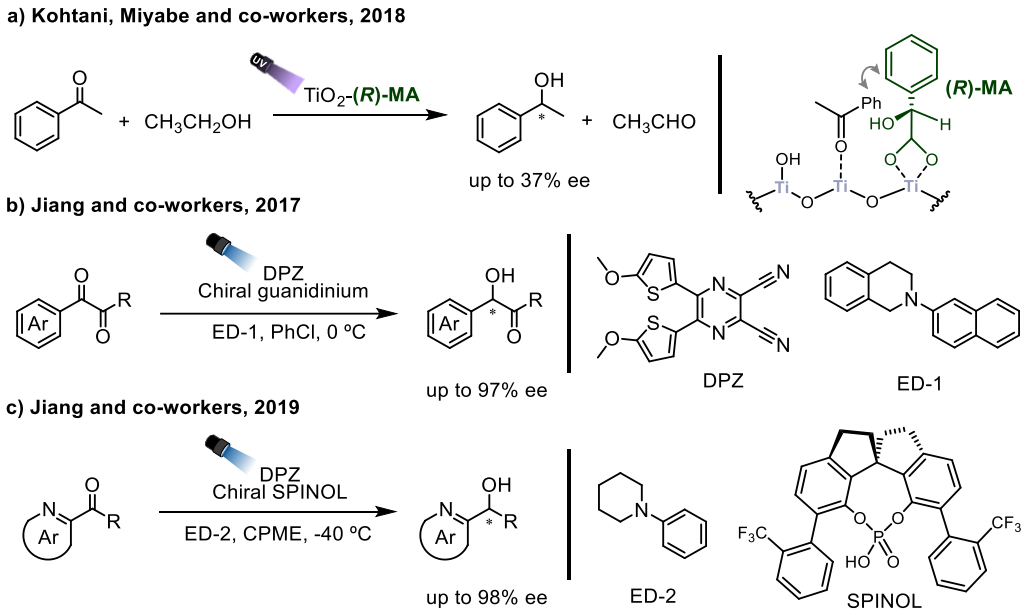

Scheme 4.4. Examples of asymmetric photocatalytic reduction of ketones in non-aqueous media.

Merging visible light as a driving force with water as a hydrogen-atom source is a very appealing approach towards green chemistry,[23] and an essential requisite in artificial photosynthesis, but very challenging (see Chapter 1). Up to now, the only reported examples of the asymmetric photocatalytic reduction of ketones in aqueous media[58] relied on enzymes.[59-61] Hyster and co-workers reported how the combination of the flavin-dependent ene-reductase *P. putida* (morphinone reductase, MorB) and the photocatalyst $Ru(bpy)_3Cl_2$ afforded chiral alcohols from acetophenone derivatives (up to 76% ee).[59] Mechanistic insights indicate that the ketone is reduced at the enzyme active binding site, where it undergoes single electron transfer (SET) from the reduced PC followed by a hydrogen atom transfer (HAT) from the reduced flavin mononucleotide (FMN). Following steps to close the catalytic cycle would likely involve SET from radical FMN to the excited PC, hydride transfer from NADH (nicotinamide adenine dinucleotide) to recover the reduced FMN and its protonation to release the product. In a comparable example, Baeg and co-workers described the visible-light-mediated regeneration of 1,4-NADPH (nicotinamide adenine dinucleotide phosphate), employing a graphene-based photocatalyst and a rhodium-

based catalyst (that reduces $NADP^+$ with triethanolamine as electron donor).[60] This system was combined with the enzyme *Lactobacillus kefir* (LKADH) for the asymmetric reduction of acetophenone derivatives (up to >99% ee).

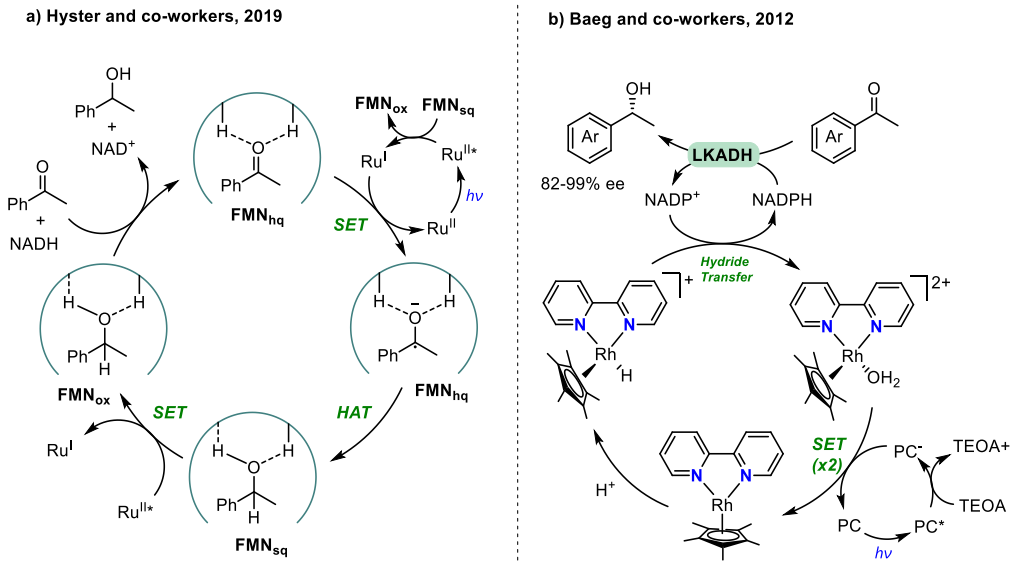

Scheme 4.5. Mechanistic proposal of selected examples for the photocatalytic ATH of ketones in aqueous media. PC = Photoredox Catalyst, TEOA = triethanolamine, SET = Single Electron Transfer, HAT = Hydrogen Atom transfer.

Yet, there is no reported example of the photocatalytic reduction of ketones where enantioselectivity is induced by transition metal catalysis. This is probably because the ATH reaction is more challenging than utilising the ketyl radical for further functionalization.[62, 63] As a matter of fact, the first example of transition metal-catalysed photoreduction of ketones in aqueous media was presented by our group in 2017.[64] The optimised catalytic system was already introduced in the previous chapter, and it involves a robust and well-defined Co complex with an aminopyridine ligand (**1_{Co}**) and a Cu photoredox catalyst (**PC_{Cu}**), using visible light as driving-force and H_2O/amine as a hydride source. The mechanistic investigations supported a SET+HAT mechanism for the photocatalytic ATH of ketones, as in the examples above. Since enantioselectivity was not the pursued objective for that project, the optimised cobalt catalyst was used as a racemic mixture of the two enantiomers; therefore, no enantioselectivity could be expected.

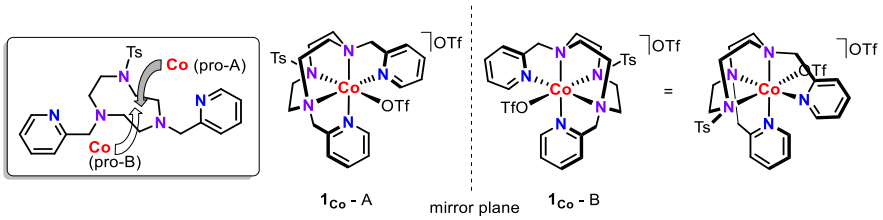

Scheme 4.6. Illustration of how two chiral-at-metal enantiomers of $\mathbf{1_{Co}}$ can be formed from the achiral precursors. Note that 'A' and 'B' are arbitrary letters.

During the optimisation stage, other catalysts were explored, and this screening revealed that tetradentate cobalt complexes such as [CoPDP(OTf)$_2$] ($\mathbf{2_{Co}}$, where PDP refers to (2*S*,2'*S*)-1,1'-bis(pyridin-2-ylmethyl)-2,2'-bipyrrolidine) and [CoMCP(OTf)$_2$] ($\mathbf{3_{Co}}$, MCP refers to (1*S*,2*S*)-*N*1,*N*2-dimethyl-*N*1,*N*2-bis(pyridin-2-ylmethyl)cyclohexane-1,2-diamine) could be potential catalysts (Scheme 4.7). However, the yield and enantioselectivity obtained by Dr. Arnau Call with these cobalt complexes with tetradentate chiral ligands were low.[65] Nevertheless, the 11% enantiomeric excess for the reaction with $\mathbf{2_{Co}}$ was encouraging to develop the system further.

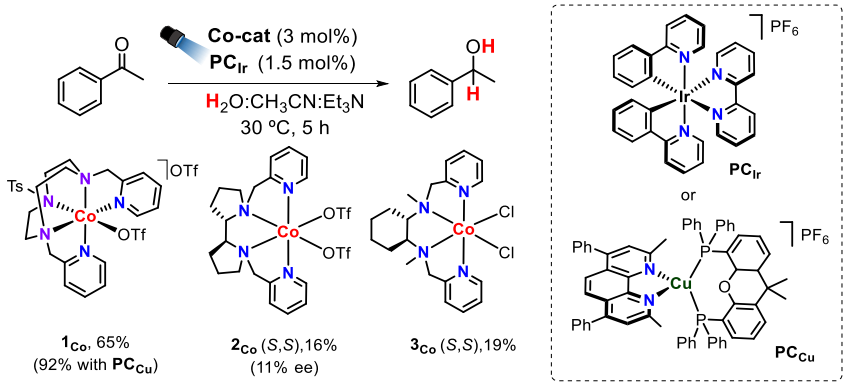

Scheme 4.7. Reactivity of the pentadentate complex $\mathbf{1_{Co}}$ and two tetradentate complexes in the early optimization stage of the photoreduction of aromatic ketones.

With this objective in mind, we first focussed on improving the product yield of ketone reduction when using tetradentate cobalt catalysts on photocatalytic ATH since these ligands are more amenable to having them chiral and tuning them. Indeed, the project is divided into two stages. First, to archive good yield levels for the reduction of

ketones by triggering the reactivity of putative cobalt hydrides towards ketyl radical anions (KRA) in water and the second stage, to promote the chirality induction.

According to our mechanistic understanding, the aromatic ketone nor the corresponding ketyl radical anion coordinates the cobalt centre. Hence, no interaction is expected between the [Co–H] and the substrate apart from the HAT. This circumstance makes the transference of chirality more challenging since, during the HAT step, the substrate is expected to be located far away from the catalytic centre. Therefore, it is expected that the substrate will have difficulties perceiving the chiral ligand effect. Indeed, in all the literature mentioned above, the ketone is near the chiral environment, surrounded by specific covalent or non-covalent interactions.[66, 67] Previous computational modelling research in our group localized the transition state related to the HAT process between the [Co–H] derived from $\mathbf{1_{Co}}$ and acetophenone. As shown in Scheme 4.8. (right), the distance between the hydrogen atom and the cobalt is 1.603 Å, and the distance between the hydride and the carbon of the ketone at the HAT transition state is 1.873 Å.[64] This last distance is longer than other values reported for the enantioselective hydride transfer to acetophenone (as low as 1.21 Å).[68-70]

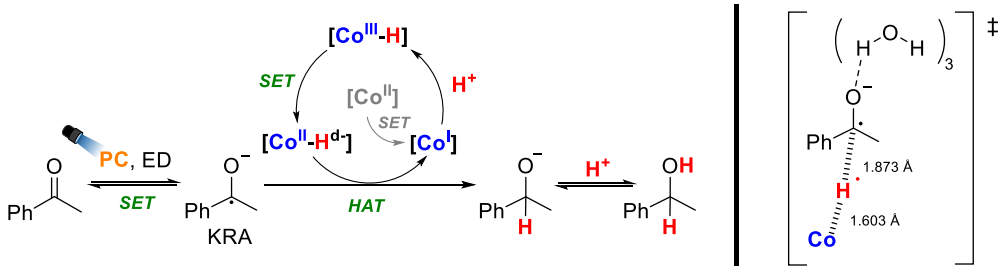

Scheme 4.8. Simplified mechanism of the proposed SET+HAT mechanism for ketone reduction. Right) illustration of how the cobalt-hydride centre interacts with the substrate through the H atom in the HAT transition state. PC = Photoredox Catalyst, ED = electron donor, KRA = Ketyl Radical anion, SET = Single Electron Transfer, HAT = Hydrogen Atom transfer.

In this chapter, we present our studies on the activation of chiral tetradentate complexes for the asymmetric reduction of ketones, taking complex $\mathbf{2_{Co}}$ (*S*,*S*) as model. We expect to contribute to the development of this methodology, which represents three main novelties: i) it unlocks the use of cobalt catalysts for the ATH of ketones (without H_2), and ii) it would constitute the first photocatalytic system based on organometallic

species for the induction of chirality on alcohols, iii) in mild aqueous media. Moreover, by refusing to harness the conventional covalent or non-covalent interactions, we endeavour to develop a distinctive strategy for asymmetric induction in the outer-sphere HAT.

4.2 Results and Discussion

4.2.1 Optimization of the photoredox catalyst

Although the reported reduction of **5a** by the tetradentate complex $\mathbf{2_{Co}}$ was notably lower than the value obtained with the pentadentate complex $\mathbf{1_{Co}}$ (using PC_{Ir} as PC, 16% and 65% yield, respectively, Scheme 4.7),[64] we anticipated that optimization of the reaction conditions could prompt the reactivity. Therefore, according to our current mechanistic hypothesis for ketone reduction (Scheme 4.8),[64] more reducing conditions should facilitate SET to form both KRA and [Co–H] species, but with more impact in the KRA generation since its redox potential is more negative. This principle was strongly supported by the competitive studies in chapter 3 where a more reducing environment accelerated the ketone reduction in front of olefin reduction. Moreover, previous studies supported this hypothesis since increasing the reducing conditions as well as increasing the reduction power of the cobalt catalyst increased the ketone reduction versus water reduction, until the point of inhibining the H_2 evolution reaction.[71]

With this aim in mind, we screened more powerful PC against reduction to analyse the performance of the dual catalysis framework. From similar conditions to those optimised for ketone reduction,[64] the reactivity of $\mathbf{2_{Co}}$ using $\mathbf{PC_{Ir}}$ (E_{red} = -1.4 V *vs* SCE) was slightly higher (22% yield, Table 4.1, entry 1). As shown in Table 4.1, more reducing photocatalysts enhanced the reactivity. However, the reactivity of the system does not only depend on the redox potential of the PC, since $\mathbf{PC_{Cu}}$ (E_{red} = -1.6 V, entry 2) yielded less product than $\mathbf{^{tBu}PC_{Ir}}$ (E_{red} = -1.5 V, entry 3). In particular, $\mathbf{^{NMe2}PC_{Ir}}$ (E_{red} = -1.8 V) gave the best result for such a dual catalytic system (entry 4). This also matches with the fact that the ketyl radical anion, formed in a higher amount when using

powerful PC (Scheme 4.8), competes with the water for the cobalt hydride intermediates as dictated by Le Chatelier's principle.[71]

Table 4.1. Optimization of the PC for the photocatalytic reduction of acetophenone using $\mathbf{2_{Co}}$.

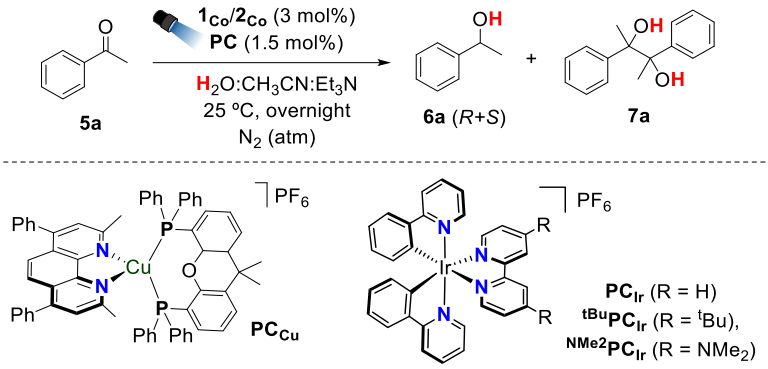

Entry	Co-cat	PC^n	E ($PC^{n/n-1}$) (V vs SCE)	Conversion (%)	Yield **6a** (%)	Ee (%)	Yield **7a** (%)
1	$\mathbf{2_{Co}}$	$\mathbf{PC_{Ir}}$	-1.4	26	22	10	0
2	$\mathbf{2_{Co}}$	$\mathbf{PC_{Cu}}$	-1.6	57	49	10	0
3	$\mathbf{2_{Co}}$	$^{tBu}\mathbf{PC_{Ir}}$	-1.5	93	85	7	0
4	$\mathbf{2_{Co}}$	$^{NMe2}\mathbf{PC_{Ir}}$	-1.8	97	91	8	0
5	$\mathbf{1_{Co}}$	$^{NMe2}\mathbf{PC_{Ir}}$	-1.8	100	93	0	0
6	$\mathbf{1_{Co}}$	$\mathbf{PC_{Cu}}$	-1.6	92	90	0	0
7	$\mathbf{2_{Co}}$	-	-	1	0	-	0
8	-	$^{NMe2}\mathbf{PC_{Ir}}$	-1.8	98	0	-	85

Conditions: Co-cat (3 mol%), PC (1.5 mol%), **5a** (10 mM) in H_2O:CH_3CN:Et_3N (0.6:0.4:0.02 mL) irradiated (447 nm) for 5 h at 25 °C under N_2. Yields after workup (average of duplicates) determined by chiral GC analysis relative to the signal of biphenyl as calibrated internal standard.

Regarding the enantioselective induction, the racemic pentadentate $\mathbf{1_{Co}}$ does not induce any enantioselectivity (Table 4.1, entries 5 and 6), while tetradentate $\mathbf{2_{Co}}$ exhibits a slight preference for the R enantiomer (Table 4.1, and see Experimental Section for further details). The ee% obtained is low (8-10%), and apparently, it does not depend on the PC (Table 4.1).[57] These values match the expected ones by an outer-sphere HAT. In addition, the starting material is recovered in the absence of PC, while the absence of cobalt leads to dimerization processes (entries 7 and 8).

4.2.2 Screening of the complexes in the group

Once we understood that the reduction capacity of the tetradentate systems is unlocked by using more reducing photocatalysts, we decided to explore other chiral complexes with the same type of ligands. In our group, we have developed during the years a library of chiral cobalt complexes, previously synthesized by group ex-members (Dr. J. Aragón, Dr. K. Michaliszyn and Dr. S. Fernández). Complexes have been here respectively named as **J1-6**, **K1-8** and **S1-2** and are represented in Scheme 4.9.[72-74]

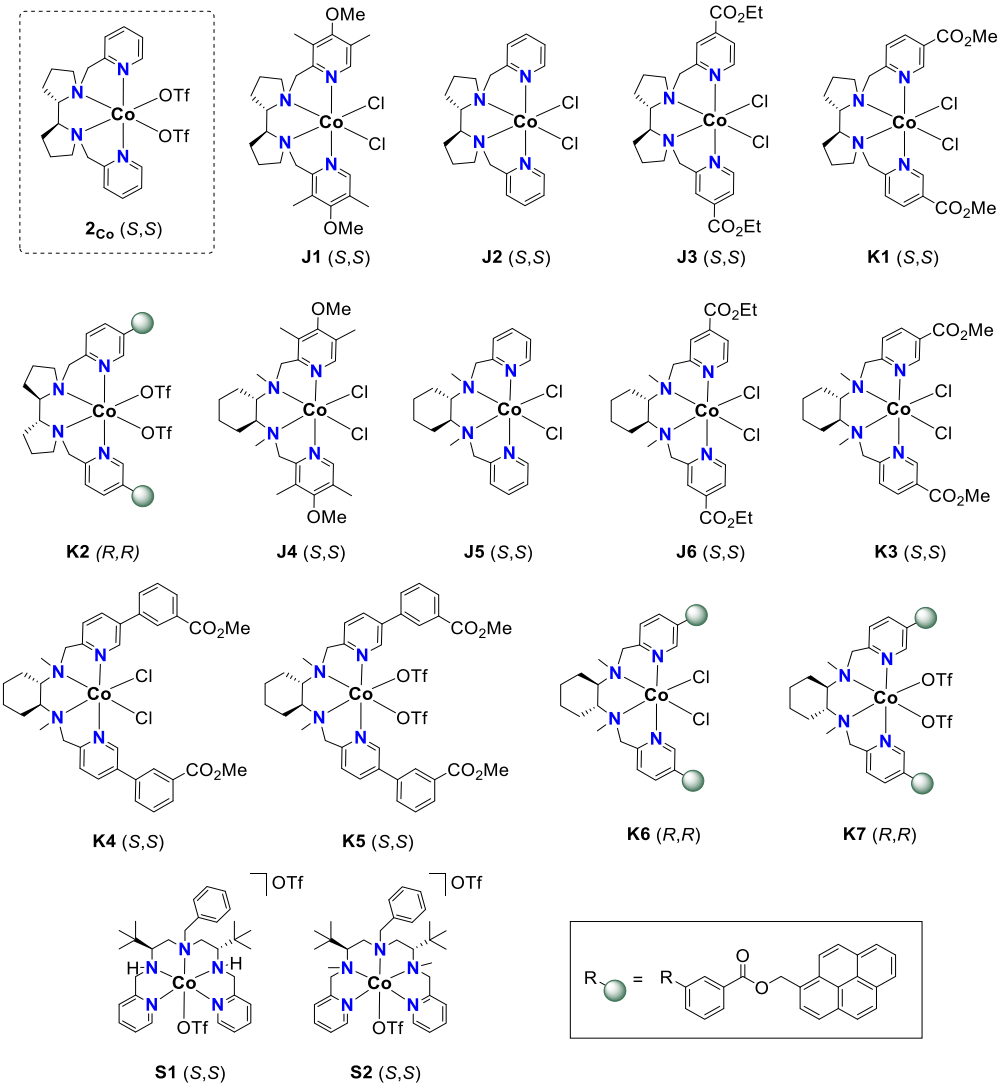

Scheme 4.9. Structures of the library of chiral cobalt complexes prepared in our group.

Most of these complexes bear chiral tetradentate ligands based on the privileged chiral backbones (*S*,*S*)-bispirrolidine and (*S*,*S*)-cyclohexanediamine (except **K2**, **K6** and **K7** being *R*,*R*). The pyridine rings present different substitution patterns. Therefore, these modifications could allow us to obtain some fundamental information. In addition, we also tested two C_2-symmetric pentacoordinate chiral complexes presenting either a –NCH_3 or –NH group, which could promote interactions of the carbonyl group.

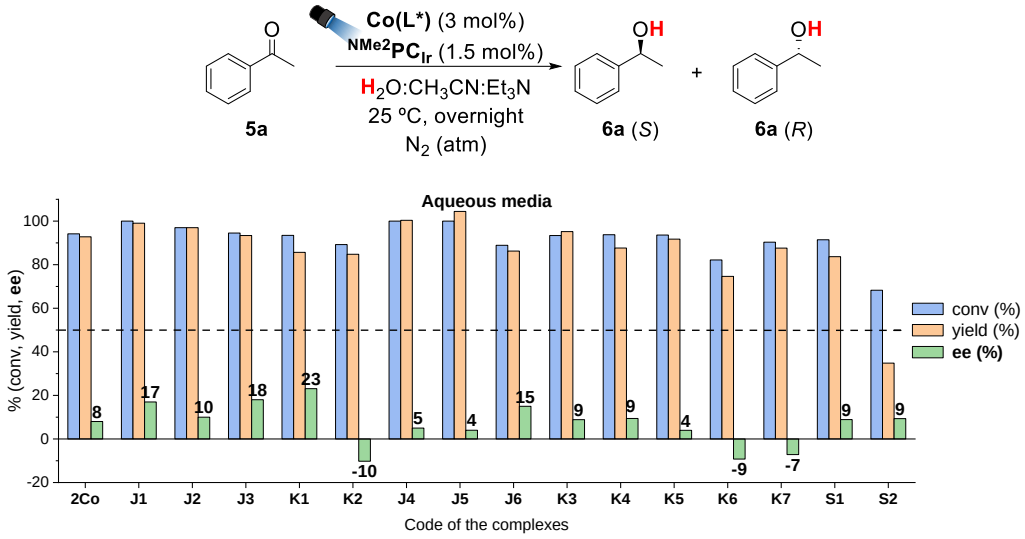

Figure 4. 1. Initial screening of cobalt chiral catalysts (colour bars: blue = conversion%, orange = yield%, green = ee%). Values of ee% are indicated in bold outside the end of each green bar. Conditions: Co(L*) (3 mol%), ^{NMe2}**PC$_{Ir}$** (1.5 mol%), **5a** (10 mM) in H_2O:CH_3CN:Et_3N (3:2:0.01 mL) mixture at 25 ºC, irradiated at 447 nm for 24 h. Yields after workup (average of duplicates) determined by chiral GC analysis relative to the signal of biphenyl as calibrated internal standard.

Differences in ee% were subtle along the screened chiral complexes without a general trend. Nevertheless, a careful analysis of the collected data revealed some valuable information. In the first place, as expected, the favoured enantiomer was (*R*)-phenylethanol except for the complexes in which the diamine backbone possessed the opposite chirality (for **K2**, **K6** and **K7**, then *R*,*R* backbone favoured enantiomer (*S*)-phenylethanol). Second, the counteranion at the exchangeable positions (Cl or OTf) was

unimportant (**2_{Co}**/**J2** or **K6**/**K7**). Third, when comparing the **J1-J6** series, we observed no correlation to the catalyst's electronic character. However, an apparent increase in the ee% was caused by substituents on the pyridine ring. Still, this apparent effect was not constant in the whole series of complexes since **K5** possessed substituted pyridines, and the ee% was lower than **J5**. Finally, the best improvement in ee% was obtained when introducing ester groups in the pyridine ring, increasing from 8% using **2_{Co}** to 18% and 23% using **J6** and **K7**, respectively. Bu the ester group is not independent since the comparison of **J2** with **J3** and **K6** suggests an interplay with other parameters.

Additionally, nickel catalysts prepared by Dr. Jordi Aragón were also tested, but exhibited neglegible reactivity for acetophenone reduction (Table 4.2).

Table 4.2. Screening of nickel chiral catalysts.

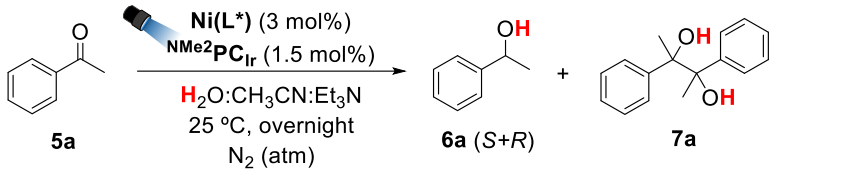

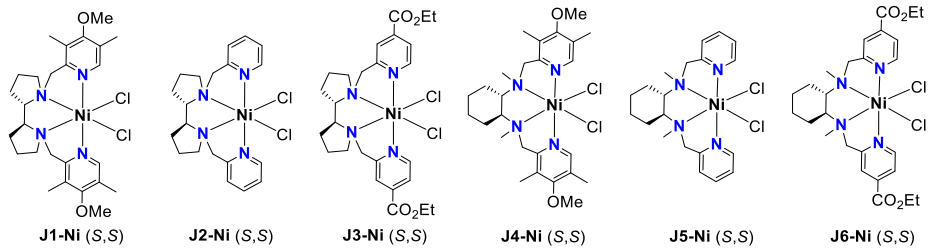

Entry	Ni-cat	Conversion (%)	Yield **6a** (%)	Yield **7a** (%)
1	**J1-Ni**	44	4	24
2	**J2-Ni**	45	3	27
3	**J3-Ni**	51	8	24
4	**J4-Ni**	44	2	25
5	**J5-Ni**	43	2	27
6	**J6-Ni**	50	6	18

Conditions: Ni-cat (3 mol%), **$^{NMe2}PC_{Ir}$** (1.5 mol%), **5a** (10 mM) in H_2O:CH_3CN:Et_3N (3:2:0.01 mL) mixture at 25 ºC, irradiated at 447 nm for 24 h. Yields after workup (average of duplicates) determined by chiral GC analysis relative to the signal of biphenyl as calibrated internal standard.

4.2.3 Effect of the reaction environment

Since the polarity of the reaction medium could alter the transition state's geometry, particularly how close the substrate is to the chiral catalyst, we hypothesized that tuning the solvent mixture could affect the ee. Although we pursued the reactivity in an aqueous solution, we screened the chiral catalysts also in methanol to study the effect of the polarity (Figure 4. 2).

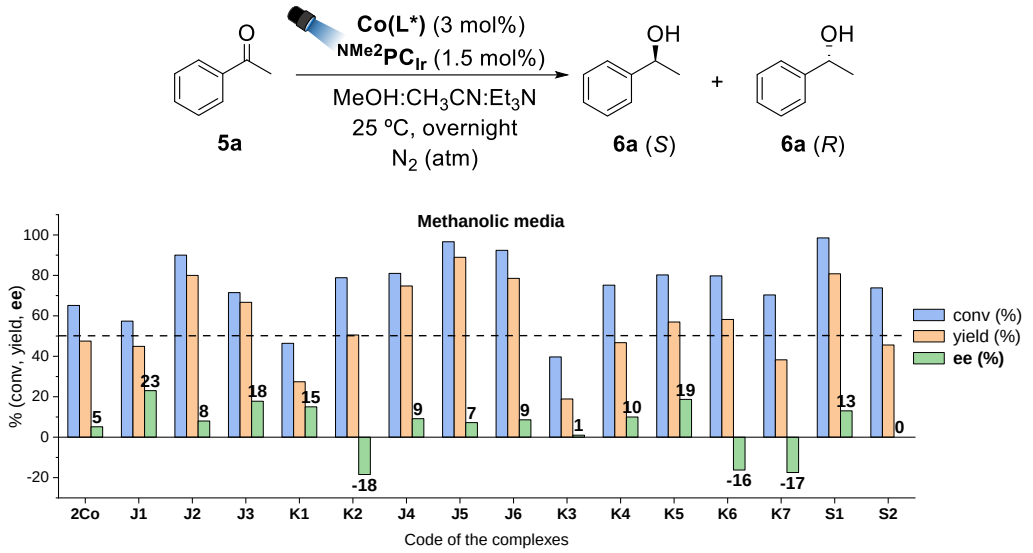

Figure 4. 2. Screening of cobalt chiral catalysts in methanolic solution (color bars: blue = conversion%, orange = yield%, green = ee%). Values of ee% are indicated in bold outside the end of each green bar. Conditions: Co(L*) (3 mol%), ^{NMe2}**PC$_{Ir}$** (1.5 mol%), **5a** (10 mM) in CH_3OH:CH_3CN:Et_3N (3:2:0.01 mL) mixture at 25 ºC, irradiated at 447 nm for 24 h. Yields after workup (average of duplicates) determined by chiral GC analysis relative to the signal of biphenyl as calibrated internal standard.

In comparison with the previous results in aqueous media, some of the reactions in methanolic solutions presented diminished conversion and yields. This could be related to changes in redox potentials. The ee was is some cases slightly increased, in particular for the complexes bearing pyrene moiety (**K2**-**K6** and **K7**). The differences of ee% values between the use of naked (**J2**, **J5**) and substituted pyridine rings (**J1** and **J3**, also **J4** and **J6**) was subtler and not general (**K3**). But unfortunately, the ee% remained in the same low range, lower than 25%. We also observed an improvement in ee% when introducing ester groups in the pyridine rings, increasing from 5% using **2$_{Co}$** to 18% and

15% using **J6** and **K7**, respectively. Again, the ester group itself is not an independent factor since the comparison between the complexes bearing cyclohexylamine backbone, from non-substituted **J2** (7%) to ester-substituted **J3** (9%) and **K3** (1%), supports the interplay with other parameters. It was unexpected that the loss of chirality transfer was observed in **S2** (ee<0.5%).

All these results exemplify how changes in the solvent mixture can influence reactivity and enantioselectivity, with a particular dependence on each chiral catalyst and without a clear relationship towards the general complex series.

4.2.4 Further studies with perylene-antenna based complexes

In the initial screening of cobalt complexes (Figure 4. 1), we had already tested the complexes **K2** and **K7**, which were designed to combine the reactivity of the tetradentate cobalt complexes with the properties of polyaromatic hydrocarbons. There were two main reasons why these complexes could be appealing: in the first place, pyrene units have served as an antenna for photosensitization[75-77] and also as redox-mediator for electron transfer[78-83] under light irradiation. Therefore, it is conceivable that incorporating this organic dye into an organometallic complex[75, 84, 85] could unify the catalytic activity of a dual system into one single structure. Second, pyrene molecules furnish a profitable connection with heterogeneous chemistry. Although polyaromatic hydrocarbons are insoluble in aqueous mixtures, they have shown host-guest interactions with macromolecules containing a hydrophobic cavity such as cyclodextrin,[86-88] enabling the organic dyes to aggregate inside and increase their water-solubility. Furthermore, species containing a pyrene ¨tail¨ structure can be anchored on the surface of carbon-based nanomaterials by strong aromatic π-π-stacking.[89-95] Mata and co-workers demonstrated how organometallic complexes with pyrene groups improved their catalytic activity when supported on reduced graphene oxide surface, providing a recyclable catalyst.[89]

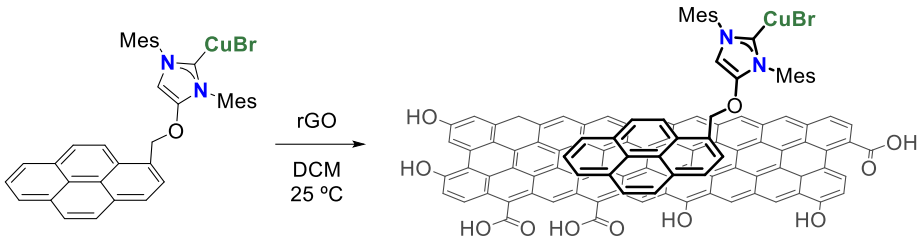

Scheme 4. 10. Example of a complex containing a pyrene unit that was anchored to the surface of rGO (reduced graphite oxide) by Mata and co-workers.

With this context in mind, Dr. Klaudia Michaliszyn also synthesized a new iridium photocatalyst bearing a pyrene group (^{pyrene}**PC$_{Ir}$**), to study if the interaction between the polyaromatic units of the different complexes (that is, **K2** and **K7**) could enhance the catalytic activity for hydrogen evolution.[72] On parallel, we herein study if these types of complexes with pyrene groups could develop profitable interactions for the enantioselective reduction of acetophenone.

The use of ^{pyrene}**PC$_{Ir}$** as a photocatalyst suppressed the reactivity for both **K2** and **K7** (Table 4.3, entries 1-4), whereas the model **2$_{Co}$** was still active but less than when using ^{NMe2}**PC$_{Ir}$** (entries 5-6). We ascribe this behaviour to a combination of the less negative redox potential of ^{pyrene}**PC$_{Ir}$** (see PCIr in Table 4.1 for comparison) and the lower insolubility of pyrene-based complexes. However, neither **K2** or **K7** revealed any profitable activity in the absence of PC (entries 7-8), which suggests that pyrene units are not working as photon receptors by themselves at 447 nm, following their absorption spectrum in acetonitrile.[72, 91] As expected, the analogous nickel-based complex **K2-Ni** did not afford the product (entries 9-11).

Table 4.3. Photocatalytic reduction of acetophenone using the complexes bearing pyrene units, the effect of the PC.

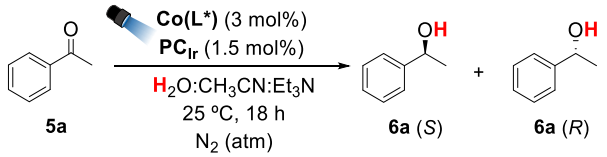

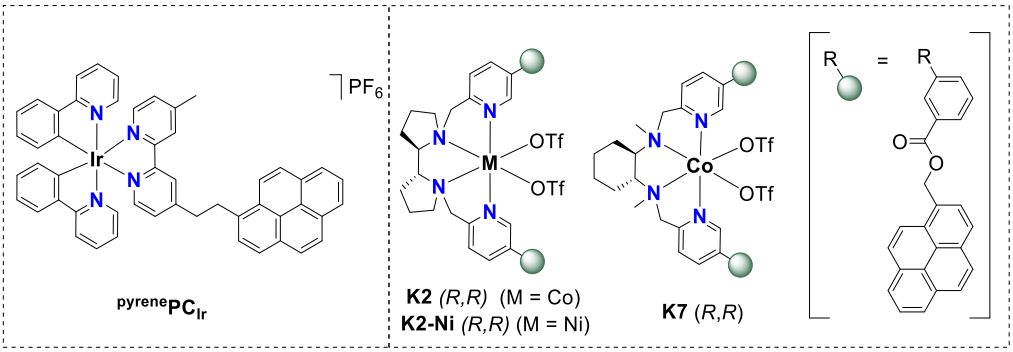

Entry	PC	Co-cat	Conv (%)	Yield (%)	ee (%)
1	^{NMe2}**PC$_{Ir}$**	**K2**	90	76	-13
2	^{NMe2}**PC$_{Ir}$**	**K7**	91	74	-8
3	^{pyrene}**PC$_{Ir}$**	**K2**	15	9	-7
4	^{pyrene}**PC$_{Ir}$**	**K7**	4	5	-6
5	^{NMe2}**PC$_{Ir}$**	**2$_{Co}$**	98	92	7
6	^{pyrene}**PC$_{Ir}$**	**2$_{Co}$**	42	40	9
7	-	**K2**	2	0	-
8	-	**K7**	-6	0	-
9	^{NMe2}**PC$_{Ir}$**	**K2-Ni**	100[a]	0	-
10	^{pyrene}**PC$_{Ir}$**	**K2-Ni**	2	0	-
11	-	**K2-Ni**	-3	0	-

Conditions: Co(L*) or **K2-Ni** (3 mol%), PC (1.5 mol%), **5a** (10 mM) in H_2O:CH_3CN:Et_3N (0.6:0.4:0.02 mL) mixture at 25 ºC under N_2, irradiated at 447 nm for 18 h. Yields after workup (average of duplicates) determined by chiral GC analysis relative to the signal of biphenyl as calibrated internal standard. [a]94% dimerization. **K2**, **K7**, **K2-Ni** and ^{pyrene}**PC$_{Ir}$** were synthesized by Dr. Klaudia Michaliszyn.

Under those circumstances, we excluded ^{pyrene}**PC$_{Ir}$** from further studies, focusing our attention again on ^{NMe2}**PC$_{Ir}$**. Given that the hypothetical π-π-stacking interactions could also favour self-aggregation of the cobalt complex,[75] we decided to study if the concentration of the catalyst could affect the catalytic response. For this reason, we raised the catalyst loading from 3% to 10% (Table 4.4, entries 1-2), which resulted in a substantial drop in the reactivity without an apparent enhancement of ee. Although a clear explanation cannot be provided yet, this observation was attributed to the intense colour of the cobalt catalyst in dispersion that might suppress PC activity. On the contrary, the concentration of catalysts can be lowered without diminishing the reactivity for acetophenone reduction, although there was no improvement in ee% (entries 3-6). From these results, we rationalised that if there are any self-aggregation effects in this range of concentrations, they are not profitable for the induction of enantioselectivity.

Table 4.4. Photocatalytic reduction of acetophenone using the complexes bearing pyrene units, the effect of the concentration of catalysts.

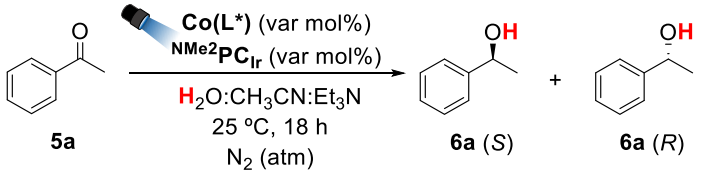

Entry	Co(L*)	Co(L*) (%)	PC (%)	Conv (%)	**6a** (%)	ee (%)	**7a** (%)
1	**K2**	10	1.5	28	17	-7	0
2	**K7**	10	1.5	51	33	-15	0
3	**K2**	0.5	1.5	100	84	-3	3
4	**K7**	0.5	1.5	100	85	-4	2
5	**K2**	0.5	0.25	88	84	-5	1
6	**K7**	0.5	0.25	96	92	-4	1

Conditions: Co(L*) (0.5 or 10 mol%), ^{NMe2}**PC$_{Ir}$** (0.25 or 1.5 mol%), **5a** (10 mM) in H_2O:CH_3CN:Et_3N (0.6:0.4:0.02 mL) mixture at 25 ºC under N_2, irradiated at 447 nm for 18 h. Yields after workup (average of duplicates) determined by chiral GC analysis relative to the signal of biphenyl as calibrated internal standard.

As mentioned at the beginning of this section, π-π-stacking interactions can also be expected between the complexes **K2** or **K7** and carbon-based macromolecules or nanomaterials. Accordingly, we decided to study if their immobilization onto certain surfaces to generate 'chiral cavities' could improve their performance on catalysis, as other authors have reported before.[89, 90] We selected nanofibers for the preliminary experiments, and we introduced it as an additive in the reaction media. For the preliminary experiments, we selected nanofibers as potential π-π-stacking additive, and to our delight we could observe that the catalytic activity of the system was not supressed (Table 4.5) while the nanomaterial did not afford **6a** in the absence of cobalt catalyst.

Table 4.5. First experiments in the presence of a nanomaterial.

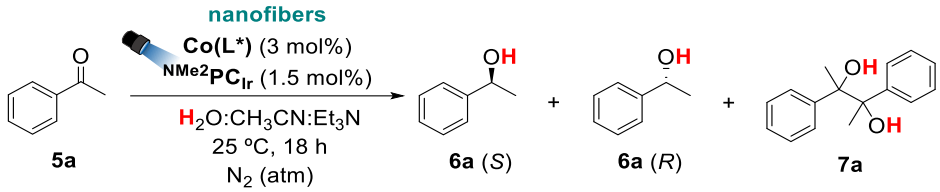

Entry	Co-cat	Conv (%)	Yield **6a** (%)	ee (%)	Yield **7a** (%)
1	**K2**	100	71	-9	0
2	**K7**	100	81	-9	0
3	-	100	0	-	88

Conditions: Co(L*) (0.5 or 10 mol%), ^{NMe2}**PC$_{Ir}$** (1.5 mol%), **5a** (10 mM) in H_2O:CH_3CN:Et_3N (0.6:0.4:0.02 mL) mixture at 25 ºC under N_2, irradiated at 447 nm overnight in the presence of nanofibers (10 times the mass of cobalt catalyst, no pre-stirring). Yields after workup (average of duplicates) determined by chiral GC analysis relative to the signal of biphenyl as calibrated internal standard.

Observing that the activity did not drop in the presence of nanofibers, we considered that other additives might positively affect the induction of chirality. Therefore, we employed fullerene (C_{60}), nanotubes (NT),[92] functionalized nanotubes with COOH (NT-COOH) and nanofibers (NF). In addition, we also explored the interaction between the complexes and cyclodextrin (γ-CD), expecting the inclusion of the pyrene units in its hydrophobic cavity.[86-88] All the reactions were stirred for 1 h

before the irradiation, expecting that the interaction between pyrene units and the additives in this lapse should stabilize the formation of the postulated chiral cavity.

Table 4.6. Screening of additives that could provide some interaction with pyrene units.

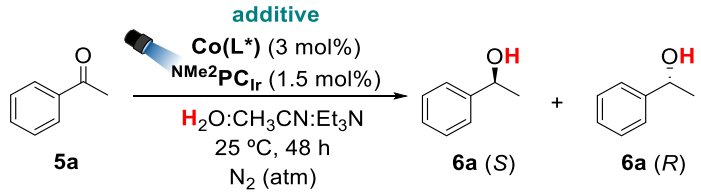

Entry	Co-cat	Material	Mat/Co	Conv (%)	Yield (%)	ee (%)
1	**K2**	none	-	100	75	-8
2	**K7**	none	-	99	82	-5
3	**K2**	CD	10	60	53	-5
4	**K7**	CD	10	100	98	-3
5	**K2**	CD	33	76	89	-8
6	**K7**	CD	33	100	81	-4
7	**K2**	NF	10	100	56	-15
8	**K7**	NF	10	100	86	-12
9	**K2**	NF	33	100	88	-10
10	**K7**	NF	33	100	93	-8
11	**K2**	C60	10	93	77	-1
12	**K7**	C60	10	68	56	-12
13	**K2**	C60	33	63	40	-1
14	**K7**	C60	33	38	11	-11
15	**K2**	NT	10	41	24	-5
16	**K7**	NT	10	61	47	-11
17	**K2**	NT	33	29	6	0
18	**K7**	NT	33	40	28	-9
19	**K2**	NT-COOH	10	6	0	-
20	**K7**	NT-COOH	10	8	0	-
21	**K2**	NT-COOH	33	8	0	-

22	**K7**	NT-COOH	33	10	0	-

Conditions for HTE screening: Co-cat (3 mol%), ^{NMe2}**PC$_{Ir}$** (1.5 mol%), **5a** (10 mM) in H_2O:CH_3CN:Et_3N (0.18:0.12:0.006 mL) irradiated (447 nm) for 48 h at 25 °C under N_2 in the presence of additives (proportion: additive being 10 or 33 times the mass of cobalt catalyst). Yields after workup (average of duplicates) determined by chiral GC analysis relative to the signal of biphenyl as calibrated internal standard. CD = cyclodextrine, NF = nanofibers, C60 = fullerene, NT = nanotubes, NT-COOH = functionalized nanotubes with COOH groups.

The enantiomeric excess values could reach -15% in the presence of nanofibers (Table 4.6, entry 7) and some observations can be outlined from the general results. First, there is an evident variation in yield between the tested materials, which tells us that these substances exhibit certain interactions with the catalytic system. Regarding yields, the reaction shows a very good tolerance to cyclodextrin, the only material soluble in the reaction media, and nanofibers. However, yields slightly dropped with the use of fullerene and carbon nanotubes, and the system's reactivity was fully inhibited when nanotubes were functionalised with COOH groups (entries 19-22).

Another general observation is that, except for nanofibers, there is a trend towards a decreased yield at higher concentrations of heterogeneous material (considering that CD is not heterogeneous). Although we still cannot explain this result, some primary hypotheses may be related to the potential EnT quenching mechanism with the nanomaterials or competitive light absorption. In addition, the adsorbed catalysts could be less active due to local environmental effects. Further spectroscopic studies are required to understand the interaction between these catalysts and materials.[72]

According to differences in ee, we suggest some interaction between the catalyst and nanomaterial caused by the immobilised. However, we can not discard the contribution in catalysis of no immobilised species between additives. In any case, we did not obtain the expected chirality induction and moved to another strategy.

4.2.5 Design of *o*-substituted chiral complexes

Our initial attempts to enhance the ee% for acetophenone reduction revealed a clear dependence on the employed catalyst (Figure 4. 1), despite being lower than 30%. Therefore, we continue the project by designing new chiral complexes. We hypothesised that increasing the steric hindrance of the ligand near the reaction centre

should impact the enantioselectivity. It is noteworthy to highlight that the previously tested chiral complexes from our group were made with different purposes (for instance, featuring different electronic properties, incorporating pyrene as an anchoring unit or strategical -NH position to bind CO_2), but not pursuing a direct effect on steric hindrance. Indeed, in all the complexes that presented substituents in the pyridine rings, those groups were located at *m*- and *p*- position, but not at *o*- (nomenclature referring to the position relative to the nitrogen atom of the pyridine ring). For this reason, from the different things that could be modified (backbone, bridge, nearby groups…), we decided to increase the bulkiness of new synthetically tailored chiral complexes, either introducing a substituent in the *o*-position or extended *N*-heterocycles (Scheme 4.11).

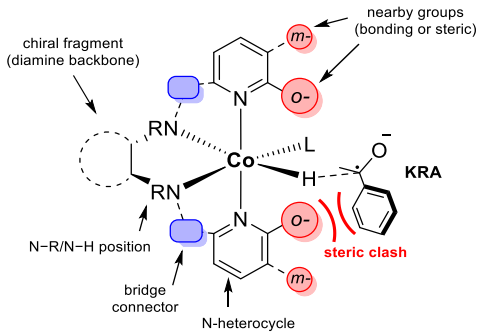

Scheme 4.11. Cobalt hydride species coordinated to a generic tetradentate aminopiridyl chiral ligand with the description of its different parts. Representation of the approaching ketyl radical anion (KRA) is also included to illustrate the expected steric effect on the hydrogen atom transfer step.

(*S*,*S*)-bispyrrolidine was the chiral backbone incorporated into the ligands type ^{X}PDP and ^{oxaz}**BP** in Scheme 4. 12 (where X refers to the different substitution patterns, $^{o\text{-}Me}$**PDP**, $^{o\text{-}Ph}$**PDP**, ^{quin}**PDP**). The preparation of these compounds was accomplished following similar procedures to the one reported in the literature.[65] Still, the crude of ^{oxaz}**BP** presented an unexpectedly complex mixture; column-chromatography purification was not straightforward, and a small isolated yield was obtained (9%).

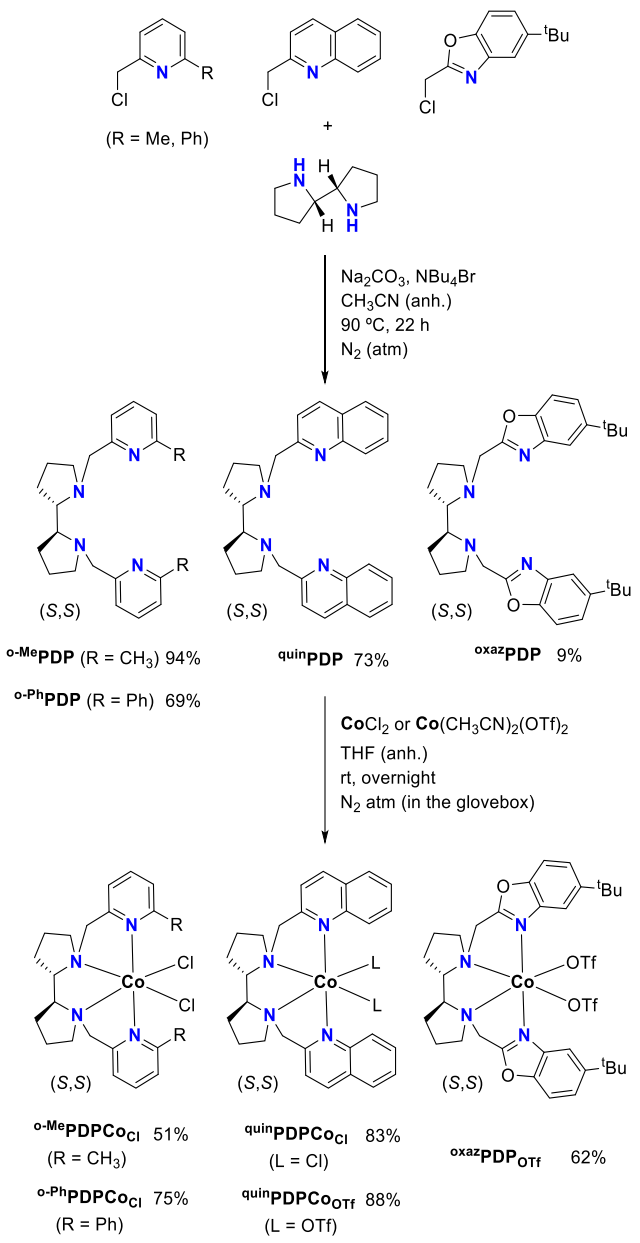

Scheme 4. 12. Synthesis of tetradentate aminopyridine ligands containing the (*S*,*S*)-bispyrrolidine backbone and their corresponding Co complexes.

The corresponding complexes were synthesized by the equimolar reaction of the tetradentate ligand with a cobalt (II) salt in a THF solution. Removal of the solvent under vacuum and slow diffusion of diethyl ether into a concentrated solution of the complexes in acetonitrile or dichloromethane afforded a colourful precipitate in good

yield (51-88%), yet no crystals were obtained except for ^{oxaz}**BPCo$_{OTf}$** (Experimental Section, Figure 4. 6). Since we do not expect that the Cl/OTf significantly affects the complexes' reactivity in ketone reduction, we indistinctly used $CoCl_2$ or $Co(CH_3CN)_2(OTf)_2$ as a source of cobalt salt. Nevertheless, to support their innocent behaviour in ee% studies, complexes bearing chlorides (^{quin}**PDPCo$_{Cl}$**) or triflates (^{quin}**PDPCo$_{OTf}$**) with the quinoline unit were prepared. All these complexes were new structures since the only reported ligands were $^{o\text{-}Me}$**PDP**, ^{quin}**PDP** which have been used for the preparation of iron complexes.[96]

4.2.6 Enantioselective catalysis with *o*-substituted complexes

Unfortunately, the reactivity of 5 *o*-substituted complexes in the photocatalytic reduction of **5a**, but lower in comparison with *m*- and *p*-substituted complexes (up to 31% yield, Table 4.7). In addition, the enantiomeric excess did not improve (up to 11%). Even though the results were not favourable, we could note that the effect of the Cl/OTf ligand was not relevant for the target reaction (entries 3-4).

Table 4.7. Reduction of **5a** using *o*-substituted cobalt complexes based on (*S*,*S*)-bispyrrolidine.

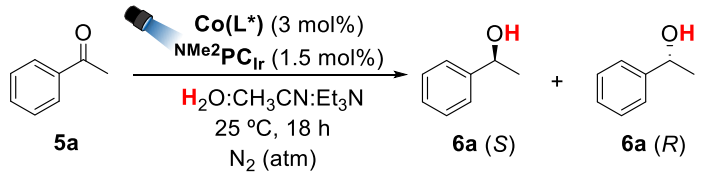

Entry	Co-cat	Conversion (%)	Yield (%)	ee (%)
1	$^{o\text{-}Me}$**PDPCo$_{Cl}$**	99	31	11
2	$^{o\text{-}Ph}$**PDPCo$_{Cl}$**	99	2	-6
3	^{quin}**PDPCo$_{Cl}$**	99	25	8
4	^{quin}**PDPCo$_{OTf}$**	99	17	10
5	^{oxaz}**BPCo$_{OTf}$**	99	2	4

Conditions: Co(L*) (3 mol%), ^{NMe2}**PC$_{Ir}$** (1.5 mol%), 5a (10 mM) in H_2O:CH_3CN:Et_3N (0.6:0.4:0.02 mL) mixture at 25 ºC under N_2, irradiated at 447 nm for 18 h. Yields after workup (average of duplicates) determined by chiral GC analysis relative to the signal of biphenyl as calibrated internal standard.

We wondered if this lack of reactivity may be due to the cobalt precatalyst failing to form the [Co–H], or if this intermediate was formed but did not react with the KRA. Given that if the [Co–H] was formed, it is expected to be active for H_2 evolution, we repeated the reaction while monitoring the pressure of the system (**1$_{Co}$** was used as a blank experiment). As seen in Figure 4. 3, no significant increment in pressure was observed for the *o*-substituted complexes, still, complexes **$^{o\text{-Me}}$PDPCo$_{Cl}$** and **^{quin}PDPCo$_{OTf}$** exhibited some activity. Once the pressure reached a plateau, we injected in GC-TCD a sample of the reaction headspace to calculate the TON for hydrogen evolution. In the case of **$^{o\text{-Me}}$PDPCo$_{Cl}$** and **^{quin}PDPCo$_{OTf}$** (TON = 4 and 1, respectively). Hydrogen evolution reaction was considerably lower than with **1$_{Co}$** (TON = 12), while no H_2 was detected for **$^{o\text{-Ph}}$PDPCo$_{Cl}$** and **^{oxaz}BPCo$_{OTf}$**. From these observations, we rationalised that the Co^{I} or [Co–H] species formation is responsible for the low catalytic activity when pyridine rings are *o*-substituted, especially for **$^{o\text{-Ph}}$PDPCo$_{Cl}$** and **^{oxaz}BPCo$_{OTf}$**, which have an excessive steric hindrance.

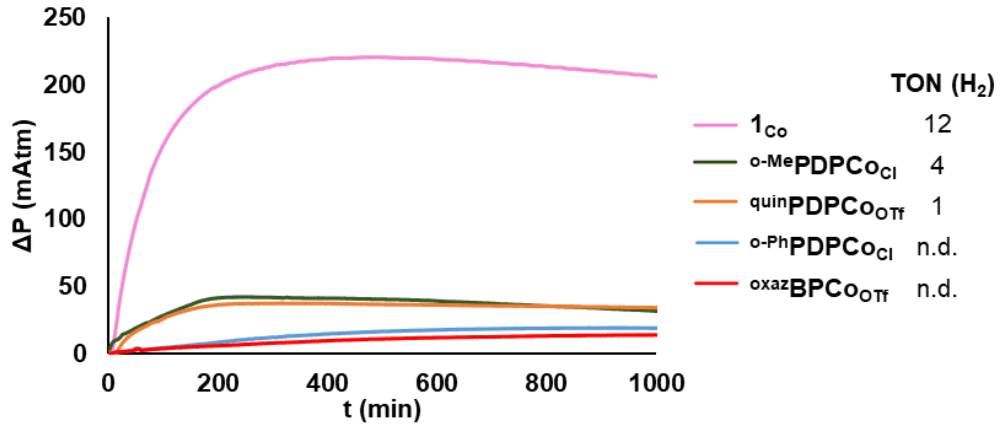

Figure 4. 3. On-line monitoring of the photochemical H_2 production for selected cobalt complexes in the presence of the substrate. Reaction conditions: **5a** (20 µmol, 10 mM), **^{NMe2}PC$_{Ir}$** (0.3 µmol, 1.5 mol%), cobalt catalyst (0.6 µmol, 3 mol%). Samples were irradiated (λ = 447 nm) at 25 °C under N_2 in a mixture of H_2O:CH_3CN:Et_3N (1.2:0.8:0.04 mL). The amount of H_2 was quantified by GC analysis when the evolved hydrogen reached a plateau.

To test that the reactivity and ee% lack of *o*-substituted complexes is not related to geometrical restrictions derived from the (*S*,*S*)-bispyrrolidine backbone, we also synthesized the chiral ligands **^{X}MCP** based on (*S*,*S*)-*N*,*N*′-dimethyl-1,2-

cyclohexanediamine (where X refers to the different substitution patterns, see **$^{o\text{-Me}}$MCP**, **^{quin}MCP** in Scheme 4. 13) and their corresponding cobalt complexes.

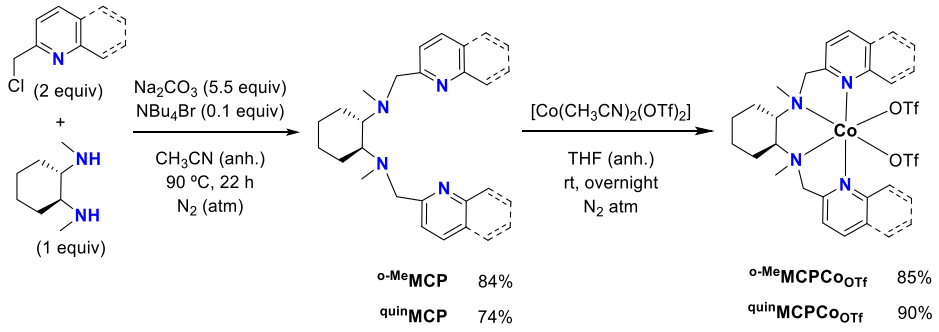

Scheme 4. 13. Synthesis of tetradentate aminopyridine ligands containing the (*S*,*S*)-cyclohexanediamine backbone, and their corresponding Co complexes.

These two cobalt complexes are novel since the corresponding ligands have only been used to coordinate with copper,[97] manganese[98-100] and iron.[101] However, despite a slight increase in yield for the reaction with complex **$^{o\text{-Me}}$MCPCo$_{OTf}$**, enantioselectivity remains low (Table 4.8).

Table 4.8. Reduction of acetophenone using the *o*-substituted cobalt complexes based on (*S*,*S*)-cyclohexanediamine.

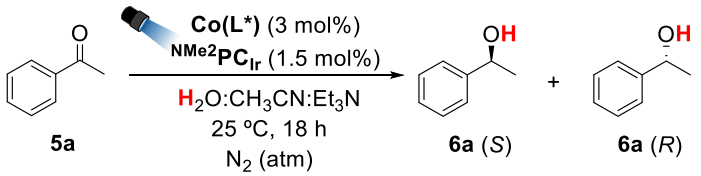

Entry	Co-cat	Conv (%)	Yield **6a** (%)	ee (%)
1	**$^{o\text{-Me}}$MCPCo$_{OTf}$**	61	40	12
2	**^{quin}MCPCo$_{OTf}$**	100	13	9

Conditions: Co(L*) (3 mol%), **^{NMe2}PC$_{Ir}$** (1.5 mol%), **5a** (10 mM) in H_2O:CH_3CN:Et_3N (0.6:0.4:0.02 mL) mixture at 25 ºC under N_2, irradiated at 447 nm for 18 h. Yields after workup (average of duplicates) determined by chiral GC analysis relative to the signal of biphenyl as calibrated internal standard.

4.2.7 Towards new sterically hindered *m*-substituted complexes

Our first approach for introducing bulky groups in the pyridine ring led us to find that the reactivity of the tetradentate cobalt complexes is too sensitive to the substitution in *o*-position. The only *o*-substituted complexes that catalysed the reduction of **5a**, and with low yields, possessed substituents with as low hindrance as a methyl group (**$^{o\text{-Me}}$PDPCo$_{Cl}$**) and a fused ring (**^{quin}PDPCo$_{Tf}$**). The introduction of bulkier moieties on that position, such as a phenyl ring (**$^{o\text{-Ph}}$PDPCo$_{Cl}$**), or the use of a tert-butyl oxazoline scaffold as heteroaromatic unit (**^{oxaz}BPCo$_{OTf}$**), limited the production of **6a** to the threshold of stoichiometric reactivity. With those experiments, we could not confirm or refute if tetradentate complexes can harness steric hindrance to increasing ee%. Under those circumstances, we considered that the presence of bulky groups not in *o*- but in *m*-position should let us test our hypothesis, anticipating an equilibrium between excess and defect of steric hindrance for appropriate asymmetric induction without compromising the reactivity.

At the initial screening of cobalt chiral complexes from our group's library of catalysts (Figure 4. 1), we have already tested some *m*-substituted complexes such as **K1** (bearing ester groups) or the even bulkier **K2** (bearing chains with pyrene groups). However, they were not strategically designed to be sterically impeded towards the reaction centre. With this intention, we were attracted by introducing a bulky quaternary carbon in *m*-position, occupied with aryl groups rather than alkyl chains, to control the degrees of freedom of the bulky moiety. Such a hypothetical tetra-arylated carbon (three aryl groups plus the pyridine ring), is a synthetic challenge itself, and the corresponding molecule would probably exhibit extreme insolubility in most organic solvents.[102] Still, we decided to focus our effort on the synthesis of structurally similar compounds where the pyridine ring is substituted in *m*-position with a tri-arylated quaternary carbon (two aryl rings plus the pyridine) that has an 'easy-to-tune' additional position (such as an ether or an ester).

In that direction, we followed reported procedures (see Section 4.1.1) to prepare the building block **py-1** (Scheme 4. 14), which can be easily tuned *via* nucleophilic attack to the ester moiety, therefore introducing two phenyl rings (**py-2**, 92% yield).

The resultant alcohol can be linked to an alkyl group by nucleophilic substitution, and the same mixture can be desilylated with a fluoride source (87% yield in the case of **py-3**). Further chlorination with thionyl chloride afforded the compound **^{qOMe}py-Cl**, which will be used as a model coupling partner to prepare the corresponding chiral ligand. Moreover, one of this synthetic route's most attractive features is that no metallic catalyst is employed.

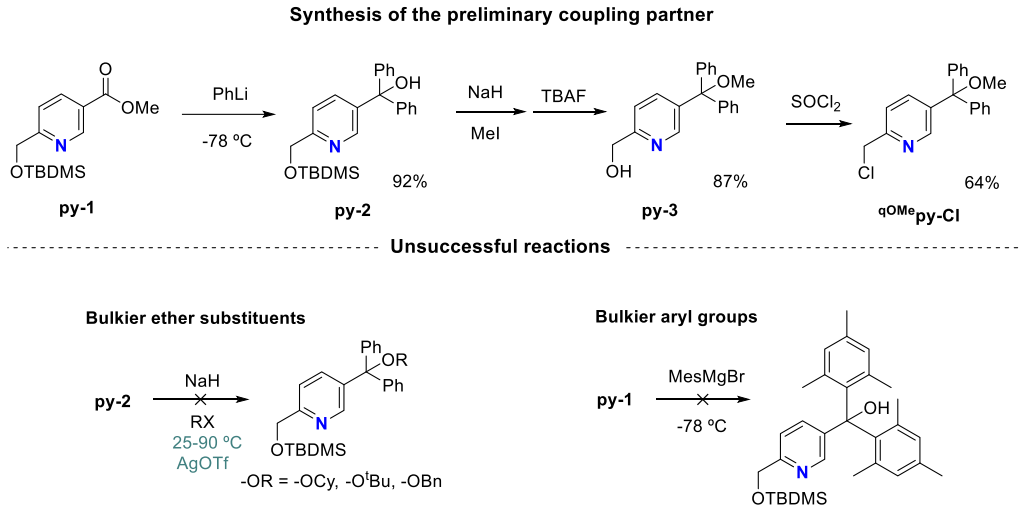

Scheme 4. 14. Top, synthetic route towards pyridine derivatives incorporating bulky quaternary carbons at *m*-position. Bottom, unsuccessful attempts to modify the substitution pattern on the quaternary carbon.

Nonetheless, the presence of the methoxy group in the model building block **^{qOMe}py-Cl** restricts the hindrance of the quaternary carbon. More impeded substituents would be more promising candidates for the target effect on chirality induction (Scheme 4.11). However, our attempts to introduce bulkier substituents (such as cyclohexyloxy, tert-butoxy or benzyloxy groups) did not afford any significant product and the starting material was recovered (Scheme 4. 14, bottom left). The incorporation of mesityl groups instead of phenyl rings also resulted in a very complex NMR mixture (Scheme 4. 14, bottom right). In front of such a recalcitrant synthetic challenge/synthetic problem, the initial scope of *m*-substituted pyridines was interrupted with one only example of chloride coupling partner that did not fulfil the expected requisite of 'all-bulky' groups. Alternatively, we considered that a more feasible route could be based on cross-coupling

reactivity towards aryl-aryl structures rather than hindered nucleophilic substitution. A trio of these coupling partners were prepared by Dr. Felix Ungeheuer and Ajdin Velic (Scheme 4. 15). It is noteworthy to mention that the structure of **$^{Ar\text{-}tBu}$py-Cl** was unexpected since the boronic did not undergo the conventional coupling with the bromide position but with a methyl group from a tert-butyl substituent.

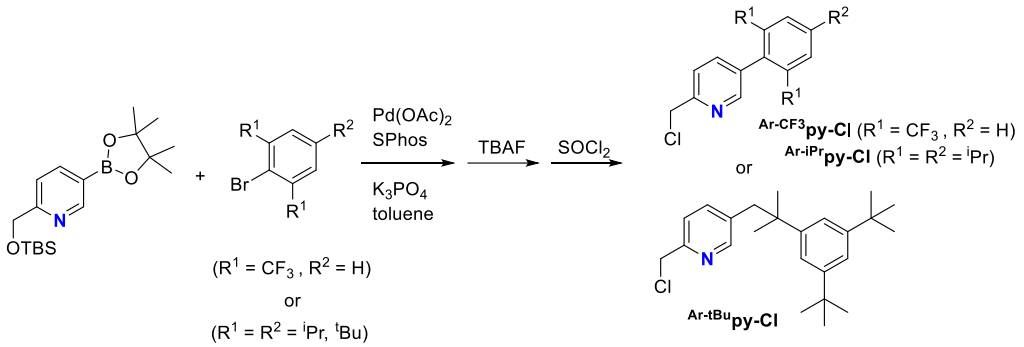

Scheme 4. 15. Synthetic route towards pyridine derivatives incorporating a bulky aryl ring at *m*-position. Starting boronic ester was prepared by Dr. Klaudia Michaliszyn. Dr. Felix Ungeheuer prepared **$^{Ar\text{-}CF3}$py-Cl**, and Ajdin Velic compounds **$^{Ar\text{-}iPr}$py-Cl** and **$^{Ar\text{-}tBu}$py-Cl**.

Having in hand these different coupling partners with substantial steric hindrance in the *m*-position, we linked them to the chiral backbone (*S*,*S*)-bispyrrolidine (20-90% yield) and then prepared the corresponding chiral cobalt triflates (77-84% yield). In this case, colourful crystals were obtained from all the complexes (despite **$^{Ar\text{-}CF3}$PDPCo$_{OTf}$** could not be diffracted). All these 4 complexes were new structures since the only previously reported ligand was **$^{Ar\text{-}CF3}$PDP**, which had been used for the preparation of an iron complex.[103]

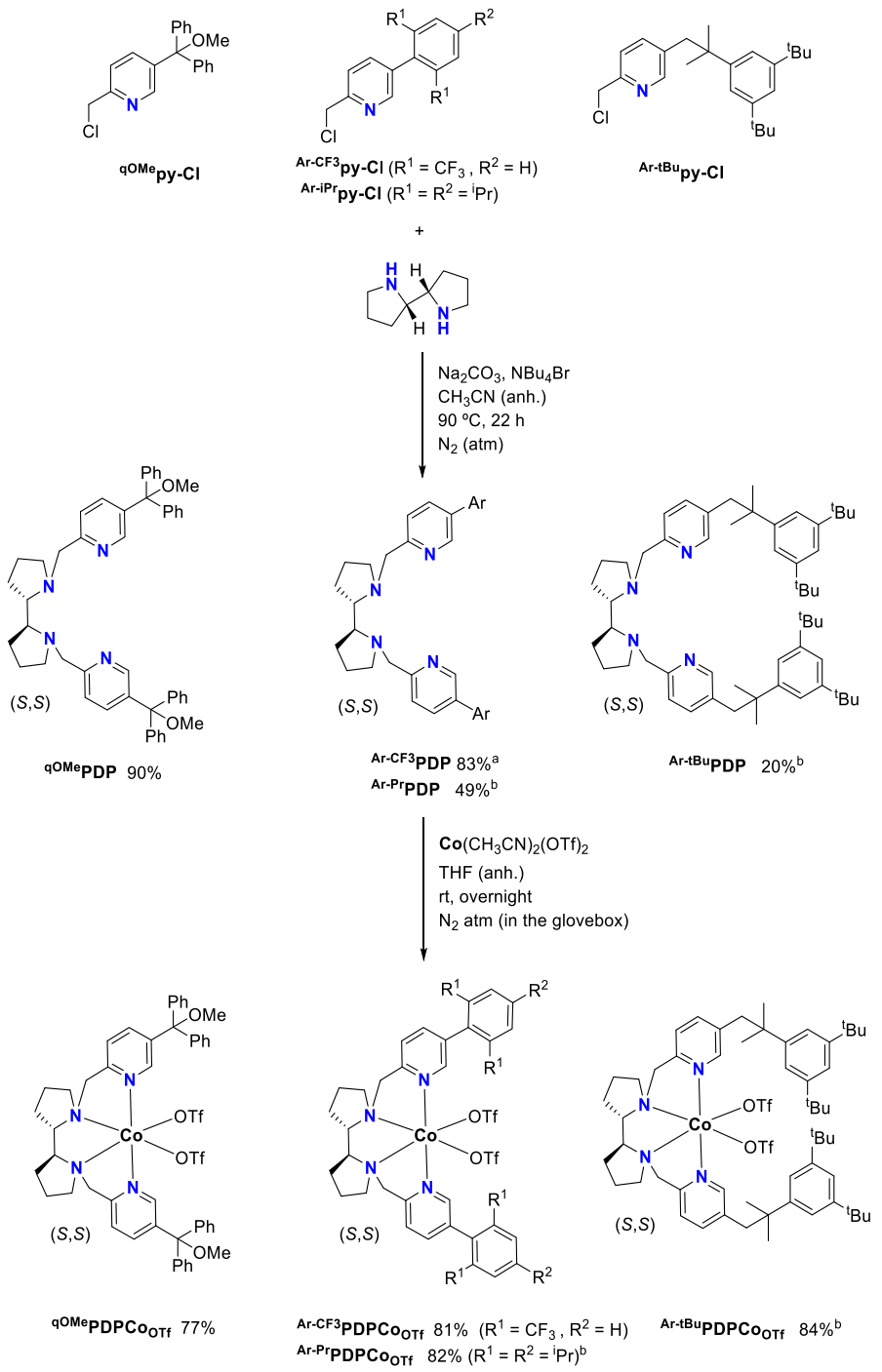

Scheme 4. 16. Synthesis of new tetradentate aminopyridine chiral ligands with *m*-substituted pyridine rings, and their corresponding Co complexes. [a]The starting chloride was prepared by Dr. Felix Ungeheuer. [b]Synthesized in collaboration with Ajdin Velic.

4.2.8 Enantioselective catalysis with *m*-substituted complexes

The four *m*-substituted complexes were tested in the photocatalytic reduction of **5a**, and we were glad to see that the sterically impeded substituents did not inhibit the reactivity. The enantiomeric excess was insignificant for ^{qOMe}**PDPCo$_{OTf}$** (3%), although this complex was derived from synthetic limitations, and its structure did not fulfil our targeted bulkiness requisites (*vide supra*). For the other complexes coming from the aryl-aryl coupling synthesis, ee% values were still very moderate but the highest up to now (up to 33% for $^{Ar\text{-}CF3}$**PDPCo$_{OTf}$**). Although more tests are needed to confirm this statement, the results discussed here suggest that synthesising complexes with hindered *meta*-substituted pyridines is on the right track to induce chirality in the ATH of ketones.

Table 4.9. Photocatalytic reduction of acetophenone using the chiral cobalt complexes with bulky substitution in *m*-position.

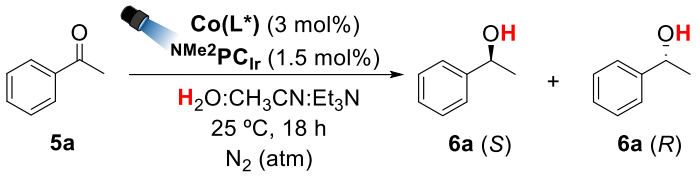

Entry	Co-cat	Conv (%)	Yield **6a** (%)	ee (%)
1	^{qOMe}**PDPCo$_{OTf}$**	100	99	3
2	$^{Ar\text{-}CF3}$**PDPCo$_{OTf}$**	100	88	33
3	$^{Ar\text{-}Pr}$**PDPCo$_{OTf}$**	87	70	23
4	$^{Ar\text{-}tBu}$**PDPCo$_{OTf}$**	69	63	29

Conditions: Co(L*) (3 mol%), ^{NMe2}**PC$_{Ir}$** (1.5 mol%), **5a** (10 mM) in H_2O:CH_3CN:Et_3N (0.6:0.4:0.02 mL) mixture at 25 ºC under N_2, irradiated at 447 nm for 18 h. Yields after workup (average of duplicates) determined by chiral GC analysis relative to the signal of biphenyl as calibrated internal standard.

4.2.9 Studying other ketones

Acetophenone has been extensively used as a model substrate for the asymmetric reduction of ketones in the literature (*vide supra*, Section 4.1 State of the art). Still, in our conditions, we could hardly improve the chirality induction in phenylethanol (**6a**), and we decided to try other substrates using our standard tetradentate catalyst **2$_{Co}$** and

the one which exhibited the best performance up to now, $^{Ar\text{-}CF3}$**PDPCo$_{OTf}$**. We have explored what happens when going from acetophenone, to derivatives with slightly more hindered substituents. Interestingly, the ee% for the reduction of **5b** was the highest we have obtained so far, both for $^{Ar\text{-}CF3}$**PDPCo$_{OTf}$** (34%) and **2$_{Co}$** (41%), although the yield drops, revealing a high dependence on the substrate both for reactivity and enantioselectivity. In the case of **5c**, the reactivity was maintained and ee% was also 'over the average' for **2$_{Co}$** (20%) despite decreasing for the other catalyst (16%). In the reaction with **5d**, the starting material was recovered.

Table 4.10. Photocatalytic reduction of other ketones.

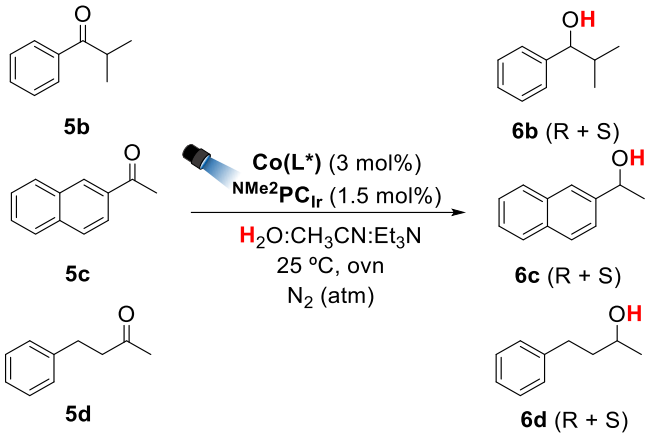

Entry	Co-cat	Substrate	Conv (%)	Yield (%)	ee (%)
1	$^{Ar\text{-}CF3}$**PDPCo$_{OTf}$**	**5b**	96	6	34
2	$^{Ar\text{-}CF3}$**PDPCo$_{OTf}$**	**5c**	100	92	16
3	**2$_{Co}$**	**5b**	23	23	41
4	**2$_{Co}$**	**5c**	100	87	20
5	**2$_{Co}$**	**5d**	0	0	0

Conditions: Co-cat (3 mol%), ^{NMe2}**PC$_{Ir}$** (1.5 mol%), Subs. (10 mM) in H_2O:CH_3CN:Et_3N (0.6:0.4:0.02 mL) irradiated (447 nm) overnight at 25 °C under N_2. Yields after workup (average of duplicates) determined by chiral GC analysis relative to the signal of biphenyl as calibrated internal standard.

In an effort to exploit the reactivity of aliphatic ketones, we employed the more active complex for ketone reduction **1$_{Co}$**, but **5d** did not react. Different triflate salts were tested ($X(OTf)_3$, where X = Gd, Al, Sc, Sm) so the cations may act as Lewis acids

to facilitate ketone reduction, and we also tried by increasing the light intensity to favour the SET. Nevertheless, in all these attempts the starting material was recovered. This could be explained either because the redox potential is not accessible[104] for $^{NMe2}PC_{Ir}^{0}$ (E = -1.8 V *vs* SCE), or because the formation of the ketyl radical anion in a non-aromatic position is so unstable that back electron transfer is more favoured than HAT, and a different mechanism is required (such as hydride transfer).

Table 4.11. Studies on the photocatalytic reduction of **5d.**

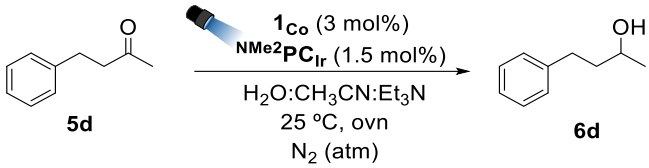

Entry	Change	$X(OTf)_3$ equiv	Conv (%)
1	-	-	<1
2	$X(OTf)_3$	1	<1
3	$X(OTf)_3$	100	<1
4[a]	7 LED	-	<1

Conditions: $\mathbf{1_{Co}}$ (3 mol%), $^{NMe2}PC_{Ir}$ (1.5 mol%), **5d** (10 mM) in H_2O:CH_3CN:Et_3N (0.6:0.4:0.02 mL) irradiated (447 nm) overnight at 25 °C under N_2. $X(OTf)_3$ represents any of the employed triflate salts ($X(OTf)_3$, where X = Gd, Al, Sc, Sm). Yields after workup (average of duplicates) determined by chiral GC analysis relative to the signal of biphenyl as calibrated internal standard. [a]Reaction irradiated with 7 LED for 2 hours.

4.2.10 Enhanced chirality induction through hydrosilylation

In a parallel study, we investigated whether the model complex $\mathbf{2_{Co}}$ could induce higher values of enantioselectivity in a different reaction. We chose the hydrosilylation of **5a**, which affords **6a** by appropriate workup in NaOH (aq). As a result, we could observe that the model complex $\mathbf{2_{Co}}$ can induce higher enantioselectivity than the reactivity in aqueous media, affording up to -67% ee. However, this result was difficult to reproduce, which could be explained due to the heterogeneous character of the reaction mixture. It is noteworthy to highlight that in this reaction, the different conditions favour the formation of the opposite enantiomer (*S*-phenylethanol) despite

using the same chiral catalyst (**2$_{Co}$** is coordinated to (*S*,*S*)-bispirrolidine through this chapter).

As a result, the ee observed is higher than under aquous conditions, which still encourage us to bealive that this type of catalysts should be able to provide good catalytic performance under the adecuate reaction conditions.

Table 4.12. Hydrosyililation of acetophenone using the model chiral cobalt complex **2$_{Co}$**.

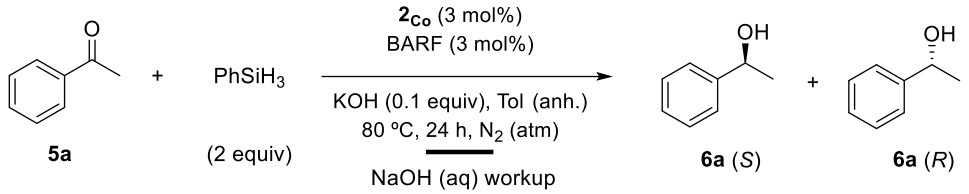

Batch	Average of	Conv (%)	Yield (%)	ee (%)
1	-	83	81	-67
2	2	50	41	-37
3	4	100	78	-15
4	4	88	77	-42

Conditions: **2$_{Co}$** (3 mol%), BARF (3 mol%), **5a** (10 mM), $PhSiH_3$ (20 mM) and dry KOH (0.1 equiv.) in dry toluene (1 mL) stirred 24 h at 80 °C under N_2. Yields after workup determined by chiral GC analysis relative to the signal of biphenyl as calibrated internal standard. [a]Reaction irradiated with 7 LED for 2 hours.

4.3 Conclusions

Although the enantioselective levels obtained are still low, some conclusions can be drawn. First, cobalt tetradentate complexes based on the chiral fragments *S*,*S*-bispyrrolidine and *S*,*S*-cyclohexanediamine can catalyse the ATH of ketones efficiently. The best results were obtained using **^{NMe2}PC$_{Ir}$** as the photocatalyst, which is attributed to its more extreme redox potential. According to the outer sphere HAT mechanism, the enantiomeric excess was very low (8% ee). Second, slight modifications in the substitution pattern of the chiral ligand's pyridines or in the media's polarity can significantly affect the enantioselectivity (upto 23% ee). Regarding the use of complexes linked to pyrene units for anchoring strategies on carbon-based surfaces, our

study indicates some interaction between the catalyst and the materials. Yet, we cannot confirm that the chiral cavity is formed at this point, and enantioselectivity values remain low (up to -15% ee).

Another important fact is that seven new tetradentate complexes with substitution in the *ortho* position of the pyridine of the chiral ligand have been prepared. The reactivity of these complexes drops drastically without observing improvements in the asymmetric induction (up to 12% ee). This inactivity is associated with excessive steric hindrance. Four other novel *m*-substituted complexes have been synthesized, and reactivity was observed when the bulky substituent is located in that position. Equally important, our current data suggest that steric hindrance in the *meta* position positively affects chirality induction (up to 33% ee). However, more studies are needed to improve the enantiomeric excess with a new generation of complexes using the guide principles obtained in this chapter.

Furthermore, reactivity and enantioselectivity are highly dependent on the substrate, as is the case with the model complex when comparing the reduction of acetophenone (92% yield, 8% ee) and isobutyrophenone (23% yield, 41% ee). Finally, the utilization of the model complex $\mathbf{2_{Co}}$ in the hydrosilylation of acetophenone allowed us to observe that it can also catalyze that transformation (up to -67%).

It is hoped that this thesis chapter will guide the continuation of this project towards the synthesis of more suitable catalysts, as well as the development of relevant models and mechanistic studies.

4.4 Experimental Section

4.4.1. Materials and reagents

Reagents and solvents were used as received from the commercial supplier unless otherwise stated. Triethylamine and diisopropylethylamine were distilled over potassium hydroxide and were stored under argon. Photocatalysts $[Ir(tbbpy)(ppy)_2](PF_6)$ ($\mathbf{^{tBu}PC_{Ir}}$), $[Ir(bpy)(ppy)_2](PF_6)$ ($\mathbf{PC_{Ir}}$),

[Cu(bathocuproine)(xantphos)](PF_6) (**PC_{Cu}**), and complexes **($Py_2^{Ts}tacn$)$Co(OTf)_2$** (**1_{Co}**), **(PDP)$Co(OTf)_2$**102 (**2_{Co}**) were synthesized according to the literature procedures. [65, 105-107] [Ir(dmabpy)$(ppy)_2$](PF_6) (**$^{NMe2}PC_{Ir}$**), was synthesized from a modified procedure from the literature. [107, 108]

For the synthesis of reagents, the solvents (DMF, hexane, Et_2O, CH_2Cl_2, CH_3CN and toluene) were used from a SPS-400, Innovative Technology solvent purification system and stored under argon with activated 4 Å molecular sieves. Anhydrous acetonitrile was purchased from Sigma-Aldrich® and water was purified with a Milli-Q Millipore Gradient AIS system. Water, methanol, ethanol, trifluoroethanol, acetonitrile, dimethylformamide, dimethylacetamide and tetrahydrofurane used for photoreactions were degassed by freeze-pump-thaw method (repeated 3 cycles) and were stored under argon.

The synthesis of air-sensitive reagents as well as the preparation of visible light photocatalytic reactions were conducted inside a nitrogen-filled glove box.

4.4.2. Instruments

Nuclear magnetic resonance (NMR). NMR spectra were recorded on Bruker Fourier300, AV400, AV500 and AVIII500 spectrometers using standard conditions (300 K). All 1H chemical shifts are reported in ppm and have been internally calibrated to the residual protons of the deuterated solvent. The 13C chemical shifts have been internally calibrated to the carbon atoms of the deuterated solvent. The coupling constants were measured in Hz.

Mass Spectrometry. High resolution Mass Spectrometry (HRMS) data was collected on a HPLC-QqTOF (Maxis Impact, Bruker Daltonics) or HPLC-TOF (MicroTOF Focus, Bruker Daltonics) mass spectrometer using 1 mM solution of the analyzed compound.

Gas chromatography analysis of liquid samples. The analysis and quantification of the starting materials and products were carried out on an Agilent 7820A gas chromatograph (HP5 column 30m, Cyclosil-B column 30m, or HP-Chiral-20B 30m)

and a flame ionization detector. GC-MS spectral analyses were performed on an Agilent 7890A gas chromatograph interfaced with an Agilent 5975c MS mass spectrometer.

Gas chromatography identification and quantification of gases. Gases at the headspace were analyzed with an Agilent 7820A GC System equipped with columns Washed Molecular Sieve 5A, 2m x 1/8'' OD, Mesh 60/80 SS and Porapak Q, 4m x 1/8'' OD, SS. Mesh: 80/100 SS and a Thermal Conductivity Detector. The quantification of the H2 obtained was measured through the interpolation of a previous calibration using different H_2/N_2 mixtures.

Parallel Pressure Transducer Hardware. The parallel pressure transducer that we used for these studies is the same that previously was developed and described for water oxidation studies.[109] This is composed by 8 differential pressure transducers (Honeywell-ASCX15DN, ± 15 psi) connected to a hardware data-acquisition system (base on Atmega microcontroller) controlled by a home-developed software program. The differential pressure transducer Honeywell-ASCX15DN is a 100 microseconds response, signal-conditioned (high level span, 4.5 V) output, calibrated and temperature compensated (0 ºC to 70 ºC) sensor. The differential sensor has two sensing ports that can be used for differential pressure measurements. The pressure calibrated devices to within ± 0.5 matm was offset and span calibrated *via* software with a high precision pressure transducer (PX409-030GUSB, 0.08 % Accuracy). Each of the 8 differential pressure transducers (Honeywell-ASCX15DN, ±15 psi) produce a voltage outputs that can directly transformed to a pressure difference between the two measuring ports. The voltage outputs were digitalized with a resolution of 0.25 matm from 0 to 175 matm and 1 matm from 176 to 1000 matm using an Atmega microcontroller with an independent voltage auto-calibration. Firmware Atmega microcontroller and control software were home-developed. The sensitivity of H_2 analytics allows quantifying the gas formed when low H_2 volumes are generated. Therefore, it could not be discarded that small amounts of H_2 were produced by inactive complexes.

4.4.3. In-house developed parallel photoreactors

Figure 4. 4. In house developed parallel photoreactors with (left) 25 positions for vials of 10 or 21 mL and (right) with 48 positions for vials of 1 mL.

Light source: The reactions were performed using Royal-Blue (λ = 447±20 nm) LUXEON Rebel ES LED, mounted on a 20 mm Square Saber - 1030 mW @ 700mA as a light source.

Temperature Control: Reaction temperature was controlled by a high-precision thermoregulation Hubber K6 cryostat. Likewise, aiming at ensuring stable irradiation, the temperature of the LEDs was controlled and set at 22 ºC.

4.4.4. Experimental procedures for photocatalysis

General procedure for catalytic tests. Inside an anaerobic box, aliquots from stock solutions in CH_3CN of **substrate** 200 mM (0.05 mL, 0.01 mmol, 1.0 eq.), cobalt or nickel **complex** 1.2 mM (0.25 mL, $3 \cdot 10^{-4}$ mmol, 3 mol%), **PC** 1.5 mM (0.1 mL, $1.5 \cdot 10^{-4}$ mmol, 1.5 mol%) were equally distributed into a vial (10 mL of headspace) that contained glass beads. The vial was sealed with a septum and removed from the anaerobic box. To each vial, degassed water was added to reach a total volume of 1 mL (total concentration of substrate 10 mM) and Et_3N (20 μL, 0.14 mmol, 14 equiv.) was injected, then the vial was placed in the photoreactor at the indicated temperature. After irradiating for a given time with blue LEDs (λ = 447 nm), the sample was opened to air and a solution of biphenyl in ethyl acetate was added as internal standard ($1.28 \cdot 10^{-3}$ mmol in 0.04 mL). Then, addition of 1 mL of more ethyl acetate formed a biphasic solution and an aliquot of the organic phase was passed through a plug of $MgSO_4$. The

resulting solution was analysed by gas chromatography. The yields reported for each reaction are given as an average of at least two runs.

Injection in the GC-FID of the separated samples of commercial (*R*)-1-Phenylethanol and (*S*)-1-Phenylethanol), allowed us to recognize that the more favoured product in the first reactions (Table 4.1) was the *R* enantiomer. Consequently, the equation to calculate the ee% in this thesis chapter is defined as:

$$ee\% = \frac{(moles\ of\ R\ enantiomer) - (moles\ of\ S\ enantiomer)}{moles\ of\ R\ enantiomer + \ moles\ of\ S\ enantiomer} \times 100$$

General procedure for the H_2 evolution monitoring. Once vials are placed in the photoreactor, each reaction vial was connected to a differential pressure transducer sensor (Honeywell-ASCX15DN) with a reference vial that contains only ^{NMe2}**PC**$_{Ir}$, electron donor and solvent. The reaction and reference vials were kept under the same experimental conditions to compensate the noise due to temperature-pressure fluctuations. The dihydrogen generated in the reaction vessels were monitored by recording the increase of pressure in the headspace, which is measured as the difference in pressure between the reaction and the reference vial.

4.4.5. Synthesis and characterization of the chloride building block

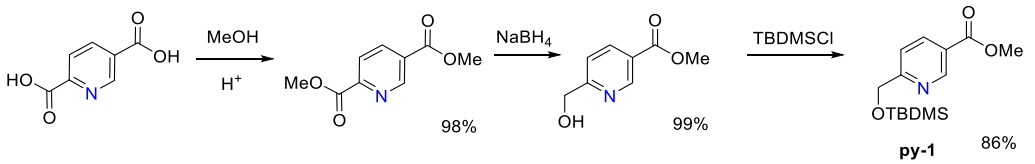

Synthesis of methyl 6-(((tert-butyldimethylsilyl)oxy)methyl)nicotinate (py-1): Starting from the commercial compound pyridine-2,5-dicarboxylic acid, procedures from the literature were applied for the sequential steps of esterification,[110] regioselective reduction[111] and silylation,[112] obtaining **py-1** in 83% yield from the three steps.

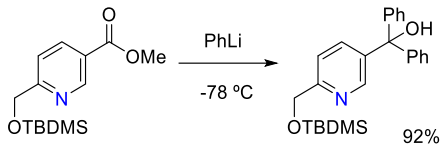

py-1 **py-2**

Synthesis of (6-(((tert-butyldimethylsilyl)oxy)methyl)pyridin-3-yl)diphenylmethanol (py-2): to a stirred solution of **py-1** (630 mg, 2.24 mmol, 1equiv.) in Et2O (5 mL) at -78 °C was added dropwise PhLi (1.8 M sol in Bu_2O, 2.61 mL, 4.70 mmol, 2.1 equiv.). The reaction was slowly warmed up to room temperature over 2 h, then quenched by small portions of dry CO_2, filtered and the filtrate was concentrated at reduced pressure. The crude was purified through silica with hexane/ethyl acetate (pure hexane, then 10:1) to give 838 mg of the desired product (92%). ^{1}H-NMR ($CDCl_3$, 400 MHz, 300 K) δ, ppm: 8.46 (s, 1H), 7.67 (d, *J*=7.4, 1H), 7.49 (d, *J*=8.1, 1H), 7.36-7.23 (m, 10H), 0.95 (s, 9H), 0.12 (s, 6H). ^{13}C[^{1}H]-NMR ($CDCl_3$, 100.6 MHz, 300 K) δ, ppm:160.2, 148.3, 146.3, 140.6, 136.4, 128.3, 127.9, 127.8, 119.2, 80.8, 65.9, 26.1, -5.2.

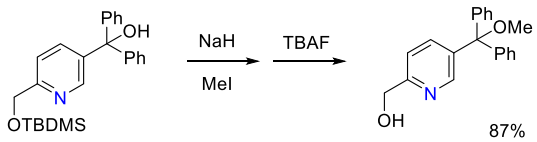

py-2 **py-3**

Synthesis of (5-(methoxydiphenylmethyl)pyridin-2-yl)methanol (py-3): In the glovebox, to a vial containing a solution of **py-2** (710 mg, 1.75 mmol, 1.00 equiv.) in THF (6 ml) was added NaH (144 mg, 5.99 mmol, 3.40 equiv.) and iodomethane (351 µL, 5.64 mmol, 3.22 equiv.). Then, the vial was crimped and the mixture was stirred for 72 hours at room temperature. Out of the glovebox, the mixture was slowly quenched with ice, then extracted in dichloromethane/water and dried over $MgSO_4$. The solvent was removed and the crude was further stirred for 4 h in 3 ml of THF with excess of tetrabutylammonium fluoride (1.37 g, 5.25 mmol, 3 equiv.). Volatiles were evaporated *in vacuo*, and the crude was purified through silica with hexane/ethyl acetate (1:2) to give 469 mg of the desired product in 87% yield. ^{1}H-NMR ($CDCl_3$, 400 MHz, 300 K) δ, ppm: 8.68 (d, *J* = 2.2 Hz, 1H), 7.83 (dd, *J* = 8.2, 2.2 Hz, 1H) 7.44-7.20 (m, 10H), 4.77 (s, 2H), 3.08 (s, 3H).

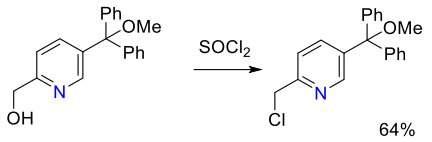

py-3 **^{qOMe}py-Cl**

Synthesis of 2-(chloromethyl)-5-(methoxydiphenylmethyl)pyridine (^{qOMe}py-Cl): py-3 (458 mg, 1.50 mmol, 1 equiv.) was dissolved in CH_2Cl_2 (4 mL) at 0 ºC. $SOCl_2$ (251 µL, 3.45 mmol, 2.3 equiv.) was cautiously added dropwise, and the mixture was stirred overnight at room temperature. The solvent was removed by bubbling nitrogen into the crude reaction mixture to minimize the amount of aqueous was added (sat., 3 ml). The organic layer was extracted in dichloromethane/water, dried over $MgSO_4$ and dried under vacuum to give 310 mg of the desired product in 64% yield. ^{1}H-NMR ($CDCl_3$, 400 MHz, 300 K) δ, ppm: 8.73 (d, *J*=1.5, 1H), 7.85 (dd, *J*=8.2, 2.4, 2H), 7.47-7.41 (m, 4H), 7.39-7.27 (m, 6H), 4.68 (s, 2H), 3.10 (s, 3H). ^{13}C[^{1}H]-NMR ($CDCl_3$, 100.6 MHz, 300 K) δ, ppm: ^{13}C NMR (101 MHz, $CDCl_3$) δ 154.7, 149.4, 142.5, 140.0, 137.0, 128.8, 128.2, 127.6, 122.0, 52.1, 46.4. GC-MS (m/z) = 323.2.

4.4.6. Synthesis and characterization of chiral ligands

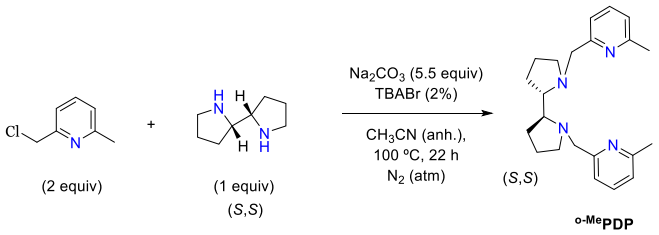

Synthesis of (2*S*,2'*S*)-1,1'-bis((6-methylpyridin-2-yl)methyl)-2,2'-bipyrrolidine ($^{o\text{-}Me}$PDP): 2-(chloromethyl)-6-methylpyridine (50.5 mg, 357 µmol), (2*S*,2'*S*)-2,2'-bipyrrolidine (25.0 mg, 178.2 µmol) and anhydrous acetonitrile (10 mL) were mixed in a 25 mL flask with Na_2CO_3 (104 mg) and tetrabutylammonium bromide (2 mg). The resulting mixture was heated at reflux under N_2 for 18 h. After cooling to room temperature, the mixture was extracted in dichloromethane/water and dried over $MgSO_4$. The crude was condensed and purified through neutral alumina with hexane/ethyl acetate (5:1) for the elution, obtaining 59 mg of a colorless oil (94%). ^{1}H-

NMR ($CDCl_3$, 400 MHz, 300 K) δ, ppm: 7.44 (t, *J* = 7.7, 1H), 7.19 (d, *J* = 7.7, 1H), 6.91 (d, *J* = 7.6, 1H), 4.12 (d, *J* = 14.6, 1H), 3.44 (d, *J* = 14.6, 1H), 2.98 (dt, *J* = 8.9, 4.3, 1H), 2.76 (p, *J* = 4.4, 1H), 2.47 (s, 3H), 2.19 (q, J = 8.5, 1H), 1.85–1.53 (m, 5H). $^{13}C[^1H]$-NMR ($CDCl_3$, 100.6 MHz, 300 K) δ, ppm: 160.0, 157.3, 136.5, 121.1, 119.4, 65.4, 61.2, 55.34, 26.0, 24.5, 23.7.

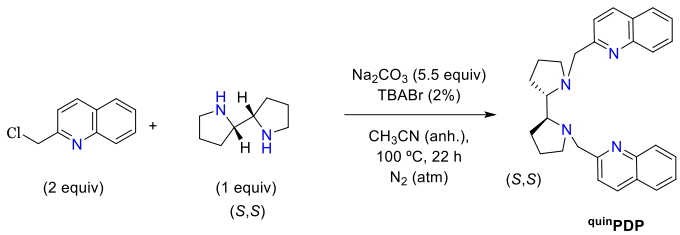

Synthesis of (2*S*,2'*S*)-1,1'-bis(quinolin-2-ylmethyl)-2,2'-bipyrrolidine (quinPDP): 2-(chloromethyl)quinoline hydrochloride (104 mg, 485 μmol), (2S,2'S)-2,2'-bipyrrolidine (34.0 mg, 242 μmol) and anhydrous acetonitrile (10 mL) were mixed in a 25 mL flask with Na_2CO_3 (141 mg) and tetrabutylammonium bromide (3 mg). The resulting mixture was heated at reflux under N_2 for 18 h. After cooling to room temperature, the mixture was extracted in dichloromethane/water and dried over $MgSO_4$. The crude was condensed and purified through neutral alumina with hexane/ethyl acetate (5:1) for the elution, obtaining 75 mg of a yellowish oil (73%). ^1H-NMR ($CDCl_3$, 400 MHz, 300 K) δ, ppm: 8.02 (dd, *J* = 13.0, 8.5, 4H), 7.73 – 7.69 (m, 2H), 7.64 (ddd, *J* = 8.4, 6.9, 1.5, 2H), 7.57 (d, *J* = 8.5, 2H), 7.44 (ddd, *J* = 8.1, 7.0, 1.1, 2H), 4.38 (d, *J* = 14.3, 2H), 3.68 (d, *J* = 14.2, 2H), 2.98–2.89 (m, 4H), 2.30 (q, *J* = 8.7, 2H), 1.93–1.77 (m, 4H), 1.75–1.66 (m, 4H). $^{13}C[^1H]$-NMR ($CDCl_3$, 100.6 MHz, 300 K) δ, ppm: 161.3, 147.5, 136.2, 129.3, 129.0, 127.5, 127.3, 125.9, 121.0, 65.6, 61.9, 55.4, 26.2, 23.8.

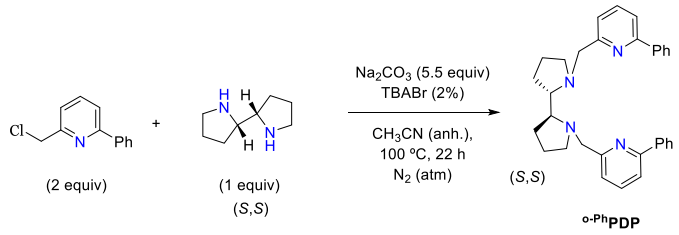

Synthesis of (2*S*,2'*S*)-1,1'-bis((6-phenylpyridin-2-yl)methyl)-2,2'-bipyrrolidine ($^{o\text{-Ph}}$PDP): 2-(chloromethyl)-6-phenylpyridine (116 mg, 570 μmol), (2S,2'S)-2,2'-bipyrrolidine (40.0 mg, 285 μmol) and anhydrous acetonitrile (10 mL) were mixed in a 25 mL flask with Na_2CO_3 (166 mg) and tetrabutylammonium bromide (2 mg). The resulting mixture was heated at reflux under N_2 for 22 h. After cooling to room temperature, the mixture was extracted in dichloromethane/water and dried over $MgSO_4$. The crude was condensed and purified through neutral alumina with hexane/ethyl acetate (5:1) for the elution, obtaining 93 mg of a yellowish oil (69%). ^{1}H-NMR ($CDCl_3$, 400 MHz, 300 K) δ, ppm: 8.00–7.95 (m, 4H), 7.64 (t, *J* = 7.7, 2H), 7.52 (d, *J* = 7.6, 2H), 7.48–7.41 (m, 4H), 7.41–7.34 (m, 4H), 4.32 (d, *J* = 14.7, 2H), 3.65 (d, *J* = 14.8, 2H), 3.09 (dt, *J* = 9.5, 4.4, 2H), 2.99-2.90 (m, 2H), 2.34 (q, *J* = 8.5, 2H), 1.92–1.69 (m, 8H). ^{13}C[^{1}H]-NMR ($CDCl_3$, 100.6 MHz, 300 K) δ, ppm: 160.6, 156.5, 139.8, 137.0, 128.7, 127.3, 121.0, 118.4, 65.5, 61.3, 55.3, 26.3, 23.8. $[\alpha]_D$ = -11.5° (measured at 25 ºC).

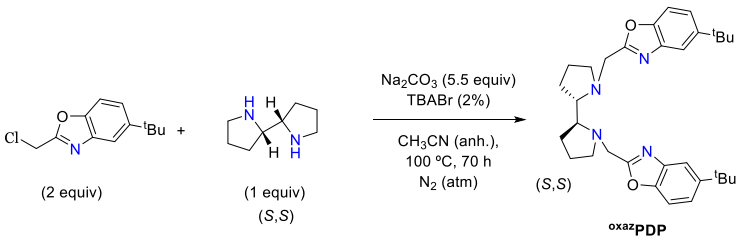

Synthesis of (2*S*,2'*S*)-1,1'-bis((5-(tert-butyl)benzo[d]oxazol-2-yl)methyl)-2,2'-bipyrrolidine (^{oxaz}BP): 5-(tert-butyl)-2-(chloromethyl)benzo[d]oxazole (47.9 mg, 214 μmol), (2S,2'S)-2,2'-bipyrrolidine (15.0 mg, 107 μmol) and anhydrous acetonitrile (10 mL) were mixed in a 25 mL flask with Na_2CO_3 (62.4 mg) and tetrabutylammonium bromide (2 mg). The resulting mixture was heated at reflux under N_2 for 70 h. After cooling to room temperature, the mixture was extracted in dichloromethane/water and dried over $MgSO_4$. The crude was condensed and purified twice through neutral alumina with hexane/ethyl acetate (10:1) for the elution, obtaining 9.9 mg of a brownish oil (9%). ^{1}H-NMR ($CDCl_3$, 400 MHz, 300 K) δ, ppm: 7.88 (m, 2H), 7.31 (m, 4H), 4.55 (d, *J* = 15.1, 2H), 3.91 (d, *J* = 15.0, 2H), 3.16 (ddd, *J* = 9.2, 6.5, 2.9, 2H), 2.90 (td, *J* = 5.3, 2.0, 2H), 2.50 (td, *J* = 9.2, 6.9, 2H), 1.91 (m, 2H), 1.70 (m, 8H), 1.35 (s, 18H). ^{13}C[^{1}H]-

NMR ($CDCl_3$, 100.6 MHz, 300 K) δ, ppm: 165.1, 147.7, 141.1, 122.5, 116.5, 109.8, 66.5, 55.3, 52.2, 31.9, 27.7, 23.8.

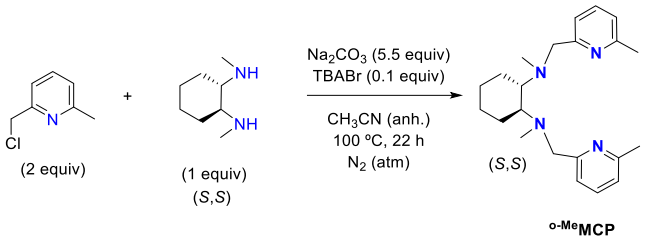

Synthesis of (1*S*,2*S*)-N1,N2-dimethyl-*N*1,*N*2-bis((6-methylpyridin-2-yl)methyl)cyclohexane-1,2-diamine ($^{o\text{-}Me}$MCP): 2-(chloromethyl)-6-methylpyridine hydrochloride (179 mg, 1.27 mmol), (2*S*,2'*S*)- (1*S*,2*S*)-*N*1,*N*2-dimethycyclohexane-1,2-diamine (90.0 mg, 633 μmol) and anhydrous acetonitrile (10 mL) were mixed in a 25 mL flask with Na_2CO_3 (369 mg) and tetrabutylammonium bromide (4 mg). The resulting mixture was heated at reflux under N_2 for 18 h. After cooling to room temperature, the mixture was extracted in dichloromethane/water and dried over $MgSO_4$. The crude was condensed and purified through neutral alumina with hexane/ethyl acetate (5:1) for the elution, obtaining 187 mg of a colourless oil (94%). ^{1}H-NMR ($CDCl_3$, 400 MHz, 300 K) δ, ppm: 7.47 (t, *J* = 7.2, 1H), 7.39 (d, *J* = 7.9, 2H), 6.97 (d, *J* = 7.4, 2H), 3.89 (d, *J* = 14.8, 2H), 3.75 (d, *J* = 14.9, 2H), 2.65 (m, 2H), 2.52 (s, 6H), 2.28 (s, 6H), 1.97 (m, 2H), 1.76 (m, 2H), 1.27 (m, 2H), 1.15 (m, 2H). ^{13}C[^{1}H]-NMR ($CDCl_3$, 100.6 MHz, 300 K) δ, ppm: 161.1, 157.2, 136.6, 121.1, 119.7, 64.9, 60.5, 36.8, 26.0, 25.9, 24.6. $[\alpha]_D$ = +8.5° (measured at 25 ºC).

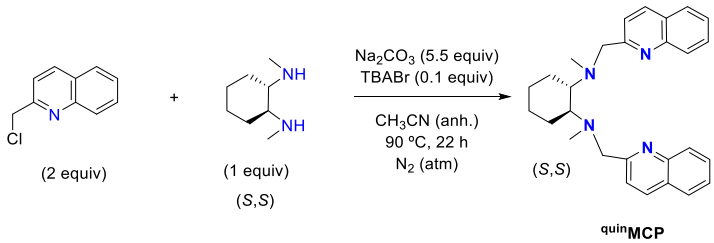

Synthesis of (1*S*,2*S*)-*N*1,*N*2-dimethyl-*N*1,*N*2-bis(quinolin-2-ylmethyl)cyclohexane-1,2-diamine (^{quin}MCP): 2-(chloromethyl)quinoline hydrochloride (151 mg, 703 μmol), (2*S*,2'*S*)- (1*S*,2*S*)-*N*1,*N*2-dimethycyclohexane-1,2-

diamine (50.0 mg, 351 μmol) and anhydrous acetonitrile (10 mL) were mixed in a 25 mL flask with Na_2CO_3 (205 mg) and tetrabutylammonium bromide (3 mg). The resulting mixture was heated at reflux under N_2 for 18 h. After cooling to room temperature, the mixture was extracted in dichloromethane/water and dried over $MgSO_4$. The crude was condensed and purified through neutral alumina with hexane/ethyl acetate (5:1) for the elution, obtaining 110 mg of a yellowish oil (74%). ^{1}H-NMR ($CDCl_3$, 400 MHz, 300 K) δ, ppm: 8.03 (d, *J* = 8.4, 2H), 7.93 (d, *J* = 8.5, 2H), 7.72 (ddd, *J* = 15.0, 8.3, 4H), 7.75-7.69 (m, 2H), 7.47–7.38 (m, 2H), 4.07 (d, *J* = 14.2, 1H), 3.88 (d, *J* = 14.2, 2H), 2.72–2.65 (m, 2H), 2.29 (s, 6H), 2.01 (d, *J*=11.7, 2H), 1.76-1.70 (m, 2H), 1.32-1.20 (m, 2H), 1.19-1.07 (m, 2H). ^{13}C[^{1}H]-NMR ($CDCl_3$, 100.6 MHz, 300 K) δ, ppm: 162.3, 147.6, 136.1, 129.2, 128.9, 127.6, 127.5, 125.9, 121.5, 64.8, 60.7, 37.0, 25.9, 25.3. $[\alpha]_D$ = +17.4° (measured at 25 ºC).

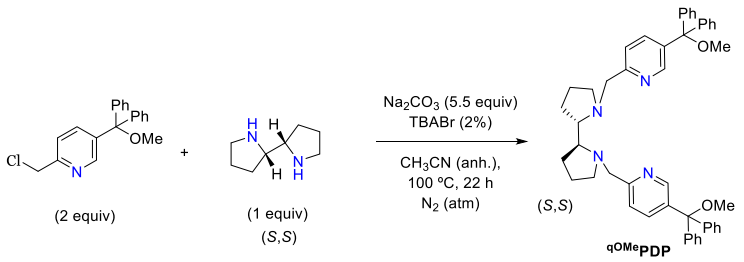

Synthesis of (2*S*,2'*S*)-1,1'-bis((5-(methoxydiphenylmethyl)pyridin-2-yl)methyl)-2,2'-bipyrrolidine (^{qOMe}PDP): 2-(chloromethyl)-5-(methoxydiphenylmethyl)pyridine (100 mg, 309 μmol), (2*S*,2'*S*)-2,2'-bipyrrolidine (19.7 mg, 140 μmol) and anhydrous acetonitrile (10 mL) were mixed in a 25 mL flask with Na_2CO_3 (164 mg) and tetrabutylammonium bromide (2 mg). The resulting mixture was heated at reflux under N_2 for 18 h. After cooling to room temperature, the mixture was extracted in dichloromethane/water and dried over $MgSO_4$. The crude was condensed and purified through neutral alumina with hexane/ethyl acetate (5:1) for the elution, obtaining 180 mg of a colorless oil (90%). ^{1}H-NMR ($CDCl_3$, 400 MHz, 300 K) δ, ppm: 8.58 (dd, *J* = 2.4, 0.4, 2H), 7.67 (dd, *J* = 8.2, 2.4, 2H), 7.44–7.37 (m, 8H), 7.31 (ddd, *J* = 10.6, 6.1, 2.3, 10H), 7.25 (s, 2H), 4.11 (d, *J* = 14.3, 2H), 3.45 (d, *J* = 14.2, 2H),

3.05 (s, 6H), 3.03-2.97 (m, 2H), 2.77-2.71 (t, *J* = 6.0, 2H), 2.23-2.15 (q, *J* = 8.6, 2H), 1.80–1.71 (m, 4H), 1.70-1.64 (m, 2H), 0.88 (s, 2H). ^{13}C NMR (101 MHz, $CDCl_3$) δ 149.2, 143.1, 136.7, 128.8, 128.1, 127.4, 122.1, 85.9, 65.6, 60.8, 55.5, 52.1, 23.6. $[\alpha]_D$ = -12.2° (measured at 25 ºC).

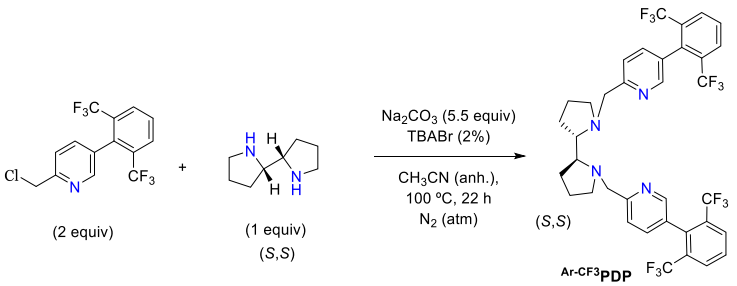

Synthesis of (2*S*,2'*S*)-1,1'-bis((5-(2,6-bis(trifluoromethyl)phenyl)pyridin-2-yl)methyl)-2,2'-bipyrrolidine (Ar-iPrPDP): 5-(2,6-bis(trifluoromethyl)phenyl)-2-(chloromethyl)pyridine (121 mg, 357 µmol), (2*S*,2'*S*)-2,2'-bipyrrolidine (25 mg, 178 µmol) and anhydrous acetonitrile (10 mL) were mixed in a 25 mL flask with Na_2CO_3 (104 mg) and tetrabutylammonium bromide (1 mg). The resulting mixture was heated at reflux under N_2 for 18 h. After cooling to room temperature, the mixture was extracted in dichloromethane/water and dried over $MgSO_4$. The crude was condensed and purified through neutral alumina with hexane/ethyl acetate (5:1) for the elution, obtaining 110 mg of a colourless oil (83%). ^{1}H NMR (CDCl3, 400 MHz), δ(ppm): 8.40 (s, 2H), 7.98 (d, *J* = 8.0, 4H), 7.66 (t, *J* = 8.0, 2H), 7.54 (d, *J* = 8.0, 2H), 7.48 (d, *J* = 8.0, 2H), 4.19 (d, *J*=14.3, 2H), 3.64 (d, *J*=14.3, 2H), 3.05 (dt, *J*=8.8, 4.3, 2H), 2.75 (t, *J*=6.1, 2H), 2.30 (q, *J*=8.5, 2H), 1.85-1.78 (m, 4H), 1.77-1.69 (m, 4H). ^{13}C NMR (101 MHz, $CDCl_3$) δ(ppm) 149.0, 137.8, 129.5, 129.4, 128.7, 121.3, 65.7, 61.3, 55.8, 26.1, 23.8. $[\alpha]_D$ = -15.6° (measured at 25 ºC).

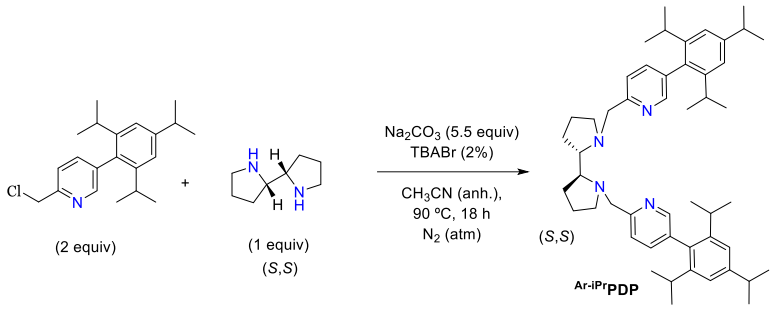

Synthesis of (2*S*,2'*S*)-1,1'-bis((5-(2,4,6-triisopropylphenyl)pyridin-2-yl)methyl)-2,2'-bipyrrolidine ($^{Ar\text{-}iPr}$PDP): To a previously dried Schlenk flask equipped with a magnetic stirring bar, (*2S,2'S*)-2,2'-bipyrrolidine (12.3 mg; 0.018 mmol; 1 eq.) was added, along with 2-(chloromethyl)-5-(2,4,6-triisopropylphenyl)pyridine (58.1 mg; 0.17 mmol; 2 eq.), Na_2CO_3 (51.3 mg; 0.43 mmol; 5.5 eq.) and tetrabutylammonium bromide (2.8 mg; 0.008 mmol; 0.1 eq.). All reaction constituents were dissolved in 8 mL of anhydrous acetonitrile, heated to 90 °C and left to reflux overnight under a nitrogen atmosphere. After 18 hours, the reaction was cooled to room temperature and 25 mL of water were added. The mixture was extracted 4 x 15 mL of DCM. All organic layers were combined, washed with brine and dried over MgSO4. The solvent was removed *in vacuo*, and the crude was obtained as a yellow-brown oil. Purification was performed by column chromatography on neutral alumina with EtOAc as the mobile phase. 1H NMR (CDCl3, 500 MHz), δ(ppm): 1.08-1.15 (m, 33H), 1.74-1.92 (m, 10H), 2.59 (hept, 6H, *J* = 6.86 Hz), 2.83-2.91 (m, 2H), 2.97 (hept, 2H, *J* = 6.89 Hz), 3.12-3.19 (m, 2H), 3.61 (d, 2H, *J* = 13.96 Hz), 4.22 (d, 2H, *J* = 14.00 Hz), 7.10 (s, 4H) 7.51 (bs, 4H), 8.41 (bs, 2H). 13C NMR (CDCl3, 125 MHz), δ(ppm): 23.9, 24.1, 24.2, 24.3, 52.7, 58.7, 65.0, 120.6, 121.1, 122.9, 131.9, 136.6, 139.6, 147.3, 149.2, 150.4. $[\alpha]_D$ = -10.7° (measured at 25 ºC).

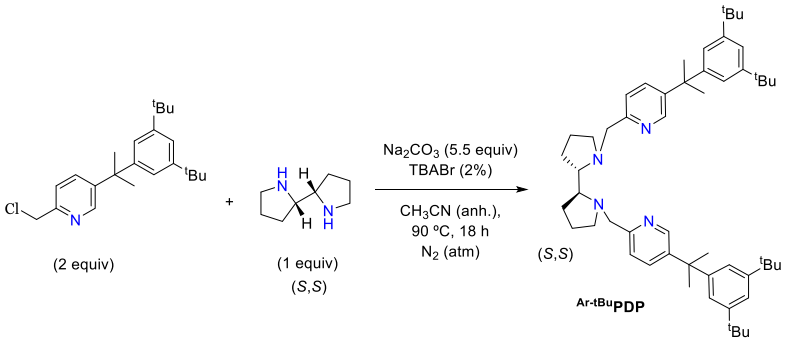

Synthesis of (2*S*,2'*S*)-1,1'-bis((5-(2-(3,5-di-tert-butylphenyl)propan-2-yl)pyridin-2-yl)methyl)-2,2'-bipyrrolidine (Ar-tBuPDP): To a previously dried Schlenk flask equipped with a magnetic stirring bar, (*2S,2'S*)-2,2'-bipyrrolidine (35.1 mg; 0.25 mmol; 1 eq.) was added, along with 2-(chloromethyl)-5-(2-(3,5-di-tert-butylphenyl)propan-2-yl)pyridine (187.0 mg; 0.5 mmol; 2 eq.), Na2CO3 (145.7 mg; 1.4 mmol; 5.5 eq.) and tetrabutylammonium bromide (8.1 mg; 0.025 mmol; 0.1 eq.). All reaction constituents were dissolved in 10 mL of anhydrous acetonitrile, heated to 90 °C and left to reflux overnight under a nitrogen atmosphere. After 18 hours, the reaction mixture changed color from white to light pink. It was cooled to room temperature and 35 mL of water were added. The mixture was extracted 4 x 15 mL of DCM. All organic layers were combined, washed with brine and dried over MgSO4. The solvent was removed *in vacuo*, and the crude was obtained as a yellow-brown oil. Purification was performed by column chromatography on neutral alumina with EtOAc as the mobile phase. 1H NMR (CDCl3, 500 MHz), δ(ppm): 1.30 (s, 30H), 1.65-1.78 (m, 8H), 2.14-2.17 (m, 2H), 2.75-2.76 (m, 2H), 2.91-2.93 (m, 2H), 3.84 (d, 2H, J = 14.07 Hz), 4.09 (d, 2H, J = 14.19 Hz), 6.80 (dd, 2H, J = 7.88 Hz, 1.73 Hz), 7.07 (d, 2H, J = 1.60 Hz), 7.12 (d, 2H, J = 7.90 Hz), 7.95 (d, 2H, J = 1.95 Hz). 13C NMR (CDCl3, 125 MHz), δ(ppm): 23.4, 31.5, 34.9, 55.2, 60.4, 60.6, 65.1, 119.7, 120.4, 121.3, 132.2, 137.9, 146.7, 150.0, 150.2, 157.7, 171.1. $[\alpha]_D$ = -11.0° (measured at 25 ºC).

4.4.7. Synthesis and characterization of chiral complexes

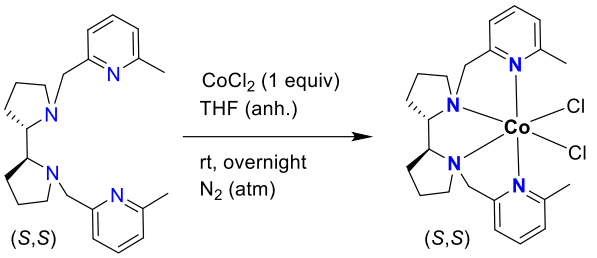

Synthesis of $^{o\text{-}Me}$PDPCo$_{Cl}$: In a glovebox, a solution of $CoCl_2$ (7.3 mg, 57 μmol) in anhydrous THF (1 mL) was added dropwise to a vigorously stirred solution of the ligand (20 mg, 57 μmol) in THF (1 mL). After few minutes, the solution become cloudy and a purple precipitate appeared. After stirring overnight, the solution was filtered off and the resulting solid dried under vacuum (14 mg, 29.0 μmol, 51%). **Anal.** Calcd (%) for $C_{22}H_{30}Cl_2CoN_4 \cdot H_2O$: C, 53.02; H, 6.25; N, 11.27; found: C 53.34, H 4.70, N: 8.74.

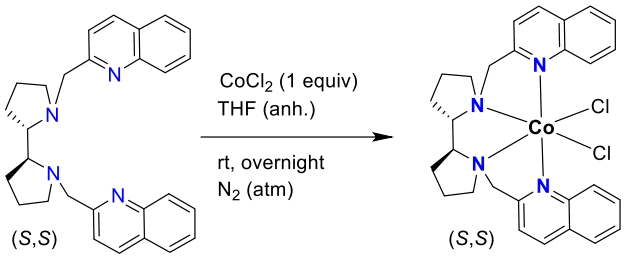

Synthesis of ^{quin}PDPCo$_{Cl}$: In a glovebox, a solution of $CoCl_2$ (10.7 mg, 82.8 μmol) in anhydrous THF (1 mL) was added dropwise to a vigorously stirred solution of the ligand (35.0 mg, 82.8 μmol) in THF (1 mL). After few minutes, the solution become cloudy and a dark green precipitate appeared. After stirring overnight the solution was filtered off and the resulting solid dried under vacuum (37.9 mg, 68.7 μmol, 83%). **Anal.** Pendant**.**

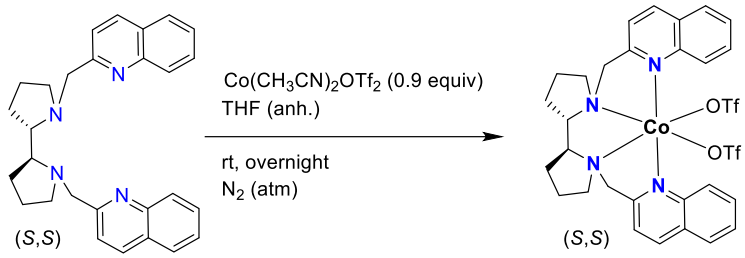

Synthesis of ^{quin}PDPCo$_{OTf}$: In a glovebox, a solution of $Co(OTf)_2(CH_3CN)_2$ (79 mg, 180 µmol) in anhydrous THF (1 mL) was added dropwise to a vigorously stirred solution of the ligand (84 mg, 200 µmol) in THF (1 mL). After few minutes, the solution become cloudy and a brown precipitate appeared. After stirring overnight the solution was filtered off through a short celite path and the resulting solid was dried under vacuum. This solid was dissolved in dichloromethane and the slow diffusion of diethyl ether into this solution produced 123.5 mg of brownish powder (158.4 µmol, 88%). **Anal.** Calcd (%) for $C_{30}H_{30}CoF_6N_4O_6S_2 \cdot 3\ H_2O$: C 43.22, H 4.35, N: 6.72; found: C 43.11, H 4.28, N: 6.59.

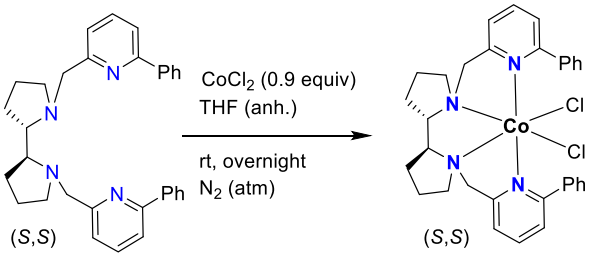

Synthesis of $^{o\text{-}Ph}$PDPCo$_{Cl}$: In a glovebox, a solution of $CoCl_2$ (17 mg, 110 µmol) in anhydrous THF (1 mL) was added dropwise to a vigorously stirred solution of the ligand (56.0 mg, 120 µmol) in THF (1 mL). After few minutes, the solution become cloudy and a dark blue precipitate appeared. After stirring overnight, the solution was filtered off and the resulting blue solid dried under vacuum (54.4 mg, 90 µmol, 75%). **Anal.** Calcd (%) for $C_{32}H_{34}Cl_2CoN_4 \cdot 7/4\ H_2O \cdot 5/2\ CH_2Cl_2$: C 48.85, H 5.05, N 6.60; found: C 48.50, H 4.88, N 6.91.

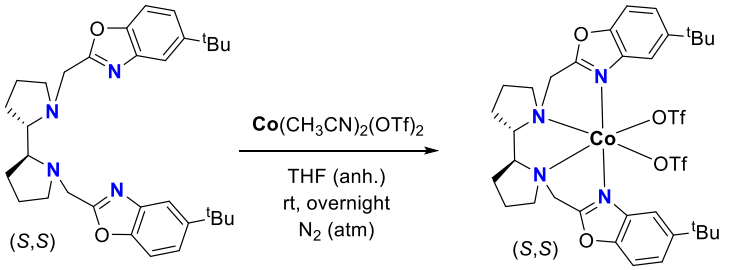

Synthesis of ^{oxaz}BPCo$_{OTf}$: In a glovebox, a solution of $Co(CH_3CN)_2(OTf)_2$ (7.3 mg, 17 μmol) in anhydrous THF (1 mL) was added dropwise to a vigorously stirred solution of the ligand (9.5 mg, 18 μmol) in THF (1 mL). After few minutes, the solution become cloudy and a dark brown precipitate appeared. After stirring overnight, the solution was filtered off and the resulting solid dried under vacuum. The residual solid was dissolved in dry DCM and placed within a container containing dry Et_2O and left to crystalize (9.6 mg, 11 μmol, 62%). **Anal.** Pendant**.**

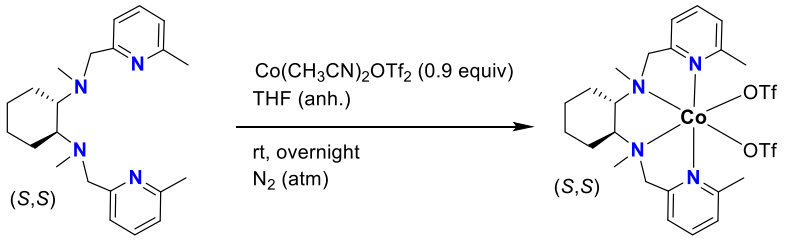

Synthesis of $^{o\text{-}Me}$MCPCo$_{OTf}$: In a glovebox, a solution of $Co(CH_3CN)_2(OTf)_2$ (83 mg, 190 μmol) in anhydrous THF (1 mL) was added dropwise to a vigorously stirred solution of the ligand (70 mg, 200 μmol) in THF (1 mL). After few minutes, the solution become cloudy and a brown precipitate appeared. After stirring overnight, the solution was filtered off and the resulting solid dried under vacuum (120 mg, 170 μmol, 85%). **Anal.** Calcd (%) for $C_{24}H_{32}CoF_6N_4O_6S_2 \cdot 2\ H_2O$: C 38.66, H 4.87, N 7.51; found: C 38.45, H 4.69, N 7.36.

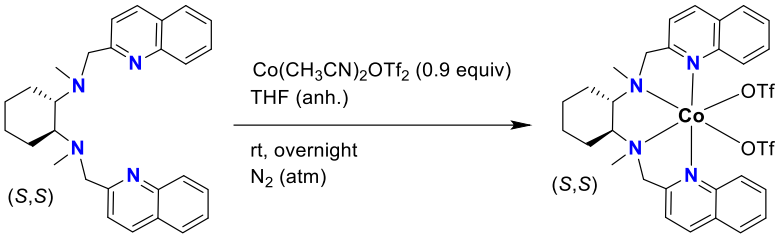

Synthesis of $^{o\text{-}Me}$MCPCo$_{OTf}$: In a glovebox, a solution of $Co(CH_3CN)_2(OTf)_2$ (79 mg, 180 µmol) in anhydrous THF (1 mL) was added dropwise to a vigorously stirred solution of the ligand (80 mg, 190 µmol) in THF (1 mL). After few minutes, the solution become cloudy and a brown precipitate appeared. After stirring overnight, the solution was filtered off and the resulting solid dried under vacuum (132 mg, 29.0 µmol, 90%). **Anal.** Calcd (%) for $C_{30}H_{32}CoF_6N_4O_6S_2 \cdot$ 3/2 H_2O : C 44.56, H 4.36, N 6.93; found: C 44.62, H 4.53, N 6.8.

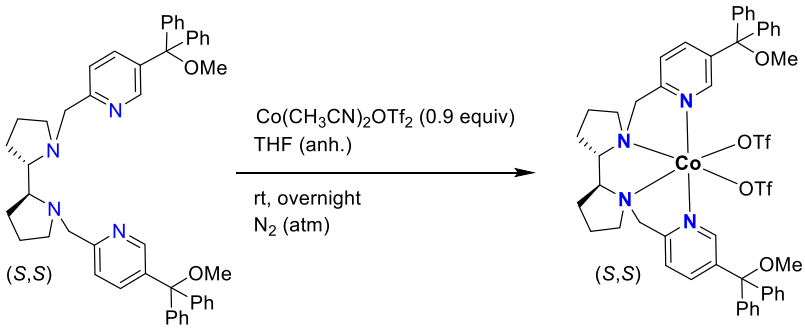

Synthesis of ^{qOMe}PDPCo$_{OTf}$: In a glovebox, a solution of $Co(CH_3CN)_2(OTf)_2$ (104 mg, 239 µmol) in anhydrous THF (1 mL) was added dropwise to a vigorously stirred solution of the ligand (175 mg, 245 µmol) in THF (1 mL). After few minutes, the solution become cloudy and a pale pink precipitate appeared. After stirring overnight, the solution was filtered off and the resulting solid dried under vacuum (155 mg, 190 µmol, 77%). **Anal.** Calcd (%) for $C_{50}H_{50}CoF_6N_4O_8S_2 \cdot$ 5/2 H_2O: C 53.76, H 4.96, N 5.02; found: C 53.71, H 4.66, N: 5.08.

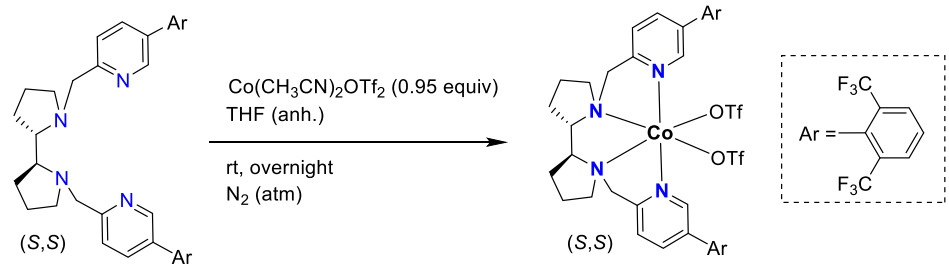

Synthesis of $^{Ar\text{-}CF3}$PDPCo$_{OTf}$: Into a vial equipped with a magnetic stirring bar $Co(CH_3CN)_2(TfO)_2$ (55.4 mg; 0.127 mmol; 0.95 eq.) was added and dissolved in 1 mL of dry THF. Into a second vial, the ligand (100 mg; 0.134 mmol; 1 eq.) was added and dissolved in 0.5 mL of dry THF. The ligand solution was added dropwise to the stirred solution of the cobalt salt. An immediate color change was observed (to pink-brown). The reaction was left stirring at room temperature under an inert atmosphere. Afterwards, the solvent was removed *in vacuo* and the residue was washed once with 1 mL of dry Et_2O, and it was removed *in vacuo* after 10 minutes of stirring at room temperature. The residual solid was dissolved in dry DCM and placed within a container containing dry Et_2O and left to crystalize. Crystals were obtained but were not diffractable (119.2 mg, 108 μmol, 81%). **Anal.** Pendant**.**

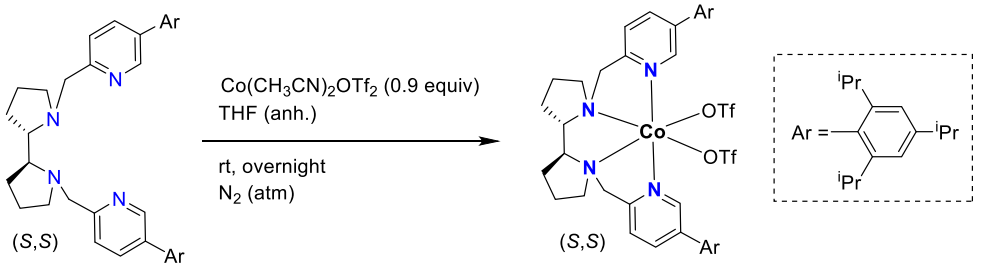

Synthesis of $^{Ar\text{-}iPr}$PDPCo$_{OTf}$: Into a vial equipped with a magnetic stirring bar $Co(CH_3CN)_2(OTf)_2$ (16.3 mg; 0.042 mmol; 0.98 eq.) was added and dissolved in 1 mL of dry THF. Into a second vial, the ligand (31.1 mg; 0.043 mmol; 1 eq.) was added and dissolved in 0.5 mL of dry THF. The ligand solution was added dropwise to the stirred solution of the cobalt salt. An immediate color change was observed (from pink to yellow-brown). The reaction was left stirring at room temperature under an inert atmosphere. Afterwards, the solvent was removed *in vacuo* and the residue was washed

once with 1 mL of dry Et_2O, and it was removed *in vacuo* after 10 minutes of stirring at room temperature. The residual solid was dissolved in dry DCM and placed within a container containing dry Et2O and left to crystalize. Pale yellow crystals were obtained (38.2 mg, 35.2 μmol, 82%). **Anal.** Pendant**.**

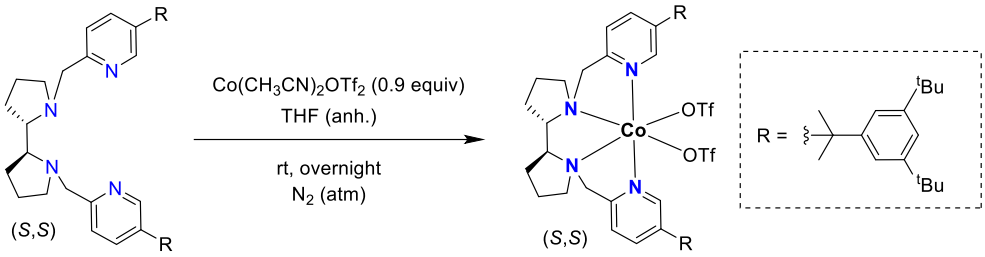

Synthesis of $^{Ar\text{-}tBu}PDPCo_{OTf}$: Into a vial equipped with a magnetic stirring bar $Co(OTf)_2(CH_3CN)_2$ (18.7 mg; 0.049 mmol; 0.98 eq.) was added and dissolved in 1 mL of dry THF. Into a second vial, L2 (40.2 mg; 0.049 mmol; 1 eq.) was added and dissolved in 0.5 mL of dry THF. The ligand solution was added dropwise to the stirred solution of the cobalt salt. An immediate color change was observed (from pink to amber). The reaction was left stirring at room temperature under an inert atmosphere. Afterwards, the solvent was removed *in vacuo* and the residue was washed once with 1 mL of dry Et_2O, and it was removed *in vacuo* after 10 minutes of stirring at room temperature. The residual solid was dissolved in dry DCM and placed within a container containing dry Et_2O and left to crystalize. Pale brown crystals were obtained (48.1 mg, 41.1 μmol, 84%). **Anal.** Pendant**.**

4.4.8. X-Ray structures

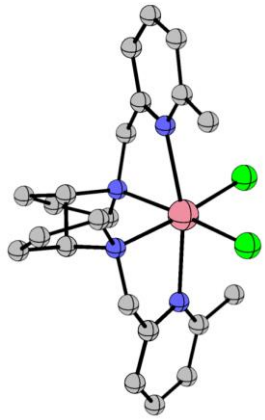

Figure 4. 5. Solid state structures by single-crystal X-Ray diffraction of complex $^{o\text{-}Me}$**PDPNi**$_{Cl}$. The hydrogen atoms are omitted for clarity.

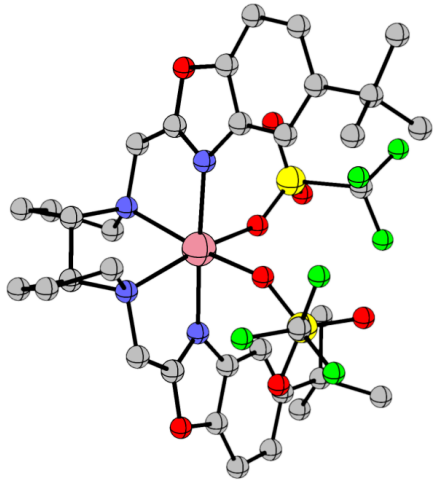

Figure 4. 6. Solid state structures by single-crystal X-Ray diffraction of complex ^{oxaz}**BPCo**$_{OTf}$. The hydrogen atoms are omitted for clarity.

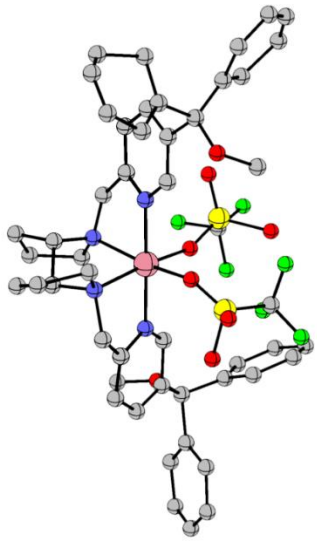

Figure 4. 7. Solid state structures by single-crystal X-Ray diffraction of complex ^{qOMe}**PDPCo**$_{OTf}$. The hydrogen atoms and solvent molecules are omitted for clarity.

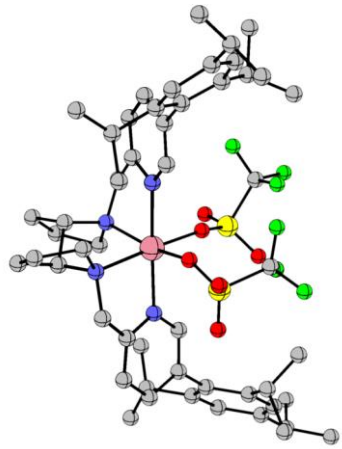

Figure 4. 8. Solid state structures by single-crystal X-Ray diffraction of complex $^{Ar\text{-}iPr}$**PDPCo**$_{OTf}$. The hydrogen atoms and solvent molecules are omitted for clarity.

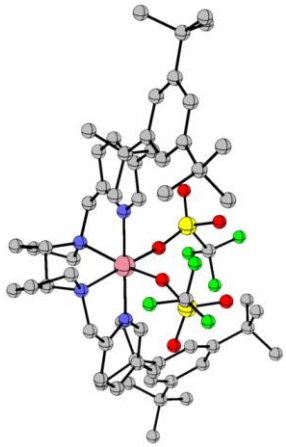

Figure 4. 9. Solid state structures by single-crystal X-Ray diffraction of complex **Ar-^{tBu}PDPCo$_{OTf}$**. The hydrogen atoms and solvent molecules are omitted for clarity.

4.4.9. Spectra collection

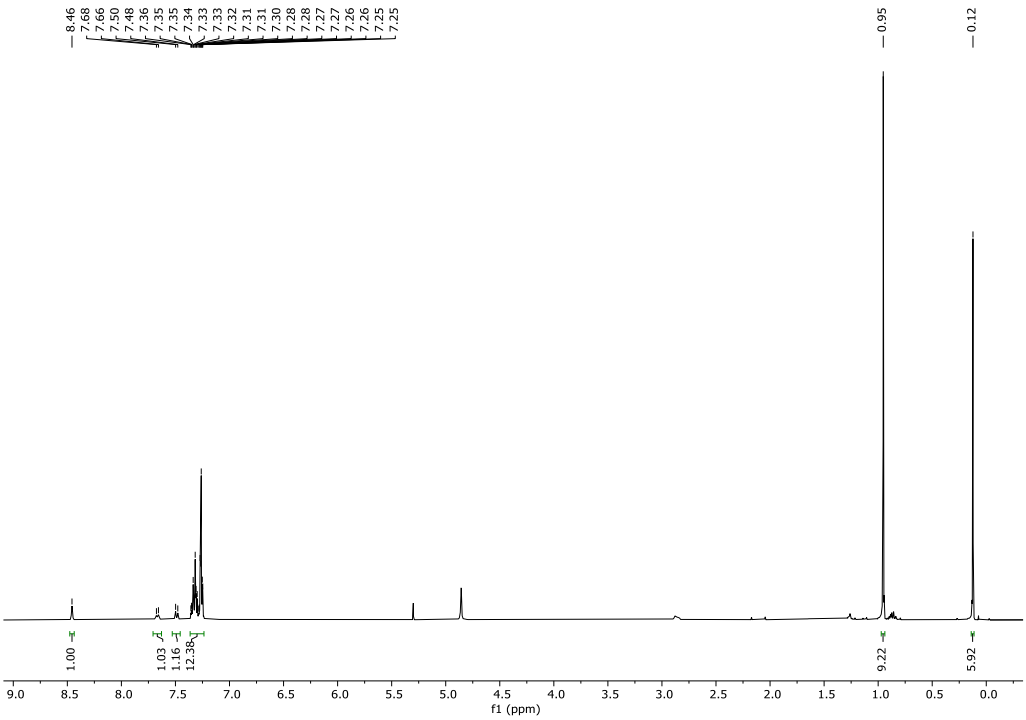

Figure 4. 10. ^{1}H-NMR ($CDCl_3$, 400 MHz, 300 K) spectrum of product **py-2**.

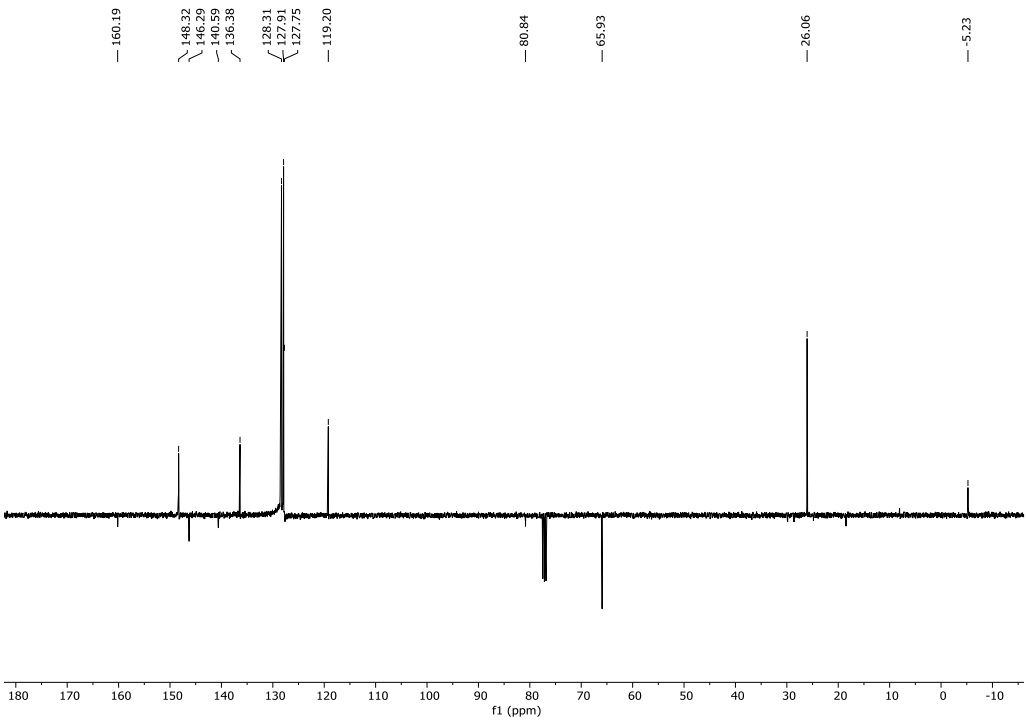

Figure 4. 11. $^{13}C[^{1}H]$-DEPTQ-135-NMR spectrum ($CDCl_3$, 100.6 MHz, 300 K) of product **py-2**.

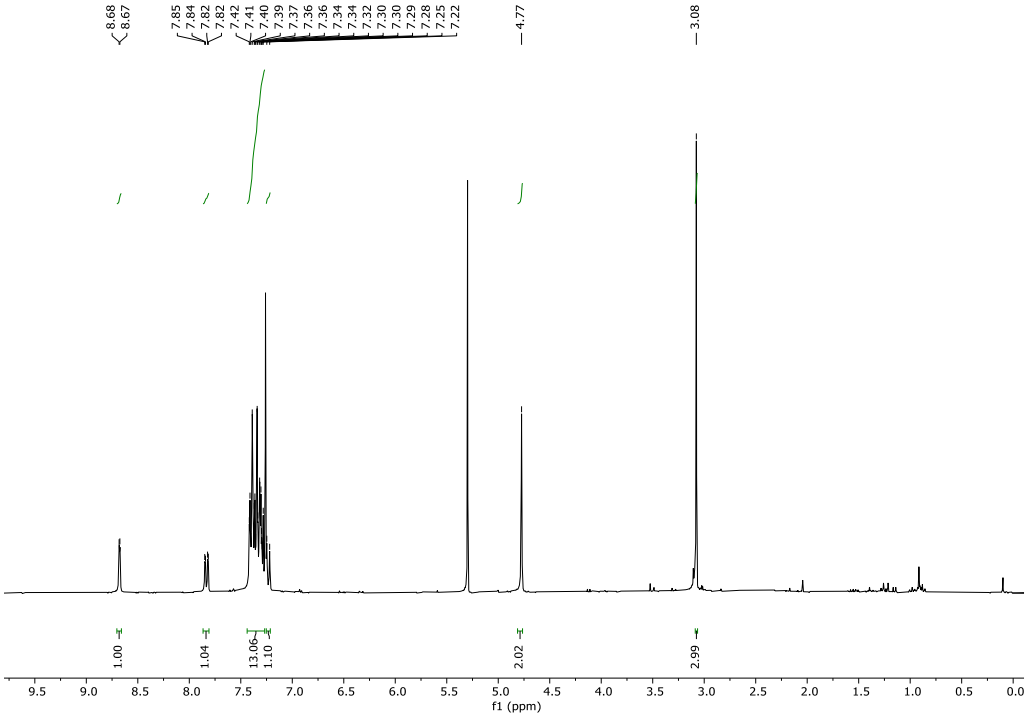

Figure 4. 12. ^{1}H-NMR ($CDCl_3$, 400 MHz, 300 K) spectrum of product **py-3**.

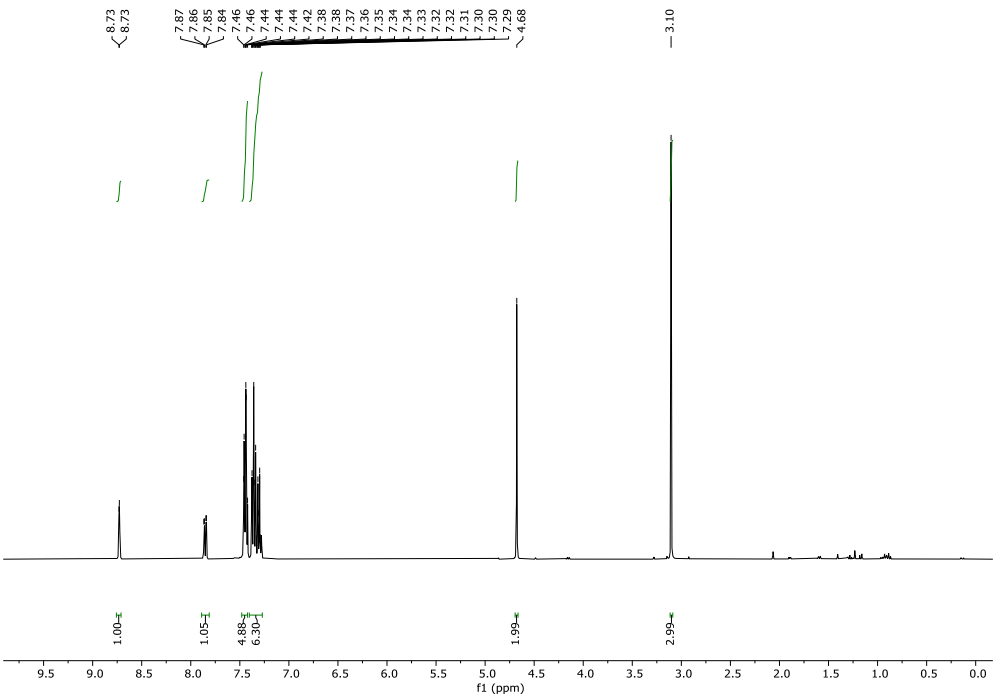

Figure 4. 13. ^{1}H-NMR ($CDCl_3$, 400 MHz, 300 K) spectrum of product **^{qOMe}py-Cl**.

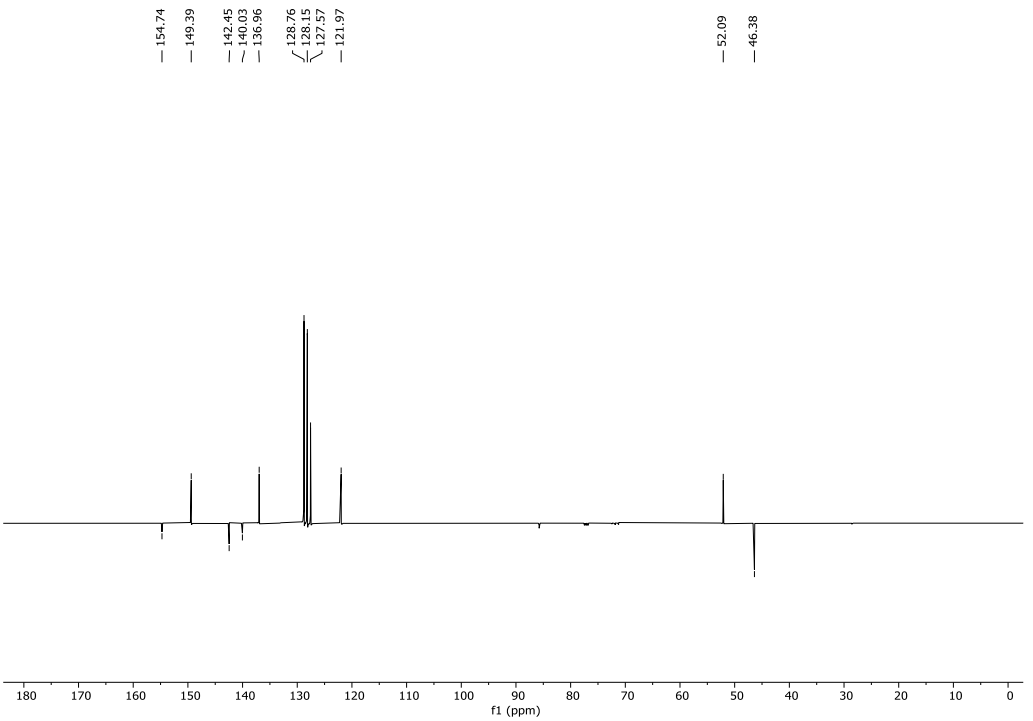

Figure 4. 14. ^{13}C[^{1}H]-DEPTQ-135-NMR spectrum ($CDCl_3$, 100.6 MHz, 300 K) of product **^{qOMe}py-Cl**.

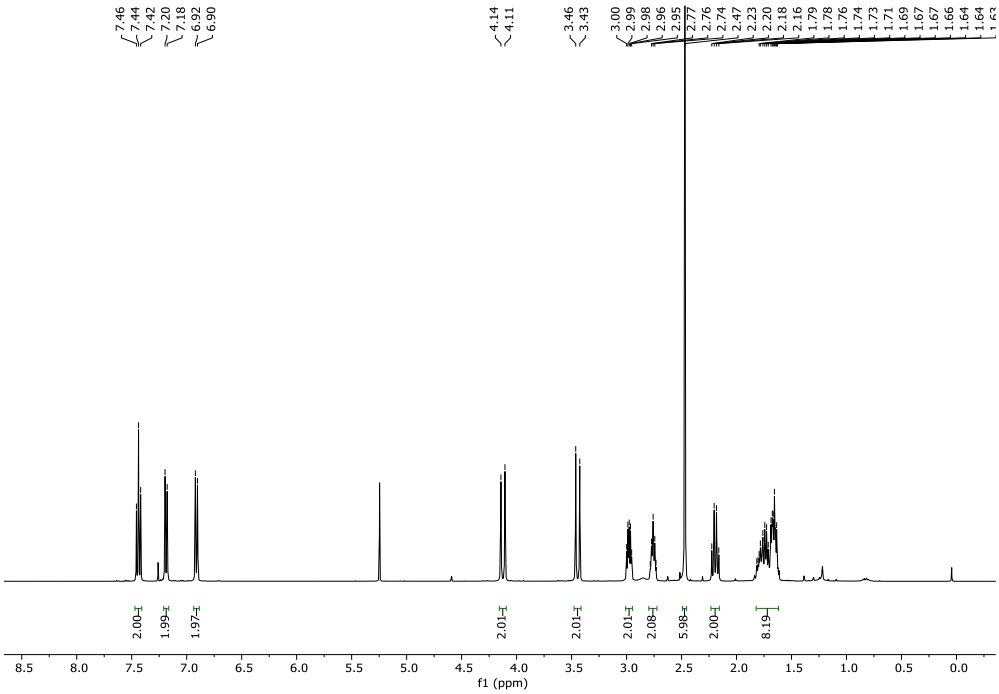

Figure 4. 15. ^{1}H-NMR ($CDCl_3$, 400 MHz, 300 K) spectrum of product **$^{o\text{-}Me}$PDP**.

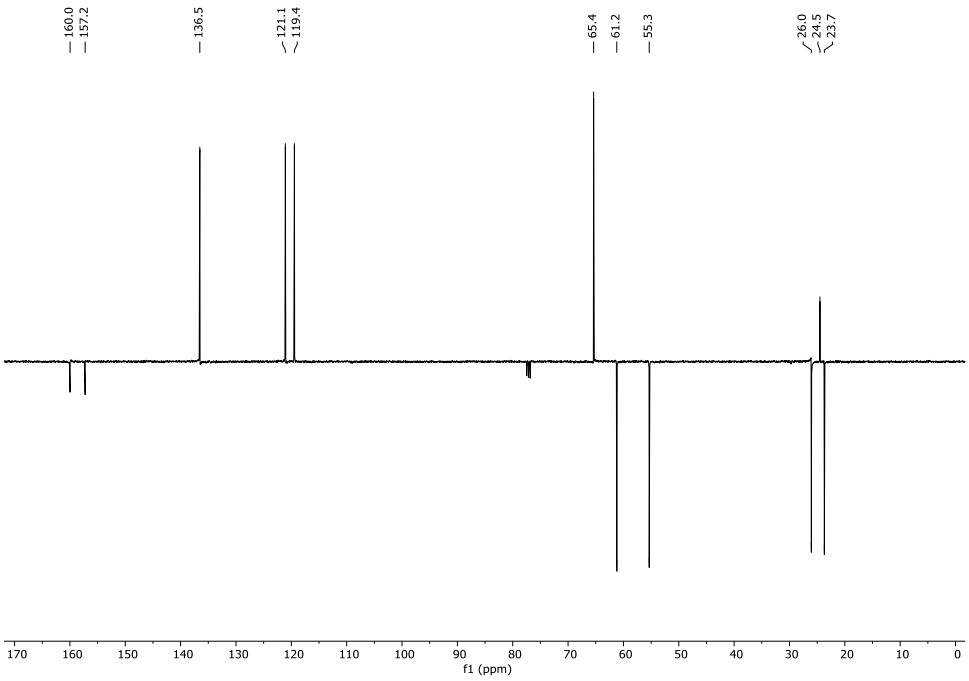

Figure 4. 16. ^{13}C[^{1}H]-DEPTQ-135-NMR spectrum ($CDCl_3$, 100.6 MHz, 300 K) of product **$^{o\text{-}Me}$PDP**.

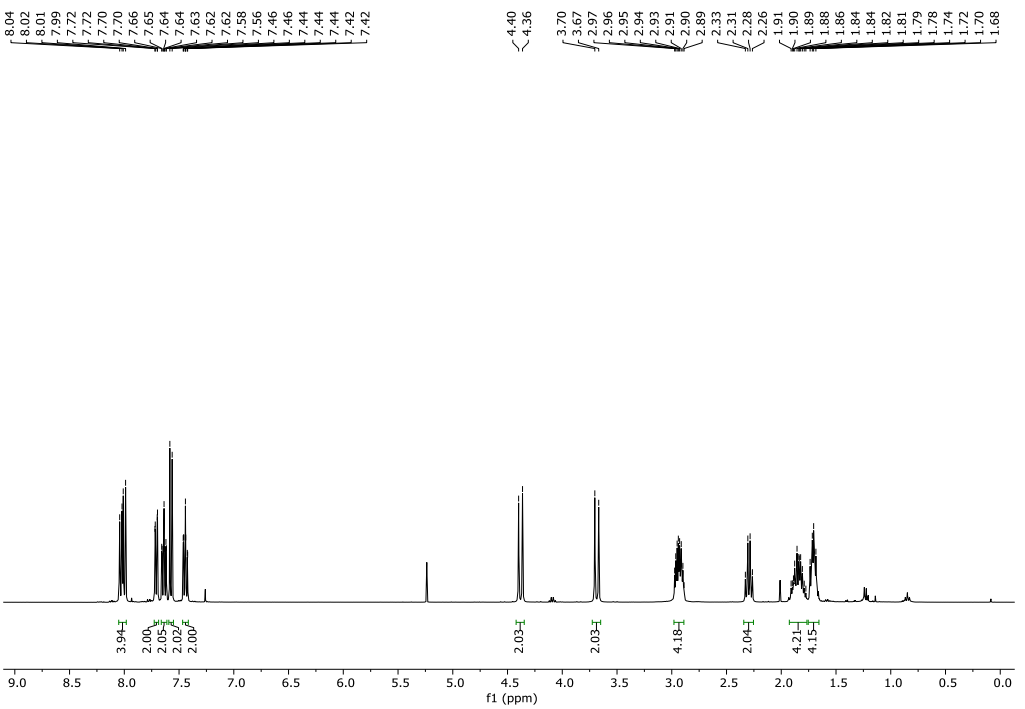

Figure 4. 17. ^{1}H-NMR ($CDCl_3$, 400 MHz, 300 K) spectrum of product **^{quin}PDP**.

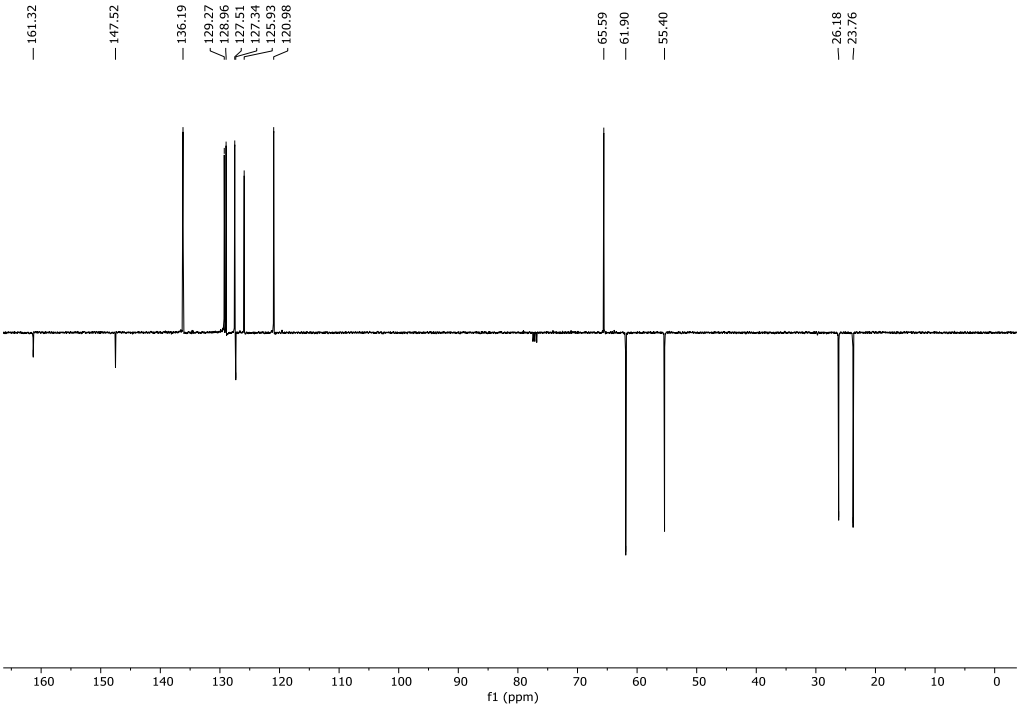

Figure 4. 18. ^{13}C[^{1}H]-DEPTQ-135-NMR spectrum ($CDCl_3$, 100.6 MHz, 300 K) of product **^{quin}PDP**.

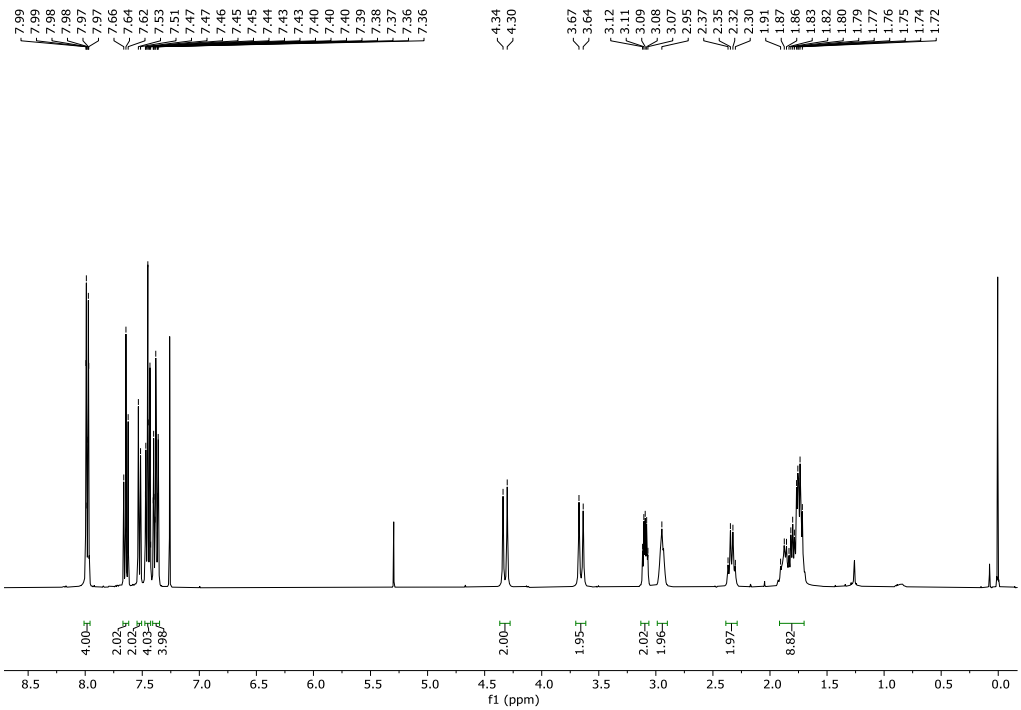

Figure 4. 19. ^{1}H-NMR ($CDCl_3$, 400 MHz, 300 K) spectrum of product **$^{o\text{-}Ph}$PDP**.

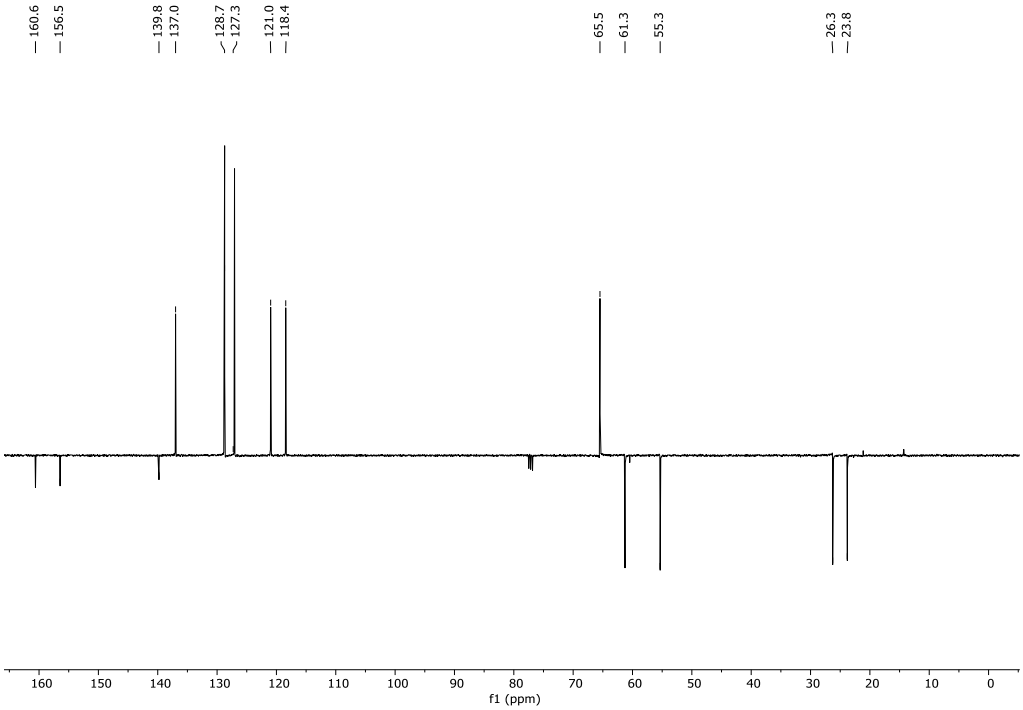

Figure 4. 20. ^{13}C[^{1}H]-DEPTQ-135-NMR spectrum ($CDCl_3$, 100.6 MHz, 300 K) of product **$^{o\text{-}Ph}$PDP**.

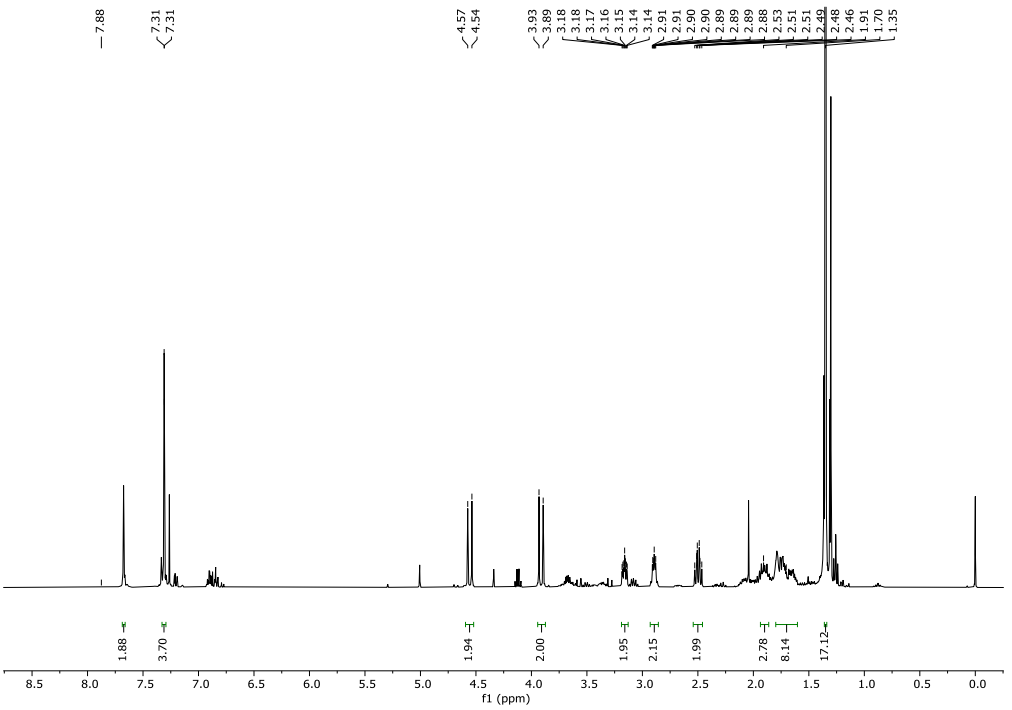

Figure 4. 21. ^{1}H-NMR ($CDCl_3$, 400 MHz, 300 K) spectrum of product **^{oxaz}PDP**.

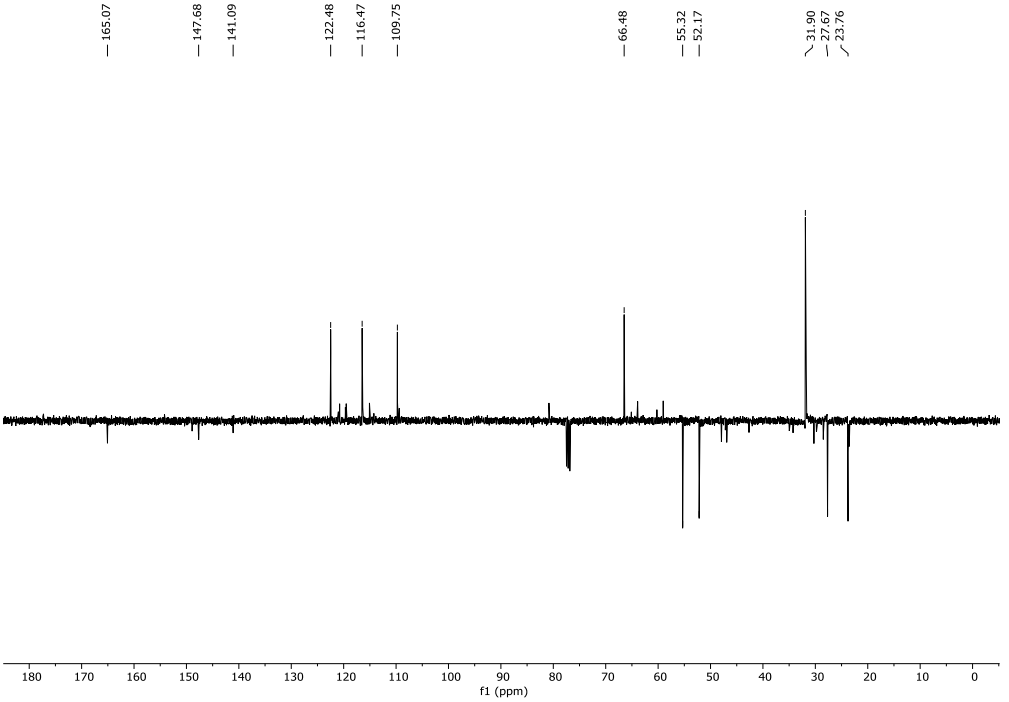

Figure 4. 22. ^{13}C[^{1}H]-DEPTQ-135-NMR spectrum ($CDCl_3$, 100.6 MHz, 300 K) of product **^{oxaz}BP**.

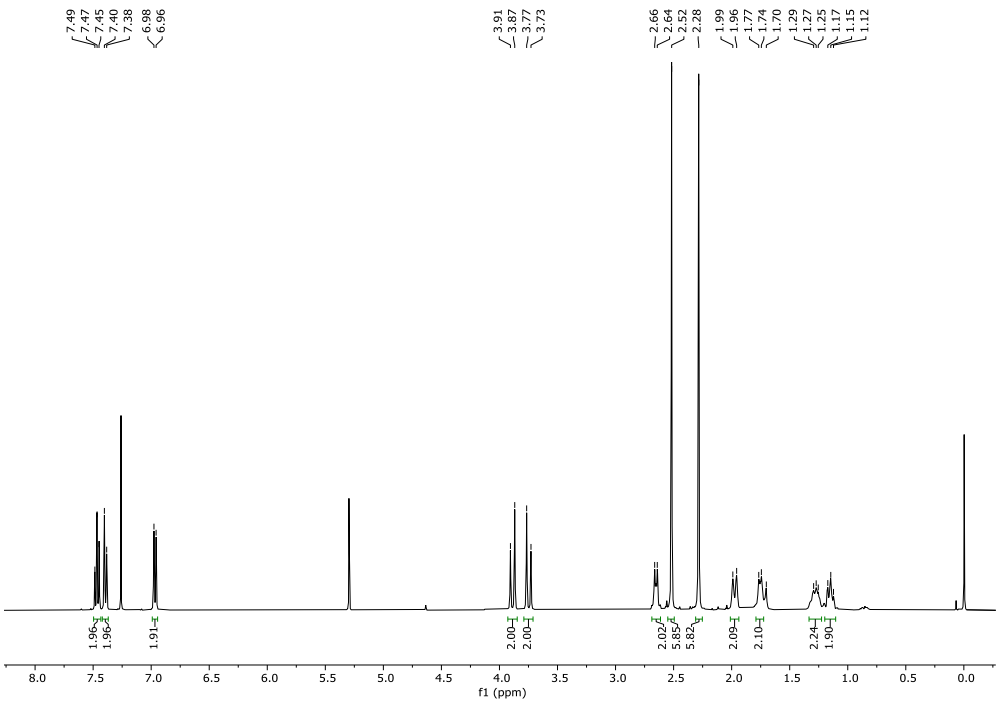

Figure 4. 23. ^{1}H-NMR ($CDCl_3$, 400 MHz, 300 K) spectrum of product **$^{o\text{-}Me}$MCP**.

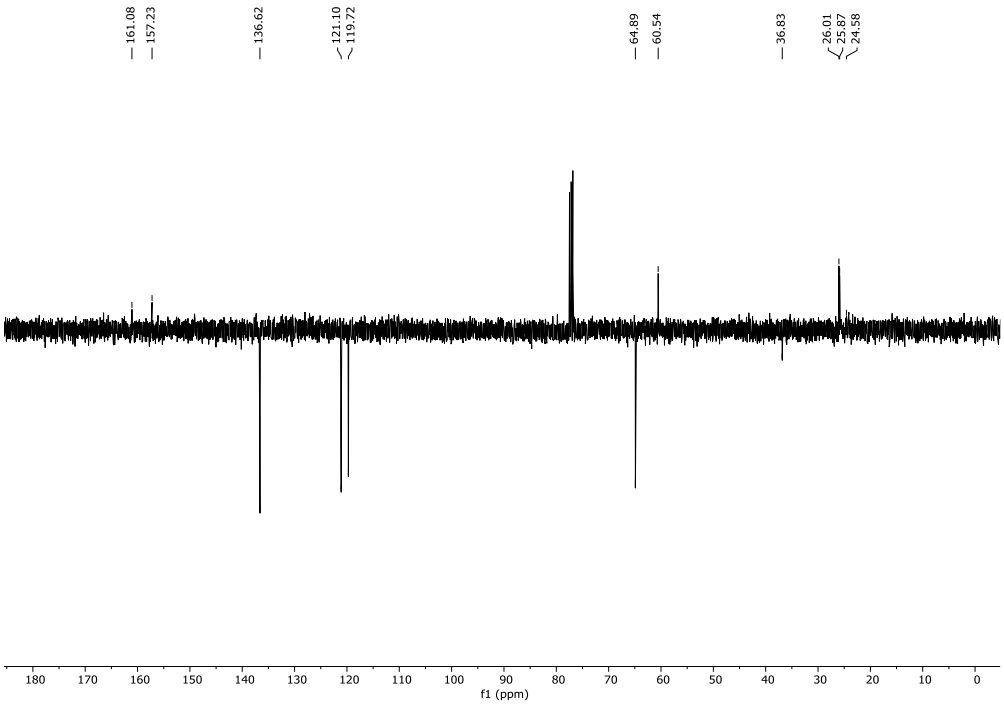

Figure 4. 24. ^{13}C[^{1}H]-DEPTQ-135-NMR spectrum ($CDCl_3$, 100.6 MHz, 300 K) of product **$^{o\text{-}Me}$MCP**.

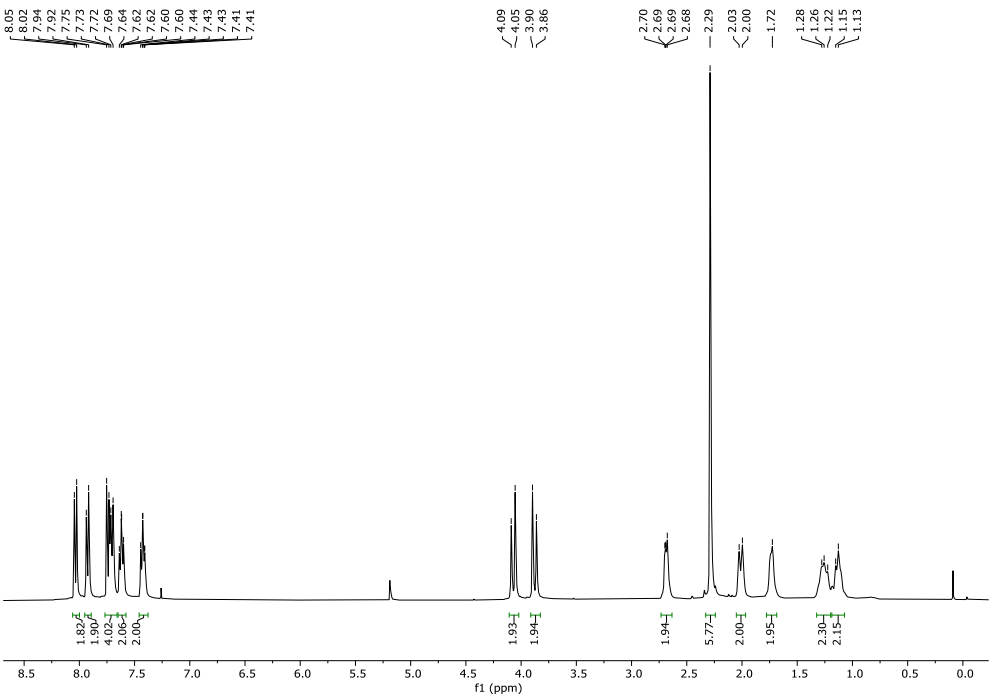

Figure 4. 25. ^{1}H-NMR ($CDCl_3$, 400 MHz, 300 K) spectrum of product **^{quin}MCP**.

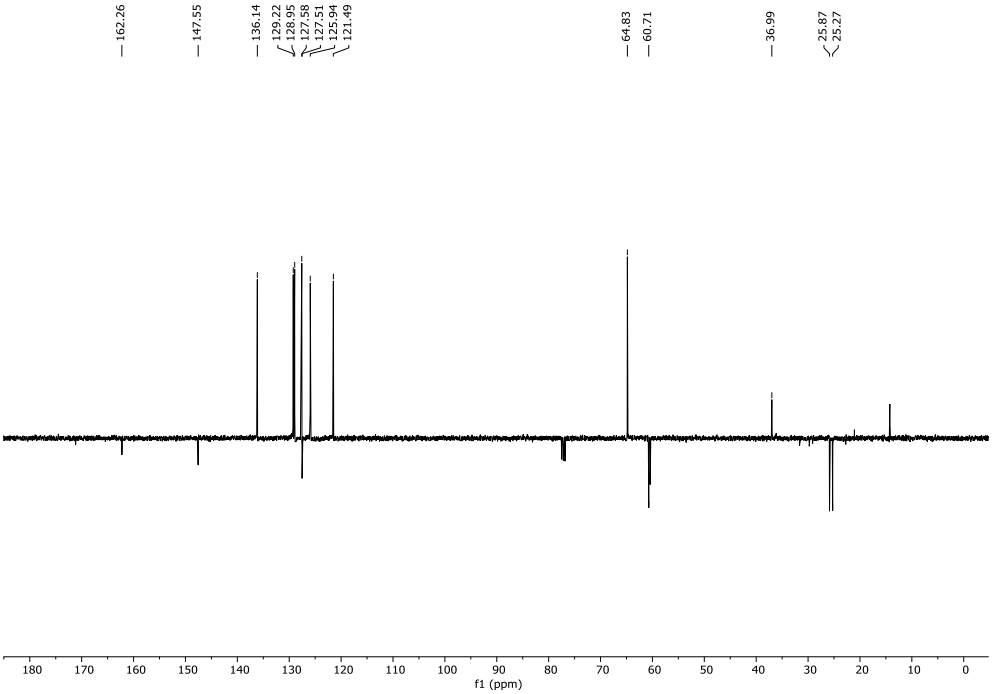

Figure 4. 26. ^{13}C[^{1}H]-DEPTQ-135-NMR spectrum ($CDCl_3$, 100.6 MHz, 300 K) of product **^{quin}MCP**.

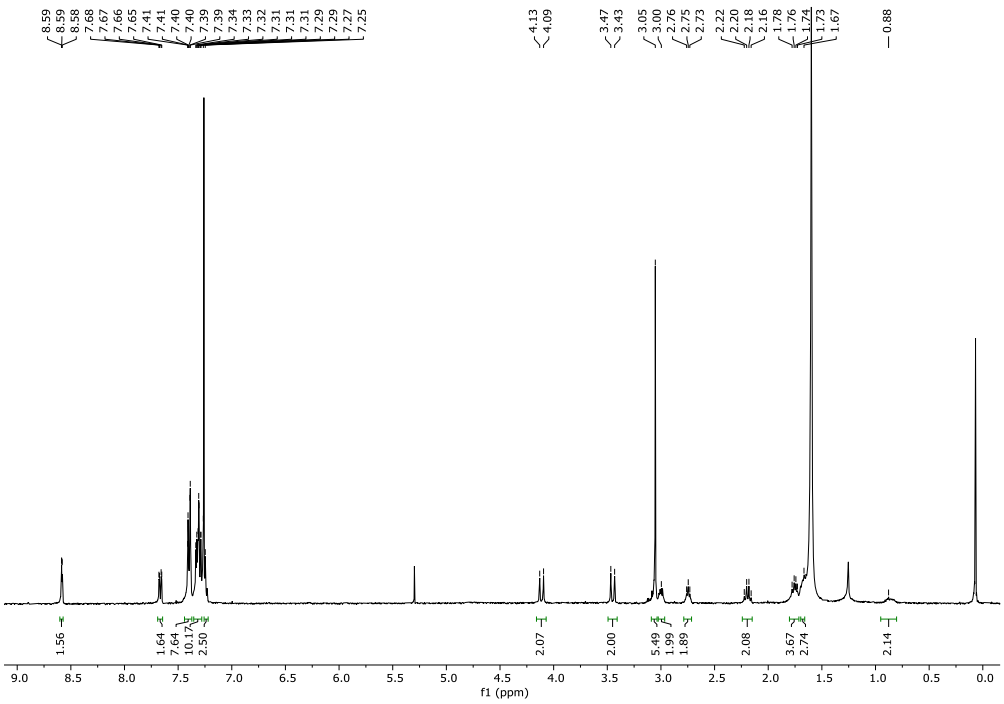

Figure 4. 27. ^{1}H-NMR ($CDCl_3$, 400 MHz, 300 K) spectrum of product **^{qOMe}PDP**.

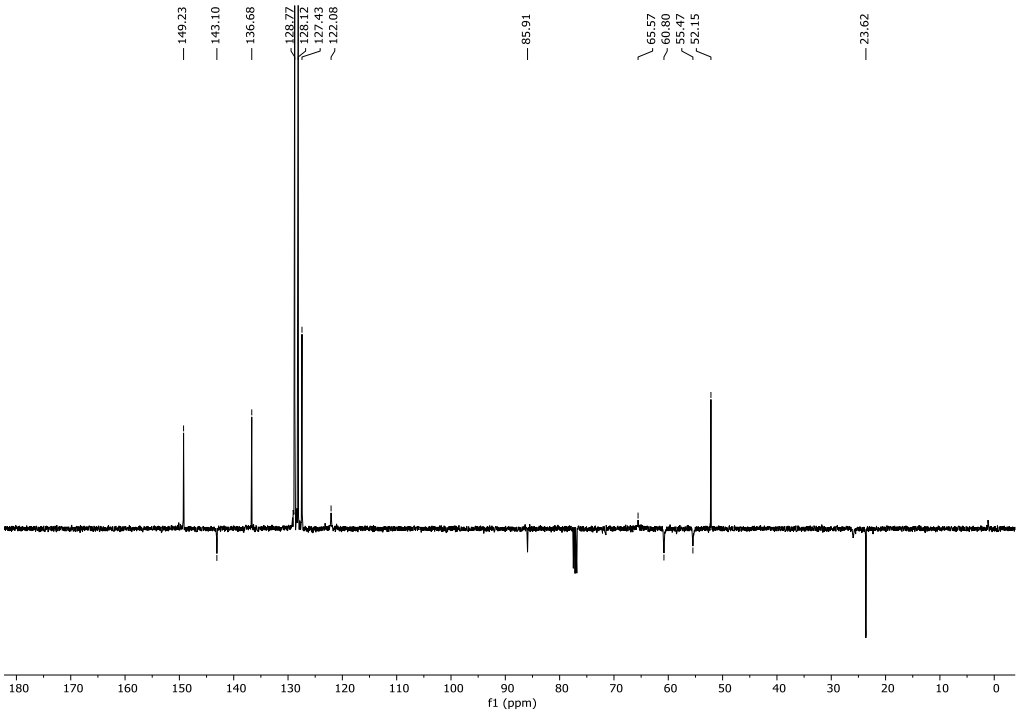

Figure 4. 28. ^{13}C[^{1}H]-DEPTQ-135-NMR spectrum ($CDCl_3$, 100.6 MHz, 300 K) of product **^{qOMe}PDP**.

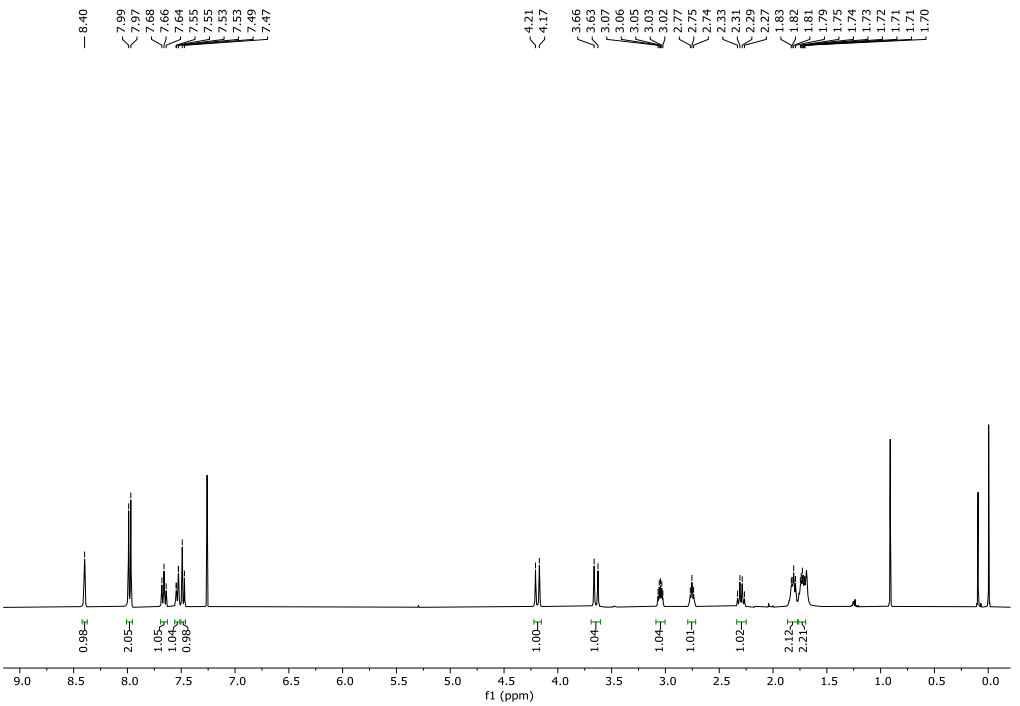

Figure 4. 29. ^{1}H-NMR ($CDCl_3$, 400 MHz, 300 K) spectrum of product **$^{Ar\text{-}CF3}$PDP**.

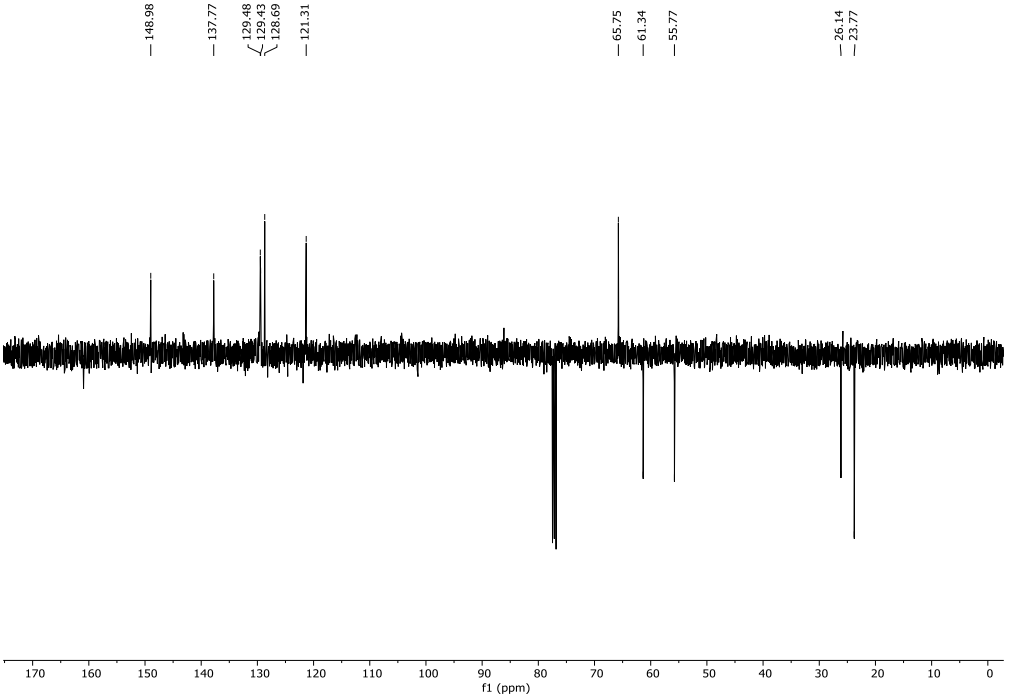

Figure 4. 30. ^{13}C[^{1}H]-DEPTQ-135-NMR spectrum ($CDCl_3$, 100.6 MHz, 300 K) of product **$^{Ar\text{-}CF3}$PDP**.

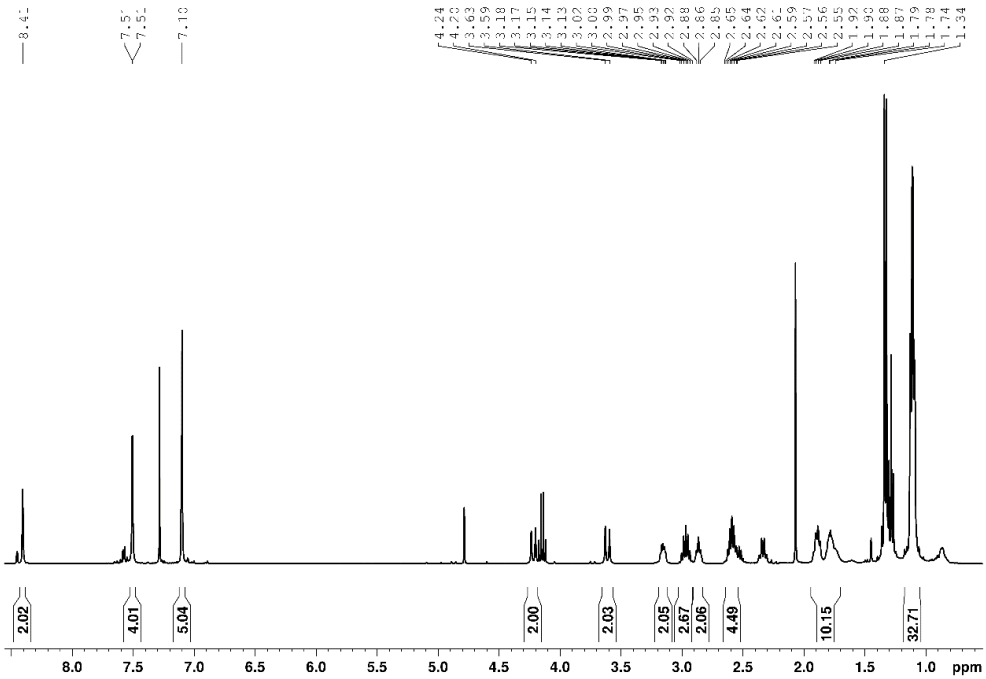

Figure 4. 31. ^{1}H-NMR ($CDCl_3$, 400 MHz, 300 K) spectrum of product **$^{Ar\text{-}iPr}$PDP**.

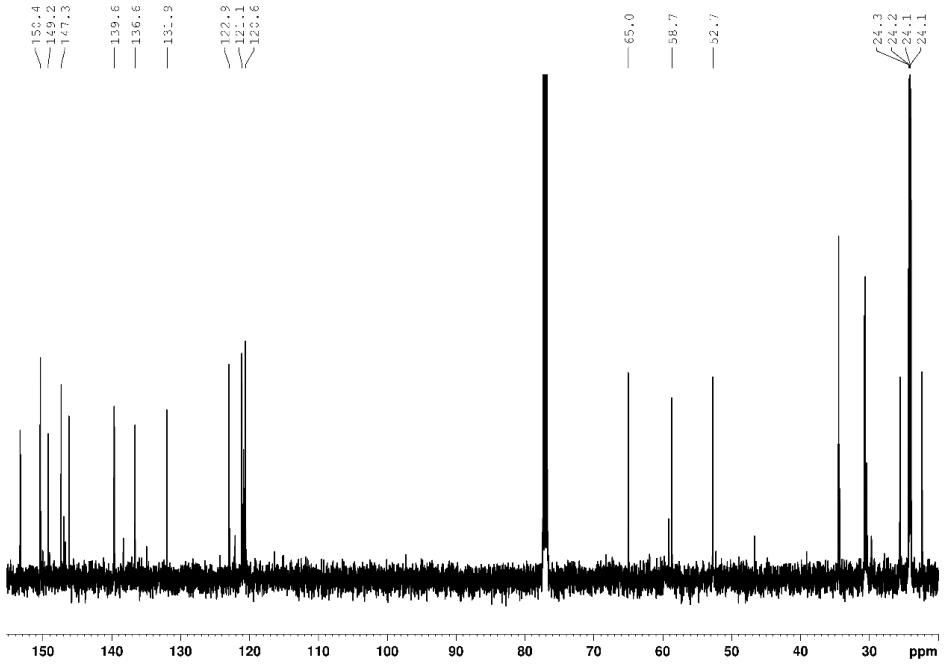

Figure 4. 32. ^{13}C NMR spectrum ($CDCl_3$, 100.6 MHz, 300 K) of product **$^{Ar\text{-}iPr}$PDP**.

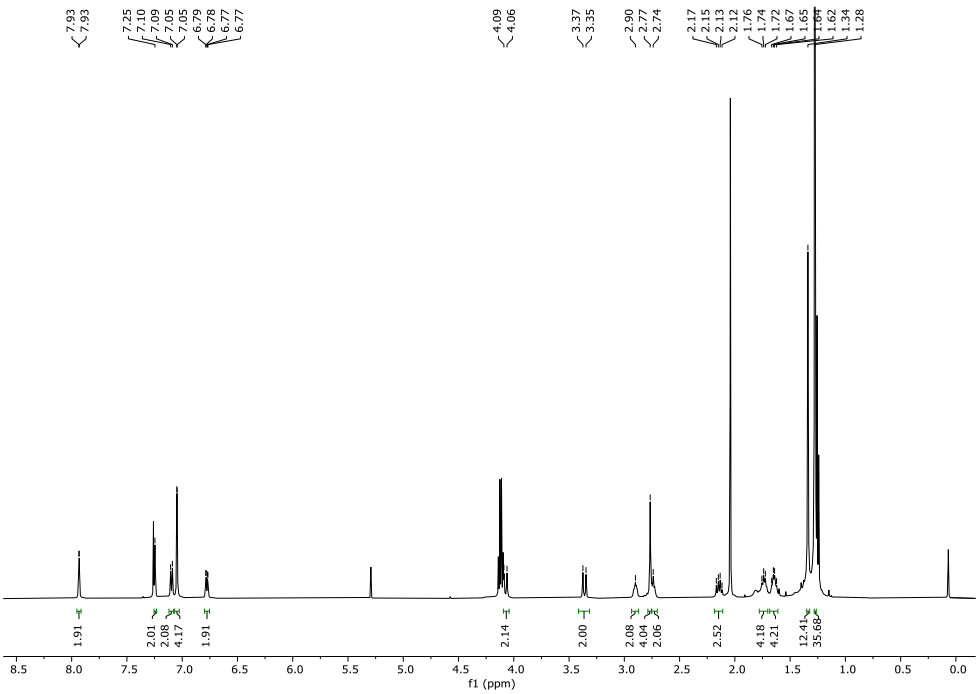

Figure 4. 33. ^{1}H-NMR ($CDCl_3$, 400 MHz, 300 K) spectrum of product **$^{Ar\text{-}tBu}$PDP**.

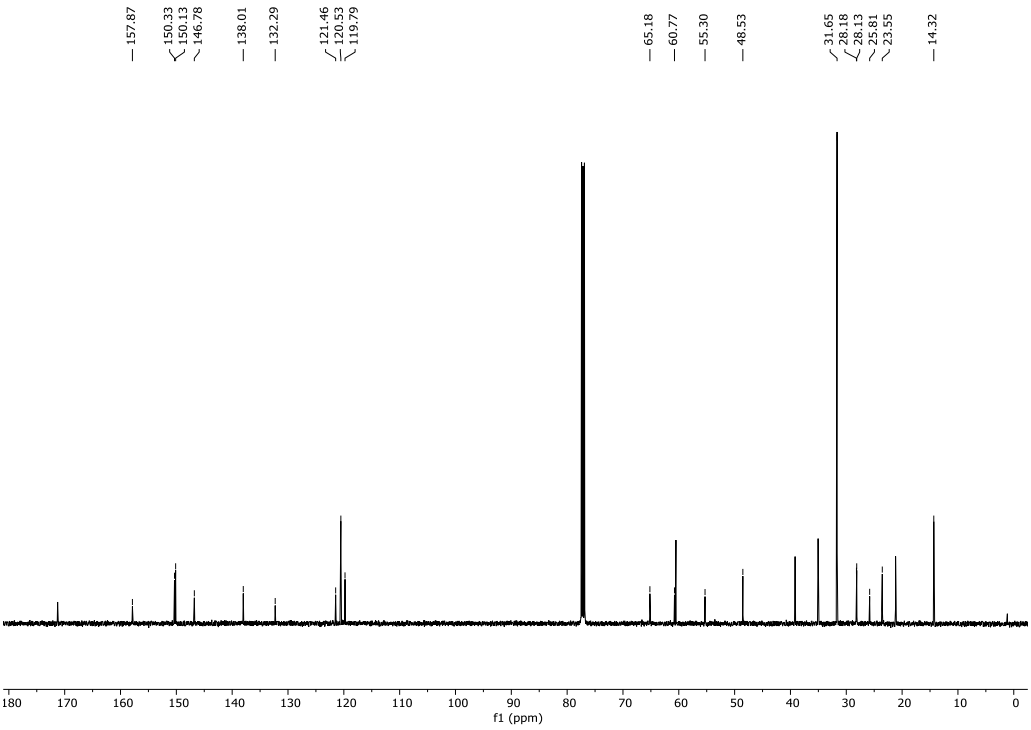

Figure 4. 34. ^{13}C NMR spectrum ($CDCl_3$, 100.6 MHz, 300 K) of product **$^{Ar\text{-}tBu}$PDP**.

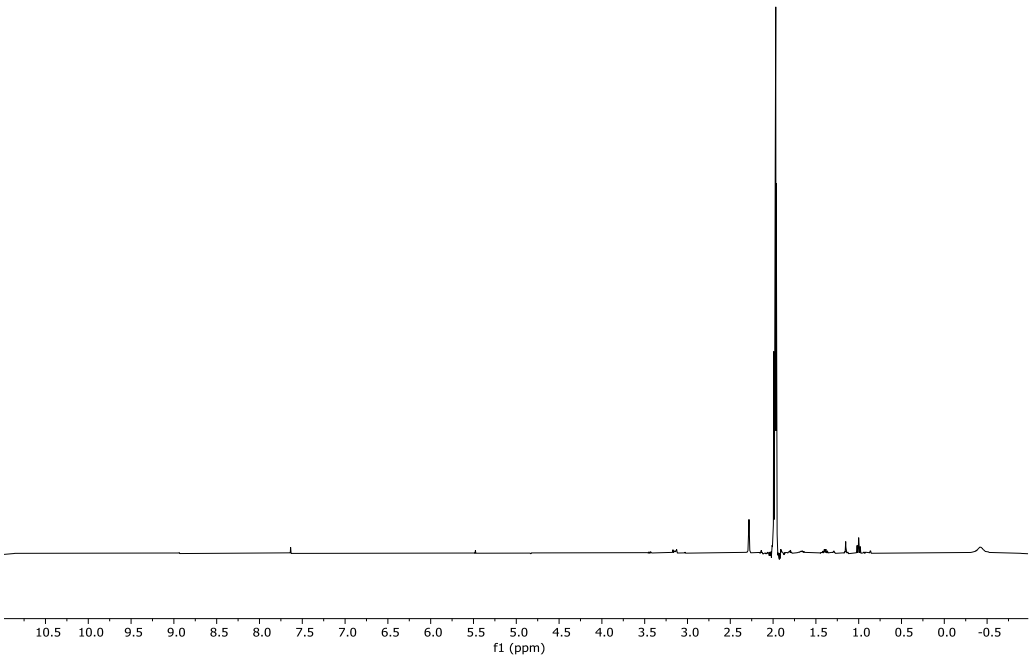

Figure 4. 35. ^{1}H-NMR (CD_3CN, 400 MHz, 300 K) spectrum of product **$^{o\text{-}Me}$PDPCo$_{Cl}$**.

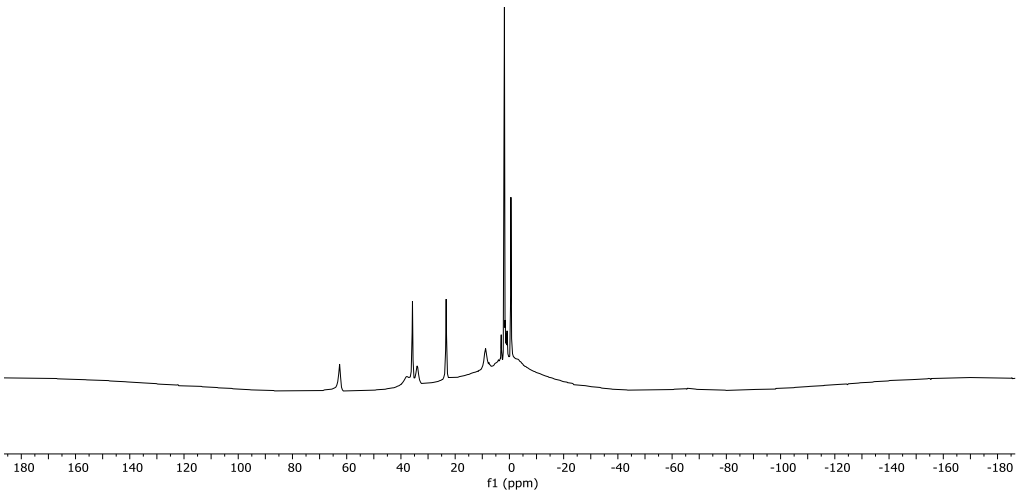

Figure 4. 36. Paramagnetic ^{1}H-NMR (CD_3CN, 400 MHz, 300 K) spectrum of product **$^{o\text{-}Me}$PDPCo$_{Cl}$**.

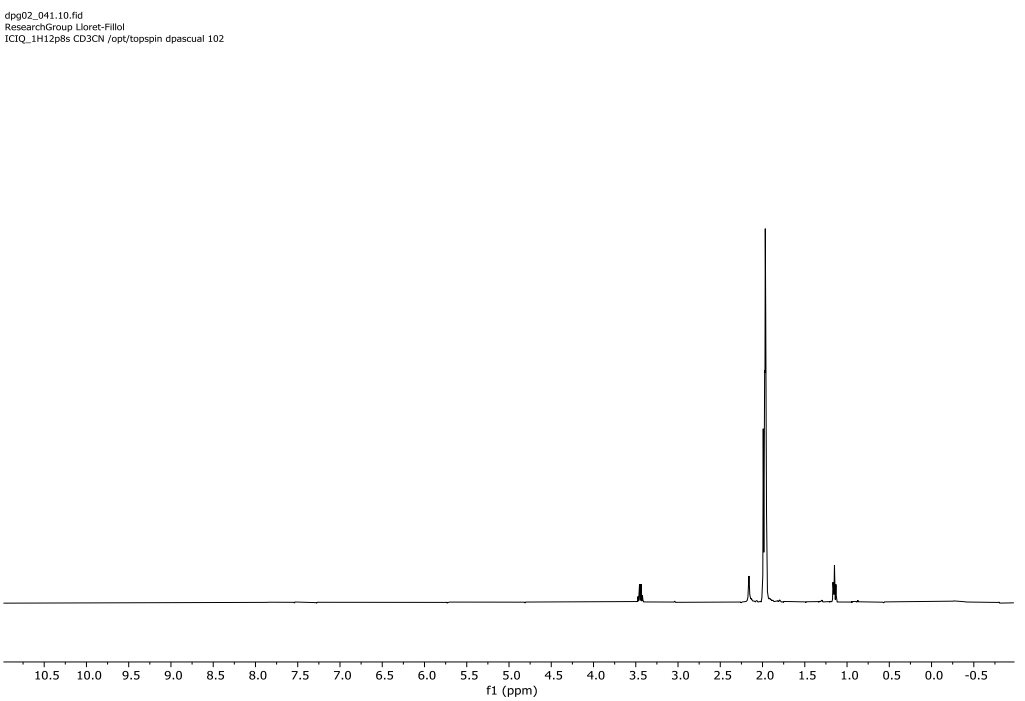

Figure 4. 37. ^{1}H-NMR (CD_3CN, 400 MHz, 300 K) spectrum of product **^{quin}PDPCo$_{Cl}$**.

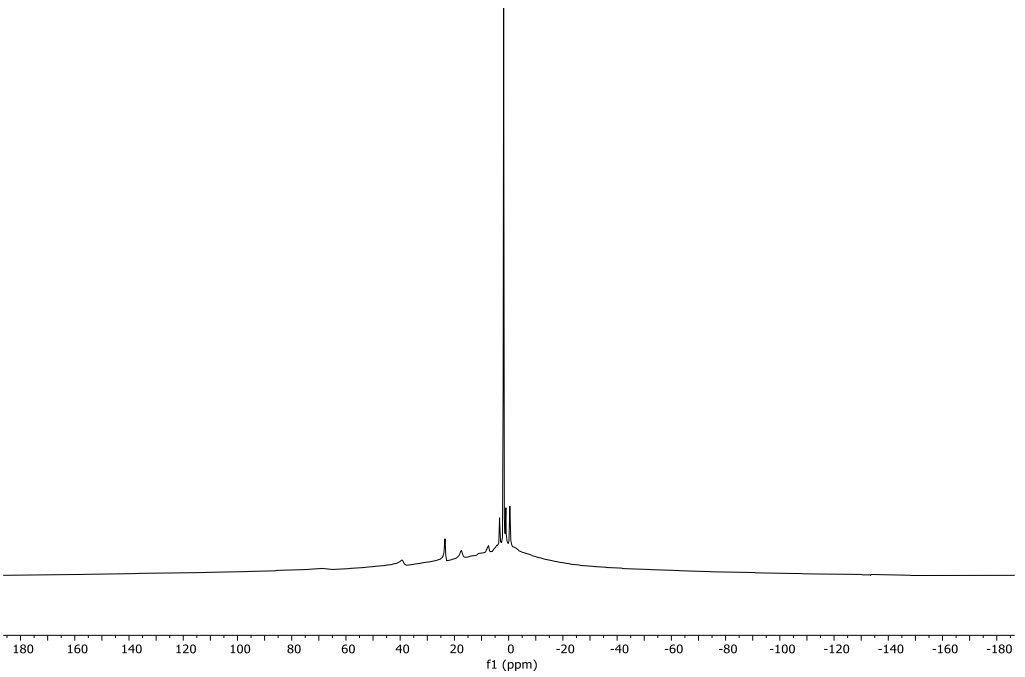

Figure 4. 38. Paramagnetic ^{1}H-NMR (CD_3CN, 400 MHz, 300 K) spectrum of product **^{quin}PDPCo$_{Cl}$**.

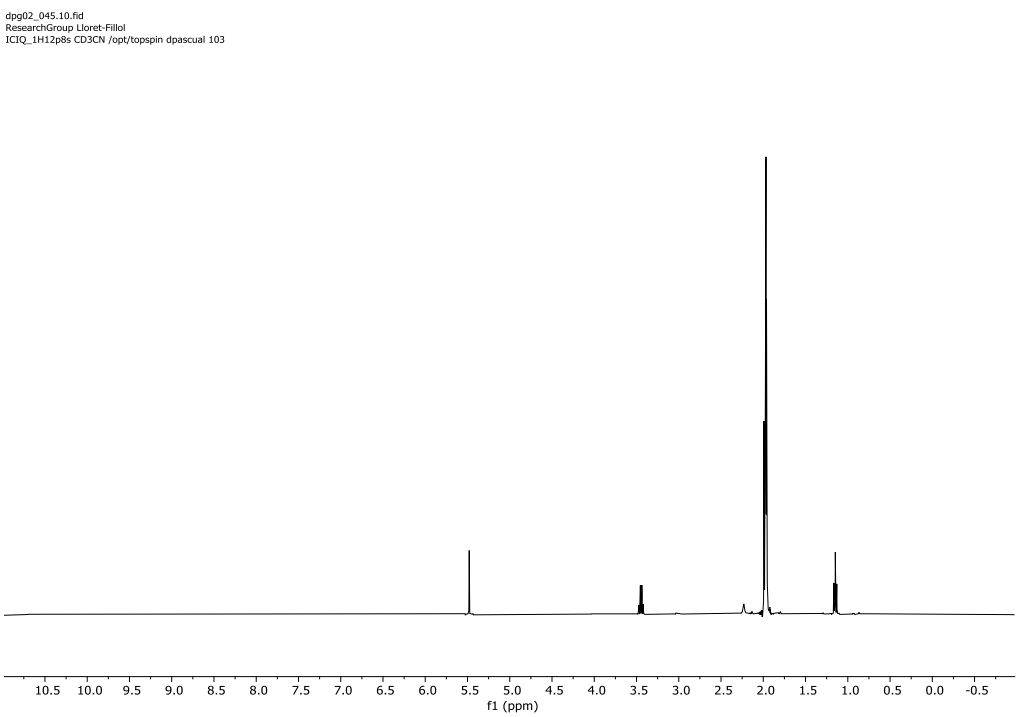

Figure 4. 39. Paramagnetic ^{1}H-NMR (CD_3CN, 400 MHz, 300 K) spectrum of product **$^{o\text{-}Ph}$PDPCo$_{Cl}$**.

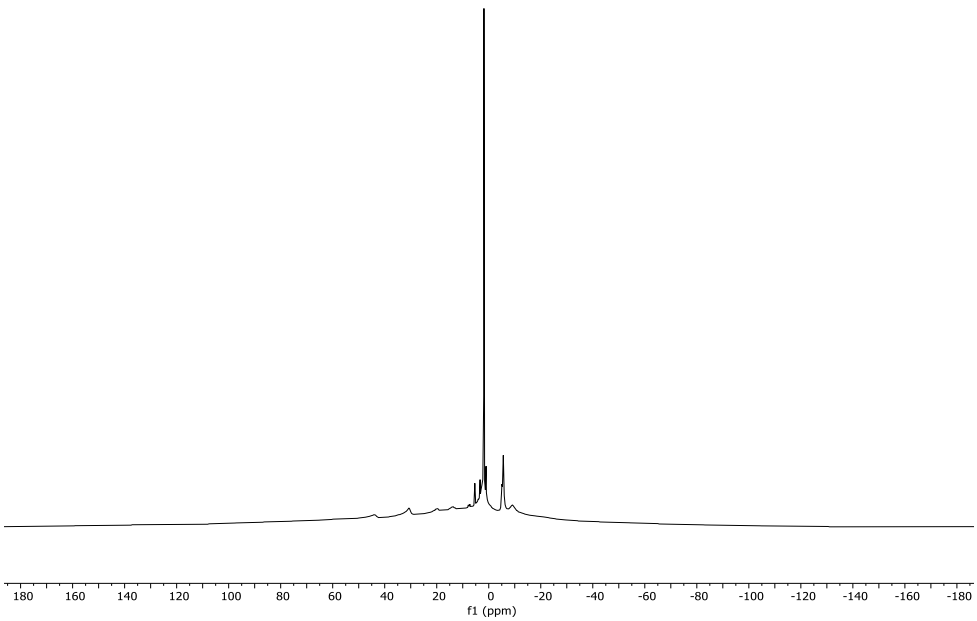

Figure 4. 40. Paramagnetic ^{1}H-NMR (CD_3CN, 400 MHz, 300 K) spectrum of product **$^{o\text{-}Ph}$PDPCo$_{Cl}$**.

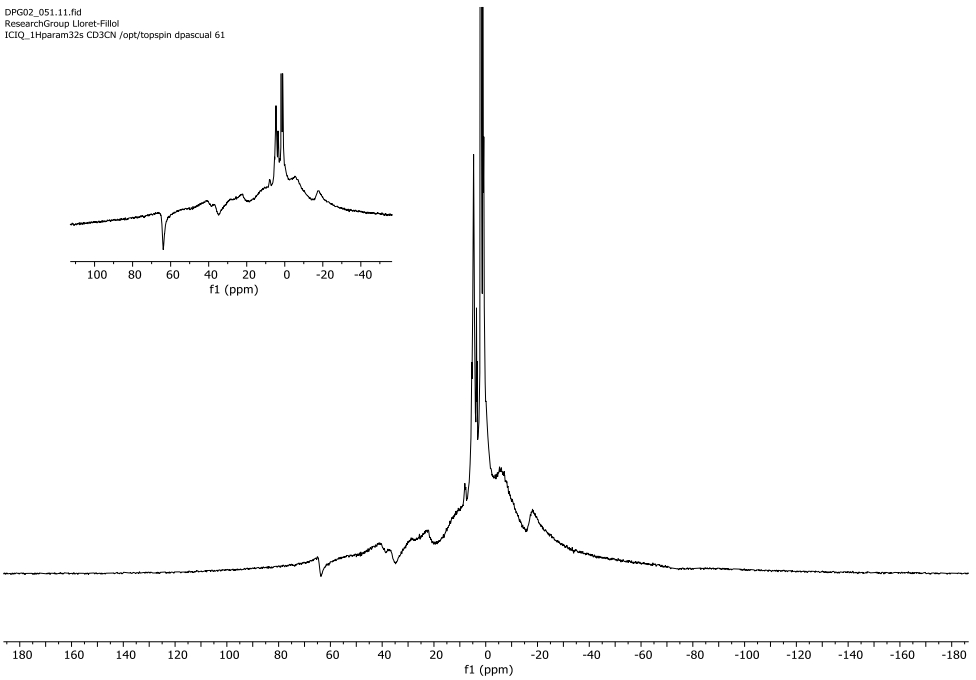

Figure 4. 41. Paramagnetic ^{1}H-NMR (CD_3CN, 400 MHz, 300 K) spectrum of product **^{quin}PDPCo$_{OTf}$**.

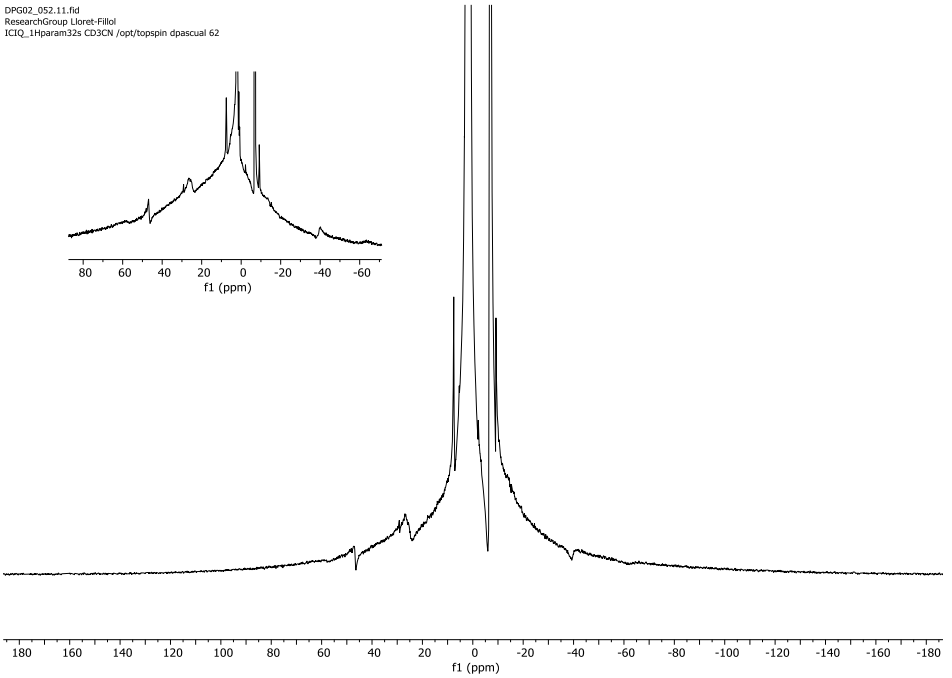

Figure 4. 42. Paramagnetic ^{1}H-NMR (CD_3CN, 400 MHz, 300 K) spectrum of product **^{quin}PDPCo$_{OTf}$**.

4.5 References

1. Nugent, W. A.; RajanBabu, T. V.; Burk, M. J., Beyond Nature's Chiral Pool: Enantioselective Catalysis in Industry. *Science* **1993,** *259* (5094), 479-483.
2. Mohr, J. T.; Krout, M. R.; Stoltz, B. M., Natural products as inspiration for the development of asymmetric catalysis. *Nature* **2008,** *455* (7211), 323-332.
3. Trost, B. M., Asymmetric catalysis: An enabling science. *Proceedings of the National Academy of Sciences* **2004,** *101* (15), 5348-5355.
4. Noyori, R., Asymmetric Catalysis: Science and Opportunities (Nobel Lecture). *Angewandte Chemie International Edition* **2002,** *41* (12), 2008-2022.
5. Tassinari, F.; Steidel, J.; Paltiel, S.; Fontanesi, C.; Lahav, M.; Paltiel, Y.; Naaman, R., Enantioseparation by crystallization using magnetic substrates. *Chemical Science* **2019,** *10* (20), 5246-5250.
6. Sevim, S.; Sorrenti, A.; Vale, J. P.; El-Hachemi, Z.; Pané, S.; Flouris, A. D.; Mayor, T. S.; Puigmartí-Luis, J., Chirality transfer from a 3D macro shape to the molecular level by controlling asymmetric secondary flows. *Nature Communications* **2022,** *13* (1), 1766.
7. Chen, X.; Gilissen, P. J.; Tinnemans, P.; Vanthuyne, N.; Rutjes, F. P. J. T.; Feringa, B. L.; Elemans, J. A. A. W.; Nolte, R. J. M., Enantiodivergent epoxidation of alkenes with a photoswitchable phosphate manganese-salen complex. *Nature Synthesis* **2022**.
8. van der Helm, M. P.; Klemm, B.; Eelkema, R., Organocatalysis in aqueous media. *Nature Reviews Chemistry* **2019,** *3* (8), 491-508.
9. Xiang, S.-H.; Tan, B., Advances in asymmetric organocatalysis over the last 10 years. *Nature Communications* **2020,** *11* (1), 3786.
10. Gaunt, M., Metals are not the only catalysts. *Nature* **2011,** *470* (7333), 183-185.
11. MacMillan, D. W. C., The advent and development of organocatalysis. *Nature* **2008,** *455* (7211), 304-308.
12. Zheng, G.-W.; Xu, J.-H., New opportunities for biocatalysis: driving the synthesis of chiral chemicals. *Current Opinion in Biotechnology* **2011,** *22* (6), 784-792.
13. Hönig, M.; Sondermann, P.; Turner, N. J.; Carreira, E. M., Enantioselective Chemo- and Biocatalysis: Partners in Retrosynthesis. *Angewandte Chemie International Edition* **2017,** *56* (31), 8942-8973.
14. Matsuda, T.; Yamanaka, R.; Nakamura, K., Recent progress in biocatalysis for asymmetric oxidation and reduction. *Tetrahedron: Asymmetry* **2009,** *20* (5), 513-557.
15. Gnas, Y.; Glorius, F., Chiral Auxiliaries - Principles and Recent Applications. *Synthesis* **2006,** *2006* (12), 1899-1930.
16. Diaz-Muñoz, G.; Miranda, I. L.; Sartori, S. K.; de Rezende, D. C.; Alves Nogueira Diaz, M., Use of chiral auxiliaries in the asymmetric synthesis of biologically active compounds: A review. *Chirality* **2019,** *31* (10), 776-812.
17. Bauer, E. B., Chiral-at-metal complexes and their catalytic applications in organic synthesis. *Chemical Society Reviews* **2012,** *41* (8), 3153-3167.
18. Zassinovich, G.; Mestroni, G.; Gladiali, S., Asymmetric hydrogen transfer reactions promoted by homogeneous transition metal catalysts. *Chemical Reviews* **1992,** *92* (5), 1051-1069.
19. Hashiguchi, S.; Fujii, A.; Takehara, J.; Ikariya, T.; Noyori, R., Asymmetric Transfer Hydrogenation of Aromatic Ketones Catalyzed by Chiral Ruthenium(II) Complexes. *Journal of the American Chemical Society* **1995,** *117* (28), 7562-7563.

20. Cramer, J.; Sager, C. P.; Ernst, B., Hydroxyl Groups in Synthetic and Natural-Product-Derived Therapeutics: A Perspective on a Common Functional Group. *Journal of Medicinal Chemistry* **2019,** *62* (20), 8915-8930.
21. Foubelo, F.; Nájera, C.; Yus, M., Catalytic asymmetric transfer hydrogenation of ketones: recent advances. *Tetrahedron: Asymmetry* **2015,** *26* (15), 769-790.
22. Xie, J.-H.; Zhou, Q.-L., Asymmetric (Transfer) Hydrogenation of Aryl and Heteroaryl Ketones. In *Asymmetric Hydrogenation and Transfer Hydrogenation*, 2021; pp 87-128.
23. Li, Y.-Y.; Yu, S.-L.; Shen, W.-Y.; Gao, J.-X., Iron-, Cobalt-, and Nickel-Catalyzed Asymmetric Transfer Hydrogenation and Asymmetric Hydrogenation of Ketones. *Accounts of Chemical Research* **2015,** *48* (9), 2587-2598.
24. Wen, J.; Wang, F.; Zhang, X., Asymmetric hydrogenation catalyzed by first-row transition metal complexes. *Chemical Society Reviews* **2021,** *50* (5), 3211-3237.
25. ter Halle, R.; Bréhéret, A.; Schulz, E.; Pinel, C.; Lemaire, M., Chiral nitrogen-metal complexes for the asymmetric reduction of ketones. *Tetrahedron: Asymmetry* **1997,** *8* (13), 2101-2108.
26. Ai, W.; Zhong, R.; Liu, X.; Liu, Q., Hydride Transfer Reactions Catalyzed by Cobalt Complexes. *Chemical Reviews* **2019,** *119* (4), 2876-2953.
27. Rhodes, C. J., Endangered elements, critical raw materials and conflict minerals. *Science Progress* **2019,** *102* (4), 304-350.
28. Gao, F.; Jin, R.; Zhang, D.; Liang, Q.; Ye, Q.; Liu, G., Flower-like mesoporous silica: a bifunctionalized catalyst for rhodium-catalyzed asymmetric transfer hydrogenation of aromatic ketones in aqueous medium. *Green Chemistry* **2013,** *15* (8), 2208-2214.
29. Echeverria, P.-G.; Férard, C.; Phansavath, P.; Ratovelomanana-Vidal, V., Synthesis, characterization and use of a new tethered Rh(III) complex in asymmetric transfer hydrogenation of ketones. *Catalysis Communications* **2015,** *62*, 95-99.
30. Lin, Z.; Li, J.; Huang, Q.; Huang, Q.; Wang, Q.; Tang, L.; Gong, D.; Yang, J.; Zhu, J.; Deng, J., Chiral Surfactant-Type Catalyst: Enantioselective Reduction of Long-Chain Aliphatic Ketoesters in Water. *The Journal of Organic Chemistry* **2015,** *80* (9), 4419-4429.
31. Farrell, K.; Müller-Bunz, H.; Albrecht, M., Synthesis, Isomerization, and Catalytic Transfer Hydrogenation Activity of Rhodium(III) Complexes Containing Both Chelating Dicarbenes and Diphosphine Ligands. *Organometallics* **2015,** *34* (24), 5723-5733.
32. Zhang, W.-J.; Ruan, S.-H.; Shen, W.-Y.; Wang, Z.; An, D.-L.; Li, Y.-Y.; Gao, J.-X., Highly enantioselective reduction of ketones in air catalyzed by Rh-based macrocycles. *Catalysis Communications* **2019,** *119*, 153-158.
33. Saidi, O.; Williams, J. M. J., Iridium-Catalyzed Hydrogen Transfer Reactions. In *Iridium Catalysis*, Andersson, P. G., Ed. Springer Berlin Heidelberg: Berlin, Heidelberg, 2011; pp 77-106.
34. Bartoszewicz, A.; Ahlsten, N.; Martín-Matute, B., Enantioselective Synthesis of Alcohols and Amines by Iridium-Catalyzed Hydrogenation, Transfer Hydrogenation, and Related Processes. *Chemistry – A European Journal* **2013,** *19* (23), 7274-7302.
35. Malacea, R.; Poli, R.; Manoury, E., Asymmetric hydrosilylation, transfer hydrogenation and hydrogenation of ketones catalyzed by iridium complexes. *Coordination Chemistry Reviews* **2010,** *254* (5), 729-752.
36. Waldron, R. W.; Weber, J. H., Asymmetric homogeneous hydrogenation catalyzed by a cobalt complex. High enantiomeric excess via statistically designed experiments and mechanistic studies. *Inorganic Chemistry* **1977,** *16* (5), 1220-1225.
37. Ohgo, Y.; Natori, Y.; Takeuchi, S.; Yoshimura, J., ASYMMETRIC HYDROGENATION CATALYZED BY BIS(DIMETHYLGLYOXIMATO)COBALT(II)-ACHIRAL BASE COMPLEX AND CHIRAL AMINOALCOHOL CONJUGATED

SYSTEMS. AN OXIDO-REDUCTASE MODEL WITH ENANTIOSELECTIVITY. *Chemistry Letters* **1974,** *3* (11), 1327-1330.
38. Ohgo, Y.; Natori, Y.; Takeuchi, S.; Yoshimura, J., ASYMMETRIC HYDROGENATION OF α-OXOCARBONYL COMPOUNDS CATALYZED BY BIS(DIMETHYLGLYOXIMATO)COBALT(II)-CHIRAL AMINE COMPLEX. *Chemistry Letters* **1974,** *3* (7), 709-712.
39. Zhang, D.; Zhu, E.-Z.; Lin, Z.-W.; Wei, Z.-B.; Li, Y.-Y.; Gao, J.-X., Enantioselective Hydrogenation of Ketones Catalyzed by Chiral Cobalt Complexes Containing PNNP Ligand. *Asian Journal of Organic Chemistry* **2016,** *5* (11), 1323-1326.
40. Wu, X.; Mo, J.; Li, X.; Hyder, Z.; Xiao, J., Green chemistry: C–C coupling and asymmetric reduction by innovative catalysis. *Progress in Natural Science* **2008,** *18* (6), 639-652.
41. Wang, B.; Zhou, H.; Lu, G.; Liu, Q.; Jiang, X., Bifunctional Oxo-Tethered Ruthenium Complex Catalyzed Asymmetric Transfer Hydrogenation of Aryl N-Heteroaryl Ketones. *Organic Letters* **2017,** *19* (8), 2094-2097.
42. Liu, Q.; Wang, C.; Zhou, H.; Wang, B.; Lv, J.; Cao, L.; Fu, Y., Iridium-Catalyzed Highly Enantioselective Transfer Hydrogenation of Aryl N-Heteroaryl Ketones with N-Oxide as a Removable ortho-Substituent. *Organic Letters* **2018,** *20* (4), 971-974.
43. Xing, Y.; Chen, J.-S.; Dong, Z.-R.; Li, Y.-Y.; Gao, J.-X., Highly efficient chiral PNNP ligand for asymmetric transfer hydrogenation of aromatic ketones in water. *Tetrahedron Letters* **2006,** *47* (26), 4501-4503.
44. Tian, C.; Gong, L.; Meggers, E., Chiral-at-metal iridium complex for efficient enantioselective transfer hydrogenation of ketones. *Chemical Communications* **2016,** *52* (22), 4207-4210.
45. Lu, J.; Dimroth, J.; Weck, M., Compartmentalization of Incompatible Catalytic Transformations for Tandem Catalysis. *Journal of the American Chemical Society* **2015,** *137* (40), 12984-12989.
46. Madern, N.; Talbi, B.; Salmain, M., Aqueous phase transfer hydrogenation of aryl ketones catalysed by achiral ruthenium(II) and rhodium(III) complexes and their papain conjugates. *Applied Organometallic Chemistry* **2013,** *27* (1), 6-12.
47. Wu, X.; Li, X.; Hems, W.; King, F.; Xiao, J., Accelerated asymmetric transfer hydrogenation of aromatic ketones in water. *Organic & Biomolecular Chemistry* **2004,** *2* (13), 1818-1821.
48. Prier, C. K.; Rankic, D. A.; MacMillan, D. W. C., Visible Light Photoredox Catalysis with Transition Metal Complexes: Applications in Organic Synthesis. *Chemical Reviews* **2013,** *113* (7), 5322-5363.
49. Hopkinson, M. N.; Sahoo, B.; Li, J.-L.; Glorius, F., Dual Catalysis Sees the Light: Combining Photoredox with Organo-, Acid, and Transition-Metal Catalysis. *Chemistry – A European Journal* **2014,** *20* (14), 3874-3886.
50. Marzo, L.; Pagire, S. K.; Reiser, O.; König, B., Visible-Light Photocatalysis: Does It Make a Difference in Organic Synthesis? *Angewandte Chemie International Edition* **2018,** *57* (32), 10034-10072.
51. Rono, L. J.; Yayla, H. G.; Wang, D. Y.; Armstrong, M. F.; Knowles, R. R., Enantioselective Photoredox Catalysis Enabled by Proton-Coupled Electron Transfer: Development of an Asymmetric Aza-Pinacol Cyclization. *Journal of the American Chemical Society* **2013,** *135* (47), 17735-17738.
52. Meggers, E., Asymmetric catalysis activated by visible light. *Chemical Communications* **2015,** *51* (16), 3290-3301.

53. Prentice, C.; Morrisson, J.; Smith, A. D.; Zysman-Colman, E., Recent developments in enantioselective photocatalysis. *Beilstein Journal of Organic Chemistry* **2020,** *16*, 2363-2441.
54. Genzink, M. J.; Kidd, J. B.; Swords, W. B.; Yoon, T. P., Chiral Photocatalyst Structures in Asymmetric Photochemical Synthesis. *Chemical Reviews* **2022,** *122* (2), 1654-1716.
55. Kohtani, S.; Kawashima, A.; Masuda, F.; Sumi, M.; Kitagawa, Y.; Yoshioka, E.; Hasegawa, Y.; Miyabe, H., Chiral α-hydroxy acid-coadsorbed TiO2 photocatalysts for asymmetric induction in hydrogenation of aromatic ketones. *Chemical Communications* **2018,** *54* (89), 12610-12613.
56. Lin, L.; Bai, X.; Ye, X.; Zhao, X.; Tan, C.-H.; Jiang, Z., Organocatalytic Enantioselective Protonation for Photoreduction of Activated Ketones and Ketimines Induced by Visible Light. *Angewandte Chemie International Edition* **2017,** *56* (44), 13842-13846.
57. Qiao, B.; Li, C.; Zhao, X.; Yin, Y.; Jiang, Z., Enantioselective reduction of azaarene-based ketones via visible light-driven photoredox asymmetric catalysis. *Chemical Communications* **2019,** *55* (52), 7534-7537.
58. Russo, C.; Brunelli, F.; Tron, G. C.; Giustiniano, M., Visible-Light Photoredox Catalysis in Water. *The Journal of Organic Chemistry* **2022**.
59. Sandoval, B. A.; Kurtoic, S. I.; Chung, M. M.; Biegasiewicz, K. F.; Hyster, T. K., Photoenzymatic Catalysis Enables Radical-Mediated Ketone Reduction in Ene-Reductases. *Angewandte Chemie International Edition* **2019,** *58* (26), 8714-8718.
60. Choudhury, S.; Baeg, J.-O.; Park, N.-J.; Yadav, R. K., A Photocatalyst/Enzyme Couple That Uses Solar Energy in the Asymmetric Reduction of Acetophenones. *Angewandte Chemie International Edition* **2012,** *51* (46), 11624-11628.
61. Choudhury, S.; Baeg, J.-O.; Park, N.-J.; Yadav, R. K., A solar light-driven, eco-friendly protocol for highly enantioselective synthesis of chiral alcohols via photocatalytic/biocatalytic cascades. *Green Chemistry* **2014,** *16* (9), 4389-4400.
62. Cao, G.-M.; Hu, X.-L.; Liao, L.-L.; Yan, S.-S.; Song, L.; Chruma, J. J.; Gong, L.; Yu, D.-G., Visible-light photoredox-catalyzed umpolung carboxylation of carbonyl compounds with CO2. *Nature Communications* **2021,** *12* (1), 3306.
63. Lee, K. N.; Ngai, M.-Y., Recent developments in transition-metal photoredox-catalysed reactions of carbonyl derivatives. *Chemical Communications* **2017,** *53* (98), 13093-13112.
64. Call, A.; Casadevall, C.; Acuña-Parés, F.; Casitas, A.; Lloret-Fillol, J., Dual cobalt–copper light-driven catalytic reduction of aldehydes and aromatic ketones in aqueous media. *Chemical Science* **2017,** *8* (7), 4739-4749.
65. Chen, M. S.; White, M. C., A Predictably Selective Aliphatic C–H Oxidation Reaction for Complex Molecule Synthesis. *Science* **2007,** *318* (5851), 783-787.
66. Proctor, R. S. J.; Colgan, A. C.; Phipps, R. J., Exploiting attractive non-covalent interactions for the enantioselective catalysis of reactions involving radical intermediates. *Nature Chemistry* **2020,** *12* (11), 990-1004.
67. Fanourakis, A.; Docherty, P. J.; Chuentragool, P.; Phipps, R. J., Recent Developments in Enantioselective Transition Metal Catalysis Featuring Attractive Noncovalent Interactions between Ligand and Substrate. *ACS Catalysis* **2020,** *10* (18), 10672-10714.
68. Meftah, Y.; Boumedjane, Y.; Fleurat-Lessard, P.; Delbecq, F.; Michel, C., Enantioselective reduction of prochiral ketones promoted by amino amide ruthenium complexes: A DFT study. *Journal of Organometallic Chemistry* **2021,** *939*, 121765.
69. Zhao, Y.; Zhang, L.; Pu, M.; Lei, M., A phosphine-free Mn(i)-NNS catalyst for asymmetric transfer hydrogenation of acetophenone: a theoretical prediction. *Dalton Transactions* **2021,** *50* (41), 14738-14744.

70. Wang, J.; Wu, K.; Qi, X., Theoretical study of the ligand effect on NHC–cobalt-catalyzed hydrogenation of ketones. *Catalysis Science & Technology* **2019,** *9* (19), 5315-5321.
71. Call, A.; Lloret-Fillol, J., Enhancement and control of the selectivity in light-driven ketone versus water reduction using aminopyridine cobalt complexes. *Chemical Communications* **2018,** *54* (69), 9643-9646.
72. Michaliszyn, K. D. Organic Transformations using Transition Metals and Photoredox Catalysts. Universidad Rovira i Virgili, 2022.
73. Fernández, S.; Cañellas, S.; Franco, F.; Luis, J. M.; Pericàs, M. À.; Lloret-Fillol, J., The Dual Effect of Coordinating −NH Groups and Light in the Electrochemical CO2 Reduction with Pyridylamino Co Complexes. *ChemElectroChem* **2021,** *8* (23), 4456-4465.
74. Artigas, J. A. Visible-light metallaphotoredox strategies for organic transformations through the cleavage of Csp3−Cl bonds. Universidad Rovira i Virgili, 2022.
75. Qiu, L.-Q.; Chen, K.-H.; Yang, Z.-W.; He, L.-N., A rhenium catalyst with bifunctional pyrene groups boosts natural light-driven CO2 reduction. *Green Chemistry* **2020,** *22* (24), 8614-8622.
76. Crivello, J. V.; Jiang, F., Development of Pyrene Photosensitizers for Cationic Photopolymerizations. *Chemistry of Materials* **2002,** *14* (11), 4858-4866.
77. Ohkubo, K.; Kohno, N.; Yamada, Y.; Fukuzumi, S., Metal-free hydrogen evolution with nanoparticles derived from pyrene via two-photon ionization induced by laser irradiation. *Chemical Communications* **2015,** *51* (57), 11515-11518.
78. Dumur, F., Recent advances on pyrene-based photoinitiators of polymerization. *European Polymer Journal* **2020,** *126*, 109564.
79. Glaser, F.; Kerzig, C.; Wenger, O. S., Sensitization-initiated electron transfer via upconversion: mechanism and photocatalytic applications. *Chemical Science* **2021,** *12* (29), 9922-9933.
80. Ghosh, I.; Shaikh, R. S.; König, B., Sensitization-Initiated Electron Transfer for Photoredox Catalysis. *Angewandte Chemie International Edition* **2017,** *56* (29), 8544-8549.
81. Marchini, M.; Bergamini, G.; Cozzi, P. G.; Ceroni, P.; Balzani, V., Photoredox Catalysis: The Need to Elucidate the Photochemical Mechanism. *Angewandte Chemie International Edition* **2017,** *56* (42), 12820-12821.
82. Coles, M. S.; Quach, G.; Beves, J. E.; Moore, E. G., A Photophysical Study of Sensitization-Initiated Electron Transfer: Insights into the Mechanism of Photoredox Activity. *Angewandte Chemie International Edition* **2020,** *59* (24), 9522-9526.
83. Brasholz, M., "Super-Reducing" Photocatalysis: Consecutive Energy and Electron Transfers with Polycyclic Aromatic Hydrocarbons. *Angewandte Chemie International Edition* **2017,** *56* (35), 10280-10281.
84. Constable, E. C.; Neuburger, M.; Rösel, P.; Schneider, G. E.; Zampese, J. A.; Housecroft, C. E.; Monti, F.; Armaroli, N.; Costa, R. D.; Ortí, E., Ligand-Based Charge-Transfer Luminescence in Ionic Cyclometalated Iridium(III) Complexes Bearing a Pyrene-Functionalized Bipyridine Ligand: A Joint Theoretical and Experimental Study. *Inorganic Chemistry* **2013,** *52* (2), 885-897.
85. Dinda, S.; Patra, S. C.; Ganguly, S., Rhodium(III) complex with pyrene-pyridyl-hydrazone: synthesis, structure, ligand redox, spectral characterization and DFT calculation. *Journal of Chemical Sciences* **2019,** *131* (3), 24.
86. Liu, P.; Sun, S.; Guo, X.; Yang, X.; Huang, J.; Wang, K.; Wang, Q.; Liu, J.; He, L., Competitive Host–Guest Interaction between β-Cyclodextrin Polymer and Pyrene-Labeled Probes for Fluorescence Analyses. *Analytical Chemistry* **2015,** *87* (5), 2665-2671.

87. Dai, N.; Qi, R.; Zhao, H.; Liu, L.; Lv, F.; Wang, S., Supramolecular Regulation of Catalytic Activity for an Amphiphilic Pyrene-Ruthenium Complex in Water. *Chemistry – A European Journal* **2021,** *27* (45), 11567-11573.
88. Dyck, A. S. M.; Kisiel, U.; Bohne, C., Dynamics for the Assembly of Pyrene−γ-Cyclodextrin Host−Guest Complexes. *The Journal of Physical Chemistry B* **2003,** *107* (42), 11652-11659.
89. Ballestin, P.; Ventura-Espinosa, D.; Martín, S.; Caballero, A.; Mata, J. A.; Pérez, P. J., Improving Catalyst Activity in Hydrocarbon Functionalization by Remote Pyrene–Graphene Stacking. *Chemistry – A European Journal* **2019,** *25* (40), 9534-9539.
90. Sabater, S.; Mata, J. A.; Peris, E., Catalyst Enhancement and Recyclability by Immobilization of Metal Complexes onto Graphene Surface by Noncovalent Interactions. *ACS Catalysis* **2014,** *4* (6), 2038-2047.
91. Modugno, G.; Syrgiannis, Z.; Bonasera, A.; Carraro, M.; Giancane, G.; Valli, L.; Bonchio, M.; Prato, M., The supramolecular design of low-dimensional carbon nano-hybrids encoding a polyoxometalate-bis-pyrene tweezer. *Chemical Communications* **2014,** *50* (38), 4881-4883.
92. Ehli, C.; Rahman, G. M. A.; Jux, N.; Balbinot, D.; Guldi, D. M.; Paolucci, F.; Marcaccio, M.; Paolucci, D.; Melle-Franco, M.; Zerbetto, F.; Campidelli, S.; Prato, M., Interactions in Single Wall Carbon Nanotubes/Pyrene/Porphyrin Nanohybrids. *Journal of the American Chemical Society* **2006,** *128* (34), 11222-11231.
93. Wang, J.; Chen, Z.; Chen, B., Adsorption of Polycyclic Aromatic Hydrocarbons by Graphene and Graphene Oxide Nanosheets. *Environmental Science & Technology* **2014,** *48* (9), 4817-4825.
94. Yoshii, T.; Umemoto, D.; Kuwahara, Y.; Mori, K.; Yamashita, H., Engineering of Surface Environment of Pd Nanoparticle Catalysts on Carbon Support with Pyrene–Thiol Ligands for Semihydrogenation of Alkynes. *ACS Applied Materials & Interfaces* **2019,** *11* (41), 37708-37719.
95. Wang, J.-W.; Gil-Sepulcre, M.; Huang, H.-H.; Solano, E.; Mu, Y.-F.; Llobet, A.; Ouyang, G., CH-π interaction boosts photocatalytic CO2 reduction activity of a molecular cobalt catalyst anchored on carbon nitride. *Cell Reports Physical Science* **2021,** *2* (12), 100681.
96. Suzuki, K.; Oldenburg, P. D.; Que Jr, L., Iron-Catalyzed Asymmetric Olefin cis-Dihydroxylation with 97 % Enantiomeric Excess. *Angewandte Chemie International Edition* **2008,** *47* (10), 1887-1889.
97. Company, A.; Güell, M.; Popa, D.; Benet-Buchholz, J.; Parella, T.; Fontrodona, X.; Llobet, A.; Solà, M.; Ribas, X.; Luis, J. M.; Costas, M., Redox-Controlled Molecular Flipper Based on a Chiral Cu Complex. *Inorganic Chemistry* **2006,** *45* (24), 9643-9645.
98. Mikata, Y.; Kuroda, Y.; Naito, K.; Murakami, K.; Yamamoto, C.; Yabe, S.; Yonemura, S.; Matsumoto, A.; Katano, H., Structure and electrochemical properties of (μ-O)2Mn2(iii,iii) and (μ-O)2Mn2(iii,iv) complexes supported by pyridine-, quinoline-, isoquinoline- and quinoxaline-based tetranitrogen ligands. *Dalton Transactions* **2021,** *50* (12), 4133-4144.
99. Vermaak, V.; Young, D. A.; Swarts, A. J., Catalytic oxidation of alcohols with novel non-heme N4-tetradentate manganese(ii) complexes. *Dalton Transactions* **2018,** *47* (46), 16534-16542.
100. Ottenbacher, R. V.; Bryliakov, K. P.; Talsi, E. P., Nonheme Manganese-Catalyzed Asymmetric Oxidation. A Lewis Acid Activation versus Oxygen Rebound Mechanism: Evidence for the "Third Oxidant". *Inorganic Chemistry* **2010,** *49* (18), 8620-8628.

101. Shan, X.; Rohde, J.-U.; Koehntop, K. D.; Zhou, Y.; Bukowski, M. R.; Costas, M.; Fujisawa, K.; Que, L., X-ray Absorption Spectroscopic Studies of High-Spin Nonheme (Alkylperoxo)iron(III) Intermediates. *Inorganic Chemistry* **2007,** *46* (20), 8410-8417.
102. Adams, R.; Hine, J.; Campbell, J., Triarylpyridylmethanes. *Journal of the American Chemical Society* **1949,** *71* (2), 387-390.
103. Gormisky, P. E.; White, M. C., Catalyst-Controlled Aliphatic C–H Oxidations with a Predictive Model for Site-Selectivity. *Journal of the American Chemical Society* **2013,** *135* (38), 14052-14055.
104. Roth, H. G.; Romero, N. A.; Nicewicz, D. A., Experimental and Calculated Electrochemical Potentials of Common Organic Molecules for Applications to Single-Electron Redox Chemistry. *Synlett* **2016,** *27* (05), 714-723.
105. Luo, S.-P.; Mejía, E.; Friedrich, A.; Pazidis, A.; Junge, H.; Surkus, A.-E.; Jackstell, R.; Denurra, S.; Gladiali, S.; Lochbrunner, S.; Beller, M., Photocatalytic Water Reduction with Copper-Based Photosensitizers: A Noble-Metal-Free System. *Angewandte Chemie International Edition* **2013,** *52* (1), 419-423.
106. Call, A.; Codolà, Z.; Acuña-Parés, F.; Lloret-Fillol, J., Photo- and Electrocatalytic H2 Production by New First-Row Transition-Metal Complexes Based on an Aminopyridine Pentadentate Ligand. *Chemistry – A European Journal* **2014,** *20* (20), 6171-6183.
107. Monos, T. M.; Sun, A. C.; McAtee, R. C.; Devery, J. J.; Stephenson, C. R. J., Microwave-Assisted Synthesis of Heteroleptic Ir(III)+ Polypyridyl Complexes. *The Journal of Organic Chemistry* **2016,** *81* (16), 6988-6994.
108. Nazeeruddin, M. K.; Wegh, R. T.; Zhou, Z.; Klein, C.; Wang, Q.; De Angelis, F.; Fantacci, S.; Grätzel, M., Efficient Green-Blue-Light-Emitting Cationic Iridium Complex for Light-Emitting Electrochemical Cells. *Inorganic Chemistry* **2006,** *45* (23), 9245-9250.
109. Fillol, J. L.; Codolà, Z.; Garcia-Bosch, I.; Gómez, L.; Pla, J. J.; Costas, M., Efficient water oxidation catalysts based on readily available iron coordination complexes. *Nature Chemistry* **2011,** *3* (10), 807-813.
110. Ohui, K.; Afanasenko, E.; Bacher, F.; Ting, R. L. X.; Zafar, A.; Blanco-Cabra, N.; Torrents, E.; Dömötör, O.; May, N. V.; Darvasiova, D.; Enyedy, É. A.; Popović-Bijelić, A.; Reynisson, J.; Rapta, P.; Babak, M. V.; Pastorin, G.; Arion, V. B., New Water-Soluble Copper(II) Complexes with Morpholine–Thiosemicarbazone Hybrids: Insights into the Anticancer and Antibacterial Mode of Action. *Journal of Medicinal Chemistry* **2019,** *62* (2), 512-530.
111. Jabre, N. D.; Respondek, T.; Ulku, S. A.; Korostelova, N.; Kodanko, J. J., A Divergent Strategy for Attaching Polypyridyl Ligands to Peptides. *The Journal of Organic Chemistry* **2010,** *75* (3), 650-659.
112. Soler, M.; Figueras, E.; Serrano-Plana, J.; González-Bártulos, M.; Massaguer, A.; Company, A.; Martínez, M. Á.; Malina, J.; Brabec, V.; Feliu, L.; Planas, M.; Ribas, X.; Costas, M., Design, Preparation, and Characterization of Zn and Cu Metallopeptides Based On Tetradentate Aminopyridine Ligands Showing Enhanced DNA Cleavage Activity. *Inorganic Chemistry* **2015,** *54* (22), 10542-10558.

'A hard fall should mean a high bounce if one is made of the right material'

- Unknown

Chapter 5
Metal to Ligand Concern Transfer: $[Ir(bpy)(ppy)_2]^+$

UNIVERSITAT ROVIRA I VIRGILI
PHOTOREDOX CATALYSIS MEDIATED BY TRANSITION METAL COMPLEXES.
TOWARDS CHALLENGING ORGANIC REDUCTIONS
David Pascual Gascón

5.1. State of the art

Cyclometalated iridium(III) polypyridine complexes are well-established photosensitizers that have been extensively used for both energy transfer (EnT, see Chapter 1) and electron transfer (ET) reactions.[1-3]. Still, recent reports in which iridium photoredox catalysts (PC) exhibited a strong reductive power are challenging to explain by classic mechanisms (see Chapter 1 and Scheme 5.1). [4-8]

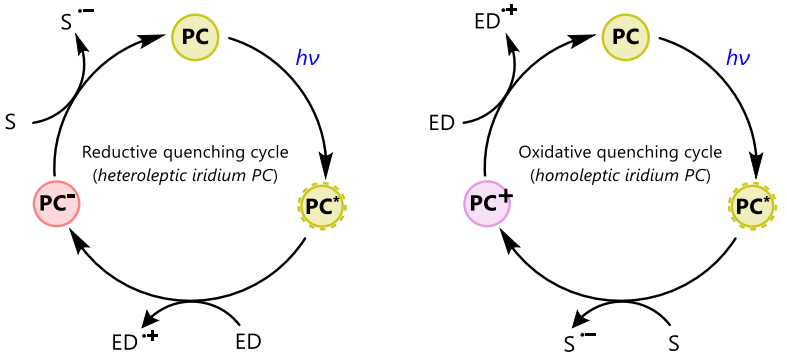

Scheme 5.1. Classic photoredox cycles. PC = Photoredox Catalyst; ED = Electron Donor; S = Substrate.

An example of hypothesizing potential new mechanisms is found in the recent publication by Theunissen and co-workers.[4] In this case, the use of [Ir(ppy)$_2$(^{tBu}bpy)]PF$_6$ (**^{tBu}PC$_{Ir}$**) or *fac*-Ir(ppy)$_3$, in combination with sacrificial electron donors (ED) under light irradiation, affords carbon-centred radicals from challenging to reduce ammonium salts (E_{red} from -1.7 V to -2.5 V *vs* SCE, Scheme 5.2). Nonetheless, the authors recognize that the expected mechanisms of reductive and oxidative quenching for **^{tBu}PC$_{Ir}$$^+$** and *fac*-Ir(ppy)$_3$, respectively, are restricted by their redox potentials and cannot directly explain the observed reactivity.

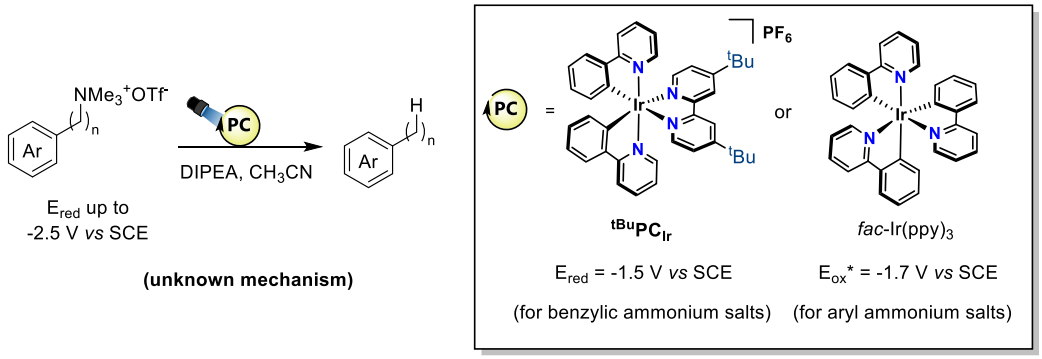

Scheme 5.2. Hydrodeamination of ammonium salts by Theunissen and co-workers.

A leading alternative mechanistic proposal corresponds to Connell and co-workers' work, who introduced in 2019 that ^{tBu}**PC$_{Ir}$** can be partially hydrogenated by the *in situ* generated radical species derived from amine oxidation. Then, the partial hydrogenation of ^{tBu}**PC$_{Ir}$** produces a more reductive PC, which operates in a tandem fashion (Scheme 5.3) to reduce aryl halides with a redox potential up to -2.7 V.[5] However, the calculated redox potential for the tandem PC system (**$^{H\text{-}tBu}$PC$_{Ir}$**, E_{ox}* = -1.7 V) does not match for the proposed electron transfer, and the authors recognize that alternative multiphoton mechanisms are likely involved.[6]

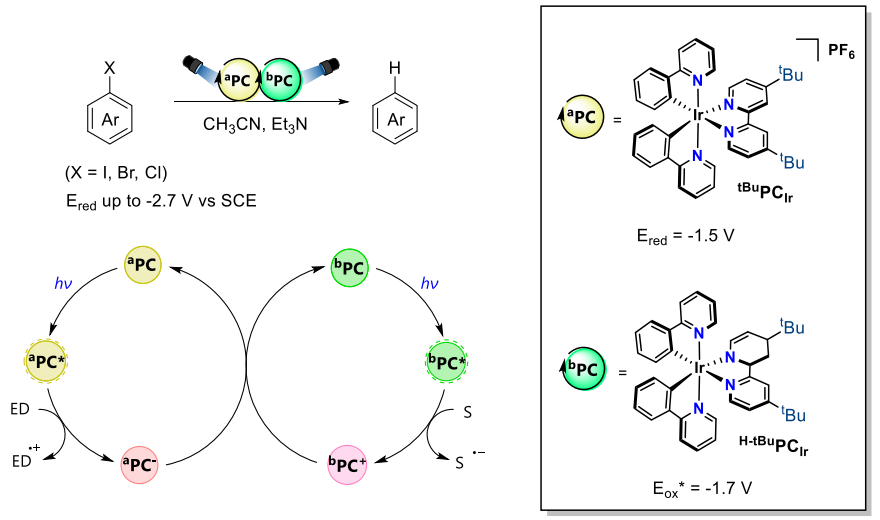

Scheme 5.3. Dehalogenation of aryl halides by Connell and co-workers. PC = Photoredox Catalyst; ED = Electron Donor; S = Substrate. Charges in the mechanistic cycle are drawn for a neutral PC for easier comparison with Scheme 5.1.

In the same year, König demonstrated that ^{tBu}**PC$_{Ir}^{+}$** could also participate in assembly-promoted single electron transfer (APSET) to non-activated alkyl chlorides (E_{red} up to -2.8 V vs SCE in DMF) prompted by the use of microstructured aqueous solutions.[7] In their work, micelles provide pre-aggregation between substrates and the *in situ* reduced ^{tBu}**PC$_{Ir}^{0}$**. This renders the desired carbon-centered radicals rather than deleterious back electron transfer to the electron donor. The proposed mechanistic hypothesis relies on the second photon absorption by the intermediate ^{tBu}**PC$_{Ir}^{0}$** to either undergo outer sphere ET with the substrate or release a solvated electron. Nonetheless, no experimental evidence was included to support a multiphoton pathway.

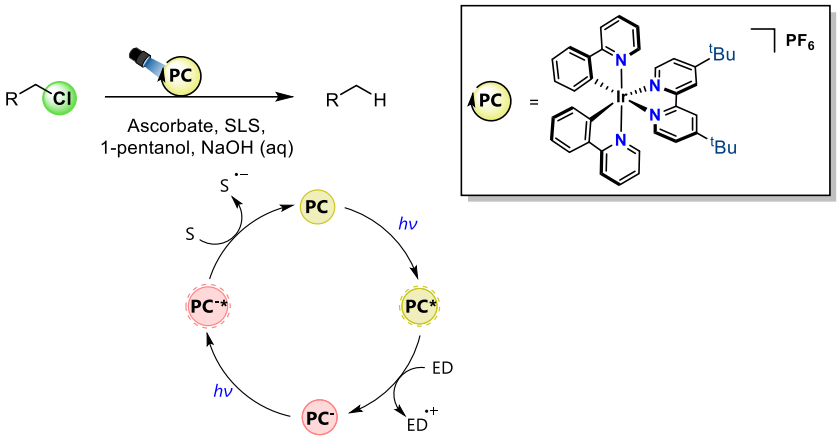

Scheme 5.4. Dehalogenation of alkyl halides by König group. The proposed mechanism implied multiphoton absorption. PC = Photoredox Catalyst; ED = Electron Donor; S = Substrate. Charges in the mechanistic cycle are drawn for a neutral PC for easier comparison with Scheme 5.1.

Wenger and co. reported in 2019 an anionic iridium catalyst that generates hydrated electrons (e^-_{aq}, E_{red} = -3.1 *vs* SCE in water) *via* two consecutive photon absorption steps (Scheme 5.5).[8] These events were strongly supported by transient absorption spectroscopy studies, and the system was applied for selected reductions in water such as the dehalogenation of chloroacetate. On the other hand, the solvated electron has been also reported in other solvents such us ammonia,[9, 10] methanol,[11, 12] tetrahydrofuran[13] or acetonitrile.[14] However, to the best of our knowledge there is no photocatalytic protocol with solid evidence of using solvated electrons in non-aqueous media, what complicates the generalization of this type of mechanism in purely organic solutions.

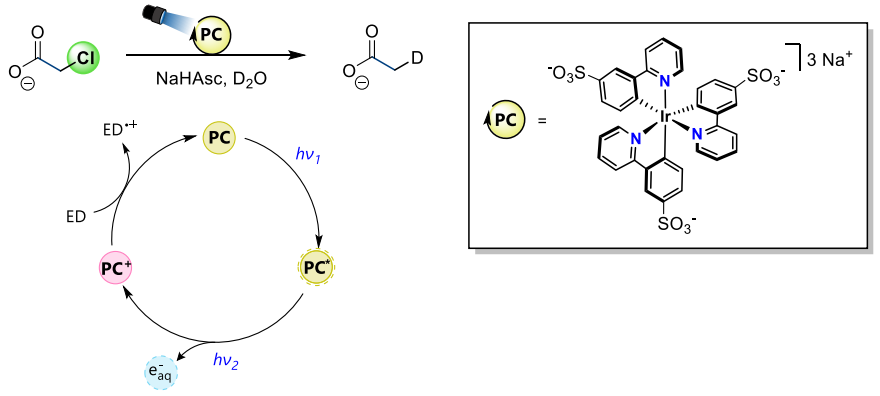

Scheme 5.5. Chloroacetate dehalogenation by Wenger and co., and the two-photon absorption mechanism proposed yielding hydrated electrons. Charges in the mechanistic cycle are drawn for a neutral PC for easier comparison with Scheme 5.1.

As it has been introduced in the previous chapters of this thesis, our group has used iridium photoredox catalysis for the development of different reductive methodologies, including hydrogen evolution,[15] the selective reduction of aromatic olefins in front of aromatic ketones (and *vice versa*),[16] and the coupling of styrene derivatives with alkyl chlorides (Scheme 5.6).[17] In all these cases, the observed reactivity could be explained based on the well-known reductive quenching mechanism (Scheme 5.1, left cycle). However, we thought studying the reduced catalytic intermediate further would help us better understand the reactivity and develop better photoredox catalytic cycles.[4-7]

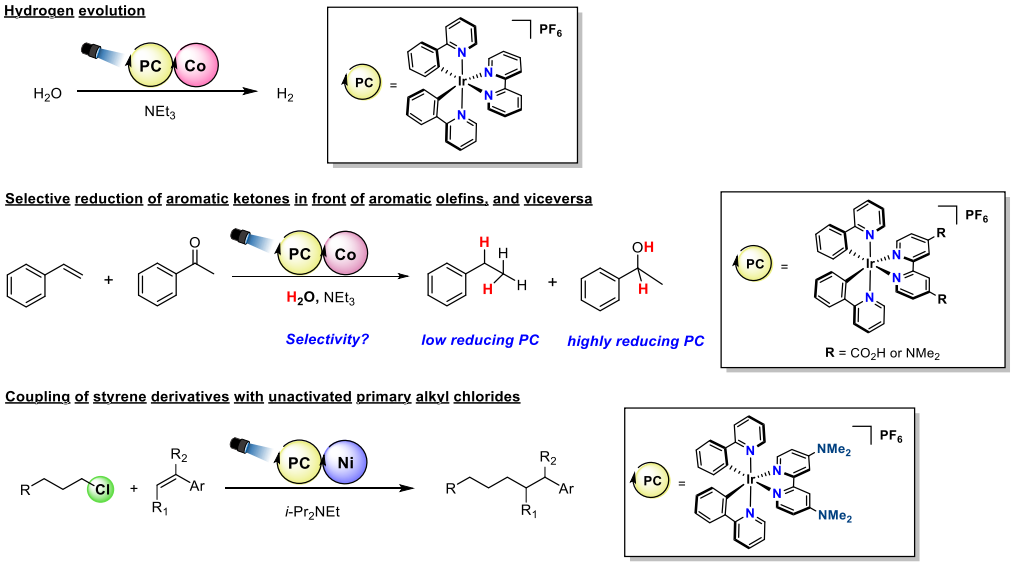

Scheme 5.6. Methodologies based on iridium photoredox catalysis developed in our group.

With this aim, we selected the non-substituted $\mathbf{PC_{Ir}^{+}}$ $[Ir(ppy)_2(bpy)]PF_6$, ppy = phenylpyridine, bpy = bipyridine) as the model complex to study and to directly study its reduced form $\mathbf{PC_{Ir}^{0}}$. Previous observations in the group suggested that isolated $\mathbf{PC_{Ir}^{0}}$ was viable, although not viable if considering the literature and its extreme reactivity. Having isolated $\mathbf{PC_{Ir}^{0}}$ could open the door for comprehensive spectroscopic characterization but, more importantly, direct characterization of their reactivity without any other molecule besides the solvent and the added substrate wanted to study. Furthermore, we will have the opportunity to study the $\mathbf{PC_{Ir}^{0}}$ excited state reactivity directly will also be studied. We expect that this study can clarify the mechanisms that $\mathbf{PC_{Ir}^{+}}$ can engage.

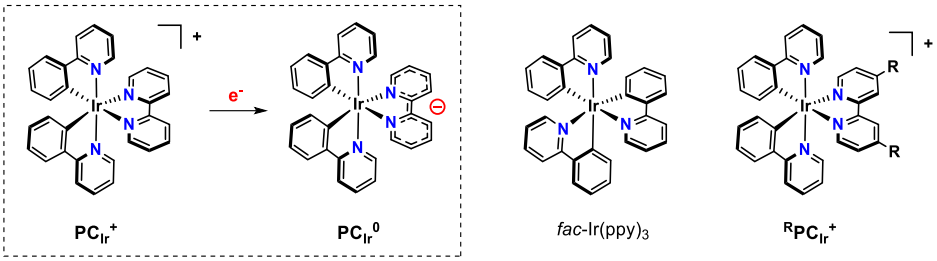

Scheme 5.7. Comparison between the commonly used *fac*-Ir(ppy)$_3$ (left), the reduced species (center) and a generic heteroleptic cyclometalated iridium complex (right). Note that **PC$_{Ir}^+$** is the chosen notation for **PC$_{Ir}$** without the PF_6 counteranion.

5.2. Results and discussion

5.2.1. Evidence of accumulation of the reduced PC$_{Ir}^0$ intermediate by UV-vis

A technique that allowed us to cleanly follow the one-electron reduction of **PC$_{Ir}^+$** to **PC$_{Ir}^0$** by UV-vis spectroelectrochemistry (see Section 5.4.2 for information about the setup). The typical experiment is carried out by monitoring a solution of **PC$_{Ir}^+$** (1 mM, 0.1 M $TBAPF_6$ in anhydrous CH_3CN) after applying an electric potential incremented slowly from the initial potential (0 V) to negative values (-1.7 V *vs* SCE). At potentials close to -1.4 V *vs* SCE, four main features appeared at 385, 450, 525 and 850 nm (Figure 5.1, top), which are characteristic of the previously reported absorption spectrum of **PC$_{Ir}^0$**.[18] Then, the **PC$_{Ir}^0$** was reversibly oxidized to **PC$_{Ir}^+$**, recovering the original spectrum of the complex **PC$_{Ir}^+$** (Experimental Section, Figure 5. 41). The absorption spectrum differs from the bipyridinium anion ($bpy^{\bullet-}$),[19] discarding a potential bpy decordination under the studied conditions.

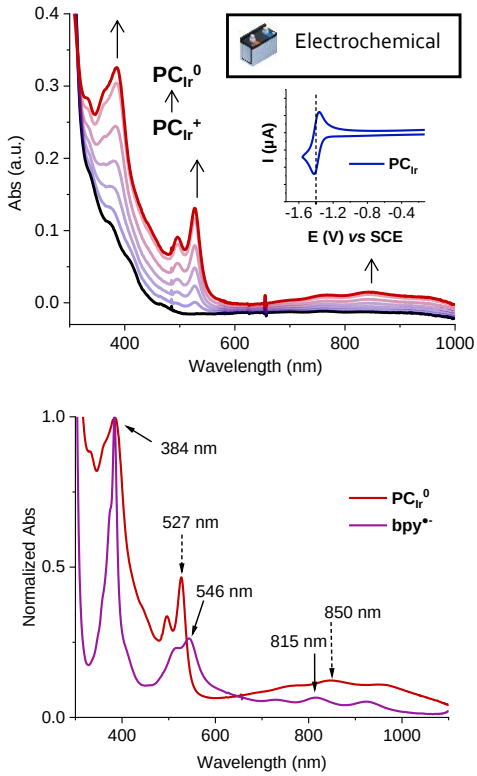

Figure 5.1. Top): evolution of the absorption spectrum during the electrochemical reduction of $\mathbf{PC_{Ir}^+}$ to $\mathbf{PC_{Ir}^0}$ in CH_3CN. Bottom): Comparison of the spectrum of $\mathbf{PC_{Ir}^0}$ and the anion $\mathbf{bpy^{\bullet-}}$.

Since the $\mathbf{PC_{Ir}^0}$ was significantly stable under the spectroelectrochemical conditions, we considered to synthesized via a chemical reduction.[20] We selected Na/Hg amalgam (1% of Na) as a chemical reductant.[21] Stirring a solution of $\mathbf{PC_{Ir}^+}$ (1 mM in CH_3CN) with Na/Hg (with 10 equiv of Na) resulted in the formation of an abundant precipitate in about 90 s. UV-Vis monitoring of the reaction showed the formation of the $\mathbf{PC_{Ir}^0}$ with significant scattering, consistent with the formation of the precipitate (Experimental section, Figure 5. 42). This observation led us to consider that the obtained powder could be the reduced species. The insolubility of $\mathbf{PC_{Ir}^0}$ could be understood since it is neutrally charged, as the highly insoluble and structurally similar neutral fac-Ir(ppy)$_3$ complexes.[22] Lowering the experiment's concentration to 100 μM resulted enough soluble to monitor the reactions without the appearance of precipitates. The naked eye can even monitor the reaction: the colour of the solution changes from yellow to orange/red after the one-electron reduction of $\mathbf{PC_{Ir}^+}$. Nevertheless, to better control the reduction of $\mathbf{PC_{Ir}^+}$ to $\mathbf{PC_{Ir}^0}$, after the one-electron reduction had finished,

the magnetic stirring was stopped to avoid over-reduction. We these considerations, **PC$_{Ir}^0$** can be cleanly obtained and studied (Figure 5.2). Replacing Na/Hg with similar chemical reductants such as KC_8 and $CoCp^*_2$ (Cp*= 1,2,3,4,5-Pentamethylcyclopentadienyl) also afforded the desired product (in Experimental section, Figure 5. 44).[23]

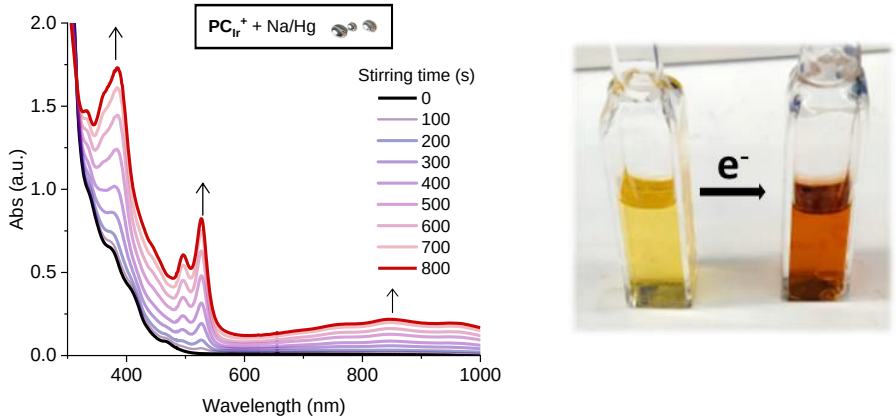

Figure 5.2. Left) evolution of the absorption spectrum during the chemical reduction of **PC$_{Ir}^+$** (100 μM) to **PC$_{Ir}^0$** with Na/Hg (10 equiv.) in CH_3CN. Right) picture of two cuvettes with **PC$_{Ir}^+$** (yellow) and **PC$_{Ir}^0$** (red) at 330 μM concentration to illustrate the intense colour change.

We employed reductive quenchers and light (LEDs, λ 447 nm) as a third way to obtain **PC$_{Ir}^0$** in the solution.[24] It is worth noticing that obtaining **PC$_{Ir}^0$** photochemically is challenging because organic electron donors can promote other processes apart from SET, such as hydrogen atom transfer (HAT)[5] or halogen atom transfer (XAT).[25-28] In particular, tertiary amines are known to generate radicals under photochemical conditions that react with the ancillary ligands of iridium photosensitizers (Scheme 5.3 and Scheme 5.8a).[6]

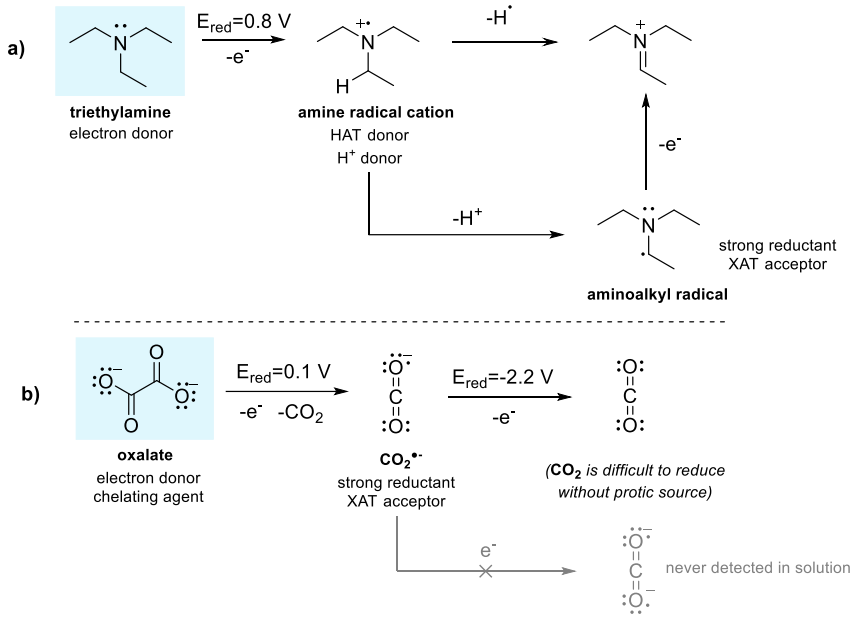

Scheme 5.8. Selected reported reactivity of a) triethylamine and b) oxalate under conventional photochemical conditions.

With this in mind, we selected tetrabutylammonium oxalate[24] (TBA_2ox, Scheme 5.8b) to promote the photoreduction of $\mathbf{PC_{Ir}^+}$. We hypothesize TBA_2ox is a good quencher since its decomposition products are CO_2 and $CO_2^{\bullet-}$.[29, 30] Although $\mathbf{CO_2^{\bullet-}}$ (E_{red} = -2.2 V *vs* SCE) can also act as a strong SET agent forms CO_2.[31] Under these conditions, the intermediate $\mathbf{PC_{Ir}^0}$ is quickly accumulated (30 s of irradiation, Figure

5.3) and the intensity of the UV-Vis band is stable in the range of minute timescale. Then, a slow decay of the 525 nm band is observed.

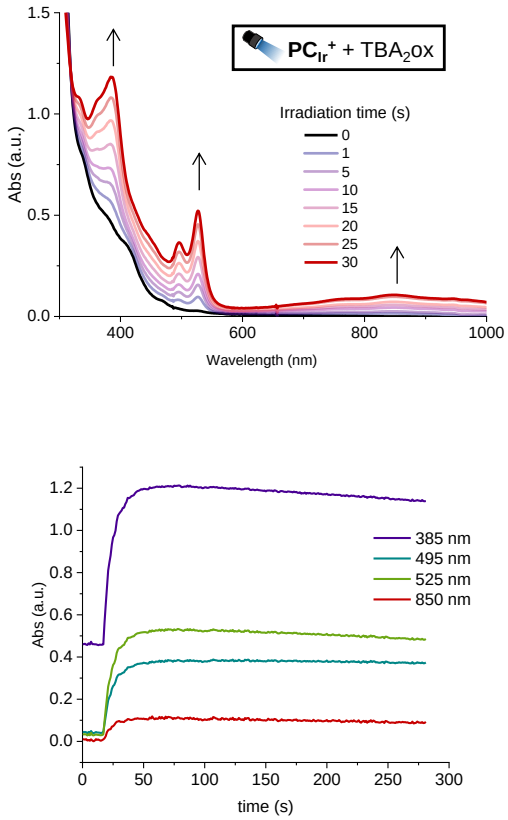

Figure 5.3. Top) absorption spectrum evolution during the **PC_{Ir}^+** (50 μM) photochemical reduction to **PC_{Ir}^0** with TBA_2ox (1.5 equiv.) in CH_3CN. Bottom) kinetic traces of selected absorption wavelengths.

For comparative reasons, we studied the effect of Et_3N as a source of electrons. In agreement with the behavior exposed by Bernhard and co-workers,[6] and consistent with previous studies in

the group[32, 33] the $\mathbf{PC_{Ir}^0}$ intermediate cannot be accumulated, although there is a short period in which it can be detected.

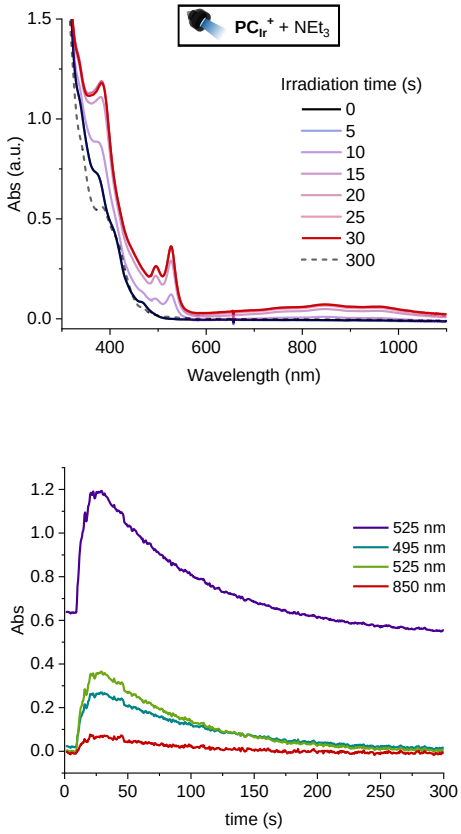

Figure 5.4. Top) Absorption spectrum evolution during the photochemical reduction of $\mathbf{PC_{Ir}^+}$ (50 μM) to $\mathbf{PC_{Ir}^0}$ with Et_3N (25 mM) in CH_3CN. Bottom) kinetic trace of selected absorption wavelengths under irradiation (started at 10 s of measurement).

ON/OFF experiments using Et_3N showed the stability of the reduced intermediate in the absence of irradiation. $\mathbf{PC_{Ir}^0}$ quickly disappeared when switching off the LED, and the concentration of $\mathbf{PC_{Ir}^0}$ was lower with each ON/OFF cycle. This behaviour matches with the quick back electron transfer (BET) to the oxidized amine in solution, together with the proposed HAT from radical species that gradually consumes the original $\mathbf{PC_{Ir}^+}$/$\mathbf{PC_{Ir}^0}$ redox pair.[6] Equivalent ON/OFF irradiation cycles with TBA_2ox instead of Et_3N shows that $\mathbf{PC_{Ir}^0}$ decays very slowly, and the recovery of the signal is larger. In this case, we hypothesize that the BET is less likely because the homolytic

oxalate cleavage is irreversible. This situation matches with a clean ET process between TBA_2ox and $\mathbf{PC_{Ir}^+}$.

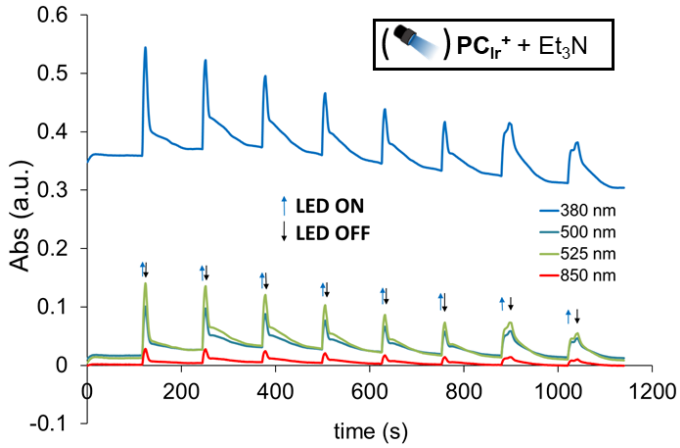

Figure 5.5. Kinetic trace of selected absorption wavelengths during ON-OFF irradiation cycles of $\mathbf{PC_{Ir}^+}$ (50 μM) in the presence of Et_3N (25 mM) in CH_3CN. The LED was turned on for the first time after 120 s without irradiation to follow up on any system changes in the absence of LED irradiation.

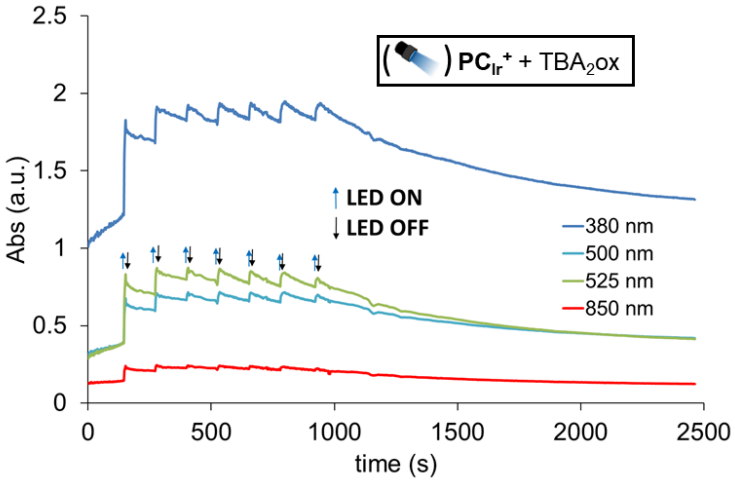

Figure 5.6. Kinetic trace of selected absorption wavelengths during ON-OFF irradiation cycles of $\mathbf{PC_{Ir}^+}$ (50 μM) in the presence of TBA_2ox (25 mM) in CH_3CN. The LED was turned on for the first time after 120 s without irradiation to follow up on any system changes in the absence of LED irradiation.

5.2.2. Isolation and characterization of the reduced intermediate

To isolate $\mathbf{PC_{Ir}^0}$ we upscaled the chemical using Na/Hg alloy (>10 mM). After filtering the dispersion and washing the precipitate with small fractions of CH_3CN, we could isolate a brown powder in 75% yield. The isolated compound was ^{1}H-NMR silent suggesting a strong paramagnetic character.[34, 35] However, the characteristic ^{1}H-NMR resonances of $\mathbf{PC_{Ir}^+}$ were detected after exposing the solution to air (in Experimental section, Figure 5. 30-37).

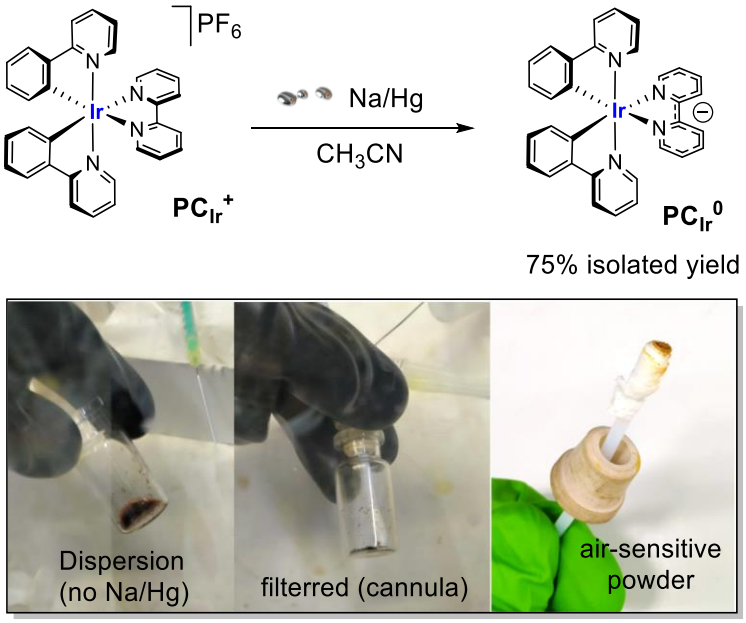

Figure 5.7. Top) reaction scheme for the chemical $\mathbf{PC_{Ir}^+}$ reduction with Na/Hg (1.5 equiv). Bottom) pictures were taken during the powder isolation. Solid dark leftovers over the cannula become yellowish when exposed to air.

The *in situ* generated $\mathbf{PC_{Ir}^0}$ in CH_3CN solution showed tolerance to a variety of solvent mixtures (in Experimental section, Table 5. **9**). However, the isolated powder was not stable in certain pure solvents (PhCN, CH_2Cl_2, $CHCl_3$, DMF), or presented bad solubility (with CH_3CN, DMSO, PhCl, dichlorobenzene, THF or even insoluble in C_6H_6, $PhCH_3$, difluorobenzene, C_6F_6, Et_2O and hexane). Systematic solvent testing revealed pyridine to solubilize $\mathbf{PC_{Ir}^0}$ with no evidence of decomposition matching with its redox-inertness (E_{red} = -2.7 V *vs* SCE in THF).[13] Indeed, $\mathbf{PC_{Ir}^0}$ powder was easily dissolved in degassed pyridine, obtaining a very dark red solution (solubility higher than 500 µM), matching the absorption spectrum with the obtained for $\mathbf{PC_{Ir}^0}$ in other solvents.

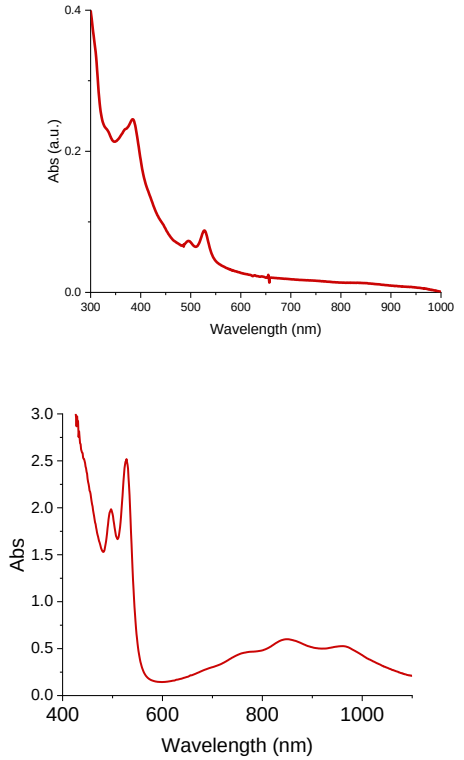

Figure 5.8. Absorption spectrum of **PC$_{Ir}^0$** in degassed Top) CH_3CN and Bottom) pyridine, in 1 mm and 1 cm optical path cuvettes, respectively.

The solubility and stability of the isolated intermediate in pyridine helped to obtain brown-to-red single crystals good enough for X-ray diffraction studies (Figure 5.9, see Experimental section for crystallization procedure). The unit cell obtained from the X-ray diffraction data of the crystals presents two molecules of the complex without anions. However, due to the high structural symmetry of **PC$_{Ir}^0$**, the C and N atoms were not distinguishable. Then, identifying the bipyridine (bpy) or phenylpyridine (ppy) ligands was not feasible. This ambiguity did not allow us to compare bond distances from **PC$_{Ir}^0$** with the structure of **PC$_{Ir}^+$**. Such an analysis would be interesting since, according to our DFT calculations, the localization of the additional electron over the **bpy$^{\bullet-}$** ligand shortens the bond distance of the C–C bond between both pyridine rings (from 1.48 Å in calculated **PC$_{Ir}^+$** to 1.43 Å in calculated **PC$_{Ir}^0$**).

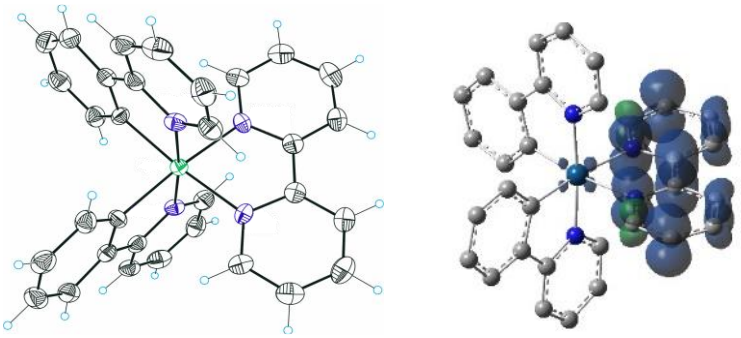

Figure 5.9. (Left) Solid-state structure of $\mathbf{PC_{Ir}^{0}}$. Thermal ellipsoids are shown at 50% probability. No counteranion or solvent molecules were found. (Right) DFT calculated spin density for $\mathbf{PC_{Ir}^{0}}$ at the uB3LYP/def2SVP level of theory. Irrelevant hydrogen atoms are omitted for clarity and an isosurface value of 0.0025 is chosen for representation. The additional unpaired electron is delocalized over the $\mathbf{bpy^{\bullet -}}$ ligand.

To break the symmetry, luckily, we were able to prepare the iridium complexes with a methyl substituent at the β position of the metalated carbon of the phenylpyridine ligand ($\mathbf{^{Me}PC_{Ir}^{+}}$/$\mathbf{^{Me}PC_{Ir}^{0}}$, Figure 5. 10). This structural change break the high symmetry without altering the electronic properties of the bpy. As expected, a comparison of the $\mathbf{^{Me}PC_{Ir}^{+}}$ and $\mathbf{^{Me}PC_{Ir}^{0}}$ X-ray structures evidenced a decrease of the C–C distance between **bpy** rings from 1.48 to 1.35 and 1.39 Å (averaged values for each structure in the crystal cells considering the error). This bpy bonding structure distortion is proof of the bpy ligand's delocalisation electron.[36]

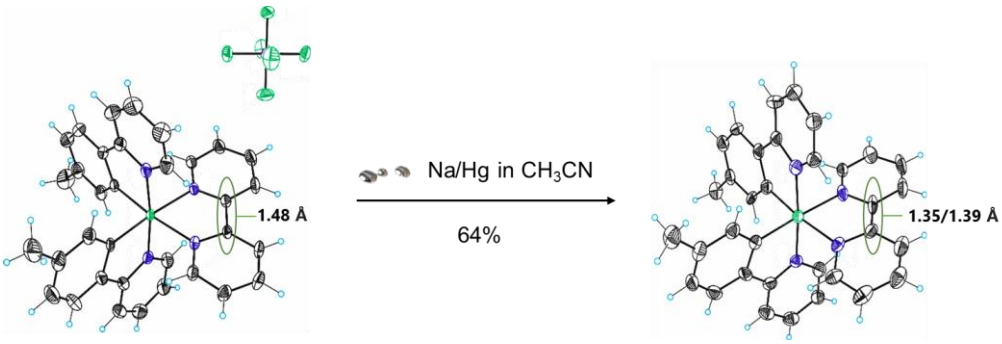

Figure 5. 10. Reaction scheme for reducing $\mathbf{^{Me}PC_{Ir}^{+}}$ with Na/Hg to form $\mathbf{^{Me}PC_{Ir}^{0}}$, including the corresponding solid-state structures. Thermal ellipsoids are shown at 50% probability. No counteranion or solvent molecules were found. Comparing both XR structures confirms the expected C–C bond shortening.

We considered that $\mathbf{PC_{Ir}^0}$ could be isolated *via* photochemical reduction using TBA_2ox as an electron donor. After 30 seconds of blue light irradiation of stirred dispersion $\mathbf{PC_{Ir}^+}$ (>10 mM) forms an abundant brown precipitate (see Experimental Section for detailed procedure). The solid was collected, filtered, and the remaining traces of tetrabutylammonium salts were quickly removed by sequential washing given their high solubility in CH_3CN (see Experimental section, Figure 5. 38), and the brown powder was isolated with 84% yield. Following our crystallization procedure, we reaffirmed the obtention of $\mathbf{PC_{Ir}^0}$, which corresponds to the first crystalline structure of a reduced PC obtained *via* reductive quenching.

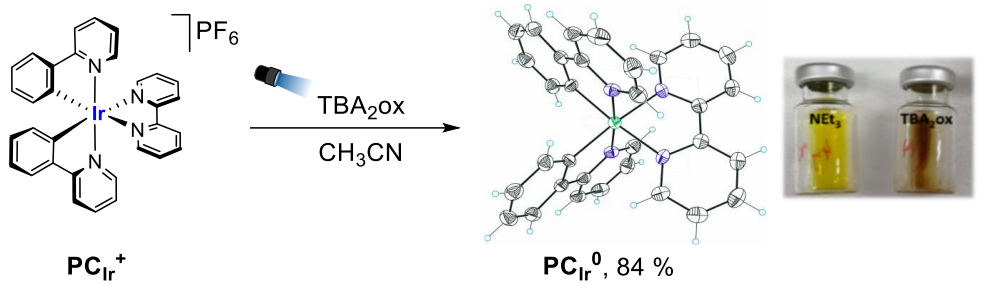

Figure 5.11. Synthesis of $\mathbf{PC_{Ir}^0}$ *via* reductive quenching with TBA_2ox. Samples of $\mathbf{PC_{Ir}^+}$ (1 mM) with Et_3N or TBA_2ox show a different colour and precipitate quantity after 30 s irradiation.

5.2.3. EPR study of $\mathbf{PC_{Ir}^0}$

After unambiguously determining the identity of the isolated solid as $\mathbf{PC_{Ir}^0}$, we measured the electron paramagnetic resonance (EPR) of a filtered oversaturated solution of $\mathbf{PC_{Ir}^0}$ powder in CH_3CN, obtaining a symmetric signal with a g value of 1.9878. Beller and co-workers reported g = 1.9840 of $\mathbf{PC_{Ir}^0}$ in a $THF/H_2O/Et_3N$ mixture generated by electrochemical reduction.[18, 37] Analogously, a solid sample prepared by mixing the $\mathbf{PC_{Ir}^0}$ powder with boron nitride resulted in a broader symmetric signal which was also slightly shifted (g = 1.9794). We attributed the small differences to the preparation methods.

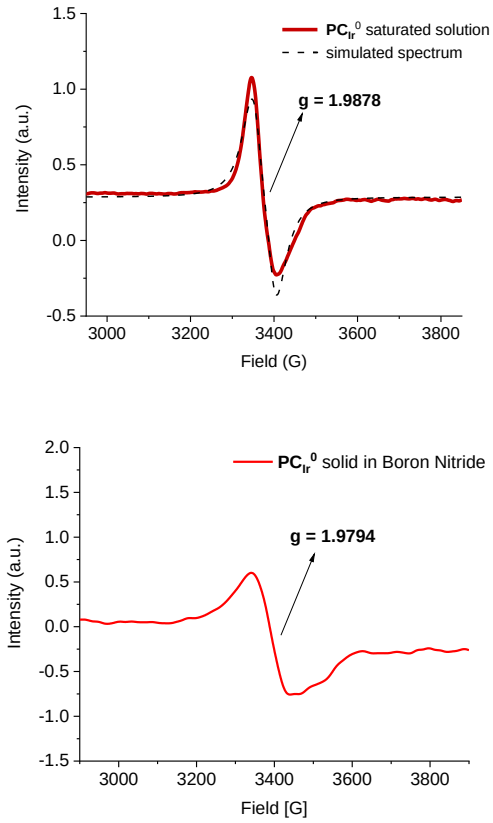

Figure 5.12. The EPR spectra registered at 77 K of a saturated solution of **PC_{Ir}^{0}** in CH_3CN (Top) and a solid state of **PC_{Ir}^{0}** powder in boron nitride (bottom). Solid samples were prepared *via* photoreduction with TBA_2ox.

The EPR spectrum was also obtained by *in situ* generation of the intermediate in CH_3CN. We found that Na/Hg and $CoCp^*_2$ can afford a signal that matches the g-factor (g = 1.98). For comparative purposes, we also prepared the photochemically reduced sample in the presence of Et_3N. However, we had to irradiate at a lower temperature to observe the desired signal. This agrees with a fast reaction of the paramagnetic

intermediate with amine sub-products after quenching.[5] All these EPR signals quickly disappeared when the sample was exposed to air.

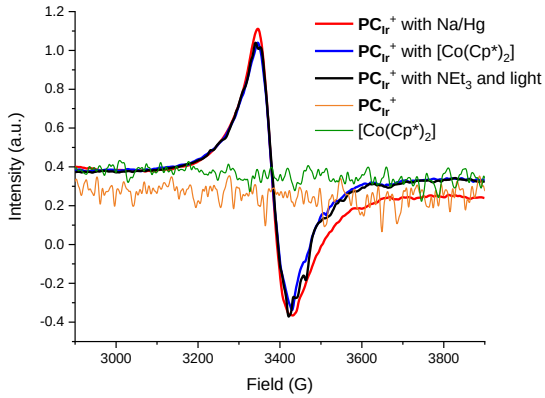

Figure 5.13. EPR spectra registered at 77 K in CH_3CN of (a) **PC$_{Ir}^+$** (0.5 mM) reduced *ex situ* with Na/Hg (red line), (b) **PC$_{Ir}^+$** (1 mM) reduced *in situ* with [CoCp*$_2$] (0.9 mM) (blue line), (c) **PC$_{Ir}^+$** (1 mM) in the presence of Et_3N (25 mM), measured after irradiating the mixture in CH_3CN for 7 s (-30 ºC) and immediately later freezing it in the EPR cavity (black line), (d) **PC$_{Ir}^+$** (1 mM) with no additive (orange line), (e) [CoCp*$_2$] (0.9 mM) in CH_3CN (green line).

Nonetheless, although the solid samples prepared by photochemical reduction of **PC$_{Ir}^+$** with TBA_2ox yielded an EPR symmetric signal, the *in situ* use of TBA_2ox led to a more intense signal with axial symmetry with g values of 1.997 and 1.949. This pattern matches with the reported EPR spectrum of **$CO_2^{\bullet-}$** species,[38, 39] but we cannot rule out the existence of ion pair formation,[40] coordination,[41-43] over reduction,[44] and C–C coupling products.[45] To check if the observed EPR spectrum belongs to species that evolved just after the reaction began, we measured a sample after exposure to ambient light for only 30 s. These mild conditions could promote only meagre photoreduction. However, the same EPR signal was obtained, while no signal was obtained under darkness. These experiments suggest that the EPR signals obtained with TBA_2ox in solution presumably correspond to **$CO_2^{\bullet-}$** together with **PC$_{Ir}^0$**.

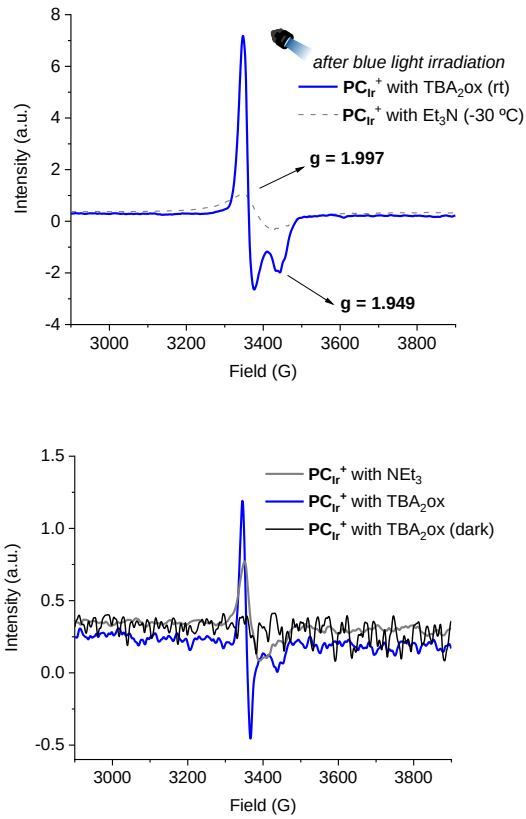

Figure 5.14. The EPR spectra registered at 77 K in CH_3CN of $\mathbf{PC_{Ir}^+}$ (1 mM). Left: in the presence of TBA_2ox (25 mM, irradiated at room temperature) or Et_3N (25 mM, irradiated at -30 ºC) after 30 seconds of irradiation. Bottom: in the presence of TBA_2ox (25 mM) or Et_3N (25 mM) after ambient light exposure at room temperature.

5.2.4. EXAFS study of $PCIr^0$

EXAFs measurements performed by Dr. Vlad Martin-Diaconescu indicated that Ir L_3-edge XAS data show intense white-lines at 11220.0 and 11220.2 eV for $\mathbf{PC_{Ir}^+}$ and the *fac*-$Ir(ppy)_3$ reference respectively (Figure 5.15), consistent with a Ir^{+3} metal center. Cauchy wavelet transforms of the EXAFS signal show 3 shells of scattering at 1.65 Å, 2.6 Å and 3.6 Å consistent with a C/N first shell coordination and longer range scattering from bpy and ppy ligands (Experimental Section, Section 5.4.8). Upon photo-($^{(hv)}\mathbf{PC_{Ir}^0}$) or chemical ($^{(chem.)}\mathbf{PC_{Ir}^0}$) reduction the EXAFs structure is maintained and no shift in the rising edge or white-line maximum is observed indicating that the reduction is ligand centered (Figure 5.15), similar to previous reports.[18] A drop in intensity however is clearly visible, which is also consistent with previous reports.[18]

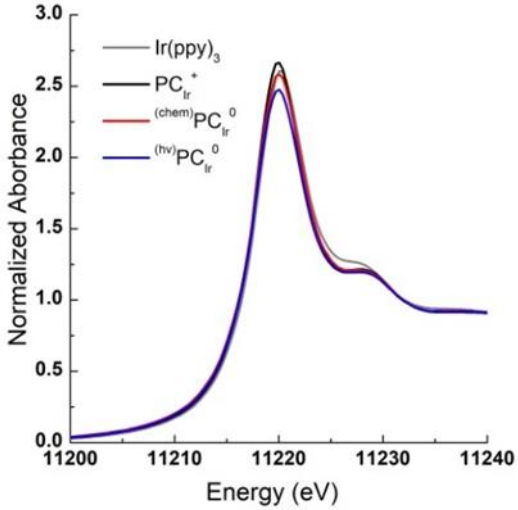

Figure 5.15. XANES and Fourier Transformed spectra (k2 weighted 3-16 Å^{-1} k-range having a Hannings window dk=1) of PC_{Ir}^+ and chemically $^{(chem)}PC_{Ir}^0$ and photo- $^{(hv)}PC_{Ir}^0$ reduced species and overlaid with $Ir(ppy)_3$ as reference.

5.2.5. Reactivity of PC_{Ir}^0 with metal complexes.

With a clean procedure for *in situ* formation of the reduced **PC_{Ir}^0** (Figure 5.2, and also in Experimental Section, *procedure V*), we tested its reactivity in SET reaction with selected metal complexes. First, we studied the stoichiometric reactivity of the **PC_{Ir}^0** ground state ($E_{1/2}$ = -1.4 V *vs* SCE) with cobaltocenium complexes $CoCp_2(PF_6)$ (Top) or $CoCp^*_2(PF_6)$ as one-electron oxidants. In agreement with their reported redox values,[23] only $CoCp_2(PF_6)$ could be reduced ($E_{1/2}$ = -1.0 V *vs* SCE). On the other hand, no reaction was observed in the case of $CoCp^*_2(PF_6)$ (E_{red} = -1.5 V *vs* SCE).

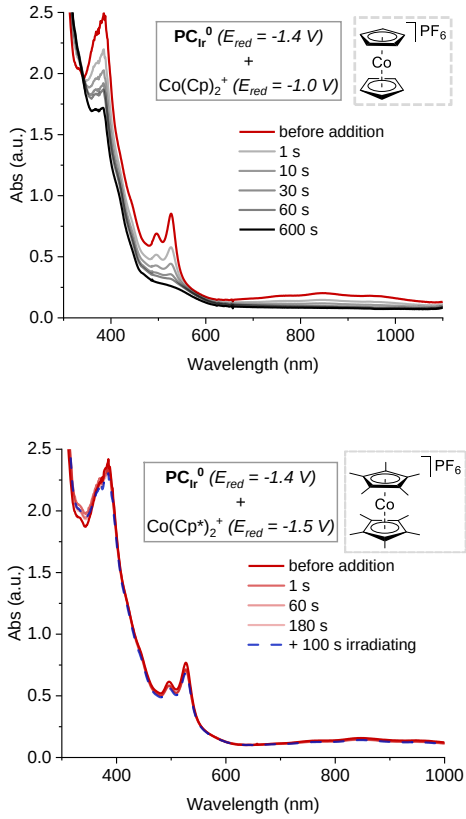

Figure 5.16. Evolution of the absorption spectrum of **PC$_{Ir}^0$** in CH_3CN after the addition of $CoCp_2(PF_6)$ (Top) or $CoCp^*_2(PF_6)$ (bottom). Turning on the LED did not show further changes for $CoCp^*_2(PF_6)$.

We also tested two selected complexes [M(OTf)(Py_2^{Ts}tacn)](OTf) (M = Co (**1$_{Co}$**), Ni (**1$_{Ni}$**)), (Py_2^{Ts}tacn = 1,4-di(picolyl)-7-(p-toluenesulfonyl)-1,4,7-triazacyclononane, OTf = trifluoromethanesulfonate anion) that were previously reported by our group in photocatalytic reductive transformations. [15-17] The almost mixing time reaction of **1$_{Co}$** with **PC$_{Ir}^0$** suggests SET. The reaction of **1$_{Ni}$** with **PC$_{Ir}^0$** produces the Ni(I) intermediate formation, characterized by an absorption band at λ_{max} of 520 nm. However, the process lasted for more than 300 s, which needs further examination to be properly understood

since it is inconsistent with a classical SET.[17, 32] Nevertheless, elaborated versions of these experiments could serve as probes for electron transfer mechanistic evidence.

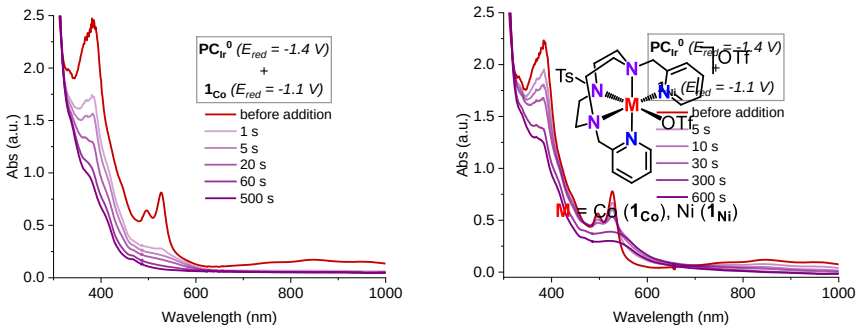

Figure 5.17. Evolution of the absorption spectrum of $\mathbf{PC_{Ir}^0}$ (100 µM) in CH_3CN after the addition of 1 equivalent of $\mathbf{1_{Co}}$ (top) or $\mathbf{1_{Ni}}$ (bottom). Structure of $\mathbf{1_{Co}}$/$\mathbf{1_{Ni}}$.

5.2.6. Reactivity with organic halides

Aromatic halides have been established as standard probes to measure the redox power of ET processes.[2, 5, 26, 46-51] We examined the reactivity of $\mathbf{PC_{Ir}^0}$ with selected organic halides comprehending a wide redox window, from -1.4 to -3.5 V *vs* SCE. We used 10 equiv. of halide to enhance the reaction over possible $\mathbf{PC_{Ir}^0}$ degradation pathways. Under darkness, the outcome follows the expected behavior, considering the redox values of the substrates (Table 5.1, yields in black). For instance, iodobiphenyl (**1a**, E_{red} = -1.4 V) was reduced via SET, and the consequent carbon-centred radicals can abstract a hydrogen atom from the solvent (65 % yield to $\mathbf{PC_{Ir}^0}$, the limiting reagent). However, the same conditions did not afford any dehalogenation from substrates with more challenging redox potential, such as bromoanisole (**1b**, E_{red} = -2.7 V) [5] or chloroanisole (**1c**, E_{red} = -2.9 V). Then, we studied if $\mathbf{PC_{Ir}^0}$ could undergo further reactivity after excitation. To our delight, **1b** and **1c** were activated under irradiation, resulting in yields higher than 70% at 30 minutes (Table 1, yields in blue). Still, we observed dehalogenation traces for **1d**, which helped us to estimate the redox potential of $\mathbf{PC_{Ir}^{0*}}$ in CH_3CN between -2.9 V and -3.5 V *vs* SCE.

Table 5.1. Stoichiometric experiment with different aryl halides.

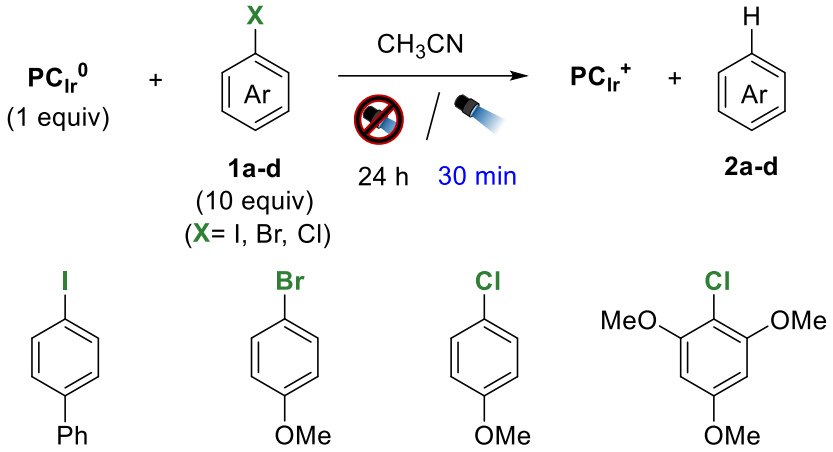

[a]**PC$_{Ir}^0$** (0.3 mM), **1** (3 mM) in CH_3CN (0.44 mL), at 25 °C under N_2. [b]Under darkness, 24 h. [c]Irradiated for 30 min (447 nm). [d]Irradiated for 24 h (447 nm). [e]Yields (average of duplicates) were determined by GC analysis relative to a calibrated internal standard.

These results have significant mechanistic implications, strongly supporting that **PC$_{Ir}^0$** excited state can be used to trigger photoreduction reactivity and possesses a redox power of at least -2.9 V *vs* SCE, which is in the range of alkali metals.[52, 53]

5.2.7. Mechanistic studies

After discovering the unprecedented **PC$_{Ir}^0$** photochemistry, we performed additional studies to gain more information about the system. First, increasing the chloroanisole equivalents enhanced the reaction rate, in concordance with a bimolecular reactivity (Table 5. 10, entries 1-15).

Then, blank experiments in the absence of light or when the sample was exposed to ambient light did not produce dehalogenation (entries 16-18). The chloroanisole was also recovered after irradiation if **PC$_{Ir}^0$** was replaced by **PC$_{Ir}^+$** (entry 19). The same result was obtained if triethylamine was added to the solution containing the chloroanisole and **PC$_{Ir}^+$** (entry 21). However, interestingly the reactivity of **PC$_{Ir}^0$** was not inhibited by triethylamine itself (entry 22), what supports that the radical species derived from tertiary amines should be the responsible to inhibit the **PC$_{Ir}^0$** exited state reactivity against chloroanisole.

Table 5. 2. Stoichiometric reactions of $\mathbf{PC_{Ir}^0}$ with chloroanisole and blank reactions.

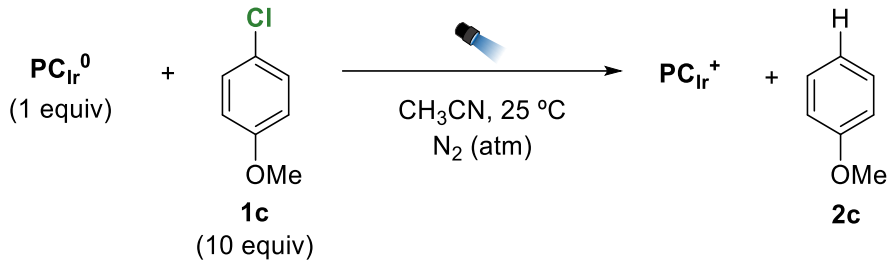

Entry	Equivalents of **1c**	Reaction time (min)	Conversion **1c** %	Yield **2** (%)
1	10[a]	60	0	0
2	10[a]	1440	0	0
3	10[b]	60	0	0
4	10[b]	60	1	0
5	-[d]	60	0	0
6	10[c,e]	720	5	4
7	10[f]	60	7	71

Standard conditions: $\mathbf{PC_{Ir}^0}$ (0.3 mM), **1c** in CH_3CN (0.44 mL) at 25 °C under N_2 under blue light irradiation (447 nm). Yields were determined by GC analysis relative to a calibrated internal standard. [a]No light. [b]Sample was exposed to ambient visible light. [c]$\mathbf{PC_{Ir}^+}$ instead of $\mathbf{PC_{Ir}^0}$. [d][**1c**] = 3 mM but without $\mathbf{PC_{Ir}^0}$. [e]In the presence of 100 equivalents of triethylamine. [f]In the presence of 10 equivalents of triethylamine.

At this point, we proceeded to the spectroscopic interrogation of the excited state of $\mathbf{PC_{Ir}^0}$ to explain its reactivity with electron-rich aryl halides. Luminescence studies revealed that $\mathbf{PC_{Ir}^{0*}}$ is not emissive, neither at room temperature nor at 77 K. The only observed emission was related to $\mathbf{PC_{Ir}^+}$ species regenerated after exposing the solution to air and freeze pumped again (Figure 5.18). Consequently, we moved then to time-resolved spectroscopic techniques to further progress on the mechanistic investigations.

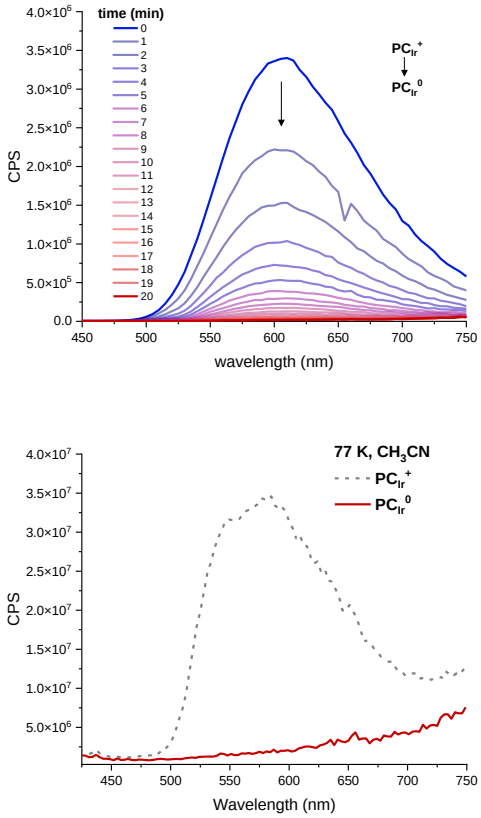

Figure 5.18. Top) emission spectra evolution of $\mathbf{PC_{Ir}^{+}}$ (300 μM) in CH_3CN when stirring at 25 ºC in the presence of Na/Hg (10 equiv.). Bottom) emission spectra of frozen $\mathbf{PC_{Ir}^{+}}$ (300 μM, dotted grey line) and $\mathbf{PC_{Ir}^{0}}$ (300 μM, solid red line).

Then, we studied the changes of the $\mathbf{PC_{Ir}^{0}}$ absorption spectrum at the nanosecond timescale in transient absorption spectroscopy (TAS) at ICIQ, and no clear signal was detected. Therefore, we assumed that the $\mathbf{PC_{Ir}^{0*}}$ excited state has a lifetime in the sub-nanosecond timescale, undergoing fast non-radiative decay back to $\mathbf{PC_{Ir}^{0}}$. In collaboration with Dr. Soranyel González from Prof. James Durrant's group, we also performed TAS measurements at the picosecond timescale. The negative bleaching of the $\mathbf{PC_{Ir}^{0}}$ signal detected is consistent with its disappearance after excitation. In addition, there is an overlapped positive signal. Since both transient signals disappear simultaneously in the 100 ps regime, recovering the $\mathbf{PC_{Ir}^{0}}$, we attribute the positive signal to the excited state absorption of $\mathbf{PC_{Ir}^{0*}}$. These experiments indicate that the lifetime of $\mathbf{PC_{Ir}^{0*}}$, in the other of 0.1 ns, what makes a diffusion SET event highly

improvable between the cloroanisole and $\mathbf{PC_{Ir}^{0*}}$.[54] Therefore, less conventional mechanisms need to be invoked.[55-59]

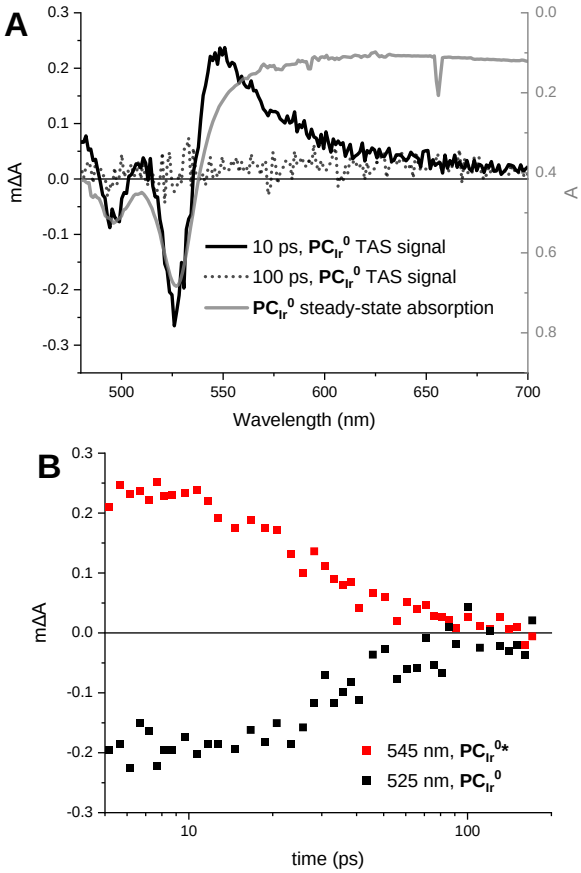

Figure 5.19. **(A)** Transient spectra (black trace) of $\mathbf{PC_{Ir}^{0}}$ after 10 (solid line) and 100 ps (dotted trace) of photoexcitation, overlapped with its negative steady-state absorption (grey) **(B)** Kinetics at 525 and 545 nm of $\mathbf{PC_{Ir}^{0}}$ in CH_3CN. Measurement conditions: $\mathbf{PC_{Ir}^{0}}$ was generated from $\mathbf{PC_{Ir}^{+}}$ (100 μM) in CH_3CN in the presence of TBA_2ox (1 mM) after 10 s of irradiation (5-200 ps).

One of the possible mechanisms that could match the sub-nanosecond lifetime of $\mathbf{PC_{Ir}^{0*}}$ is the formation of an electron donor-acceptor complex (EDA)[57, 60-63] between $\mathbf{PC_{Ir}^{0}}$ and chloroanisole. A ground state EDA complex can photo-trigger a SET that is not limited to the longer timescale of diffusion events. However, a chloroanisole excess (100 equiv.) does not induce any substantial change in the absorption or emission

spectra of $\mathbf{PC_{Ir}^0}$. Therefore, there are no signs of EDA complex formation with $\mathbf{PC_{Ir}^0}$ or $\mathbf{PC_{Ir}^+}$.

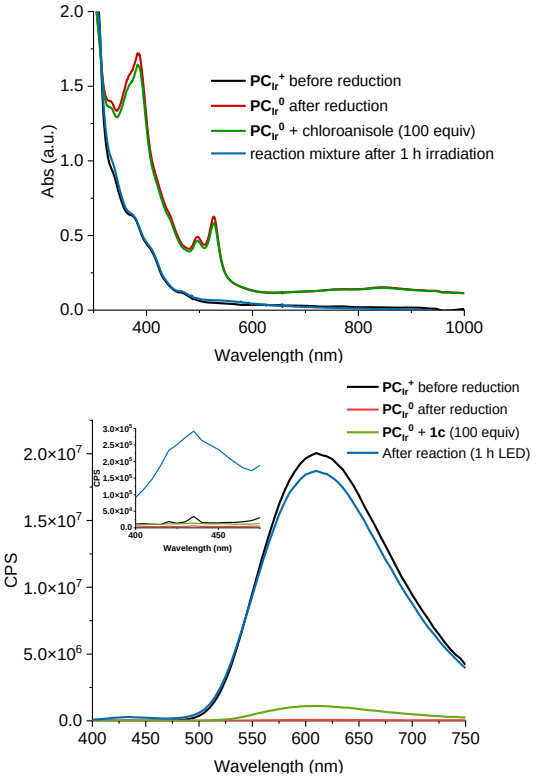

Figure 5.20. Evidence $\mathbf{PC_{Ir}^+}$ recovery after the reaction of $\mathbf{PC_{Ir}^0}$ with an excess of chloroanisole (**1c**, 100 equiv.) in CH_3CN, according to the absorption (top) and emission spectra (bottom) evolution.

Another possible mechanism that might be compatible with the sub-nanosecond lifetime of $\mathbf{PC_{Ir}^{0*}}$ is the photoinduced ejection of a solvated electron.[8, 64-66] Despite further studies on transient spectroscopy would be required to directly detect the solvated electron in acetonitrile,[14, 67, 68] we envisioned that the hypothetical electron should exhibit some reactivity. Indeed, solvated electrons have been studied in acetonitrile at 77 K, and they are known to enable the reductive cleavage of the C–CN bond of acetonitrile. The generation of either CN^- and $CH_3^\bullet$, or $CNCH_2^-$ and $H^\bullet$, unleashes HAT events.[69] In this way, H/D scrambling between CH_3CN and CD_3CN and the generation of CH_4 or H_2 could be symptomatic of a solvated electron. Indeed, 5 h

irradiation of a CD_3CN/CH_3CN (9:1) solution containing $\mathbf{PC_{Ir}^0}$ (300 μM) provoked scrambling, but no CH_4 or H_2 was observed by NMR spectra.

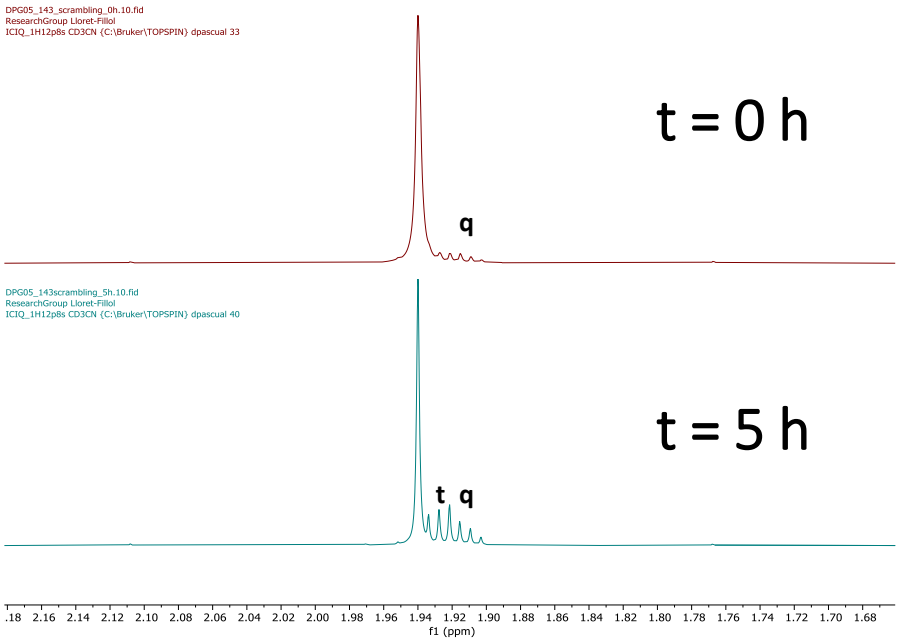

Figure 5.21. ^{1}H-NMR spectra (400 MHz, 8 scans) of $\mathbf{PC_{Ir}^0}$ (0.3 mM) after 0 h (top) and 5 h (bottom) of 447 nm irradiation in CD_3CN/CH_3CN (9:1) mixture.

We also identified the electronic transition that could unlock the unexplored reactivity of $\mathbf{PC_{Ir}^0}$. TD-DFT calculations performed by Dr. Sergio Fernández for $\mathbf{PC_{Ir}^0}$ in CH_3CN revealed valuable information. In the first place, electronic transitions involving the $bpy^{\bullet-}$ unpaired electron involve high energy orbitals inaccessible by the promotion of other electrons (137A, 140A in Figure 5.22). On the other hand, electronic transitions of lower energy electrons led to orbitals of similar energy to those accessible from $\mathbf{PC_{Ir}^+}$ under blue light irradiation. Second, the main electronic transitions for this unpaired electron are two: a low energy transition (686 nm in Figure 5.22, associated with the experimental band at 850 nm in Figure 5.1) and a higher energy transition calculated as 417 nm (associated with the experimental 450-525 nm bands, see Figure 5.1).

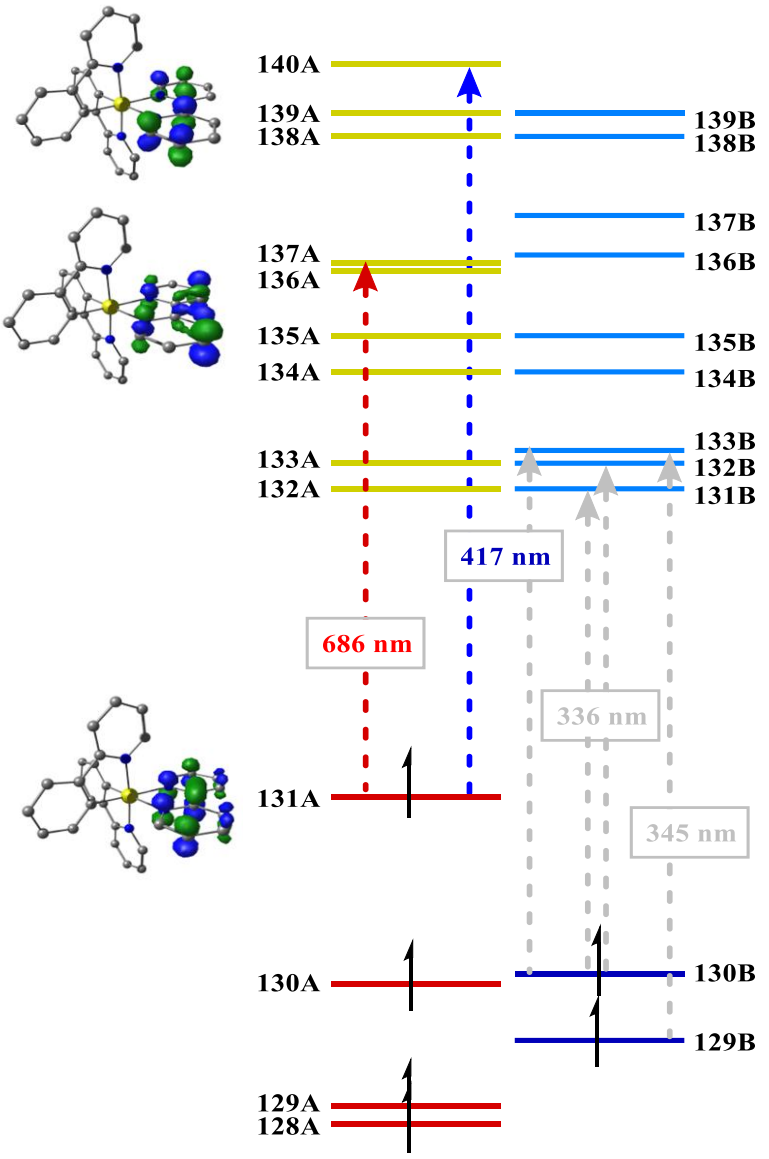

Figure 5.22. TD-DFT calculated by Dr. Sergio Fernández. Level of theory: cam-B3LYP (N = 22) using LANL2DZ for Ir and 6-31G* for C, N, H.

A priori, both transitions could be responsible for the reactivity since blue LEDs (447 nm) could populate both orbitals via direct excitation of the electron to 140A, or more likely by the subsequent relaxation event from 140A to 137A. As mentioned in Chapter 1, conventional photoexcitation processes are followed by relaxation to the lowest energy orbital from which reactivity occurs (Kasha rule). To test the behaviour

of our system, we repeated the dehalogenation of chloroanisole irradiating at different wavelengths (Table 5. 6). We found that 447 nm and 530 nm irradiation was able to photoinduced the reactivity of **PC$_{Ir}^0$**. In contrast, we did not observe reactivity when irradiating at 590, 660 and 850 nm.

Table 5.3. Reactivity of **PC$_{Ir}^0$** irradiating at different wavelengths.

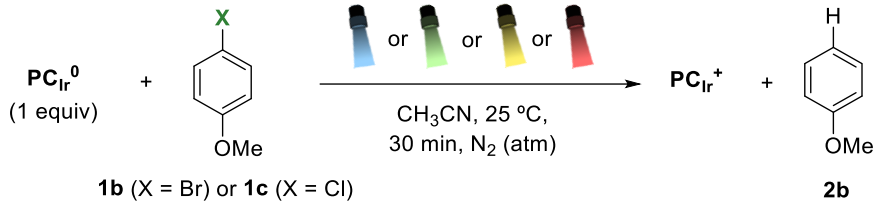

Entry	λ (nm)	Substrate	Conversion **1** (%)	Yield **2b** (%)
1	530	**1b**	6	56
2	530	**1c**	8	49
3	590	**1b**	1	0
4	590	**1c**	0	0
5	660	**1b**	0	0
6	660	**1c**	0	0
7	850	**1b**	4	0
8	850	**1c**	0	0

Standard conditions: **PC$_{Ir}^+$** (0.3 mM), **1** (3 mM) in CH_3CN (0.44 mL) at 25 °C under N_2, irradiating at different wavelengths for 30 minutes. Yields were determined by GC analysis relative to a calibrated internal standard.

Therefore, the excitation on the broad bands at 700-1100 nm is not productive for dechlorination. This means that the excited state responsible for the reactivity is not the lowest in energy (anti-Kasha process[70, 71]), and according to our TD-DFT we should invoke an unusual highly energetic π(bpy)-π*(bpy) transition,[66] corresponding with the absorption bands at the region of 450-550 nm.

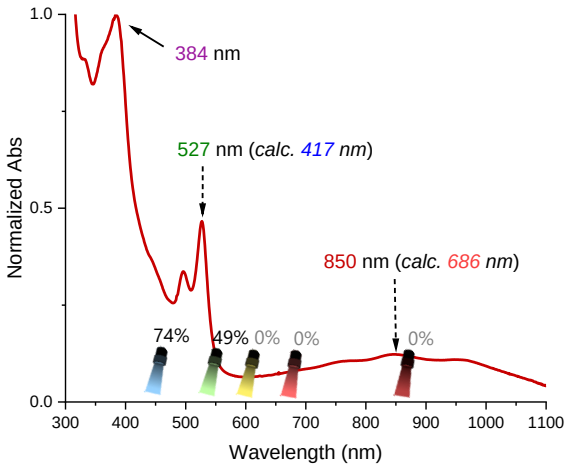

Figure 5.23. Experimental absorption spectrum of $\mathbf{PC_{Ir}^{0}}$ in CH_3CN with a summary of the measured and TD-DFT calculated absorption maxima. Coloured torches indicate the yields for chloroanisole dehalogenation when irradiating with different LEDs wavelengths (447, 530, 590, 660 and 850 nm).

5.2.8. The bpy role in $\mathbf{PC_{Ir}^{0}}$.

The previously discussed UV-vis spectrum obtained from TD-DFT calculations suggests that the reactivity of $\mathbf{PC_{Ir}^{0*}}$ comes from a transition between orbitals located in the $\mathbf{bpy^{\bullet-}}$ ligand. Moreover, a similar transition has been described for $\mathbf{bpy^{\bullet-}}$ by Noble and Peacock.[19] Therefore, we hypothesized that the $\mathbf{bpy^{\bullet-}}$ could have the same reactivity without iridium,[65, 66] and we studied the dehalogenation of chloroanisole again, with $\mathbf{bpy^{\bullet-}}$ (Table 5. 4, entry 1). To our delight, 22% of dehalogenation was observed at [$\mathbf{bpy^{\bullet-}}$] (15 mM) under blue light irradiation, which slightly increased to 30% using [$\mathbf{bpy^{\bullet-}}$] (90 mM), while no anisole was observed under darkness. The higher reactivity of $\mathbf{bpy^{\bullet-}}$ exited state at higher concentrations was attributed to the high instability of $\mathbf{bpy^{\bullet-}}$, which even reacts with CH_3CN (see below). The $\mathbf{bpy^{\bullet-}}$ can access this productive

transition also by irradiating at 530, 590 and 660 nm, but not at 850 nm. In the reactions, a colour change from wine to yellow was already observable at 30 min (Figure 5.24).

Table 5. 4. Reactivity of **bpy**$^{\bullet-}$ irradiating at different wavelengths.

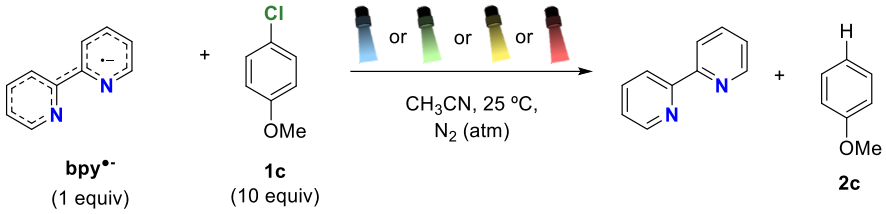

Entry	[**bpy**$^{\bullet-}$] (mM)	Reaction time (min)	Wavelength (nm)	Yield **2c** (%)
1	0.3	2160	447	0
2	3	2160	447	5
3	15	30	447	21
4	15	720	447	22
5	90	30	447	30
6	90	30	530	28
7	90	30	590	26
8	90	30	660	22
9	90	30	850	0
10	15	2160	darkness	0

Standard conditions: **bpy**$^{\bullet-}$ (variable concentration), **1c** (10 equiv.) in CH_3CN (0.1 mL) at 25 °C under N_2 under light irradiation. Yields were determined by GC analysis relative to a calibrated internal standard.

These results also match the previous observations in which an unproductive transition is associated with the high energy band (700-100 nm) while irradiation at the higher energy bands (450-700 nm) unlocks the desired anti-Kasha reactivity.

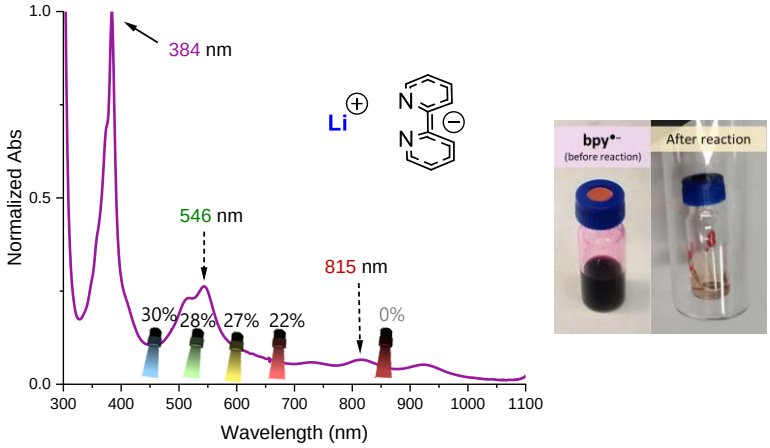

Figure 5.24. Left) **bpy**$^{\bullet-}$ normalized absorption spectrum in CH_3CN. Coloured torches indicate the irradiating wavelengths (447, 530, 590, 660 and 850 nm), and the values are the chloroanisole dehalogenation yields. Right) pictures of GC-vials with **bpy**$^{\bullet-}$ in CH_3CN before (wine colour) and after (yellow) 30 min of irradiation to illustrate the colour change.

It was surprising that the yield did not progress over time. Careful analysis of the GC-MS chromatograms revealed a signal corresponding with a mass of 82 g/mol. This value matches with 3-aminocrotonitrile (**3a**). The reaction repeated in the absence of substrate yield and ^{1}H-NMR of the crude consistent with compound **3a,** as a mixture of E/Z diastereomers. **3a** was also found under darkness after long reaction time (Experimental Section, Figure 5. 59 -Figure 5. **61**). The **3a** estimated yield by ^{1}H-NMR reaches up to 158%, meaning that the role of **bpy**$^{\bullet-}$ is catalytic due to its highly basic character and not because of the photochemical reactivity. Hence, **bpy**$^{\bullet-}$ cannot be very

productive for dehalogenation in CH_3CN and the best option is to change to another solvent.

Table 5.5. Reactivity of **bpy$^{\bullet-}$** with acetonitrile.

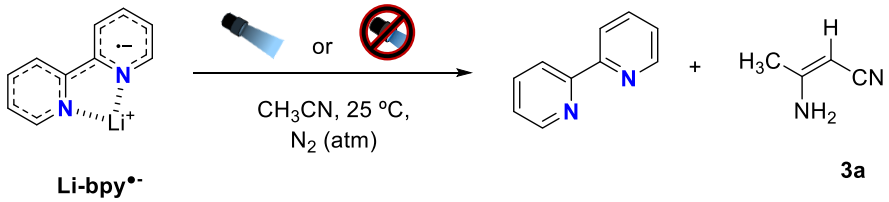

Entry	Irradiation	Reaction time (h)	Yield **3a** (%)
1	-	0	0
2	yes	1	66
3	yes	36	158
4	no	1	28
5	no	36	110

Standard conditions: **bpy$^{\bullet-}$** (15 mM), in CH_3CN (1.5 mL) at 25 °C under N_2 under light irradiation or darkness (covered with aluminium foil). Yields were estimated by ^{1}H-NMR, taking bipyridine as the internal standard.

THF as solvent is a good candidate since it solubilizes the bipyridine salt and should be stable to the basicity of the **bpyLi** salt.[19] To our delight, the chloroanisole was smoothly dehalogenated (up to 77% yield after 36 h) when **bpy$^{\bullet-}$** (0.3 mM) was irradiated, and no product was observed under dark.

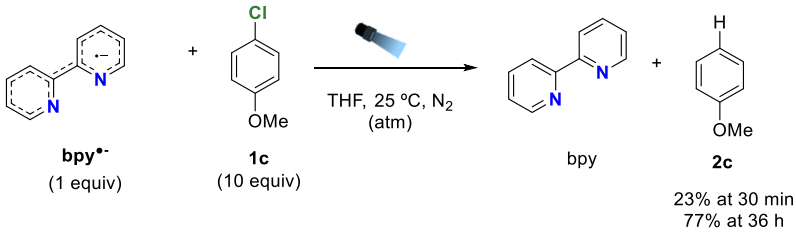

Scheme 5.9. Reactivity of **bpy$^{\bullet-}$** with chloroanisole in THF.

5.2.9. From stoichiometric to catalytic: the role of sacrificial ED

Encouraged by the highly reductive power of the system, we anticipated that **PC$_{Ir}^0$** should be recyclable from **PC$_{Ir}^+$** in the presence of a suitable source of electrons. (Scheme 5.11, left cycle). The first photon produces the **PC$_{Ir}^+$** excitation with further reductive quenching with the sacrificial ED to form **PC$_{Ir}^0$**, while a second photon should promote the electron transfer from **PC$_{Ir}^0$** to the substrate. On the other hand, if using a more

potent reductant, the transformation of $\mathbf{PC_{Ir}^{+}}$ to $\mathbf{PC_{Ir}^{0}}$ can occur without the need of the first photon (right cycle).

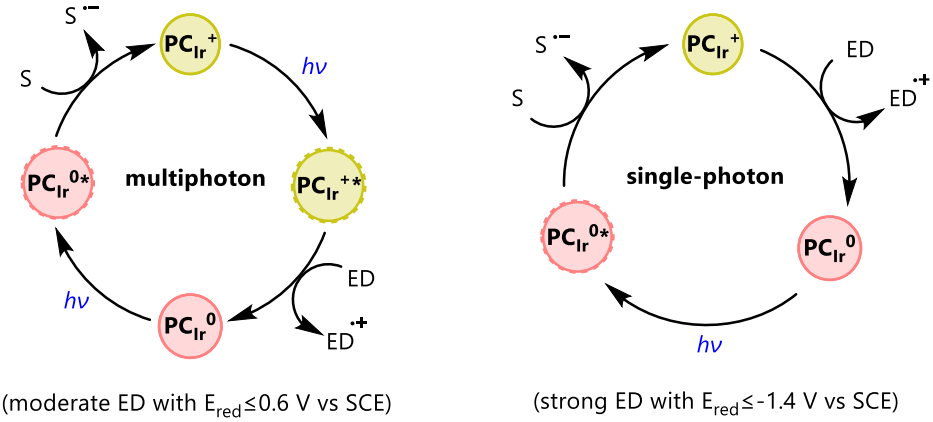

Scheme 5.10. Proposed photochemical mechanisms in which $\mathbf{PC_{Ir}^{0}}$ can be catalytically profitable.

The utilization of a sacrificial ED involves two main challenges. On the one hand, the oxidized $\mathbf{ED^{\bullet+}}$ can undergo back electron transfer processes (BET) to recover the ED and $\mathbf{PC_{Ir}^{+}}$. This unproductive process, already possible from $\mathbf{PC_{Ir}^{0}}$, could be much more favoured from the extreme reductant $\mathbf{PC_{Ir}^{0*}}$. Therefore, catalysis will be frustrated if $\mathbf{PC_{Ir}^{0*}}$ reacts faster with $\mathbf{ED^{\bullet+}}$ than with the substrate. On the other hand, common electron donors evolve into radical species that participate in other processes, such as XAT or HAT (*vide supra*). Side reactivity can be profitable from some methodologies, but it complicates the mechanistic study. In particular, alkyl amines are among the most common sacrificial agent for reductive photochemistry, but we proved that triethylamine is inappropriate (Table 5. **10**, entry 21). This is probably due to the formation of radicals derived from tertiary amines that favour the partial hydrogenation of the bpy ligand.[5] If the bpy ligand is hydrogenated[5] or substituted by other ligand,[2] the herein described bpy-bpy transition is eliminated and the PC cannot reduce substrates as inactivated as **1c**. Moreover, in the presence of Et_3N, the ancillary bpy ligand of different PC can also be released to form $Ir(ppy)_2(CH_3CN)_2^{+}$ at relatively short times (in Experimental Section, Figure 5. 65 and Figure 5. 70).[72] This species is not photoactive (in Experimental Section, Figure 5. 71), but its participation in chemical transformations cannot be discarded.

Alternatively, **$\mathbf{TBA_2ox}$** is a practical ED for synthesising $\mathbf{PC_{Ir}^{0}}$. The catalytic system operates up to TON value of 4.3. However, since it has been reported that $\mathbf{CO_2^{\bullet-}}$ can

also cleave inactivated carbon-halide bonds,[25, 44] we cannot prove that the observed reactivity is based on the $\mathbf{PC_{Ir}^0}$.

Table 5.6. Photocatalytic activity of $\mathbf{PC_{Ir}^+}$ with different electron donors (ED).

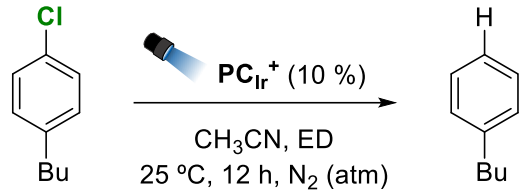

1e, 3 mM **2e**

Entry	ED	ED (mM)	Conv (%)	Yield (%)
1	none	0	0	0
2	NEt_3	100	5	4
3	TAEA	100	7	7
4	TBA_2ox	10	57	43
5	$CoCp^*_2$	10	99	68

Standard conditions: $\mathbf{PC_{Ir}^+}$ (0.3 mM), **1e** (3 mM) and ED (100 or 10 mM) in CH_3CN (0.44 mL) at 25 °C under N_2. Irradiated for 12 h (447 nm). Yields were determined by GC analysis relative to a calibrated internal standard.

On the other hand, we have tried to use a strong enough reductant to accumulate $\mathbf{PC_{Ir}^0}$ (right catalytic cycle in Scheme 5.11, for ED with $E_{ox} < -1.4$ V). The reactivity should also be accessible, and the unproductive BET should not be favoured. To avoid the generation of organic radicals, we selected decamethylcobaltocene (**$CoCp^*_2$**). In collaboration with Marina D'Ottavio, initial experiments indicated that **$CoCp^*_2$** could exhibit a suitable role as a sacrificial electron donor for the model reaction (Table 5.7, entry 2). However, blank experiments revealed that **$CoCp^*_2$** is not an innocent source of electrons, since the dehalogenation product was also observed when irradiating **$CoCp^*_2$** in the absence of $\mathbf{PC_{Ir}^+}$ (entry 3). This unexpected result can motivate to explore cobaltocene derivatives,[73-75] for photochemical transformations.[76]

Table 5.7. Preliminary studies of the photochemical activity of **CoCp*$_2$**.

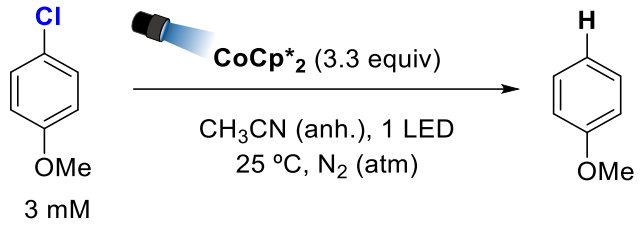

Entry	Changes	Wavelength (nm)	Conv (%)	Yield (%)
1	**PC$_{Ir}^+$** (0.1 equiv)	447	58	47
2	**PC$_{Ir}^+$** (0.1 equiv), 12 h	447	99	68
3	-	447	100	46
3	-	No light	0	0
5	60 °C	447	100	50
6	60 °C	No light	0	0

[a]Standard reaction conditions: **CoCp*$_2$** (3.3 equiv), Subs. (3 mM) in anhydrous CH_3CN (1 mL) irradiated (447 nm) for 1 hour at 25 °C under N_2. Yields after workup (average of duplicates) determined by GC analysis relative to the calibrated internal standard.

We notice that **CoCp*$_2$** is playing a different role than **PC$_{Ir}^0$**. We also confirmed that its reactivity is not thermal but photochemical (Table 5.7, entries 5-6 and in Experimental Section, Figure 5. 94), and that the reactivity does not come from the $[Cp^*]^-$ ligand or from the cobalt itself (in Experimental Section, Table 5. 13). Moreover, the reagent was proven to be highly reactive under irradiation not only for reductive chemistry but also for a novel redox-neutral reaction as the double addition of CH_3CN to 4-phenylbutan-2-one in a deoxygenative fashion (Scheme 5.11). These results illustrate that the excitation of **CoCp*$_2$** can unlock very interesting reactivity.

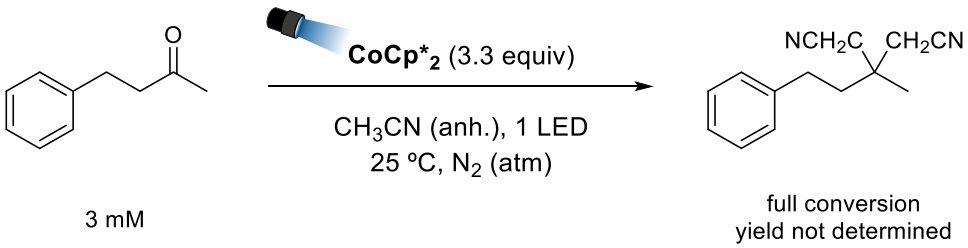

Scheme 5.11. Deoxygenative double addition of CH_3CN to 4-phenylbutan-2-one (**5d**).

5.2.10. Removing the sacrificial ED: Electrophotocatalysis

Given that sacrificial electron donors introduce uncertainty to the mechanistic picture, we envisioned that electrophotochemistry should provide adequate conditions for catalysis. Furthermore, this approach can unlock challenging redox transformations without sacrificial agents. Indeed, electrophotochemistry has been reported by organic catalysts to be very efficient.[47, 48, 55, 77] Our hypothesis is also supported by the reversible accumulation of $\mathbf{PC_{Ir}^0}$ in the spectroelectrochemical cell (in Experimental Section, Figure 5. 41).

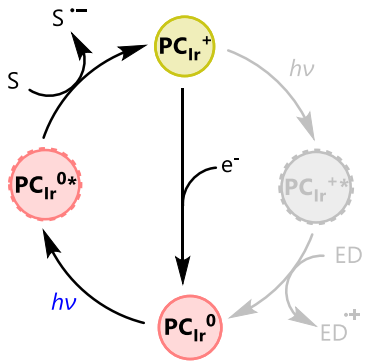

Scheme 5.12. Proposed catalytic electrophotochemical mechanism with $\mathbf{PC_{Ir}^0}$.

With this aim, in collaboration with Dr. Sergio Fernández and Dr. Geyla Dubed, we initially verified that there is no organic transformation when performing a controlled potential electrolysis at an applied potential of -1.5 V *vs* SCE to accumulate a stoichiometric amount of $\mathbf{PC_{Ir}^0}$ in the presence of 10 equivalents of **1e** (

Figure 5. **25**, the initial white region in the graph). Next, in this same experiment, electrodes are disconnected; no potential is applied, and then the solution was irradiated, resulting in 78% of **2e** dehalogenated (TON = 0.78, blue region in the graph). To confirm the recyclability, the same solution was exposed again to sequential

electrochemical reduction followed by irradiation, giving rise to an additional 84% yield ($TON_{(total)}$ = 1.62) which successfully goes beyond the stoichiometric threshold.

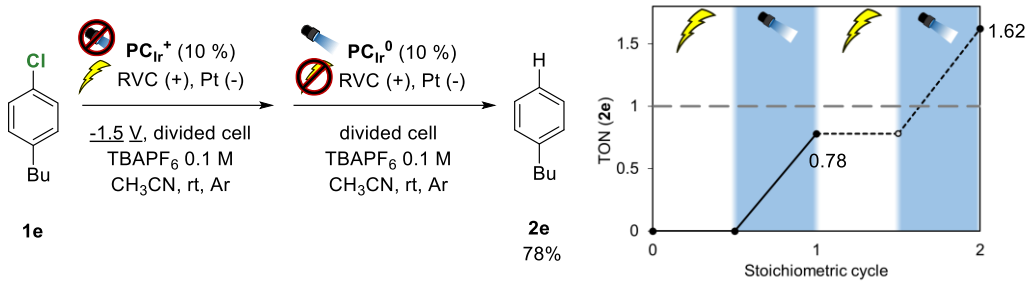

Figure 5. 25. Consecutive two-sequential stoichiometric experiments (first step: reduction under darkness; second step: irradiation with disconnected electrodes) demonstrating the recyclability of **PC$_{Ir}^{0}$**. Blue background areas indicate irradiation cycles, and white background areas indicate non-irradiation periods.

This last experiment strongly indicates that **PC$_{Ir}^{+}$** is a good candidate for electrophotocatalytic reductions. Next, we moved to the target reaction, where the electric bias and the LED source are turned on simultaneously. Under those conditions, the system exhibits catalysis without further optimization (TON (**2e**) = 5.5, and TON (**2c**) up to 6.3). Moreover, the observed reactivity follows a redox limit that agrees with our stoichiometric experiments since substrate **1d** afforded only 5% of transformation. Finally, as a blank, no dehalogenation of chloroanisole was observed in the absence of iridium by applying the same potential range (corrected *vs* Fc^{+}/Fc couple) and irradiation.

Table 5.8. Electrophotocatalytic experiments in the presence of different aryl chlorides.

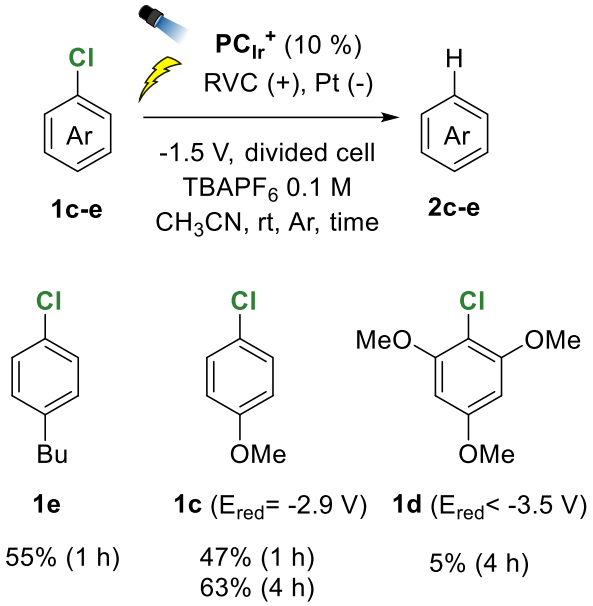

Standard conditions: **PC$_{Ir}^+$** (0.3 mM), **1e** (3 mM) in CH_3CN (4 mL) with $TBAPF_6$ (0.1 M) at 25 °C under Ar. Irradiated with 16 LEDs (447 nm). Yields were determined by GC analysis relative to a calibrated internal standard.

An unexpected observation was related to the colour changes during the catalytic reactions. In the stoichiometric experiment, electrochemical reduction with the substrate (no irradiation) transforms the yellow solution into orange (characteristic change from **PC$_{Ir}^+$** to **PC$_{Ir}^0$**, see Figure 5.2 and Figure 5.26), and after the consecutive irradiation, the yellow colour is recovered (from **PCIr^0** to **PC$_{Ir}^+$**). However, the simultaneous application of a fixed potential and irradiation results in intense dark colour. Moreover, after exposition to air for 5-10 minutes, the dark solution becomes yellow again.

Figure 5.26. Pictures of the electrochemical setup illustrating the colour of the reaction mixture (a) before applying any potential (yellow solution), (b) after applying a potential until reaching a plateau of transmitted electric current (orange solution), (c) after electrophotocatalytic experiment (dark solution).

We also tried the electrophotocatalytic dehalogenation using bipyridine (E_{red} = -2.2 V). Applying a -2.3 V fixed potential and light irradiation did not produce dehalogenation. It could be possible that the low concentration **bpy**$^{\bullet-}$ is quickly consumed by the solvent (CH_3CN), producing 3-aminocrotononitrile. Still, in a stoichiometric experiment at a higher concentration ([bpy] = 15 mM), 8% of dehalogenation was observed. As mentioned before, studies in THF could help control the reactivity of bpy$^{\bullet-}$, and will be performed in the future. Further optimization is required to unlock the productive use of bpy as a catalyst for highly reductive transformations, as we have found for **PC$_{Ir}^{+}$**. However, we envision that similar systems containing bpy units can also be used at milder applied potentials,[65, 77] and the present work opens the door to the reactivity of reduced intermediates.

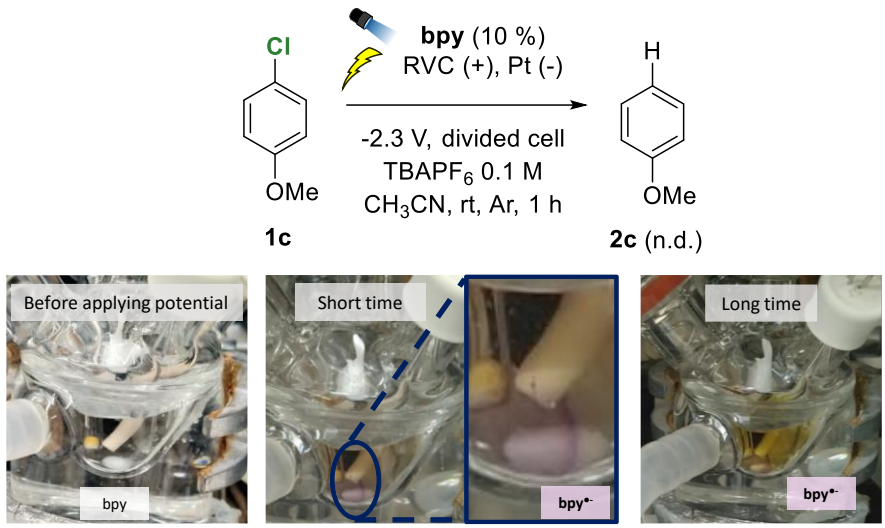

Figure 5.27. Electrophotocatalytic dechlorination using bpy as a catalyst in acetonitrile. Pictures of a non-irradiated experiment, a purple gradient precedent from the reduction in the electrode foam, but it quickly vanishes in bulk, which gets more and more yellow with time, consistent with the accumulation of 3-aminocrotononitrile.

5.3. Conclusions

Although iridium complexes are well-established photoredox catalysts, the reduced intermediate after reductive quenching has never been isolated, and indirect studies have led to mechanistic controversy during the last years. Herein, we have unambiguously determined the structure of the reduced [Ir(bpy)(ppy)$_2$]^0 (**PC$_{Ir}^0$**) and the homologous [Ir(bpy)(^{Me}ppy)$_2$]^0 (**^{Me}PC$_{Ir}^0$**). This has allowed us to confirm that the unpaired electron is mainly located at the bipyridine ligand, in agreement with the shortening in the C–C bonds between the pyridine rings. Moreover, **PC$_{Ir}^0$** was obtained photochemically by reductive quenching by **PC$_{Ir}^0$** with tetrabutylammonium oxalate, and isolated, crystalized, and the X-ray structure resolved.

Direct measurements have allowed us to confirm previously reported spectroscopic information such as absorption or EPR spectrum. The absence of emission or the ps-lifetime of **PC$_{Ir}^{0*}$** in acetonitrile suggested a mechanism that should not be controlled by diffusion.

The stoichiometric reactivity of the ground and exited states is a precedent for other photocatalytic systems. For instance, to evaluate the effect of additives in solution or to

corroborate the existence of EnT *vs* ET processes. Indeed, ur studies cannot conclude yet which is the particular mechanism operative under this reactivity, and our current understanding points towards the formation of solvated electrons more than an electron donor-acceptor complex.

TD-DFT calculations allowed us to note that the transition responsible for this reactivity is a bpy-bpy transition associated with the absorption bands at 450-550 nm, and not with lower energy transitions as the Kasha rule generally dictates. This is strongly supported by the unprecedented reactivity of **bpy$^{\bullet-}$**, which could also reduce chloroanisole by irradiating the broad active band in the region from 450 to 660 nm.

Finally, we developed electrophotocatalytic reaction with **PC$_{Ir}^{+}$** as a suitable catalyst, as illustrated in the dehalogenation of unactivated aryl chlorides (E_{red} up to -2.9 V *vs* SCE). We envision that the reactivity of **PC$_{Ir}^{0}$** could extend to other complexes, including simple bpy derivates, and shed light on the previous mechanistic ambiguity.

5.4. Experimental section

5.4.1. General Experimental details

All procedures were carried out under N_2 using standard vacuum Schlenk line, and inert atmosphere glovebox techniques. Reagents and solvents were purchased from commercial sources as used as received unless otherwise stated. [Ir(bpy)(ppy)$_2$]PF$_6$ (**PC$_{Ir}^{+}$**), [Ir(bpy)(Meppy)$_2$]PF$_6$ (**^{Me}PC$_{Ir}^{+}$**), and [Ir(tbbpy)(ppy)$_2$]PF$_6$ (**^{tBu}PC$_{Ir}^{+}$**) were synthesized according to literature procedures.[78, 79] Tetrabutylammonium oxalate (TBA_2ox) was synthesized following a reported procedure.[80] Triethylamine anhydrous (≥99%, NEt_3) was purchased from Sigma Aldrich and deoxygenated before preparing the samples. Anhydrous CH_3CN was purchased from Sigma Aldrich and further deoxygenated by freeze-pump-thaw cycle. All the solvents were strictly degassed and stored in anaerobic conditions. The synthesis of air sensitive compounds as well as the preparation of visible light photocatalytic reactions were conducted inside a nitrogen-filled glove box (mBraun Unilab) with concentrations of O_2 and H_2O lower than 0.5 ppm and using Schlenk techniques under argon atmosphere.

5.4.2. Instruments

Spectroscopic methods

The solution of $[Ir(ppy)_2(bpy)](PF_6)$ (**PC_{Ir}^+**) was prepared in neat CH_3CN solvent. The reference cuvette was used with the same solvent. UV-Vis measurements were carried out on a Shimadzu UV-2401PC spectrophotometer equipped with a photomultiplier detector, double beam optics and D_2 and W light sources. The absorption kinetics were studied on an Agilent 8453 diode array spectrophotometer (190–1100 nm range) in 1 cm quartz cells. A cryostat from Unisoku Scientific Instruments was used for the temperature control under inert atmosphere.

UV-Vis measurements with on-line irradiation

The UV-Vis measurements with on-line irradiation were performed on a self-made apparatus using 1 cm quartz fluorescence cuvette in a fluorescence cuvette holder. LED (Royal blue, 447 nm) was placed perpendicular to the optical pathway of Agilent 8453 diode array spectrophotometer (190-1100 nm range). A cryostat from Unisoku Scientific Instruments was used for the temperature control.

Luminescence measurements

Fluorescence measurements were carried out on a Fluorolog Horiba Jobin Yvon spectrofluorimeter equipped with photomultiplier detector (or InGaAs if using the nitrogen cooled detector), double monochromator and Xenon light source. Sample preparation was same as that of absorption experiments in 1 cm quartz cells.

Electrochemistry

All the electrochemical experiments were carried out with a VSP potentiostat from Bio-Logic, equipped with the EC-Lab software. A double-wall jacketed single-compartment cell was used. It was filled with Ar $TBAPF_6/CH_3CN$ (0.1 M) electrolyte solutions of the complex under study.

For Cyclic Voltammetry (CV) measurements, 1 mm diameter glassy carbon (GC) disks were used as working electrodes, a Pt wire as a counter electrode and an Ag/AgCl wire as pseudo-reference, immerged in a bridge tube containing the same electrolyte solution (0.1 M, $TBAPF_6/CH_3CN$) and separated from the working solution by a porous tip. Ferrocene (Fc) was used as an internal standard and all the potentials were referenced vs. the $Fc^{+/0}$ redox couple, then converted to reference *vs* SCE.

For Controlled-Potential electrolysis (CPE), the cathodic compartment of an H-type electrochemical cell was filled with 4 ml of $TBAPF_6/CH_3CN$ (0.1 M) solution of the catalyst, is maintained under constant stirring in the course of the experiment. Reticulated Vitreous Carbon (RVC, ERG Materials and Aerospace, 80 ppi) was used as a working electrode, and an Ag/AgCl wire as a pseudo-reference, immerged in a bridge tube filled with the same electrolyte solution (0.1 M, $TBAPF_6/CH_3CN$) and separated

from the working solution by a porous tip. The redox potential of the $Fc^{+/0}$ couple was checked in a separate cell prior to and after electrolysis.

Spectroelectrochemistry (SEC)

SEC experiments were performed by using a SP-50 potentiostat from Bio-Logic. Under an inert (N_2) atmosphere, a 1 mM solution of complex in $TBAPF_6/CH_3CN$ (0.1 M) filled an optically transparent thin-layer electrode (OTTLE) cell, equipped with a Pt minigrid working and auxiliary electrodes, an Ag microwire pseudo-reference electrode and a CaF_2 window. Blank $TBAPF_6/CH_3CN$ (0.1 M) solutions were used for solvent subtractions.

Gas chromatography analysis

The analysis and quantification of the starting materials and products were carried out on an Agilent 7820A gas chromatograph (HP5 column, 30m or Cyclosil-B column, 30m) and a flame ionization detector. GC-MS spectral analyses were performed on an Agilent 7890A gas chromatograph interfaced with an Agilent 5975c MS mass spectrometer.

Transient Absorption Spectroscopy (ns)

Laser flash photolysis experiments in ns time scale were carried out by using the third harmonics (355 nm) of a pulsed Nd-YAG laser from Quantel as a pump source. The single pulses were ca. 10 ns duration and the energy of the laser beam was 2 mJ/pulse. A pulsed xenon lamp was employed as the monitoring light source. The signal from the monochromator/photomultiplier detection system was captured by a Yokohama DLM2052 oscilloscope. The output signal from the oscilloscope was transferred to a personal computer for study. Samples were prepared in 1x1 cm cells quartz and were deaerated with dry nitrogen prior to use.

The studies of transient absorptions at micro-milisecond timescale were carried out by the same pump source used in the nanosecond system, but employing a different optical workbench. A highly stable 150 W tungsten lamp (400-950 nm) combined with two monochromators Minuteman MM151, were used as probe light. The two monochromator setup with single wavelength detection was chosen to minimize the sample's exposure to probe light and to remove most of the phosphorescence emitted by the photosensitizer. The detection part consists in a silicon photodiode (Hamamatsu S3883) and a homebuilt current amplifier. A homebuilt FPGA datalogger allows to register data frames of 200 ms at 200MS/s with 16 bit of resolution. Thereafter, there is a decimation process that consists on downsampling at different time intervals (1 ms, 10 ms and 100 ms). In this manner, all time resolution was kept up to 1 ms and

progressively reduced at the cue part. The sample was stored in a sealed 10 mm quartz cuvette. For each single wavelength, kinetic traces were recorded after an average of 100 laser shots.

Transient Absorption Spectroscopy (ps)

The investigated samples were prepared under N_2 atmosphere in a glovebox, and contained 100 µM of the corresponding iridium complex in CH_3CN and 1 mM TBA_2ox. The samples were irradiated for 10 s with a homemade LED photoreactor (Royal Blue, 447 nm). For the samples containing 15 mM NEt_3, it was added using Schlenk techniques out of the glovebox, and those samples were not irradiated with LED.

The picosecond to nanosecond transient absorption measurements were done with a Helios setup from Ultrafast Systems, with excitation pulses (92 fs, 355 nm, ~2 µJ/cm2) hitting the sample at a repetition rate of 1 kHz. Both the pump and the probe beams originated from an 800-nm seed beam produced by a regeneratively amplified Ti:sapphire laser (Solstice, Spectra-Physics), which was split into the probe and the pump beams by a semi-transparent mirror. The wavelength of the pump beam was tuned with an optical parametric amplifier (TOPAS Prime, Light Conversion) and a frequency mixer (NirUVis, Light Conversion). The power of the laser pulses was measured with an Ophir Photonics PE9 energy meter.

Electronic paramagnetic resonance (EPR)

An EMX Micro X-band EPR spectrometer from Bruker was used to collect the data using a finger dewar for measurements at 77 K. Data was acquired in perpendicular mode with a modulation frequency of 100 KHz, a modulation amplitude of 10 G, a 5.1 ms time constant and 21.4 ms conversion time and a microwave power of 0.18 mW. Spectra was simulated using the EasySpin software package.

Nuclear magnetic resonance (NMR)

NMR spectra were recorded on Bruker Fourier300, AV400, AV500 and AVIII500 spectrometers using standard conditions (300 K). All 1H chemical shifts are reported in ppm and have been internally calibrated to the residual protons of the deuterated solvent. The 13C chemical shifts have been internally calibrated to the carbon atoms of the deuterated solvent. The coupling constants were measured in Hz.

Mass Spectrometry

High resolution Mass Spectrometry (HRMS) data was collected on a HPLC-QqTOF (Maxis Impact, Bruker Daltonics) or HPLC-TOF (MicroTOF Focus, Bruker Daltonics) mass spectrometer using 1 mM solution of the analyzed compound.

5.4.3. In-house developed parallel photoreactor

The reactions were performed using LUXEON Rebel ES LED, mounted on a 20 mm Square Saber - 1030 mW @ 700mA (Datasheet: https://www.luxeonstar.com/assets/downloads/ds68.pdf) as a light source. Reaction temperature was controlled by a high precision thermoregulation Hubber K6 cryostat. Likewise, aiming for a stable irradiation the temperature of the LEDs was controlled and set at 22 ºC.

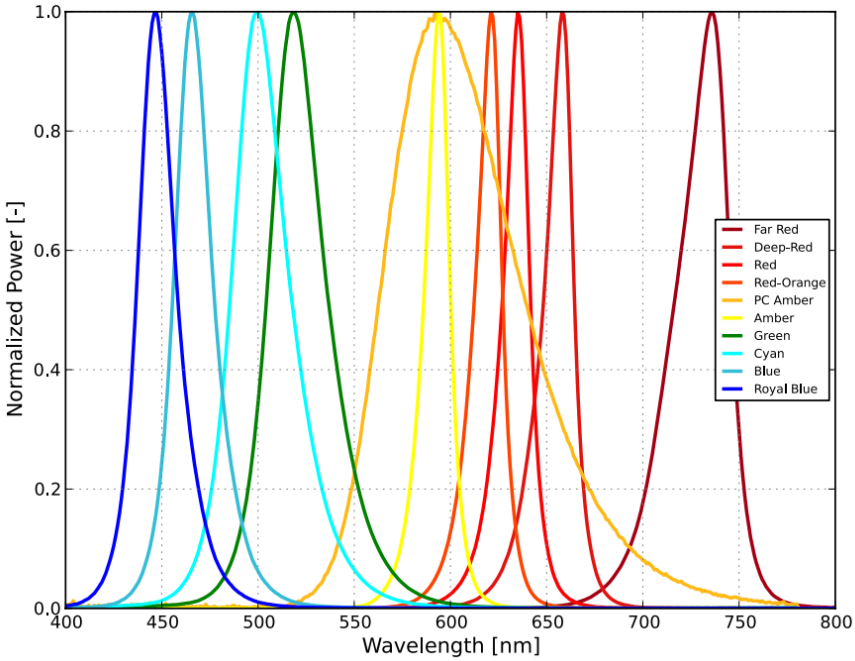

Figure 5. 28. Normalized power *vs* wavelength range for LUXEON Rebel LEDs at 25 ºC.

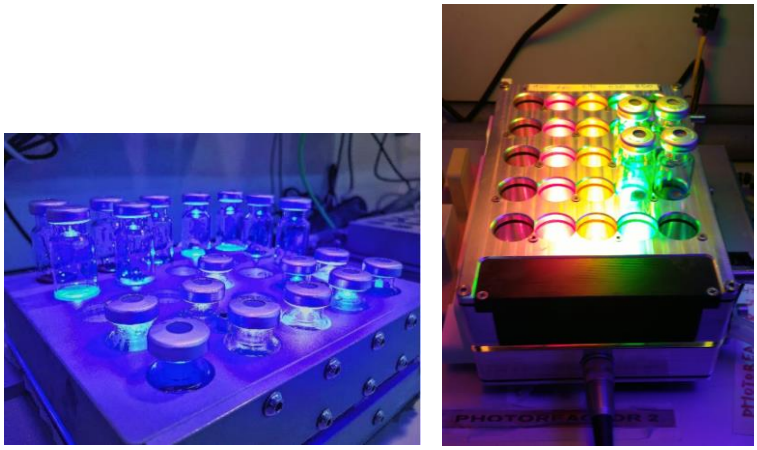

Figure 5. 29. In-house developed parallel photoreactors with 25 positions for vials of 10 or 21 ml.

5.4.4. Procedures for the synthesis of the reduced intermediate

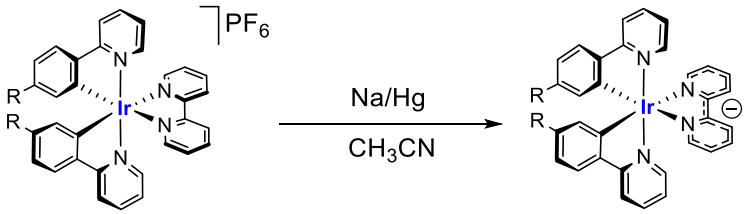

Procedure I. Isolation of reduced PC by chemical electron transfer: An overnight oven-dried reaction vial is introduced to the glovebox to weigh on it **PC$_{Ir}^+$** (1 equiv, 12.5 μmol, 10.0 mg) or **^{Me}PC$_{Ir}^+$** (1 equiv, 12.5 μmol, 10.4 mg) and Na/Hg alloy (1.15 equiv, 14.37 μmol, 33.0 mg), to finally add 1 ml of anhydrous CH_3CN and stir for 1 minute. The dispersion containing the precipitate is removed from the metallic sphere and transferred to a second dry vial. To clean leftover iridium from the Na/Hg alloy, stir 0.2 ml of additional CH_3CN and then transfer the fresh dispersion to the second vial. To remove CH_3CN from the dispersed **PC$_{Ir}^0$**, filter using a teflon cannula. Wash the powder three times with minimal amount of CH_3CN (around 0.2 ml), and inject some volume of nitrogen to dry the collected powder, which can also be dried in the prechamber for about 3 minutes and weighed (6.2 mg, 75 % for **PC$_{Ir}^0$**, and 5.5 mg, 64 % for **^{Me}PC$_{Ir}^0$**).

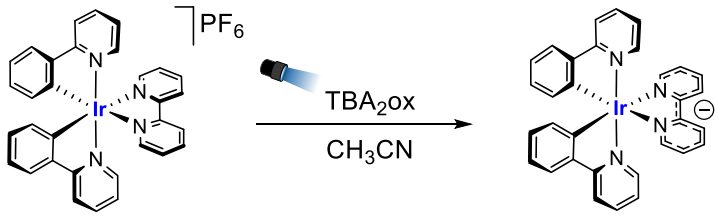

PC_{Ir}^{+} PC_{Ir}^{0}, 84 %

Procedure II. Isolation of reduced PC by photochemical electron transfer: An overnight oven-dried reaction vial is introduced to the glovebox to weigh on it $\mathbf{PC_{Ir}^{+}}$ (1 equiv, 12.5 µmol, 10.0 mg) and 1.5 equiv of TBA_2ox (18.75 µmol, 10.7 mg), to finally add 1 ml of anhydrous CH_3CN and stir for 30 seconds irradiating with a kessyl lamp while stirred. To remove CH_3CN and tetrabutylammonium salts from the dispersed $\mathbf{PC_{Ir}^{0}}$, filter using a cannula. Wash the powder three times with minimal amount of CH_3CN (around 0.2 ml), and inject some volume of nitrogen to dry the collected powder, which can also be dried in the prechamber for about 3 minutes and weighed (6.9 mg, 84 %). At this step, NMR in degassed anhydrous CD_3CN can confirm that there are no more tetrabutylammonium signals.

Procedure III. Crystallization of reduced PC: In a glovebox, $\mathbf{PC_{Ir}^{0}}$ or $\mathbf{^{Me}PC_{Ir}^{0}}$ powder is dissolved in the minimum amount of degassed pyridine to be transferred to an NMR tube. Carefully add a top layer of diethyl ether and leave closed for some days until red-brown crystals are obtained.

Procedure IV. Crystallization of $\boldsymbol{^{Me}PC_{Ir}^{+}}$: we found that $\mathbf{^{Me}PC_{Ir}^{+}}$ crystal structure was not reported and we screened multiple solvents for its recrystallization in a GC-vial with a needle for slow evaporation. Despite the crystals obtained with some of the solvents decomposed when diffracting at low temperature (crystals in methanol), evaporation of dichloroethane resulted in successful orange crystals stable both at room and low temperature.

5.4.5. NMR spectra collection from the isolation of PC_{Ir}^{0}

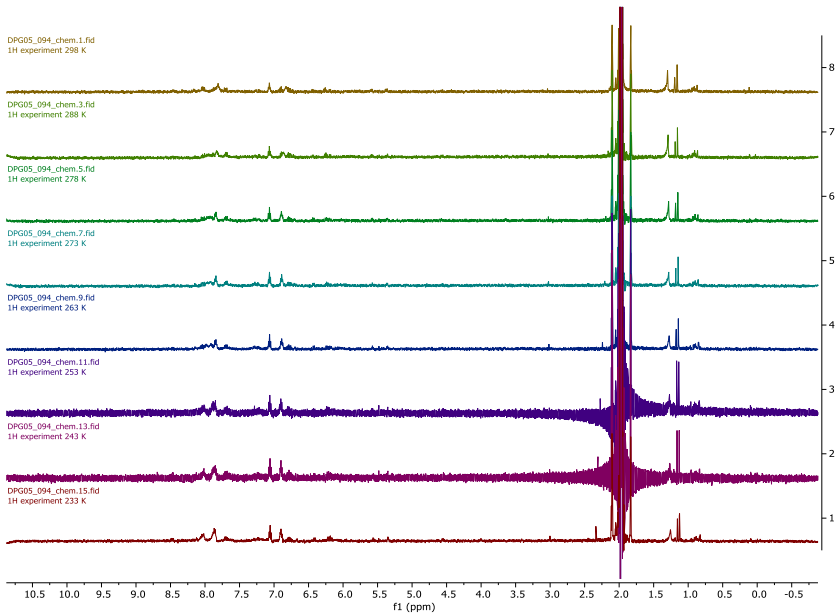

Figure 5. 30. ^{1}H-NMR spectra at different temperatures (from top to bottom: 298, 288, 278, 273, 263, 253, 243, 233 K) of **PC$_{Ir}^0$** collected from chemical reduction with Na/Hg in CD_3CN.

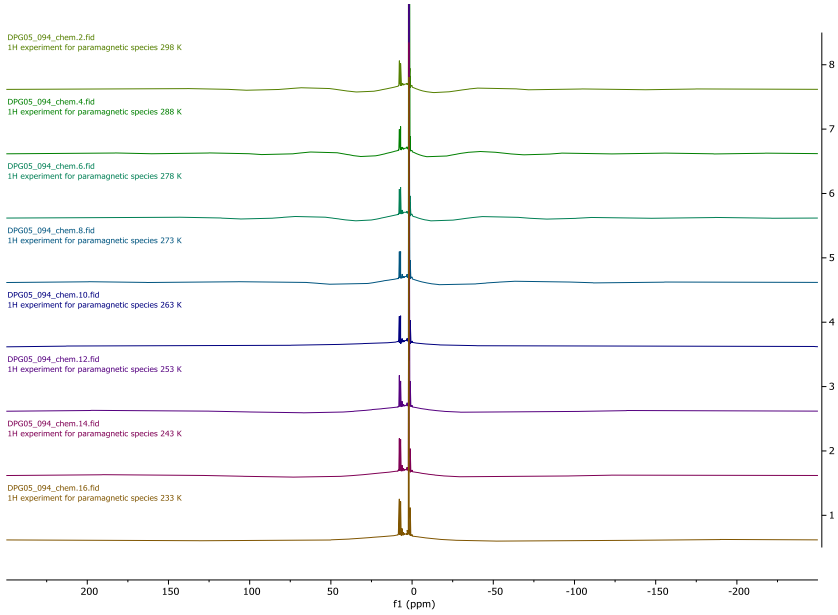

Figure 5. 31. Paramagnetic ^{1}H-NMR spectra at different temperatures (from top to bottom: 298, 288, 278, 273, 263, 253, 243, 233 K) of **PC$_{Ir}^0$** collected from chemical reduction with Na/Hg in CD_3CN.

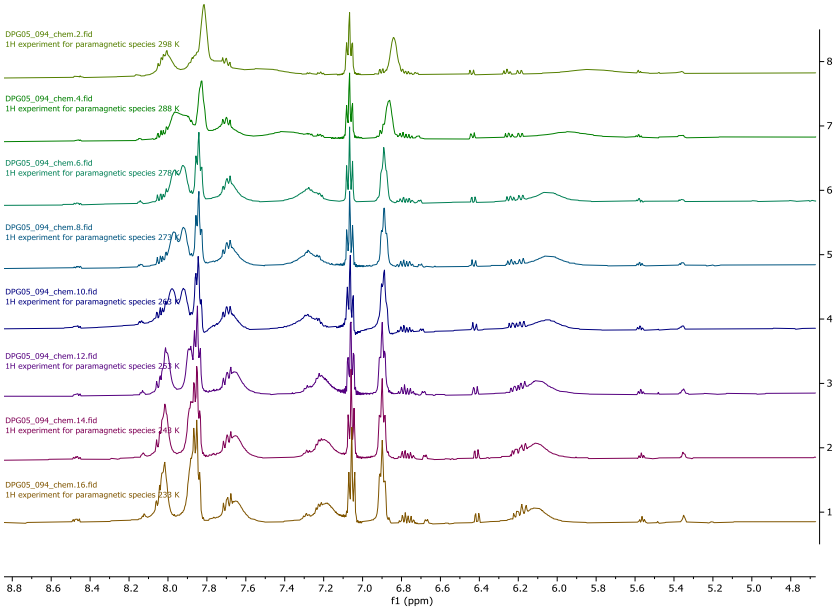

Figure 5. 32. Inset of the 4.8-8.8 ppm region of the paramagnetic ^{1}H-NMR spectra at different temperatures (from top to bottom: 298, 288, 278, 273, 263, 253, 243, 233 K) of $\mathbf{PC_{Ir}^{0}}$ collected from chemical reduction with Na/Hg in CD_3CN.

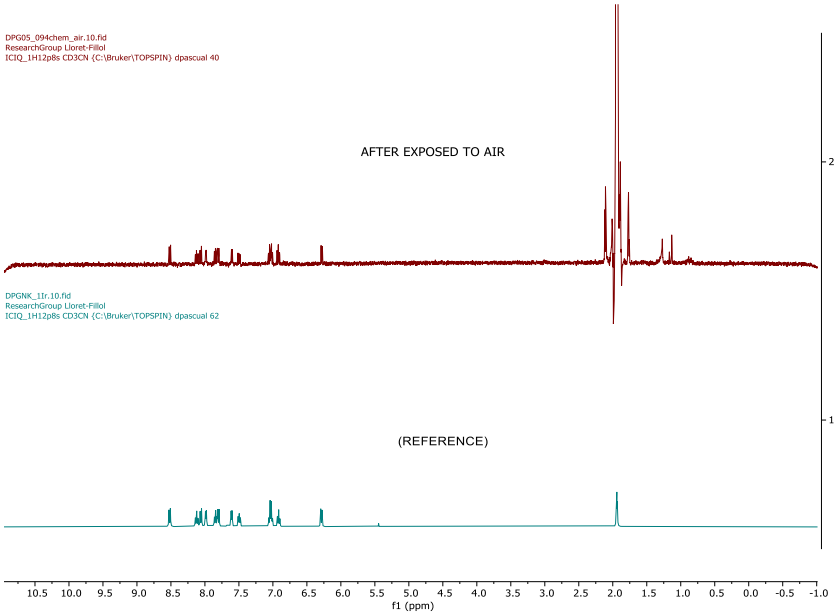

Figure 5. 33. ^{1}H-NMR spectra of (top) a $\mathbf{PC_{Ir}^{0}}$ sample collected from chemical reduction with Na/Hg in CD_3CN, after opening to air, and (bottom) a reference sample containing $\mathbf{PC_{Ir}^{+}}$ in CD_3CN.

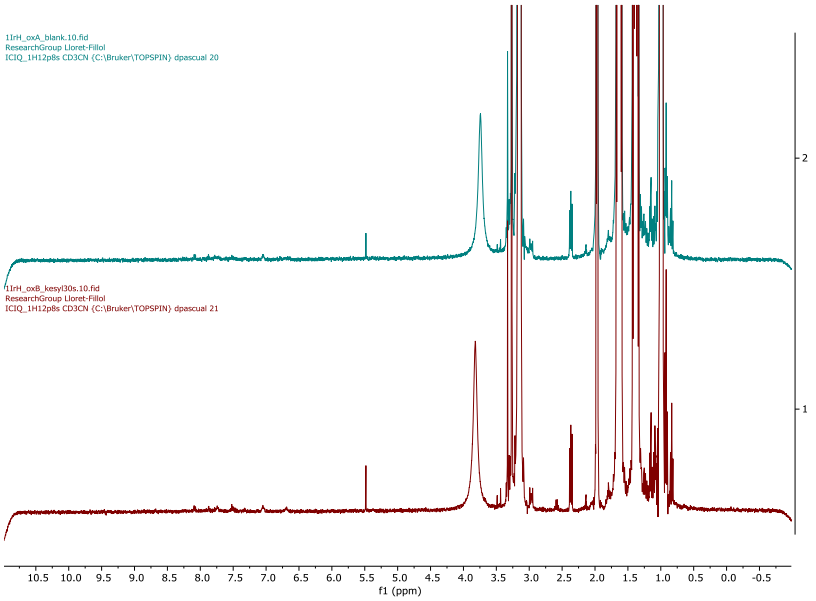

Figure 5. 34. ^{1}H-NMR spectra of **PC$_{Ir}^+$** 5 mM in the presence of 5 equiv. of TBA$_2$ox. Top: exposed to ambient light. Bottom: irradiated 30 s with kessyl lamp.

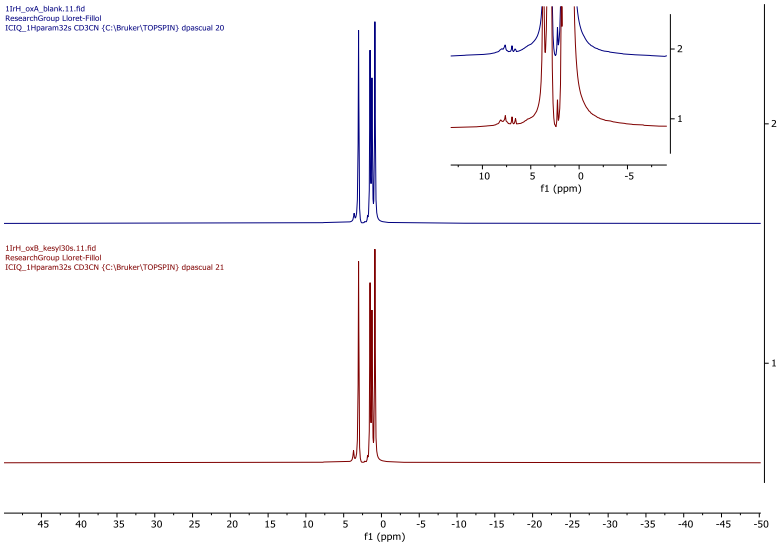

Figure 5. 35. Paramagnetic ^{1}H-NMR spectra of **PC$_{Ir}^+$** 5 mM in the presence of 5 equiv. of TBA$_2$ox. Top: exposed to ambient light. Bottom: irradiated 30 s with kessyl lamp.

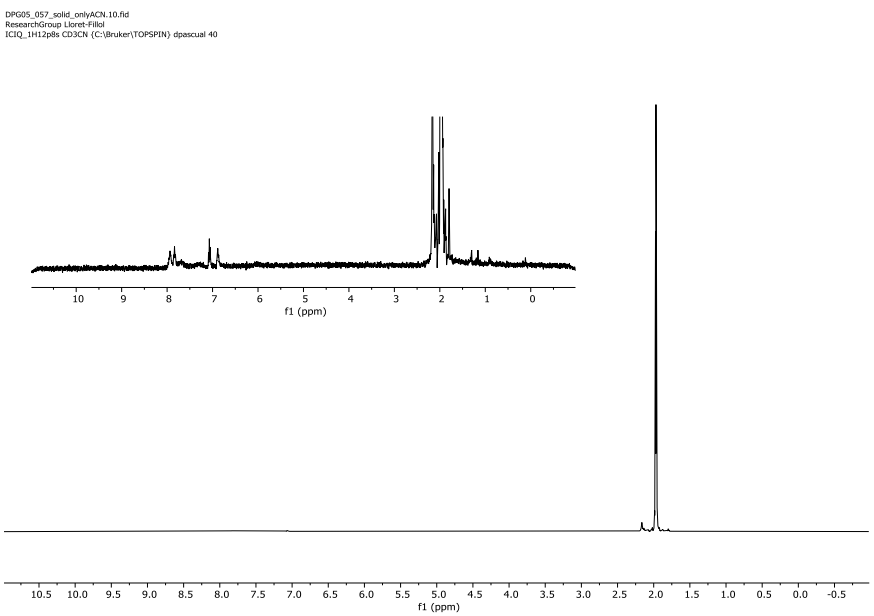

Figure 5. 36. ^{1}H-NMR spectra of $\mathbf{PC_{Ir}^{0}}$ isolated powder dispersed in CD_3CN after the photoreduction with TBA_2ox.

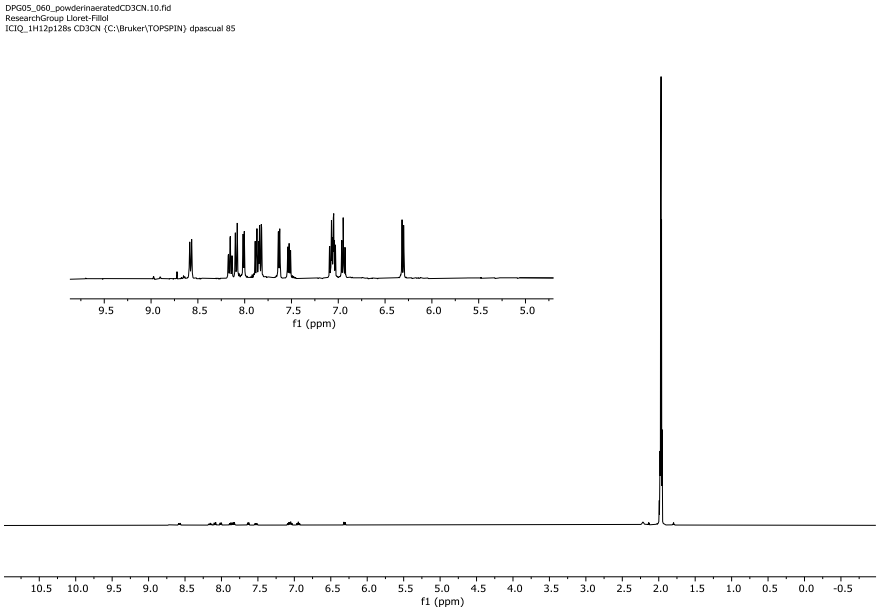

Figure 5. 37. ^{1}H-NMR spectra of $\mathbf{PC_{Ir}^{0}}$ isolated powder dispersed in CD_3CN after the photoreduction with TBA_2ox, after opening the Young NMR tube to air.

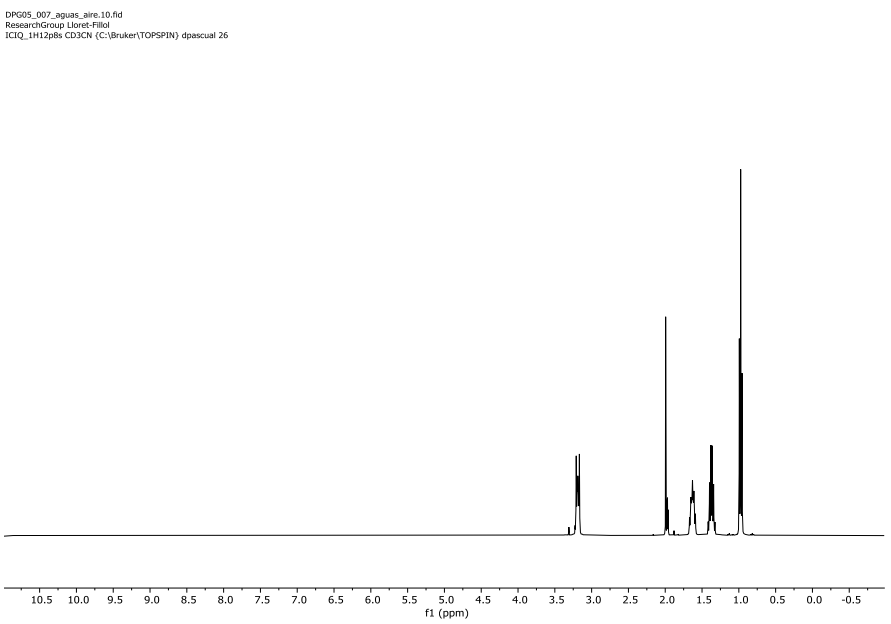

Figure 5. 38. ^{1}H-NMR spectra in CD_3CN of the filtered solution removed during the photoreduction with TBA_2ox containing the remainder of tetrabutylammonium salts.

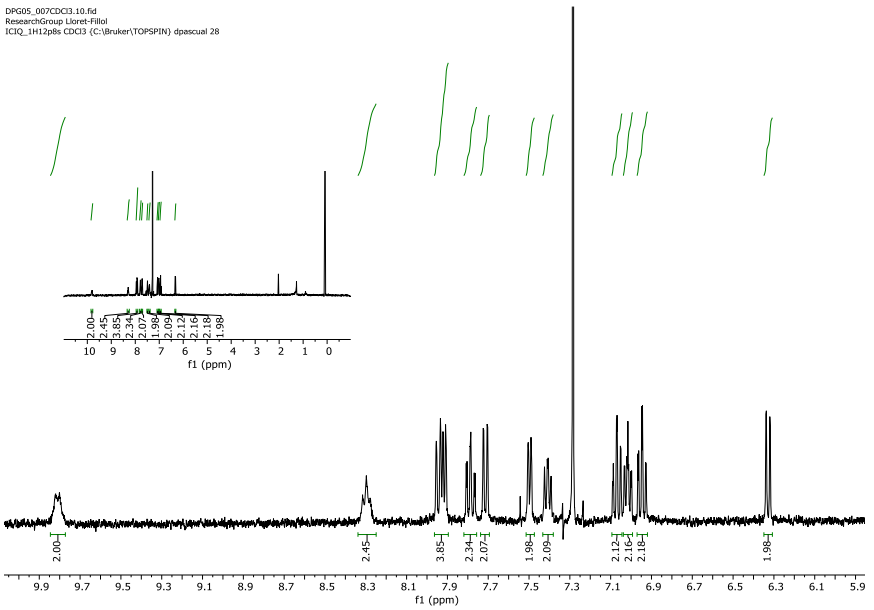

Figure 5. 39. ^{1}H-NMR spectra of $\mathbf{PC_{Ir}^0}$ isolated powder in $CDCl_3$, measured under nitrogen atmosphere in a Young-NMR tube, corresponding with the formation of the chloride salt of $\mathbf{PC_{Ir}^+}$ as reported elsewhere.[81, 82]

5.4.6. Solvent tolerance list of the *in situ* reduced species

Table 5. 9. Colour changes after adding an organic solvent to the isolated $\mathbf{PC_{Ir}^0}$.

Entry	Solvent	Color change
1	CH_3CN	-
2	PhCN	Yellow-white
3	DMF	-
4	DMA	-
5	DMSO	-
6	DMPU	-
7	NMP	-
8	HMPI	Yellow
9	C_6H_6	-
10	$PhCH_3$	-
11	$PhCF_3$	Yellow
12	PhCl	-
13	pyridine	-
14	Et_2O	-
15	THF	-
16	$CH2Cl_2$	Yellow
17	$CHCl_3$	Yellow
18	H_2O	Yellow
19	CH_3OH	Yellow
20	^{t}BuOH	-

Standard conditions: $\mathbf{PC_{Ir}^0}$ (300 μM solution) in CH_3CN (0.2 mL) at 25 °C under N_2. In the glovebox, additional 20 μL of other solvent are introduced to each vial. After 10 minutes without significant changes, all the red samples were opened to air and become yellow.

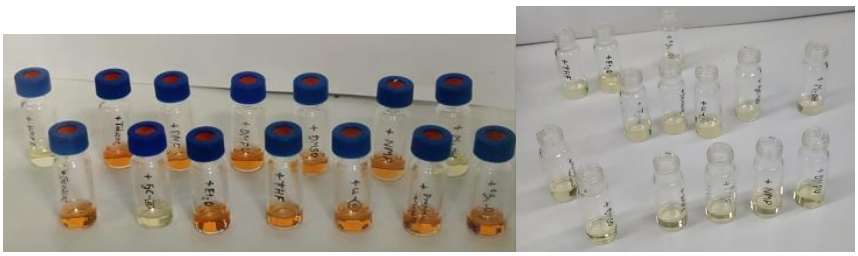

Figure 5. 40. Pictures of vials containing different solvent mixtures before and after opening to air.

5.4.7. Spectroscopic studies of PC_{Ir}^0 in solution

Electrochemical reduction was studied in a spectroelectrochemical cell containing a 1 mM $\mathbf{PC_{Ir}^+}$ solution (0.1 M, $TBAPF_6/CH_3CN$) under inert atmosphere. The observed features corresponding with $\mathbf{PC_{Ir}^0}$ which appear during the reductive wave, also disappear in a reversible manner during the oxidative wave.

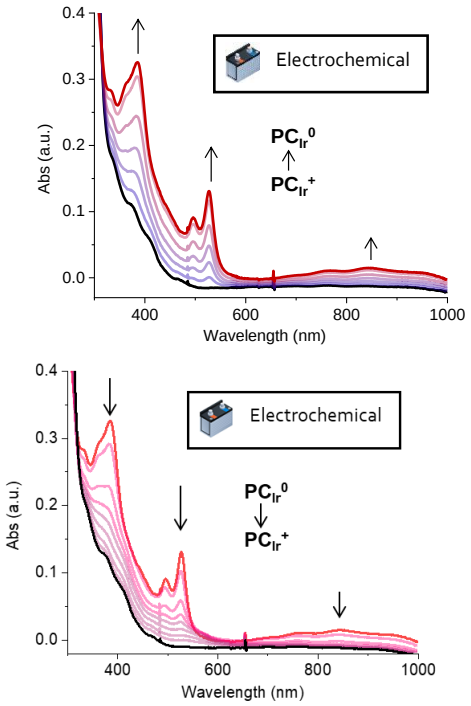

Figure 5. 41. Evolution of the absorption spectrum during the spectroelectrochemical reduction of $\mathbf{PC_{Ir}^+}$ to $\mathbf{PC_{Ir}^0}$ in CH_3CN (top: reductive wave) and its reoxidation (bottom: oxidative wave).

Chemical reduction was studied in a cuvette (1 cm path) containing a 0.3 mM $\mathbf{PC_{Ir}^+}$ inert solution in CH_3CN in the presence of 10 equivalents of Na/Hg (1% mass) under vigorous magnetic stirring.

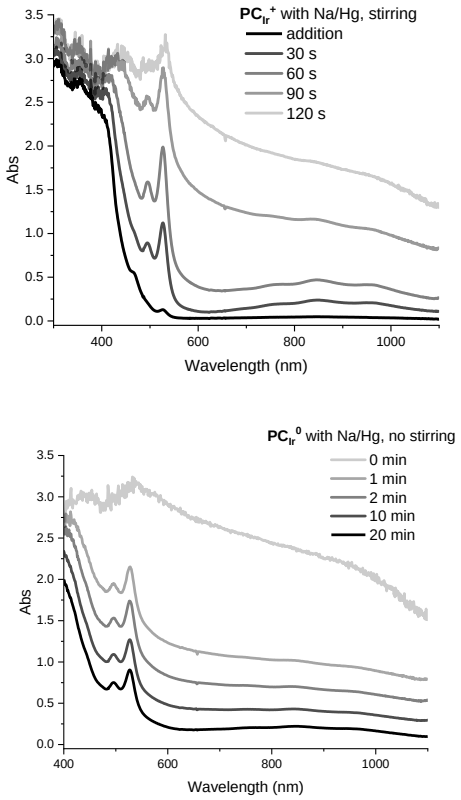

Figure 5. 42. Evolution of the absorption spectrum during the chemical reduction of **PC$_{Ir}^{+}$** (1 mM) to **PC$_{Ir}^{0}$** with Na/Hg (10 equiv.) in CH_3CN. The baseline is highly distorted do to the apparition of an abundant precipitate.

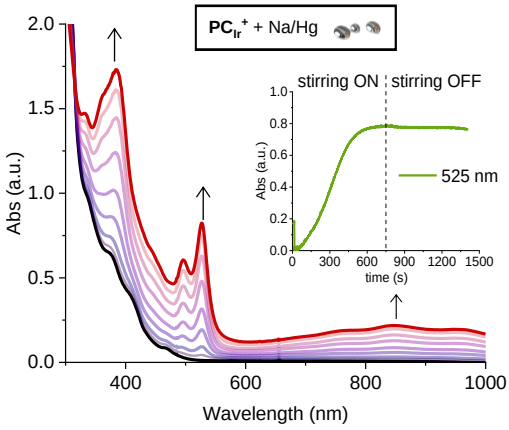

Figure 5. 43. Detailed evolution of the absorption spectrum during the chemical reduction of **PC$_{Ir}^+$** to **PC$_{Ir}^0$** with Na/Hg in CH_3CN.

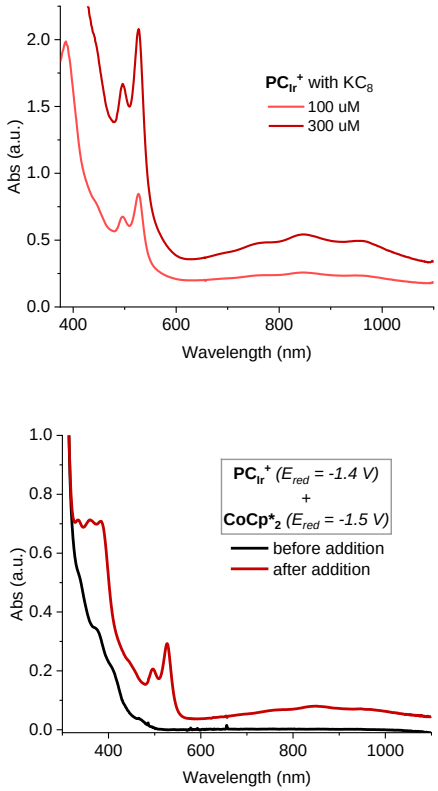

Figure 5. 44. (*top)* Absorption spectra of **PC$_{Ir}^+$** in the presence of KC_8 (10 equiv.) in CH_3CN after stirring at room temperature until the absorption is maximum. (*bottom)* Absorption spectra of **PC$_{Ir}^+$** (1 mM) at room temperature in the absence and presence of [CoCp*$_2$] (0.9 equiv) in

CH_3CN under N_2 atmosphere, reduced sample was taken from EPR experiment and measured in 1 mm cuvette.

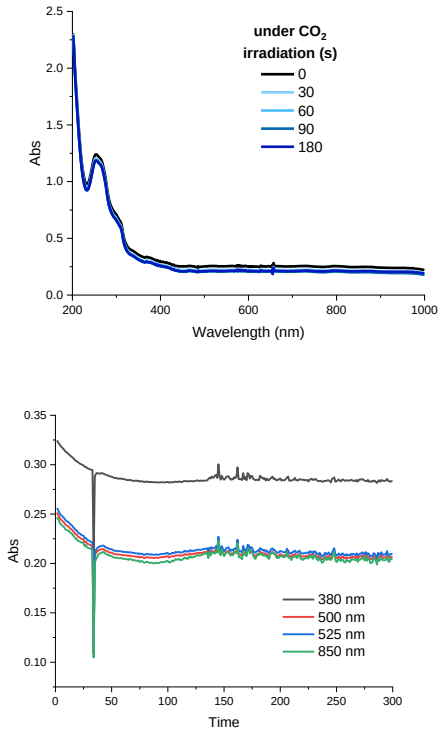

Figure 5. 45. Top: evolution of the absorption spectrum during the photochemical reduction of $\mathbf{PC_{Ir}^{+}}$ (25 μM) to $\mathbf{PC_{Ir}^{0}}$ with TBA2ox (125 μM) in CH_3CN under CO_2 atmosphere (saturated by 5 min bubbling). Bottom: kinetic trace of selected absorption wavelengths under irradiation (started at 30 s of measurement).

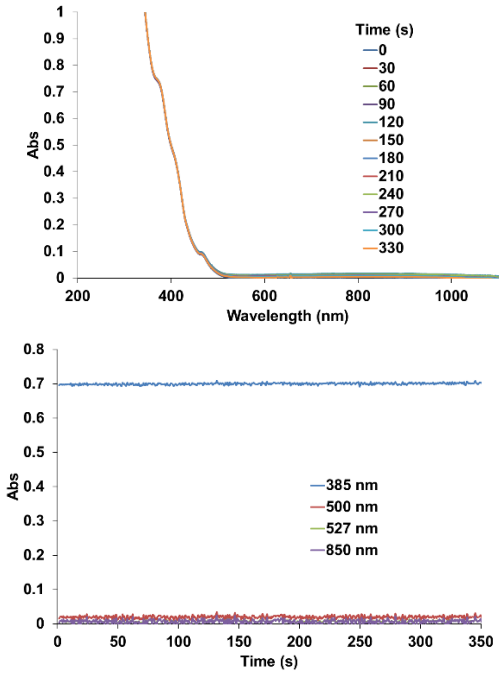

Figure 5. 46. Top: evolution of the absorption spectrum during the photochemical reduction of $\mathbf{PC_{Ir}^{+}}$ (50 μM) to $\mathbf{PC_{Ir}^{0}}$ with DABCO (100 mM) in CH_3CN. Bottom: kinetic trace of selected absorption wavelengths under irradiation (started at 10 s of measurement).

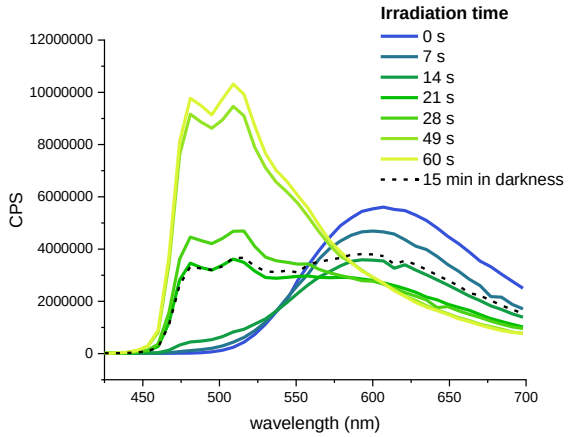

Figure 5. 47. Evolution of the luminiscence of a sample containing $\mathbf{PC_{Ir}^{+}}$ (25μM) and Et3N (50 mM) in degassed CH_3CN under 447 nm LED irradiation. Every irradiation lapse was preceeded of 2 minutes under darkness to favour the system equilibrium.

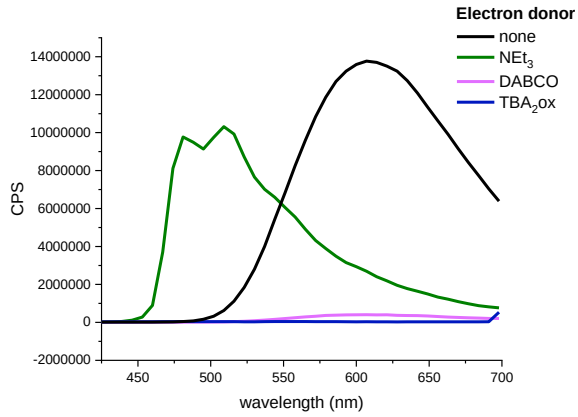

Figure 5. 48. Comparison of the luminiscence of samples containing $\mathbf{PC_{Ir}^{+}}$ (25μM) and different electron donors (50 mM) in degassed CH_3CN after 30 seconds of 447 nm LED irradiation.

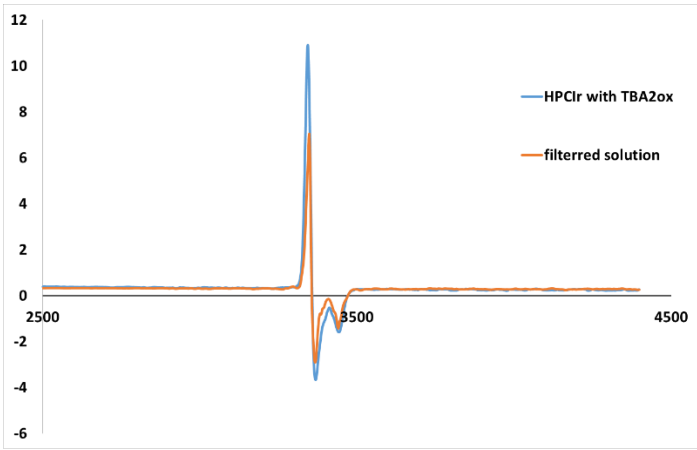

Figure 5. 49. Comparison of the EPR spectrum of $\mathbf{PC_{Ir}^{+}}$ irradiated in the presence of TBA_2ox and the filtered solution obtained when isolating $\mathbf{PC_{Ir}^{0}}$ following the procedure II.

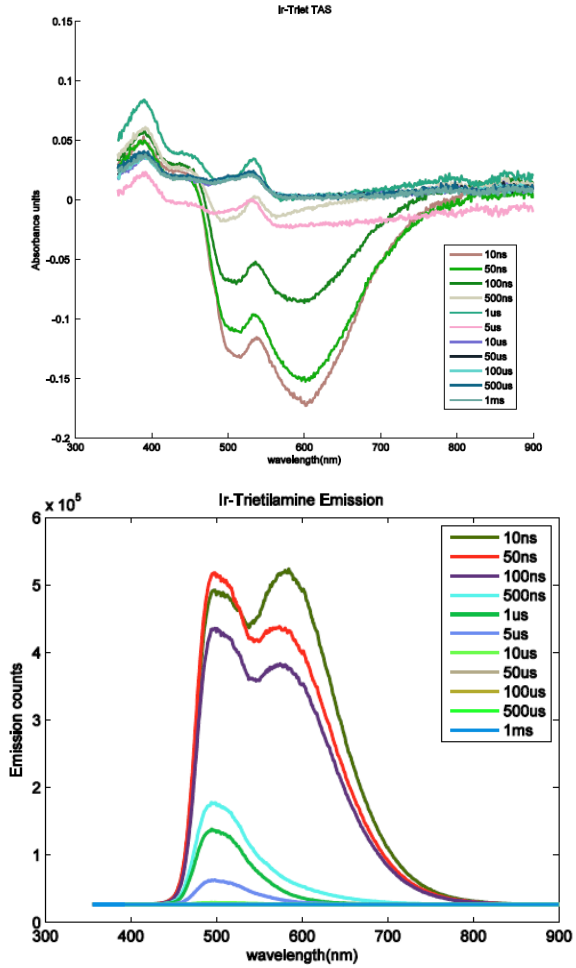

Figure 5. 50. Transient absorption spectra of **PC$_{Ir}^+$** (50 μM) irradiated in the presence of Et_3N (25 mM).

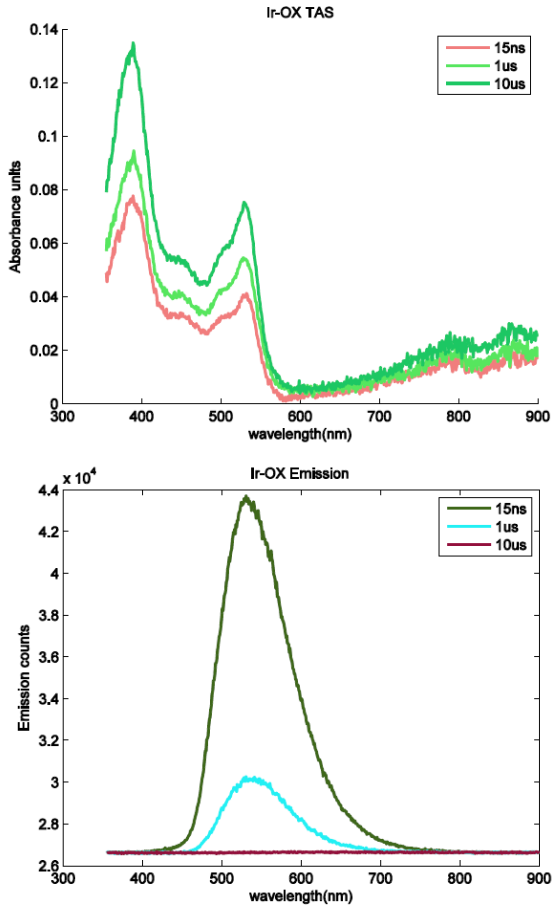

Figure 5. 51. Transient absorption spectra of $\mathbf{PC_{Ir}}^{+}$ (50 μM) irradiated in the presence of TBA_2ox (25 mM).

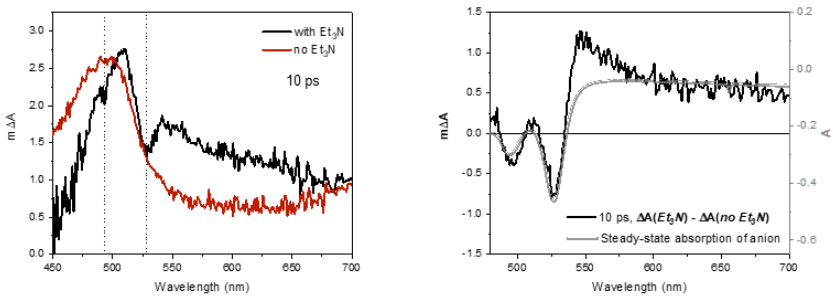

Figure 5. 52. **(left)** Transient absorption of $\mathbf{PC_{Ir}}^{+}$ with Et_3N. **(right)** Difference between transient absorption with and without Et_3N (black) overlapped with the negative steady-state absorption of the anion (*grey*, spectrum corresponding to 70s after under constant irradiation in a flow cell).

Measurement conditions: $\mathbf{PC_{Ir}}^+$ 50 μM in ACN with Et_3N 7.5 mM. Experiment measured by Dr. Carlota Bozal-Ginesta.

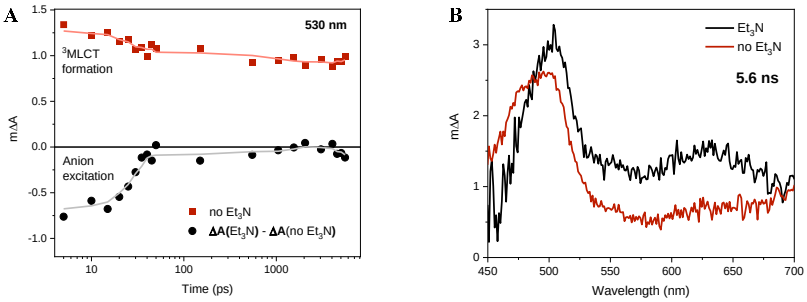

Figure 5. 53. **(A)** Kinetics at 530 nm of $\mathbf{PC_{Ir}}^+$ without Et_3N in ACN (*red* trace) and $\mathbf{PC_{Ir}}^0$ (*black* trace, calculated by subtracting the kinetics of $\mathbf{PC_{Ir}}^+$ with and without Et_3N in ACN). (B) Transient spectra of $\mathbf{PC_{Ir}}^+$ after 5.6 ns of photoexcitation in ACN with and without Et_3N. Experiment measured by Dr. Carlota Bozal-Ginesta.

5.4.8. Suplementary EXAFs information

Data was collected at the ALBA synchrotron CLAESS beamline at cryogenic temperatures (20K) using a Si311 double crystal monochromator. Samples were prepared as powders diluted in cellulose with spectra collected in transmission mode. The Athena software package was used for data averaging, normalization and energy scale calibration.[83] The energy was calibrated to the first inflection point of the L_3-edge of Pt foil taken as 11564 eV. XANES features were fit using a Gaussian-Lorentzian sum function with 60% Gaussian character together with a cumulative Gaussian-Lorentzian sum for the edge jump. Lastly, the experimental spectra were correlated with theoretically calculated spectra following previously published procedures.[84, 85] XAS spectra were calculated with the ORCA software package,[86] using a TD-DFT method employing the Tamm-Dancoff approximation[87, 88] and a BP86 functional with a def2-TZVP basis set together with a def2-TZVP/J auxiliary basis set on all atoms,[89, 90] as well as the ZORA relativistic approximation.[91, 92]

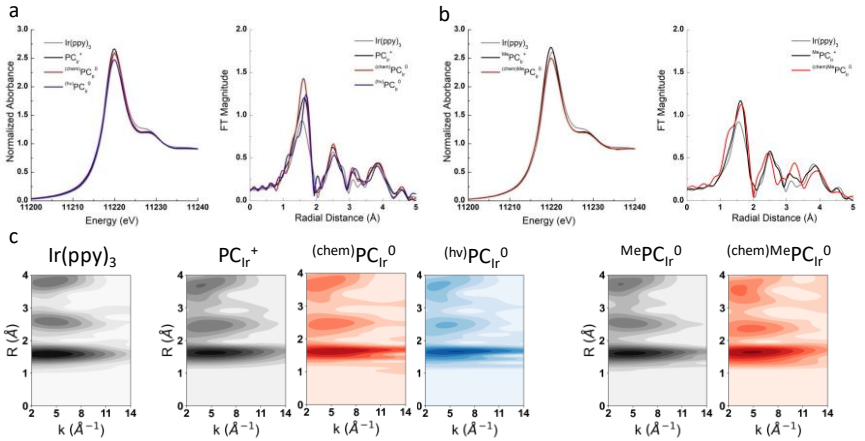

Figure 5. 54*:* (a) XANES and Fourier Transformed spectra (k^2 weighted 3-16 $Å^{-1}$ k-range having a Hannings window dk=1) of PC_{Ir}^{+} and chemically and photo- reduced species $^{(chem)}PC_{Ir}^{0}$ and PC_{Ir}^{0} overlaid with $Ir(ppy)_3$ as reference. (b) XANES and Fourier Transformed spectra (k^2 weighted 3-12 $Å^{-1}$ k-range having a Hannings window dk=1) of $^{Me}PC_{Ir}^{+}$ and chemically and photo- reduced species $^{(chem)Me}PC_{Ir}^{0}$ and $^{Me}PC_{Ir}^{0}$ overlaid with $Ir(ppy)_3$ as reference. (c) Cauchy wavelet-transform of the samples showing structural integrity and comparable long range interaction dominated by C/N/O scattering paths. Experiment measured by Dr. Vlad Martin-Diaconescu.

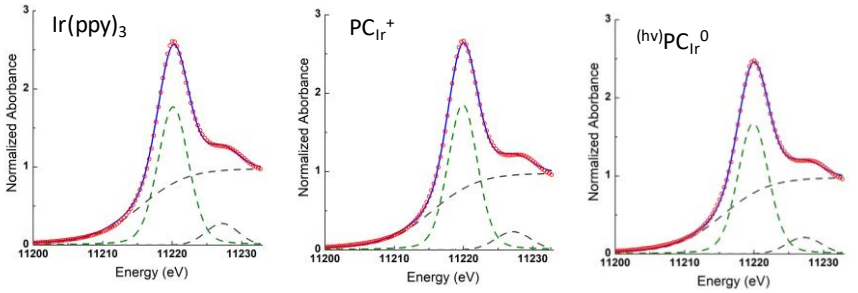

Figure 5. 55*:* XANES peak-fits for $Ir(ppy)_3$, PC_{Ir}^{+} and PC_{Ir}^{0} as described in the experimental section. Experiment measured by Dr. Vlad Martin-Diaconescu.

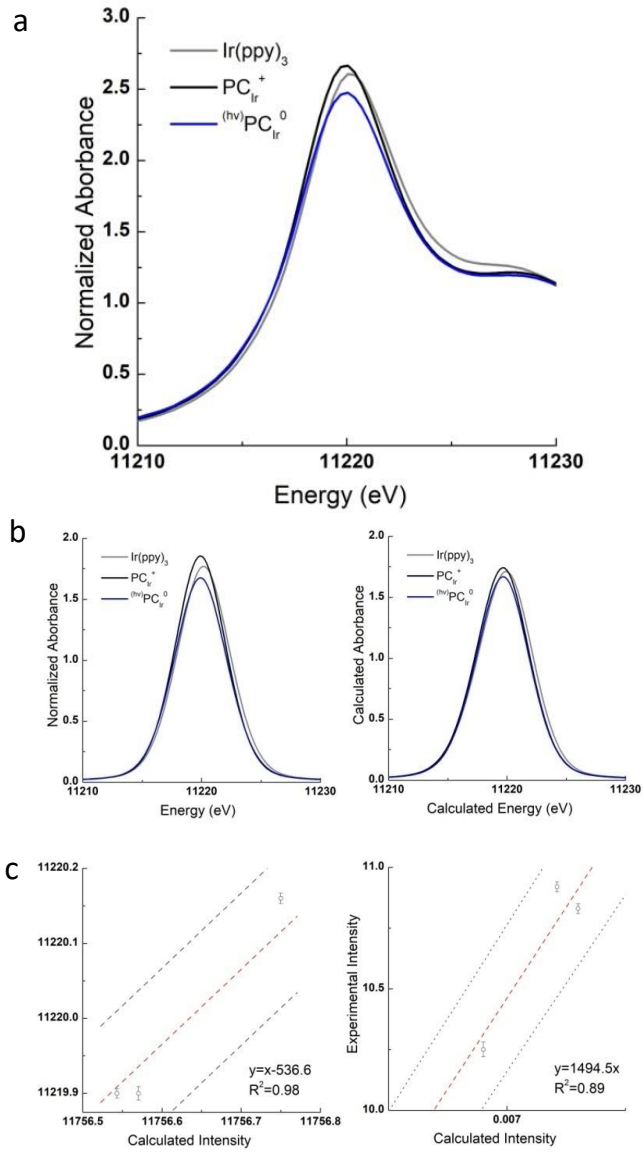

Figure 5. 56*:* Correlation of theoretical spectra to experiment for $Ir(ppy)_3$, PC_{Ir}^+ and PC_{Ir}^0 as described in the experimental section. (a) Normalized Experimental XANES region. (b) Fitted experimental white-lines and calculated white-lines (shifted -536.6eV with the intensity multiplied by a factor of 1494.5. (c) Correlation of experimental and calculated whitelines. Experiment measured by Dr. Vlad Martin-Diaconescu.

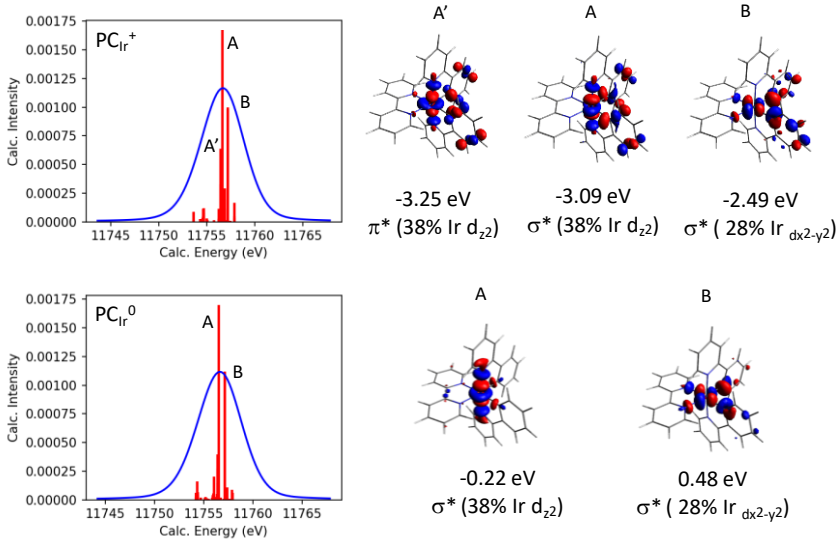

Figure 5. 57*:* Calculated transitions and corresponding acceptor orbitals (isovalue 0.03) showing ground state orbital energies and % Ir$_d$ for, PC_{Ir}^{+} and PC_{Ir}^{0}. Calculated by Dr. Vlad Martin-Diaconescu.

5.4.9. Procedures for reactivity studies

Procedure V (for stoichiometric studies followed by UV-vis): A 2.8 ml solution with 100 μM **PC_{Ir}^{+}** was stirred in the presence of Na/Hg (10 equiv., an excess is used to enhance reaction rate), followed the kinetic of the reduction by UVvis absorption spectroscopy in a long-neck 10 mm cuvette closed with a septum. Once the absorbance signal is maximum (plateau), stirring is stopped and the cuvette is transferred to the glovebox, where 2.5 ml of the solution are removed from the supernatant using a long needle and then dispensed into a clean dry cuvette with a stir bar. The SET agent was injected during the absorption kinetic measurement with a 25 μL Hamilton syringe under inert conditions. The cooling system maintained the temperature at 25 ºC and a magnetic stirring plate is used to stir the reactions. Depending on the experiment (irradiation or darkness), the external LED source is turned on or kept turned off.

Procedure VI (for stoichiometric studies followed by GC): A 2.8 ml solution with 330 μM **PC_{Ir}^{+}** was stirred in the presence of Na/Hg (10 equiv., an excess is used to enhance reaction rate), followed the kinetic of the reduction by UVvis absorption spectroscopy in a long-neck 10 mm cuvette closed with a septum. Once the absorbance signal is maximum (plateau), stirring is stopped and the cuvette is transferred to the glovebox, where 0.4 ml of the solution are removed from the supernatant using a long needle, and

then dispensed into 6 GC-vials, followed by addition of 10 equivalents of the substrate in 40 μL from a 33 μM substrate stock (total volume is 0.44 ml). Each GC-vial is closed and put into a flask fitting with our homemade photoreactor shape, which is closed with a white rubber septum to keep it under nitrogen. The cooling system maintained the temperature at 25 ºC and orbital shaking is used to stir the reactions. Depending on the experiment (irradiation or darkness), the LED source is turned on or kept turned off. After that an internal standard is added to measure samples in GC-FID.

Procedure VII (for stoichiometric reactivity of the powder): The powder of **PC$_{Ir}^0$** was prepared in a glovebox according to *Procedure I* (*vide supra*). From the resultant mass, 4.3 mg (6.6 μmol) were dispersed in 2 ml of anhydrous CH_3CN (3.3 mM). Quickly, 0.4 ml of the dispersion were transferred to vials containing 1 equivalent of the corresponding substrate in 40 μl (total volume, 440 μl). The vials were left overnight stirring at 25 ºC either under light irradiation or under darkness. After that an internal standard is added to measure samples in GC-FID.

Procedure VIII (for photocatalytic experiments): The reactions were prepared in glass vials in the glovebox, where **PC$_{Ir}^+$** and **1e** were dispensed from stock solutions. TBA_2ox was also dispensed inside of the glovebox, while degassed anhydrous Et_3N was injected out of the glovebox using the Schlenk line. The reactions were kept in our in-house developed parallel photoreactors overnight. Once opened, an internal standard was added to the reaction mixture, followed by biphasic extraction of the organic phase (water/AcOEt) and filtration through a short $MgSO_4$ path before GC analysis.

Procedure IX (for photocatalytic experiments): The reactions were prepared in glass vials in the glovebox, where **PC$_{Ir}^+$** and **1e** were dispensed from stock solutions. TBA_2ox was also dispensed inside of the glovebox, while degassed anhydrous Et_3N was injected out of the glovebox using the Schlenk line. The reactions were kept in our in-house developed parallel photoreactors overnight. Once opened, an internal standard was added to the reaction mixture, followed by biphasic extraction of the organic phase (water/AcOEt) and filtration through a short $MgSO_4$ path before GC analysis.

5.4.10. Additional reactivity studies with PC$_{Ir}^0$

Table 5. 10. Stoichiometric reactions of **PC$_{Ir}^0$** with chloroanisole and blank reactions.

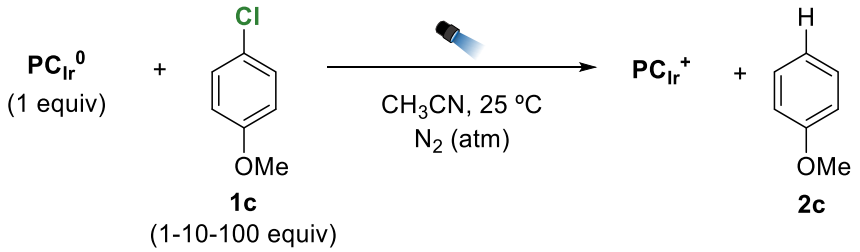

Entry	Equivalents of **1c**	Reaction time (min)	Conversion **1c** %	Yield **2** (%)
1	1	0	0	0
2	1	5	18	15
3	1	15	42	40
4	1	60	57	57
5	1	1440	91	79
6	10	0	0	0
7	10	5	4	33
8	10	15	6	58
9	10	60	8	79
10	10	1440	9	95
11	100	0	0	0
12	100	5	1	77
13	100	15	1	88
14	100	60	1	97
15	100	1440	1	99

Standard conditions: **PC$_{Ir}^{0}$** (0.3 mM), **1c** in CH_3CN (0.44 mL) at 25 °C under N_2 under blue light irradiation (447 nm). Yields were determined by GC analysis relative to a calibrated internal standard.

Table 5. 11. Reactivity of the isolated powder.

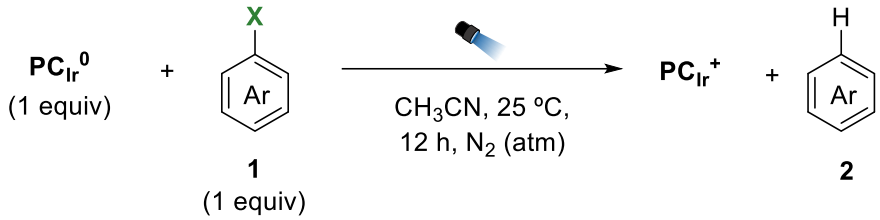

Entry	Aryl halide	Light exposure	Conv (%)	Yield (%)
1	**1c**	447 nm LED	23	20
2	**1c**	dark	0	0
3	**1a**	447 nm LED	25	24
4	**1a**	dark	30	28

Standard conditions: **PC$_{Ir}^0$** (3 mM dispersion), **1** (3 mM) in CH_3CN (0.44 mL) at 25 °C under N_2. Irradiated for 12 h (447 nm). Yields were determined by GC analysis relative to a calibrated internal standard.

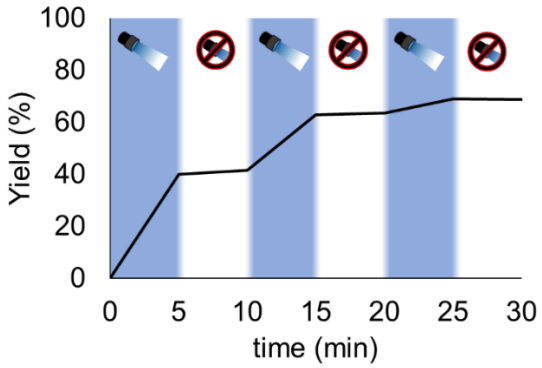

Figure 5. 58. Dehalogenation of chloroanisole (**1c**) when performing ON/OFF cycles with a 447 nm LED. Blue areas indicate irradiation cycles and white areas indicate non-irradiation periods.

5.4.11. NMR spectra from reactivity

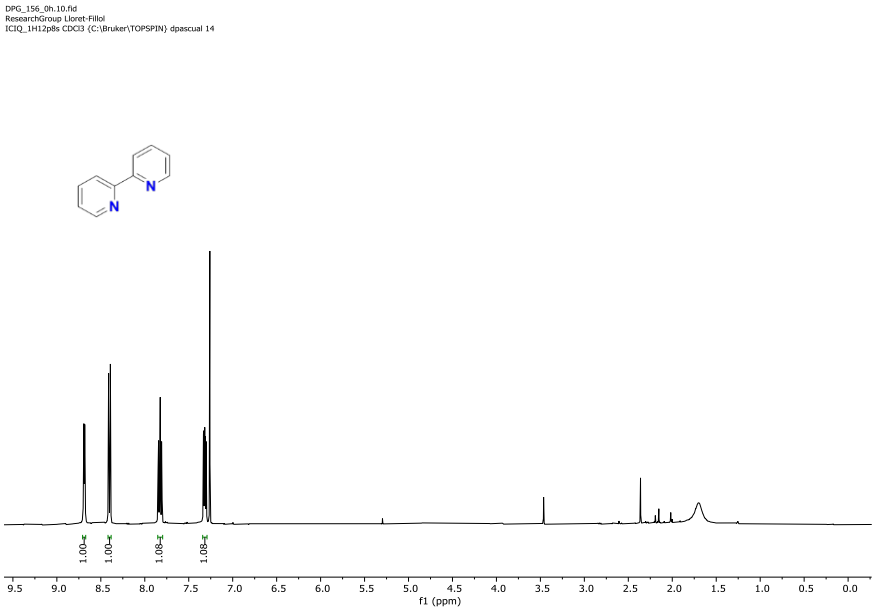

Figure 5. 59. ^{1}H-NMR spectra in $CDCl_3$ of the reaction crude of **bpy$^{\bullet-}$** (15 mM) in acetonitrile at time zero.

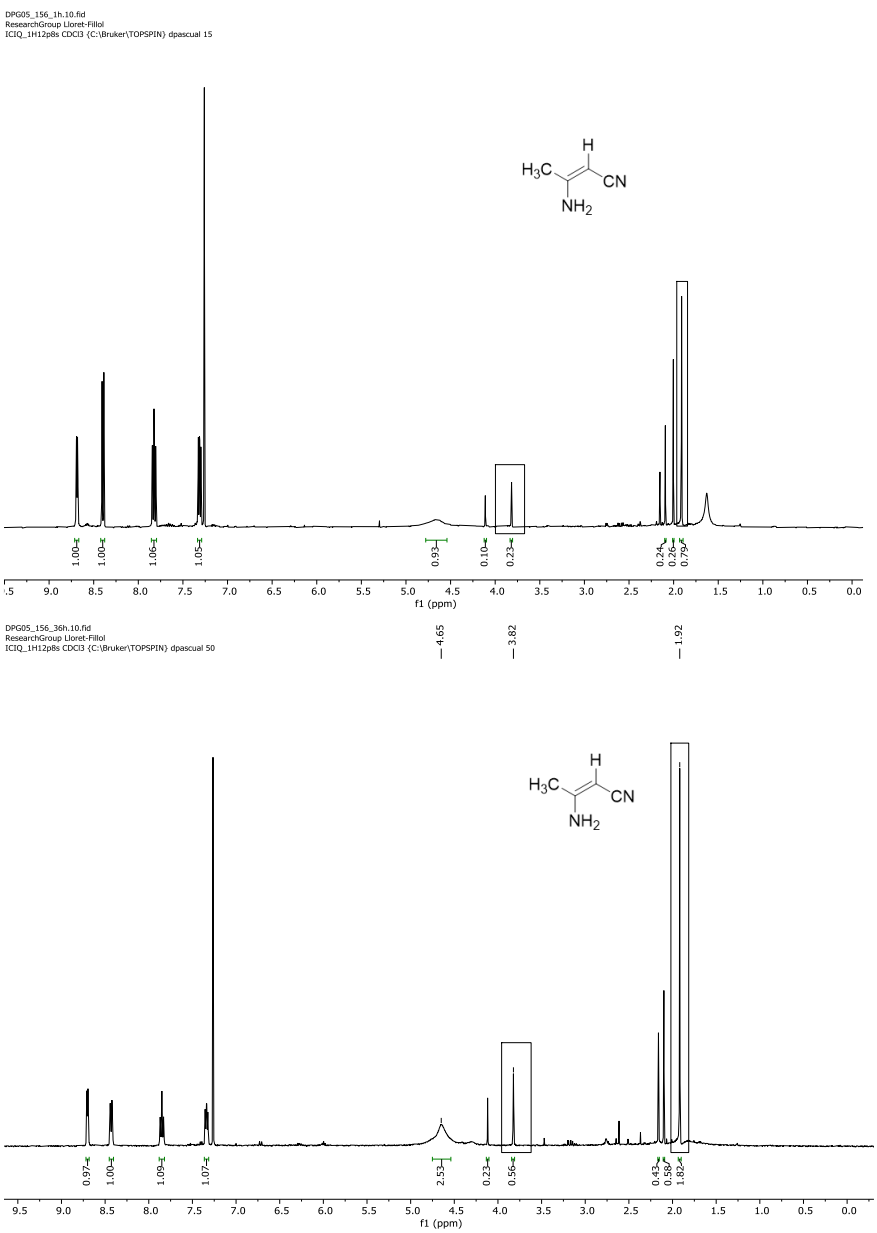

Figure 5. 60. ^{1}H-NMR spectra in $CDCl_3$ of the reaction crude of **bpy$^{\bullet-}$** (15 mM) in acetonitrile after 1 h (top) and 36 h (bottom) of irradiation (447 nm). Highlighted signals correspond with the ones attributed to the predominant diastereomer of 3-aminocrotononitrile according to the reported spectra.[93]

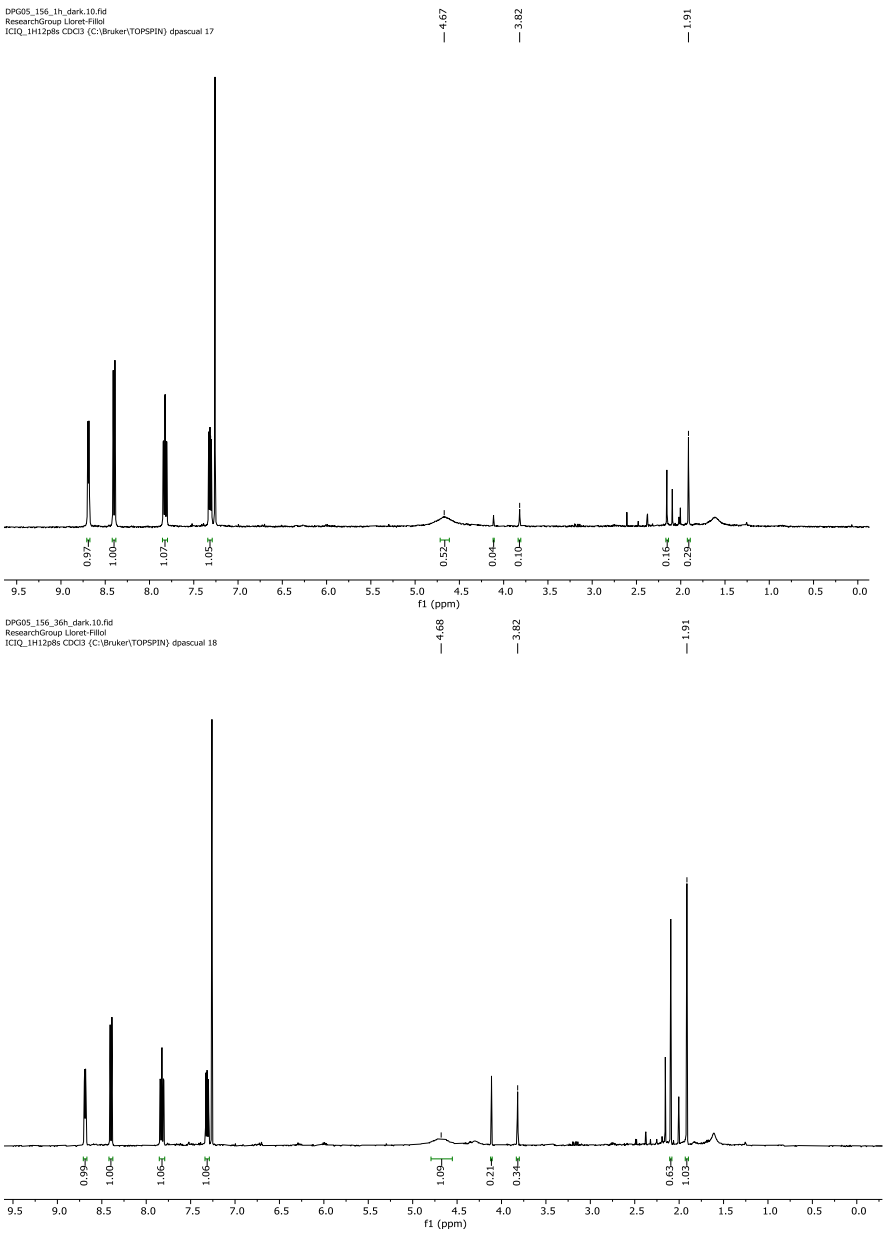

Figure 5. 61. ^{1}H-NMR spectra in $CDCl_3$ of the reaction crude of **bpy**$^{\bullet-}$ (15 mM) in acetonitrile after 1 h (top) and 36 h (bottom) under darkness.

5.4.12. Studies on the release of the bpy in the presence of triethylamine

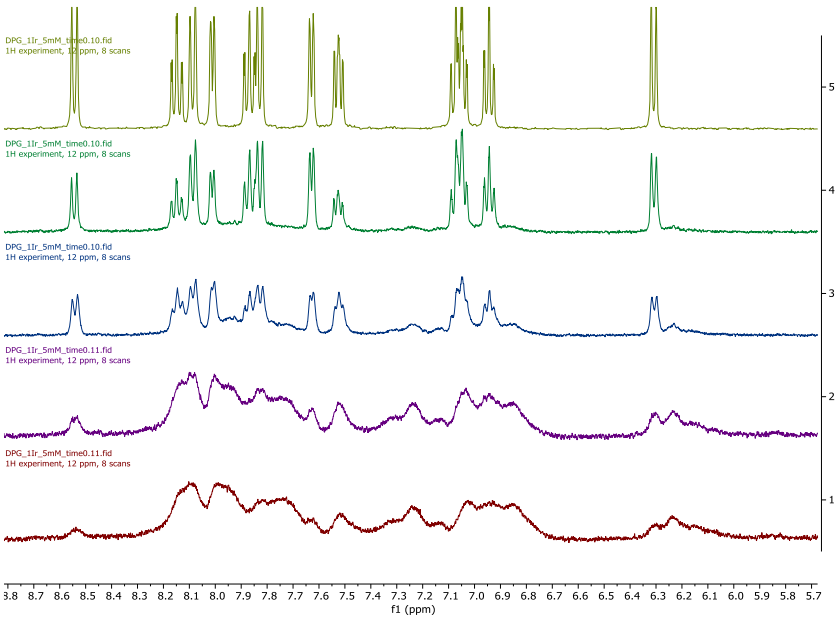

Figure 5. 62. ^{1}H-NMR spectra of **PC$_{Ir}^+$** 5 mM in the presence of 10 equiv. of Et3N after different irradiation times (up to down corresponding with 0, 1, 2, 5 and 10 min of irradiation), signal broadening is related with the generation of paramagnetic species.

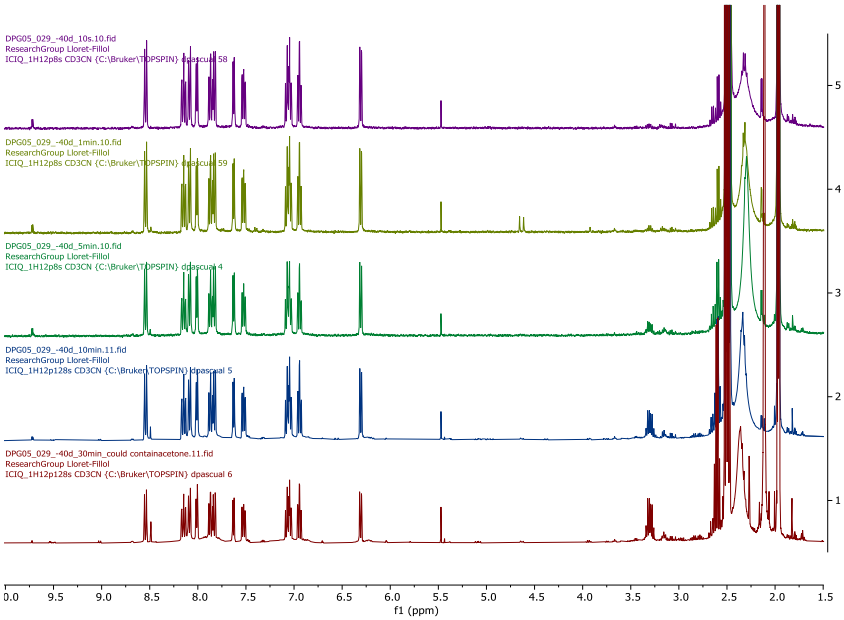

Figure 5. 63. ^{1}H-NMR spectra of **PC$_{Ir}^{+}$** 5 mM in the presence of 10 equiv. of Et_3N at -40 ºC after different irradiation times (from top to bottom, 10 s, 1 min, 5 min, 10 min and 30 min).

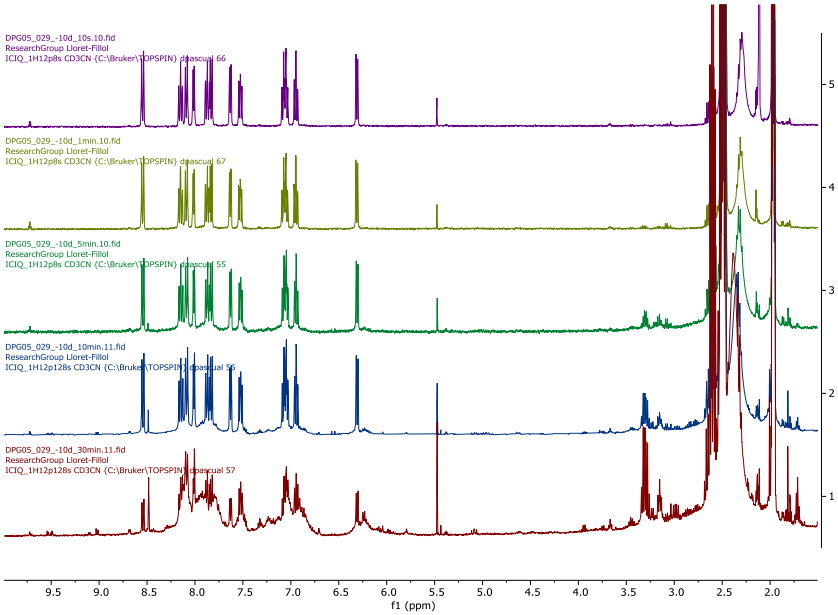

Figure 5. 64. ^{1}H-NMR spectra of **PC$_{Ir}^{+}$** 5 mM in the presence of 10 equiv. of Et_3N at -10 ºC after different irradiation times (from top to bottom, 10 s, 1 min, 5 min, 10 min and 30 min).

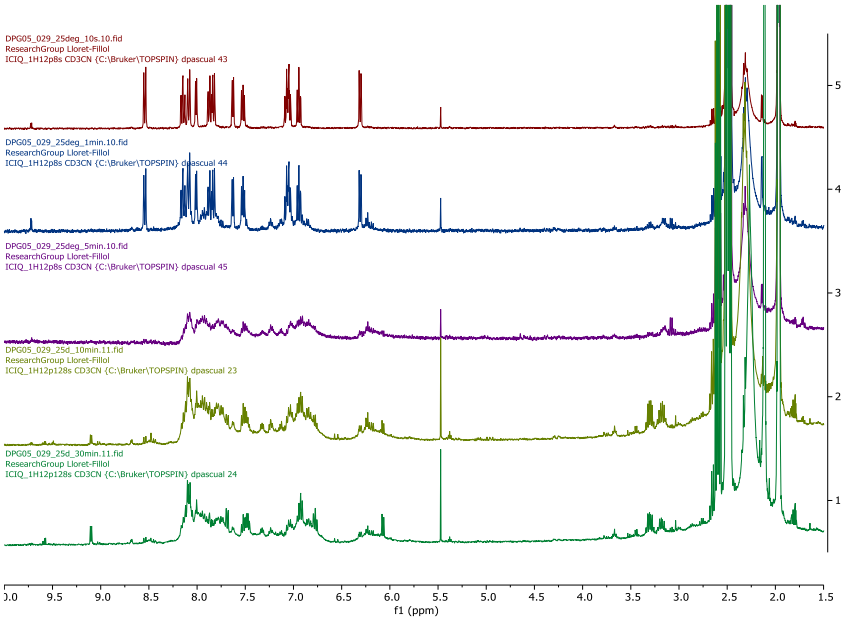

Figure 5. 65. ^{1}H-NMR spectra of **PC$_{Ir}^+$** 5 mM in the presence of 10 equiv. of Et_3N at 25 ºC after different irradiation times (from top to bottom, 10 s, 1 min, 5 min, 10 min and 30 min).

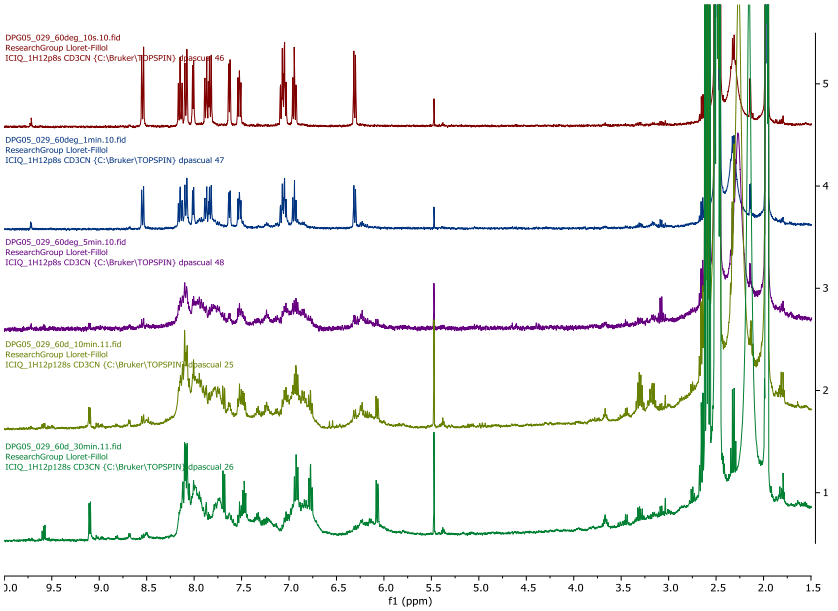

Figure 5. 66. ^{1}H-NMR spectra of **PC$_{Ir}^+$** 5 mM in the presence of 10 equiv. of Et_3N at 60 ºC after different irradiation times (from top to bottom, 10 s, 1 min, 5 min, 10 min and 30 min).

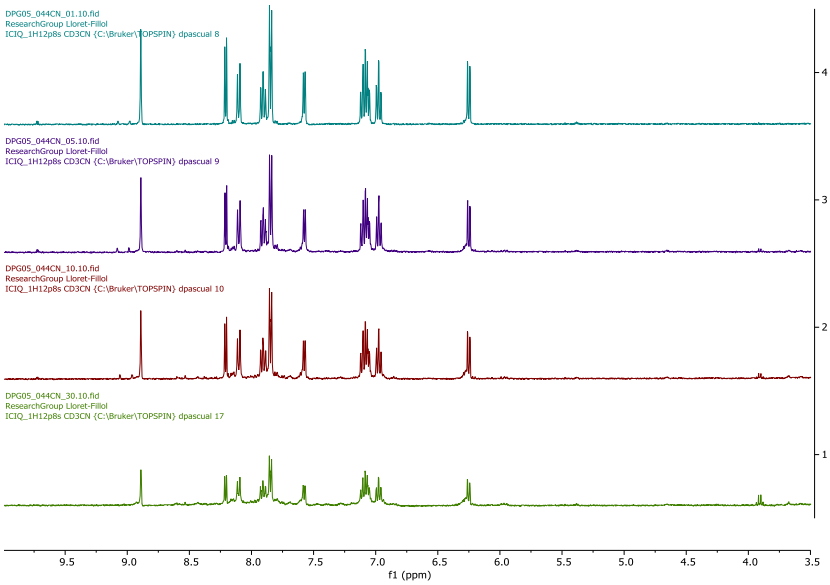

Figure 5. 67. ^{1}H-NMR spectra of ^{CN}**PC$_{Ir}^{+}$** 5 mM in the presence of 10 equiv. of Et_3N at 25 ºC after different irradiation times (from top to bottom, 1 min, 5 min, 10 min and 30 min).

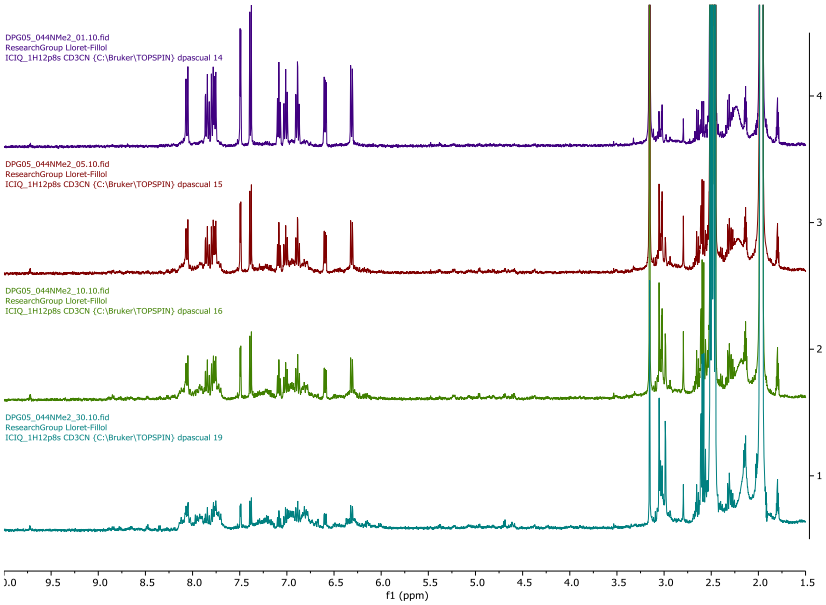

Figure 5. 68. ^{1}H-NMR spectra of ^{NMe2}**PC$_{Ir}^{+}$** 5 mM in the presence of 10 equiv. of Et_3N at 25 ºC after different irradiation times (from top to bottom, 1 min, 5 min, 10 min and 30 min).

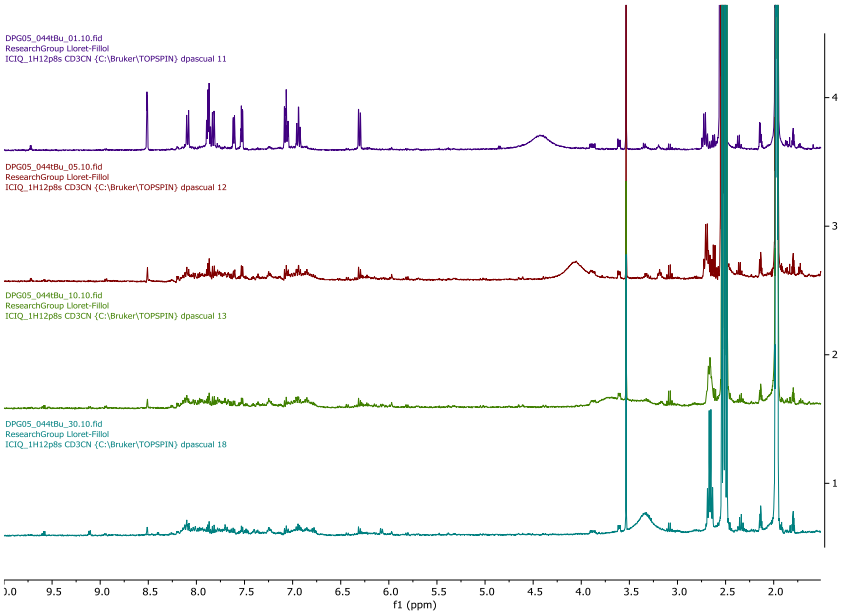

Figure 5. 69. ^{1}H-NMR spectra of **^{tBu}PC$_{Ir}^+$** 5 mM in the presence of 10 equiv. of Et_3N at 25 ºC after different irradiation times (from top to bottom, 1 min, 5 min, 10 min and 30 min).

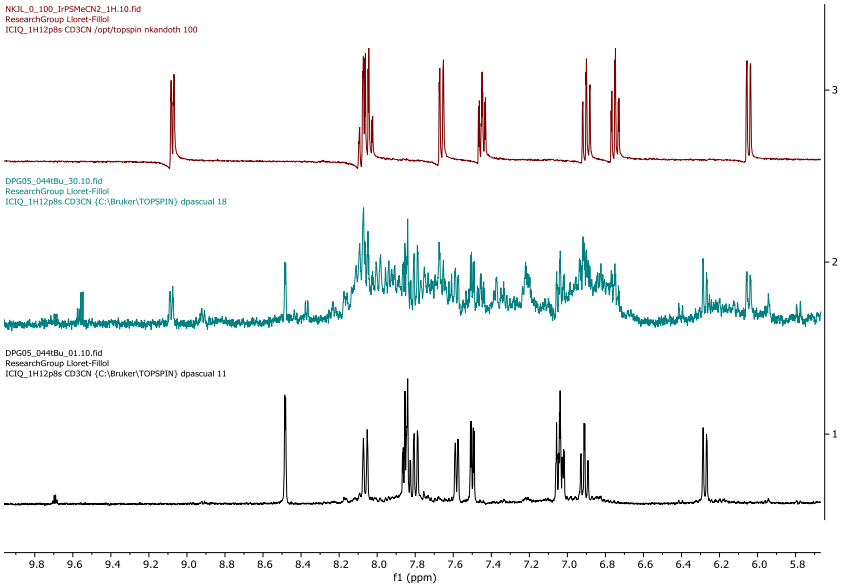

Figure 5. 70. Comparison of the ^{1}H-NMR spectra of (up) $[Ir(ppy)_2(CH_3CN)_2]PF_6$, (medium) **^{tBu}PC$_{Ir}^+$** 5 mM in the presence of 10 equiv. of Et_3N at 25 ºC after 30 min of irradiation, and (bottom) **^{tBu}PC$_{Ir}^+$** 5 mM in the presence of 10 equiv. of Et_3N at 25 ºC before irradiation.

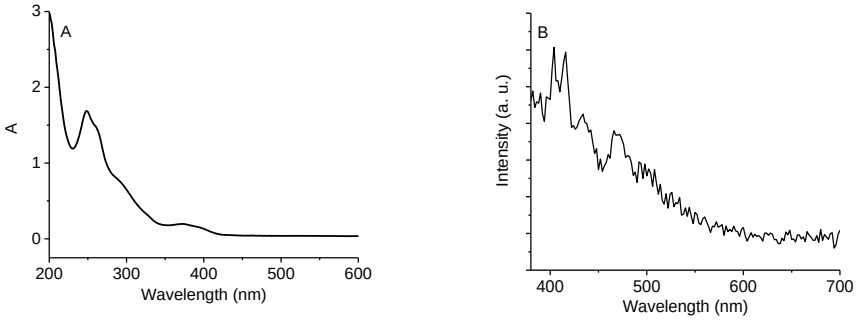

Figure 5. 71. Absorption and emission spectra of $[Ir(ppy)_2(CH_3CN)_2]PF_6$ in CH_3CN (λ_{ex}= 355 nm). Measured by Dr. Noufal Kandoth.

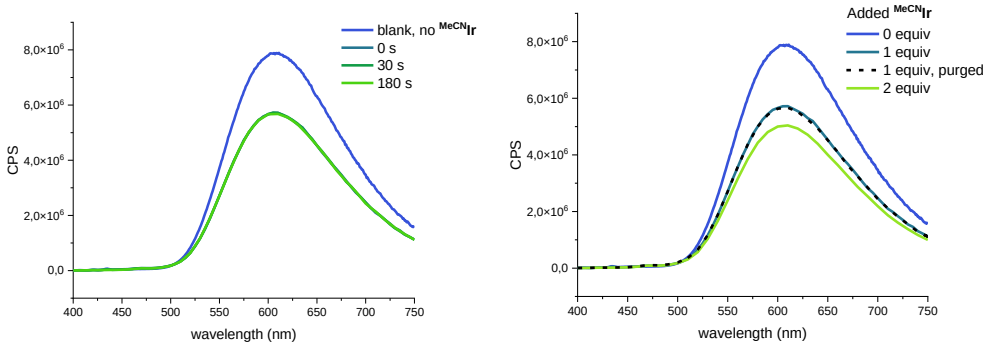

Figure 5. 72. (top) Emission spectra of $\mathbf{PC_{Ir}}^+$ (25 uM) in the presence of $[Ir(ppy)_2(CH_3CN)_2]PF_6$ (25 uM) in CH_3CN (λex= 385 nm). (bottom) Emission spectra of $\mathbf{PC_{Ir}}^+$ (25 uM) confirming that $\mathbf{PC_{Ir}}^{+*}$ undergoes some interaction with $[Ir(ppy)_2(CH_3CN)_2]PF_6$.

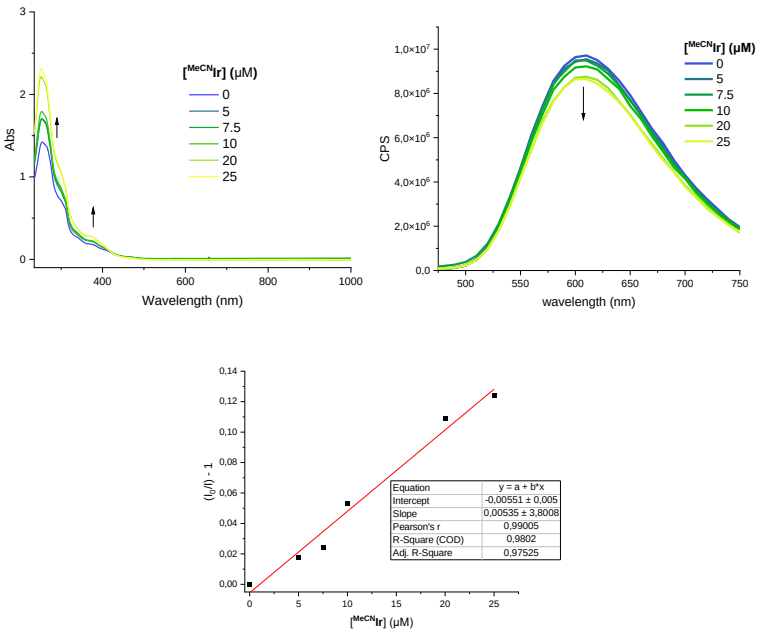

Figure 5. 73. (Left) Absorption spectra of HCPIr (25 uM) modifying the concentration of MeCNIr in CH_3CN. (Right) Emission spectra of HPCIr (25 uM) modifying the concentration of MeCNIr in CH_3CN. In a next step, we wondered if there could be an observable interaction between the PC and the MeCNIr in substoichiometric amount, what was confirmed and supported by Stern-Volmer studies (R^2=0.98).

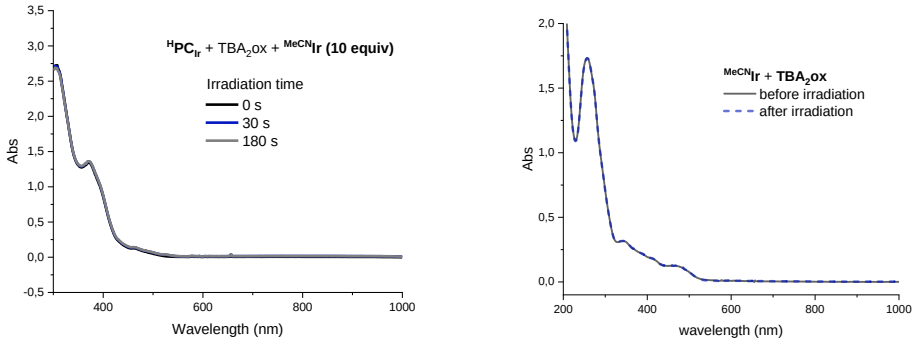

Figure 5. 74. (Top) Absorption spectra of a mixture of HCPIr (25 uM), TBA2ox (31.25 uM) and MeCNIr (250 uM) in CH_3CN under irradiation. (Bottom) Absorption spectra of MeCNIr (25 uM) in the presence of TBA2ox (62.5 uM) before and after 30 s of 447 nm LED irradiation.

5.4.13. Collection of spectroscopic studies with other iridium complexes

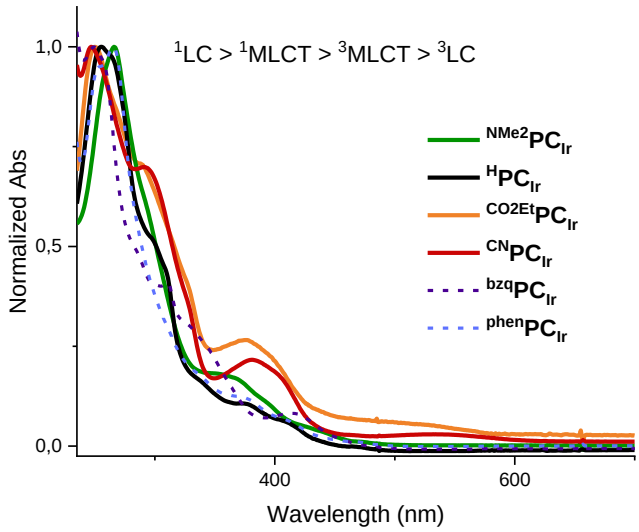

Figure 5. 75. Normalized absorbance of selected complexes in their charged form.

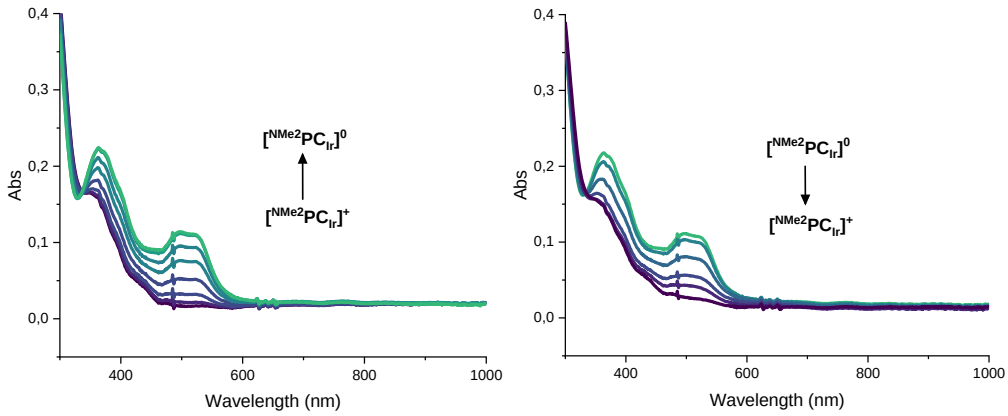

Figure 5. 76. SEC-UVvis spectra of NMe2PCIr (1 mM) at room temperature in the presence of TBAPF6 (0.2 M) in CH_3CN under N_2 atmosphere. The potential is tuned upon negative values (top) and then back to its original point (bottom).

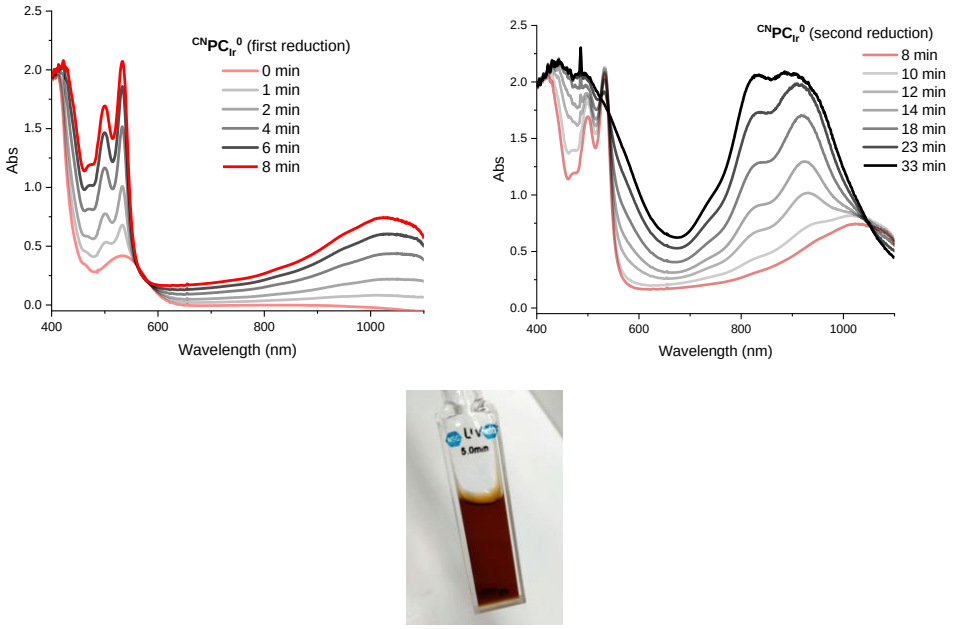

Figure 5. 77. Evolution of the absorption spectrum during the chemical reduction of $^{CN}PC_{Ir}{}^{+}$ (1 mM) to $^{CN}PC_{Ir}{}^{0}$ and presumably $^{CN}PC_{Ir}{}^{-}$ with Na/Hg (20 equiv) in CH_3CN in a 5 mm cuvette. Picture of the cuvette illustrates the color of the solution at the end of the experiment.

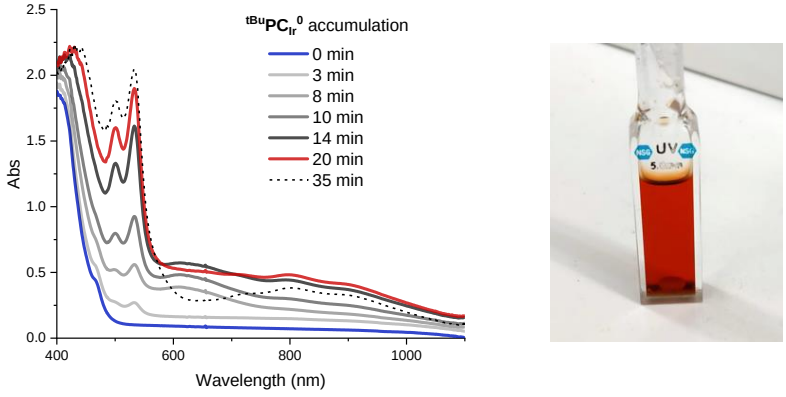

Figure 5. 78. Evolution of the absorption spectrum during the chemical reduction of $^{tBu}PC_{Ir}{}^{+}$ (1 mM) to $^{tBu}PC_{Ir}{}^{0}$ with Na/Hg (20 equiv) in CH_3CN in a 5 mm cuvette. Picture of the cuvette illustrates the color of the solution at the end of the experiment.

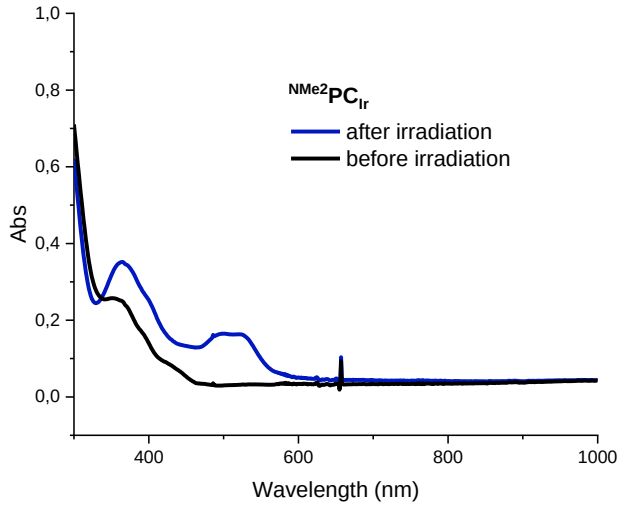

Figure 5. 79. Absorption spectra of NMe2PCIr (25µM) before (black trace) and after (blue trace) 30 s of irradiation with a 447 nm LED in the presence of TBA2ox (125µM) in degassed CH_3CN.

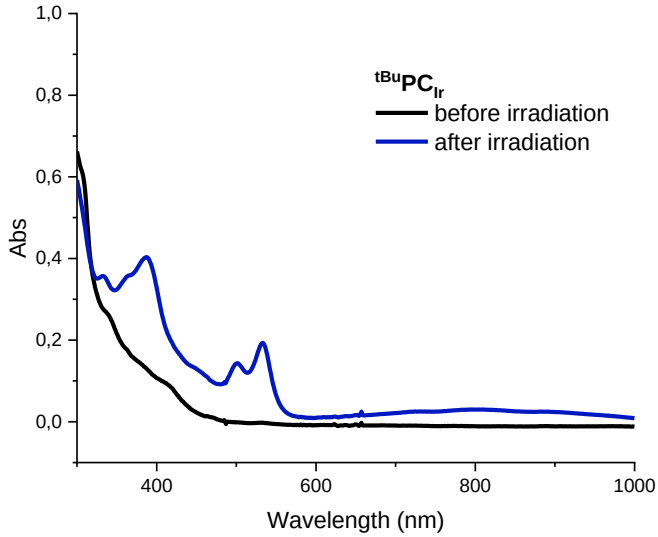

Figure 5. 80. Absorption spectra of tBuPCIr (25µM) before (black trace) and after (blue trace) 30 s of irradiation with a 447 nm LED in the presence of TBA2ox (125µM) in degassed CH_3CN.

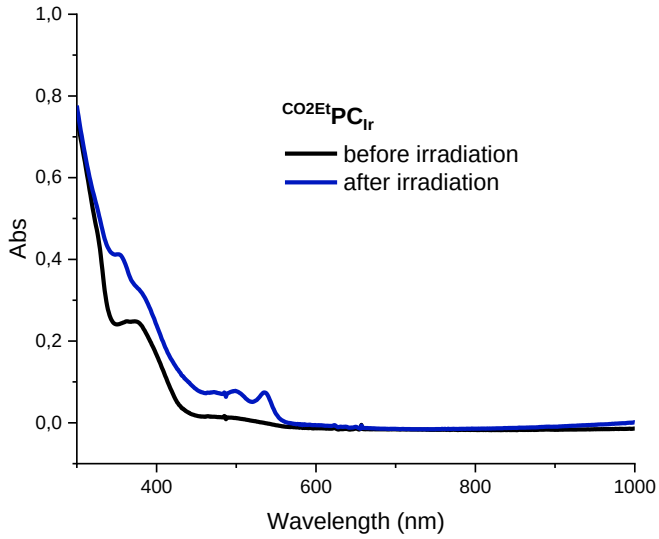

Figure 5. 81. Absorption spectra of CO2EtPCIr (25μM) before (black trace) and after (blue trace) 30 s of irradiation with a 447 nm LED in the presence of TBA2ox (125μM) in degassed CH_3CN.

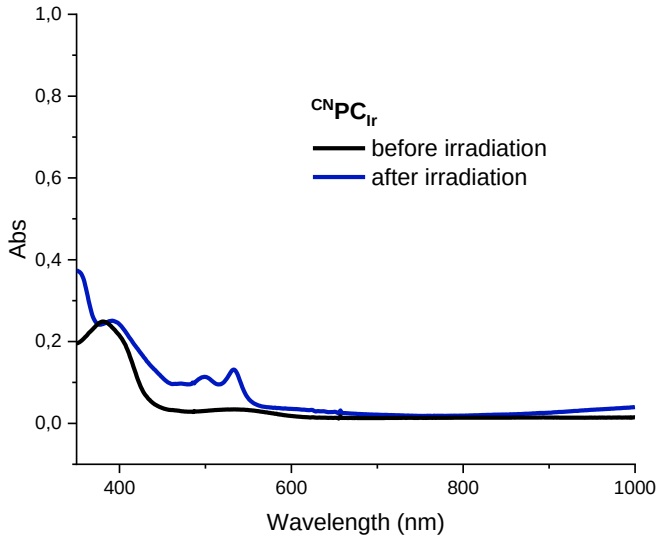

Figure 5. 82. Absorption spectra of CNPCIr (25μM) before (black trace) and after (blue trace) 30 s of irradiation with a 447 nm LED in the presence of TBA2ox (125μM) in degassed CH_3CN.

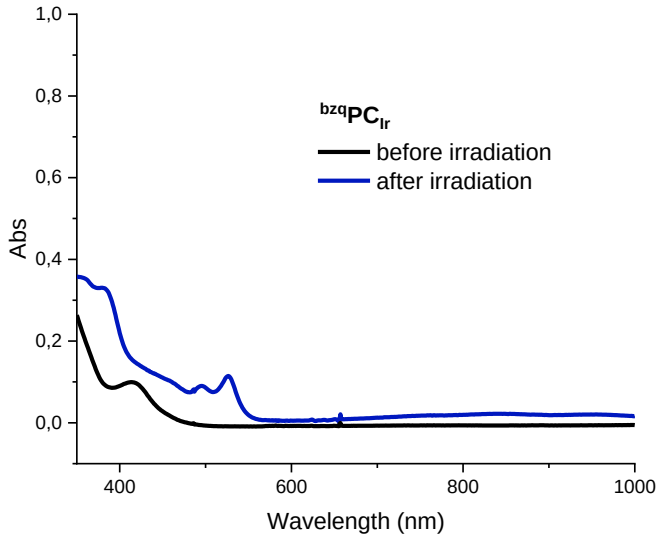

Figure 5. 83. Absorption spectra of bzqPCIr (25µM) before (black trace) and after (blue trace) 30 s of irradiation with a 447 nm LED in the presence of TBA2ox (125µM) in degassed CH_3CN.

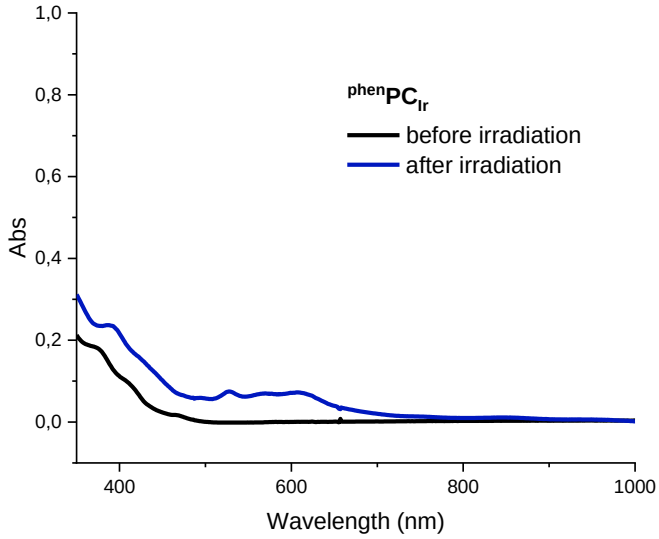

Figure 5. 84. Absorption spectra of phenPCIr (25µM) before (black trace) and after (blue trace) 30 s of irradiation with a 447 nm LED in the presence of TBA2ox (125µM) in degassed CH_3CN.

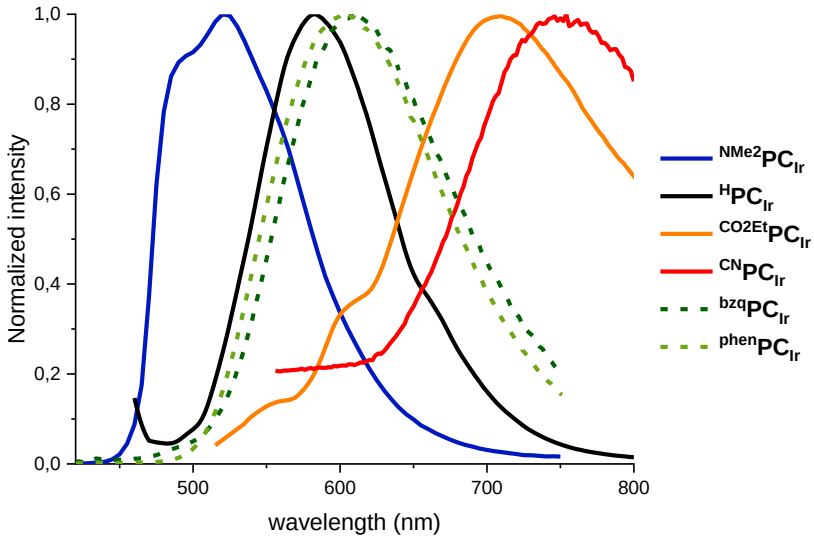

Figure 5. 85. Normalized emission spectra of selected complexes in CH3CN.

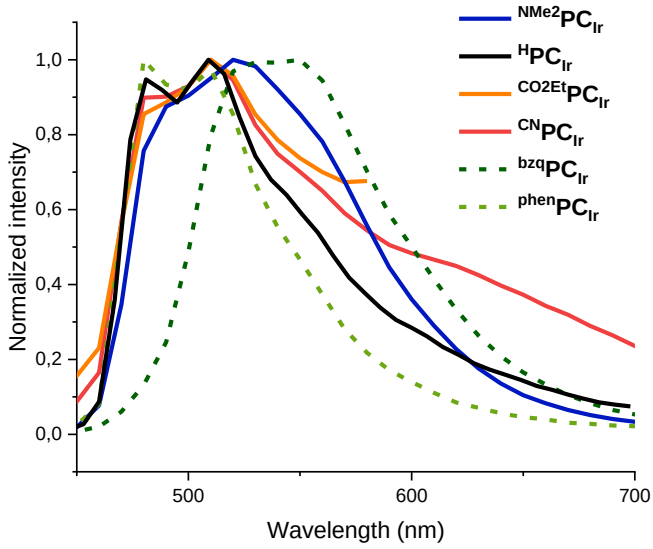

Figure 5. 86. Normalized emission of the new signals obtained from different complexes (25μM) after enough irradiation time (up to 300 s) in the presence of Et3N (50 mM) in degassed CH_3CN.

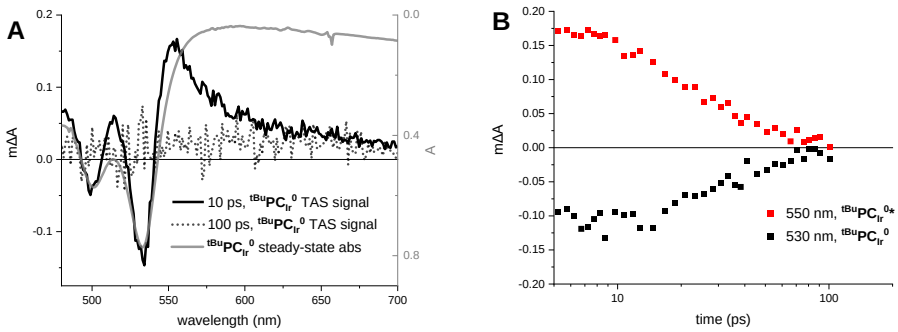

Figure 5. 87. **(A)** Transient spectra (black trace) of $^{tBu}PC_{Ir}^{0}$ after 10 (solid line) and 100 ps (dotted trace) of photoexcitation, overlapped with the negative steady-state absorption of $^{tBu}PC_{Ir}^{0}$ for comparison (grey) **(B)** Kinetics at 530 and 550 nm of $^{tBu}PC_{Ir}^{0}$ in CH_3CN. Measurement conditions: $^{tBu}PC_{Ir}^{0}$ was generated from $^{tBu}PC_{Ir}^{+}$ 100 μM in CH_3CN in the presence of TBA_2ox 1 mM after 10 s of irradiation (5-100 ps).

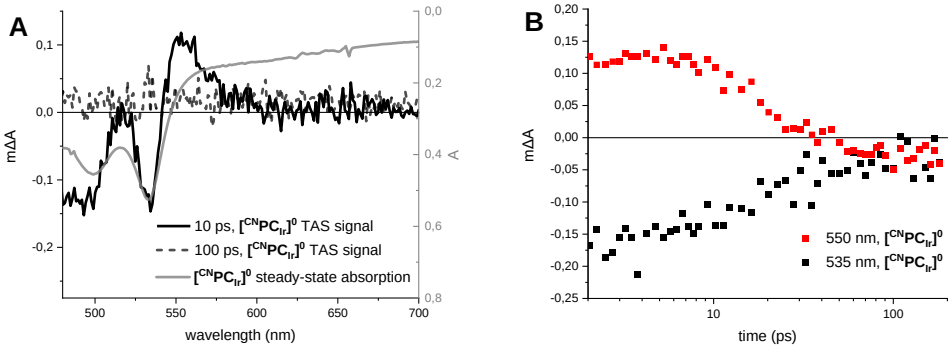

Figure 5. 88. **(A)** Transient spectra (*black* trace) of $[^{CN}PC_{Ir}]^{0}$ after 10 (solid line) and 100 ps (dotted trace) of photoexcitation, overlapped with the negative steady-state absorption of $[^{CN}PC_{Ir}]^{0}$ for comparison (*grey*). **(B)** Kinetics at 535 and 550nm of $[^{CN}PC_{Ir}]^{0}$ in ACN. Measurement conditions: $[^{CN}PC_{Ir}]^{0}$ was generated from $^{CN}PC_{Ir}$ 100 μM in ACN in the presence of TBA_2ox 1 mM after 10 s of irradiation (2-200 ps).

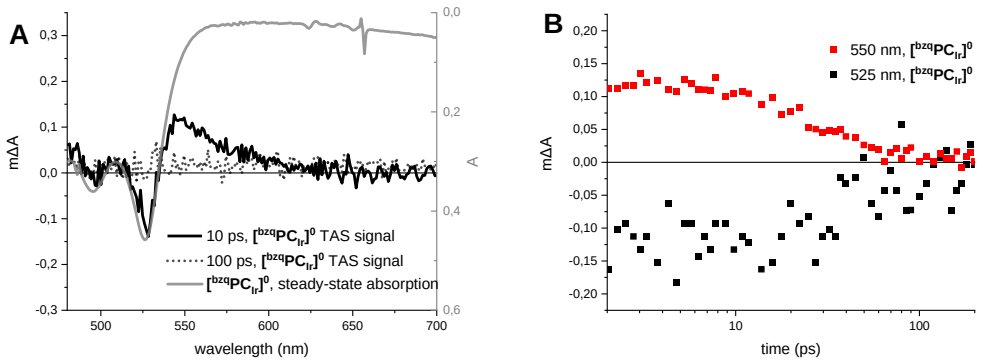

Figure 5. 89. **(A)** Transient spectra (*black* trace) of $[^{bzq}PC_{Ir}]^0$ after 10 ps of photoexcitation, overlapped with the negative steady-state absorption of $[^{bzq}PC_{Ir}]^0$ for comparison (*grey*). **(B)** Kinetics at 525 and 550 nm of $[^{bzq}PC_{Ir}]^0$ in ACN. Measurement conditions: $[^{bzq}PC_{Ir}]^0$ was generated from $^{bzq}PC_{Ir}$ 100 μM in ACN in the presence of TBA_2ox 1 mM after 10 s of irradiation (2-200 ps).

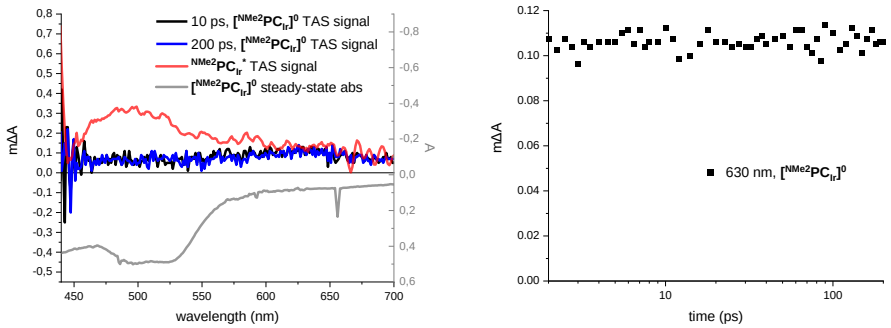

Figure 5. 90. **(A)** Transient spectra of $[^{NMe2}PC_{Ir}]^0$ after 10 ps (*black* trace) and 200 ps (*blue* trace) of photoexcitation, overlapped with its negative steady-state absorption (*grey*) and the excited state transient absorption measured in the absence of quencher (*red*, emission substracted) **(B)** Kinetics at 630 nm of $[^{NMe2}PC_{Ir}]^0$ in ACN. Measurement conditions: $[^{NMe2}PC_{Ir}]^0$ was generated from $^{NMe2}PC_{Ir}$ 100 μM in ACN in the presence of TBA_2ox 1 mM after 10 s of irradiation (2-200 ps).

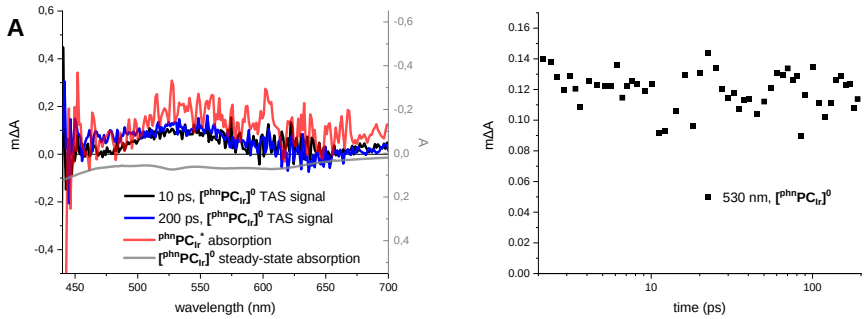

Figure 5. 91. **(A)** Transient spectra of **[^{phn}PC$_{Ir}$]^{0}** after 10 ps (*black* trace) and 200 ps (*blue* trace) of photoexcitation, overlapped with its steady-state absorption (*grey*) and the excited state transient absorption measured in the absence of quencher (*red*, emission substracted) **(B)** Kinetics at 530 nm of **[^{phn}PC$_{Ir}$]^{0}** in ACN. Measurement conditions: **[^{phn}PC$_{Ir}$]^{0}** was generated from **^{phn}PC$_{Ir}$** 100 μM in ACN in the presence of TBA_2ox 1 mM after 10 s of irradiation (2-200 ps).

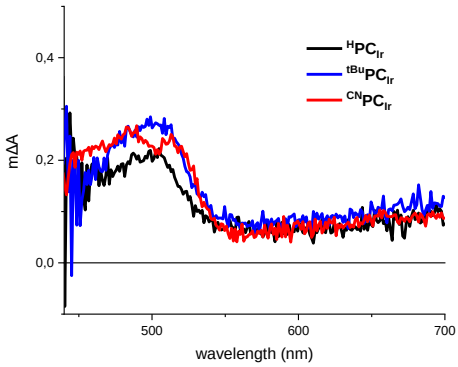

Figure 5. 92. Transient spectra of **^{H}PC$_{Ir}$** (black), **^{tBu}PC$_{Ir}$** (blue), and **^{CN}PC$_{Ir}$** (red) in pure CH_3CN after 10 ps of photoexcitation.

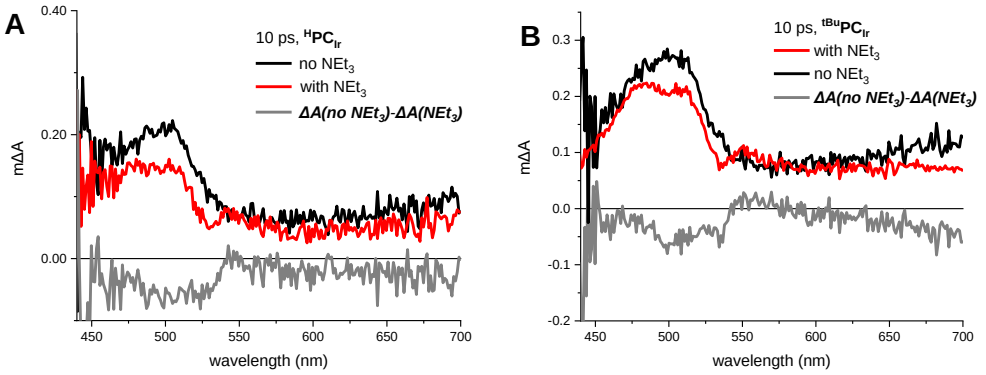

Figure 5. 93. **(A)** Transient spectra of **^{H}PC$_{Ir}$** after 10 ps of photoexcitation, in the presence (*red* trace) and absence (*black*) of triethylamine, and the difference between transient absorption with and without NEt_3 (*grey*) **(B)** Transient spectra of **^{tBu}PC$_{Ir}$** after 10 ps of photoexcitation, in the presence (*red* trace) and absence (*black*) of triethylamine, and the difference between transient absorption with and without NEt_3 (*grey*) Measurement conditions: **PC$_{Ir}$** 100 μM in ACN in the presence or absence of NEt_3 15 mM.

5.4.14. Further reactivity studies about $CoCp^*_2$

Table 5. 12. Effect of the concentration, light and wavelength on the photoactivity of $CoCp^*_2$.

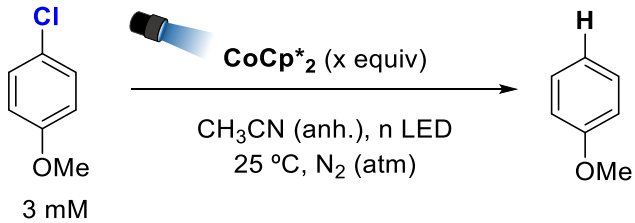

Entry	Changes	Conv (%)	Yield (%)
1	3 mM **$CoCp^*_2$**	38	12
2	6 mM **$CoCp^*_2$**	84	34
3	9.9 mM **$CoCp^*_2$** filterred	96	44

4	0.1 LED	38	19
10	16 LED	100	40
6	530	10	8
7	590	0	0
8	660	0	0
9	850	0	0

[a]Standard reaction conditions: **$CoCp^*_2$** (different concentrations), Subs. (3 mM) in anhydrous CH_3CN (1 mL) irradiated (447 nm) for 24 hour at 25 °C under N_2. Yields after workup (average of duplicates) determined by GC analysis relative to calibrated internal standard.

Table 5. 13. Photoreactions using species structurally comparable with $CoCp^*_2$.

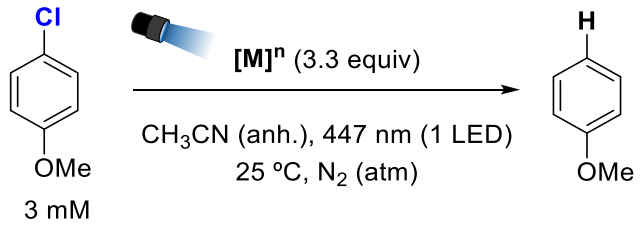

Entry	Changes	Conv (%)	Yield (%)
1	$CoCp^*_2{}^+$	4	0
2	Cc^0	6	5
3	Fc^0	0	0
4	LiCp* (6.6 equiv)	0	0
5	LiCp* (6.6 equiv) + $Co(OTf)_2(CH_3CN)_2$ (3.3 equiv)	0	0

[a]Standard reaction conditions: metallocene (3.3 equiv), Subs. (3 mM) in anhydrous CH_3CN (1 mL) irradiated (447 nm) for 1 hour at 25 °C under N_2. Yields after workup (average of duplicates) determined by GC analysis relative to calibrated internal standard.

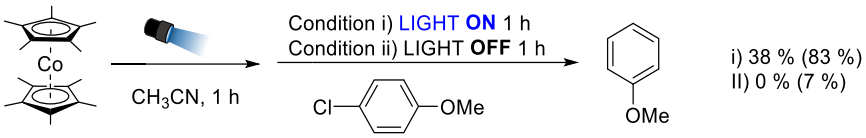

Scheme 5. 13. Stepwise reaction.

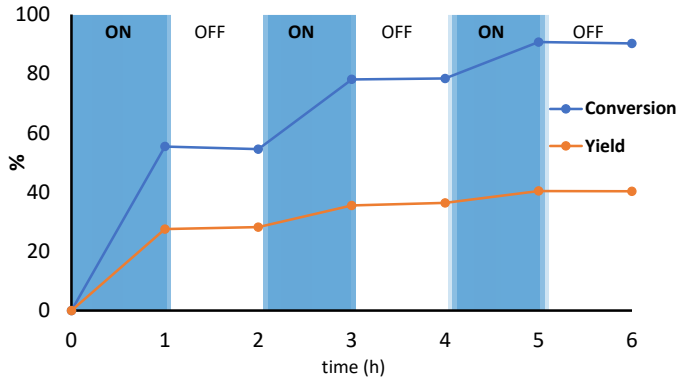

Figure 5. 94. ON-OFF cycles for the reaction of chloroanisole with $CoCp^*_2$ under standard conditions. Blue areas indicate irradiation cycles and white areas indicate non-irradiation periods.

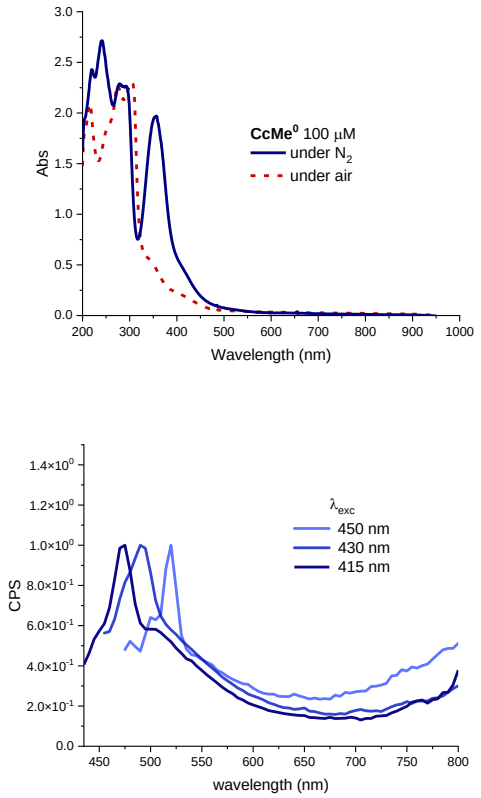

Figure 5. 95. Absorption and luminescence measurements of $CoCp^*_2$. The peak in the emission spectra corresponds with a Raman band from the solvent.

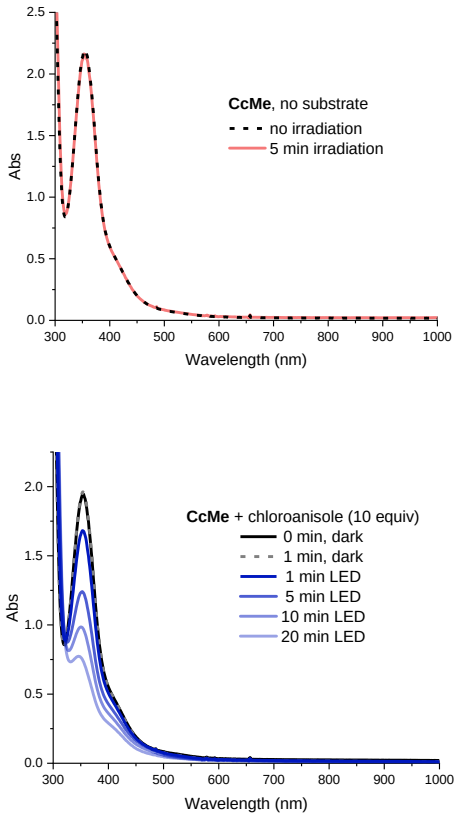

Figure 5. 96. Absorption and luminescence measurements of $CoCp^*_2$. The peak in the emission spectra corresponds with a Raman band from the solvent.

Table 5. 14. Photoreactions with $CoCp^*_2$ under non inert atmosphere.

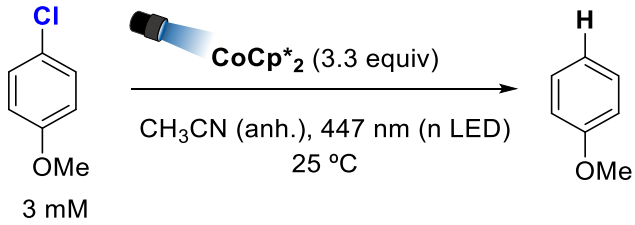

Entry	Changes	Conv (%)	Yield (%)
1	Under CO_2	5	5

2	Under O_2	4	0

[a]Standard reaction conditions: **CcMe** (3.3 equiv), Subs. (3 mM) in anhydrous CH_3CN (1 mL) irradiated (447 nm) for 1 hour at 25 °C under N_2. Yields after workup (average of duplicates) determined by GC analysis relative to calibrated internal standard.

Table 5. 15. Exploration of the reactivity with $CoCp^*_2$ in front of different substrates.

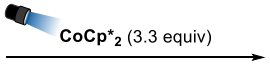

Substrate	Product	Yield (%)
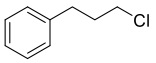	none	0
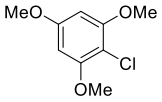	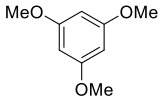	87* (rough estimation, almost full conversion)
		39
		27
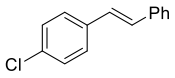	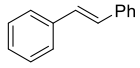	traces (green light)
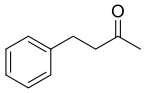	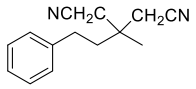	to be estimated by NMR
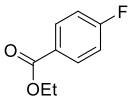	not observed (could it decarboxylate?)	0 (full conversion)
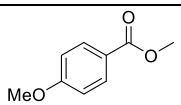	not observed (could it decarboxylate + sth else?)	0 (full conversion)
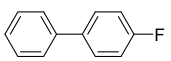	none* (cannot be discarded that signals were not separable)	0

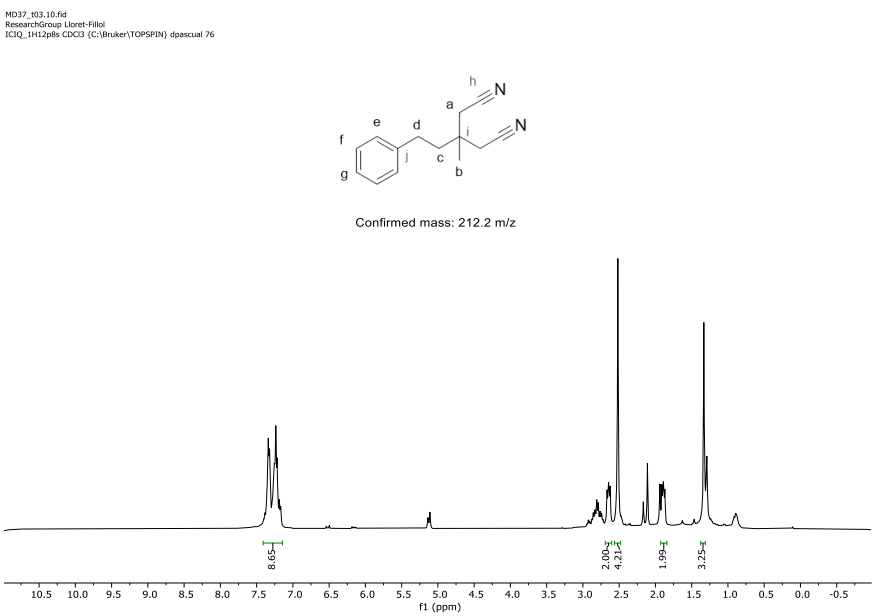

Figure 5. 97. ^{1}H-NMR spectra in $CDCl_3$ of the cleanest fraction isolated from the reaction between **CoCp*$_2$** and 4-phenylbutan-2-one.

5.4.15. DFT calculations details

DFT calculations have been performed with the Gaussian09 software package[ref: Gaussian 09, Revision E.01, Frisch et. al. Gaussian, Inc., Wallingford CT, 2009]. Geometry optimizations and frequency calculations at the ground state structure have been performed at the uB3LYP/def2SVP level of theory. Solvent effects and London interactions are considered through the SMD[94] model for CH_3CN and Grimme-D3 correction[95], respectively.

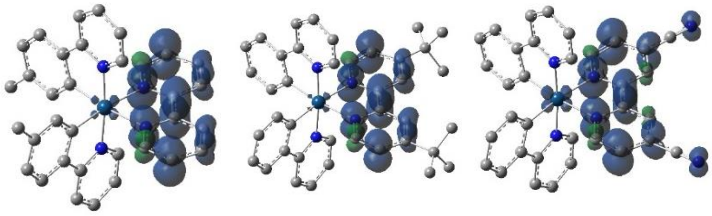

Figure 5. 98. Calculated spin density for (left) **^{Me}PC$_{Ir}^{0}$** (middle), **^{tBu}PC$_{Ir}^{0}$** and (right) **^{CN}PC$_{Ir}^{0}$** calculated at the uB3LYP/def2SVP level of theory. Unrelevant hydrogen atoms are omitted for clarity and an isosurface value of 0.0025 is chosen for representation. The additional unpaired

electron is clearly delocalized over the bipyridine ligand as expected according to similar reported complexes.[18]

5.5. References

1. Kandoth, N.; Pérez Hernández, J.; Palomares, E.; Lloret-Fillol, J., Mechanisms of photoredox catalysts: the role of optical spectroscopy. *Sustainable Energy & Fuels* **2021,** *5* (3), 638-665.
2. Shon, J.-H.; Kim, D.; Rathnayake, M. D.; Sittel, S.; Weaver, J.; Teets, T. S., Photoredox catalysis on unactivated substrates with strongly reducing iridium photosensitizers. *Chemical Science* **2021,** *12* (11), 4069-4078.
3. Monos, T. M.; Stephenson, C. R. J., Photoredox Catalysis of Iridium(III)-Based Photosensitizers. In *Iridium(III) in Optoelectronic and Photonics Applications*, 2017; pp 541-581.
4. Annibaletto, J.; Jacob, C.; Theunissen, C., Ammonium Salts as Convenient Radical Precursors Using Iridium Photoredox Catalysis. *Organic Letters* **2022,** *24* (23), 4170-4175.
5. Connell, T. U.; Fraser, C. L.; Czyz, M. L.; Smith, Z. M.; Hayne, D. J.; Doeven, E. H.; Agugiaro, J.; Wilson, D. J. D.; Adcock, J. L.; Scully, A. D.; Gómez, D. E.; Barnett, N. W.; Polyzos, A.; Francis, P. S., The Tandem Photoredox Catalysis Mechanism of [Ir(ppy)2(dtb-bpy)]+ Enabling Access to Energy Demanding Organic Substrates. *Journal of the American Chemical Society* **2019,** *141* (44), 17646-17658.
6. Bawden, J. C.; Francis, P. S.; DiLuzio, S.; Hayne, D. J.; Doeven, E. H.; Truong, J.; Alexander, R.; Henderson, L. C.; Gómez, D. E.; Massi, M.; Armstrong, B. I.; Draper, F. A.; Bernhard, S.; Connell, T. U., Reinterpreting the Fate of Iridium(III) Photocatalysts─Screening a Combinatorial Library to Explore Light-Driven Side-Reactions. *Journal of the American Chemical Society* **2022,** *144* (25), 11189-11202.
7. Giedyk, M.; Narobe, R.; Weiß, S.; Touraud, D.; Kunz, W.; König, B., Photocatalytic activation of alkyl chlorides by assembly-promoted single electron transfer in microheterogeneous solutions. *Nature Catalysis* **2020,** *3* (1), 40-47.
8. Kerzig, C.; Guo, X.; Wenger, O. S., Unexpected Hydrated Electron Source for Preparative Visible-Light Driven Photoredox Catalysis. *Journal of the American Chemical Society* **2019,** *141* (5), 2122-2127.
9. Buttersack, T.; Mason, P. E.; McMullen, R. S.; Schewe, H. C.; Martinek, T.; Brezina, K.; Crhan, M.; Gomez, A.; Hein, D.; Wartner, G.; Seidel, R.; Ali, H.; Thürmer, S.; Marsalek, O.; Winter, B.; Bradforth, S. E.; Jungwirth, P., Photoelectron spectra of alkali metal–ammonia microjets: From blue electrolyte to bronze metal. *Science* **2020,** *368* (6495), 1086-1091.
10. Chaban, V. V.; Prezhdo, O. V., Electron Solvation in Liquid Ammonia: Lithium, Sodium, Magnesium, and Calcium as Electron Sources. *The Journal of Physical Chemistry B* **2016,** *120* (9), 2500-2506.

11. Nishitani, J.; Yamamoto, Y.-i.; West, C. W.; Karashima, S.; Suzuki, T., Binding energy of solvated electrons and retrieval of true UV photoelectron spectra of liquids. *Science Advances 5* (8), eaaw6896.
12. Hara, A.; Yamamoto, Y.-i.; Suzuki, T., Solvated electron formation from the conduction band of liquid methanol: Transformation from a shallow to deep trap state. *The Journal of Chemical Physics* **2019,** *151* (11), 114503.
13. Kadhum, A. A. H.; Salmon, G. A., Reactivity of solvated electrons in tetrahydrofuran. *Journal of the Chemical Society, Faraday Transactions 1: Physical Chemistry in Condensed Phases* **1986,** *82* (8), 2521-2530.
14. Grills, D. C.; Lymar, S. V., Solvated Electron in Acetonitrile: Radiation Yield, Absorption Spectrum, and Equilibrium between Cavity- and Solvent-Localized States. *The Journal of Physical Chemistry B* **2022,** *126* (1), 262-269.
15. Call, A.; Lloret-Fillol, J., Enhancement and control of the selectivity in light-driven ketone versus water reduction using aminopyridine cobalt complexes. *Chemical Communications* **2018,** *54* (69), 9643-9646.
16. Casadevall, C.; Pascual, D.; Aragón, J.; Call, A.; Casitas, A.; Casademont-Reig, I.; Lloret-Fillol, J., Light-driven reduction of aromatic olefins in aqueous media catalysed by aminopyridine cobalt complexes. *Chemical Science* **2022,** *13* (15), 4270-4282.
17. Aragón, J.; Sun, S.; Pascual, D.; Jaworski, S.; Lloret-Fillol, J., Photoredox Activation of Inert Alkyl Chlorides for the Reductive Cross-Coupling with Aromatic Alkenes. *Angewandte Chemie International Edition* **2022,** *61* (21), e202114365.
18. Bokarev, S. I.; Hollmann, D.; Pazidis, A.; Neubauer, A.; Radnik, J.; Kühn, O.; Lochbrunner, S.; Junge, H.; Beller, M.; Brückner, A., Spin density distribution after electron transfer from triethylamine to an [Ir(ppy)2(bpy)]+ photosensitizer during photocatalytic water reduction. *Physical Chemistry Chemical Physics* **2014,** *16* (10), 4789-4796.
19. Noble, B. C.; Peacock, R. D., Spectroscopic studies on the bipyridinium anion. *Spectrochimica Acta Part A: Molecular Spectroscopy* **1990,** *46* (3), 407-412.
20. Connelly, N. G.; Geiger, W. E., Chemical Redox Agents for Organometallic Chemistry. *Chemical Reviews* **1996,** *96* (2), 877-910.
21. Balej, J., Standard potential of sodium amalgam at 25°C. *Electrochimica Acta* **1976,** *21* (11), 953-956.
22. Jespersen, D.; Keen, B.; Day, J. I.; Singh, A.; Briles, J.; Mullins, D.; Weaver, J. D., III, Solubility of Iridium and Ruthenium Organometallic Photoredox Catalysts. *Organic Process Research & Development* **2019,** *23* (5), 1087-1095.
23. Hwang, B.; Park, M.-S.; Kim, K., Ferrocene and Cobaltocene Derivatives for Non-Aqueous Redox Flow Batteries. *ChemSusChem* **2015,** *8* (2), 310-314.
24. Pellegrin, Y.; Odobel, F., Sacrificial electron donor reagents for solar fuel production. *Comptes Rendus Chimie* **2017,** *20* (3), 283-295.
25. Chmiel, A. F.; Williams, O. P.; Chernowsky, C. P.; Yeung, C. S.; Wickens, Z. K., Non-innocent Radical Ion Intermediates in Photoredox Catalysis: Parallel Reduction

Modes Enable Coupling of Diverse Aryl Chlorides. *Journal of the American Chemical Society* **2021,** *143* (29), 10882-10889.
26. Glaser, F.; Larsen, C. B.; Kerzig, C.; Wenger, O. S., Aryl dechlorination and defluorination with an organic super-photoreductant. *Photochemical & Photobiological Sciences* **2020,** *19* (8), 1035-1041.
27. Constantin, T.; Zanini, M.; Regni, A.; Sheikh, N. S.; Juliá, F.; Leonori, D., Aminoalkyl radicals as halogen-atom transfer agents for activation of alkyl and aryl halides. *Science* **2020,** *367* (6481), 1021-1026.
28. Aydogan, A.; Bangle, R. E.; De Kreijger, S.; Dickenson, J. C.; Singleton, M. L.; Cauët, E.; Cadranel, A.; Meyer, G. J.; Elias, B.; Sampaio, R. N.; Troian-Gautier, L., Mechanistic investigation of a visible light mediated dehalogenation/cyclisation reaction using iron(iii), iridium(iii) and ruthenium(ii) photosensitizers. *Catalysis Science & Technology* **2021,** *11* (24), 8037-8051.
29. You, Y.; Kanna, W.; Takano, H.; Hayashi, H.; Maeda, S.; Mita, T., Electrochemical Dearomative Dicarboxylation of Heterocycles with Highly Negative Reduction Potentials. *Journal of the American Chemical Society* **2022,** *144* (8), 3685-3695.
30. Kim, S.; Park, G.; Cho, E. J.; You, Y., Coreactant Strategy for the Photoredox Catalytic Generation of Trifluoromethyl Radicals under Low-Energy Photoirradiation. *The Journal of Organic Chemistry* **2016,** *81* (16), 7072-7079.
31. Paparo, A.; Okuda, J., Carbonite, the dianion of carbon dioxide and its metal complexes. *Journal of Organometallic Chemistry* **2018,** *869*, 270-274.
32. Call, A.; Casadevall, C.; Acuña-Parés, F.; Casitas, A.; Lloret-Fillol, J., Dual cobalt–copper light-driven catalytic reduction of aldehydes and aromatic ketones in aqueous media. *Chemical Science* **2017,** *8* (7), 4739-4749.
33. Call, A.; Codolà, Z.; Acuña-Parés, F.; Lloret-Fillol, J., Photo- and Electrocatalytic H2 Production by New First-Row Transition-Metal Complexes Based on an Aminopyridine Pentadentate Ligand. *Chemistry – A European Journal* **2014,** *20* (20), 6171-6183.
34. Gould, S. J.; Melville, C. R., NMR silent, naturally-occurring quinones: A case of radicals. *Tetrahedron Letters* **1997,** *38* (9), 1473-1476.
35. Bruch, Q. J.; Connor, G. P.; Chen, C.-H.; Holland, P. L.; Mayer, J. M.; Hasanayn, F.; Miller, A. J. M., Dinitrogen Reduction to Ammonium at Rhenium Utilizing Light and Proton-Coupled Electron Transfer. *Journal of the American Chemical Society* **2019,** *141* (51), 20198-20208.
36. Wang, M.; England, J.; Weyhermüller, T.; Wieghardt, K., Electronic Structures of “Low-Valent” Neutral Complexes [NiL2]0 (S = 0; L = bpy, phen, tpy) – An Experimental and DFT Computational Study. *European Journal of Inorganic Chemistry* **2015,** *2015* (9), 1511-1523.
37. Hollmann, D.; Gärtner, F.; Ludwig, R.; Barsch, E.; Junge, H.; Blug, M.; Hoch, S.; Beller, M.; Brückner, A., Insights into the Mechanism of Photocatalytic Water Reduction by DFT-Supported In Situ EPR/Raman Spectroscopy. *Angewandte Chemie International Edition* **2011,** *50* (43), 10246-10250.

38. Nosenko, V. V.; Vorona, I. P.; Baran, N. P.; Ishchenko, S. S.; Vysotskyi, B. V.; Krakhmalnaya, T. V.; Semenov, Y. A., Comparative EPR study CO2− radicals in modern and fossil tooth enamel. *Radiation Measurements* **2015,** *78*, 53-57.
39. Schramm, D. U.; Rossi, A. M., EPR and ENDOR studies on CO2− radicals in γ-irradiated B-type carbonated apatites. *Physical Chemistry Chemical Physics* **2000,** *2* (6), 1339-1343.
40. Prasad, D. R.; Hoffman, M. Z.; Mulazzani, Q. G.; Rodgers, M. A. J., Pulsed-laser flash and continuous photolysis of aqueous solutions of methylviologen, oxalate, and their ion-pair complexes. *Journal of the American Chemical Society* **1986,** *108* (17), 5135-5142.
41. Han, Y.-F.; Lin, Y.-J.; Jia, W.-G.; Weng, L.-H.; Jin, G.-X., Stepwise Formation of Tetra- and Hexanuclear Iridium and Rhodium Complexes Containing Oxalato Ligands. *Organometallics* **2007,** *26* (24), 5848-5853.
42. Fernández-Alvarez, F. J.; Iglesias, M.; Oro, L. A.; Polo, V., CO2 Activation and Catalysis Driven by Iridium Complexes. *ChemCatChem* **2013,** *5* (12), 3481-3494.
43. Vogt, M.; Nerush, A.; Diskin-Posner, Y.; Ben-David, Y.; Milstein, D., Reversible CO2 binding triggered by metal–ligand cooperation in a rhenium(i) PNP pincer-type complex and the reaction with dihydrogen. *Chemical Science* **2014,** *5* (5), 2043-2051.
44. List, B.; Leinung, W., Visible-Light Photoredox-Catalytic Coupling of Aryl Chlorides via Radical Anions. *Synfacts* **2021,** *17* (10), 1143.
45. Devery Iii, J. J.; Douglas, J. J.; Nguyen, J. D.; Cole, K. P.; Flowers Ii, R. A.; Stephenson, C. R. J., Ligand functionalization as a deactivation pathway in a fac-Ir(ppy)3-mediated radical addition. *Chemical Science* **2015,** *6* (1), 537-541.
46. Czyz, M. L.; Taylor, M. S.; Horngren, T. H.; Polyzos, A., Reductive Activation and Hydrofunctionalization of Olefins by Multiphoton Tandem Photoredox Catalysis. *ACS Catalysis* **2021,** *11* (9), 5472-5480.
47. Kim, H.; Kim, H.; Lambert, T. H.; Lin, S., Reductive Electrophotocatalysis: Merging Electricity and Light To Achieve Extreme Reduction Potentials. *Journal of the American Chemical Society* **2020,** *142* (5), 2087-2092.
48. Cowper, N. G. W.; Chernowsky, C. P.; Williams, O. P.; Wickens, Z. K., Potent Reductants via Electron-Primed Photoredox Catalysis: Unlocking Aryl Chlorides for Radical Coupling. *Journal of the American Chemical Society* **2020,** *142* (5), 2093-2099.
49. Xu, J.; Cao, J.; Wu, X.; Wang, H.; Yang, X.; Tang, X.; Toh, R. W.; Zhou, R.; Yeow, E. K. L.; Wu, J., Unveiling Extreme Photoreduction Potentials of Donor–Acceptor Cyanoarenes to Access Aryl Radicals from Aryl Chlorides. *Journal of the American Chemical Society* **2021,** *143* (33), 13266-13273.
50. Li, Y.; Ye, Z.; Lin, Y.-M.; Liu, Y.; Zhang, Y.; Gong, L., Organophotocatalytic selective deuterodehalogenation of aryl or alkyl chlorides. *Nature Communications* **2021,** *12* (1), 2894.
51. Ghosh, I., Excited radical anions and excited anions in visible light photoredox catalysis. **2019,** *4* (12).

52. Scordilis-Kelley, C.; Fuller, J.; Carlin, R. T.; Wilkes, J. S., Alkali Metal Reduction Potentials Measured in Chloroaluminate Ambient-Temperature Molten Salts. *Journal of The Electrochemical Society* **1992,** *139* (3), 694.
53. MacKenzie, I. A.; Wang, L.; Onuska, N. P. R.; Williams, O. F.; Begam, K.; Moran, A. M.; Dunietz, B. D.; Nicewicz, D. A., Discovery and characterization of an acridine radical photoreductant. *Nature* **2020,** *580* (7801), 76-80.
54. Rieth, A. J.; Gonzalez, M. I.; Kudisch, B.; Nava, M.; Nocera, D. G., How Radical Are "Radical" Photocatalysts? A Closed-Shell Meisenheimer Complex Is Identified as a Super-Reducing Photoreagent. *Journal of the American Chemical Society* **2021,** *143* (35), 14352-14359.
55. Jeong, D. Y.; Lee, D. S.; Lee, H. L.; Nah, S.; Lee, J. Y.; Cho, E. J.; You, Y., Evidence and Governing Factors of the Radical-Ion Photoredox Catalysis. *ACS Catalysis* **2022,** *12* (10), 6047-6059.
56. Beckwith, J. S.; Aster, A.; Vauthey, E., The excited-state dynamics of the radical anions of cyanoanthracenes. *Physical Chemistry Chemical Physics* **2022,** *24* (1), 568-577.
57. Cole, J. P.; Chen, D.-F.; Kudisch, M.; Pearson, R. M.; Lim, C.-H.; Miyake, G. M., Organocatalyzed Birch Reduction Driven by Visible Light. *Journal of the American Chemical Society* **2020,** *142* (31), 13573-13581.
58. Fujitsuka, M.; Majima, T., Reaction dynamics of excited radical ions revealed by femtosecond laser flash photolysis. *Journal of Photochemistry and Photobiology C: Photochemistry Reviews* **2018,** *35*, 25-37.
59. Haimerl, J.; Ghosh, I.; König, B.; Vogelsang, J.; Lupton, J. M., Single-molecule photoredox catalysis. *Chemical Science* **2019,** *10* (3), 681-687.
60. Tasnim, T.; Ryan, C.; Christensen, M. L.; Fennell, C. J.; Pitre, S. P., Radical Perfluoroalkylation Enabled by a Catalytically Generated Halogen Bonding Complex and Visible Light Irradiation. *Organic Letters* **2022,** *24* (1), 446-450.
61. Liang, X.; Li, Y.; Xia, Q.; Cheng, L.; Guo, J.; Zhang, P.; Zhang, W.; Wang, Q., Visible-light-driven electron donor–acceptor complex induced sulfonylation of diazonium salts with sulfinates. *Green Chemistry* **2021,** *23* (22), 8865-8870.
62. Zhou, Q.; Sun, C. G.; Liu, X.; Li, X.; Shao, Z.; Tan, K.; Shen, Y., Electron donor–acceptor complex-catalyzed photoredox reactions mediated by DIPEA and inorganic carbonates. *Organic Chemistry Frontiers* **2022,** *9* (19), 5264-5271.
63. de Pedro Beato, E.; Spinnato, D.; Zhou, W.; Melchiorre, P., A General Organocatalytic System for Electron Donor–Acceptor Complex Photoactivation and Its Use in Radical Processes. *Journal of the American Chemical Society* **2021,** *143* (31), 12304-12314.
64. Goez, M.; Zubarev, V., Light intensity dependence of a two-photon catalytic cycle: photoionization via absorption–electron transfer–absorption. *Chemical Physics* **2000,** *256* (1), 107-116.
65. Naumann, R.; Goez, M., First Micelle-Free Photoredox Catalytic Access to Hydrated Electrons for Syntheses and Remediations with a Visible LED or even Sunlight. *Chemistry – A European Journal* **2018,** *24* (66), 17557-17567.

66. Goez, M.; Kerzig, C.; Naumann, R., An “All-Green” Catalytic Cycle of Aqueous Photoionization. *Angewandte Chemie International Edition* **2014,** *53* (37), 9914-9916.
67. Singh, A.; Gesser, H. D.; Scott, A. R., Solvated electron in acetonitrile. *Chemical Physics Letters* **1968,** *2* (5), 271-273.
68. Svejda, P.; Volman, D. H., Photochemical formation of free radicals from acetonitrile as studied by electron spin resonance. *The Journal of Physical Chemistry* **1970,** *74* (9), 1872-1875.
69. Bonin, M. A.; Tsuji, K.; Williams, F., Electron Spin Resonance Evidence for a Trapped Electron and its Reversible Reaction in Gamma-irradiated Acetonitrile-d3. *Nature* **1968,** *218* (5145), 946-948.
70. Braslavsky, S. E., Glossary of terms used in photochemistry, 3rd edition (IUPAC Recommendations 2006). **2007,** *79* (3), 293-465.
71. Demchenko, A. P.; Tomin, V. I.; Chou, P.-T., Breaking the Kasha Rule for More Efficient Photochemistry. *Chemical Reviews* **2017,** *117* (21), 13353-13381.
72. Tinker, L. L.; McDaniel, N. D.; Curtin, P. N.; Smith, C. K.; Ireland, M. J.; Bernhard, S., Visible Light Induced Catalytic Water Reduction without an Electron Relay. *Chemistry – A European Journal* **2007,** *13* (31), 8726-8732.
73. Silva Valverde, M. F.; Schweyen, P.; Gisinger, D.; Bannenberg, T.; Freytag, M.; Kleeberg, C.; Tamm, M., N-Heterocyclic Carbene Stabilized Boryl Radicals. *Angewandte Chemie International Edition* **2017,** *56* (4), 1135-1140.
74. Arashiba, K.; Eizawa, A.; Tanaka, H.; Nakajima, K.; Yoshizawa, K.; Nishibayashi, Y., Catalytic Nitrogen Fixation via Direct Cleavage of Nitrogen–Nitrogen Triple Bond of Molecular Dinitrogen under Ambient Reaction Conditions. *Bulletin of the Chemical Society of Japan* **2017,** *90* (10), 1111-1118.
75. Nakazato, T.; Takekoshi, H.; Sakurai, T.; Shinokubo, H.; Miyake, Y., Synthesis and Characterization of 16π Antiaromatic 2,7-Dihydrodiazapyrenes: Antiaromatic Polycyclic Hydrocarbons with Embedded Nitrogen. *Angewandte Chemie International Edition* **2021,** *60* (25), 13877-13881.
76. Thander, A.; Basak, D.; Mallik, B., Spectroscopic studies on the photoeffects on some metallocenes in the presence of chloroform molecules confined in poly(methyl methacrylate) thin films. *Spectrochimica Acta Part A: Molecular and Biomolecular Spectroscopy* **2004,** *60* (10), 2393-2398.
77. Chernowsky, C. P.; Chmiel, A. F.; Wickens, Z. K., Electrochemical Activation of Diverse Conventional Photoredox Catalysts Induces Potent Photoreductant Activity**. *Angewandte Chemie International Edition* **2021,** *60* (39), 21418-21425.
78. Monos, T. M.; Sun, A. C.; McAtee, R. C.; Devery, J. J.; Stephenson, C. R. J., Microwave-Assisted Synthesis of Heteroleptic Ir(III)+ Polypyridyl Complexes. *The Journal of Organic Chemistry* **2016,** *81* (16), 6988-6994.
79. Lepeltier, M.; Graff, B.; Lalevée, J.; Wantz, G.; Ibrahim-Ouali, M.; Gigmes, D.; Dumur, F., Heteroleptic iridium (III) complexes with three different ligands: Unusual triplet emitters for light-emitting electrochemical cells. *Organic Electronics* **2016,** *37*, 24-34.

80. Beattie, J. W.; White, D. S.; Bheemaraju, A.; Martin, P. D.; Groysman, S., Recyclable chemosensor for oxalate based on bimetallic complexes of a dinucleating bis(iminopyridine) ligand. *Dalton Transactions* **2014,** *43* (21), 7979-7986.
81. Zhou, Y.; Jia, J.; Wang, X.; Guo, W.; Wu, Z.; Xu, N., Protein Staining Agents from Cationic and Neutral Luminescent Iridium(III) Complexes. *Chemistry – A European Journal* **2016,** *22* (47), 16796-16800.
82. Horiuchi, S.; Tanaka, H.; Sakuda, E.; Arikawa, Y.; Umakoshi, K., Encapsulation and Enhanced Luminescence Properties of IrIII Complexes within a Hexameric Self-Assembled Capsule. *Chemistry – A European Journal* **2016,** *22* (49), 17533-17537.
83. Ravel, B.; Newville, M., ATHENA, ARTEMIS, HEPHAESTUS: data analysis for X-ray absorption spectroscopy using IFEFFIT. *Journal of Synchrotron Radiation* **2005,** *12*, 537-541.
84. Bjornsson, R.; Delgado-Jaime, M. U.; Lima, F. A.; Sippel, D.; Schlesier, J.; Weyhermüller, T.; Einsle, O.; Neese, F.; DeBeer, S., Molybdenum L-Edge XAS Spectra of MoFe Nitrogenase. *Z. Anorg. Allg. Chem.* **2015,** *641* (1), 65-71.
85. Van Kuiken, B. E.; Valiev, M.; Daifuku, S. L.; Bannan, C.; Strader, M. L.; Cho, H.; Huse, N.; Schoenlein, R. W.; Govind, N.; Khalil, M., Simulating Ru L3-Edge X-ray Absorption Spectroscopy with Time-Dependent Density Functional Theory: Model Complexes and Electron Localization in Mixed-Valence Metal Dimers. *J Phys Chem A* **2013,** *117* (21), 4444-4454.
86. Neese, F., The ORCA program system. *Wiley Interdiscip. Rev.: Comput. Mol. Sci.* **2012,** *2* (1), 73-78.
87. DeBeer George, S.; Petrenko, T.; Neese, F., Time-dependent density functional calculations of ligand K-edge X-ray absorption spectra. *Inorg. Chim. Acta* **2008,** *361* (4), 965-972.
88. DeBeer George, S.; Petrenko, T.; Neese, F., Prediction of Iron K-Edge Absorption Spectra Using Time-Dependent Density Functional Theory. *J Phys Chem A* **2008,** *112* (50), 12936-12943.
89. Schäfer, A.; Horn, H.; Ahlrichs, R., Fully optimized contracted Gaussian basis sets for atoms Li to Kr. *J Chem Phys* **1992,** *97* (4), 2571-2577.
90. Weigend, F.; Ahlrichs, R., Balanced basis sets of split valence, triple zeta valence and quadruple zeta valence quality for H to Rn: Design and assessment of accuracy. *Phys. Chem. Chem. Phys.* **2005,** *7* (18), 3297-3305.
91. van Wüllen, C., Molecular density functional calculations in the regular relativistic approximation: Method, application to coinage metal diatomics, hydrides, fluorides and chlorides, and comparison with first-order relativistic calculations. *J Chem Phys* **1998,** *109* (2), 392-399.
92. Pantazis, D. A.; Chen, X.-Y.; Landis, C. R.; Neese, F., All-Electron Scalar Relativistic Basis Sets for Third-Row Transition Metal Atoms. *J. Chem. Theor. Comp.* **2008,** *4* (6), 908-919.
93. Li, J.; Chen, W.-C.; Liu, H.; Chen, Z.; Chai, D.; Lee, C.-S.; Yang, C., Double-twist pyridine–carbonitrile derivatives yielding excellent thermally activated delayed

fluorescence emitters for high-performance OLEDs. *Journal of Materials Chemistry C* **2020,** *8* (2), 602-606.

94. Marenich, A. V.; Cramer, C. J.; Truhlar, D. G., Universal Solvation Model Based on Solute Electron Density and on a Continuum Model of the Solvent Defined by the Bulk Dielectric Constant and Atomic Surface Tensions. *The Journal of Physical Chemistry B* **2009,** *113* (18), 6378-6396.

95. Grimme, S.; Ehrlich, S.; Goerigk, L., Effect of the damping function in dispersion corrected density functional theory. *Journal of Computational Chemistry* **2011,** *32* (7), 1456-1465.

Chapter 6

General conclusions

UNIVERSITAT ROVIRA I VIRGILI
PHOTOREDOX CATALYSIS MEDIATED BY TRANSITION METAL COMPLEXES.
TOWARDS CHALLENGING ORGANIC REDUCTIONS
David Pascual Gascón

In *Chapter 3*, we established that $\mathbf{1_{Co}/PC_{Cu}}$ is an excellent dual combination of catalysts for olefin reduction, exhibiting excellent selectivity. The selected system expanded the methodology to prepare deuterated alkanes. Thus, the deuteration was consistent with an irreversible HAT step. Based on our mechanistic understanding, evaluation of other photosensitizers and conditions reached a dual Co/Ir system capable of selectively reducing acetophenone *versus* styrene and vice versa. This unique behaviour is rationalized by the different reduction mechanisms that each substrate undergoes.

In *Chapter 4*, we found that cobalt tetradentate complexes based on the chiral fragments *S*,*S*-bispyrrolidine and *S*,*S*-cyclohexanediamine can catalyze the ATH of aromatic ketones efficiently in the presence of $\mathbf{^{NMe2}PC_{Ir}}$ as the photocatalyst. However, when substituting the *ortho*-position of the pyridine of the chiral ligand, the reactivity of these complexes drops drastically. We associated this lack of reactivity with excessive steric hindrance. Our current data suggest bulky meta-position substitution positively affects chirality induction. Nonetheless, further studies are required. Lastly, both reactivity and enantioselectivity are highly dependent on the substrate.

In *Chapter V*, we have isolated and unambiguously determined the structure of $[Ir(bpy)(ppy)_2]^0$ ($\mathbf{PC_{Ir}^0}$), which corresponds with the first crystalline structure of a catalytic intermediate obtained *via* reductive quenching (to the best of our knowledge). In our spectroscopic characterization of this species, we observed the excitation of the reduced intermediate of an iridium PC for the first time, which had previously been only proposed as a mechanistic hypothesis. However, the isolated intermediate under irradiation could reduce aryl chlorides (up to -2.9 V *vs* SCE), which becomes catalytic under electrophotochemical conditions. Furthermore, TD-DFT calculations and experimental results demonstrated that the reductive reactivity came from the $\mathbf{bpy^{\bullet -}}$ ligand.

As a general conclusion, these results show that the selectivity of metal hydrides in basic media can be controlled and directed to reduce organic functionalities. For this reason, we envision that other readily available H_2O reduction catalysts could also perform selective organic reductions using visible light as the driving force and H_2O as

a clean source of hydrides. We also expect that the herein disclosed reductive reactivity of $\mathbf{PC_{Ir}^0}$ and $\mathbf{bpy^{\bullet -}}$ will be extended to other bipyridine-based molecules for further transformations. These studies can help to shed light on the mechanistic ambiguity around multiphoton mechanisms.

UNIVERSITAT ROVIRA I VIRGILI
PHOTOREDOX CATALYSIS MEDIATED BY TRANSITION METAL COMPLEXES.
TOWARDS CHALLENGING ORGANIC REDUCTIONS
David Pascual Gascón

UNIVERSITAT ROVIRA I VIRGILI
PHOTOREDOX CATALYSIS MEDIATED BY TRANSITION METAL COMPLEXES.
TOWARDS CHALLENGING ORGANIC REDUCTIONS
David Pascual Gascón

UNIVERSITAT ROVIRA I VIRGILI
PHOTOREDOX CATALYSIS MEDIATED BY TRANSITION METAL COMPLEXES.
TOWARDS CHALLENGING ORGANIC REDUCTIONS
David Pascual Gascón

UNIVERSITAT ROVIRA I VIRGILI
PHOTOREDOX CATALYSIS MEDIATED BY TRANSITION METAL COMPLEXES.
TOWARDS CHALLENGING ORGANIC REDUCTIONS
David Pascual Gascón

UNIVERSITAT
ROVIRA i VIRGILI